Characterization of Toll-Like Receptor 8 and Its Modulation through Novel Small-Molecule Antagonists

Dissertation

zur

Erlangung des Doktorgrades (Dr. rer. nat.)

der

Mathematisch-Naturwissenschaftlichen Fakultät

der

Rheinischen Friedrich-Wilhelms-Universität Bonn

vorgelegt von

Troy Matziol

aus

Frechen

Bonn 2026

Angefertigt mit Genehmigung der Mathematisch-Naturwissenschaftlichen Fakultät der
Rheinischen Friedrich-Wilhelms-Universität Bonn

Gutachter/Betreuer: Prof. Dr. Günther Weindl

Gutachter: Prof. Dr. Gerhard Wolber

Tag der Promotion: 04.05.2026

Erscheinungsjahr: 2026

Die vorliegende Arbeit wurde in der Zeit von Februar 2022 bis Juli 2025 unter Leitung von Herrn Prof. Dr. Günther Weindl am Pharmazeutischen Institut der Rheinischen Friedrich-Wilhelms-Universität Bonn angefertigt.

Table of Contents

List of Abbreviations

AIM2	Absent in Melanoma 2
ALR	Absent in Melanoma 2 (AIM2)-like receptor
ASC	Apoptosis-associated speck-like protein containing a CARD
BMDMs	Bone Marrow-Derived Macrophages
CD	Cluster of Differentiation
cGAS	Cyclic GMP-AMP Synthase
CLR	C-type Lectin Receptor
CNS	Central Nervous System
Co-IP	Co-immunoprecipitation
Da	Dalton
DAMP	Damage-Associated Molecular Pattern
DC	Dendritic Cell
DD	Death Domain
DMR	Dynamic Mass Redistribution
DNA	Deoxyribonucleic Acid
dsRNA	Double-Stranded RNA
ELISA	Enzyme-Linked Immunosorbent Assay
ER	Endoplasmic Reticulum
GOF	Gain-of-Function
GPCR	G Protein-Coupled Receptor
IFN	Interferon
IL	Interleukin

ILC	Innate Lymphoid Cells
IRAK	Interleukin-1 Receptor-Associated Kinase
IRF	Interferon Regulatory Factor
KO	(genetic) Knockout
LDH	Lactate Dehydrogenase
LGP2	Laboratory of Genetics and Physiology 2
LPS	Lipopolysaccharide
LRR	Leucine-Rich Repeat
MAPK	Mitogen-Activated Protein Kinase
MAVS	Mitochondrial Antiviral-Signaling Protein
MD	Molecular Dynamics
MDA5	Melanoma Differentiation-Associated Protein 5
MHC	Major Histocompatibility Complex
MyD88	Myeloid Differentiation Primary Response 88
NACHT	Neuronal Apoptosis Inhibitor Protein, CIITA, HET-E, TP1
NET	Neutrophil Extracellular Trap
NF-κB	Nuclear Factor Kappa-Light-Chain-Enhancer of Activated B Cells
NK Cells	Natural Killer Cells
NLR	NOD-Like Receptor
NLRP3	NLR Family Pyrin Domain Containing 3
NOD	Nucleotide-Binding Oligomerization Domain
PAMP	Pathogen-Associated Molecular Pattern
PBMCs	Peripheral Blood Mononuclear Cells
PRR	Pattern Recognition Receptor
RA	Rheumatoid Arthritis

RIG-I	Retinoic Acid Inducible Gene I
RLR	RIG-I-Like Receptor
RNA	Ribonucleic Acid
ROS	Reactive Oxygen Species
SAR	Structure–Activity Relationship
SLC15A4	Solute Carrier Family 15, member 4
SLE	Systemic Lupus Erythematosus
SMOC	Supramolecular Organizing Center
SOCS	Suppressor of Cytokine Signaling
ssRNA	Single-Stranded RNA
STING	Stimulator of Interferon Genes
TAK1	Transforming Growth Factor-β-Activated Kinase 1
TASL	TLR Adaptor interacting with SLC15A4 on the Lysosome
TBK1	TANK-Binding Kinase 1
TH Cell	T Helper Cell
TIR	Toll/IL-1 Receptor
TLR	Toll-Like Receptor
TNF	Tumor Necrosis Factor
TRAF6	TNF Receptor Associated Factor 6
τRAMD	τ-Random Acceleration Molecular Dynamics
TRIF	TIR-Domain-Containing Adapter-Inducing Interferon-β
UNC93B1	Unc-93 Homolog B1

List of Figures

List of Schemes

List of Tables

List of Appendices

1 Introduction

1.1 Preface

Autoimmune and inflammatory diseases affect hundreds of millions of people worldwide, presenting a growing global health challenge. As of now, approximately 5% of the world's population suffer of these conditions.[1] The disease spectrum contains more than 100 distinct conditions, including rheumatoid arthritis, multiple sclerosis, systemic lupus erythematosus, type 1 diabetes, and Crohn's disease, collectively demonstrating one of the highest non-communicable disease burdens worldwide.[2,3] The prevalence of autoimmune diseases has been increasing steadily by 3–5% annually, making the identification of underlying pathogenic mechanisms and the development of targeted therapeutic interventions an increasingly urgent priority.[4]

The innate immune system serves as the body's first line of defense, operating through a limited repertoire of germline-encoded receptors that detect molecular patterns associated with pathogens and cellular stress. Among these pattern recognition receptors (PRRs), Toll-like receptors (TLRs) play a central role in initiating immune responses by sensing pathogen- and damage-associated molecular patterns, thereby triggering inflammatory signaling cascades.[5] Human Toll-like receptor 8 (TLR8) has emerged as a critical endosomal receptor for its roles in host defense, vaccine efficacy, and immunotherapy, although many aspects of its function remain incompletely understood.[6] Dysregulated TLR8 signaling has been implicated in driving autoimmune syndromes and chronic inflammation, making its selective modulation a promising scientific and clinical strategy.[7]

Recent advances have elucidated mechanisms of ligand recognition and signaling of endosomal TLRs, with TLR8 now recognized as a pivotal yet still partly characterized regulator of antiviral and inflammatory responses.[8] A comprehensive investigation of TLR8 signaling, structure, and pharmacological modulation therefore provides novel insights into immune regulation and offer promising therapeutic opportunities for autoimmune and inflammatory diseases.

1.2 The Immune System

1.2.1 General Principles

The innate immune system is the host's first and most ancient line of defense, delivering a rapid, non-specific response to infectious pathogens and endogenous danger signals. This system is evolutionarily conserved and provides the critical signals that are required to activate and shape the more specialized adaptive immune response.[5] A core principle of innate immunity is its ability to recognize conserved molecular patterns rather than specific antigens.[9] These patterns are broadly categorized into two groups: pathogen-associated molecular patterns (PAMPs), which are unique to microorganisms (e.g., lipopolysaccharide (LPS), bacterial flagellin, viral RNA), and danger-associated molecular patterns (DAMPs), which are host-derived molecules released from damaged or stressed cells.[10,11] The ability of the immune system to distinguish between these danger signals and harmless self-molecules is fundamental for initiating an appropriate inflammatory response while maintaining tolerance.[12] Within minutes to hours, the innate immune system mobilizes a diverse repertoire of defense mechanisms comprising physical barriers, cellular effectors, and soluble mediators (Figure 1). Cellular responses include phagocytosis and degranulation by neutrophils and macrophages, as well as natural killer (NK) cell-mediated cytotoxicity. Concurrently, soluble factors such as complement proteins, reactive oxygen species, and an array of inflammatory cytokines, including tumor necrosis factor (TNF), interleukin (IL)-1, IL-6, and type I interferons (IFNs) amplify and coordinate the immune response.[13]

The adaptive immune system in contrast, provides a delayed but highly antigen-specific response mediated by B and T lymphocytes. This response enables precise pathogen clearance and long-lived immunological memory. Activation depends on the presentation of antigens via major histocompatibility complex (MHC) class I and II together with co-stimulatory signals, which are induced by innate sensing and consequently couple adaptive responses to the tissue context of infection or injury.[14] Key effector mechanisms include cytotoxic T cell-mediated elimination of infected or malignant cells, T helper (Th) cell polarization directing immune responses, and germinal center B cell differentiation involving class switch recombination and affinity maturation to generate high-affinity, isotype-switched antibodies (Figure 1).[14,15] Following activation, memory T and B cells provide rapid, robust recall responses upon re-exposure, with tolerance checkpoints limiting autoreactivity. Notably, cytokines and co-stimulation produced downstream of endosomal TLRs, particularly TLR8 in human myeloid cells, critically shape the magnitude and quality of adaptive immune responses, thus bridging

innate pathogen recognition with durable, specific immunity.[7] The complement system, comprising more than 30 plasma and membrane-bound proteins, bridges innate and adaptive immunity by opsonizing pathogens, promoting chemotaxis, and inducing cell lysis through membrane attack complex formation.[16] Beyond its defensive functions, inappropriate complement activation can damage host tissues and has been implicated in autoimmune and inflammatory disorders such as systemic lupus erythematosus (SLE) and rheumatoid arthritis (RA).[17]

1.2.2 Cells of the Innate Immune System

The innate immune system compromises a diverse set of cellular effectors that provide a rapid, non-specific defense against invading pathogens and danger signals. Neutrophils are the most abundant type of white blood cell in human blood and are typically the first responders to sites of infection or tissue injury. They control antimicrobial activity through phagocytosis, degranulation, the release of reactive oxygen species and neutrophil extracellular traps (NETs), which limits the spread of pathogens in the early stages of infection.[18] Monocytes and macrophages also serve as professional phagocytes, but they play a central role in mediating inflammation by secretion of cytokines such as TNF and IL-1β. Tissue-resident macrophages further contribute to homeostasis and clearance of apoptotic cells, linking host defense to tissue repair.[19]

Dendritic cells (DCs) act as a key connector between innate and adaptive immunity. Conventional myeloid DCs are highly enriched in TLRs and specialize in antigen uptake, processing, and presentation to T cells via MHC molecules, while plasmacytoid DCs specialize in the rapid production of type I IFNs in response to viral nucleic acids.[5,20,21] Natural killer (NK) cells present another subset of innate effectors that induce direct cytotoxicity against virally infected or malignant cells by releasing perforin and granzymes. They also produce IFN-γ to promote macrophage activation and Th1 polarization (Figure 1).[22]

Additional innate populations provide complementary functions. Mast cells and basophils release histamine, proteases, and lipid mediators that drive immediate hypersensitivity and parasite defense. Eosinophils play a distinct role in anti-helminth immunity and allergic inflammation pathogenesis.[23] Finally, although lacking antigen-specific receptors, innate lymphoid cells (ILCs) produce effector cytokines that mirror T helper cell subsets (Th1-, Th2-, and Th17-like responses), thereby providing an early layer of immune regulation and tissue-specific protection.[24]

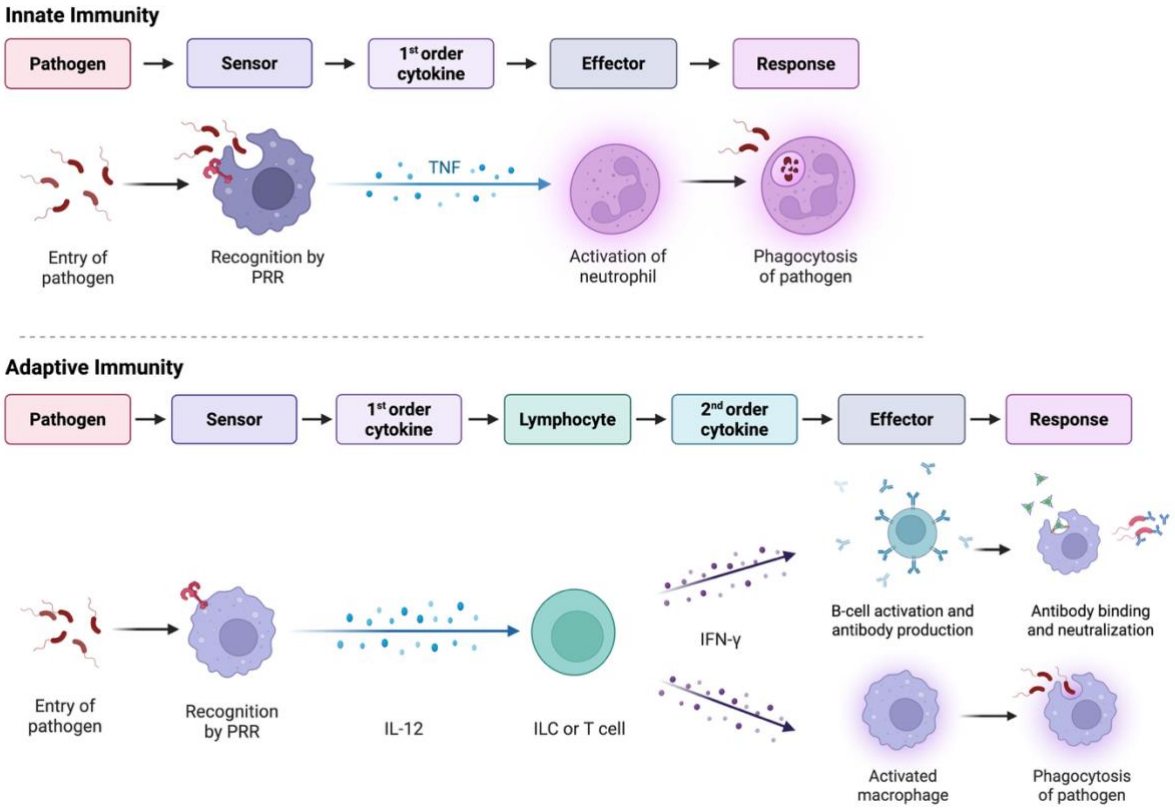

Figure 1. Overview of innate and adaptive immunity. In the innate immunity pathway, a pathogen enters the body and is recognized by sensor cells such as macrophages via PRRs, e.g. TLR8. This recognition triggers the release of primary cytokines like TNF, which rapidly activate effector cells such as neutrophils. Activated neutrophils then perform phagocytosis, eliminating the pathogen, demonstrating the innate immune system's fast, non-specific defense mechanism. In contrast, the adaptive immunity pathway starts similarly with pathogen recognition by PRRs on macrophages, leading to the secretion of primary cytokines such as IL-12. IL-12 activates lymphocytes, including innate lymphoid cells or T cells, which produce secondary cytokines such as IFN-γ. These cytokines further activate effector cells including macrophages. The adaptive response divides into two major arms: B cells are activated to produce antibodies that specifically bind and neutralize the pathogen, while activated macrophages partake in enhanced phagocytosis. Created with BioRender.com.

1.2.3 Pattern Recognition Receptors

Recognition of PAMPs and DAMPs is mediated by a limited number of germline-encoded PRRs.[5] The major families of PRRs include the Toll-like receptors (TLRs), the NOD-like receptors (NLRs), the RIG-I-like receptors (RLRs), C-type lectin receptors (CLRs), and absent in melanoma 2 (AIM2)-like receptors (ALRs).[25] TLRs are type I transmembrane proteins that consist of an extracellular leucine-rich repeat (LRR) domain for ligand binding and a cytosolic

Toll/IL-1 receptor (TIR) domain for signaling. TLRs will be discussed in detail in section 1.3. CLRs are a large family of transmembrane and soluble receptors characterized by a carbohydrate-recognition domain, which depend on Ca^{2+} for ligand binding, although C-type lectin-like receptors (CTLRs) function independently.[26] Canonical CLRs such as Dectin-1 and Dectin-2 detect fungal β-glucans and mannans, whereas others recognize a broader spectrum of ligands including lipids and proteins.[27] CLR signaling integrates antifungal defense, antigen uptake and T cell polarization.[28] RLRs are cytosolic RNA helicases that detect viral RNA and initiate type I interferon responses. This family includes RIG-I, MDA5, and LGP2. RIG-I senses short double-stranded RNAs with 5′triphosphate ends, while MDA5 responds to longer double-stranded RNA (dsRNAs).[29,30] Upon recognition, RLRs signal via the mitochondrial adaptor MAVS, activating TBK1 and IRF3/7, and coupling RNA detection to interferon release.[31] NLRs represent the fourth major PRR class, functioning as cytosolic proteins that sense microbial ligands, cellular injury, or metabolic stress. These receptors share a tripartite architecture consisting of a C-terminal LRR domain for ligand sensing, a central NACHT domain for oligomerization and variable N-terminal effector domains such as caspase-recruitment domains (CARDs, as in NLRC proteins) or pyrin domains (PYDs, as in NLRPs).[32] Certain NLRs, including NLRP3, NLRP1, and NLRC4, assemble into inflammasomes. These a large multiprotein complexes that activate caspase-1 (and caspase-4/5 in humans, caspase-11 in mice).[33] Caspase-1 then cleaves pro-IL-1β and pro-IL-18 into their mature forms, inducing pyroptosis via gasdermin D pore formation.[34,35] Dysregulation of NLR activity contributes to autoinflammatory diseases and metabolic syndromes, highlighting its clinical relevance.[36]

Beyond the canonical PRR families, additional cytosolic DNA sensors have been identified. ALRs, such as AIM2 and IFI16, recognize double-stranded DNA (dsDNA) via HIN200 domains.[37] AIM2 forms an inflammasome with ASC, activating caspase-1 and driving the release of IL-1β/IL-18.[38] The cGAS–STING pathway is another central mechanism of DNA-sensing. Upon binding to cytosolic dsDNA, cGAS synthesizes cyclic GMP-AMP (cGAMP), which activates the ER-resident adaptor STING. This leads to the recruitment of TBK1 and the induction of type I IFNs.[39,40] These pathways expand the scope of innate surveillance to include viral and endogenous DNA, thereby linking infection control to autoimmunity and cancer.[41,42]

Among these receptors, the TLR family stands out due to its well-defined signaling pathways and its high potential to pharmacological modulation, making it a particularly attractive target for drug targeting and discovery.[43–45]

1.3 The Toll-like Receptor Family

1.3.1 Overview

Toll-like receptor research originated with the identification of the *Toll* gene in *Drosophila melanogaster* genetic screens conducted by Anderson and Nüsslein-Volhard in 1985.[46] Subsequent studies revealed that TLRs are central to innate immunity because they detect pathogen invasion, initiate inflammatory cascades, and activate antigen-presenting cells to prime antigen specific adaptive immunity beyond mere nonspecific barriers.[21,45] TLRs have emerged as a principal PRR family extensively studied for their essential roles in linking innate pathogen recognition to adaptive immune instruction, as well as their involvement in autoimmune and inflammatory pathologies.[10] These transmembrane proteins are defined by a conserved structural pattern, featuring an LRR ectodomain for ligand binding, a single transmembrane helix, and a TIR domain in the intracellular region responsible for initiating downstream signaling.[47] The human TLR family includes ten functional members (TLR1–TLR10) that are divided into two functional subgroups. Cell-surface TLRs (TLR1, 2, 4, 5, 6, and 10) are located on the plasma membrane and primarily recognize molecular patterns from extracellular pathogens.[48] For example, TLR5 recognizes bacterial flagellin (Figure 2).[49] In contrast, endosomal TLRs (TLR3, 7, 8, and 9) are located within intracellular endosomes and detect nucleic acids from internalized pathogens (Figure 2).[48,50] TLRs undergo conformational rearrangements that promote dimerization of their ectodomains.[51] This brings the intracellular TIR domains into close proximity, enabling the recruitment of adaptor proteins such as MyD88 or TRIF, and therefore initiating downstream signaling cascades that lead to the activation of NF-κB.[7,10]

1.3.2 Nucleic Acid-sensing TLRs

Endosomal TLRs are crucial for host defense yet also play a role in autoimmune diseases. Each endosomal TLR is differentiated by its specific ligand, for example, TLR3 recognizes dsRNA,[52] while TLR7 and TLR8 both recognize single-stranded RNA (ssRNA).[50,53] TLR9 is activated by unmethylated CpG-DNA motifs, commonly found in bacterial and viral genomes (Figure 2).[54,55] This unique localization within the endosomes and occasionally lysosomes is a critical regulatory mechanism that ensures they encounter only internalized pathogen components (like those from phagocytosed viruses and bacteria), while largely avoiding the host's own nucleic acids in the cytoplasm and preventing inappropriate immune activation.[56] The trafficking of these receptors from the endoplasmic reticulum (ER) to the endosomes is carefully controlled

by the chaperone protein UNC93B1, a multipass transmembrane protein that directly regulates the packaging of TLRs into vesicles for ER exit.[57] UNC93B1 remains associated with TLRs through multiple post-Golgi sorting steps, and mediates differential trafficking of individual endosomal TLRs through distinct cellular pathways. For instance, TLR9 requires UNC93B1-mediated recruitment of adaptor protein complex 2 (AP-2) for clathrin-dependent endocytosis and delivery to endolysosomes, whereas TLR7 utilize alternative, AP-2-independent trafficking routes.[58] Additionally, endosomal TLRs require proteolytic cleavage and acidic pH for activation, providing additional regulatory checkpoints that prevent aberrant signaling. The proteolytic processing separates the full-length receptor into functional fragments within the acidic endolysosomal environment, a maturation step essential for ligand recognition and downstream signaling.[59] Dysregulation of these tightly controlled pathways is strongly implicated in autoimmune diseases like SLE. Specific UNC93B1 variants that enhance TLR7 and TLR8 trafficking and signaling have been identified in SLE patients, highlighting the balance required for optimal immune homeostasis.[60] For a more detailed description of nucleic sensing TLRs, please refer to Publication I, which is reproduced in chapter 2 of this thesis.

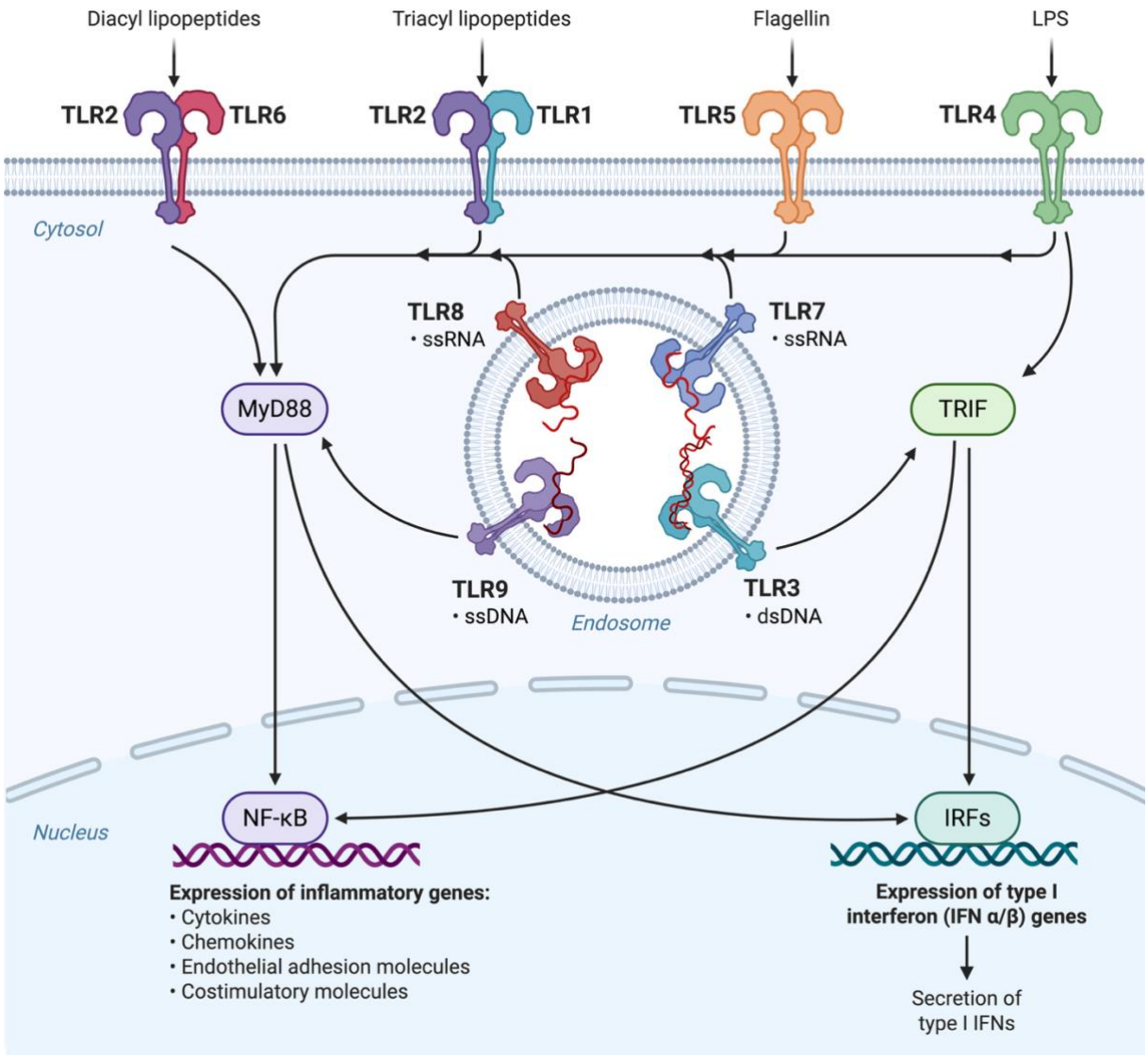

Figure 2. Overview of TLR signaling pathways. Localization, ligands, and downstream signaling of cell-surface and endosomal TLRs. Cell-surface TLRs (TLR1/2, TLR2/6, TLR4, and TLR5) detect bacterial and viral components such as lipopeptides, LPS and flagellin. Endosomal TLRs (TLR3, TLR7, TLR8, and TLR9) recognize nucleic acids. Ligand binding induces dimerization and recruits adaptor proteins that promote signaling. Most TLRs signal through MyD88, which leads to the activation of NF-κB and the transcription of inflammatory mediators, including cytokines, chemokines, adhesion molecules, and co-stimulatory molecules. In contrast, TLR3 and partially TLR4 signal via TRIF, which activates IRFs to induce type I IFN gene expression. Together, these pathways regulate immediate inflammatory responses and the induction of adaptive immunity. Created with BioRender.com.

1.4 Toll-like Receptor 8

1.4.1 Biology and Function

In humans, TLR8 is predominantly expressed in monocytes, macrophages, and myeloid dendritic cells (mDCs). These cells function as professional antigen-presenting cells by phagocytosing pathogens, producing diverse cytokines and activating T cells.[5,21] While other cells, such as neutrophils and NK cells, also contribute to innate immunity, their role in TLR8 signaling is less prominent than that of the myeloid lineage.[61] Within these cells, TLR8 localizes to late endosomes and lysosomes, where its activation drives strong proinflammatory responses.[62]

Natural ligands of human TLR8 include microbial ssRNA and certain RNA degradation products,[63,64] but it can also be potently activated by various synthetic ligands, including small-molecules, and specific oligonucleotides.[63,65,66] Physiologically, human TLR8 activation is crucial for antiviral and antibacterial immunity, driving the production of cytokines that help clear infections. However, TLR8 dysregulation contributes to chronic inflammation in autoimmune diseases such as SLE and RA.[6,67] Additionally, TLR8 is also being explored for its potential role in modulating the anti-tumor response in cancer immunotherapy.[7,68] In contrast to human, the murine TLR8 ortholog is largely nonfunctional when stimulated with known TLR8 ligands, presenting a key species-specific difference.[69,70] For a more detailed description of the TLR8 biology and function, please refer to Publication I (chapter 2).

1.4.2 Signaling Pathways

Upon ligand binding, TLR8 dimerizes, and its cytoplasmic TIR domains recruit the key adaptor protein MyD88.[71,48] This initiates a signaling cascade in which MyD88 acts as a scaffold to recruit and activate the kinase IRAK4, which subsequently phosphorylates IRAK1. Recent structural and cell biological insights reveal that MyD88-dependent TLR signaling proceeds through assembly of the Myddosome, a location-specific supramolecular organizing center (SMOC), in which increased local concentrations of signaling components facilitate the weak allosteric interactions required for kinase activation.[72–74] This complex acts as a central hub from which the entire downstream TLR signaling cascade is executed.[75] The Myddosome is a helical oligomeric complex formed by the death domains (DDs) of MyD88 and the kinases IRAK4 and IRAK1/2.[76] Structural studies (e.g., cryo-EM and crystallography) show that MyD88 provides the nucleation seed via its DD, enabling the sequential recruitment of six to eight IRAK4 molecules and up to four IRAK1/2 molecules into a left-handed helical

assembly.[77] The cascade continues with the recruitment of TRAF6, a crucial E3 ubiquitin ligase that activates the TAK1 complex, leading to the phosphorylation and activation of NF-κB and MAPK signaling pathways.[78] This results in the induction of key pro-inflammatory cytokines such as TNF and IL-1β, alongside the upregulation of co-stimulatory molecules CD80 and CD86, which are essential for T cell activation and shaping of the adaptive immune response.[7,78,79] Negative feedback mechanisms, involving proteins such as IRAK-M and suppressor of cytokine signaling (SOCS) family members tightly regulate this pathway to prevent excessive and potentially damaging inflammation.[80]

Beyond this canonical model, recent advances have substantially deepened our understanding of endosomal TLR8 signaling. TLR7 and 8 are activated not by full-length RNA, but by specific RNA degradation products generated by lysosomal RNases such as RNase T2, PLD3/PLD4, and RNase 6 from bacterial RNA.[81,82] This activation relies on a cooperative dual-site mechanism, requiring both uridine-containing fragments and short oligoribonucleotides binding distinct sites on the receptor.[64,83] As such, TLR8 detects intermediates of RNA breakdown, directly linking nucleic acid catabolism to innate immune signaling.[84] Downstream of the receptor, signaling selectivity is increasingly understood to involve adaptor-level checkpoints. The SLC15A4–TASL complex has recently been identified as a crucial determinant for IRF5 activation, which is a key transcription factor for type I IFN responses downstream of TLR7/8/9 activation.[85,86] High-resolution structural studies demonstrate how the adaptor TASL docks within the SLC15A4 transporter, providing an anchoring motive for IRF5 recruitment and activation.[87] This adaptor-level checkpoint explains how TLR7/8/9 can differentially regulate cytokine production. Specifically, IRF5 activation drives the production of type I IFNs and pro-inflammatory cytokines, which are strongly linked to autoimmunity.[88] Therefore, pharmacological targeting of the SLC15A4–TASL axis is emerging as a druggable target for modulating immune responses downstream TLR7/8/9.[88] In addition, recent work has identified the serine/threonine kinase STK25 as a novel positive regulator of TLR8 signaling, mediating its effects through direct phosphorylation and activation of IRF5.[89] STK25 expression is upregulated upon TLR7/8/9 stimulation, and genetic loss of STK25 significantly attenuates TLR8-driven inflammatory responses in primary immune cells. This highlights STK25 as a potential therapeutic target for ameliorating TLR8-mediated pathological inflammation and autoimmunity. For a more detailed description of the TLR8 signaling pathway, please refer to Publication I (chapter 2).

1.4.3 Receptor Structure and Ligand Binding

TLR8 is a type I transmembrane glycoprotein composed of an N-terminal leucine-rich repeat (LRR) ectodomain (~800 amino acids (aa)), a single-pass transmembrane helix (~20 hydrophobic residues), and a C-terminal TIR domain (~150 aa) that engages adaptor proteins upon activation (Figure 3).[90,91] The ectodomain forms the hallmark horseshoe-shaped solenoid made of tandem LRRs that mediates ligand recognition. A distinctive architectural element is the Z-loop inserted between LRRs 14-15 (Figure 3). In acidified endosomes, this loop undergoes a proteolytic cleavage, a crucial step that relieves autoinhibition, enables homodimerization, and activates the receptor competent for signaling. Subsequently, the receptor's ectodomains form an inter-subunit interface that is essential for ligand-mediated activation.[64,92]

X-Ray crystallographic structures revealed that TLR8 recognizes uridine-rich ssRNA degradation products through two cooperative binding sites. Site 1 is located between LRRs 11-14 in TLR8; and LRRs 16*-18* in TLR8* in the dimer interface and accommodates uridine as well as many small-molecule ligands. Site 2 sits on the concave LRR surface of one protomer and binds short oligoribonucleotides.[64] While uridine alone binds site 1, this interaction is insufficient to trigger the full conformational change necessary for receptor activation. Instead, simultaneous binding of a short RNA fragment to site 2 induces a conformational closure of the TLR8 ectodomains into a signaling-competent dimer, thereby explaining the synergistic effect of RNA degradation products.[64] The natural ligands for these two sites are generated by the lysosomal endoribonuclease RNase T2, which produces 5′-uridine-containing fragments and 2′,3′-cyclic-phosphate-terminated adenine/guanine oligoribonucleotides matching the binding preferences of site 1 and site 2, respectively.[83] This dual-site recognition mechanism clarifies TLR8’s pharmacology: synthetic monovalent agonists can activate TLR8 by binding site 1 alone, whereas physiologic RNA ligands typically require engagement of both site 1 (uridine) and site 2 (short oligoribonucleotide) to achieve the receptor’s active conformation.[64] Additionally, natural modifications of nucleosides, like substitution of uridine with pseudouridine or other natural modifications, can modulate recognition by TLR7 and TLR8 and thereby reduce receptor activation and subsequent cytokine production.[93] This observation has been critical for the development of therapeutic mRNA technologies that evade innate immune activation by these receptors.[94]

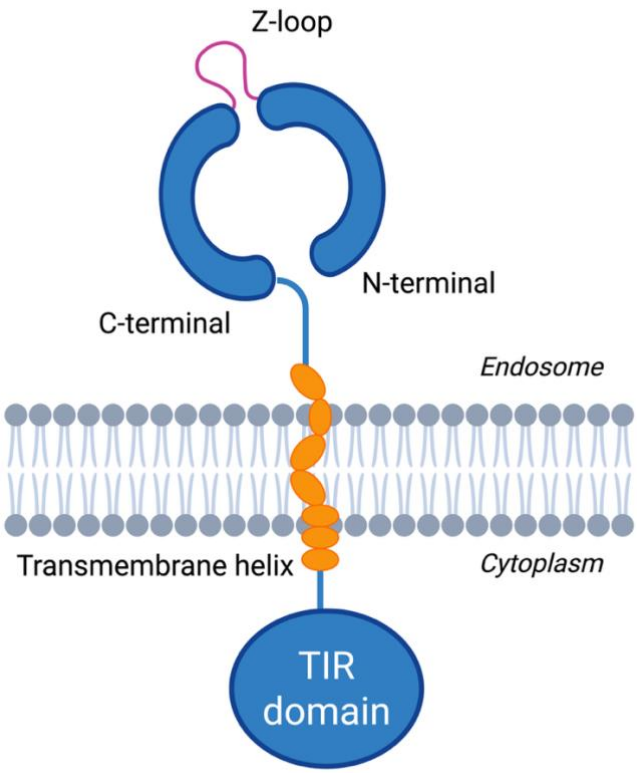

Figure 3. Domain architecture of TLR8. Modular organization of a prototypical endosomal TLR, such as TLR8. The extracellular leucine-rich repeat (LRR) ectodomain is depicted with its N-terminal and C-terminal regions, interrupted by the characteristic Z-loop, a short-inserted sequence that requires proteolytic cleavage in acidic endosomes to enable receptor dimerization and activation. The ectodomain is anchored in the endosomal membrane via a single transmembrane helix, which connects to the cytoplasmic TIR domain. The TIR domain is responsible for recruiting adaptor proteins such as MyD88, initiating downstream signaling cascades. Created with BioRender.com.

Moreover, crystal structures of TLR8 ectodomains have demonstrated that TLR8 antagonists, such as the CU-CPT9 series, bind specifically at the protein–protein dimer interface (Site 1), locking the receptor's ectodomains in an inactive, open conformation.[95] Key residues mediating antagonist binding include Phe346, Tyr348, Asn312, Val378, Asp543, Asp545, and Thr574, which form a composite interaction network spanning both monomers. Hydrophobic residues such as Leu351, Val520, and Leu573 support shape complementarity of the antagonist scaffold, while Asp543 and Thr574 engage in hydrogen bonding that anchors antagonists and inhibits conformational closure of the dimer. Molecular dynamics (MD) simulations and τRAMD (τ-random acceleration molecular dynamics) unbinding pathway analysis have further demonstrated that antagonists with ionic head groups, particularly those interacting with

Glu427 and Tyr567, prefer the internal dissociation path, enhancing residence time and pharmacological stability.[96] Collectively, these interactions maintain TLR8 in its resting architecture and effectively inhibit the inter-subunit rotation required for MyD88 recruitment and downstream signal transduction.[95] For a more detailed description of TLR8 structure and ligand binding, please refer to Publication I (chapter 2).

1.5 TLRs as a Therapeutic Target

1.5.1 TLR8 in Human Disease

Abnormal TLR8 activity has been associated with a wide range of immune-mediated, infectious, malignant, and hyperinflammatory conditions (Figure 4). Rare gain-of-function (GOF) variants in TLR8 cause an immune dysregulation syndrome, which is characterized by neutropenia, antibody deficiency, lymphoproliferation, and bone-marrow failure, underlining the tightly balanced TLR8 signaling in humans.[97,98] In the tumor microenvironment, TLR8 recognizes tumor-secreted microRNAs, including miR-21 and miR-29a, which function as paracrine agonists that activate TLR8 in surrounding immune cells. This microRNA-TLR8 interaction triggers a prometastatic inflammatory program characterized by NF-κB activation and secretion of proinflammatory cytokines, thereby establishing a direct mechanistic link between solid tumors and tumor-associated inflammation.[99] Among endosomal TLRs, TLR8 specifically contributes to chronic inflammation in RA, with TLR8 agonists inducing significant TNF production from synovial membranes.[100] Peripheral blood mononuclear cells from psoriasis patients exhibit significantly increased expression of intracellular TLRs including TLR8, accompanied by elevated inflammatory cytokine gene expression of TNF and IFN-γ.[101] Beyond psoriasis, monocytes from patients with systemic sclerosis exhibit altered cytokine responses upon TLR8 stimulation, demonstrating disease-specific dysregulation of the pathway.[102] Genetic and functional studies also associate TLR8 polymorphisms with tuberculosis susceptibility, highlighting a host-determinant role at the population level.[103,104] At the systemic level, excessive TLR8 signaling contributes to hyperinflammatory states such as cytokine storm and sepsis by promoting NF-κB and MAPK signaling and elevating IL-6, TNF, and other inflammatory mediators, resulting in multiorgan dysfunction.[105,106] In addition, recent investigations showed that endogenous microRNAs, particularly miR-574-5p, drive autoimmune inflammation in conditions like SLE through IFN production, B cell activation and autoantibody generation.[107] Similarly, in Sjögren's disease, TLR8-positive monocytes and macrophages infiltrate salivary gland lesions in patients, where they express elevated levels of

CD86 and contribute to adaptive immune responses through enhanced antigen presentation and T cell activation.[108] For a more detailed description of TLR8 in human disease, please refer to Publication I (chapter 2).

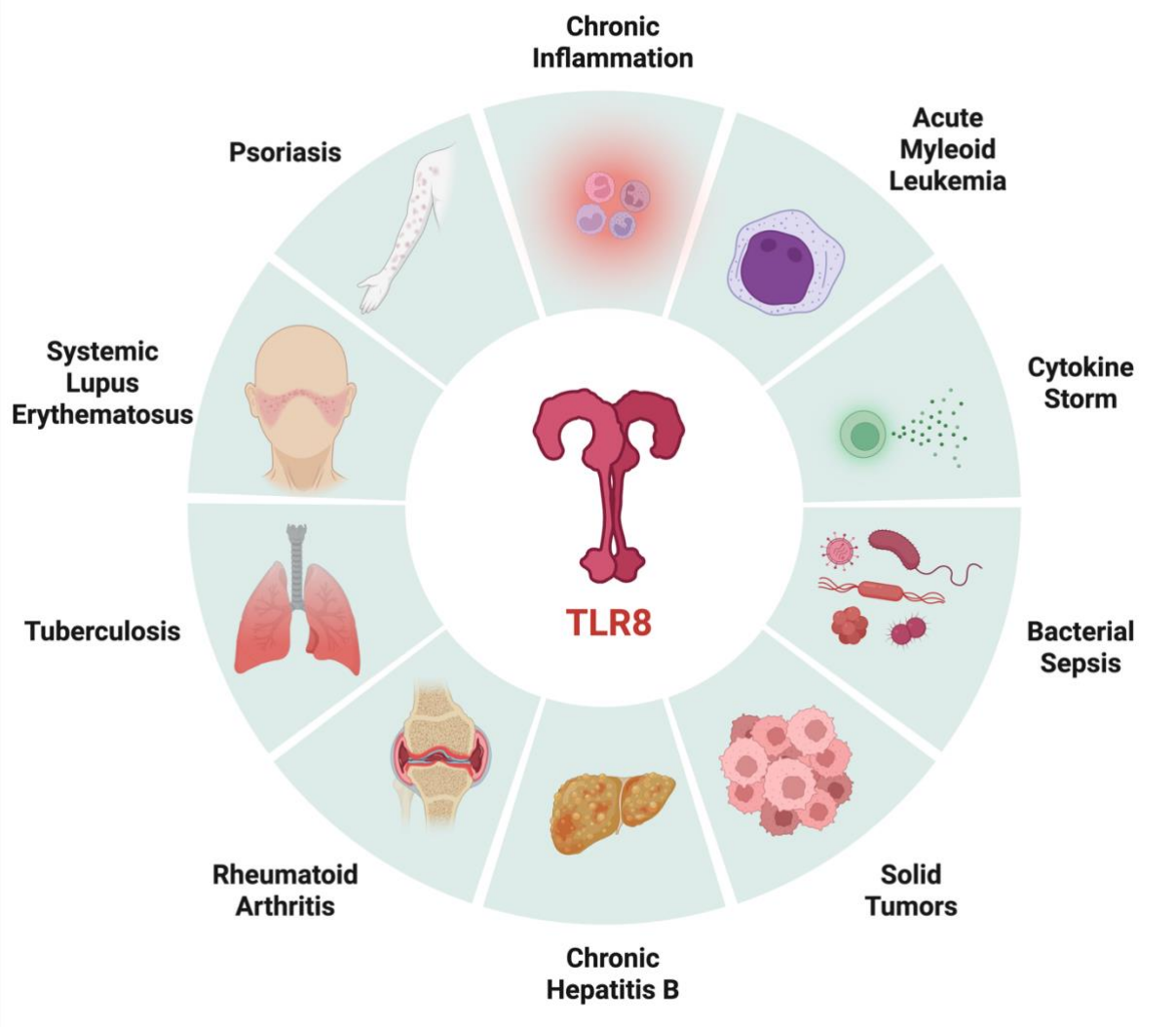

Figure 4. Diseases and pathological conditions linked to TLR8. Highlighted conditions include chronic inflammation, autoimmune diseases (rheumatoid arthritis, psoriasis, systemic lupus erythematosus), infections (tuberculosis, chronic hepatitis B, bacterial sepsis), cytokine storm, solid tumors and hematologic malignancies (acute myeloid leukemia), underlining the diverse roles of TLR8 in immune regulation and pathology. Created with BioRender.com.

1.5.2 Therapeutic Rationale

Pharmacological modulation of TLR8 can be broadly classified into two principal approaches. The first involves the development of TLR8 agonists to potentiate adaptive immune responses, positioning these compounds as promising vaccine adjuvants. Notably, TLR8 agonists are being investigated for their capacity to mediate robust Th1-polarized immune responses, with

applications in cancer immunotherapy and the enhancement of antiviral immunity.[109,110] Building on these findings, a range of TLR8 or 7/8 agonists have progressed into clinical treatment for solid tumors. These agents are investigated for use in combination with established therapies such as immune checkpoint inhibitors, with the goal of amplifying anti-tumor immune responses and overcoming resistance mechanisms within the tumor microenvironment. EIK1001, a systemically delivered TLR7/8 co-agonist, recently has demonstrated encouraging anti-tumor activity in Phase I trials across various solid tumors and is currently being evaluated in Phase II/III studies as first-line treatment for advanced melanoma and in Phase II trials for both squamous and non-squamous non-small cell lung cancer (NSCLC).[8,111] In hematologic malignancies, TLR8 activation in acute myeloid leukemia (AML) cells and their microenvironment promotes differentiation and inhibits proliferation in preclinical models.[112] TLR8 agonists like motolimod induce inflammatory cell death in AML cells, positioning TLR8 as a promising therapeutic target.[113] In chronic hepatitis B, the oral TLR8 agonist selgantolimod (GS-9688) enhances antiviral immune functions and has advanced into phase 2 clinical testing, demonstrating on-target immunologic activity and acceptable safety profile in virally suppressed patients on nucleoside therapy.[114,115] Moreover, preclinical studies have explored TLR8 agonists in combination with low-dose cisplatin, showing synergistic effects in boosting anti-tumor immunity.[116]

In contrast, the primary rationale for TLR8 antagonists is their potential to treat autoimmune and chronic inflammatory diseases, where TLR8 overactivation by endogenous nucleic acids drives a persistent inflammatory state.[117–119] Several compounds exhibiting dual TLR7/8 antagonism have been reported and advanced into clinical development.[8,120] Enpatoran (M5049), a dual TLR7/8 antagonist, is the most clinically advanced candidate and has demonstrated significant improvements in disease indicators and type I IFN gene signatures in Phase II trials for cutaneous lupus erythematosus, with good tolerability profiles confirmed.[121] Supporting preclinical data from E6742 further highlight the promise of this approach in models of lupus-like disease.[122] Similarly, BMS-986256 (Afimetoran) has shown efficacy in patients with CLE, improving CLASI-A scores by >50%.[123]

However, while dual antagonism holds promise for autoimmune indications, the preservation of TLR7 function is crucial given its predominant role in plasmacytoid dendritic cells (pDCs) that regulate type IFN-mediated antiviral responses, in contrast to TLR8, which is principally expressed in monocytes and macrophages. Non-selective inhibition of both TLR7 and TLR8 may disrupt antiviral defenses and impair dendritic cell regulatory capacity due to their distinct

expression patterns and transcriptional outputs.[124,125] In conditions such as RA, psoriasis, and cytokine storm syndromes, overactivation of myeloid TLR8 drives pathologic tissue damage via excessive cytokine release. Selective inhibition of TLR8, but not TLR7, can therefore suppress pathological NF-κB signaling and tissue-destructive inflammation, while simultaneously maintaining TLR7's antiviral, tolerogenic, and immune-modulatory benefits.[126] Despite these advances, no TLR8-selective drug has received regulatory approval to date.

Although there are currently no approved TLR8-directed medicines, several other TLR-modulating agents are licensed in the U.S./EU, primarily as agonists used topically or as vaccine adjuvants. The TLR7 agonist imiquimod is approved as a topical immunomodulatory therapy for external genital and perianal warts, actinic keratosis, and superficial basal cell carcinoma (e.g., Aldara/Zyclara), with its mechanism of action well-documented in the immunology literature.[127,128] Among vaccines, monophosphoryl lipid A (MPL), a TLR4 agonist, is an established component of advanced adjuvant formulations such as AS01B used in the Shingrix zoster vaccine and AS01E in Arexvy, an RSV vaccine.[129–131] MPL is also used in AS04 (MPL adsorbed onto aluminum salts) for the HPV vaccine Cervarix and the hepatitis B vaccine Fendrix, indicated for patients with renal insufficiency.[132,133] Furthermore, HEPLISAV-B, an adult hepatitis B vaccine, contains CpG 1018, a TLR9 agonist oligonucleotide adjuvant.[134]

In summary, TLR8 acts as a critical regulator between immunity and disease. Selective inhibition of TLR8 offers therapeutic promise for reducing maladaptive myeloid inflammation in autoimmune, infectious, and tumor-associated contexts, while preserving the essential antiviral functions of TLR7. Robust preclinical and clinical data support advancing potent, selective TLR8 inhibitors for pathological RNA sensing and cytokine-driven diseases. For a more detailed description of the TLR8 therapeutic rationale, I refer to Publication I (chapter 2).

1.6 Objective and Scope of this Thesis

1.6.1 Overall Aim

This thesis focuses on identifying, characterizing, and mechanistically evaluating novel, selective small-molecule antagonists that target human TLR8. The primary objective is to evaluate their pharmacological potential in various immunological cell lines. Specifically, this work advances basic immunology by investigating the molecular details of antagonistic effects on TLR8 signaling and mapping the key binding interactions and amino acid residues that are essential for ligand recognition. Furthermore, this thesis supports medicinal chemistry efforts by providing potent, selective lead compounds that could form the basis of new immunomodulatory therapies.

1.6.2 Thesis Structure

This dissertation comprises three publications and one unpublished chapter that collectively address the knowledge gaps identified above.

Chapter 1 covers a review article that thoroughly summarizes the current state of knowledge regarding the biology and pharmacology of endosomal TLRs 7, 8, and 9. It places this thesis in the context of ongoing research efforts and discusses potential future immunotherapeutic strategies.

Chapter 2 investigates the structural insights and further optimization of previously discovered pyrimidine-based scaffolds, revealing their potential to antagonize TLR8 and therefore providing a framework for rational design of future TLR8 directed antagonists.

Chapter 3 describes the discovery and initial pharmacological characterization of a novel isoxazole-based scaffold, acting as a potent selective TLR8 antagonist and providing the first-in-class structure–activity relationships (SAR) for this chemotype with comprehensive pharmacological characterization.

Chapter 4 focuses on the rational optimization of a pyrimidine-based antagonist scaffold, building upon the insights from Chapters 2 and 3. Through systematic exploration of SAR, this chapter demonstrates how targeted molecular modifications enhance both TLR8 selectivity and inhibitory potency, discovering a lead compound that achieves performance comparable to the most potent selective TLR8 antagonists reported to date.

Chapter 2

Structure-guided approaches to modulate endosomal toll-like receptors TLR7, TLR8 and TLR9: advances, challenges and therapeutic promise

Troy Matziol*, Valerij Talagayev*, Günther Weindl, Gerhard Wolber

Drug Discov. Today. 2025;30(11):104495

*Troy Matziol and Valerij Talagayev contributed equally to this work.

Please refer to Appendix I for the publication's full text.

2.1 Publication summary

Endosomal TLRs are a specialized subgroup within the TLR superfamily. They are responsible for mediating host responses to viral and bacterial nucleic acids, and they play a crucial role in connecting innate and adaptive immunity. In recent years, our mechanistic understanding of these receptors has expanded significantly, covering not only ligand recognition and receptor dynamics, but also how these insights can be used to develop rational pharmacological treatments for complex diseases such as cancer, autoimmunity, and chronic viral infection. This review of endosomal TLRs (TLR7/8/9) provides a comprehensive overview of the latest advances in their structural biology, signaling pathways, pharmacological modulation and therapeutic potential. Combining recent structural insights with translational pharmacology, the review reveals new opportunities and ongoing challenges in precise immunomodulation through endosomal TLRs.

Endosomal TLRs 7/8/9 share a conserved leucine-rich repeat ectodomain architecture and function as ligand-activated homodimers. TLR8 exists as a pre-formed dimer with two spatially distinct binding sites: one at the dimerization interface for small agonists and a concave pocket for oligoribonucleotide fragments. TLR7 employs an analogous strategy with sites for guanosine analogs and uridine-rich RNA sequences. TLR9 uses stimulatory CpG DNA as bivalent molecular glue that threads through both receptor protomers to form an active 2:2 complex. While each of these receptors has evolved distinct binding modes to discriminate between diverse nucleic acid structures, structural studies consistently demonstrate that ligand-induced conformational changes represent a conserved requirement for signal initiation.

Recent studies give insight into the signaling mechanism of TLR7/8/9, which is mediated by the MyD88-dependent assembly of a higher-order Myddosome complex. This supramolecular complex further triggers the activation of NF-κB and IRFs (mainly IRF5 and IRF7), driving the production of proinflammatory cytokines and type I interferons. New players have emerged in this signaling pathway, including the adaptor TASL and the transporter SLC15A4. These proteins specifically scaffold IRF5 phosphorylation downstream of TLR7 and 9 in plasmacytoid dendritic cells and B cells, revealing a critical layer of signaling compartmentalization for IFN-driven autoimmunity and antiviral defense.

From a drug discovery perspective, the review outlines structure-guided advances in TLR modulator development, enabled by high-resolution crystal structures revealing molecular mechanisms of ligand recognition. Agonists typically use nucleoside-mimetic scaffolds such as imidazoquinolines, while antagonists stabilize inactive conformations through hydrophobic interface binding. Recent therapeutic innovations reach out beyond traditional small molecules to address key translational challenges. Brain-penetrant TLR antagonists have been developed to target neuroinflammatory cascades in CNS (central nervous system) disorders, while advanced delivery platforms overcome systemic toxicity limitations. Antibody-drug conjugates carrying TLR agonist payloads enable tumor-selective immune activation and engineered nanoparticle systems provide spatiotemporal control of TLR stimulation. These targeted approaches localize TLR modulation to disease-relevant compartments while minimizing off-target effects.

Despite these advances, clinical development of TLR modulators faces ongoing challenges including immune-related adverse effects, insufficient target selectivity due to the structural similarities among endosomal TLRs, and heterogeneous context-dependent signaling across cell types and disease stages. Nevertheless, several TLR7/8 antagonists with improved selectivity and brain penetration have advanced to clinical trials for lupus and other autoimmune diseases. These compounds show great potential for reducing disease symptoms by decreasing pathogenic interferon responses and therefore reduce TLR7/8-driven autoimmunity.

Emerging biological insights further enrich the therapeutic landscape. Natural 2′-O-methylated RNA fragments serve as endogenous TLR7/8 antagonists and can be used as templates to design immunomodulators that suppress unwanted cytokine induction. Regulatory roles of UNC93B1 and adaptor complexes such as TASL/TASL2 in receptor trafficking and signaling are being investigated, suggesting novel intervention points. Moreover, recent evidence implicates TLR8

as a critical sensor of endogenous ssRNA released during tissue damage and infection. This role links it to chronic inflammation and autoimmunity, thereby underscoring the need for cell-type-selective modulation.

Deepening knowledge of how TLR7, TLR8, and TLR9 function at the structural and mechanistic level reveals valuable opportunities to target their immunomodulatory functions. Advances in drug design and delivery technologies, as well as the use of clinical biomarkers enable more targeted immunotherapies centered on endosomal TLRs.

2.2 Author contribution

Within this review, I was responsible for compiling and evaluating the literature on endosomal TLR7, TLR8, and TLR9, specifically on pharmacology, therapeutic applications of ligands, and challenges in achieving receptor selectivity. I prepared the figure describing the signaling pathway and the table displaying compounds investigated in clinical trials, incorporated the references, and contributed to the overall manuscript structure. I revised the manuscript in close collaboration with my co-first author and the corresponding authors.

Chapter 3

Optimization of 6-(trifluoromethyl)pyrimidine derivatives as TLR8 antagonists

Nika Strašek Benedik, Valerij Talagayev, Troy Matziol, Ana Dolšak, Izidor Sosič, Günther Weindl, Gerhard Wolber, Matej Sova

Acta Pharm. 2025;75(2):159–183

Please refer to Appendix II for the publication's full text and supporting information.

3.1 Publication summary

TLR8 has gained significant attention as a central player in human innate immunity, acting as a sensor of RNA catabolites within endolysosomes and therefore creating strong proinflammatory responses. While this function is essential for antimicrobial defense, aberrant or chronic TLR8 activation has been strongly linked to autoimmune disorders such as SLE, psoriasis, and RA. Despite a growing interest in developing selective small-molecule antagonists for TLR8, only a limited number have been successfully created. A major challenge in designing TLR8 modulators is achieving favorable pharmacokinetic properties while minimizing off-target and cytotoxic effects.

The main goal of this study was to design and synthesize a novel series of small-molecule inhibitors as selective TLR8 antagonists. These new compounds were developed and optimized based on previously identified 6-(trifluoromethyl)pyrimidin-2-amines.[135,136] The rational design focused on selective modifications at two critical positions on the scaffold. Selection of substituents was guided by molecular dynamics simulations to systematically investigate SAR in TLR8 binding pocket. The chemical modifications enhanced binding affinities by strengthening hydrogen bonding interactions, modulating hydrophobic contacts, and addressing steric constraints within the TLR8 uridine-binding pocket, which has been characterized through crystallographic and computational studies as essential for ligand recognition and receptor inhibition. Further mechanistic insights were obtained through docking studies and protein-ligand interaction frequency analyses (Dynophore clouds), which clarified the SAR drivers responsible for observed variations in potency and cytotoxicity.

Biological evaluation used hTLR8-transfected HEK293 cells with an NF-κB SEAP reporter to quantify the inhibition of TLR8 activation with agonist TL8-506. Out of 15 tested compounds, none showed agonistic activity, while several ones antagonized TLR8-dependent NF-κB

signaling with low-micromolar potencies in this cellular system. Two compounds, 14 and 26, were selected for more detailed profiling. Compound 14 of the first series displayed robust inhibition of TLR8 signaling with IC_{50} value in low micromolar range, but reduced cell viability at higher concentrations raised concerns about cytotoxicity. By contrast, compound 26 achieved a similar potency while preserving cellular viability, making it the most promising lead candidate of the second series. Structure–activity relationship analysis revealed that a 4-hydroxyphenyl ring positioned two carbon atoms from the main scaffold proved essential for binding in the first series, while the pyrrole ring at position 4 significantly contributed to antagonistic activity in the second series. Substitutions with furan or pyrazole rings generally resulted in a loss of activity. Incorporation of biphenyl substituents or modification of linker length resulted in reduced potency, underscoring the importance of optimal spatial geometry and electronic properties for productive receptor engagement.

New key insights from this article:

(1) The pyrimidin-2-amine scaffold can be effectively modified using targeted synthetic methods to create potent TLR8 antagonists.
(2) SAR studies showed that even minor chemical alterations can have a major impact on both compound activity and its toxicity.
(3) Compound 26 emerged as a lead candidate with an optimal balance of high potency and full cellular viability, avoiding the cytotoxic effects observed with other potent compounds such as compound 14.

In conclusion, this work demonstrates that systematic scaffold optimization of 6-(trifluoromethyl)pyrimidin-2-amines yields potent, non-toxic antagonists of TLR8. While further studies are required to confirm selectivity, in vivo efficacy and pharmacokinetic properties, the identification of compound 26 provides a promising candidate for further investigation due to its balanced profile of potency and safety. Future development strategies include exploring alternative substituents at position 6 beyond trifluoromethyl groups and introducing modifications to the pyrrole ring at position 2. Importantly, halogen selection critically impacts compound safety. Chlorine and bromine substitutions should be avoided to minimize cytotoxicity, while fluorine incorporation at strategic positions enhances both potency and cellular viability. Collectively, the resulting chemical scaffolds offer a validated platform for developing selective TLR8-targeted immunomodulatory agents.

3.2 Author contribution

Within this project, I was responsible for designing, executing, and analyzing all biological experiments. In collaboration with co-authors, I contributed to experimental design and evaluated structure–activity relationships through biological data interpretation. I prepared biological figures, wrote the corresponding sections of the manuscript, and participated in manuscript revision.

Chapter 4

Discovery of Novel Isoxazole-Based Small-Molecule Toll-Like Receptor 8 Antagonists

Troy Matziol*, Valerij Talagayev*, Tjaša Slokan, Nika Strašek Benedik, Janine Holze, Matej Sova, Gerhard Wolber, and Günther Weindl

J Med Chem. 2025;68(4):4888–4907

*Troy Matziol and Valerij Talagayev contributed equally to this work.

Please refer to Appendix III for the publication's full text.

4.1 Publication summary

Targeting TLR8 with selective small-molecule antagonists represents a promising therapeutic strategy to reduce pathogenic inflammation while preserving beneficial host defense mechanisms. Despite growing research interest, the development of potent, selective, and clinically viable TLR8 antagonists remains challenging due to structural complexities of the receptor and the similarity of its ligand-binding domains to related TLRs, notably TLR7.

The objective of this research was to discover and characterize new molecular scaffolds capable of acting as potent, selective, and bioavailable antagonists of TLR8, with proven functional inhibition in human immune cell models. To achieve this, a three-dimensional pharmacophore model was constructed by analyzing multiple crystal structures and identifying conserved interactions essential for effective antagonism. Virtual screening of a library of 2.7 million compounds and subsequent molecular docking identified 42 hits. Among these, the isoxazole scaffold was prioritized due to its novelty and predicted fit within the antagonist binding pocket.

Initial screening in hTLR8-transfected HEK293 reporter cells identified compounds 10 and 12 as lead molecules with submicromolar IC_{50} values for TLR8 inhibition, matching the potency of the clinical-stage dual TLR7/8 antagonist enpatoran.[121,137] Cytotoxicity assays confirmed favorable safety profiles for lead compounds over a wide concentration range in various cell lines. Selectivity assessments demonstrated a strong preference for TLR8 over other TLR family members, notably showing minimal affinity towards TLR7, highlighting the precision of antagonism achieved. Functionally, our study links TLR8 antagonism of compound 10 to the reduction of inflammasome-associated cytokine release by interfering with TLR8-dependent priming rather than directly blocking inflammasome assembly. This was further confirmed

when cells were primed with TLR8 agonist TL8-506 and subsequently challenged with canonical inflammasome activators. Compound 10 reduced IL-1β production without affecting cell viability, suggesting selective inhibition of the TLR8 priming pathway rather than non-specific cytotoxicity or direct inflammasome blockade. Western blot analysis of downstream signaling components provided mechanistic confirmation. Compound 10 blocked stimulus-induced phosphorylation of the NF-κB subunit p65 and prevented IκBα degradation, demonstrating effective inhibition of the canonical TLR8-mediated NF-κB pathway.

Pharmacological characterization via Schild analysis confirmed competitive antagonism at the TLR8 agonist binding site. This orthosteric mechanism was experimentally validated through site-directed mutagenesis studies: mutations disrupting the predicted binding pocket prevented both agonist activation and antagonist sensitivity, while aromatic substitution preserved agonist responsiveness and maintained antagonist susceptibility. Co-immunoprecipitation (co-IP) experiments showed reduced MyD88 recruitment to TLR8 in the presence of compound 10, representing the first direct evidence of this mechanism for a TLR8 antagonist. Molecular docking and molecular dynamics simulations provided structural support for these experimental findings. Dynamic mass redistribution (DMR) assays confirmed selective TLR8 inhibition, with compound 10 suppressing TLR8 signaling while other TLR responses remained intact.

The following insights were gained from this research paper:

(1) Discovery of a novel isoxazole-based scaffold, compound 10, that selectively antagonizes human TLR8 in nanomolar range without cross-inhibiting other TLRs and high selectivity over TLR7.
(2) Identification of Gly351, Val378, Phe495, and Ala518 as crucial residues that shape antagonist binding and guide SAR optimization strategies.
(3) Pharmacological proof-of-concept in both immortalized and primary human immune cells, showing TNF suppression without off-target effects on other TLRs.
(4) Selective blockade of TLR8-dependent priming, which inhibited subsequent IL-1β release following canonical inflammasome activation.
(5) Mutagenesis validation of key binding pocket residues and confirmation of competitive binding through Schild analysis.
(6) Mechanism of action at the uridine-binding site, demonstrated through co-IP experiments, effectively blocking MyD88 recruitment and downstream NF-κB/IRF activation.

The integration of crystallographic data, computational modeling, chemical synthesis, and functional pharmacology demonstrates an effective interdisciplinary approach for challenging targets like TLR8. This study expands the repertoire of TLR8-targeted molecules and establishes a comprehensive way of rational drug design that may be applicable to other pattern recognition receptors.

4.2 Author contribution

Within this project, I was the experimental and investigative lead for all biological assays and performed all biological experiments, except the DMR. I designed the biological experiments in close collaboration with the medicinal chemistry team, supported structure–activity relationship interpretation through biological data analysis, and prepared all figures and tables concerning biological data. I contributed equally to writing and revising the manuscript with the co-author and all corresponding authors.

Chapter 5

Design, synthesis and biological evaluation of novel pyrimidine and quinazoline-based small-molecule Toll-like receptor 8 antagonists

Troy Matziol[1#], Valerij Talagayev[2#], Nika Strašek Benedik[3], Paula von Kempis[1], Tjaša Slokan[3], Janine Holze[1], Günther Weindl[1], Gerhard Wolber[2], Matej Sova[3]

[#]Troy Matziol and Valerij Talagayev contributed equally to this work.

Chapter 5 was written by Troy Matziol and revised by Günther Weindl, Matej Sova and Gerhard Wolber. The parts of Chapter 5 covering molecular modeling were written and revised by Valerij Talagayev and Gerhard Wolber. The parts of Chapter 5 covering molecular design, synthesis and preparation of compounds were written and revised by Tjaša Slokan and Matej Sova. Gerhard Wolber and Matej Sova kindly provided compounds and reagents.

[1] University of Bonn, Pharmaceutical Institute, Pharmacology and Toxicology Section, Gerhard-Domagk-Str. 3, 53121 Bonn, Germany

[2] Freie Universität Berlin, Institute of Pharmacy, Pharmaceutical and Medicinal Chemistry, Königin-Luise-Str. 2+4, 14195 Berlin, Germany

[3] University of Ljubljana, Faculty of Pharmacy, The Department of Pharmaceutical Chemistry, Aškerčeva 7, SI-1000 Ljubljana, Slovenia

Please refer to Appendix IV for supporting information.

5.1 Introduction

Toll-like receptors (TLRs) are type I integral membrane glycoproteins that play a central role in innate immunity.[5] As a family of pattern-recognition receptors in mammals they recognize chemically diverse microbial structures known as pathogen-associated molecular patterns (PAMPs), as well as molecules derived from damaged cells known as damage-associated molecular patterns (DAMPs).[10,138] After ligand binding, recruitment of adaptor proteins such as MyD88 triggers proinflammatory signaling cascades leading to activation of the transcription factor nuclear factor-kappaB (NF-κB), which regulates the induction of proinflammatory cytokines and chemokines.[78] In humans, ten different types of TLRs have been identified. These are located either on the cell membrane (TLRs 1, 2, 4, 5, 6 and 10) or within endosomal compartments (TLRs 3, 7, 8 and 9).[48] Endosomal TLRs recognize nucleic acids from pathogens or damaged host cells, such as double-stranded RNAs (TLR3), single-stranded RNAs (TLR7

and TLR8) or single-stranded DNAs (TLR9).[53] Therefore, they have been implicated in the immune response following viral infection as well as the pathogenesis of various inflammatory and autoimmune diseases.[139–141] TLR8 in particular is associated with the development of systemic lupus erythematosus (SLE),[142] rheumatoid arthritis[100] and psoriasis.[101] Targeting TLR8 with antagonists has therefore been investigated as a potential strategy to attenuate cytokine production and alleviate the symptoms of these autoimmune diseases.[143]

Several chemotypes of TLR8 inhibitors have been reported in recent years,[6,66,136,143] however, none has reached the market so far. There are many challenges associated with the development of novel TLR8 modulators. The first is the absence of suitable rodent models, as TLR8 is nonfunctional in both mice and rats.[70,95] Consequently, the role of TLR8 in murine physiology is not well established, resulting in limited disease model data that could clarify its involvement in autoimmunity.[144] Additionally, some TLR ligands suffer from suboptimal pharmacokinetic properties, such as short half-lives and poor bioavailability.[145] Finally, achieving receptor selectivity within the structurally homologous Toll-like receptor family remains one of the principal challenges in the design and development of TLR8 inhibitors.[146] The selectivity issue is particularly evident for TLR7 and TLR8, which share substantial sequence and structural similarity as well as overlapping ligand recognition profiles – both are able to bind single-stranded RNA and nonselective small-molecule ligands.[63] As a result, many dual TLR7/8 antagonists have been reported in recent years.[8,147] Notably, enpatoran (M5049),[137,144,148,149] afimetoran (BMS-986256),[123] E6742,[122,150] and MHV370[151–153] are TLR7/8 dual antagonists in clinical development for the treatment of COVID-19 pneumonia, SLE or other systemic autoimmune diseases. More recently, KBD4466[154] has been reported as a potent TLR7/8 inhibitor demonstrating therapeutic efficacy in an SLE animal model. Structure-based rational design has also enabled the discovery of SMU-39, a potent TLR7/8 antagonist that effectively ameliorated psoriasis in mice and exhibited no signs of systemic toxicity.[155] Two additional compounds, ETI41 and ETI60, exhibited potent inhibition of endosomal TLR-mediated proinflammatory signaling, displaying nanomolar potency across cellular, biophysical, and *in vivo* assays.[156] Despite these advances, only a few small-molecule ligands show selective inhibition of TLR8, including the 1,2,4-triazole derivative TH-1027 (**1**),[157] the pyrazolo[1,5-a]pyrimidine derivative CU-CPT8m (**2**),[95] the quinoline derivative CU-CPT9a (**3**),[146] the 6-(trifluoromethyl)pyrimidin-2-amine derivative **4**,[136] and the isoxazole derivative **5**[158] (Figure 5). For the reasons outlined above, there is a strong need to develop new chemotypes of selective TLR8 antagonists.

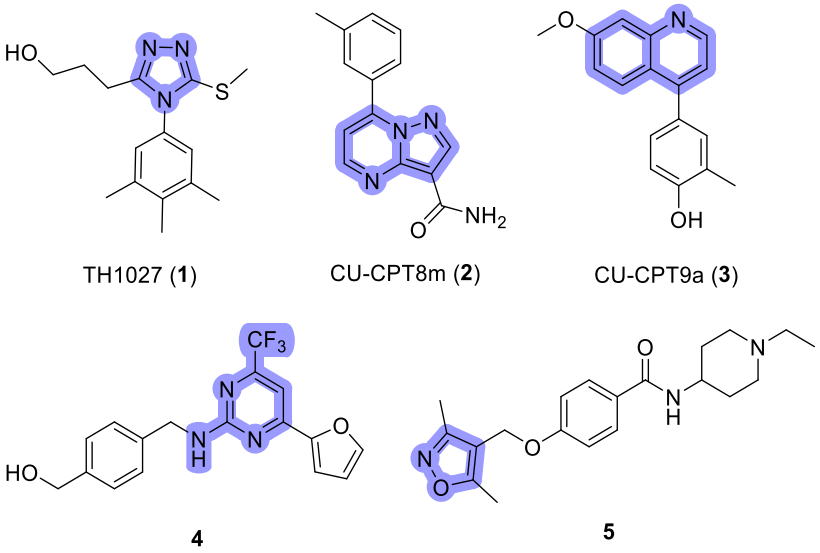

Figure 5. Structures of selective TLR8 antagonists. The main scaffolds are highlighted in purple.

In this study, novel selective TLR8 antagonists were identified through *in silico* design. Previously, isoxazole-based antagonists, which targeted the uridine binding site at TLR8 homodimer interface (Figure 6A) and showed inhibition in the nanomolar range, were discovered.[158] The isoxazole-containing compounds consisted of three key components: (i) an isoxazole scaffold that interacted with the backbone amide of Gly351, (ii) a linker containing a positively charged nitrogen that formed an ionic interaction with Glu427, and (iii) a variable rest that differed among the synthesized compounds (Figure 6B).

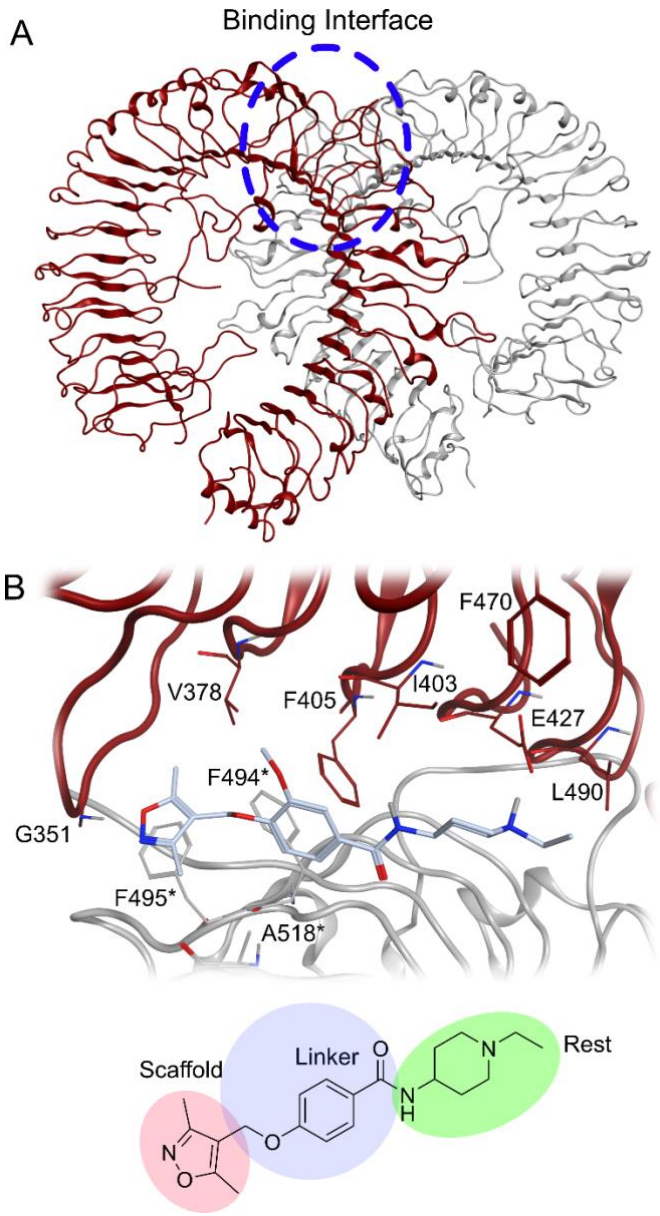

Figure 6. TLR8 protein structure. (A) TLR8 homodimer protein structure with the uridine binding site. (B) Binding mode of the most potent isoxazole-based TLR8 antagonist identified in previous study[158] consisting of a scaffold, linker and rest. Color code: brown and grey ribbons and atoms, TLR8 protein structure; light blue atoms, isoxazole-based TLR8 antagonist.

Our approach focused on replacing the isoxazole scaffold with a pyrimidine scaffold, previously identified as a key component for TLR8 inhibition.[136,146] By retaining the linker to preserve critical interactions, this modification aimed to enhance antagonist potency. Using this strategy, pyrimidine-based TLR8 antagonists with diverse substituents attached to the amide group were designed (Figure 7).

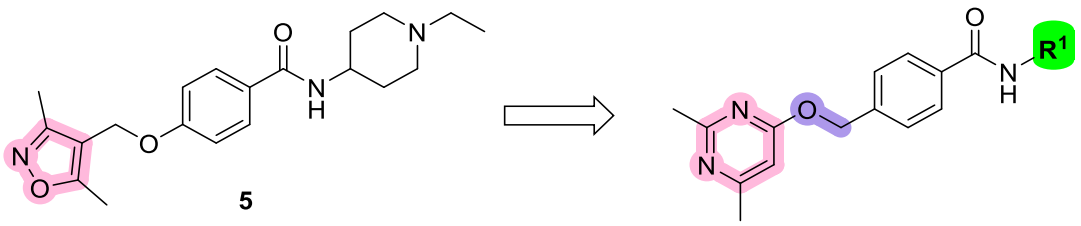

Figure 7. Design of a pyrimidine-based TLR8 antagonist from isoxazole derivative **5**. The scaffolds are highlighted in pink, and the structural changes are shown in purple and green.

5.2 Results and discussion

5.2.1 Design, synthesis, and initial biological evaluation of pyrimidine-based TLR8 antagonists

We used our in-house library of building blocks containing a primary amine for a nucleophilic substitution, along with an additional amine necessary for ionic interactions. These building blocks were used to replace the ethylpiperidine-4-yl rest present in isoxazole derivative **5** to create a database of pyrimidine-based TLR8 antagonists. The molecules in this database were subjected to computational molecular docking studies to determine their binding modes within the uridine binding site of TLR8 (Table S1). The predicted binding modes were evaluated based on key protein-ligand interactions, specifically the hydrogen bond between the pyrimidine nitrogen and the backbone amine of Gly351, and the ionic interaction between the protonated amine and the side chain of Glu427. Additionally, we assessed the structural and conformational integrity of the binding modes. Based on these criteria, we selected 13 molecules (compounds **9**–**17**, **20**–**23**) with promising binding profiles for synthesis and experimental validation.

The synthesis started with methyl 4-(hydroxymethyl)benzoate (**6**) (Scheme 1). Nucleophilic substitution with 4-chloro-2,6-dimethylpyrimidine afforded methyl 4-(((2,6-dimethylpyrimidin-4-yl)oxy)methyl)benzoate (**7**), which was hydrolyzed in the presence of 1 M NaOH to yield carboxylic acid **8**. The coupling reaction using **8**, HATU and the appropriate amine provided amides **9**–**17**. Similarly, *tert*-butyl 4-(4-(((2,6-dimethylpyrimidin-4-yl)oxy)methyl)benzamido)piperidine-1-carboxylate (**9**) was obtained by a coupling reaction using **8**, HATU and *tert*-butyl 4-aminopiperidine-1-carboxylate. The Boc protecting group was then removed with trifluoroacetic acid and the resulting piperidine derivative **19** was alkylated with the corresponding alkyl bromide to yield final compounds **20**–**23**.

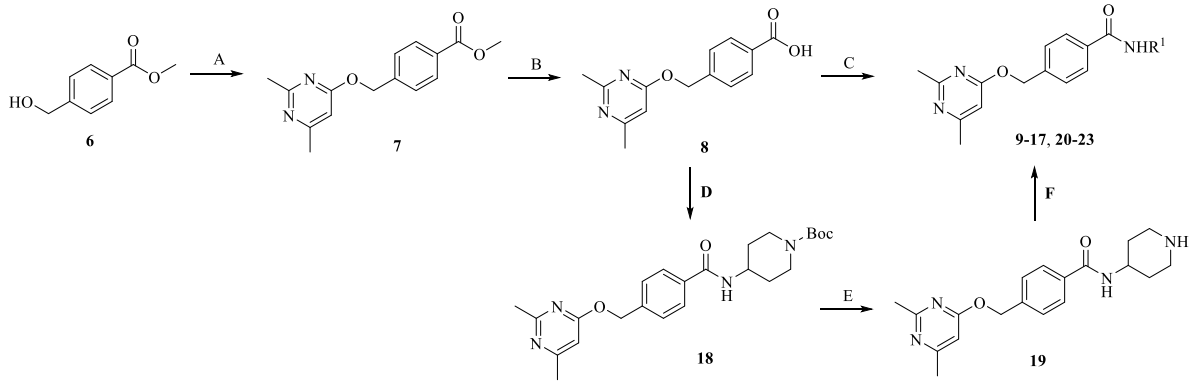

Scheme 1. Synthesis of pyrimidine-based compounds **9**–**17** and **20**–**23**. Reagents and conditions: (A) NaH, 4-chloro-2,6-dimethylpyrimidine, DMF, 60 °C, 6 h, then room temperature (rt) overnight; (B) 1 M NaOH, 1,4-dioxane, rt, 24 h; (C) HATU, amine (R^1NH_2), DIPEA, THF, rt, 24 h; (D) HATU, *tert*-butyl 4-aminopiperidine-1-carboxylate, DIPEA, THF, rt, 24 h; (E) TFA, DCM, rt, 24 h; (F) alkyl bromide, K_2CO_3, KI, acetonitrile, reflux, 2 h.

To validate the *in silico* predictions, compounds **9**–**17**, **20**–**23** were screened using HEK293 reporter cells expressing hTLR8.[135,136,158–160] All tested candidates showed strong inhibition of TLR8-mediated NF-κB signaling, with at least 80% inhibition at 10 μM (Figure S1A and Table 1). MTT assay results confirmed no significant cytotoxic effects at concentrations up to 50 μM, and no agonistic activity was observed at either 10 or 25 μM (Figure S1B, C). The most promising candidates, demonstrating at least 90% inhibition at 10 μM in hTLR8-HEK293 reporter cells, were selected for IC_{50} analysis (Figure S2, Table 1). All tested compounds showed IC_{50} values around 1 μM, with compound **16** demonstrating the most potent inhibitory activity, with an IC_{50} of 0.3 μM against the TLR8-selective agonist TL8-506, outperforming our previously reported isoxazole-based antagonists.[158] Furthermore, no cytotoxic effects were observed in hTLR8-HEK293 cells at concentrations up to 100 μM (Figure S3).

Table 1. Inhibition of TL8-506-stimulated TLR8-dependent NF-κB activity and IC_{50} values of compounds **9**–**17** and **20**–**23** in hTLR8-HEK293 reporter cells. Normalized percent inhibition data are mean ± SEM of three to four independent experiments. One-sample *t*-test vs. 100% NF-κB activity. ***P ≤ 0.001, ****P ≤ 0.0001. n.d., not determined. IC_{50} values were derived from concentration-response curves (Figure S2). Data are mean of four independent experiments with 95% CI in parentheses.

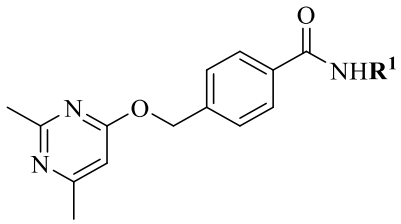

Compound	Amine (R^1NH_2)	% inhibition at 10 µM ± SEM hTLR8-HEK293	IC_{50} [µM] (95% CI) hTLR8-HEK293
9	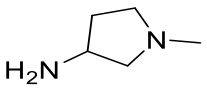	97 ± 0.4****	2.73 (2.23–3.31)
10	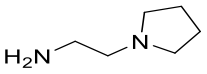	80 ± 2***	n.d.
11	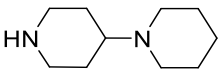	86 ± 1****	n.d.
12	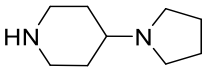	84 ± 1***	n.d.
13	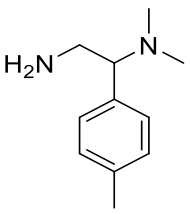	93 ± 1****	2.10 (1.53–2.83)
14	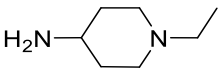	100 ± 0.2****	1.17 (1.02–1.35)
15	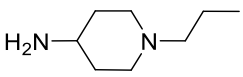	98 ± 0.5****	0.575 (0.350–0.884)
16	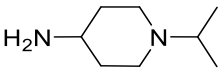	100 ± 0.3****	0.300 (0.162–0.494)

17	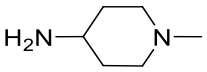	95 ± 2****	1.11 (0.662–1.76)
20	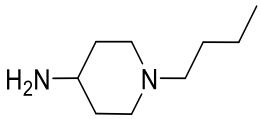	98 ± 1****	1.08 (0.633–1.81)
21	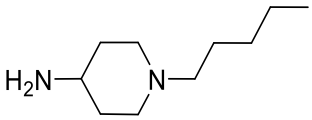	97 ± 1****	2.11 (1.75–2.53)
22	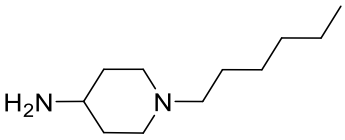	95 ± 2****	2.04 (1.73–2.38)
23	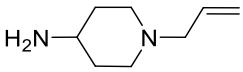	100 ± 0.2****	0.693 (0.441–1.04)

5.2.2 Structure–activity relationships and molecular dynamics of pyrimidine-based TLR8 antagonists

The first synthesized compound was derivative **9**, which has 1-methylpyrrolidin-3-amine attached to the main scaffold via the amide bond. It showed TLR8 antagonist activity in the low micromolar range (IC_{50} of 2.73 μM). When a linker is present between the amino group and the pyrrolidine ring (compound **10**), the activity is lost. Similarly, the introduction of 1,4'-bipiperidine or 4-(pyrrolidin-1-yl)piperidine leads to the inactive compounds **11** and **12**, respectively**.** Based on the active isoxazole derivative **5** from our previous study,[158] we synthesized *N*-(2-(dimethylamino)-2-(*p*-tolyl)ethyl)-4-(((2,6-dimethylpyrimidin-4-yl)oxy)methyl)benzamide (**13**), which has fourfold lower potency compared to the parent compound. The most optimal substitution for TLR8 antagonist activity was 1-alkylpiperidin-4-amine with the length of the alkyl substituent playing an important role for potency. Shorter (methyl in **17** and ethyl in **14**) and longer substituents (butyl, pentyl or hexyl as in **20**, **21** and **22**, respectively) than propyl (compound **15**) resulted in derivatives with lower potencies. When propyl was replaced by an allyl substituent (compound **23**), the IC_{50} value remained in the

nanomolar range. Finally, the most potent pyrimidine derivative (IC_{50} of 0.3 μM) was compound **16** with the branched substituent isopropyl.

Comparison of the binding hypotheses for compounds **15**, **16**, and **23** reveals that all three form a hydrogen bond between the nitrogen N1 of the pyrimidine ring and the backbone amine of Gly351. The methyl groups make hydrophobic contacts with the side chains of residues Lys350, Val378, Phe494* and Phe495*, with the asterisk indicating the chain B of the homodimer. The phenyl ring of **15**, **16**, and **23** establishes hydrophobic contacts with I403 and A518*, while the amine group of the piperidine ring forms an ionic interaction with Glu427. The main difference between these compounds lies in the hydrophobic interactions formed by the groups attached to the piperidine ring. The propyl group of **15** forms hydrophobic contacts with Phe346 and Phe470, while the isopropyl group of **16** interacts only with Leu490. The allyl rest of **23** shows a hydrophobic contact with Phe470. These observations suggest that the isopropyl group is more favorable for potency, likely due to its interaction with Leu490 (Figure 8).

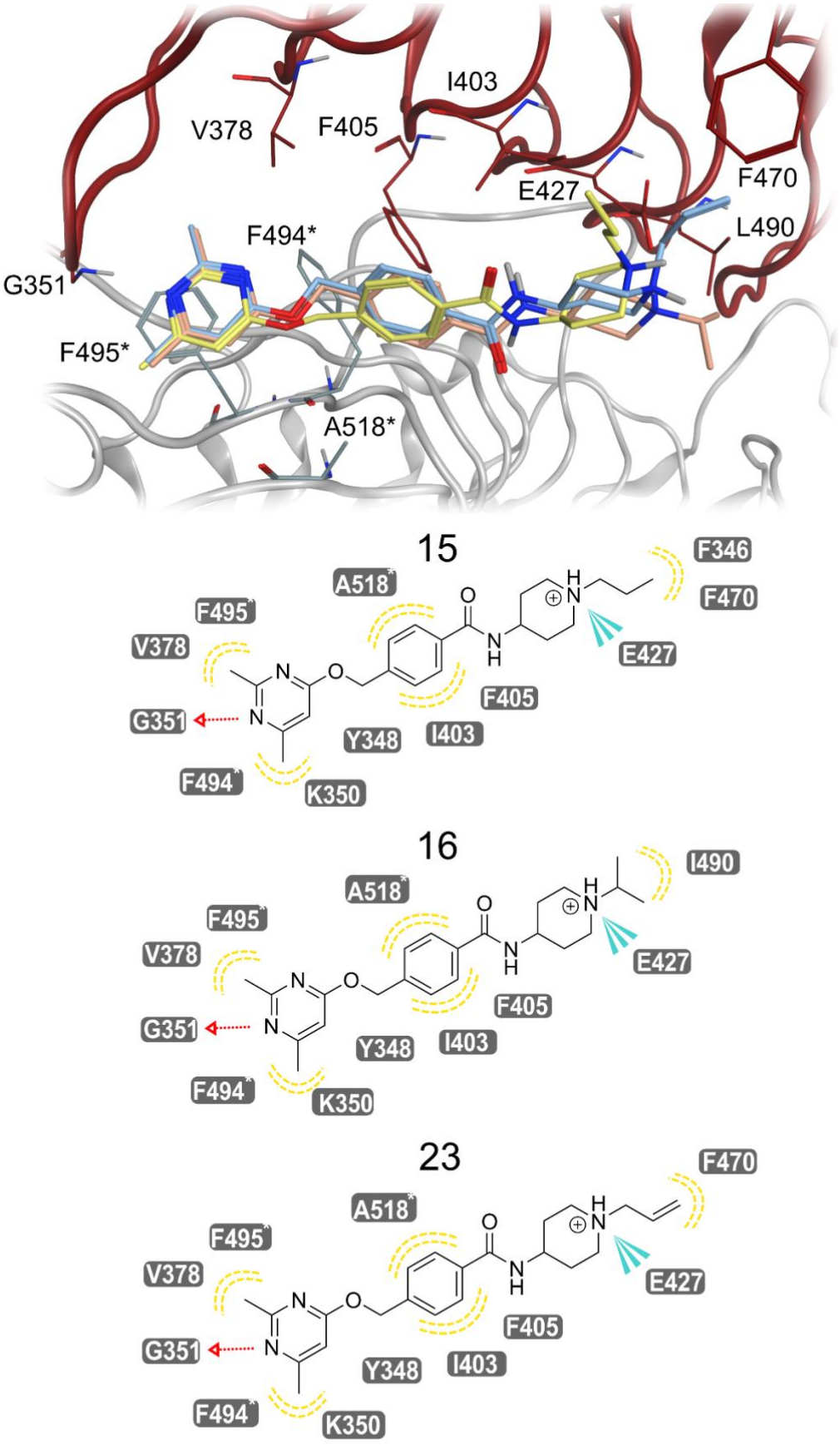
I403
V378
F405
F470
E427
L490
F494*
G351
F495*
A518*
15
F346
A518*
F470
F495*
V378
E427
F405
G351
Y348
I403
F494*
K350
16
I490
A518*
F495*
V378
E427
F405
G351
Y348
I403
F494*
K350
23
F470
A518*
F495*
V378
E427
F405
G351
Y348
I403
F494*
K350
Hydrophobic
Hydrogen bond acceptor
Positive ionizable

Figure 8. 3D and 2D representations of the binding hypothesis for compounds **15**, **16** and **23**. These compounds show identical interactions except for the substituent located on the piperidine ring, which shows a hydrophobic contact with Phe346 and Phe470 in compound **15**, with Leu490 in compound **16** and with Phe470 in compound **23**. Compound **16** shows higher inhibitory potency, indicating that interaction with Leu490 is preferred for TLR8 inhibition. The asterisk denotes chain B. Color code: brown and gray ribbons and atoms, TLR8 protein structure (PDB ID: 6V9U); yellow molecule, compound **15**; pink molecule, compound **16**; light blue molecule, compound **23**.

To further investigate the interactions of compounds **15**, **16** and **23**, molecular dynamics simulations were performed. The trajectories of the simulations were analyzed using the OpenMMDL Analysis part of the OpenMMDL workflow,[161] which analyzes the frequency of interactions of the protein with the ligands throughout the trajectories of the simulations, with the methodology incorporating the concept of Dynophores, employed in our previous studies.[136,158,162] The analysis shows that the hydrogen bond interaction between the backbone of Gly351 and the pyrimidine nitrogen is present in 98–99% of the simulation duration for compounds **15**, **16** and **23**. The methyl groups on the pyrimidine ring show hydrophobic contacts in 73–94% of the trajectory. The phenyl ring maintains hydrophobic contacts in 97–98% of the simulation duration. The piperidine amine maintains an ionic interaction with the side chain of Glu427 in 98% of the frames during the simulation with compound **15**, 89% of the frames during the simulation with compound **16** and 11% of the frames during the simulation with compound **23**. This interaction potentially affects the inhibition potency of compound **23**. The propyl group of **15** shows hydrophobic contacts in 46% of the simulation frames, while the ethyl group of **23** shows hydrophobic contacts in 38% of the frames. The methyl groups of the isopropyl in **16** show hydrophobic contacts during 23% and 35% of the simulation respectively (Table S2–S4). Additionally, the root mean square deviation (RMSD) was calculated for simulations of compounds **15**, **16** and **23**. The average RMSD for simulations of **15**, **16** and **23** was 2.78 Å, 2.54 Å and 3.58 Å, respectively (Figure S4–S6).

5.2.3 Optimization of the pyrimidine scaffold toward potent quinazoline derivative 35

To evaluate the importance of methyl groups on the pyrimidine ring, three additional compounds **30**, **31** and **32** were synthesized (Scheme 2 and Table 2). Removal of the methyl groups (compound **30**) results in approximately 7-fold lower potency compared with **16**.

Introduction of a methyl group at position 6 of the pyrimidine ring (compound **32**) does not improve potency, whereas the presence of a methyl group at position 2 increases potency, indicating that this substitution is important for potent antagonistic activity on TLR8. In the next step, compounds in which benzene or cyclopentane was fused to the 2-methylpyrimidine ring were synthesized to obtain quinazoline and 6,7-dihydro-5H-cyclopenta[d]pyrimidine derivatives **35** and **38**, respectively (Scheme 2 and Table 2). Both modifications enhanced potency, with quinazoline derivative **35** identified as the most potent TLR8 antagonist, with an IC_{50} value in the low nanomolar range, resulting in approximately 10-fold greater potency compared to **16** (Table 1 and 2).

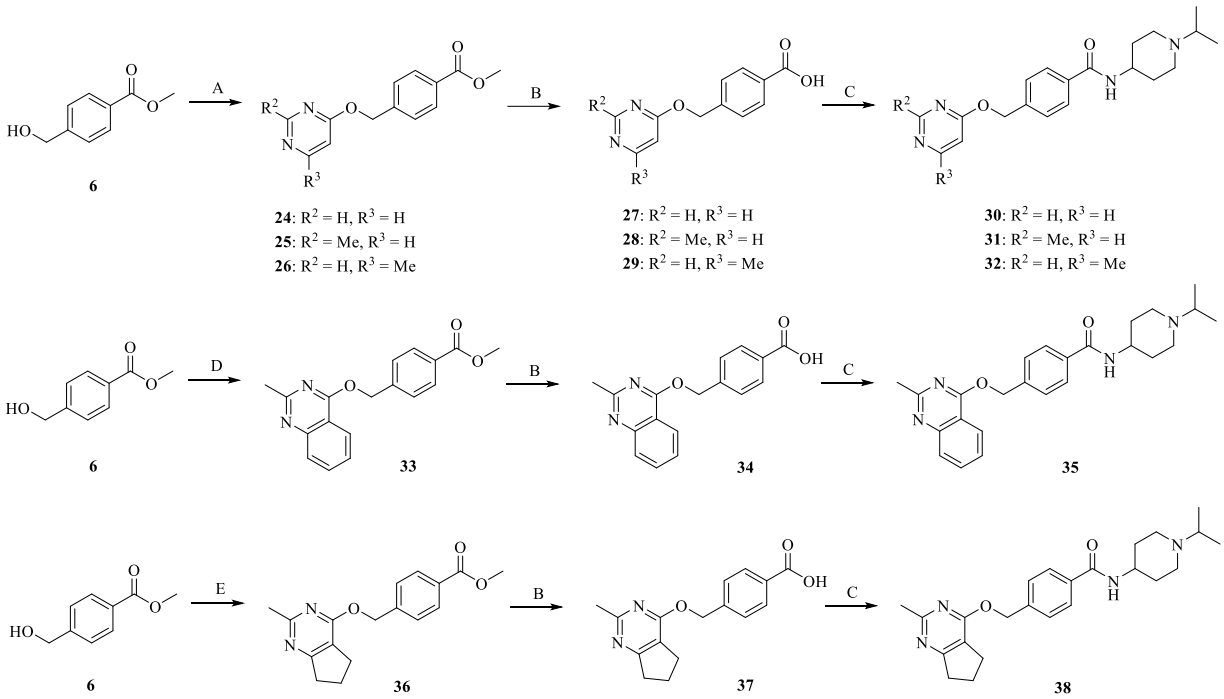

Scheme 2. Synthesis of compounds **30**–**32**, **35** and **38.** Reagents and conditions: (A) NaH, appropriate 4-chloropyrimidine, anhydrous THF or DMF, 60 °C for 4 h or 24 h at rt; (B) 1 M NaOH, 1,4-dioxane, rt, 24 h; (C) HATU, DIPEA, 1-isopropylpiperidin-4-amine, THF, rt, 24 h; (D) NaH, 4-chloro-2-methylquinazoline, anhydrous DMF, rt, 24h; (E) NaH, 4-chloro-2-methyl-6,7-dihydro-5H-cyclopenta[d]pyrimidine, anhydrous DMF, rt, 24 h.

Table 2. Inhibition of TL8-506-stimulated TLR8-dependent NF-κB activity and IC_{50} values of compounds **30**–**32**, **35** and **38** in hTLR8-HEK293 reporter cells. Normalized percent inhibition data are mean ± SEM of three or four independent experiments. One-sample *t*-test vs. 100% NF-κB activity. ***P ≤ 0.001, ****P ≤ 0.0001. IC_{50} values were derived from concentration-

response curves (Figure S2). Data are mean of four independent experiments with 95% CI in parentheses.

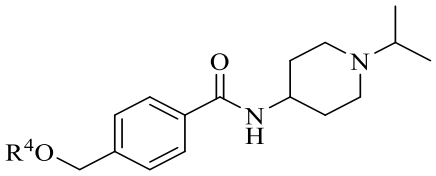

Compound	R^4	% inhibition at 10 µM ± SEM hTLR8-HEK293	IC_{50} [µM] (95% CI) hTLR8-HEK293
30	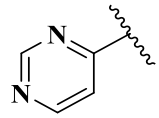	98 ± 0.5****	1.98 (1.33–3.41)
31	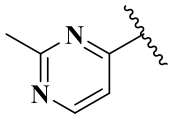	100 ± 0.4***	0.50 (0.36–0.69)
32	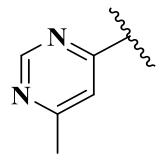	96 ± 1****	3.23 (2.11–6.22)
35	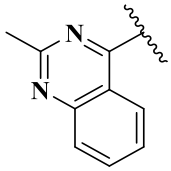	100 ± 0.2****	0.032 (0.015–0.052)
38	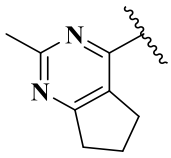	100 ± 0.3***	0.160 (0.083–0.260)

The binding hypotheses for compounds **35** and **38** indicate that both compounds form a hydrogen bond interaction between the nitrogen N1 of the pyrimidine ring and the backbone amide of Gly351. The methyl group makes hydrophobic contacts with the side chains of Tyr348, Val378 and Phe494* in both compounds. The phenyl ring of **35** and the cyclopentane ring of **38** establish hydrophobic contacts with the side chain of Lys350. A π-stacking interaction is observed between the pyrimidine ring and the side chain of Phe494* in both **35** and **38**. The phenyl ring of both compounds **35** and **38** forms hydrophobic contacts with Ile403, Phe405 and Ala518*. The amine of the piperidine ring forms an ionic interaction with the side chain of Glu427 in both **35** and **38,** and the isopropyl group makes a hydrophobic contact with the side chain of Leu490 (Figure 9). The presence of a bicyclic ring scaffold, such as the quinazoline scaffold in compound **35**, results in an additional π-stacking interaction with Phe494*. This interaction is absent in compounds **15** and **16**. The presence or absence of this interaction affects inhibition potency, with compound **35** displaying higher inhibitory potency than compounds **15** and **16**.

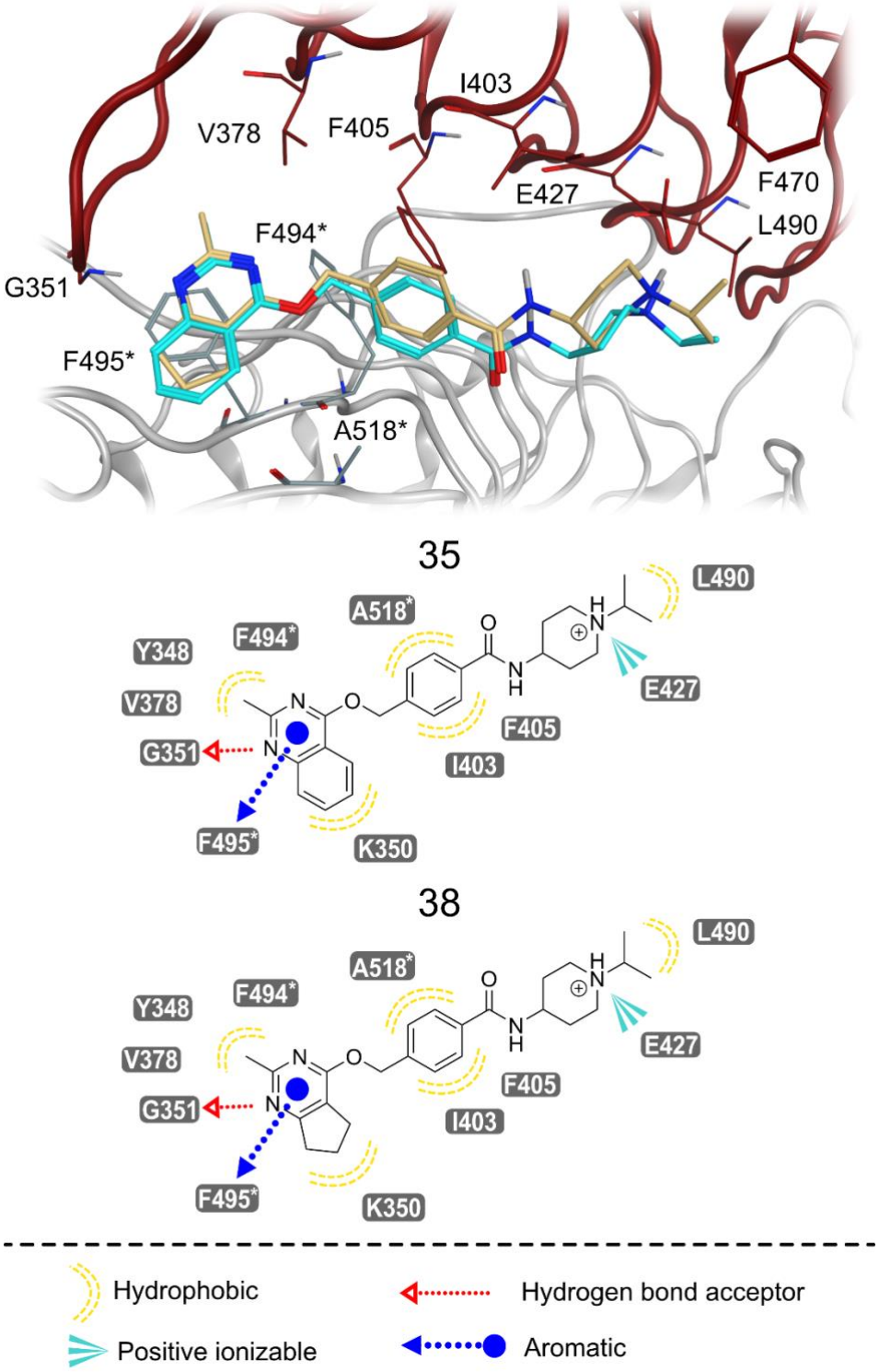

Figure 9. 3D and 2D representations of the binding hypothesis for compounds **35** and **38**. Both compounds show identical interactions in the binding site interface of TLR8 and display an aromatic interaction between the pyrimidine ring and Phe495* that is not present in the binding hypothesis for compounds **15**, **16** and **23**. The asterisk denotes chain B. Color code: brown and gray ribbons and atoms, TLR8 protein structure (PDB ID: 6V9U); turquoise molecule, compound **35**; light brown molecule, compound **38**.

To further evaluate the binding hypothesis for **35** and **38** MD simulations were performed and the previously described OpenMMDL Analysis part of the OpenMMDL workflow was used to calculate protein-ligand interaction frequencies. The analysis showed that the nitrogen N1 of the pyrimidine ring in **35** and **38** forms hydrogen bond interactions with the backbone amine of Gly351 in 95% and 99% of the frames during the simulation, respectively. The pyrimidine ring shows hydrophobic contacts in 52–55% of the simulation duration, while the methyl group shows hydrophobic contacts in 94–96% of the frames. The phenyl ring maintains interactions in 98% of the simulation duration. The carbamide oxygen forms a hydrogen bond in 16–20% of the simulation frames, while the piperidine amine maintains an ionic interaction with the side chain of Glu427 in 91–92% of the simulation duration. Both methyl groups of the isopropyl form hydrophobic contacts in 14–16% and 23–28% of the simulation respectively. The main noticeable difference between **35** and **38** is the frequency of aromatic interactions formed by the pyrimidine ring. The pyrimidine ring of **35** forms an aromatic interaction in 66% of the frames, while the pyrimidine ring of **38** only forms an aromatic interaction in 35% of the frames, highlighting the importance of the aromatic interaction of the pyrimidine ring for potency (Table S5, S6). RMSD values were calculated for **35** and **38** during the simulations. The average RMSD for **35** was 3.48 Å, while the average RMSD for **38** was 3.16 Å (Figure S7, S8).

5.2.4 Biological characterization of compounds 16 and 35 as selective TLR8 antagonists

Since compound **16** was identified as the most potent antagonist from the first series, its TLR selectivity across a panel of TLR ligands targeting TLR2/1, TLR2/6, TLR3, TLR4, TLR5, TLR7, TLR8, and TLR9 using HEK293 reporter cells was evaluated. The results confirmed high specificity of compound **16** for hTLR8, with no significant inhibition of other TLRs (Figure 10A). Given the high structural similarity between TLR8 and TLR7, IC_{50} analysis was performed in hTLR7-expressing cells (Figure S9A), revealing a significantly higher IC_{50} (29.8 µM) compared to hTLR8 (0.313 µM), corresponding to a selectivity factor exceeding 95-fold in favor of hTLR8.

To further validate the functional relevance of compound **16**, its inhibitory activity was assessed in THP-1 macrophages and human peripheral mononuclear blood cells (PBMCs), representing more physiologically relevant cells. Compound **16** demonstrated concentration-dependent inhibition of TNF secretion, with IC_{50} values of 0.232 µM (95% CI: 0.126–0.388 µM) in THP-1 macrophages and 0.849 µM (95% CI: 0.662–1.16 µM) in PBMCs (Figure 10B and Table 3). LDH assays confirmed the absence of cytotoxic effects up to 50 µM, the highest concentration

tested (Figure S10). When stimulated with TLR8 or TLR4 agonists in THP1-Dual MD2-CD14-TLR4 cells (hereafter referred to as THP-1 Dual cells), compound **16** selectively inhibited key downstream signaling pathways of TLR8, including NF-κB and IRF signaling, while having no effect on TLR4 activation (Figure 10C). Using label-free optical biosensor technology,[158,160] we confirmed that compound **16** inhibits TLR8-mediated cell responses. The concentration-effect curve for dynamic mass redistribution (DMR) signals (Figure 10D) showed an IC_{50} of 3.52 μM (95% CI: 1.76–6.67 μM) for compound **16** in TLR8-activated THP-1 Dual cells. These findings further highlight the efficacy of compound **16** in modulating pro-inflammatory pathways in relevant cellular contexts.

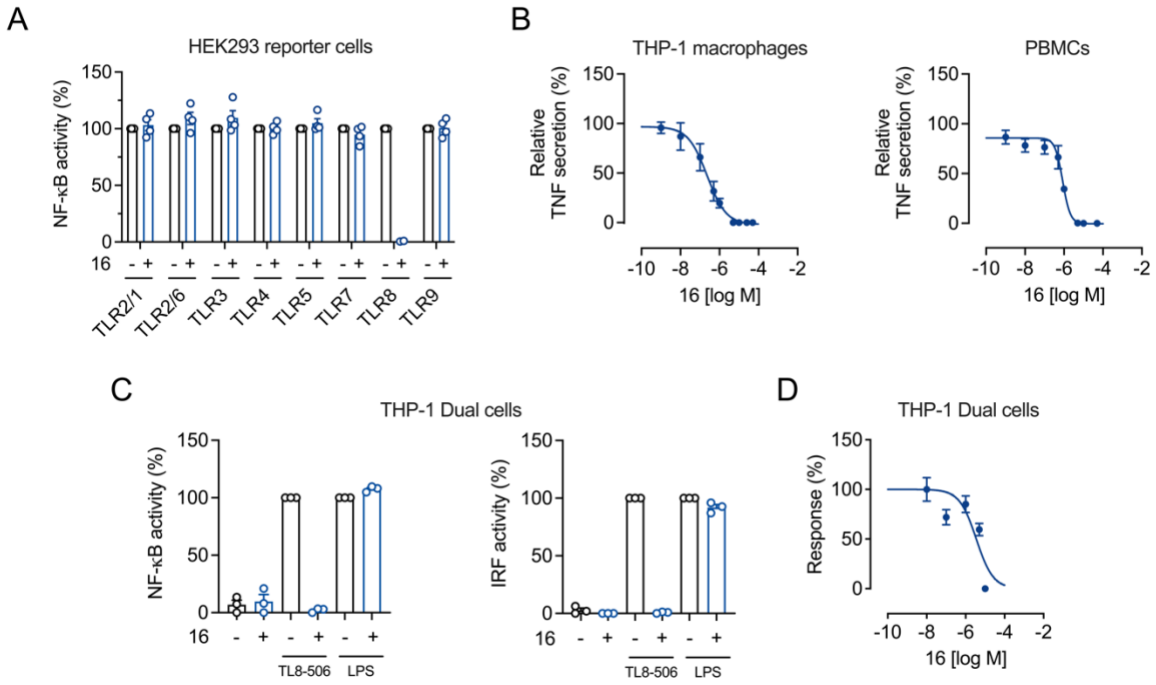

Figure 10. Compound **16** selectively inhibits TLR8-mediated inflammation and signaling. (A) hTLR-HEK293 reporter cells were preincubated with or without compound **16** (10 µM) for 1 h, and then stimulated with ligands for TLR2/1 (Pam_3CSK_4, 10 ng/mL), TLR2/6 (Pam_2CSK_4, 1 ng/mL), TLR3 (poly(I:C) HMW, 10 µg/mL), TLR4 (LPS *E. coli*, 10 ng/mL), TLR5 (flagellin, 100 ng/mL), TLR7 (CL307, 0.8 µM), TLR8 (TL8-506, 1.5 µM), or TLR9 (ODN2006, 5 µM). Supernatants were analyzed for TLR-mediated NF-κB activation by SEAP reporter assay using QuantiBlue (OD_{620}) and normalized to the respective TLR agonist alone. Data are presented as mean + SEM (n=3). (B) PBMCs or THP-1 macrophages were preincubated with increasing concentrations of compound **16** for 1 h and then stimulated with TL8-506 (0.6 µM) for 4 h. TNF release in the cell culture supernatants was determined by ELISA. For the calculation of the concentration-response curve nonlinear regression with variable slope (four parameters) was used. IC_{50} values are shown in Table 3. Data are mean ± SEM (n=3–4). (C) THP1-Dual MD2-CD14-TLR4 cells (THP-1 Dual cells) were preincubated with 10 µM of compound **16** for 1 h, and then stimulated with TL8-506 (6 µM) or LPS from *Escherichia coli* (*E. coli*) (10 ng/mL) for 24 h. Supernatants were analyzed for NF-κB activation by SEAP reporter assay using QuantiBlue (OD_{620}) or for IRF activation by Lucia luciferase using QuantiLuc. Data are mean + SEM (n=3). (D) Inhibitory concentration-response curves resulting from DMR traces. THP1-Dual MD2-CD14-TLR4 cells (THP-1 Dual cells) were preincubated with increasing concentrations of compound **16** for 1.5 h and then stimulated with TL8-506 (6 µM). For the calculation of the concentration-response curve nonlinear regression with variable slope (four

parameters) was used. The concentration-response curve was derived from DMR signals recorded at 250 min. Data are mean ± SEM (n=4).

Since compound **35** emerged as a highly potent antagonist from the third series, we next evaluated its TLR selectivity profile using a panel of TLR ligands in HEK293 reporter cells. Similar to compound **16**, compound **35** showed strong specificity for hTLR8, with no detectable inhibition of other TLRs (Figure 11A). To further assess selectivity, IC_{50} analysis was performed in hTLR7-expressing cells (Figure S9B). The IC_{50} value for hTLR7 was markedly higher (9.27 μM; 95% CI: 8.21–10.09 μM) compared with hTLR8 (0.032 μM; 95% CI: 0.015–0.052 μM), corresponding to a selectivity factor over 280-fold in favor of hTLR8.

Table 3. Potency (IC_{50}, μM) of compounds **16**, **35**, and **CU-CPT9a** in TLR8 reporter cells and immune cell assays. IC_{50} values were derived from concentration-response curves (Figure 10, 11, S2). Data are mean of four independent experiments with 95% CI in parentheses. For each cell type, the logIC_{50} values of compound **35** were compared to those of **CU-CPT9a**. *P ≤ 0.05, ***P ≤ 0.001, not significant (ns) = p >0.05.

Compound	**IC_{50} [μM] (95% CI)**		
	hTLR8-HEK293	**THP-1 macrophages**	**PBMCs**
16	0.300 (0.162–0.494)	0.232 (0.126–0.388)	0.849 (0.662–1.16)
35	0.032^{***} (0.015–0.052)	0.014^{ns} (0.009–0.022)	0.107^{*} (0.085–0.137)
CU-CPT9a	0.097 (0.067–0.119)	0.010 (0.003–0.028)	0.066 (0.045–0.091)

To assess its functional relevance in more physiologically representative systems, compound **35** was further tested in THP-1 macrophages and PBMCs. Compound **35** demonstrated concentration-dependent inhibition of TNF secretion, with IC_{50} values of 13.86 nM (95% CI: 9.26–22.08 nM) in THP-1 macrophages and 107.3 nM (95% CI: 84.73–136.7 nM) in PBMCs (Figure 11B and Table 3). The most potent TLR8 antagonist reported to date, **CU-CPT9a**[95,146], showed IC_{50} values of 10.05 nM (95% CI: 2.91–28.48 nM) in THP-1 macrophages and 66.56 nM (95% CI: 45.18–91.22 nM) in PBMCs, placing compound **35** within a comparable potency range (Figure 11C and Table 3). LDH release assays confirmed the absence of cytotoxicity up

to 50 µM (Figure S10). Further confirmation of TLR8 antagonism was obtained using label-free optical biosensor technology. In DMR assays using TLR8-stimulated THP-1 macrophages, **35** resulted in a concentration-dependent reduction in cellular responses, with an IC_{50} of 2.205 nM (95% CI: 0.175–27.79 nM), equipotent to **CU-CPT9a**, which demonstrated an IC_{50} of 0.436 nM (95% CI: 0.030–6.321 nM) (Figure 11D).

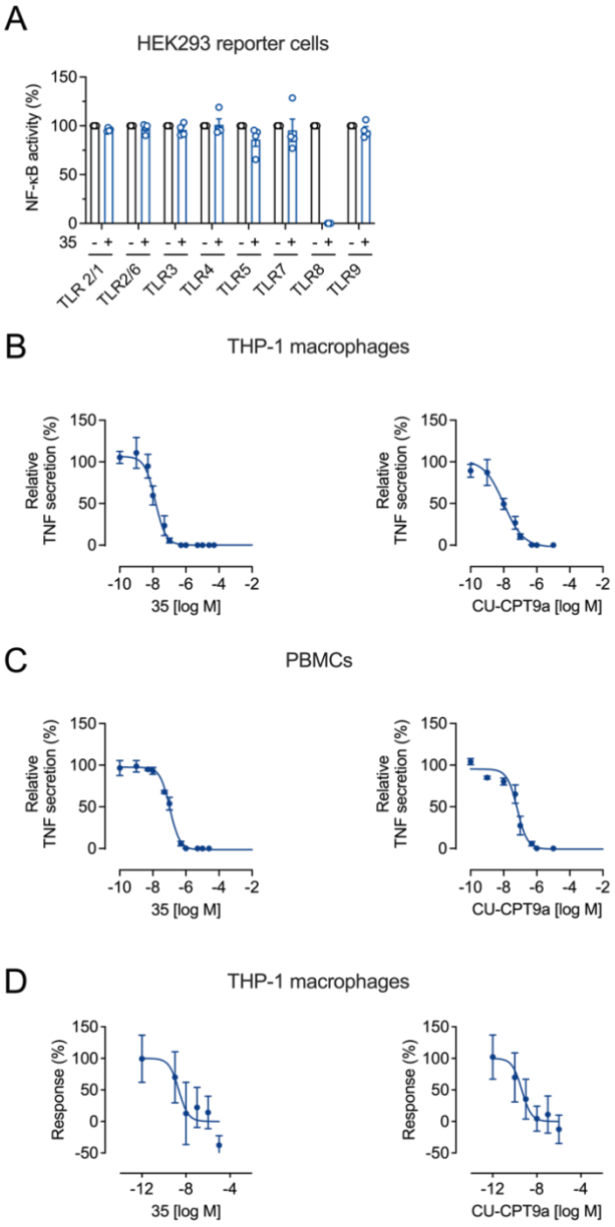

Figure 11. Compound **35** selectively inhibits TLR8-mediated inflammation and signaling. (A) hTLR-HEK293 reporter cells were preincubated with or without compound **35** (1 µM) for 1 h, and then stimulated with ligands for TLR2/1 (Pam_3CSK_4, 10 ng/mL), TLR2/6 (Pam_2CSK_4, 1 ng/mL), TLR3 (poly(I:C) HMW, 10 µg/mL), TLR4 (LPS *E. coli*, 10 ng/mL), TLR5 (flagellin, 100 ng/mL), TLR7 (CL307, 0.8 µM), TLR8 (TL8-506, 1.5 µM), or TLR9 (ODN2006, 5 µM). Supernatants were analyzed for TLR-mediated NF-κB activation by SEAP reporter assay using

QuantiBlue (OD_{620}) and normalized to the respective TLR agonist alone. Mean + SEM (n=4). (B) THP-1 macrophages or (C) PBMCs were preincubated with increasing concentrations of compound **35** or **CU-CPT9a** for 1 h and then stimulated with TL8-506 (0.6 μM) for 4 h. TNF release in the cell culture supernatants was determined by ELISA. For calculation of the concentration-response curve nonlinear regression with variable slope (four parameters) was used. IC_{50} values are shown in Table 3. Mean ± SEM (n=4). (D) Inhibitory concentration-response curves resulting from DMR traces. THP-1 macrophages were preincubated with increasing concentrations of compound **35** or **CU-CPT9a** for 1.5 h and then stimulated with TL8-506 (6 μM). For calculation of the concentration-response curve nonlinear regression with variable slope (four parameters) was used. The concentration-response curve was derived from DMR signals calculated from the area under the curve. Mean ± SEM (n=4–8).

5.2.5 Binding mode characterization of lead compound 35

Computational studies were performed to analyze the binding mode of compound **35**. Mutations at glycine 351 (G351P), valine 378 (V378M), and phenylalanine 495 (F495L*)[158] were introduced separately, and molecular docking studies with compound **35** were performed. The G351P mutation affects the protein backbone and prevents compound **35** from interacting with Gly351 leading to loss of activity (Figure 12A,B). The V378M mutation leads to an increase of the side chain size with the introduction of the methionine, thereby sterically restricting compound **35** from entering the binding site (Figure 12C,D), while the F495L* also causes steric hindrance due to the introduced L495* side chain being located closer to Gly351 and thus restricting the molecules from forming an interaction with the backbone of Gly351 (Figure 12E,F). To experimentally validate the *in silico* predictions for compound **35**, site-directed mutations were introduced into TLR8 and expressed in HEK293 cells.[158] Given the preserved activity of the F495L mutant, we investigated whether compound **35** or **CU-CPT9a** could access the TLR8 binding pocket. Both compound **35** and the reference antagonist **CU-CPT9a** nearly completely inhibited TL8-506-induced receptor activation (Figure 12G). Structural studies have shown that TLR8 agonists bind a defined pocket, and the crystal structure of **CU-CPT9a** confirms its engagement of the same site.[95] Taken together with our modeling data, these observations support the conclusion that compound **35** targets the same binding site as TL8-506 and **CU-CPT9a**, likely acting through direct competition with the agonist.

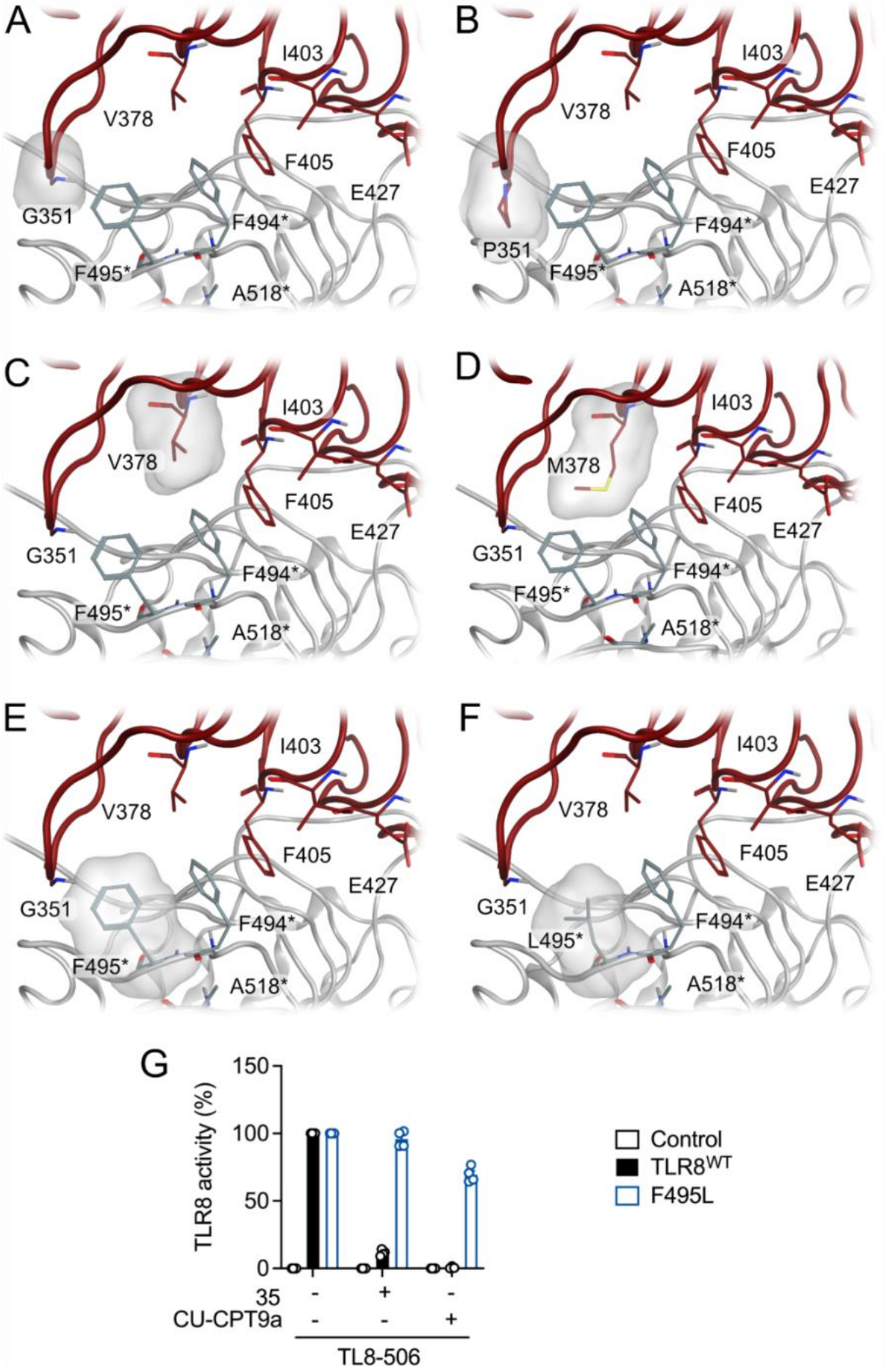
A
I403
V378
F405
E427
G351
F494*
F495*
A518*
B
I403
V378
F405
E427
P351
F494*
F495*
A518*
C
I403
V378
F405
E427
G351
F494*
F495*
A518*
D
I403
M378
F405
E427
G351
F494*
F495*
A518*
E
I403
V378
F405
E427
G351
F494*
F495*
A518*
F
I403
V378
F405
E427
G351
F494*
L495*
A518*
G
TLR8 activity (%)
150
100
50
0
35
CU-CPT9a
- - +
- + -
TL8-506
Control
TLR8WT
F495L

Figure 12. Compound **35** binds to the pocket of chemical ligands within the TLR8 dimerization interface. (A–F) Computational TLR8 binding site mutational studies. TLR8 binding site interface with the highlighted surface shape of (A) G351 and the (B) P351 mutation, preventing a hydrogen bond interaction with the backbone. (C) V378 and the (D) M378 mutation with the extended side chain preventing **35** from entering the binding site. (E) F495* and the (F) L495* mutation, pointing towards Gly351 and preventing **35** from entering the binding site and performing an interaction with the backbone of Gly351. (G) HEK293 reporter control cells were transfected with mutant or wildtype TLR8 plasmid. Cells were preincubated with either compound **35** (1 μM) or **CU-CPT9a** (1 μM) for 1 h and then stimulated with TL8-506 (3 μM) for 24 h. Supernatants were analyzed for TLR8-mediated NF-κB activation by the SEAP reporter assay using QuantiBlue (OD_{620}) and normalized to TL8-506. Mean + SEM (n=4).

5.2.6 Physicochemical and pharmacokinetic characterization of compounds 16 and 35

Next, the physicochemical properties, i.e. log D and kinetic solubility, of the most potent compounds from the first (compound **16**) and the third series (compound **35**) were determined (Table 4). The kinetic solubility of a compound is the maximum solubility of the fastest precipitating species of the compound[163] and the goal for drug discovery compounds is to achieve solubility higher as 60 μg/mL.[164] Compounds **16** and **35** displayed favorable solubility characteristics, with kinetic solubility values of 78.3 μg/mL and 91.3 μg/mL, respectively.

Table 4. Log D and kinetic solubility for compounds **16** and **35**.

Compound	**Log D**	**Kinetic Solubility in Phosphate Buffer pH 7.4**	
		(μM)	**(μg/mL)**
16	1.27	205	78.3
35	2.37	218	91.3

The next step was to determine pharmacokinetic properties such as metabolic stability in liver microsomes (Table 5) and plasma protein binding (Table 6) for compounds **16** and **35**. Metabolic stability was assessed in human and mouse liver microsomes. Key parameters

determined were *in vitro* half-life ($t_{1/2}$), microsomal intrinsic clearance ($CL_{int(mic)}$) and *in vivo* hepatic intrinsic clearance ($CL_{int(liver)}$) by methods described in the experimental section. Both compounds showed good metabolic stability, with $t_{1/2}$ values greater than 70 minutes and low clearance. Metabolic stability was higher in human liver microsomes compared to mouse liver microsomes, with $t_{1/2}$ values exceeding 145 minutes (Table 5).

Table 5. Metabolic stability of selected compounds in human and mouse liver microsomes.

Compound	**Human liver microsomes**			**Mouse liver microsomes**		
	$t_{1/2}$ (min)	$CL_{int(mic)}$[a] (μL/min/mg)	$CL_{int(liver)}$[b] (mL/min/kg)	$t_{1/2}$ (min)	$CL_{int(mic)}$ (μL/min/mg)	$CL_{int(liver)}$ (mL/min/kg)
16	>145	<9.6	<8.6	>145	<9.6	<38.0
35	>145	<9.6	<8.6	73.6	18.8	74.6
Testosterone	15.5	89.2	80.2	4.5	308.6	1222.2
Diclofenac	5.2	264.1	237.7	47.3	29.3	116.2
Propafenone	6.7	205.7	185.1	2.0	710.9	2815.3

[a] Microsomal intrinsic clearance, $CL_{int(mic)} = 0.693/t_{1/2}$/mg microsome protein per mL.

[b] Hepatic intrinsic clearance, $CL_{int(liver)} = CL_{int(mic)} \times$ mg microsomal protein/g liver weight × g liver weight/kg body weight

Prediction of plasma protein binding is important because it significantly affects volume of distribution, clearance and drug half-life ($t_{1/2}$).[165] The $t_{1/2}$ is usually longer for drugs with high protein binding. In our study, compound **16** exhibited moderate binding, while compound **35** showed higher binding to human plasma proteins (Table 6).

Table 6. Plasma protein binding of compounds **16** and **35** (mean ± SD, n=3).

Compound	Human		
	%Unbound	%Bound	%Recovery
16	43.7 ± 2.3	56.3	97.9 ± 5.1
35	11.4 ± 1.3	88.6	93.2 ± 6.2
Warfarin	0.8 ± 0.0	99.2	104.9 ± 8.5

5.3 Conclusion

Overactivation of TLR8, which recognizes microbial RNA and triggers the release of proinflammatory cytokines, contributes to inflammatory and autoimmune diseases. Many new scaffolds of TLR8 antagonists have been reported, however, none have yet reached the market. In this work, novel pyrimidine-based TLR8 antagonists were designed and synthesized by replacing the isoxazole ring from our previous study with a pyrimidine ring. A structure–activity relationship study revealed that the most optimal substituent on the amide bond is 1-isopropylpiperidine. The most potent compound **16**, with an IC_{50} value of 300 nM, selectively inhibited TLR8-mediated signaling and demonstrated concentration-dependent inhibition of TNF secretion in THP-1 cells and PBMCs. In the next step, the pyrimidine ring was fused with benzene, resulting in the quinazoline derivative **35**, which exhibited approximately 10-fold higher potency. Compound **35** inhibited TNF secretion in THP-1 cells and PBMCs comparably to the antagonist **CU-CPT9a**. Computational modeling and mutagenesis of the TLR8 binding cavity confirmed ligand-receptor interactions within the same pocket as **CU-CPT9a**, indicating competitive antagonism at the agonist site for chemical ligands. The high specificity and potency of compound **35**, combined with favorable kinetic solubility and metabolic stability in human and mouse liver microsomes with a $t_{1/2}$ exceeding 145 minutes, make it a promising candidate for further development of selective TLR8 antagonists. Its superior performance over previously developed antagonists highlights its potential for therapeutic applications, especially in diseases driven by TLR8-mediated inflammation.

5.4 Materials and methods

5.4.1 Chemistry

Reagents and solvents were obtained from commercial sources (e.g., BLDpharm, Apollo Scientific, Sigma-Aldrich, Acros Organics, Enamine, TCI). Reactions were monitored by thin-layer chromatography on silica gel plates (Merck DC Fertigplatten Kieselgel 60 GF254) and visualized under UV light. If necessary, staining with the appropriate staining reagents was also performed. Flash column chromatography was carried out on silica gel 60 (mesh size 70–230; Merck) using the indicated solvents. Flash column chromatography of some final compounds was performed on an Isolera One (Biotage) using Biotage Sfär C18 D - Duo 100 Å 30 µm column. The flow rate was 25 mL/min; detection was performed at 254 nm; and the eluent system consisted of 0.1% aqueous trifluoroacetic acid (A) and acetonitrile (B) was used. The following gradient was used: 0–3 min, 100% A, 3–18 min 0-100% B, 18–20 min 100% B. Yields refer to purified products and were not optimized. ^{1}H and ^{13}C NMR spectra were recorded at 295 K in $CDCl_3$ or acetone-d_6 (Avance III NMR spectrometer; Bruker, MA, USA) using a decoupling inverse 1H probe (Broadband). Coupling constants (*J*) are given in Hz, and the splitting patterns are labeled as follows: s, singlet; bs, broad singlet; d, doublet; t, triplet; q, quartet; dd, doublet of doublets; dt, doublet of triplets; m, multiplet. Mass spectra (Expression CMS mass spectrometer; Advion, NY, USA) and high-resolution mass measurements (Exactive Plus Orbitrap mass spectrometer; Thermo Fisher Scientific, MA, USA) were performed at the Faculty of Pharmacy, University of Ljubljana, Slovenia. HPLC analyses were performed using the Thermo Scientific UltiMate 3000 modular system (Thermo Fisher Scientific Inc.) equipped with a quaternary pump and a multi-wavelength detector. An ACQUITY UPLC HSS C18 column (2.1 x 50 mm; 1.8 µm), thermostatted to 40 °C was used. The flow rate was 0.4 mL/min; detection was performed at 254 nm; and the eluent system consisted of 0.1% aqueous trifluoroacetic acid (A) and acetonitrile (B) was used. The following gradient was used: 0–7 min, 5–95% B; 7–8 min, 95% B. All compounds are >95% pure by HPLC analysis.

5.4.2 Experimental procedures and characterization data for compounds 7–23

Methyl 4-(((2,6-dimethylpyrimidin-4-yl)oxy)methyl)benzoate (7)

To a cooled solution of methyl 4-(hydroxymethyl)benzoate (**6**) (15.00 mmol, 2.49 g) in anhydrous DMF (30 mL), NaH (15 mmol, 0.360 g of 60% dispersion in mineral oil) was added. After 1 h, the solution was removed from the ice bath and 4-chloro-2,6-dimethylpyrimidine (10.00 mmol, 1.43 g) was added. The reaction mixture was stirred for 6 h at 60 °C and then

overnight at room temperature. A 30% solution of NH_4Cl (50 mL) and diethyl ether (100 mL) were added to the reaction mixture. The phases were separated and the organic phase was washed with water (50 mL) and a saturated solution of NaCl (50 mL), dried over anhydrous Na_2SO_4, and filtered. The solvent was removed under reduced pressure, and the residue was purified by flash column chromatography. Yield 31%; colorless oil; Rf = 0.13 (EtOAc/ n-hexane, 1:2, v/v); ^{1}H NMR (400 MHz, DMSO-*d*$_6$): δ (ppm) = 2.34 (s, 3H), 2.47 (s, 3H), 3.86 (s, 3H), 5.47 (s, 2H), 6.70 (s, 1H), 7.55 – 7.60 (m, 2H), 7.96 – 7.99 (m, 2H).

4-(((2,6-Dimethylpyrimidin-4-yl)oxy)methyl)benzoic acid (8)

Methyl 4-(((2,6-dimethylpyrimidin-4-yl)oxy)methyl)benzoate (**7**) (4.69 mmol, 1.59 g) was dissolved in 1M NaOH (15 mL) and dioxane (15 mL) and stirred overnight at room temperature. Diethyl ether (30 mL) was added to the reaction mixture and the phases were separated. 1 M HCl was added to the aqueous phase and the product precipitated. Yield 77%; white solid; Rf = 0.67 (DCM/MeOH, 9:1, v/v); ^{1}H NMR (400 MHz, DMSO-*d*$_6$): δ (ppm) = 2.34 (s, 3H), 2.47 (s, 3H), 5.46 (s, 2H), 6.69 (s, 1H), 7.55 (d, *J* = 8.4 Hz, 2H), 7.93 – 8.00 (m, 2H), 13.01 (s, 1H).

General procedure A (synthesis of amide)

A corresponding acid (1 equiv.) was dissolved in anhydrous THF under argon atmosphere and HATU (1.5 equiv.) was added. After 15 minutes, a corresponding amine (1 equiv.) and DIPEA (4 equiv.) were added to the stirred solution. The reaction mixture was stirred overnight at room temperature. EtOAc was then added and the reaction mixture washed with saturated solution of $NaHCO_3$. The organic phase was dried over anhydrous Na_2SO_4, filtered, and evaporated under reduced pressure. The residue was purified by flash column chromatography.

4-(((2,6-Dimethylpyrimidin-4-yl)oxy)methyl)-*N*-(1-methylpyrrolidin-3-yl)benzamide (9)

Synthesized from 4-(((2,6-dimethylpyrimidin-4-yl)oxy)methyl)benzoic acid (**8**) (0.58 mmol, 0.150 g), HATU (0.87 mmol, 0.331 g), 1-methylpyrrolidin-3-amine (0.58 mmol, 0.058 g) and DIPEA (2.32 mmol, 0.404 mL) via general procedure A. The compound was purified by flash column chromatography using DCM/MeOH = 9/1 (v/v) as the eluent. Yield 41%; white solid; Rf = 0.16 (DCM/MeOH, 9:1, v/v); ^{1}H NMR (400 MHz, $CDCl_3$): δ (ppm) = 1.73 – 1.81 (m, 1H), 2.22 – 2.28 (m, 1H), 2.38 – 2.47 (m, 1H), 2.40 (s, 3H), 2.41 (s, 3H), 2.54 – 2.57 (m, 1H), 2.58 (s, 3H), 2.79 (dd, *J* = 10.1, 0.9 Hz, 1H), 3.00 (td, *J* = 8.6, 3.3 Hz, 1H), 4.65 – 4.72 (m, 1H), 5.44 (s, 2H), 6.45 (s, 1H), 6.61 (d, *J* = 8.2 Hz, 1H), 7.41 – 7.57 (m, 2H), 7.70 – 7.86 (m, 2H); ^{13}C NMR (100 MHz, $CDCl_3$): δ (ppm) = 23.86, 25.89, 33.31, 41.79, 49.64, 55.06, 63.12, 66.87, 103.82, 127.16, 127.94, 134.01, 140.17, 166.43, 167.46, 169.15; HRMS (ESI+) *m/z*

calcd. for $C_{19}H_{25}N_4O_2$ $[M+H]^+$ 341.19720, found 341.19700; HPLC purity 95.30% at 254 nm (t_R = 1.807 min).

4-(((2,6-Dimethylpyrimidin-4-yl)oxy)methyl)-*N*-(2-(pyrrolidin-1-yl)ethyl)benzamide (10)

Synthesized from 4-(((2,6-dimethylpyrimidin-4-yl)oxy)methyl)benzoic acid (**8**) (0.58 mmol, 0.150 g), HATU (0.87 mmol, 0.331 g), 2-(pyrrolidin-1-yl)ethan-1-amine (0.58 mmol, 0.066 g) and DIPEA (2.32 mmol, 0.404 mL) via general procedure A. The compound was purified by flash column chromatography using DCM/MeOH = 9/1 (v/v) as the eluent. Yield 15%; yellow solid; Rf = 0.18 (DCM/MeOH, 9:1, v/v); ^{1}H NMR (400 MHz, $CDCl_3$): δ (ppm) = 1.80 – 1.84 (m, 4H), 2.40 (s, 3H), 2.58(s, 3H), 2.59 – 2.65 (m, 4H), 2.75 (t, *J* = 5.9 Hz, 2H), 3.58 (q, *J* = 5.5 Hz, 2H), 5.44 (s, 2H), 6.44 (s, 1H), 6.96 (br s, 1H), 7.48 – 7.59 (m, 2H), 7.80 – 7.82 (m, 2H); ^{13}C NMR (100 MHz, $CDCl_3$): δ (ppm) = 23.53, 23.86, 25.90, 38.33, 53.96, 54.69, 66.92, 103.83, 127.28, 127.95, 134.27, 140.02, 167.16, 167.46, 169.17; HRMS (ESI+) *m/z* calcd. for $C_{20}H_{27}N_4O_2$ $[M+H]^+$ 355.21285, found 355.21252; HPLC purity 100.00% at 254 nm (t_R = 1.897 min).

[1,4'-Bipiperidin]-1'-yl(4-(((2,6-dimethylpyrimidin-4-yl)oxy)methyl)phenyl)methanone (11)

Synthesized from 4-(((2,6-dimethylpyrimidin-4-yl)oxy)methyl)benzoic acid (**8**) (0.58 mmol, 0.150 g), HATU (0.87 mmol, 0.331 g), 1,4'-bipiperidine (0.58 mmol, 0.098 g) and DIPEA (2.32 mmol, 0.404 mL) via general procedure A. The compound was purified by flash column chromatography using DCM/MeOH = 9/1 (v/v) as the eluent. Yield 32%; white solid; Rf = 0.23 (DCM/MeOH, 9:1, v/v); ^{1}H NMR (400 MHz, acetone-d_6): δ (ppm) = 1.60 – 1.66 (m, 2H), 1.75 – 1.89 (m, 6H), 2.15 (br s, 2H), 2.34 (s, 3H), 2.48 (s, 3H), 3.25 – 3.30 (m, 4H), 3.43 – 3.51 (m, 1H), 4.02 (s, 4H), 5.45 (s, 2H), 6.56 (s, 1H), 7.44 – 7.47 (m, 2H), 7.54 – 7.57 (m, 2H); ^{13}C NMR (100 MHz, acetone-d_6): δ (ppm) = 22.73, 23.72, 24.54, 25.88, 27.48, 51.32, 55.89, 64.88, 67.47, 104.20, 127.96, 128.95, 136.57, 139.56, 167.87, 168.71, 170.09, 170.13; HRMS (ESI+) *m/z* calcd. for $C_{24}H_{33}N_4O_2$ $[M+H]^+$ 409.25980, found 409.25945; HPLC purity 100.00% at 254 nm (t_R = 1.997 min).

(4-(((2,6-Dimethylpyrimidin-4-yl)oxy)methyl)phenyl)(4-(pyrrolidin-1-yl)piperidin-1-yl)methanone (12)

Synthesized from 4-(((2,6-dimethylpyrimidin-4-yl)oxy)methyl)benzoic acid (**8**) (0.58 mmol, 0.150 g), HATU (0.87 mmol, 0.331 g), 4-(pyrrolidin-1-yl)piperidine (0.58 mmol, 0.090 g) and DIPEA (2.32 mmol, 0.404 mL) via general procedure A. The compound was purified by flash column chromatography using DCM/MeOH = 9/1 (v/v) as the eluent. Yield 22%; orange oil;

Rf = 0.20 (DCM/MeOH, 9:1, v/v); ^{1}H NMR (400 MHz, acetone-*d*$_6$): δ (ppm) = 1.44 – 1.58 (m, 2H), 1.70 – 1.77 (m, 4H), 1.81 – 1.98 (m, 2H), 2.34 (s, 3H), 2.35 – 2.39 (m, 1H), 2.49 (s, 3H), 2.54 – 2.64 (m, 4H), 3.07 (br s, 2H), 5.46 (s, 2H), 6.56 (s, 1H), 7.41 – 7.43 (m, 2H), 7.53 – 7.55 (m, 2H); ^{13}C NMR (100 MHz, acetone-*d*$_6$): δ (ppm) = 23.73, 24.00, 25.90, 31.96, 49.60, 51.81, 61.89, 67.57, 104.24, 127.91, 128.82, 137.47, 139.05, 167.89, 168.66, 169.77, 170.15. HRMS (ESI+) *m/z* calcd. for $C_{23}H_{31}N_4O_2$ $[M+H]^+$ 395.24415, found 395.24411; HPLC purity 95.96% at 254 nm (t_R = 1.870 min).

_N_-(2-(Dimethylamino)-2-(p-tolyl)ethyl)-4-(((2,6-dimethylpyrimidin-4-yl)oxy)methyl)benzamide (13)

Synthesized from 4-(((2,6-dimethylpyrimidin-4-yl)oxy)methyl)benzoic acid (**8**) (0.58 mmol, 0.150 g), HATU (0.87 mmol, 0.331 g), N^1, N^1-dimethyl-1-(*p*-tolyl)ethane-1,2-diamine (0.58 mmol, 0.104 g), and DIPEA (2.32 mmol, 0.404 ml) via general procedure A. The compound was purified by flash column chromatography using DCM/MeOH = 9/1 (v/v) as the eluent. Yield 20%; yellow solid; Rf = 0.45 (DCM/MeOH, 9:1, v/v); ^{1}H NMR (400 MHz, $CDCl_3$): δ (ppm) = 2.37 (s, 3H), 2.40 (s, 9H), 2.58 (s, 3H), 3.66 – 3.74 (m, 1H), 3.88 – 3.94 (m 1H), 4.01 – 4.08 (m, 1H), 5.43 (s, 2H), 6.44 (s, 1H), 6.86 (t, *J* = 5.0 Hz, 1H), 7.18 – 7.22 (m, 4H), 7.48 (d, *J* = 8.3 Hz, 2H), 7.75 (d, *J* = 8.3 Hz, 2H); ^{13}C NMR (100 MHz, $CDCl_3$): δ (ppm) = 21.17, 23.86, 25.89, 41.24, 41.77, 66.83, 68.77, 103.80, 127.30, 127.98, 128.92, 129.50, 130.93, 133.47, 138.91, 140.47, 167.46, 167.49, 167.95, 169.13; HRMS (ESI+) *m/z* calcd. for $C_{25}H_{31}N_4O_2$ $[M+H]^+$ 419.24415, found 419.24377; HPLC purity 100.00% at 254 nm (t_R = 2.623 min).

4-(((2,6-Dimethylpyrimidin-4-yl)oxy)methyl)-_N_-(1-ethylpiperidin-4-yl)benzamide (14)

Synthesized from 4-(((2,6-dimethylpyrimidin-4-yl)oxy)methyl)benzoic acid (**8**) (0.39 mmol, 0.100 g), HATU (0.59 mmol, 0.222 g), 1-ethylpiperidin-4-amine (0.39 mmol, 0.050 g), and DIPEA (1.56 mmol, 0.272 ml) via general procedure A. The compound was purified by flash column chromatography using DCM/MeOH = 9/1 (v/v) as the eluent. Yield 27%; white solid; Rf = 0.11 (DCM/MeOH, 9:1, v/v); ^{1}H NMR (400 MHz, $CDCl_3$): δ (ppm) = 1.11 (t, *J* = 7.2 Hz, 3H), 1.54 – 1.64 (m, 2H), 2.06 – 2.17 (m, 4H), 2.41 (s, 3H), 2.46 (q, *J* = 7.2 Hz, 2H), 2.58 (s, 3H), 2.94 (d, *J* = 11.5 Hz, 2H), 3.97 – 4.07 (m, 1H), 5.44 (s, 2H), 5.95 (d, *J* = 7.9 Hz, 1H), 6.45 (s, 1H), 7.49 – 7.51 (m, 2H), 7.75 – 7.77 (m, 2H); ^{13}C NMR (100 MHz, $CDCl_3$): δ (ppm) = 12.18, 23.86, 25.90, 32.26, 47.09, 52.01, 52.35, 66.84, 103.82, 127.05, 128.02, 134.35, 140.19, 166.49, 167.45, 167.47, 169.13; HRMS (ESI+) *m/z* calcd. for $C_{21}H_{29}N_4O_2$ $[M+H]^+$ 369.22850, found 369.22837; HPLC purity 100.00% at 254 nm (t_R = 1.910 min).

4-(((2,6-Dimethylpyrimidin-4-yl)oxy)methyl)-*N*-(1-propylpiperidin-4-yl)benzamide (15)

Synthesized from 4-(((2,6-dimethylpyrimidin-4-yl)oxy)methyl)benzoic acid (**8**) (0.58 mmol, 0.150 g), HATU (0.87 mmol, 0.331 g), 1-propylpiperidin-4-amine (0.58 mmol, 0.092 ml), and DIPEA (2.32 mmol, 0.404 ml) via general procedure A. The compound was purified by flash column chromatography using DCM/MeOH = 9/1 (v/v) as the eluent. Yield 68%; white solid; Rf = 0.37 (DCM/MeOH, 9:1, v/v); ^{1}H NMR (400 MHz, $CDCl_3$): δ (ppm) = 0.91 (t, *J* = 7.4 Hz, 3H), 1.47 – 1.62 (m, 4H), 2.05 (dd, *J* = 12.4, 3.1 Hz, 2H), 2.03 – 2.17 (m, 2H), 2.30 – 2.34 (m, 2H), 2.41 (s, 3H), 2.58 (s, 3H), 2.86 – 2.94 (m, 2H), 3.96 – 4.06 (m, 1H), 5.44 (s, 2H), 5.96 (d, *J* = 7.8 Hz, 1H), 6.45 (s, 1H), 7.48 – 7.50 (m, 2H), 7.74 – 7.76 (m, 2H); ^{13}C NMR (100 MHz, $CDCl_3$): δ (ppm) = 11.99, 20.24, 23.85, 25.89, 32.29, 47.10, 52.43, 60.69, 66.85, 103.82, 127.05, 128.02, 134.39, 140.17, 166.49, 167.45, 167.47, 169.14. HRMS (ESI+) *m/z* calcd. for $C_{22}H_{31}N_4O_2$ $[M+H]^+$ 383.24415, found 383.24321; HPLC purity 100.00% at 254 nm (t_R = 2.073 min).

4-(((2,6-Dimethylpyrimidin-4-yl)oxy)methyl)-*N*-(1-isopropylpiperidin-4-yl)benzamide (16)

Synthesized from 4-(((2,6-dimethylpyrimidin-4-yl)oxy)methyl)benzoic acid (**8**) (0.58 mmol, 0.150 g), HATU (0.87 mmol, 0.331 g), 1-isopropylpiperidin-4-amine (0.58 mmol, 0.083 g), and DIPEA (2.32 mmol, 0.404 ml) via general procedure A. The compound was purified by flash column chromatography using DCM/MeOH = 9/1 (v/v) as the eluent. Yield 39%; white solid; Rf = 0.37 (DCM/MeOH, 9:1, v/v); ^{1}H NMR (400 MHz, $CDCl_3$): δ (ppm) = 1.06 (d, *J* = 6.6 Hz, 6H), 1.49 – 1.58 (m, 2H), 2.05 – 2.09 (m, 2H), 2.29 – 2.36 (m, 2H), 2.41 (s, 3H), 2.58 (s, 3H), 2.72 – 2.79 (m, 1H), 2.84 – 2.90 (m, 2H), 3.94 – 4.04 (m, 1H), 5.44 (s, 2H), 5.93 (d, *J* = 7.8 Hz, 1H), 6.45 (s, 1H), 7.48 – 7.50 (m, 2H), 7.74 – 7.76 (m, 2H); ^{13}C NMR (100 MHz, $CDCl_3$): δ (ppm) = 18.39, 23.86, 25.89, 32.60, 47.32, 47.56, 54.61, 66.86, 103.83, 127.05, 128.02, 134.42, 140.16, 166.45, 167.46, 167.48, 169.14. HRMS (ESI+) *m/z* calcd. for $C_{22}H_{31}N_4O_2$ $[M+H]^+$ 383.24415, found 383.24305; HPLC purity 100.00% at 254 nm (t_R = 2.027 min).

4-(((2,6-Dimethylpyrimidin-4-yl)oxy)methyl)-*N*-(1-methylpiperidin-4-yl)benzamide (17)

Synthesized from 4-(((2,6-dimethylpyrimidin-4-yl)oxy)methyl)benzoic acid (**8**) (0.58 mmol, 0.150 g), HATU (0.87 mmol, 0.331 g), 1-methylpiperidin-4-amine (0.58 mmol, 0.073 ml), and DIPEA (2.32 mmol, 0.404 ml) via general procedure A. The compound was purified by flash column chromatography using DCM/MeOH = 9/1 (v/v) as the eluent. Yield 33%; white solid; Rf = 0.20 (DCM/MeOH, 9:1, v/v); ^{1}H NMR (400 MHz, $CDCl_3$): δ (ppm) = 1.55– 1.64 (m, 2H), 2.02 – 2.10 (m, 2H), 2.15 – 2.24 (m, 2H), 2.34 (s, 3H), 2.41 (s, 3H), 2.58 (s, 3H), 2.82 – 2.90

(m, 2H), 3.95 – 4.05 (m, 1H), 5.44 (s, 2H), 5.95 (d, *J* = 7.4 Hz, 1H), 6.45 (s, 1H), 7.49 (d, *J* = 7.7 Hz, 2H), 7.76 (d, *J* = 7.8 Hz, 2H); ^{13}C NMR (100 MHz, $CDCl_3$): δ (ppm) = 23.86, 25.89, 32.25, 46.17, 46.51, 54.55, 66.84, 103.82, 127.06, 128.03, 134.30, 140.23, 166.55, 167.45, 167.49, 169.14; HRMS (ESI+) *m/z* calcd. for $C_{20}H_{27}N_4O_2$ $[M+H]^+$ 355.21285, found 355.21193; HPLC purity 99.68% at 254 nm (t_R = 1.840 min).

***Tert*-butyl 4-(4-(((2,6-dimethylpyrimidin-4-yl)oxy)methyl)benzamido)piperidine-1-carboxylate (18)**

Synthesized from 4-(((2,6-dimethylpyrimidin-4-yl)oxy)methyl)benzoic acid (**8**) (4.09 mmol, 1.060 g), HATU (6.14 mmol, 2.333 g), *tert*-butyl 4-aminopiperidine-1-carboxylate (4.09 mmol, 0.820 g), and DIPEA (16.36 mmol, 2.850 ml) via general procedure A. The compound was purified by flash column chromatography using DCM/MeOH = 30/1 (v/v) as the eluent. Yield 95%; colorless oil; Rf = 0.70 (DCM/MeOH, 9:1, v/v); ^{1}H NMR (400 MHz, $CDCl_3$): δ (ppm) = 1.47 (s, 9H), 2.03 (dd, *J* = 12.5, 2.6 Hz, 2H), 2.41 (s, 3H), 2.58 (s, 3H), 2.91 (t, *J* = 11.8 Hz, 2H), 3.19 (q, *J* = 7.4 Hz, 1H), 3.67 – 3.76 (m, 1H), 4.12 (s, 3H), 5.45 (s, 2H), 5.93 (d, *J* = 8.0 Hz, 1H), 6.45 (s, 1H), 7.50 (d, *J* = 8.1 Hz, 2H), 7.75 (d, *J* = 8.0 Hz, 2H).

Deprotection of Boc group

4-(((2,6-dimethylpyrimidin-4-yl)oxy)methyl)-*N*-(piperidin-4-yl)benzamide (19)

Tert-butyl 4-(4-(((2,6-dimethylpyrimidin-4-yl)oxy)methyl)benzamido)piperidine-1-carboxylate (**18**) ((4.09 mmol, 1.80 g) and trifluoroacetic acid (40.86 mmol, 3.13 ml) were dissolved in DCM (10 ml) and stirred at room temperature for 24 h. Solvents were evaporated and the compound was purified by flash column chromatography using DCM/isopropanol = 7/3 (v/v) + 1% NH_3 as the eluent. Yield 30%; colorless oil; Rf = 0.13 (DCM/MeOH, 9:1, v/v); ^{1}H NMR (400 MHz, $CDCl_3$): δ (ppm) = 1.86 – 2.00 (m, 2H), 2.21 – 2.29 (m, 2H), 2.42 (s, 3H), 2.59 (s, 3H), 3.02 (t, *J* = 12.7 Hz, 2H), 3.45 – 3.52 (m, 2H), 4.22 – 4.32 (m, 1H), 5.45 (s, 2H), 6.33 (d, *J* = 7.8 Hz, 1H), 6.46 (s, 1H), 7.51 (d, *J* = 8.3 Hz, 2H), 7.77 (d, *J* = 8.3 Hz, 2H), 1H from NH is exchanged; ^{13}C NMR (100 MHz, $CDCl_3$): δ (ppm) = 23.84, 25.89, 28.85, 43.49, 44.88, 67.00, 104.05, 127.33, 128.21, 133.50, 140.79, 166.80, 167.54, 169.31. HRMS (ESI+) *m/z* calcd. for $C_{19}H_{25}N_4O_2$ $[M+H]^+$ 341.19720, found 341.19699; HPLC purity 99.32% at 254 nm (t_R = 1.830 min).

General procedure B (alkylation of amine)

4-(((2,6-Dimethylpyrimidin-4-yl)oxy)methyl)-*N*-(piperidin-4-yl)benzamide (**19**) (1 equiv.) was dissolved in anhydrous acetonitrile and the appropriate alkyl halide (2 equiv.), K_2CO_3 (1.5

equiv.) and KI (catalytic amount) were added. The reaction mixture was stirred at reflux for 2 h. The solvent was removed under reduced pressure, and the residue was dissolved in DCM and extracted with water. The organic phase was dried over anhydrous Na_2SO_4, filtered and the solvent was removed under reduced pressure. The residue was purified by flash column chromatography.

_N_-(1-butylpiperidin-4-yl)-4-(((2,6-dimethylpyrimidin-4-yl)oxy)methyl)benzamide (20)

Synthesized from 4-(((2,6-dimethylpyrimidin-4-yl)oxy)methyl)-*N*-(piperidin-4-yl)benzamide (**19**) (0.29 mmol, 0.100 g), K_2CO_3 (0.44 mmol, 0.061 g), 1-chlorobutane (0.59 mmol, 0.062 ml), and KI (cat.) via general procedure B. The compound was purified by flash column chromatography using DCM/MeOH = 9/1 (v/v) as the eluent. Yield 44%; white solid; Rf = 0.48 (DCM/MeOH, 9:1, v/v); ^{1}H NMR (400 MHz, $CDCl_3$): δ (ppm) = 0.93 (t, *J* = 7.3 Hz, 3H), 1.29 – 1.39 (m, 2H), 1.51 – 1.59 (m, 2H), 1.70 – 1.75 (m, 2H), 2.04 – 2.12 (m, 2H), 2.20 – 2.29 (m, 2H), 2.41 (s, 3H), 2.42 – 2.46 (m, 2H), 2.58 (s, 3H), 2.98 – 3.05 (m, 2H), 4.01 – 4.11 (m, 1H), 5.44 (s, 2H), 6.01 (d, *J* = 8.1 Hz, 1H), 6.45 (s, 1H), 7.49 – 7.52 (m, 2H), 7.73 – 7.76 (m, 2H); ^{13}C NMR (100 MHz, $CDCl_3$): δ (ppm) = 13.98, 20.74, 23.85, 25.89, 28.78, 31.80, 46.78, 52.42, 58.35, 66.84, 103.82, 127.08, 128.00, 134.21, 140.23, 166.52, 167.44, 167.47, 169.13; HRMS (ESI+) *m/z* calcd. for $C_{23}H_{33}N_4O_2$ $[M+H]^+$ 397.25980, found 397.25954; HPLC purity 98.13% at 254 nm (t_R = 2.293 min).

4-(((2,6-Dimethylpyrimidin-4-yl)oxy)methyl)-*N*-(1-pentylpiperidin-4-yl)benzamide (21)

Synthesized from 4-(((2,6-dimethylpyrimidin-4-yl)oxy)methyl)-*N*-(piperidin-4-yl)benzamide (**19**) (0.29 mmol, 0.100 g), K_2CO_3 (0.44 mmol, 0.061 g), 1-bromopentane (0.59 mmol, 0.073 ml), and KI (cat.) via general procedure B. The compound was purified by flash column chromatography using DCM/MeOH = 9/1 (v/v) as the eluent. Yield 19%; white solid; Rf = 0.40 (DCM/MeOH, 9:1, v/v); ^{1}H NMR (400 MHz, $CDCl_3$): δ (ppm) = 0.91 (t, *J* = 7.0 Hz, 3H), 1.25 – 1.37 (m, 4H), 1.55 – 1.63 (m, 2H), 1.72 – 1.81 (m, 2H), 2.06 – 2.13 (m, 2H), 2.24 – 2.32 (m, 2H), 2.41 (s, 3H), 2.45 – 2.49 (m, 2H), 2.58 (s, 3H), 3.02 – 3.09 (m, 2H), 4.03 – 4.12 (m, 1H), 5.44 (s, 2H), 6.04 (d, *J* = 7.2 Hz, 1H), 6.45 (s, 1H), 7.49 – 7.51 (m, 2H), 7.75 – 7.77 (m, 2H); ^{13}C NMR (100 MHz, $CDCl_3$): δ (ppm) = 14.01, 22.52, 23.86, 25.89, 26.16, 29.65, 31.60, 46.61, 52.40, 58.57, 66.83, 103.83, 127.07, 128.03, 134.14, 140.30, 166.53, 167.48, 169.13; HRMS (ESI+) *m/z* calcd. for $C_{24}H_{35}N_4O_2$ $[M+H]^+$ 411.27550, found 411.27500; HPLC purity 99.48% at 254 nm (t_R = 2.570 min).

4-(((2,6-dimethylpyrimidin-4-yl)oxy)methyl)-*N*-(1-hexylpiperidin-4-yl)benzamide (22)

Synthesized from 4-(((2,6-dimethylpyrimidin-4-yl)oxy)methyl)-*N*-(piperidin-4-yl)benzamide (**19**) (0.29 mmol, 0.100 g), K_2CO_3 (0.44 mmol, 0.061 g), 1-bromohexane (0.59 mmol, 0.083 mL) and KI (cat.) via general procedure B. The compound was purified by flash column chromatography using DCM/MeOH = 9/1 (v/v) as the eluent. Yield 41%; white solid; Rf = 0.42 (DCM/MeOH, 9:1, v/v); ^{1}H NMR (400 MHz, $CDCl_3$): δ (ppm) = 0.89 (t, *J* = 6.8 Hz, 3H), 1.26 – 1.34 (m, 6H), 1.53 – 1.60 (m, 2H), 1.69 – 1.78 (m, 2H), 2.06 – 2.10 (m, 2H), 2.22 – 2.28 (m, 2H), 2.41 (s, 3H), 2.43 – 2.47 (m, 2H), 2.58 (s, 3H), 2.98 – 3.07 (m, 1H), 4.01 – 4.11 (m, 1H), 5.44 (s, 2H), 6.05 (d, *J* = 8.0 Hz, 1H), 6.45 (s, 1H), 7.48 – 7.51 (m, 2H), 7.75 – 7.77 (m, 2H); ^{13}C NMR (100 MHz, $CDCl_3$): δ (ppm) = 14.03, 22.57, 23.84, 25.88, 26.54, 27.19, 31.67, 46.72, 52.41, 58.62, 66.84, 103.82, 127.12, 127.97, 134.20, 140.20, 166.55, 167.44, 167.46, 169.13; HRMS (ESI+) *m/z* calcd. for $C_{25}H_{37}N_4O_2$ $[M+H]^+$ 425.29110, found 425.29051; HPLC purity 100.00% at 254 nm (t_R = 2.880 min).

***N*-(1-allylpiperidin-4-yl)-4-(((2,6-dimethylpyrimidin-4-yl)oxy)methyl)benzamide (23)**

Synthesized from 4-(((2,6-dimethylpyrimidin-4-yl)oxy)methyl)-*N*-(piperidin-4-yl)benzamide (**19**) (0.29 mmol, 0.100 g), K_2CO_3 (0.44 mmol, 0.061 g), 3-bromoprop-1-ene (0.59 mmol, 0.051 ml), and KI (cat.) via general procedure B. The compound was purified by flash column chromatography using DCM/MeOH = 30/1 (v/v) as the eluent. Yield 14%; yellow solid; Rf = 0.67 (DCM/MeOH, 9:1, v/v); ^{1}H NMR (400 MHz, $CDCl_3$): δ (ppm) = 1.55 – 1.64 (m, 2H), 2.04 – 2.07 (m, 2H), 2.13 – 2.19 (m, 2H), 2.40 (s, 3H), 2.58 (s, 3H), 2.91 – 2.94 (m, 2H), 3.02 – 3.04 (m, 2H), 3.97 – 4.06 (m, 1H), 5.16 – 5.23 (m, 2H), 5.44 (s, 2H), 5.83 – 5.93 (m, 1H), 6.06 (d, *J* = 7.2 Hz, 1H), 6.45 (s, 1H), 7.48 – 7.50 (m, 2H), 7.75 – 7.77 (m, 2H); ^{13}C NMR (100 MHz, $CDCl_3$): δ (ppm) = 23.84, 25.88, 31.88, 46.77, 52.17, 61.53, 66.83, 68.15, 103.81, 119.06, 127.09, 127.99, 128.01, 133.98, 140.23, 166.55, 167.44, 169.12; HRMS (ESI+) *m/z* calcd. for $C_{22}H_{29}N_4O_2$ $[M+H]^+$ 381.22850, found 381.22818; HPLC purity 97.78% at 254 nm (t_R = 2.043 min).

General procedure C

To a cooled solution of methyl 4-(hydroxymethyl)benzoate (1.1 equiv.) in anhydrous DMF or THF (30 mL), NaH (1.2 equiv, 60% dispersion in mineral oil) was added. After 20 minutes, the solution was removed from the ice bath, and the appropriate pyrimidine derivative (1 equiv.) was added. The reaction mixture was stirred at 60 ºC for 4 h or at room temperature for 24 h. Then, a 30% solution of NH_4Cl (50 mL) and diethyl ether (100 mL) were added to the reaction mixture. The phases were separated, and the organic phase was washed with water (50 mL) and

a saturated solution of NaCl (50 mL), dried over anhydrous Na_2SO_4, and filtered. The solvent was removed under reduced pressure, and the residue was purified by flash column chromatography.

Methyl 4-((pyrimidin-4-yloxy)methyl)benzoate (24)

Synthesized from methyl 4-(hydroxymethyl)benzoate (**6**) (22 mmol, 3.656 g), NaH (42 mmol, 1.680 g of 60% dispersion in mineral oil) and 4-chloropyrimidine hydrochloride (20 mmol, 3.02 g) in DMF (30 mL) at room temperature for 24 h. The compound was purified by flash column chromatography using EtOAc/n-hexane = 1/2 (v/v) as the eluent. Yield 23%; yellow - white solid; Rf = 0.18 (EtOAc/n-hexane, 1:2, v/v); ^{1}H NMR (400 MHz, DMSO-d_6): δ (ppm) = 3.92 (s, 3H), 5.49 (s, 2H), 6.82 (d, J = 5.8, 1.2 Hz, 1H), 7.43 – 7.52 (m, 2H), 8.02 – 8.08 (m, 2H), 8.46 (d, J = 5.8 Hz, 1H), 8.78 (s, 1H).

Methyl 4-(((2-methylpyrimidin-4-yl)oxy)methyl)benzoate (25)

Synthesized from methyl 4-(hydroxymethyl)benzoate (**6**) (11 mmol, 1.83 g), NaH (12 mmol, 0.48 g of 60% dispersion in mineral oil) and 4-chloro-2-methylpyrimidine (10 mmol, 1.286 g) in THF (40 mL) at 60 ºC for 4 h. The compound was purified by flash column chromatography using EtOAc/n-hexane = 1/2 (v/v) as an eluent. Yield 24%; yellow-white solid; Rf = 0.18 (EtOAc/n-hexane, 1:2, v/v); ^{1}H NMR (400 MHz, DMSO-d_6): δ (ppm) = 2.62 (s, 3H), 3.92 (s, 3H), 5.47 (s, 2H), 6.61 (d, J = 5.5 Hz, 1H), 7.47 – 7.54 (m, 2H), 8.02 – 8.09 (m, 2H), 8.35 (d, J = 4.8 Hz, 1H).

Methyl 4-(((6-methylpyrimidin-4-yl)oxy)methyl)benzoate (26)

Synthesized from methyl 4-(hydroxymethyl)benzoate (**6**) (22 mmol, 3.656 g), NaH (24 mmol, 0.960 g of 60% dispersion in mineral oil) and 4-chloro-6-methylpyrimidine (20 mmol, 2.571 g) in THF (40 mL) at 60 ºC for 4 h. The compound was purified by flash column chromatography using EtOAc/n-hexane = 1/2 (v/v) as the eluent. Yield 17%; white solid; Rf = 0.18 (EtOAc/n-hexane, 1:2, v/v); ^{1}H NMR (400 MHz, DMSO-d_6): δ (ppm) = 2.46 (s, 3H), 3.92 (s, 3H), 5.48 (s, 2H), 6.67 (s, 1H), 7.47 – 7.52 (m, 2H), 8.03 – 8.07 (m, 2H), 8.67 (d, J = 0.6 Hz, 1H).

Methyl 4-(((2-methylquinazolin-4-yl)oxy)methyl)benzoate (**33**)

Synthesized from methyl 4-(hydroxymethyl)benzoate (**6**) (22 mmol, 3.656 g), NaH (24 mmol, 0.960 g of 60% dispersion in mineral oil) and 4-chloro-2-methylquinazoline (20 mmol, 3.572 g) in THF (40 mL) at 60 ºC for 4 h. The compound was purified by flash column chromatography using EtOAc/n-hexane = 1/2 (v/v) as the eluent. Yield 17%; white solid; Rf = 0.18 (EtOAc/n-hexane, 1:2, v/v); ^{1}H NMR (400 MHz, DMSO-d_6): δ (ppm) = 2.74 (s, 3H), 3.93

(s, 3H), 5.68 (s, 2H), 7.50 (ddd, *J* = 8.1, 6.8, 1.3 Hz, 1H), 7.58 – 7.61 (m, 2H), 7.80 (ddd, *J* = 8.4, 6.8, 1.5 Hz, 1H), 7.85 – 7.87 (m, 1H), 8.07 – 8.10 (m, 2H), 8.17 (ddd, *J* = 8.2, 1.4, 0.6 Hz, 1H).

Methyl 4-(((2-methyl-6,7-dihydro-5*H*-cyclopenta[*d*]pyrimidin-4-yl)oxy)methyl)benzoate (36)

Synthesized from methyl 4-(hydroxymethyl)benzoate (**6**) (6.19 mmol, 1.029 g), NaH (6.76 mmol, 0.270 g of 60% dispersion in mineral oil) and 4-chloro-2-methyl-6,7-dihydro-5H-cyclopenta[d]pyrimidine (5.63 mmol, 0.949 g) in THF (40 mL) at 60 ºC for 4 h. The compound was purified by flash column chromatography using EtOAc/n-hexane = 1/2 (v/v) as the eluent. Yield 48%; white solid; Rf = 0.52 (EtOAc/n-hexane, 1:1, v/v); ^{1}H NMR (400 MHz, DMSO-*d*$_6$): δ (ppm) = 2.03 – 2.12 (m, 2H), 2.59 (s, 3H), 2.83 (t, *J* = 7.4 Hz, 2H), 2.90 (t, *J* = 7.8 Hz, 2H), 3.89 (s, 3H), 5.47 (s, 2H), 7.47 – 7.49 (m, 2H), 8.01 – 8.03 (m, 2H).

General procedure D

The appropriate methyl ester (1 equiv.) was dissolved in 1 M NaOH (15 mL) and dioxane (15 mL) and stirred overnight at room temperature. Dioxane was evaporated, and diethyl ether (30 mL) was added. The phases were separated. 1M HCl was added to the aqueous phase, and the solid that precipitated was filtered off.

4-((Pyrimidin-4-yloxy)methyl)benzoic acid (27)

Synthesized from methyl 4-((pyrimidin-4-yloxy)methyl)benzoate (**24**) (4.6 mmol, 1.13 g). Yield 90%; white solid; Rf = 0.49 (DCM/MeOH, 9:1, v/v); ^{1}H NMR (400 MHz, DMSO-*d*$_6$): δ (ppm) = 5.52 (s, 2H), 7.11 (d, *J* = 5.8 Hz, 1H), 7.56 (d, *J* = 8.1 Hz, 2H), 7.95 (d, *J* = 8.1 Hz, 2H), 8.59 (d, *J* = 5.9 Hz, 1H), 8.86 (s, 1H), 12.81 (bs, 1H).

4-(((2-Methylpyrimidin-4-yl)oxy)methyl)benzoic acid (28)

Synthesized from methyl 4-(((2-methylpyrimidin-4-yl)oxy)methyl)benzoate (**25**) (5.0 mmol, 1.29 g). Yield 64%; white solid; Rf = 0.25 (EtOAc); ^{1}H NMR (400 MHz, DMSO-*d*$_6$): δ (ppm) = 2.53 (s, 3H), 5.39 (s, 2H), 6.79 (d, *J* = 5.8 Hz, 1H), 7.35 (d, *J* = 8.0 Hz, 2H), 7.88 (d, *J* = 8.0 Hz, 2H), 8.41 (d, *J* = 5.8 Hz, 1H), 1H from COOH is exchanged.

4-(((6-Methylpyrimidin-4-yl)oxy)methyl)benzoic acid (29)

Synthesized from methyl 4-(((6-methylpyrimidin-4-yl)oxy)methyl)benzoate (2**6**) (3.19 mmol, 0.823 g). Yield 73%; white solid; Rf = 0.26 (EtOAc); ^{1}H NMR (400 MHz, DMSO-*d*$_6$): δ (ppm) = 2.38 (s, 3H), 5.48 (s, 2H), 6.90 (s, 1H), 7.53 (d, *J* = 7.6 Hz, 2H), 7.95 (d, *J* = 7.6 Hz, 2H), 8.65 (s, 1H), 12.99 (bs, 1H).

4-(((2-Methylquinazolin-4-yl)oxy)methyl)benzoic acid (34)

Synthesized from methyl 4-(((2-methylquinazolin-4-yl)oxy)methyl)benzoate (**33**) (5.1 mmol, 1.57 g). Yield 43%; white solid; Rf = 0.57 (DCM/MeOH, 9:1, v/v); ^{1}H NMR (400 MHz, DMSO-d_6): δ (ppm) = 2.66 (s, 3H), 5.72 (s, 2H), 7.61 – 7.65 (m, 1H), 7.67 – 7.69 (m, 2H), 7.85– 7.96 (m, 2H), 7.98 – 8.00 (m, 2H), 8.18 (dd, *J* = 8.2, 0.7 Hz, 1H), 12.98 (bs, 1H).

4-(((2-Methyl-6,7-dihydro-5*H*-cyclopenta[*d*]pyrimidin-4-yl)oxy)methyl)benzoic acid (37)

Synthesized from methyl 4-(((2-methyl-6,7-dihydro-5H-cyclopenta[d]pyrimidin-4-yl)oxy)methyl)benzoate (3**6**) (2.7 mmol, 0.805 g). Yield 69%; white solid; Rf = 0.58 (DCM/MeOH, 9:1, v/v); ^{1}H NMR (400 MHz, DMSO-d_6): δ (ppm) = 1.98 – 2.05 (m, 2H), 2.47 (s, 3H), 2.76 (t, *J* = 7.4 Hz, 2H), 2.82 (t, *J* = 7.7 Hz, 2H), 5.49 (s, 2H), 7.54 (d, *J* = 8.1 Hz, 2H), 7.94 (d, *J* = 8.1 Hz, 2H), 12.99 (bs, 1H).

General procedure E (synthesis of amide)

To the corresponding acid (1 equiv.) dissolved in anhydrous THF (10 mL) and DMF (2 mL), DIPEA (2 equiv.) and HATU (1.5 equiv.) were added under an argon atmosphere. After 15 minutes, the corresponding amine (1 equiv.) was added to the stirred solution. The reaction mixture was stirred overnight at room temperature. THF was then evaporated under reduced pressure. The residue was dissolved in EtOAc (50 mL) and washed with saturated solution of $NaHCO_3$ (50 mL), water (50 mL), and brine (50 mL). The organic phase was dried over anhydrous Na_2SO_4, filtered, and evaporated under reduced pressure. The residue was purified by flash column chromatography.

4-((Pyrimidin-4-yloxy)methyl)-*N*-(1-isopropylpiperidin-4-yl)benzamide (30)

Synthesized from 4-((pyrimidin-4-yloxy)methyl)benzoic acid (**27**) (1.5 mmol, 0.345 g), DIPEA (3.0 mmol, 0.523 mL), HATU (1.8 mmol, 0.684 g), and 1-isopropylpiperidin-4-amine (1.5 mmol, 0.236 mL) via general procedure E. The compound was purified by flash column chromatography on Biotage Isolera One. Yield 39%; white solid; Rf = 0.25 (DCM/MeOH, 9:1, v/v); ^{1}H NMR (400 MHz, $CDCl_3$): δ (ppm) = 1.06 (d, *J* = 6.4 Hz, 6H), 1.56 – 1.64 (m, 2H), 2.03 – 2.06 (m, 2H), 2.29 – 2.35 (m, 2H), 2.75 – 2.81 (m, 1H), 2.87 – 2.90 (m, 2H), 3.90 – 4.07 (m, 1H), 5.46 (s, 2H), 6.44 (d, *J* = 7.6 Hz, 1H), 6.80 (d, *J* = 5.6 Hz, 1H), 7.47 (d, *J* = 7.9 Hz, 2H), 7.79 (d, *J* = 7.9 Hz, 2H), 8.44 (d, *J* = 5.7 Hz, 1H), 8.77 (s, 1H); ^{13}C NMR (100 MHz, $CDCl_3$): δ (ppm) = 18.28, 32.22, 47.32, 47.53, 54.61, 67.24, 108.82, 127.24, 127.88, 134.57, 139.42, 157.27, 158.33, 166.44, 168.48. HRMS (ESI+) *m/z* calcd. for $C_{20}H_{27}N_4O_2$ $[M+H]^+$ 355.21285, found 355.21236; HPLC purity 100.00% at 254 nm (t_R = 2.013 min).

4-(((2-Methylpyrimidin-4-yl)oxy)methyl)-*N*-(1-isopropylpiperidin-4-yl)benzamide (31)

Synthesized from 4-(((2-methylpyrimidin-4-yl)oxy)methyl)benzoic acid (**28**) (1.2 mmol, 0.293 g), DIPEA (2.4 mmol, 0.418 mL), HATU (1.44 mmol, 0.548 g), and 1-isopropylpiperidin-4-amine (1.5 mmol, 0.189 mL) via general procedure E. The compound was purified by flash column chromatography on Biotage Isolera One. Yield 16%; white solid; Rf = 0.25 (DCM/MeOH, 9:1, v/v); ^{1}H NMR (400 MHz, $CDCl_3$): δ (ppm) = 1.06 (d, *J* = 6.6 Hz, 6H), 1.51 – 1.60 (m, 2H), 2.05 – 2.07 (m, 2H), 2.29 – 2.35 (m, 2H), 2.61 (s, 3H), 2.71 – 2.81 (m, 1H), 2.86 – 2.89 (m, 2H), 3.94 – 4.03 (m, 1H), 5.45 (s, 2H), 6.11 (d, *J* = 7.5 Hz, 1H), 6.59 (d, *J* = 5.8 Hz, 1H), 7.49 (d, *J* = 8.1 Hz, 2H), 7.77 (d, *J* = 8.2 Hz, 1H), 8.34 (d, *J* = 5.8 Hz, 1H); ^{13}C NMR (100 MHz, $CDCl_3$): δ (ppm) = 18.47, 26.01, 32.69, 47.48, 47.63, 54.62, 67.04, 105.53, 127.20, 128.12, 134.61, 139.90, 157.42, 166.51, 168.16, 168.60. HRMS (ESI+) *m/z* calcd. for $C_{21}H_{29}N_4O_2$ $[M+H]^+$ 369.22850, found 369.22797; HPLC purity 95.00% at 254 nm (t_R = 2.327 min).

4-(((6-Methylpyrimidin-4-yl)oxy)methyl)-*N*-(1-isopropylpiperidin-4-yl)benzamide (32)

Synthesized from 4-(((6-methylpyrimidin-4-yl)oxy)methyl)benzoic acid (**29**) (1.2 mmol, 0.293 g), DIPEA (2.4 mmol, 0.418 mL), HATU (1.44 mmol, 0.548 g), and 1-isopropylpiperidin-4-amine (1.5 mmol, 0.189 mL) via general procedure E. The compound was purified by flash column chromatography on Biotage Isolera One. Yield 33%; white solid; Rf = 0.23 (DCM/MeOH, 9:1, v/v); ^{1}H NMR (400 MHz, $CDCl_3$): δ (ppm) = 1.05 (d, *J* = 6.5 Hz, 6H), 1.51 – 1.61 (m, 2H), 2.03 – 2.06 (m, 2H), 2.28 – 2.33 (m, 2H), 2.44 (s, 3H), 2.71 – 2.81 (m, 1H), 2.86 – 2.89 (m, 2H), 3.92 – 4.02 (m, 1H), 5.45 (s, 2H), 6.25 (d, *J* = 7.9 Hz, 1H), 6.65 (s, 1H), 7.46 (d, *J* = 8.1 Hz, 2H), 7.77 (d, *J* = 8.2 Hz, 1H), 8.66 (s, 1H); ^{13}C NMR (100 MHz, $CDCl_3$): δ (ppm) = 18.39, 23.83, 32.56, 47.43, 47.56, 54.56, 67.12, 107.17, 127.19, 127.85, 134.54, 139.77, 157.79, 166.47, 167.60, 169.08. HRMS (ESI+) *m/z* calcd. for $C_{21}H_{29}N_4O_2$ $[M+H]^+$ 369.22850, found 383.22801; HPLC purity 98.18% at 254 nm (t_R = 2.023 min).

***N*-(1-Isopropylpiperidin-4-yl)-4-(((2-methylquinazolin-4-yl)oxy)methyl)benzamide** (**35**)

Synthesized from 4-(((2-methylquinazolin-4-yl)oxy)methyl)benzoic acid (**34**) (1.2 mmol, 0.353 g), DIPEA (2.4 mmol, 0.418 ml), HATU (1.44 mmol, 0.548 g), and 1-isopropylpiperidin-4-amine (1.5 mmol, 0.189 mL) via general procedure E. The compound was purified by flash column chromatography on Biotage Isolera One. Yield 22%; white solid; Rf = 0.25 (DCM/MeOH, 9:1, v/v); ^{1}H NMR (400 MHz, $CDCl_3$): δ (ppm) = 1.07 (d, *J* = 6.5 Hz, 6H), 1.54 – 1.64 (m, 2H), 2.06 – 2.09 (m, 2H), 2.31 – 2.37 (m, 2H), 2.73 (s, 3H), 2.74 – 2.81 (m, 1H), 2.88 – 2.91 (m, 2H), 3.96 – 4.05 (m, 1H), 5.66 (s, 2H), 6.12 (d, *J* = 7.8 Hz, 1H), 7.47 – 7.51

(m, 1H), 7.58 (d, *J* = 8.1 Hz, 2H), 7.77 – 7.86 (m, 4H), 8.15 (d, *J* = 8.0 Hz, 1H); ^{13}C NMR (100 MHz, $CDCl_3$): δ (ppm) = 18.45, 26.50, 32.60, 47.43, 47.65, 54.73, 67.62, 114.56, 123.39, 126.29, 127.08, 127.27, 128.17, 133.71, 134.66, 139.92, 151.61, 163.76, 166.08, 166.54. HRMS (ESI+) *m/z* calcd. for $C_{25}H_{31}N_4O_2$ $[M+H]^+$ 419.24415, found 419.24364; HPLC purity 98.24% at 254 nm (t_R = 2.313 min).

***N*-(1-isopropylpiperidin-4-yl)-4-(((2-methyl-6,7-dihydro-5H-cyclopenta[d]pyrimidin-4-yl)oxy)methyl)benzamide (38)**

Synthesized from 4-(((2-methyl-6,7-dihydro-5H-cyclopenta[d]pyrimidin-4-yl)oxy)methyl)benzoic acid (**37**) (1.2 mmol, 0.341 g), DIPEA (2.4 mmol, 0.418 mL), HATU (1.44 mmol, 0.548 g), and 1-isopropylpiperidin-4-amine (1.5 mmol, 0.189 mL) via general procedure E. The compound was purified by flash column chromatography on Biotage Isolera One. Yield 62%; white solid; Rf = 0.30 (DCM/MeOH, 9:1, v/v); ^{1}H NMR (400 MHz, $CDCl_3$): δ (ppm) = 1.08 (d, *J* = 6.5 Hz, 6H), 1.56 – 1.64 (m, 2H), 2.01 – 2.14 (m, 4H), 2.32 – 2.37 (m, 2H), 2.58 (s, 3H), 2.76 – 2.94 (m, 7H), 3.93 – 4.07 (m, 1H), 5.48 (s, 2H), 6.16 (d, *J* = 7.6 Hz, 1H), 7.49 (d, *J* = 7.9 Hz, 2H), 7.76 (d, *J* = 7.9 Hz, 1H); ^{13}C NMR (100 MHz, $CDCl_3$): δ (ppm) = 18.39, 21.93, 25.65, 26.50, 32.47, 34.28, 47.31, 47.64, 54.79, 66.60, 116.69, 127.14, 127.98, 134.35, 140.50, 165.13, 166.42, 166.59, 175.21. HRMS (ESI+) *m/z* calcd. for $C_{24}H_{33}N_4O_2$ $[M+H]^+$ 409.25980, found 409.25868; HPLC purity 100% at 254 nm (t_R = 2.240 min).

5.4.3 Cell culture

Human Embryonic Kidney (HEK)-Blue Null1, HEK-Blue hTLR2-TLR1, HEK-Blue hTLR2-TLR6, HEK-Blue hTLR4, HEK-Blue hTLR5, HEK-Blue hTLR7, HEK-Blue hTLR8, and HEK-Blue hTLR9 cells (InvivoGen, Toulouse, France) were cultured in Dulbecco's modified Eagle's medium (PAN-Biotech, Aidenbach, Germany) containing 10% (v/v) heat inactivated fetal bovine serum (FBS; S0615), 100 U/mL penicillin, 100 mg/mL streptomycin (P4333), 2 mM L-glutamine (G7513) (all from Sigma Aldrich, Taufkirchen, Germany), 100 µg/mL normocin and selective antibiotics HEK-Blue Selection (hTLR2-TLR1, hTLR2-TLR6, hTLR4), 100 µg/mL zeocin (Null1) and 100 µg/mL zeocin with 10 µg/mL (hTLR7, hTLR9) resp. 30 µg/mL (hTLR5, hTLR8) blasticidin (all from InvivoGen, Toulouse, France). THP1-Dual MD2-CD14-TLR4 cells (InvivoGen, Toulouse, France) were cultured in RPMI-1640 medium supplemented with 10% FBS, penicillin (100U/mL), streptomycin (100 µg/mL), L-glutamine (2mM), HEPES (25 mM), normocin (100 µg/mL) and selective antibiotics (blasticidin: 10 µg/mL, zeocin: 100 µg/mL) following the manufacturer’s instructions.

THP-1 cells (ACC 16, DSMZ-German Collection of Microorganisms and Cell Cultures GmbH, Braunschweig, Germany) were cultured in RPMI 1640 (11530586, Fisher Scientific, Schwerte, Germany) containing 100 U/mL penicillin, 100 µg/mL streptomycin (P4333), 2 mM L-glutamine (G7513, both from Sigma-Aldrich, Taufkirchen, Germany) and 10% heat-inactivated FBS (S0615, Sigma-Aldrich, Taufkirchen, Germany) at a density of 4×10^5 cells/mL. To generate THP-1-derived macrophages, THP-1 monocytes were seeded into 24-well plates at a density of 4×10^5 cells/mL in growth medium containing 25 ng/mL PMA (phorbol 12-myristate 13-acetate; tlrl-pma, InvivoGen, Toulouse, France). After 48 h, adherent cells were carefully washed with PBS (phosphate buffered saline; P04-53500, Pan-Biotech, Aidenbach, Germany) and rested in PMA-free medium for 24 h. All cell lines were maintained at 37 °C in a humidified atmosphere of 5% CO2 and 95% air and were regularly tested negative for mycoplasma contamination (VenorGeM Classic Mycoplasma PCR detection kit, Minerva Biolabs, Berlin, Germany).

Peripheral blood mononuclear cells (PBMCs) were obtained from buffy-coat donations (Institute of Experimental Haematology and Transfusion Medicine, University Clinic Bonn) and isolated by density gradient centrifugation using Biocoll separation media (Bio&Sell, Nuremberg, Germany). PBMCs were washed three times with PBS containing EDTA and then seeded in 24-well plates (5×10^6 cells/well). The studies with human blood were approved by the ethics committee of the University Clinic Bonn (315/22) and written informed consent was obtained from all healthy donors.

5.4.4 Cell stimulation

HEK-Blue cells ($4\text{-}5\times10^4$ cells/well) and THP-1 macrophages (4×10^4 cells/well, 4×10^5 cells/well) were seeded in 96-well or 24-well plates (PS, Sarstedt, Germany), respectively. For stimulation experiments, cells were washed with phosphate-buffered saline (PBS, Sigma Aldrich) and medium was replaced with OptiMEM (Thermo Fisher Scientific, Darmstadt, Germany). For inhibition studies, the cells were preincubated with TLR8 antagonists for 1 h and then stimulated with TLR agonists for 24 h. The following TLR ligands were used: Pam_2CSK_4, Pam_3CSK_4, poly(I:C) (HMW), LPS from *E. coli* O111:B4 (LPS-EB Ultrapure), flagellin from *Bacillus subtilis* (flagellin-BS Ultrapure), CL307, TL8-506, ODN2006 and CU-CPT9a (all from InvivoGen, Toulouse, France), and enpatoran (BIOZOL Diagnostika, Germany). After 24 h, NF-κB activity was measured using QuantiBlue solution (InvivoGen, Toulouse, France) following manufactures instructions.

THP1-Dual MD2-CD14-TLR4 cells (InvivoGen, Toulouse, France) were seeded in 96-well plates at a density of $1x10^5$ cells per well and immediately preincubated with designated antagonists for 1 h and then stimulated with TLR agonists. After 24 h, NF-κB activity was measured using SEAP reporter assay with QuantiBlue solution (InvivoGen, Toulouse, France) and ISRE activity was measured via Lucia luciferase using QuantiLuc solution (InvivoGen, Toulouse, France), both following manufacturer's instructions.

The synthesized TLR8 antagonists were dissolved in DMSO as 12.5–50 mM stock solutions. Final DMSO concentrations in cell culture were below 0.2% (v/v). Cells were first incubated with the antagonists for 1 h and then stimulated with the respective TLR agonist.

5.4.5 Cell viability

Effects on cell viability were assessed by MTT and LDH assays. For the MTT assay HEK-Blue hTLR8 cells or differentiated THP-1 macrophages (40,000 cells/well, 96 well plate) were incubated with TLR8 antagonists for 20 h. Subsequently, 25 µl MTT (3-(4,5-dimethylthiazol-2-yl)-2,5-diphenyltetrazolium bromide, 5 mg/ml) was added and the plate was incubated for 4 h at 37 °C. After removing supernatants, DMSO (4720.1, Carl Roth, Karlsruhe, Germany) was added and absorption at 540 nm was measured. Viability of the untreated cells was defined as 100%. DMSO (10% v/v; A994.1, Carl Roth, Karlsruhe, Germany) served as a positive control.

The LDH assay was performed according to the manufacturer's instructions (Thermo Fisher Scientific, Darmstadt, Germany). The percentage of LDH release was calculated compared to 100% cell lysis control.

5.4.6 ELISA

Following 4 h of stimulation with the respective TLR agonists, cell culture supernatants from THP-1 macrophages or PBMCs were collected and TNF concentrations were analyzed using a commercially available human TNF ELISA kit (88–7346-88; Thermo Fisher Scientific, Darmstadt, Germany).

5.4.7 Dynamic mass redistribution (DMR) label-free assay

DMR assays were conducted using the EPIC system (Corning) as previously described.[158,160] Briefly, DMR measurements were performed using the Epic biosensor and following baseline readings, 10 µL of the agonist TL8-506 (6 µM) was added to each well (40 µL total volume) using a semiautomated liquid handler, Selma (Analytik Jena AG, Jena, Germany). Increasing concentrations of compound **16**, **35** or **CU-CPT9a** were preincubated for 1.5 h before the addition of TL8-506. DMR signals were recorded for 250 min, and the data were analyzed and

exported using the Epic Analyzer Software (Corning, New York, NY, USA). All signals were baseline-corrected, and responses were recorded as picometer (picosecond) shifts over time (minutes) following baseline normalization. Experiments were performed at 37 °C in triplicate or quadruplicate. For data normalization of the concentration-effect curves, indicated as relative response (%), the top levels of the concentration-effect curves were set to 100% and bottom levels to 0%.

5.4.8 Statistical analysis

Data are expressed as means ± SEM. Statistical differences were assessed by one-sample *t*-test against 100% and considered significant at *P ≤ 0.05, **P ≤ 0.01, ***P ≤ 0.001, ****P ≤ 0.0001. Curve fitting was performed using four-parameter nonlinear regression.

Statistical comparison of best-fit parameters ($logIC_{50}$) of nonlinear regressions from concentration response curves was conducted with the extra-sum-of-squares F-test. DMR data were normalized and expressed as relative response (%), with the top levels of the concentration-effect curves at 250 minutes set to 100% and the bottom levels to 0%. Statistical analysis was performed using GraphPad Prism (version 8.0, GraphPad software, San Diego, USA).

5.4.9 Protein structure preparation

The protein structure of human TLR8 with a co-crystallized ligand containing a positive ionizable interaction with Glu427 with the highest resolution (PDB ID: 6V9U)[166] was selected for *in silico* studies. The protein structure was prepared using MOE 2022 (Chemical Computing Group, Montreal, Canada). Crystallographic waters and buffer additives were removed, with the ligand being retained. The missing side chain modeling and capping were performed using the Structure Preparation utility implemented in MOE. The protein was protonated using the Protonate 3D function[167] at pH 7 and temperature 300 K.

5.4.10 Molecular docking studies

The obtained hits were docked into the prepared crystal structure of 6V9U using GOLD 5.8.2[168] with the binding site being defined as a radius of 6 Å around the co-crystallized ligand. For each molecule, 50 genetic algorithm runs were conducted using the ChemPLP scoring function.[169] Docking poses were minimized with the Merck molecular force field 94 (MMFF94).[170] Binding poses for the compounds were selected according to the fulfillment of the requirement of containing at least one hydrogen bond acceptor and one positive ionizable interaction. For the final step, the binding modes of the molecules were visually inspected

focusing on the interactions in addition to the conformational and structural sanity of the binding modes.

5.4.11 Molecular dynamics simulations

Molecular dynamics (MD) simulations were performed on RTX2080Ti and RTX3090 graphics processing units (NVIDIA Corporation, Santa Clara). Simulations of the TLR8 complex for compounds **15**, **16** and **23** were prepared using Maestro 11.7 (Schrödinger, LLC, New York, USA). The hydrogen bond network in the TLR8 complex systems was optimized at pH 7.0 and temperature 310 K. The complex was placed into a TIP3P water box with a padding distance of 10 Å from the protein surface. The system was isotonized with 0.15 M NaCl. The system was parameterized using the OPLS 2005 force field and relaxed using the default Desmond protocol. MD simulations were performed with a constant number of particles, pressure, and temperature (NPT ensemble). During the MD simulation, a constant temperature of 310 K was maintained using the Nose–Hoover thermostat. Constant pressure of 1.01325 bar was preserved during the simulation using the Martyna-Tobias-Klein method. Five replicas, each with a duration of 50 ns, were simulated, with each replica generating 1000 frames. The replicas were concatenated using VMD. The combined trajectories were analyzed using the OpenMMDL Analysis part of the OpenMMDL workflow, with default settings being used during the analysis. For the RMSD calculations, the MDAnalysis package was used.[171]

5.4.12 Determination of log D

The log D determination was performed by WuXi AppTec (Shanghai, China). The preparation of 100 mM phosphate buffer (PB) with the pH at 7.4: 15 mL of 100 mM Na_2HPO_4 (prepared by dissolving 5.999 g of Na_2HPO_4 in 500 mL of water) was added to a 50 mL tube, and the pH was then adjusted to 7.4 ± 0.05 with 100 mM NaH_2PO_4 (prepared by dissolving 7.098 g of NaH_2PO_4 in 500 mL of water). PB (pH 7.4) saturated with 1-octanol was prepared by the addition of 10 mL of 1-octanol into 100 mL of 100 mM PB (pH 7.4) and the mixture was shaken vigorously and left standing overnight at room temperature before use. 1-Octanol saturated with PB (pH 7.4) was prepared by adding 10 mL of 100 mM PB (pH 7.4) into 100 mL of 1-octanol and the mixture was shaken vigorously and left standing overnight at room temperature before use. 2 μL of stock solution of test compounds and control compounds were aliquoted into tubes in duplicate. Then 149 μL of 1-octanol saturated with PB (pH 7.4) was added into the tubes, and 149 μL of PB (pH 7.4) saturated with 1-Octanol was added to the corresponding tubes. Each tube was mixed vigorously for 2 minutes and then shaken for 1 hour at 800 rpm at room temperature, followed by centrifugation at 4000 rpm for 5 minutes at room temperature. Then

appropriate volumes of buffer layer samples and 1-octanol layer samples were aliquoted. These samples were diluted and analyzed by using the LC-MS/MS method without running a calibration curve. The log D value for each compound was calculated using the following equation:

$$Log\ D_{octanol/buffer} = \log10(\frac{Mean\ Octanol\ Layer\ Peak\ Area\ Ratio\ *\ Octanol\ Layer\ Dilution\ Factor}{Mean\ Buffer\ Layer\ Peak\ Area\ Ratio\ *\ Buffer\ Layer\ Dilution\ Factor})$$

5.4.13 Determination of kinetic solubility

The kinetic solubility assay was performed by WuXi AppTec (Shanghai, China). The preparation of 50 mM phosphate buffer (PB) with the pH at 7.4: 15 mL of 100 mM Na_2HPO_4 (prepared by dissolving 3.000 g of Na_2HPO_4 in 500 mL of water) was added into a 50 mL tube, and the pH was then adjusted to 7.4 ± 0.05 with 100 mM NaH_2PO_4 (prepared by dissolving 3.549 g of NaH_2PO_4 in 500 mL of water). The 10 mM stock solutions of the test compounds were prepared in DMSO. 10 μL of stock solution of test and control compounds was added into each well of a 96-well plate. Then, 490 μL of medium was added to each well of the 96-well plate. The solubility samples were vortexed for at least 2 minutes. The 96-well plate was shaken at room temperature at 800 rpm for 24 hours and then centrifuged at 25 ℃ for 10 minutes (e.g. 4000 rpm). The supernatant was transferred into a filter plate, and then the filtrates were collected into a new 96-well plate by centrifuging for at least 5 minutes. The concentrations of the filtrates were quantified by the LC-UV system. Materials: MultiScreen Solvinert (PTFE Filter Media with polyolefin copolymer device) from Millipore Merck.

5.4.14 Determination of metabolic stability in human and mouse liver microsomes

Microsome stability tests were conducted by WuXi AppTec (Shanghai, China). The 10 mM stock solutions of the test and control compounds (testosterone, diclofenac and propafenone) were prepared in DMSO and diluted to 100 μM with acetonitrile. Empty 'Incubation' plates T60 and NCF60 were pre-warmed at 37 °C for 10 min. Microsome working solution (445 μL) was transferred into pre-warmed 'Incubation' plates T60 and NCF60, followed by a 10-minute incubation at 37 °C. Microsome working solution (54 μL) was transferred to a Blank60 plate, followed by the addition of 6 μL NADPH cofactor and 180 μL of stop solution into each well. Compound working solution (5 μL) was added to the 'Incubation' plates (T60 and NCF60) containing microsomes. For the 'Incubation' plate NCF60, 50 μL of PB buffer was added, and the plate was incubated at 37 °C for 60 min. Stop solution (180 μL) and NADPH working solution (6 μL) were added to the T0 plate. Then, a mixture (54 μL) was removed from the 'Incubation' plate T60 and transferred to the T0 plate. For the 'Incubation' plate T60, NADPH

working solution (44 µL) was added, followed by a 60-minute incubation at 37 °C. At 5, 15, 30, 45, and 60 min, 60 µL of each sample at each time point was transferred to a well containing 180 µL of stop solution, followed by mixing. All sampling plates were shaken for 10 min, then centrifuged at 3220 ×g for 20 min at 4 °C. The supernatant (80 µL) was transferred into 240 µL of pure water and mixed using a plate shaker for 10 min. Each bioanalysis plate was sealed and shaken for 10 min prior to LC-MS/MS analysis. The stability of the compounds was determined as *in vitro* half-life ($t_{1/2}$) and intrinsic clearance (CL_{int}). The microsomal intrinsic clearance ($CL_{int(mic)}$) was calculated using the following equation: $CL_{int(mic)} = 0.693/t_{1/2}$/mg microsomal protein per mL. Hepatic intrinsic clearance ($CL_{int(liver)}$) was estimated from liver microsomal data using the following equation and appropriate scaling factors: $CL_{int(liver)} = CL_{int(mic)}$ × mg microsomal protein/g liver weight × g liver weight/kg body weight. Scaling factors: 45 mg microsomal protein per gram liver tissue, 88 g (mouse) or 20 g (human) liver tissue per kilogram body weight.[172,173] The equation of first-order kinetics was used to calculate $t_{1/2}$:

Equation of first-order kinetics:

$$C_t = C_0 \times e^{-k \times t}$$

$$When\ C_t = \frac{1}{2} C_0$$

$$T_{1/2} = \frac{ln2}{k_e} = \frac{0.693}{k_e}$$

5.4.15 Determination of plasma protein binding

Phosphate Buffered Saline (PBS) Solution Preparation (100 mM sodium phosphate and 150 mM NaCl, pH 7.4 ± 0.1): BupH Phosphate Buffered Saline Pack, supplied by Thermo Fisher Scientific under Product #28372, contained 0.1 M sodium phosphate and 0.15 M sodium chloride with a pH of 7.2, when the pouch contents were dissolved in a final volume of 500 mL ultrapure water. Before use, the pH value was adjusted to 7.4 ± 0.1 using 1% phosphoric acid or 1 N sodium hydroxide.

On the day of the experiment, plasma (Biomex) was thawed under running cold tap water and centrifuged at 3220 ×g for 5 min to remove any clots. The pH value was checked and recorded. The pH of the resulting plasma was measured and adjusted to 7.4 ± 0.1 using 1% phosphoric acid or 1 M sodium hydroxide, as needed. Working solutions (400 µM) of test compounds were prepared by diluting 4 µL of the stock solution (10 mM) with 96 µL DMSO. Working solutions (400 µM) of control compounds were prepared by diluting 4 µL of the stock solution (10 mM) with 96 µL DMSO. Loading matrix solutions (2 µM) of test compounds were prepared by

diluting 5 μL of working solutions with 995 μL of blank matrix and mixed thoroughly. Loading matrix solutions (2 μM) of control compounds were prepared by diluting 5 μL of working solutions with 995 μL of blank matrix and mixed thoroughly. Aliquots of 50 μL loading matrix containing test compounds or control compounds were transferred in triplicate to Sample Collection Plate, respectively. The samples were matched with opposite blank PBS to obtain a final volume of 100 μL with a volume ratio of matrix: PBS at 1: 1 (v: v) in each well immediately. The stop solution (500 μL, acetonitrile with 0.1% formic acid containing tolbutamide at 250 nM and labetalol at 250 nM) was added to these T0 samples of test and control compound. The plate was sealed and shaken at 800 rpm for 10 min. These T0 samples were then stored at 2 ~ 8 °C pending further processing along with other post-dialysis samples. The rapid equilibrium dialysis base plate(s) with inserts (Thermo Scientific Base Plate - Made of PTFE material (catalog number 89811) and Thermo Scientific Rapid Equilbrium Dialysis (RED) Device Inserts, 8 kDa MWCO, catalog number 89810 or 89809) were assembled following the manufacturer's instructions. The PBS chambers (the white ring) were loaded with the appropriate volume of PBS, and then the corresponding volume of spiked sample matrix was loaded into the sample chambers of the RED insert, identified by the red ring, in triplicate (200 μL matrix - 350 μL PBS). At the end of dialysis, aliquots of 50 μL of samples were taken from both the PBS (receiver) side and the matrix (donor) side of the dialysis device. These samples were transferred into new 96-well plates (the sample collection plates). Each sample was mixed with an equal volume of opposite blank PBS or matrix to reach a final volume of 100 μL with a volume ratio of matrix: PBS (1: 1, v: v) in each well. All samples were further processed by adding 500 μL of stop solution containing internal standards. The mixture was vortexed and centrifuged at 4000 rpm for about 20 min. An aliquot of 100 μL of supernatant of all samples was then removed for LC-MS/MS analysis. Single blank samples were prepared by transferring 50 μL of blank matrix to a 96 well plate and adding 50 μL of blank PBS to each well. The matrix-matched samples were then further processed by adding 500 μL of stop solution containing internal standards, following the same sample processing method as the dialysis samples.

The %Unbound, %Bound and %Recovery were calculated using the following equations:

$$\%Unbound = 100 \times \frac{F}{T}$$

$$\%Bound = 100 - \%Unbound$$

$$\%Recovery = 100 \times \frac{(F \times 350 + T \times 200)}{(T_0 \times 200)}$$

F = the peak area ratio of compound and internal standard on the receiver side of the membrane after 4 hours of incubation; T = the peak area ratio of compound and internal standard on the donor side of the membrane after 4 hours of incubation; T_0 = the peak area ratio of compound and internal standard at time zero

6 Summary

In recent years, TLRs have emerged as therapeutic targets. Agonists potentiate vaccine-induced immunity and anti-tumor responses, whereas antagonists reduce pathological inflammation in autoimmune diseases such as psoriasis, RA and SLE.[174–176] This thesis investigated the discovery and development of selective TLR8 antagonists, their effect on TLR8 signaling pathways, and their functional validation reducing pathological cytokine release. The resulting compounds exhibit potency and selectivity profiles suitable for further development as therapeutic agents targeting autoimmune disorders driven by aberrant TLR8 activation.

Chapter 2 reviewed how recent studies have revitalized work on endosomal receptors TLR7, TLR8, and TLR9. Over the past decade, high-resolution cryo-EM structures of all three receptors have guided ligand design, discovering dozens of chemotypes. These advances have translated into promising clinical programs. The oral dual TLR7/8 inhibitor enpatoran recently reduced lupus disease activity in the Phase II WILLOW study (NCT05162586), with safety and efficacy being investigated in current trials (NCT05540327). Furthermore, TLR8 agonist selgantolimod (GS-9688) reached Phase II for chronic hepatitis B (NCT05551273). Intratumoral TLR9 agonists like tilsotolimod (IMO-2125) combined with checkpoint inhibitors, have extended progression-free survival in melanoma and head-and-neck cancer.[109] Ongoing efforts to achieve selective TLR8 ligands have produced potent compounds such as ZG0895, a nanomolar TLR8-specific agonist now in Phase I oncology testing,[177] and the CU-CPT9 series antagonists that demonstrated a breakthrough in antagonism by locking the receptor in its open conformation.[95]

Beyond pharmacological selectivity, formulation strategies and delivery platforms offer crucial spatial control over TLR modulation. Chemical modification of oligoribonucleotides at the 2′-sugar position confers TLR7 selectivity by preventing RNase-mediated cleavage that would otherwise generate TLR8-activating uridine monomers.[178] Core-cross-linked diselenide nanoparticles enable radio responsive release of TLR7/8 agonists within irradiated tumor fields, synchronizing immune activation with radiotherapy effectively minimizing systemic cytokine release.[179] In parallel, recent advances in smart nanoparticle technologies allow targeting of specific immune cell subsets, further highlighting the adaptability of modern delivery systems for precise and context-dependent modulation of TLR signaling.[180]

Despite significant progress in TLR-targeted therapeutics, a critical gap persists. No selective TLR8 modulator has obtained regulatory approval. Most clinically advanced candidates exhibit dual TLR7/8 activity, reflecting fundamental challenges in achieving receptor selectivity. TLR7

and TLR8 share extensive structural homology, particularly within the ligand-binding pocket, with human sequences differing by only a few key residues.[181] This similarity extends to overlapping signaling outputs, complicating efforts to evaluate receptor-specific contributions to therapeutic efficacy. Moreover, functional crosstalk among TLRs and other pattern recognition receptors such as RIG-I-like helicases adds mechanistic complexity, as selective modulation of one pathway may inadvertently influence others.[182,183] Nevertheless, recent advances offer promising solutions. Computational approaches including molecular dynamics simulations and machine learning-guided design are elucidating receptor activation mechanisms and identifying structural features that guide TLR8 selectivity.[96,184] Additionally, the discovery of endogenous antagonistic mechanisms mediated by 2′-O-methylated RNA fragments provides insights into natural regulatory checkpoints with therapeutic potential.[185] These findings collectively highlight both the challenges and opportunities facing next-generation TLR8-selective drug development.

Chapters 3, 4, and 5 focus on the development and characterization of selective TLR8 antagonists to address the significant unmet need for targeted inhibition of TLR8 signaling. Chapter 3 describes the optimization of a previously discovered molecule, transforming it into a focused series of 6-(trifluoromethyl)pyrimidine antagonists. Guided by SAR, the original substituents at positions 2 and 4 of the pyrimidine core were replaced with systematically varied aromatic rings. Compounds 14 and 26 reached low-micromolar potency without measurable cytotoxicity at working concentrations. Molecular dynamics simulations confirmed stable hydrogen bonding between pyrimidine N-3 and Gly351, while the CF_3 group anchored hydrophobically against Tyr348, Val378, and Phe495*, rationalizing the observed SAR.

Although this series remained less potent than the original scaffold, it introduces a chemically accessible template whose activity can be enhanced by utilizing the newly mapped pyrrole vector or modulating the CF_3 pocket. However, valuable SAR data for the pyrimidine scaffold were obtained, demonstrating that rational design grounded in structural insight can rapidly evolve TLR8 ligands, paving the way for selective antagonists capable of suppressing pathological TLR8 signaling in autoimmune disease.

Building on the structural insights from Chapter 3, Chapter 4 employed an iterative structure-guided approach to develop TLR8 antagonists with enhanced potency. Virtual screening against the ectodomain uridine pocket of human TLR8 identified a novel isoxazole scaffold as a chemically distinct starting point. Molecular modeling predicted a binding mode in which the

isoxazole nitrogen forms a critical hydrogen bond with Gly351, while a piperidine substituent extends toward Glu427 and a phenyl ring occupies a hydrophobic cavity defined by Tyr348, Val378*, and Phe495*. Systematic SAR exploration revealed that lengthening the piperidine N-alkyl group and trimming a meta-methoxy substituent on the aryl ring tighten these contacts, improving potency from micromolar to nanomolar range.

The ligand-binding site in TLR8 was explored using both *in silico* predictions and experimental mutagenesis of key amino acid residues. Mutations in the TLR8 binding pocket at Gly351 and Val378, which define the uridine pocket, disrupted both agonist and antagonist activity underscoring their essential role for ligand engagement. The F495L mutation maintained the key Gly351 hydrogen bond while removing edge-to-face π-stacking yet caused only partial loss of antagonist activity. This suggests that Phe495 plays a supportive, but not essential, role in ligand binding. To confirm competitive antagonism, Schild plots were performed for the lead compound 10. Schild regression analysis yielded parallel right-shifts with unit slope, suggesting that compound 10 competes directly for the ligand site previously defined for CU-CPT9 series.[95] These findings connect directly to the current structural models of TLR8 activation and Myddosome formation.[75] Active TLR8 signaling requires ectodomain closure to juxtapose the two intracellular TIR domains, creating a platform for six MyD88 death domains to nucleate the helical tower that subsequently recruits IRAK4 and IRAK2.[77] By stabilizing the open ectodomain, compound 10 prevents TIR domain approximation, thereby blocking the geometric trigger for Myddosome assembly and leaving MyD88 dispersed in the cytosol. Co-IP experiments in THP-1 macrophages confirmed that the agonist induced TLR8-MyD88 complex is reduced in the presence of compound 10. Western blots demonstrated the functional consequence. IκBα remained undegraded and phospho-p65 levels were reduced, suggesting that the signaling cascade is inhibited at the adaptor-recruitment step rather than downstream in the kinase chain. Preventing the MyD88 recruitment and preserving IκBα further suppressed both NF-κB and IRF arms of the pathway and decreased IL-1β secretion from inflammasome-primed macrophages.

Beyond classical pharmacology, DMR, a label-free optical biosensor assay introduced for TLR research recently by our working group, was adopted.[160] Our previous studies captured real-time signaling fingerprints for plasma-membrane and endosomal TLRs, yet no antagonist data for TLR8 were available. Application of DMR using THP-1 cells treated with compound 10 revealed reduction of the TLR8 agonist-induced signal. Since DMR detects cytoskeletal rearrangements driven by early adaptor engagement,[186] the reduced signal corroborates the co-

IP and Western blot findings showing impaired MyD88 recruitment. Together, these approaches provide real-time, whole-cell confirmation that compound 10 intercepts Myddosome formation at its earliest step. These insights represent the first direct protein–protein interaction proof that a small-molecule TLR8 antagonist can block this supramolecular assembly, thereby completing the mechanistic understanding initiated with CU-CPT9a but never biochemically validated. Finally, this work establishes a comprehensive structure–activity framework for targeting the TLR8 uridine-binding pocket. The identification of a selective, nanomolar lead compound provides a strong foundation for pharmacokinetic characterization and advances the development of this novel antagonist class.

Chapter 5 explored scaffold optimization by replacing the isoxazole core from Chapter 4 with the 2,6-dimethylpyrimidine scaffold from Chapter 3. This approach aimed to enhance antagonist potency while preserving key binding interactions. SAR studies demonstrate that maintaining critical interactions such as the Gly351 hydrogen bond and Glu427 salt bridge while creating additional room for hydrophobic optimization is essential for activity. Incorporation of an isopropyl group on the piperidine nitrogen increases potency 10-fold over the isoxazole by engaging Leu490. Furthermore, fusing the ring system to form a quinazoline adds a π-stacking interaction with Phe494*, resulting in low-nanomolar antagonist activity. The lead compound 35 matched the benchmark antagonist CU-CPT9a in potency and exhibited 280-fold selectivity over TLR7. DMR assays in THP-1 macrophages confirmed that both pyrimidine lead 16 and quinazoline lead 35 completely block agonist-induced receptor signaling. Docking studies place 35 deep in the uridine pocket, where its pyrimidine N1 hydrogen-bonds to Gly351, the isopropyl tail interacts with Leu490 and Phe470, and the fused ring π-stacks with Phe494*. Mutation of Gly351 or Val378 reduced antagonist activity, while substituting Phe495 with leucine only weakened it, confirming that compound 35 occupies the same ligand site as CU-CPT9 derivatives and the previously discovered isoxazole compound 10.

Compound 16 and compound 35 both met critical drug-like benchmarks, showing good water solubility, moderate polarity, and robust metabolic stability in human and mouse liver microsomes. However, their pharmacokinetic profiles showed clear distinctions: compound 16 stands out for its higher proportion of unbound drug in plasma, while compound 35 is characterized by much stronger plasma protein binding, which could extend its half-life while lowering free circulating levels. Importantly, compound 35 displayed higher selectivity, low-nanomolar potency comparable to the activity observed for CU-CPT9a and evident engagement of the TLR8 uridine pocket. Despite its higher protein binding, compound 35 suppresses TNF

release in primary immune cells at very low concentrations, confirming its effectiveness. The favorable pharmacokinetic and physicochemical properties of quinazoline 35, combined with its high selectivity and metabolic stability, position it as a promising lead compound for further development. These attributes make compound 35 a valuable tool for investigating TLR8-targeted therapies in inflammatory diseases.

This thesis presents a comprehensive approach to TLR8 antagonist development, integrating immunological insights, structure-based drug design, and mechanistic characterization to establish potent and selective lead compounds. These studies demonstrate that selective, potent modulation of TLR8 is feasible and therapeutically promising, thus further addressing the considerable burden of autoimmune and inflammatory diseases. Benchmarking against CU-CPT9a strengthens translational relevance, as these compounds achieve clinical-level potency with enhanced selectivity, which is essential for avoiding immune-mediated adverse effects. The initial challenges of attaining nanomolar potency, receptor-subtype selectivity, and desirable pharmacokinetic properties have been progressively overcome, evidenced by the transition from pyrimidine cores to novel isoxazole and optimized quinazoline derivatives.

In the future, *in silico* approaches integrating TLR8 polymorphisms with clinical factors could improve predictive accuracy for treatment response. This precision-medicine paradigm, combining genetic and clinical biomarkers, may guide patient stratification for TLR8 antagonist therapy.[187] Furthermore, cutting-edge cell-type-resolved transcriptomic studies have highlighted the importance of recognizing the heterogeneous roles of innate immune pathways across different immune and tissue cell types.[188,189] Such studies reinforce that TLR signaling and its downstream effects are highly cell-type- and context-dependent, advocating for therapeutic strategies that are targeted and adaptable to cellular context. These advances collectively emphasize the potential for next-generation, precision-guided immunotherapies that minimize off-target effects while maximizing efficacy for specific patient subgroups.[126,190]

However, ongoing progress in understanding the pharmacology of TLR8 reveals that both structural and species differences are critical for successful antagonist design. As human TLR8 contains two separate ligand-binding pockets with synergistic activation requiring occupancy of both sites, it remains unclear whether therapeutic targeting should engage both pockets simultaneously, or whether such engagement produces signal loss or unintended off-target effects. An alternative strategy to achieve synergistic effects involves combining TLR8 antagonists with complementary immunomodulators, a concept previously demonstrated for

agonists.[109,191] Addressing these questions will require detailed computational modeling such as molecular dynamics simulations of ligand-pocket interactions and systematic binding-site mutagenesis, building on the paradigm of structure-guided design that has driven recent progress in the field.

Another critical consideration in TLR8 antagonist discovery is the presence of species differences. Human and murine TLR8 exhibit different ligand preferences and activation mechanisms, which presents a significant challenge for the translatability of preclinical studies.[50,192,193] However, recent preclinical data indicate that although mTLR8 was historically regarded as non-functional due to its lack of response to established TLR8 ligands, it can be robustly activated by certain nucleoside–polynucleotide combinations, such as uridine or guanosine together with poly-dT.[194] These findings provide a novel pharmacological basis for targeting TLR8 in murine models, potentially unlocking important knowledge about TLR8 function and providing a new tool to explore therapeutic approaches. Despite the promise of new murine models, the translational development path remains challenging. While humanized mouse models can offer complex immunological readouts, their complexity and resource requirements are considerable, and validation in non-human primates is often still necessary to obtain the most clinically relevant immunological data.[195]

7 References

(1) Hayter, S. M.; Cook, M. C. Updated Assessment of the Prevalence, Spectrum and Case Definition of Autoimmune Disease. *Autoimmun. Rev.* **2012**, *11* (10), 754–765. https://doi.org/10.1016/j.autrev.2012.02.001.

(2) Conrad, N.; Misra, S.; Verbakel, J. Y.; Verbeke, G.; Molenberghs, G.; Taylor, P. N.; Mason, J.; Sattar, N.; McMurray, J. J. V.; McInnes, I. B.; Khunti, K.; Cambridge, G. Incidence, Prevalence, and Co-Occurrence of Autoimmune Disorders over Time and by Age, Sex, and Socioeconomic Status: A Population-Based Cohort Study of 22 Million Individuals in the UK. *The Lancet* **2023**, *401* (10391), 1878–1890. https://doi.org/10.1016/S0140-6736(23)00457-9.

(3) Abend, A. H.; He, I.; Bahroos, N.; Christianakis, S.; Crew, A. B.; Wise, L. M.; Lipori, G. P.; He, X.; Murphy, S. N.; Herrick, C. D.; Avasarala, J.; Weiner, M. G.; Zelko, J. S.; Matute-Arcos, E.; Abajian, M.; Payne, P. R. O.; Lai, A. M.; Davis, H. A.; Hoberg, A. A.; Ortman, C. E.; Gode, A. D.; Taylor, B. W.; Osinski, K. I.; Di Florio, D. N.; Rose, N. R.; Miller, F. W.; Tsokos, G. C.; Fairweather, D. Estimation of Prevalence of Autoimmune Diseases in the United States Using Electronic Health Record Data. *J. Clin. Invest.* **2025**, *135* (4), e178722. https://doi.org/10.1172/JCI178722.

(4) Miller, F. W. The Increasing Prevalence of Autoimmunity and Autoimmune Diseases: An Urgent Call to Action for Improved Understanding, Diagnosis, Treatment, and Prevention. *Curr. Opin. Immunol.* **2023**, *80*, 102266. https://doi.org/10.1016/j.coi.2022.102266.

(5) Akira, S.; Uematsu, S.; Takeuchi, O. Pathogen Recognition and Innate Immunity. *Cell* **2006**, *124* (4), 783–801. https://doi.org/10.1016/j.cell.2006.02.015.

(6) Bian, F.; Yan, D.; Wu, X.; Yang, C. A Biological Perspective of TLR8 Signaling in Host Defense and Inflammation. *Infect. Microbes Dis.* **2023**, *5* (2), 44–55. https://doi.org/10.1097/IM9.0000000000000119.

(7) Duan, T.; Du, Y.; Xing, C.; Wang, H. Y.; Wang, R.-F. Toll-Like Receptor Signaling and Its Role in Cell-Mediated Immunity. *Front. Immunol.* **2022**, *13*, 812774. https://doi.org/10.3389/fimmu.2022.812774.

(8) Matziol, T.; Talagayev, V.; Weindl, G.; Wolber, G. Structure-Guided Approaches to Modulate Endosomal Toll-like Receptors TLR7, TLR8 and TLR9: Advances, Challenges and Therapeutic Promise. *Drug Discov. Today* **2025**, *30* (11), 104495. https://doi.org/10.1016/j.drudis.2025.104495.

(9) Medzhitov Ruslan; Janeway Charles. Innate Immunity. *N. Engl. J. Med.* **2000**, *343* (5), 338–344. https://doi.org/10.1056/NEJM200008033430506.

(10) Fitzgerald, K. A.; Kagan, J. C. Toll-like Receptors and the Control of Immunity. *Cell* **2020**, *180* (6), 1044–1066. https://doi.org/10.1016/j.cell.2020.02.041.

(11) Iwasaki, A.; Medzhitov, R. Regulation of Adaptive Immunity by the Innate Immune System. *Science* **2010**, *327* (5963), 291–295. https://doi.org/10.1126/science.1183021.

(12) Matzinger, P. The Danger Model: A Renewed Sense of Self. *Science* **2002**, *296* (5566), 301–305. https://doi.org/10.1126/science.1071059.

(13) Turvey, S. E.; Broide, D. H. Innate Immunity. *J. Allergy Clin. Immunol.* **2010**, *125* (2), S24–S32. https://doi.org/10.1016/j.jaci.2009.07.016.

(14) Chi, H.; Pepper, M.; Thomas, P. G. Principles and Therapeutic Applications of Adaptive Immunity. *Cell* **2024**, *187* (9), 2052–2078. https://doi.org/10.1016/j.cell.2024.03.037.

(15) Ratajczak, W.; Niedźwiedzka-Rystwej, P.; Tokarz-Deptuła, B.; Deptuła, W. Immunological Memory Cells. *Cent. Eur. J. Immunol.* **2018**, *43* (2), 194–203. https://doi.org/10.5114/ceji.2018.77390.

(16) Dunkelberger, J. R.; Song, W.-C. Complement and Its Role in Innate and Adaptive Immune Responses. *Cell Res.* **2010**, *20* (1), 34–50. https://doi.org/10.1038/cr.2009.139.

(17) Coss, S. L.; Zhou, D.; Chua, G. T.; Aziz, R. A.; Hoffman, R. P.; Wu, Y. L.; Ardoin, S. P.; Atkinson, J. P.; Yu, C.-Y. The Complement System and Human Autoimmune Diseases. *Cell. Mol. Mech. Autoimmun.* **2023**, *137*, 102979. https://doi.org/10.1016/j.jaut.2022.102979.

(18) Rosales, C. Neutrophils at the Crossroads of Innate and Adaptive Immunity. *J. Leukoc. Biol.* **2020**, *108* (1), 377–396. https://doi.org/10.1002/JLB.4MIR0220-574RR.

(19) Viola, A.; Munari, F.; Sánchez-Rodríguez, R.; Scolaro, T.; Castegna, A. The Metabolic Signature of Macrophage Responses. *Front. Immunol.* **2019**, *10*, 1462. https://doi.org/10.3389/fimmu.2019.01462.

(20) Wculek, S. K.; Cueto, F. J.; Mujal, A. M.; Melero, I.; Krummel, M. F.; Sancho, D. Dendritic Cells in Cancer Immunology and Immunotherapy. *Nat. Rev. Immunol.* **2020**, *20* (1), 7–24. https://doi.org/10.1038/s41577-019-0210-z.

(21) Kawai, T.; Akira, S. The Role of Pattern-Recognition Receptors in Innate Immunity: Update on Toll-like Receptors. *Nat. Immunol.* **2010**, *11* (5), 373–384. https://doi.org/10.1038/ni.1863.

(22) Freud, A. G.; Mundy-Bosse, B. L.; Yu, J.; Caligiuri, M. A. The Broad Spectrum of Human Natural Killer Cell Diversity. *Immunity* **2017**, *47* (5), 820–833. https://doi.org/10.1016/j.immuni.2017.10.008.

(23) Stone, K. D.; Prussin, C.; Metcalfe, D. D. IgE, Mast Cells, Basophils, and Eosinophils. *J. Allergy Clin. Immunol.* **2010**, *125* (2), S73–S80. https://doi.org/10.1016/j.jaci.2009.11.017.

(24) Vivier, E.; Artis, D.; Colonna, M.; Diefenbach, A.; Di Santo, J. P.; Eberl, G.; Koyasu, S.; Locksley, R. M.; McKenzie, A. N. J.; Mebius, R. E.; Powrie, F.; Spits, H. Innate Lymphoid Cells: 10 Years On. *Cell* **2018**, *174* (5), 1054–1066. https://doi.org/10.1016/j.cell.2018.07.017.

(25) Li, D.; Wu, M. Pattern Recognition Receptors in Health and Diseases. *Signal Transduct. Target. Ther.* **2021**, *6* (1), 291. https://doi.org/10.1038/s41392-021-00687-0.

(26) Chiffoleau, E. C-Type Lectin-Like Receptors As Emerging Orchestrators of Sterile Inflammation Represent Potential Therapeutic Targets. *Front. Immunol.* **2018**, *9*, 227. https://doi.org/10.3389/fimmu.2018.00227.

(27) Dambuza, I. M.; Brown, G. D. C-Type Lectins in Immunity: Recent Developments. *Innate Immun.* **2015**, *32*, 21–27. https://doi.org/10.1016/j.coi.2014.12.002.

(28) Speakman, E. A.; Dambuza, I. M.; Salazar, F.; Brown, G. D. T Cell Antifungal Immunity and the Role of C-Type Lectin Receptors. *Trends Immunol.* **2020**, *41* (1), 61–76. https://doi.org/10.1016/j.it.2019.11.007.

(29) Hornung, V.; Ellegast, J.; Kim, S.; Brzózka, K.; Jung, A.; Kato, H.; Poeck, H.; Akira, S.; Conzelmann, K.-K.; Schlee, M.; Endres, S.; Hartmann, G. 5'-Triphosphate RNA Is the Ligand for RIG-I. *Science* **2006**, *314* (5801), 994–997. https://doi.org/10.1126/science.1132505.

(30) Pichlmair, A.; Schulz, O.; Tan, C. P.; Näslund, T. I.; Liljeström, P.; Weber, F.; Reis e Sousa, C. RIG-I-Mediated Antiviral Responses to Single-Stranded RNA Bearing 5'-Phosphates. *Science* **2006**, *314* (5801), 997–1001. https://doi.org/10.1126/science.1132998.

(31) Takeuchi, O.; Akira, S. Innate Immunity to Virus Infection. *Immunol. Rev.* **2009**, *227* (1), 75–86. https://doi.org/10.1111/j.1600-065X.2008.00737.x.

(32) Lamkanfi, M.; Dixit, V. M. Mechanisms and Functions of Inflammasomes. *Cell* **2014**, *157* (5), 1013–1022. https://doi.org/10.1016/j.cell.2014.04.007.

(33) Latz, E.; Xiao, T. S.; Stutz, A. Activation and Regulation of the Inflammasomes. *Nat. Rev. Immunol.* **2013**, *13* (6), 397–411. https://doi.org/10.1038/nri3452.

(34) Kayagaki, N.; Stowe, I. B.; Lee, B. L.; O'Rourke, K.; Anderson, K.; Warming, S.; Cuellar, T.; Haley, B.; Roose-Girma, M.; Phung, Q. T.; Liu, P. S.; Lill, J. R.; Li, H.; Wu, J.; Kummerfeld, S.; Zhang, J.; Lee, W. P.; Snipas, S. J.; Salvesen, G. S.; Morris, L. X.; Fitzgerald, L.; Zhang, Y.; Bertram, E. M.; Goodnow, C. C.; Dixit, V. M. Caspase-11 Cleaves Gasdermin D for Non-Canonical Inflammasome Signalling. *Nature* **2015**, *526* (7575), 666–671. https://doi.org/10.1038/nature15541.

(35) Shi, J.; Zhao, Y.; Wang, K.; Shi, X.; Wang, Y.; Huang, H.; Zhuang, Y.; Cai, T.; Wang, F.; Shao, F. Cleavage of GSDMD by Inflammatory Caspases Determines Pyroptotic Cell Death. *Nature* **2015**, *526* (7575), 660–665. https://doi.org/10.1038/nature15514.

(36) Yao, J.; Sterling, K.; Wang, Z.; Zhang, Y.; Song, W. The Role of Inflammasomes in Human Diseases and Their Potential as Therapeutic Targets. *Signal Transduct. Target. Ther.* **2024**, *9* (1), 10. https://doi.org/10.1038/s41392-023-01687-y.

(37) Unterholzner, L.; Keating, S. E.; Baran, M.; Horan, K. A.; Jensen, S. B.; Sharma, S.; Sirois, C. M.; Jin, T.; Latz, E.; Xiao, T. S.; Fitzgerald, K. A.; Paludan, S. R.; Bowie, A. G. IFI16 Is an Innate Immune Sensor for Intracellular DNA. *Nat. Immunol.* **2010**, *11* (11), 997–1004. https://doi.org/10.1038/ni.1932.

(38) Hornung, V.; Ablasser, A.; Charrel-Dennis, M.; Bauernfeind, F.; Horvath, G.; Caffrey, Daniel. R.; Latz, E.; Fitzgerald, K. A. AIM2 Recognizes Cytosolic dsDNA and Forms a Caspase-1-Activating Inflammasome with ASC. *Nature* **2009**, *458* (7237), 514–518. https://doi.org/10.1038/nature07725.

(39) Ishikawa, H.; Barber, G. N. STING Is an Endoplasmic Reticulum Adaptor That Facilitates Innate Immune Signalling. *Nature* **2008**, *455* (7213), 674–678. https://doi.org/10.1038/nature07317.

(40) Wu, J.; Sun, L.; Chen, X.; Du, F.; Shi, H.; Chen, C.; Chen, Z. J. Cyclic GMP-AMP Is an Endogenous Second Messenger in Innate Immune Signaling by Cytosolic DNA. *Science* **2013**, *339* (6121), 826–830. https://doi.org/10.1126/science.1229963.

(41) Man, S. M.; Karki, R.; Kanneganti, T.-D. AIM2 Inflammasome in Infection, Cancer, and Autoimmunity: Role in DNA Sensing, Inflammation, and Innate Immunity. *Eur. J. Immunol.* **2016**, *46* (2), 269–280. https://doi.org/10.1002/eji.201545839.

(42) Motwani, M.; Pesiridis, S.; Fitzgerald, K. A. DNA Sensing by the cGAS–STING Pathway in Health and Disease. *Nat. Rev. Genet.* **2019**, *20* (11), 657–674. https://doi.org/10.1038/s41576-019-0151-1.

(43) Brikos, C.; O'Neill, L. A. J. Signalling of Toll-Like Receptors. In *Toll-Like Receptors (TLRs) and Innate Immunity*; Bauer, S., Hartmann, G., Eds.; Springer Berlin Heidelberg: Berlin, Heidelberg, 2008; pp 21–50. https://doi.org/10.1007/978-3-540-72167-3_2.

(44) Hennessy, E. J.; Parker, A. E.; O'Neill, L. A. J. Targeting Toll-like Receptors: Emerging Therapeutics? *Nat. Rev. Drug Discov.* **2010**, *9* (4), 293–307. https://doi.org/10.1038/nrd3203.

(45) Takeda, K.; Akira, S. Toll-like Receptors in Innate Immunity. *Int. Immunol.* **2005**, *17* (1), 1–14. https://doi.org/10.1093/intimm/dxh186.

(46) Nüsslein-Volhard, C. The Toll Gene in Drosophila Pattern Formation. *Trends Genet.* **2022**, *38* (3), 231–245. https://doi.org/10.1016/j.tig.2021.09.006.

(47) Botos, I.; Segal, D. M.; Davies, D. R. The Structural Biology of Toll-like Receptors. *Structure* **2011**, *19* (4), 447–459. https://doi.org/10.1016/j.str.2011.02.004.

(48) Kawasaki, T.; Kawai, T. Toll-Like Receptor Signaling Pathways. *Front. Immunol.* **2014**, *Volume 5-2014*. https://doi.org/10.3389/fimmu.2014.00461.

(49) Yoon, S.; Kurnasov, O.; Natarajan, V.; Hong, M.; Gudkov, A. V.; Osterman, A. L.; Wilson, I. A. Structural Basis of TLR5-Flagellin Recognition and Signaling. *Science* **2012**, *335* (6070), 859–864. https://doi.org/10.1126/science.1215584.

(50) Lind, N. A.; Rael, V. E.; Pestal, K.; Liu, B.; Barton, G. M. Regulation of the Nucleic Acid-Sensing Toll-like Receptors. *Nat. Rev. Immunol.* **2022**, *22* (4), 224–235. https://doi.org/10.1038/s41577-021-00577-0.

(51) Jin, M. S.; Lee, J.-O. Structures of the Toll-like Receptor Family and Its Ligand Complexes. *Immunity* **2008**, *29* (2), 182–191. https://doi.org/10.1016/j.immuni.2008.07.007.

(52) Liu, L.; Botos, I.; Wang, Y.; Leonard, J. N.; Shiloach, J.; Segal, D. M.; Davies, D. R. Structural Basis of Toll-Like Receptor 3 Signaling with Double-Stranded RNA. *Science* **2008**, *320* (5874), 379–381. https://doi.org/10.1126/science.1155406.

(53) Miyake, K.; Shibata, T.; Fukui, R.; Sato, R.; Saitoh, S.-I.; Murakami, Y. Nucleic Acid Sensing by Toll-Like Receptors in the Endosomal Compartment. *Front. Immunol.* **2022**, *13*, 941931. https://doi.org/10.3389/fimmu.2022.941931.

(54) Dalpke, A.; Frank, J.; Peter, M.; Heeg, K. Activation of Toll-Like Receptor 9 by DNA from Different Bacterial Species. *Infect. Immun.* **2006**, *74* (2), 940–946. https://doi.org/10.1128/IAI.74.2.940-946.2006.

(55) Kumagai, Y.; Takeuchi, O.; Akira, S. TLR9 as a Key Receptor for the Recognition of DNA☆. *Adv. Drug Deliv. Rev.* **2008**, *60* (7), 795–804. https://doi.org/10.1016/j.addr.2007.12.004.

(56) Barton, G. M.; Kagan, J. C. A Cell Biological View of Toll-like Receptor Function: Regulation through Compartmentalization. *Nat. Rev. Immunol.* **2009**, *9* (8), 535–542. https://doi.org/10.1038/nri2587.

(57) Pelka, K.; Phulphagar, K.; Zimmermann, J.; Stahl, R.; Schmid-Burgk, J. L.; Schmidt, T.; Spille, J.-H.; Labzin, L. I.; Agrawal, S.; Kandimalla, E. R.; Casanova, J.-L.; Hornung, V.; Marshak-Rothstein, A.; Höning, S.; Latz, E. Cutting Edge: The UNC93B1 Tyrosine-Based Motif Regulates Trafficking and TLR Responses via Separate Mechanisms. *J. Immunol.* **2014**, *193* (7), 3257–3261. https://doi.org/10.4049/jimmunol.1301886.

(58) Lee, B. L.; Moon, J. E.; Shu, J. H.; Yuan, L.; Newman, Z. R.; Schekman, R.; Barton, G. M. UNC93B1 Mediates Differential Trafficking of Endosomal TLRs. *eLife* **2013**, *2*, e00291. https://doi.org/10.7554/eLife.00291.

(59) Park, B.; Brinkmann, M. M.; Spooner, E.; Lee, C. C.; Kim, Y.-M.; Ploegh, H. L. Proteolytic Cleavage in an Endolysosomal Compartment Is Required for Activation of Toll-like Receptor 9. *Nat. Immunol.* **2008**, *9* (12), 1407–1414. https://doi.org/10.1038/ni.1669.

(60) David, C.; Arango-Franco, C. A.; Badonyi, M.; Fouchet, J.; Rice, G. I.; Didry-Barca, B.; Maisonneuve, L.; Seabra, L.; Kechiche, R.; Masson, C.; Cobat, A.; Abel, L.; Talouarn, E.; Béziat, V.; Deswarte, C.; Livingstone, K.; Paul, C.; Malik, G.; Ross, A.; Adam, J.; Walsh, J.; Kumar, S.; Bonnet, D.; Bodemer, C.; Bader-Meunier, B.; Marsh, J. A.; Casanova, J.-L.; Crow, Y. J.; Manoury, B.; Frémond, M.-L.; Bohlen, J.; Lepelley, A.

Gain-of-Function Human UNC93B1 Variants Cause Systemic Lupus Erythematosus and Chilblain Lupus. *J. Exp. Med.* **2024**, *221* (8), e20232066. https://doi.org/10.1084/jem.20232066.

(61) Schmidt, A.; Coughlin, M.; Catalina, M. D.; Przetak, M.; Kalatskaya, I.; Studham, M.; Shaw, J.; Bender, A. T.; Strand, F. Toll-like Receptor 8 Activation Induces a Neutrophil Inflammatory Phenotype: Therapeutic Implications for the Utility of Toll-like Receptor 8 Inhibition. *J. Leukoc. Biol.* **2025**, *117* (5), qiaf036. https://doi.org/10.1093/jleuko/qiaf036.

(62) Gorden, K. B.; Gorski, K. S.; Gibson, S. J.; Kedl, R. M.; Kieper, W. C.; Qiu, X.; Tomai, M. A.; Alkan, S. S.; Vasilakos, J. P. Synthetic TLR Agonists Reveal Functional Differences between Human TLR7 and TLR8. *J. Immunol.* **2005**, *174* (3), 1259–1268. https://doi.org/10.4049/jimmunol.174.3.1259.

(63) Tanji, H.; Ohto, U.; Shibata, T.; Miyake, K.; Shimizu, T. Structural Reorganization of the Toll-Like Receptor 8 Dimer Induced by Agonistic Ligands. *Science* **2013**, *339* (6126), 1426–1429. https://doi.org/10.1126/science.1229159.

(64) Tanji, H.; Ohto, U.; Shibata, T.; Taoka, M.; Yamauchi, Y.; Isobe, T.; Miyake, K.; Shimizu, T. Toll-like Receptor 8 Senses Degradation Products of Single-Stranded RNA. *Nat. Struct. Mol. Biol.* **2015**, *22* (2), 109–115. https://doi.org/10.1038/nsmb.2943.

(65) Sakaniwa, K.; Shimizu, T. Targeting the Innate Immune Receptor TLR8 Using Small-Molecule Agents. *Acta Crystallogr. Sect. Struct. Biol.* **2020**, *76* (7), 621–629. https://doi.org/10.1107/S2059798320006518.

(66) Patinote, C.; Karroum, N. B.; Moarbess, G.; Cirnat, N.; Kassab, I.; Bonnet, P.-A.; Deleuze-Masquéfa, C. Agonist and Antagonist Ligands of Toll-like Receptors 7 and 8: Ingenious Tools for Therapeutic Purposes. *Eur. J. Med. Chem.* **2020**, *193*, 112238. https://doi.org/10.1016/j.ejmech.2020.112238.

(67) Sun, H.; Li, Y.; Zhang, P.; Xing, H.; Zhao, S.; Song, Y.; Wan, D.; Yu, J. Targeting Toll-like Receptor 7/8 for Immunotherapy: Recent Advances and Prospectives. *Biomark. Res.* **2022**, *10* (1), 89. https://doi.org/10.1186/s40364-022-00436-7.

(68) Martínez-Espinoza, I.; Guerrero-Plata, A. The Relevance of TLR8 in Viral Infections. *Pathogens* **2022**, *11* (2), 134. https://doi.org/10.3390/pathogens11020134.

(69) Heil, F.; Hemmi, H.; Hochrein, H.; Ampenberger, F.; Kirschning, C.; Akira, S.; Lipford, G.; Wagner, H.; Bauer, S. Species-Specific Recognition of Single-Stranded RNA via

Toll-like Receptor 7 and 8. *Science* **2004**, *303* (5663), 1526–1529. https://doi.org/10.1126/science.1093620.

(70) Liu, J.; Xu, C.; Hsu, L.-C.; Luo, Y.; Xiang, R.; Chuang, T.-H. A Five-Amino-Acid Motif in the Undefined Region of the TLR8 Ectodomain Is Required for Species-Specific Ligand Recognition. *Mol. Immunol.* **2010**, *47* (5), 1083–1090. https://doi.org/10.1016/j.molimm.2009.11.003.

(71) Kawai, T.; Akira, S. TLR Signaling. *Cell Death Differ.* **2006**, *13* (5), 816–825. https://doi.org/10.1038/sj.cdd.4401850.

(72) Kagan, J. C.; Magupalli, V. G.; Wu, H. SMOCs: Supramolecular Organizing Centres That Control Innate Immunity. *Nat. Rev. Immunol.* **2014**, *14* (12), 821–826. https://doi.org/10.1038/nri3757.

(73) Motshwene, P. G.; Moncrieffe, M. C.; Grossmann, J. G.; Kao, C.; Ayaluru, M.; Sandercock, A. M.; Robinson, C. V.; Latz, E.; Gay, N. J. An Oligomeric Signaling Platform Formed by the Toll-like Receptor Signal Transducers MyD88 and IRAK-4*. *J. Biol. Chem.* **2009**, *284* (37), 25404–25411. https://doi.org/10.1074/jbc.M109.022392.

(74) Latty, S. L.; Sakai, J.; Hopkins, L.; Verstak, B.; Paramo, T.; Berglund, N. A.; Cammarota, E.; Cicuta, P.; Gay, N. J.; Bond, P. J.; Klenerman, D.; Bryant, C. E. Activation of Toll-like Receptors Nucleates Assembly of the MyDDosome Signaling Hub. *eLife* **2018**, *7*, e31377. https://doi.org/10.7554/eLife.31377.

(75) Fisch, D.; Zhang, T.; Sun, H.; Ma, W.; Tan, Y.; Gygi, S. P.; Higgins, D. E.; Kagan, J. C. Molecular Definition of the Endogenous Toll-like Receptor Signalling Pathways. *Nature* **2024**, *631* (8021), 635–644. https://doi.org/10.1038/s41586-024-07614-7.

(76) De Nardo, D.; Balka, K. R.; Cardona Gloria, Y.; Rao, V. R.; Latz, E.; Masters, S. L. Interleukin-1 Receptor–Associated Kinase 4 (IRAK4) Plays a Dual Role in Myddosome Formation and Toll-like Receptor Signaling. *J. Biol. Chem.* **2018**, *293* (39), 15195–15207. https://doi.org/10.1074/jbc.RA118.003314.

(77) Lin, S.-C.; Lo, Y.-C.; Wu, H. Helical Assembly in the MyD88–IRAK4–IRAK2 Complex in TLR/IL-1R Signalling. *Nature* **2010**, *465* (7300), 885–890. https://doi.org/10.1038/nature09121.

(78) Kawai, T.; Akira, S. Signaling to NF-κB by Toll-like Receptors. *Trends Mol. Med.* **2007**, *13* (11), 460–469. https://doi.org/10.1016/j.molmed.2007.09.002.

(79) Jin, B.; Sun, T.; Yu, X.-H.; Yang, Y.-X.; Yeo, A. E. T. The Effects of TLR Activation on T-Cell Development and Differentiation. *Clin. Dev. Immunol.* **2012**, *2012*, 1–32. https://doi.org/10.1155/2012/836485.

(80) Liew, F. Y.; Xu, D.; Brint, E. K.; O'Neill, L. A. J. Negative Regulation of Toll-like Receptor-Mediated Immune Responses. *Nat. Rev. Immunol.* **2005**, *5* (6), 446–458. https://doi.org/10.1038/nri1630.

(81) Bérouti, M.; Lammens, K.; Heiss, M.; Hansbauer, L.; Bauernfried, S.; Stöckl, J.; Pinci, F.; Piseddu, I.; Greulich, W.; Wang, M.; Jung, C.; Fröhlich, T.; Carell, T.; Hopfner, K.-P.; Hornung, V. Lysosomal Endonuclease RNase T2 and PLD Exonucleases Cooperatively Generate RNA Ligands for TLR7 Activation. *Immunity* **2024**, *57* (7), 1482-1496.e8. https://doi.org/10.1016/j.immuni.2024.04.010.

(82) Nunes, I. V.; Breitenbach, L.; Pawusch, S.; Eigenbrod, T.; Ananth, S.; Schad, P.; Fackler, O. T.; Butter, F.; Dalpke, A. H.; Chen, L.-S. Bacterial RNA Sensing by TLR8 Requires RNase 6 Processing and Is Inhibited by RNA 2'O-Methylation. *EMBO Rep.* **2024**, *25* (11), 4674–4692. https://doi.org/10.1038/s44319-024-00281-9.

(83) Greulich, W.; Wagner, M.; Gaidt, M. M.; Stafford, C.; Cheng, Y.; Linder, A.; Carell, T.; Hornung, V. TLR8 Is a Sensor of RNase T2 Degradation Products. *Cell* **2019**, *179* (6), 1264-1275.e13. https://doi.org/10.1016/j.cell.2019.11.001.

(84) Hu, T.; Suter, S. R.; Mumbleau, M. M.; Beal, P. A. TLR8 Activation and Inhibition by Guanosine Analogs in RNA: Importance of Functional Groups and Chain Length. *Bioorg. Med. Chem.* **2018**, *26* (1), 77–83. https://doi.org/10.1016/j.bmc.2017.11.020.

(85) Heinz, L. X.; Lee, J.; Kapoor, U.; Kartnig, F.; Sedlyarov, V.; Papakostas, K.; César-Razquin, A.; Essletzbichler, P.; Goldmann, U.; Stefanovic, A.; Bigenzahn, J. W.; Scorzoni, S.; Pizzagalli, M. D.; Bensimon, A.; Müller, A. C.; King, F. J.; Li, J.; Girardi, E.; Mbow, M. L.; Whitehurst, C. E.; Rebsamen, M.; Superti-Furga, G. TASL Is the SLC15A4-Associated Adaptor for IRF5 Activation by TLR7–9. *Nature* **2020**, *581* (7808), 316–322. https://doi.org/10.1038/s41586-020-2282-0.

(86) Zhang, H.; Bernaleau, L.; Delacrétaz, M.; Hasanovic, E.; Drobek, A.; Eibel, H.; Rebsamen, M. SLC15A4 Controls Endolysosomal TLR7–9 Responses by Recruiting the Innate Immune Adaptor TASL. *Cell Rep.* **2023**, *42* (8), 112916. https://doi.org/10.1016/j.celrep.2023.112916.

(87) Chen, X.; Xie, M.; Zhang, S.; Monguió-Tortajada, M.; Yin, J.; Liu, C.; Zhang, Y.; Delacrétaz, M.; Song, M.; Wang, Y.; Dong, L.; Ding, Q.; Zhou, B.; Tian, X.; Deng, H.; Xu, L.; Liu, X.; Yang, Z.; Chang, Q.; Na, J.; Zeng, W.; Superti-Furga, G.; Rebsamen, M.; Yang, M. Structural Basis for Recruitment of TASL by SLC15A4 in Human Endolysosomal TLR Signaling. *Nat. Commun.* **2023**, *14* (1), 6627. https://doi.org/10.1038/s41467-023-42210-9.

(88) Boeszoermenyi, A.; Bernaleau, L.; Chen, X.; Kartnig, F.; Xie, M.; Zhang, H.; Zhang, S.; Delacrétaz, M.; Koren, A.; Hopp, A.-K.; Dvorak, V.; Kubicek, S.; Aletaha, D.; Yang, M.; Rebsamen, M.; Heinz, L. X.; Superti-Furga, G. A Conformation-Locking Inhibitor of SLC15A4 with TASL Proteostatic Anti-Inflammatory Activity. *Nat. Commun.* **2023**, *14* (1), 6626. https://doi.org/10.1038/s41467-023-42070-3.

(89) Rice, M. R.; Matta, B.; Wang, L.; Luo, Q.; De Guzman, J.; Srinivasan, D.; Ludwig, K. R.; Indukuri, S.; Brune, L.; Tan, S.-L.; Barnes, B. J. TLR-Induced STK25 Activation Promotes IRF5-Mediated Inflammation. *Life Sci. Alliance* **2025**, *8* (9), e202503343. https://doi.org/10.26508/lsa.202503343.

(90) Ohto, U.; Tanji, H.; Shimizu, T. Structure and Function of Toll-like Receptor 8. *Microbes Infect.* **2014**, *16* (4), 273–282. https://doi.org/10.1016/j.micinf.2014.01.007.

(91) Ohto, U.; Shimizu, T. Structural Aspects of Nucleic Acid-Sensing Toll-like Receptors. *Biophys. Rev.* **2016**, *8* (1), 33–43. https://doi.org/10.1007/s12551-015-0187-1.

(92) Tanji, H.; Ohto, U.; Motoi, Y.; Shibata, T.; Miyake, K.; Shimizu, T. Autoinhibition and Relief Mechanism by the Proteolytic Processing of Toll-like Receptor 8. *Proc. Natl. Acad. Sci.* **2016**, *113* (11), 3012–3017. https://doi.org/10.1073/pnas.1516000113.

(93) Bérouti, M.; Wagner, M.; Greulich, W.; Piseddu, I.; Gärtig, J.; Hansbauer, L.; Müller-Hermes, C.; Heiss, M.; Pichler, A.; Tölke, A. J.; Witte, G.; Hopfner, K.-P.; Anz, D.; Sattler, M.; Carell, T.; Hornung, V. Pseudouridine RNA Avoids Immune Detection through Impaired Endolysosomal Processing and TLR Engagement. *Cell* **2025**, *188* (18), 4880-4895.e15. https://doi.org/10.1016/j.cell.2025.05.032.

(94) Karikó, K.; Buckstein, M.; Ni, H.; Weissman, D. Suppression of RNA Recognition by Toll-like Receptors: The Impact of Nucleoside Modification and the Evolutionary Origin of RNA. *Immunity* **2005**, *23* (2), 165–175. https://doi.org/10.1016/j.immuni.2005.06.008.

(95) Zhang, S.; Hu, Z.; Tanji, H.; Jiang, S.; Das, N.; Li, J.; Sakaniwa, K.; Jin, J.; Bian, Y.; Ohto, U.; Shimizu, T.; Yin, H. Small-Molecule Inhibition of TLR8 through Stabilization of Its Resting State. *Nat. Chem. Biol.* **2018**, *14* (1), 58–64. https://doi.org/10.1038/nchembio.2518.

(96) Talagayev, V.; Wolber, G.; Nunes-Alves, A. Agonists and Antagonists Show Different Unbinding Paths from the TLR8 Receptor. *J. Chem. Inf. Model.* **2025**, *65* (14), 7678–7688. https://doi.org/10.1021/acs.jcim.5c00496.

(97) Aluri, J.; Bach, A.; Kaviany, S.; Chiquetto Paracatu, L.; Kitcharoensakkul, M.; Walkiewicz, M. A.; Putnam, C. D.; Shinawi, M.; Saucier, N.; Rizzi, E. M.; Harmon, M. T.; Keppel, M. P.; Ritter, M.; Similuk, M.; Kulm, E.; Joyce, M.; De Jesus, A. A.; Goldbach-Mansky, R.; Lee, Y.-S.; Cella, M.; Kendall, P. L.; Dinauer, M. C.; Bednarski, J. J.; Bemrich-Stolz, C.; Canna, S. W.; Abraham, S. M.; Demczko, M. M.; Powell, J.; Jones, S. M.; Scurlock, A. M.; De Ravin, S. S.; Bleesing, J. J.; Connelly, J. A.; Rao, V. K.; Schuettpelz, L. G.; Cooper, M. A. Immunodeficiency and Bone Marrow Failure with Mosaic and Germline TLR8 Gain of Function. *Blood* **2021**, *137* (18), 2450–2462. https://doi.org/10.1182/blood.2020009620.

(98) Bleesing, J. Gain-of-Function Defects in Toll-like Receptor 8 Shed Light on the Interface between Immune System and Bone Marrow Failure Disorders. *Front. Immunol.* **2022**, *13*, 935321. https://doi.org/10.3389/fimmu.2022.935321.

(99) Fabbri, M.; Paone, A.; Calore, F.; Galli, R.; Gaudio, E.; Santhanam, R.; Lovat, F.; Fadda, P.; Mao, C.; Nuovo, G. J.; Zanesi, N.; Crawford, M.; Ozer, G. H.; Wernicke, D.; Alder, H.; Caligiuri, M. A.; Nana-Sinkam, P.; Perrotti, D.; Croce, C. M. MicroRNAs Bind to Toll-like Receptors to Induce Prometastatic Inflammatory Response. *Proc. Natl. Acad. Sci.* **2012**, *109* (31), E2110–E2116. https://doi.org/10.1073/pnas.1209414109.

(100) Sacre, S. M.; Lo, A.; Gregory, B.; Simmonds, R. E.; Williams, L.; Feldmann, M.; Brennan, F. M.; Foxwell, B. M. Inhibitors of TLR8 Reduce TNF Production from Human Rheumatoid Synovial Membrane Cultures. *J. Immunol.* **2008**, *181* (11), 8002–8009. https://doi.org/10.4049/jimmunol.181.11.8002.

(101) Kim, H. J.; Kim, S. H.; Je, J. H.; Shin, D. Y.; Kim, D. S.; Lee, M.-G. Increased Expression of Toll-like Receptors 3, 7, 8 and 9 in Peripheral Blood Mononuclear Cells in Patients with Psoriasis. *Exp. Dermatol.* **2016**, *25* (6), 485–487. https://doi.org/10.1111/exd.12974.

(102) Ehlers, C.; Thiele, T.; Biermann, H.; Traidl, S.; Bruns, L.; Ziegler, A.; Schefzyk, M.; Bartsch, L. M.; Kalinke, U.; Witte, T.; Graalmann, T. Toll-Like Receptor 8 Is Expressed in Monocytes in Contrast to Plasmacytoid Dendritic Cells and Mediates Aberrant Interleukin-10 Responses in Patients With Systemic Sclerosis. *Arthritis Rheumatol.* **2024**, art.42964. https://doi.org/10.1002/art.42964.

(103) Salie, M.; Daya, M.; Lucas, L. A.; Warren, R. M.; Van Der Spuy, G. D.; Van Helden, P. D.; Hoal, E. G.; Möller, M. Association of Toll-like Receptors with Susceptibility to Tuberculosis Suggests Sex-Specific Effects of TLR8 Polymorphisms. *Infect. Genet. Evol.* **2015**, *34*, 221–229. https://doi.org/10.1016/j.meegid.2015.07.004.

(104) Eigenbrod, T.; Pelka, K.; Latz, E.; Kreikemeyer, B.; Dalpke, A. H. TLR8 Senses Bacterial RNA in Human Monocytes and Plays a Nonredundant Role for Recognition of *Streptococcus Pyogenes*. *J. Immunol.* **2015**, *195* (3), 1092–1099. https://doi.org/10.4049/jimmunol.1403173.

(105) Kumar, V. Toll-like Receptors in Sepsis-Associated Cytokine Storm and Their Endogenous Negative Regulators as Future Immunomodulatory Targets. *Int. Immunopharmacol.* **2020**, *89*, 107087. https://doi.org/10.1016/j.intimp.2020.107087.

(106) Karki, R.; Kanneganti, T.-D. The 'Cytokine Storm': Molecular Mechanisms and Therapeutic Prospects. *Trends Immunol.* **2021**, *42* (8), 681–705. https://doi.org/10.1016/j.it.2021.06.001.

(107) Wang, T.; Song, D.; Li, X.; Luo, Y.; Yang, D.; Liu, X.; Kong, X.; Xing, Y.; Bi, S.; Zhang, Y.; Hu, T.; Zhang, Y.; Dai, S.; Shao, Z.; Chen, D.; Hou, J.; Ballestar, E.; Cai, J.; Zheng, F.; Yang, J. Y. MiR-574-5p Activates Human TLR8 to Promote Autoimmune Signaling and Lupus. *Cell Commun. Signal.* **2024**, *22* (1), 220. https://doi.org/10.1186/s12964-024-01601-1.

(108) Yan, L.; Miyahara, Y.; Sakamoto, M.; Kaneko, N.; Chen, H.; Sameshima, J.; Kido, H.; Yokomizo, S.; Sueyoshi, T.; Nagano, H.; Ohyama, Y.; Nakamura, S.; Kawano, S.; Moriyama, M. Possible Involvement of Toll-like Receptor 8-Positive Monocytes/Macrophages in the Pathogenesis of Sjögren's Disease. *Front. Immunol.* **2024**, *Volume 15-2024*. https://doi.org/10.3389/fimmu.2024.1480675.

(109) Rolfo, C.; Giovannetti, E.; Martinez, P.; McCue, S.; Naing, A. Applications and Clinical Trial Landscape Using Toll-like Receptor Agonists to Reduce the Toll of Cancer. *Npj Precis. Oncol.* **2023**, *7* (1), 26. https://doi.org/10.1038/s41698-023-00364-1.

(110) Jeon, D.; Hill, E.; McNeel, D. G. Toll-like Receptor Agonists as Cancer Vaccine Adjuvants. *Hum. Vaccines Immunother.* **2024**, *20* (1), 2297453. https://doi.org/10.1080/21645515.2023.2297453.

(111) Wolf, E.; Sacchi de Camargo Correia, G.; Li, S.; Zhao, Y.; Manochakian, R.; Lou, Y. Emerging Immunotherapies for Advanced Non-Small-Cell Lung Cancer. *Vaccines* **2025**, *13* (2). https://doi.org/10.3390/vaccines13020128.

(112) Ignatz-Hoover, J. J.; Wang, H.; Moreton, S. A.; Chakrabarti, A.; Agarwal, M. K.; Sun, K.; Gupta, K.; Wald, D. N. The Role of TLR8 Signaling in Acute Myeloid Leukemia Differentiation. *Leukemia* **2015**, *29* (4), 918–926. https://doi.org/10.1038/leu.2014.293.

(113) Yang, W.; Sun, X.; Liu, S.; Xu, Y.; Li, Y.; Huang, X.; Liu, K.; Mao, L.; Min, S.; Liu, L.; Li, S.; Zhu, Y.; Zhang, Y.; Xie, X.; Xu, K.; Sun, C.; Yan, J.; Li, Z. TLR8 Agonist Motolimod-Induced Inflammatory Death for Treatment of Acute Myeloid Leukemia. *Biomed. Pharmacother.* **2023**, *163*, 114759. https://doi.org/10.1016/j.biopha.2023.114759.

(114) Amin, O. E.; Colbeck, E. J.; Daffis, S.; Khan, S.; Ramakrishnan, D.; Pattabiraman, D.; Chu, R.; Micolochick Steuer, H.; Lehar, S.; Peiser, L.; Palazzo, A.; Frey, C.; Davies, J.; Javanbakht, H.; Rosenberg, W. M. C.; Fletcher, S. P.; Maini, M. K.; Pallett, L. J. Therapeutic Potential of TLR8 Agonist GS-9688 (Selgantolimod) in Chronic Hepatitis B: Remodeling of Antiviral and Regulatory Mediators. *Hepatology* **2021**, *74* (1), 55–71. https://doi.org/10.1002/hep.31695.

(115) Gane, E. J.; Dunbar, P. R.; Brooks, A. E.; Zhang, F.; Chen, D.; Wallin, J. J.; Van Buuren, N.; Arora, P.; Fletcher, S. P.; Tan, S. K.; Yang, J. C.; Gaggar, A.; Kottilil, S.; Tang, L. Safety and Efficacy of the Oral TLR8 Agonist Selgantolimod in Individuals with Chronic Hepatitis B under Viral Suppression. *J. Hepatol.* **2023**, *78* (3), 513–523. https://doi.org/10.1016/j.jhep.2022.09.027.

(116) Wu, S.; Xiang, R.; Zhong, Y.; Zhao, S.; Zhang, Z.; Kou, Z.; Zhang, S.; Zhao, Y.; Zu, C.; Zhao, G.; Xiao, Y.; Ren, S.; Gao, X.; Wang, B. TLR7/8/9 Agonists and Low-Dose Cisplatin Synergistically Promotes Tertiary Lymphatic Structure Formation and Antitumor Immunity. *Npj Vaccines* **2025**, *10* (1), 13. https://doi.org/10.1038/s41541-024-01055-z.

(117) Kawai, T.; Ikegawa, M.; Ori, D.; Akira, S. Decoding Toll-like Receptors: Recent Insights and Perspectives in Innate Immunity. *Immunity* **2024**, *57* (4), 649–673. https://doi.org/10.1016/j.immuni.2024.03.004.

(118) Guiducci, C.; Gong, M.; Cepika, A.-M.; Xu, Z.; Tripodo, C.; Bennett, L.; Crain, C.; Quartier, P.; Cush, J. J.; Pascual, V.; Coffman, R. L.; Barrat, F. J. RNA Recognition by Human TLR8 Can Lead to Autoimmune Inflammation. *J. Exp. Med.* **2013**, *210* (13), 2903–2919. https://doi.org/10.1084/jem.20131044.

(119) Lin, Y.-S.; Chang, Y.-C.; Pu, T.-Y.; Chuang, T.-H.; Hsu, L.-C. Involvement of Nucleic Acid-Sensing Toll-like Receptors in Human Diseases and Their Controlling Mechanisms. *J. Biomed. Sci.* **2025**, *32* (1), 56. https://doi.org/10.1186/s12929-025-01151-9.

(120) Kalliolias, G. D.; Basdra, E. K.; Papavassiliou, A. G. Targeting TLR Signaling Cascades in Systemic Lupus Erythematosus and Rheumatoid Arthritis: An Update. *Biomedicines* **2024**, *12* (1), 138. https://doi.org/10.3390/biomedicines12010138.

(121) Morand, E.; Dall'Era, M.; Sanchez-Guerrero, J.; Pearson, D.; Werth, V. P.; Wenzel, J.; Roy, S.; Kleinmond, C.; Fernandez-Ruiz, R.; Klopp-Schulze, L.; Gühring, H.; Moreau, F.; Furie, R. A. LB0004 RANDOMISED, PLACEBO-CONTROLLED PHASE II STUDY OF ORAL ENPATORAN, A FIRST-IN-CLASS TOLL-LIKE RECEPTOR 7/8 INHIBITOR, IN SYSTEMIC LUPUS ERYTHEMATOSUS. *Ann. Rheum. Dis.* **2025**, *84*, 316–317. https://doi.org/10.1016/j.ard.2025.05.391.

(122) Yamakawa, N.; Tago, F.; Nakai, K.; Kitahara, Y.; Ikari, S.; Hojo, S.; Hall, N.; Aluri, J.; Hussein, Z.; Gevorkyan, H.; Maruyama, T.; Ishizaka, S.; Yagi, T. First-in-Human Study of the Safety, Tolerability, Pharmacokinetics, and Pharmacodynamics of E6742, a Dual Antagonist of Toll-like Receptors 7 and 8, in Healthy Volunteers. *Clin. Pharmacol. Drug Dev.* **2023**, *12* (4), 363–375. https://doi.org/10.1002/cpdd.1176.

(123) Hosein, F.; Ignatenko, S.; Chadwick, K. D.; Zhu, L.; Baribaud, F.; Saini, J.; Bach, T.; Aras, U.; Zhang, W.; Karabeber, H.; Dawes, M.; Harrison, M.; Carayannopoulos, L. N.; Krishna, G. Safety, Tolerability, Efficacy, Pharmacokinetics, and Pharmacodynamics of Afimetoran, a Toll-Like Receptor 7 and 8 Inhibitor, in Patients With Cutaneous Lupus Erythematosus: A Phase 1b Randomized, Double-Blind, Placebo-Controlled Study. *ACR Open Rheumatol.* **2025**, *7* (7), e70059. https://doi.org/10.1002/acr2.70059.

(124) Bao, M.; Liu, Y.-J. Regulation of TLR7/9 Signaling in Plasmacytoid Dendritic Cells. *Protein Cell* **2013**, *4* (1), 40–52. https://doi.org/10.1007/s13238-012-2104-8.

(125) De Marcken, M.; Dhaliwal, K.; Danielsen, A. C.; Gautron, A. S.; Dominguez-Villar, M. TLR7 and TLR8 Activate Distinct Pathways in Monocytes during RNA Virus Infection. *Sci. Signal.* **2019**, *12* (605), eaaw1347. https://doi.org/10.1126/scisignal.aaw1347.

(126) Bender, A. T.; Tzvetkov, E.; Pereira, A.; Wu, Y.; Kasar, S.; Przetak, M. M.; Vlach, J.; Niewold, T. B.; Jensen, M. A.; Okitsu, S. L. TLR7 and TLR8 Differentially Activate the IRF and NF-κB Pathways in Specific Cell Types to Promote Inflammation. *ImmunoHorizons* **2020**, *4* (2), 93–107. https://doi.org/10.4049/immunohorizons.2000002.

(127) Wang Yichuan; Abel Kristina; Lantz Katherine; Krieg Arthur M.; McChesney Michael B.; Miller Christopher J. The Toll-Like Receptor 7 (TLR7) Agonist, Imiquimod, and the TLR9 Agonist, CpG ODN, Induce Antiviral Cytokines and Chemokines but Do Not Prevent Vaginal Transmission of Simian Immunodeficiency Virus When Applied Intravaginally to Rhesus Macaques. *J. Virol.* **2005**, *79* (22), 14355–14370. https://doi.org/10.1128/jvi.79.22.14355-14370.2005.

(128) U.S. Food & Drug Administration. Aldara (Imiquimod) Prescribing Information, 2024. https://www.accessdata.fda.gov/drugsatfda_docs/label/2024/020723s028lbl.pdf (accessed 2025-08-15).

(129) Mata-Haro, V.; Cekic, C.; Martin, M.; Chilton, P. M.; Casella, C. R.; Mitchell, T. C. The Vaccine Adjuvant Monophosphoryl Lipid A as a TRIF-Biased Agonist of TLR4. *Science* **2007**, *316* (5831), 1628–1632. https://doi.org/10.1126/science.1138963.

(130) U.S. Food & Drug Administration. SHINGRIX Prescribing Information, 2025. https://www.fda.gov/vaccines-blood-biologics/vaccines/shingrix (accessed 2025-08-15).

(131) U.S. Food & Drug Administration. AREXVY Prescribing Information, 2025. https://www.fda.gov/vaccines-blood-biologics/arexvy (accessed 2025-08-15).

(132) European Medicines Agency. Cervarix – EPAR Product Information, 2023. https://www.ema.europa.eu/en/medicines/human/EPAR/cervarix (accessed 2025-08-15).

(133) European Medicines Agency. Fendrix – EPAR Product Information, 2023. https://www.ema.europa.eu/en/medicines/human/EPAR/fendrix (accessed 2025-08-15).

(134) U.S. Food & Drug Administration. HEPLISAV-B Prescribing Information, 2024. https://www.fda.gov/vaccines-blood-biologics/vaccines/heplisav-b (accessed 2025-08-15).

(135) Šribar, D.; Grabowski, M.; Murgueitio, M. S.; Bermudez, M.; Weindl, G.; Wolber, G. Identification and Characterization of a Novel Chemotype for Human TLR8 Inhibitors. *Eur. J. Med. Chem.* **2019**, *179*, 744–752. https://doi.org/10.1016/j.ejmech.2019.06.084.

(136) Dolšak, A.; Šribar, D.; Scheffler, A.; Grabowski, M.; Švajger, U.; Gobec, S.; Holze, J.; Weindl, G.; Wolber, G.; Sova, M. Further Hit Optimization of 6-(Trifluoromethyl)Pyrimidin-2-Amine Based TLR8 Modulators: Synthesis, Biological Evaluation and Structure–Activity Relationships. *Eur. J. Med. Chem.* **2021**, *225*, 113809. https://doi.org/10.1016/j.ejmech.2021.113809.

(137) Port, A.; Shaw, J. V.; Klopp-Schulze, L.; Bytyqi, A.; Vetter, C.; Hussey, E.; Mammasse, N.; Ona, V.; Bachmann, A.; Strugala, D.; Reh, C.; Goteti, K. Phase 1 Study in Healthy Participants of the Safety, Pharmacokinetics, and Pharmacodynamics of Enpatoran (M5049), a Dual Antagonist of Toll-like Receptors 7 and 8. *Pharmacol. Res. Perspect.* **2021**, *9* (5), e00842. https://doi.org/10.1002/prp2.842.

(138) Goulopoulou, S.; McCarthy, C. G.; Webb, R. C. Toll-like Receptors in the Vascular System: Sensing the Dangers Within. *Pharmacol. Rev.* **2016**, *68* (1), 142–167. https://doi.org/10.1124/pr.114.010090.

(139) O'reilly, S.; Duffy, L. Toll-like Receptors in the Pathogenesis of Autoimmune Diseases: Recent and Emerging Translational Developments. *ImmunoTargets Ther.* **2016**, *Volume 5*, 69–80. https://doi.org/10.2147/ITT.S89795.

(140) Gao, W.; Xiong, Y.; Li, Q.; Yang, H. Inhibition of Toll-Like Receptor Signaling as a Promising Therapy for Inflammatory Diseases: A Journey from Molecular to Nano Therapeutics. *Front. Physiol.* **2017**, *Volume 8-2017*. https://doi.org/10.3389/fphys.2017.00508.

(141) Hamerman, J. A.; Barton, G. M. The Path Ahead for Understanding Toll-like Receptor-Driven Systemic Autoimmunity. *Curr. Opin. Immunol.* **2024**, *91*, 102482. https://doi.org/10.1016/j.coi.2024.102482.

(142) Webster, H. UNC93B1 Variants Promote SLE via TLR Activation. *Nat. Rev. Rheumatol.* **2024**, *20* (9), 528–528. https://doi.org/10.1038/s41584-024-01147-z.

(143) Wu, Y.; Tang, W.; Zuo, J. Toll-like Receptors: Potential Targets for Lupus Treatment. *Acta Pharmacol. Sin.* **2015**, *36* (12), 1395–1407. https://doi.org/10.1038/aps.2015.91.

(144) Vlach, J.; Bender, A. T.; Przetak, M.; Pereira, A.; Deshpande, A.; Johnson, T. L.; Reissig, S.; Tzvetkov, E.; Musil, D.; Morse, N. T.; Haselmayer, P.; Zimmerli, S. C.; Okitsu, S. L.; Walsky, R. L.; Sherer, B. Discovery of M5049: A Novel Selective Toll-Like Receptor 7/8 Inhibitor for Treatment of Autoimmunity. *J. Pharmacol. Exp. Ther.* **2021**, *376* (3), 397–409. https://doi.org/10.1124/jpet.120.000275.

(145) Engel, A. L.; Holt, G. E.; Lu, H. The Pharmacokinetics of Toll-like Receptor Agonists and the Impact on the Immune System. *Expert Rev. Clin. Pharmacol.* **2011**, *4* (2), 275–289. https://doi.org/10.1586/ecp.11.5.

(146) Hu, Z.; Tanji, H.; Jiang, S.; Zhang, S.; Koo, K.; Chan, J.; Sakaniwa, K.; Ohto, U.; Candia, A.; Shimizu, T.; Yin, H. Small-Molecule TLR8 Antagonists via Structure-Based Rational Design. *Cell Chem. Biol.* **2018**, *25* (10), 1286-1291.e3. https://doi.org/10.1016/j.chembiol.2018.07.004.

(147) Wang, X.; Liu, Y.; Han, X.; Zou, G.; Zhu, W.; Shen, H.; Liu, H. Small Molecule Approaches to Treat Autoimmune and Inflammatory Diseases (Part II): Nucleic Acid Sensing Antagonists and Inhibitors. *Bioorg. Med. Chem. Lett.* **2021**, *44*, 128101. https://doi.org/10.1016/j.bmcl.2021.128101.

(148) Klopp-Schulze, L.; Gopalakrishnan, S.; Yalkinoglu, Ö.; Kuroki, Y.; Lu, H.; Goteti, K.; Krebs-Brown, A.; Nogueira Filho, M.; Gradhand, U.; Fluck, M.; Shaw, J.; Dong, J.; Venkatakrishnan, K. Asia-Inclusive Global Development of Enpatoran: Results of an Ethno-Bridging Study, Intrinsic/Extrinsic Factor Assessments and Disease Trajectory Modeling to Inform Design of a Phase II Multiregional Clinical Trial. *Clin. Pharmacol. Ther.* **2024**, *115* (6), 1346–1357. https://doi.org/10.1002/cpt.3216.

(149) Witte, T.; Fernandez-Ruiz, R.; Abramova, N.; Weinelt, D.; Moreau, F.; Klopp-Schulze, L.; Shaw, J.; Denis, D.; Wenzel, J. Enpatoran, a First-in-Class, Selective, Orally Administered Toll-like Receptor 7/8 Inhibitor, in Systemic and Cutaneous Lupus Erythematosus: Results from a Randomised, Placebo-Controlled Phase Ib Study. *Lupus Sci. Med.* **2025**, *12* (2), e001705. https://doi.org/10.1136/lupus-2025-001705.

(150) Ishizaka, S. T.; Hawkins, L.; Chen, Q.; Tago, F.; Yagi, T.; Sakaniwa, K.; Zhang, Z.; Shimizu, T.; Shirato, M. A Novel Toll-like Receptor 7/8–Specific Antagonist E6742

Ameliorates Clinically Relevant Disease Parameters in Murine Models of Lupus. *Eur. J. Pharmacol.* **2023**, *957*, 175962. https://doi.org/10.1016/j.ejphar.2023.175962.

(151) Alper, P.; Betschart, C.; André, C.; Boulay, T.; Cheng, D.; Deane, J.; Faller, M.; Feifel, R.; Glatthar, R.; Han, D.; Hemmig, R.; Jiang, T.; Knoepfel, T.; Maginnis, J.; Mutnick, D.; Pei, W.; Ruzzante, G.; Syka, P.; Zhang, G.; Zhang, Y.; Zink, F.; Zipfel, G.; Hawtin, S.; Junt, T.; Michellys, P.-Y. Discovery of the TLR7/8 Antagonist MHV370 for Treatment of Systemic Autoimmune Diseases. *ACS Med. Chem. Lett.* **2023**, *14* (8), 1054–1062. https://doi.org/10.1021/acsmedchemlett.3c00136.

(152) Hawtin, S.; André, C.; Collignon-Zipfel, G.; Appenzeller, S.; Bannert, B.; Baumgartner, L.; Beck, D.; Betschart, C.; Boulay, T.; Brunner, H. I.; Ceci, M.; Deane, J.; Feifel, R.; Ferrero, E.; Kyburz, D.; Lafossas, F.; Loetscher, P.; Merz-Stoeckle, C.; Michellys, P.; Nuesslein-Hildesheim, B.; Raulf, F.; Rush, J. S.; Ruzzante, G.; Stein, T.; Zaharevitz, S.; Wieczorek, G.; Siegel, R.; Gergely, P.; Shisha, T.; Junt, T. Preclinical Characterization of the Toll-like Receptor 7/8 Antagonist MHV370 for Lupus Therapy. *Cell Rep. Med.* **2023**, *4* (5), 101036. https://doi.org/10.1016/j.xcrm.2023.101036.

(153) Shisha, T.; Posch, M. G.; Lehmann, J.; Feifel, R.; Junt, T.; Hawtin, S.; Schuemann, J.; Avrameas, A.; Danekula, R.; Misiolek, P.; Siegel, R.; Gergely, P. First-in-Human Study of the Safety, Pharmacokinetics, and Pharmacodynamics of MHV370, a Dual Inhibitor of Toll-Like Receptors 7 and 8, in Healthy Adults. *Eur. J. Drug Metab. Pharmacokinet.* **2023**, *48* (5), 553–566. https://doi.org/10.1007/s13318-023-00847-3.

(154) Yuan, Y.; Wei, Y.; Jia, Z.; Chu, H.; Kong, D.; Lei, F.; Ye, F.; Qian, X.; Zhang, J.; Zhou, X.; Zhu, X.; Li, Z.; Liang, X.; Chen, W. Discovery of KBD4466, a Selective TLR 7/8 Inhibitor, for the Treatment of Autoimmune Diseases. *J. Med. Chem.* **2025**. https://doi.org/10.1021/acs.jmedchem.5c00656.

(155) Wu, P.; Fu, Q.; Zhou, S.; Huang, L.; Cheng, K.; Chen, Z. Structure-Based Rational Design of TLR7/8 Antagonists through Agonist Scaffold Reengineering for Psoriasis Therapy. *Eur. J. Med. Chem.* **2025**, *299*, 118063. https://doi.org/10.1016/j.ejmech.2025.118063.

(156) Jeong, U.; Lee, W. H.; Choi, Y. S.; Haseeb, M.; Baek, W.-Y.; Han, J. H.; Choi, H.; Kim, M. S.; Suh, C.-H.; Kim, W.; Choi, S. Discovery of ETI41 and ETI60: Novel Selective Endosomal Toll-like Receptor Inhibitors for the Treatment of Autoimmune Diseases. *Exp. Mol. Med.* **2025**. https://doi.org/10.1038/s12276-025-01526-w.

(157) Jiang, S.; Tanji, H.; Yin, K.; Zhang, S.; Sakaniwa, K.; Huang, J.; Yang, Y.; Li, J.; Ohto, U.; Shimizu, T.; Yin, H. Rationally Designed Small-Molecule Inhibitors Targeting an Unconventional Pocket on the TLR8 Protein–Protein Interface. *J. Med. Chem.* **2020**, *63* (8), 4117–4132. https://doi.org/10.1021/acs.jmedchem.9b02128.

(158) Matziol, T.; Talagayev, V.; Slokan, T.; Strašek Benedik, N.; Holze, J.; Sova, M.; Wolber, G.; Weindl, G. Discovery of Novel Isoxazole-Based Small-Molecule Toll-Like Receptor 8 Antagonists. *J. Med. Chem.* **2025**, *68* (4), 4888–4907. https://doi.org/10.1021/acs.jmedchem.4c03148.

(159) Grabowski, M.; Bermudez, M.; Rudolf, T.; Šribar, D.; Varga, P.; Murgueitio, M. S.; Wolber, G.; Rademann, J.; Weindl, G. Identification and Validation of a Novel Dual Small-Molecule TLR2/8 Antagonist. *Biochem. Pharmacol.* **2020**, *177*, 113957. https://doi.org/10.1016/j.bcp.2020.113957.

(160) Holze, J.; Lauber, F.; Soler, S.; Kostenis, E.; Weindl, G. Label-Free Biosensor Assay Decodes the Dynamics of Toll-like Receptor Signaling. *Nat. Commun.* **2024**, *15* (1), 9554. https://doi.org/10.1038/s41467-024-53770-9.

(161) Talagayev, V.; Chen, Y.; Doering, N. P.; Obendorf, L.; Denzinger, K.; Puls, K.; Lam, K.; Liu, S.; Wolf, C. A.; Noonan, T.; Breznik, M.; Knaus, P.; Wolber, G. OpenMMDL - Simplifying the Complex: Building, Simulating, and Analyzing Protein–Ligand Systems in OpenMM. *J. Chem. Inf. Model.* **2025**, *65* (4), 1967–1978. https://doi.org/10.1021/acs.jcim.4c02158.

(162) Benedik, N. S.; Talagayev, V.; Matziol, T.; Dolšak, A.; Sosič, I.; Weindl, G.; Wolber, G.; Sova, M. Optimization of 6-(Trifluoromethyl)Pyrimidine Derivatives as TLR8 Antagonists. *Acta Pharm.* **2025**, *75* (2), 159–183. https://doi.org/10.2478/acph-2025-0011.

(163) Sou, T.; Bergström, C. A. S. Automated Assays for Thermodynamic (Equilibrium) Solubility Determination. *Physicochem. Characterisation Drug Discov.* **2018**, *27*, 11–19. https://doi.org/10.1016/j.ddtec.2018.04.004.

(164) Edward H. Kerns; Li Di; Guy T. Carter. In Vitro Solubility Assays in Drug Discovery. *Curr. Drug Metab.* **2008**, *9* (9), 879–885. https://doi.org/10.2174/138920008786485100.

(165) Ghafourian, T.; Amin, Z. QSAR Models for the Prediction of Plasma Protein Binding. *Bioimpacts* **2013**, *3* (1), 21–27. https://doi.org/10.5681/bi.2013.011.

(166) Mussari, C. P.; Dodd, D. S.; Sreekantha, R. K.; Pasunoori, L.; Wan, H.; Posy, S. L.; Critton, D.; Ruepp, S.; Subramanian, M.; Watson, A.; Davies, P.; Schieven, G. L.; Salter-Cid, L. M.; Srivastava, R.; Tagore, D. M.; Dudhgaonkar, S.; Poss, M. A.; Carter, P. H.; Dyckman, A. J. Discovery of Potent and Orally Bioavailable Small Molecule Antagonists of Toll-like Receptors 7/8/9 (TLR7/8/9). *ACS Med. Chem. Lett.* **2020**, *11* (9), 1751–1758. https://doi.org/10.1021/acsmedchemlett.0c00264.

(167) Labute, P. Protonate3D: Assignment of Ionization States and Hydrogen Coordinates to Macromolecular Structures. *Proteins Struct. Funct. Bioinforma.* **2009**, *75* (1), 187–205. https://doi.org/10.1002/prot.22234.

(168) Jones, G.; Willett, P.; Glen, R. C.; Leach, A. R.; Taylor, R. Development and Validation of a Genetic Algorithm for Flexible docking11Edited by F. E. Cohen. *J. Mol. Biol.* **1997**, *267* (3), 727–748. https://doi.org/10.1006/jmbi.1996.0897.

(169) Korb, O.; Stützle, T.; Exner, T. E. Empirical Scoring Functions for Advanced Protein−Ligand Docking with PLANTS. *J. Chem. Inf. Model.* **2009**, *49* (1), 84–96. https://doi.org/10.1021/ci800298z.

(170) Halgren, T. A. Merck Molecular Force Field. I. Basis, Form, Scope, Parameterization, and Performance of MMFF94. *J. Comput. Chem.* **1996**, *17* (5–6), 490–519. https://doi.org/10.1002/(SICI)1096-987X(199604)17:5/6%253C490::AID-JCC1%253E3.0.CO;2-P.

(171) Naughton, F. B.; Alibay, I.; Barnoud, J.; Barreto-Ojeda, E.; Beckstein, O.; Bouysset, C.; Cohen, O.; Gowers, R. J.; MacDermott-Opeskin, H.; Matta, M.; Melo, M. N.; Reddy, T.; Wang, L.; Zhuang, Y. MDAnalysis 2.0 and beyond: Fast and Interoperable, Community Driven Simulation Analysis. *Biophys. J.* **2022**, *121* (3), 272a–273a. https://doi.org/10.1016/j.bpj.2021.11.1368.

(172) Davies, B.; Morris, T. Physiological Parameters in Laboratory Animals and Humans. *Pharm. Res.* **1993**, *10* (7), 1093–1095. https://doi.org/10.1023/A:1018943613122.

(173) Obach, R. S.; Baxter, J. G.; Liston, T. E.; Silber, B. M.; Jones, B. C.; Macintyre, F.; Rance, D. J.; Wastall, P. The Prediction of Human Pharmacokinetic Parameters from Preclinical and In Vitro Metabolism Data. *J. Pharmacol. Exp. Ther.* **1997**, *283* (1), 46–58. https://doi.org/10.1016/S0022-3565(24)36999-X.

(174) Thwaites, R.; Chamberlain, G.; Sacre, S. Emerging Role of Endosomal Toll-Like Receptors in Rheumatoid Arthritis. *Front. Immunol.* **2014**, *Volume 5-2014*. https://doi.org/10.3389/fimmu.2014.00001.

(175) Sun, L.; Liu, W.; Zhang, L. The Role of Toll-Like Receptors in Skin Host Defense, Psoriasis, and Atopic Dermatitis. *J. Immunol. Res.* **2019**, *2019*, 1–13. https://doi.org/10.1155/2019/1824624.

(176) Mukherjee, S.; Patra, R.; Behzadi, P.; Masotti, A.; Paolini, A.; Sarshar, M. Toll-like Receptor-Guided Therapeutic Intervention of Human Cancers: Molecular and Immunological Perspectives. *Front. Immunol.* **2023**, *Volume 14-2023*. https://doi.org/10.3389/fimmu.2023.1244345.

(177) Sun, Y.; Chai, X.; Wang, Z.; Qu, S.; Wu, L.; Liu, L.; Liu, Y.; Zhu, J. First-in-Human Study of ZG0895, a TLR8 Selective Agonist, as Monotherapy in Patients with Advanced Solid Tumors. *J. Clin. Oncol.* **2024**, *42* (16_suppl), e15103–e15103. https://doi.org/10.1200/JCO.2024.42.16_suppl.e15103.

(178) Tong, A.-J.; Leylek, R.; Herzner, A.-M.; Rigas, D.; Wichner, S.; Blanchette, C.; Tahtinen, S.; Kemball, C. C.; Mellman, I.; Haley, B.; Freund, E. C.; Delamarre, L. Nucleotide Modifications Enable Rational Design of TLR7-Selective Ligands by Blocking RNase Cleavage. *J. Exp. Med.* **2024**, *221* (2), e20230341. https://doi.org/10.1084/jem.20230341.

(179) Wu, Y.; Qin, J.; Gu, Y.; Zhao, G.; Xu, P.; Lin, S.; Cheng, X.; Zhang, L. W.; Wang, Y.; Wang, Y. Radioresponsive Delivery of Toll-like Receptor 7/8 Agonist for Tumor Radioimmunotherapy Enabled by Core-Cross-Linked Diselenide Nanoparticles. *ACS Nano* **2024**, *18* (4), 2800–2814. https://doi.org/10.1021/acsnano.3c05882.

(180) Thakur, N.; Thakur, S.; Chatterjee, S.; Das, J.; Sil, P. C. Nanoparticles as Smart Carriers for Enhanced Cancer Immunotherapy. *Front. Chem.* **2020**, *Volume 8-2020*. https://doi.org/10.3389/fchem.2020.597806.

(181) Behzadi, P.; García-Perdomo, H. A.; Karpiński, T. M. Toll-Like Receptors: General Molecular and Structural Biology. *J. Immunol. Res.* **2021**, *2021*, 1–21. https://doi.org/10.1155/2021/9914854.

(182) Kawai, T.; Akira, S. Toll-like Receptors and Their Crosstalk with Other Innate Receptors in Infection and Immunity. *Immunity* **2011**, *34* (5), 637–650. https://doi.org/10.1016/j.immuni.2011.05.006.

(183) Loo, Y.-M.; Gale, M. Immune Signaling by RIG-I-like Receptors. *Immunity* **2011**, *34* (5), 680–692. https://doi.org/10.1016/j.immuni.2011.05.003.

(184) Bzówka, M.; Bagrowska, W.; Góra, A. Recent Advances in Studying Toll-like Receptors with the Use of Computational Methods. *J. Chem. Inf. Model.* **2023**, *63* (12), 3669–3687. https://doi.org/10.1021/acs.jcim.3c00419.

(185) Alharbi, A. S.; Sapkota, S.; Zhang, Z.; Jin, R.; Jayasekara, W. S. N.; Rupasinghe, E.; Speir, M.; Wilkinson-White, L.; Gamsjaeger, R.; Cubeddu, L.; Ellyard, J. I.; Wenholz, D. S.; McAllan, A. L.; Rezwan, R.; Ying, L.; Far, H. H.; Bones, J.; He, S.; Yu, D.; Lennox, K. A.; Hertzog, P. J.; Vinuesa, C. G.; Behlke, M. A.; Ohto, U.; Laczka, O. F.; Corry, B.; Shimizu, T.; Gantier, M. P. 2'-O-Methyl-Guanosine 3-Base RNA Fragments Mediate Essential Natural TLR7/8 Antagonism. *bioRxiv* **2024**, *605091*. https://doi.org/10.1101/2024.07.25.605091.

(186) Schröder, R.; Schmidt, J.; Blättermann, S.; Peters, L.; Janssen, N.; Grundmann, M.; Seemann, W.; Kaufel, D.; Merten, N.; Drewke, C.; Gomeza, J.; Milligan, G.; Mohr, K.; Kostenis, E. Applying Label-Free Dynamic Mass Redistribution Technology to Frame Signaling of G Protein–Coupled Receptors Noninvasively in Living Cells. *Nat. Protoc.* **2011**, *6* (11), 1748–1760. https://doi.org/10.1038/nprot.2011.386.

(187) Wei, J.; Kurumi, H.; Isomoto, H.; Ogihara, R.; Matsushima, K.; Machida, H.; Ishida, T.; Hirayama, T.; Yamaguchi, N.; Yoshida, Y.; Tsukamoto, K. Toll-like Receptor Gene Polymorphisms as Predictive Biomarkers for Response to Infliximab in Japanese Patients with Crohn's Disease. *Diagnostics* **2025**, *15* (8). https://doi.org/10.3390/diagnostics15080971.

(188) Hu, A.; Sun, L.; Lin, H.; Liao, Y.; Yang, H.; Mao, Y. Harnessing Innate Immune Pathways for Therapeutic Advancement in Cancer. *Signal Transduct. Target. Ther.* **2024**, *9* (1), 68. https://doi.org/10.1038/s41392-024-01765-9.

(189) Le, J.; Dian, Y.; Zhao, D.; Guo, Z.; Luo, Z.; Chen, X.; Zeng, F.; Deng, G. Single-Cell Multi-Omics in Cancer Immunotherapy: From Tumor Heterogeneity to Personalized Precision Treatment. *Mol. Cancer* **2025**, *24* (1), 221. https://doi.org/10.1186/s12943-025-02426-3.

(190) Mu, Z.; Wei, W.; Fair, B.; Miao, J.; Zhu, P.; Li, Y. I. The Impact of Cell Type and Context-Dependent Regulatory Variants on Human Immune Traits. *Genome Biol.* **2021**, *22* (1), 122. https://doi.org/10.1186/s13059-021-02334-x.

(191) Nouri-Shirazi, M.; Tamjidi, S.; Nourishirazi, E.; Guinet, E. Combination of TLR8 and TLR4 Agonists Reduces the Degrading Effects of Nicotine on DC-NK Mediated Effector T Cell Generation. *Int. Immunopharmacol.* **2018**, *61*, 54–63. https://doi.org/10.1016/j.intimp.2018.05.012.

(192) Forsbach, A.; Nemorin, J.-G.; Montino, C.; Müller, C.; Samulowitz, U.; Vicari, A. P.; Jurk, M.; Mutwiri, G. K.; Krieg, A. M.; Lipford, G. B.; Vollmer, J. Identification of RNA Sequence Motifs Stimulating Sequence-Specific TLR8-Dependent Immune Responses. *J. Immunol.* **2008**, *180* (6), 3729–3738. https://doi.org/10.4049/jimmunol.180.6.3729.

(193) Cervantes, J. L.; Weinerman, B.; Basole, C.; Salazar, J. C. TLR8: The Forgotten Relative Revindicated. *Cell. Mol. Immunol.* **2012**, *9* (6), 434–438. https://doi.org/10.1038/cmi.2012.38.

(194) Hinkelmann, L.; Brehm, M.; Kumbol, V.; McGurran, H.; Krüger, C.; Kleinau, G.; Scheerer, P.; Golenbock, D.; Alexopoulou, L.; Gantier, M. P.; Bauer, S.; Lehnardt, S. Murine Toll-like Receptor 8 Is a Nucleic Acid Multi-Sensor Detecting 2',3'-Cyclic Monophosphate Guanosine as Well as Combinations of Ribo-, Deoxy-, Cyclic Nucleotides, and Nucleosides. *bioRxiv* **2025**, 2025.10.14.682277. https://doi.org/10.1101/2025.10.14.682277.

(195) Kugelberg, E. Making Mice More Human the TLR8 Way. *Nat. Rev. Immunol.* **2014**, *14* (1), 6–6. https://doi.org/10.1038/nri3587.

8 Appendix

This appendix comprises the full-length publications corresponding to Chapters 2, 3, and 4, including all supporting information associated with these works. Furthermore, it presents supplementary data related to the unpublished research described in Chapter 5. The appendix also includes NMR spectra for all newly synthesized compounds and HPLC chromatograms for final compounds documented in Chapters 3, 4, and 5. Copyright information for the published articles, available under Creative Commons Attribution 4.0 International (CC BY 4.0) license or under Creative Commons Attribution-NonCommercial-NoDerivatives 4.0 (CC BY-NC-ND 4.0) license, is provided in the respective copyright statements.

Appendix I. Publication I: Structure-guided approaches to modulate endosomal toll-like receptors TLR7, TLR8 and TLR9: advances, challenges and therapeutic promise

The following pages include the article “Structure-guided approaches to modulate endosomal toll-like receptors TLR7, TLR8 and TLR9: advances, challenges and therapeutic promise” as it was published in Drug Discovery Today by ScienceDirect, part of Elsevier.

Reprinted with permission from:

Troy Matziol, Valerij Talagayev, Günther Weindl, Gerhard Wolber. Structure-guided approaches to modulate endosomal toll-like receptors TLR7, TLR8 and TLR9: advances, challenges and therapeutic promise. Drug Discov. Today. 2025;30(11):104495.

Doi: 10.1016/j.drudis.2025.104495

Structure-guided approaches to modulate endosomal toll-like receptors TLR7, TLR8 and TLR9: advances, challenges and therapeutic promise

Troy Matziol [1,#], Valerij Talagayev [2,#], Günther Weindl [1,*], Gerhard Wolber [2,*]

[1] University of Bonn, Pharmaceutical Institute, Pharmacology and Toxicology Section, Gerhard-Domagk-Str. 3, 53121 Bonn, Germany
[2] Freie Universität Berlin, Institute of Pharmacy, Pharmaceutical and Medicinal Chemistry, Königin-Luise-Str. 2+4, 14195 Berlin, Germany

TLR7, TLR8 and TLR9 are endosomal immune receptors central to antiviral defense, autoimmunity and cancer immunotherapy. Recent structural insights have revealed distinct ligand-binding mechanisms and conformational dynamics, enabling the design of selective small-molecule agonists and antagonists. This review summarizes key advances in TLR7/8/9 biology, pharmacology and structure-guided drug discovery. We highlight clinical progress, delivery strategies and translational challenges including species-specific differences and immune-related toxicities. Novel approaches such as nanoparticle systems and endogenous RNA mimetics promise targeted modulation of TLR activity. Together, these developments emphasize the therapeutic potential of precision TLR modulation in immunologically complex diseases.

Keywords: Toll-like receptors; endosomal immunity; small-molecule modulators; structure-guided drug design

Introduction

Toll-like receptors (TLRs) are a family of innate immune receptors that detect pathogen-associated molecular patterns (PAMPs) and damage-associated molecular patterns (DAMPs), playing a crucial part in the immune response.(p1) In humans, ten TLRs have been identified, distributed either on the cell surface (e.g., TLRs 1/2/4/5/6 and 10) or within endosomal compartments (e.g., TLRs 3/7/8/9).(p1),(p2) Whereas surface TLRs primarily recognize microbial components such as lipopolysaccharides and flagellin, endosomal TLRs detect nucleic acids from pathogens or damaged cells.(p3) Ligand binding initiates downstream signaling pathways, typically mediated by signaling adaptors such as MyD88 for TLR7/8/9, resulting in the activation of nuclear factor (NF)-κB and interferon (IFN) regulatory factors (IRFs). This, in turn, drives the production of proinflammatory cytokines and chemokines essential for immune defense, including tumor necrosis factor (TNF), interleukin (IL)-6 and IL-1β.(p2) Besides their role in pathogen sensing, TLR7, TLR8 and TLR9 contribute to autoimmune diseases such as systemic lupus erythematosus (SLE), systemic sclerosis and Sjögren's syndrome.(p4) Advances in structural biology and receptor pharmacology have led to the development of agonists and antagonists targeting these TLRs, with several candidates advancing into clinical trials. However, challenges remain, including species-specific receptor differences (notably in TLR8), the lack of crystal structures for the (ligand-bound) human TLR9 receptor, context-dependent signaling and adverse immune activation by TLR9 agonists.(p3),(p4) In this review we provide an overview of the biology, disease relevance and therapeutic TLR7/8/9 targeting strategies. The repertoire of ligands for the remaining endosomal TLR3 is sparse and has been recently summarized elsewhere.(p5) We highlight current drug discovery efforts, discuss the translational hurdles, and outline future perspectives for exploiting these receptors in immunotherapy and other therapeutic applications.

* *Corresponding authors. Weindl, G. (guenther.weindl@uni-bonn.de), Wolber, G. (gerhard.wolber@fu-berlin.de).*
# These authors contributed equally to this work.

https://doi.org/10.1016/j.drudis.2025.104495

Dimerization and ligand recognition in TLR7/8/9

TLR7/8/9 are endosomal sensors that share a conserved leucine-rich repeat (LRR) ectodomain architecture and function as ligand-activated homodimer (Figure 1a–d).[p6] High-resolution structures have illuminated similar conformational behaviors among these receptors.[p7],[p8],[p9] TLR8 exists as a pre-formed ectodomain dimer even in the absence of a ligand and contains two spatially separate ligand-binding sites. One site, located at the dimerization interface, accommodates small agonists whereas a second 'concave' pocket on the protein surface binds short oligoribonucleotide fragments (Figure 1a,b).[p8] Synthetic agonists or natural ligands induce TLR7 dimerization by binding two sites analogous to TLR8: a primary site at the dimer interface for small ligands and a secondary site spanning the concave surface for uridine-rich RNA.[p10] In TLR7 and TLR8, agonist binding produces a closed M-shaped dimer that juxtaposes the C-terminal signaling domains, priming the receptor to recruit adaptor proteins.[p8],[p10] Antagonists bind within the TLR7 ectodomain interface and lock the receptor in an open dimer conformation (~69 Å C-terminal separation), preventing Toll/interleukin-1 receptor (TIR) domain juxtaposition and signaling, a stark structural contrast to agonist-induced ~36 Å 'closed' dimers.[p11] TLR8-selective antagonists like CU-CPT9a similarly occupy the hydrophobic interface pocket, stabilizing the receptor in an inactive dimeric state while the binding of agonists leads to structural reorganization leading to the homodimers moving closer (Figure 1d).[p12] Moreover, molecular dynamics simulations show that agonists and antagonists dissociate from TLR8 through distinct pathways, reflecting differences in interactions and allosteric effects.[p13]

TLR9 similarly undergoes dramatic conformational changes upon ligand binding. Stimulatory CpG DNA acts as a bivalent ligand or 'molecular glue' that wraps across two TLR9 protomers, forming a 2:2 receptor–DNA complex. The CpG-containing oligonucleotide threads through the lateral groove of one TLR9 ectodomain and into the concave face of the other, effectively bridging the two receptors and inducing the active dimer conformation.[p16] A second DNA-binding pocket, corresponding to the small nucleoside-binding site of TLR7/8, has also been identified in TLR9 and appears to cooperatively regulate its activation (Figure 1c).[p15] These structural insights point to a shared mechanism: ligand-induced dimerization is required for signaling, yet the receptors have evolved multiple ligand-binding pockets and dimerization modes to sense complex nucleic-acid-based stimuli.[p8],[p12]

TLR7/8/9 signaling pathways in immunity and autoimmunity

MyD88-dependent endosomal TLRs are predominantly expressed in specialized immune cells [e.g., plasmacytoid dendritic cells (pDCs) for TLR7/9], where they function as sentinels for viral RNA or bacterial DNA. Activation of TLR7/8/9 triggers a MyD88-dependent signaling cascade that leads to the activation of NF-κB and IRF7 or IRF5, resulting in the production of proinflammatory cytokines and type I IFNs (Figure 2). Recent findings reveal that MyD88 assembles into barrel-shaped supramolecular complexes called Myddosomes.[p17] TASL has been identified as a crucial adaptor for IRF5 activation downstream of TLR7 and TLR9 in pDCs and B cells, although being dispensable for TLR4 or IRF3/7 signaling.[p18] The SLC15A4–TASL/TASL2 complex is essential for full IRF5 activation and the induction of IFN/IL-6 responses in these cells.[p19],[p20] Therefore, selectively targeting SLC15A4–TASL interactions could offer new strategies to modulate TLR-driven IFN responses in autoimmunity, as exemplified by the recent identification of feeblin – a small-molecule inhibitor that binds SLC15A4 to destabilize TASL and disrupt TLR7/8–IRF5 signaling.[p21]

Agonist engagement of TLR7/8 leads to robust induction of IFN-α/β and inflammatory mediators, demonstrating their crucial role in antiviral immunity and as immune adjuvants.[p22] TLR9 activation by CpG-rich DNA likewise triggers strong Th1-polarizing cytokine responses; indeed, synthetic CpG oligodeoxynucleotides (ODNs) have advanced as vaccine adjuvants in infectious disease and cancer.[p23] Topical TLR7/8 agonists are therapeutically used to enhance local immune responses against skin tumors and viral lesions, whereas systemically administered TLR agonists are being explored as immunotherapy adjuvants owing to their ability to potentiate DC and T cell activity.[p24],[p25]

Dysregulated TLR7/8/9 signaling, however, is implicated in autoimmunity and chronic inflammation. Aberrant sensing of self RNA or DNA can pathologically activate these receptors, as seen in SLE where endogenous nucleic acids drive unwanted type I IFN production.[p26] As a result, TLR antagonists have gained attention as potential immunomodulators for restoring immune homeostasis. Blocking TLR7/8 ameliorates lupus-like disease in preclinical models.[p27],[p28] Likewise, TLR9 inhibition is being studied to prevent overproduction of IFN and autoantibody stimulation in conditions ranging from lupus to certain autoinflammatory syndromes.[p29] Importantly, the nuanced understanding of TLR structures and ligand interactions now allows the design of antagonists that specifically target disease-relevant TLR pathways while sparing protective immune functions. For example, selectively antagonizing TLR7/8 in pDCs can dampen pathogenic IFN-α in lupus without globally suppressing other TLRs needed for host defense.[p27] In summary, the pharmacological modulation of TLR7/8/9 holds considerable promise in drug discovery for cancer immunotherapy, infectious diseases and autoimmune disorders.

Optimizing TLR7/8/9 activation for immunotherapy and vaccine use

A wide range of small-molecule agonists has been developed to mimic the natural ligands of MyD88-dependent endosomal TLRs and exploit their immune-activating properties. Many TLR7/8 agonists are heterocyclic base analogs that bind in the nucleoside pocket of the receptor dimer interface, thereby inducing the active closed conformation. The imidazoquinolines imiquimod and resiquimod were among the first antiviral TLR7 agonists identified. These molecules, resembling guanine analogs, directly occupy the same site that endogenous purines bind, triggering TLR dimerization and downstream IFN production. Imidazoquinolines remain an important scaffold for TLR7 agonists, with ongoing research focused on optimizing potency and selectivity. Moreover they have inspired the identification of novel TLR7

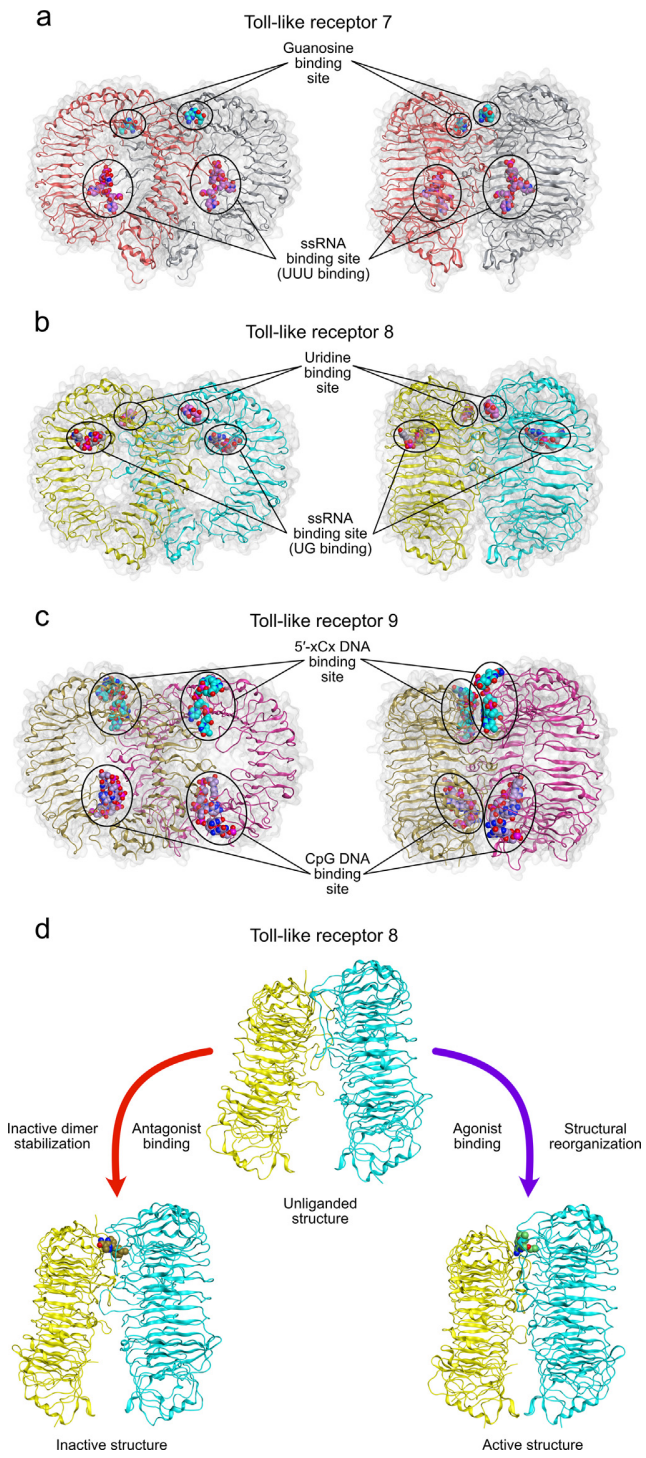

FIGURE 1

Binding sites of TLR7/8/9 and TLR8 conformational change. **(a)** TLR7 contains two binding sites, with the guanosine binding site for small ligands and an single-stranded RNA (ssRNA) binding site (PDB: 5GMF).[p10] **(b)** TLR8 contains two binding sites with the uridine binding site for small-molecule binding and an ssRNA binding site (PDB: 4R08).[p14] **(c)** TLR9 contains two DNA binding sites, with both cooperatively regulating the receptor activation (PDB: 5Y3M).[p15] **(d)** TLR8 conformational change. In the unliganded structure both homodimers are distanced away from each other (PDB: 3W3G).[p8] Antagonist binding leads to an inactive dimer stabilization with the homodimers remaining distanced from each other (PDB: 5WYX).[p12] Agonist binding leads to a structural reorganization, with the homodimers reducing their distance (PDB: 3W3L).[p8]

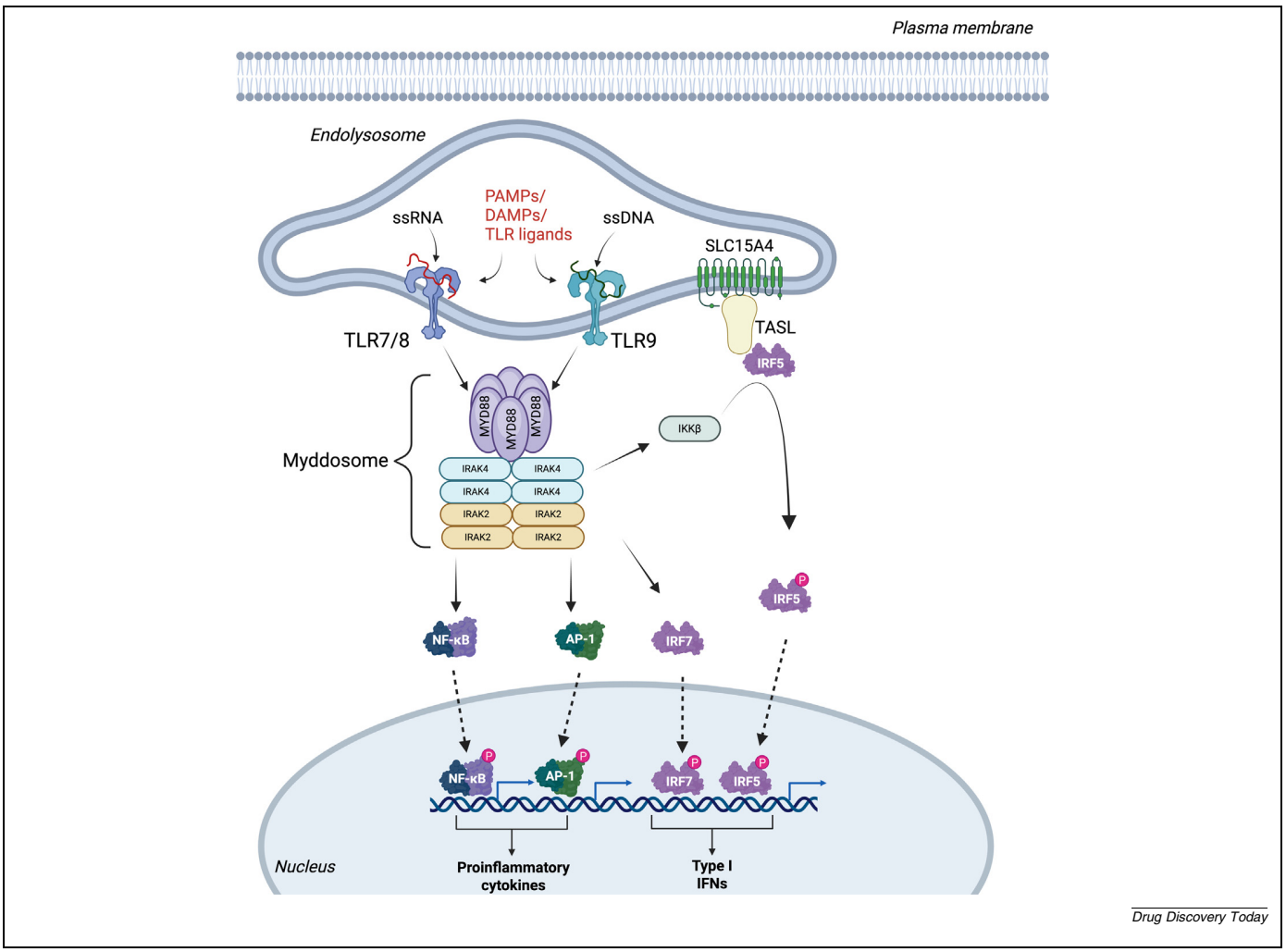

FIGURE 2

Endosomal TLR7/8/9 signaling pathways. TLR7 and TLR8 detect ssRNA, whereas TLR9 recognizes unmethylated CpG DNA within endosomes. Ligand engagement induces receptor dimerization and recruitment of the adaptor protein, which oligomerizes into a higher order signaling platform known as the Myddosome. This complex includes multiple MyD88 and interleukin-1 receptor–associated kinase (IRAK) molecules and serves as the core signaling hub. Activation of the Myddosome leads to phosphorylation and nuclear translocation of transcription factors NF-κB, AP-1 and further of IRF7. SLC15A4, a lysosomal transporter, recruits the adaptor protein TASL, which scaffolds IRF5 to the endolysosomal membrane. This spatial organization facilitates IRF5 phosphorylation by IKKβ, promoting its dimerization and nuclear translocation.

agonist scaffolds, such as imidazo-thienopyridine-based TLR7 agonists (Table 1).[p30],[p31],[p32],[p33] Structural studies confirm that such agonists can effectively substitute for one of the two RNA degradation products normally required for full activation. In TLR8, a small agonist in the interface pocket can replace uridine, whereas in TLR7 a single synthetic ligand can simultaneously engage both protomers to promote dimerization.[p34] In the case of TLR9, agonists are typically synthetic CpG DNA oligonucleotides rather than small molecules. These CpG ODNs bind bivalently and induce a potent immunostimulatory signal, and several compounds are in clinical use or in trials as vaccine adjuvants.[p25] Among TLR7 agonists, clinical trials investigating intratumoral and systemic administration for oncology indications have progressed significantly (Table 2). For TLR9, clinical development has primarily focused on oligonucleotide-based agonists such as IMO-2125, currently undergoing late-stage clinical evaluation for refractory melanoma and solid tumors in combination with checkpoint inhibitors (Table 2).

Cooperative binding mechanisms are a hallmark of TLR7/8 agonism. TLR7 can be activated by the combined presence of two ligand components: uridine-rich short RNA and a small guanosine-like compound, which occupy its two distinct pockets and act in concert (Figure 1a).[p10],[p45] TLR8 requires simultaneous binding of two ligands: uridine at the interface site and an oligoribonucleotide fragment at the concave site. This dual occupancy is essential to induce the conformational change necessary for activation.[p8],[p14] Synthetic single molecules have been designed to fulfill both binding requirements. For example, certain agonists are molecular ‘twin’ designs that can simultaneously engage both sites or two protomers, thereby bypassing the need for separate RNA fragments. This approach is exemplified by isoxazole-pyrimidine-based agonists reported as selective

TABLE 1

Selected TLR7/8/9-targeting scaffolds and compounds in clinical development TLR7/8/9-targeting scaffolds that have been identified as modulators of TLR7, TLR8 and TLR9. Each scaffold class is listed alongside its primary TLR target(s) and a representative compound.

Scaffold class	Target	Structure
Benzanilides[p35]	TLR7/8	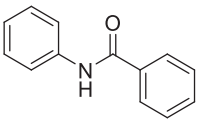
Benzimidazoles[p36]	TLR8	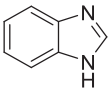
Benzoxazoles[p35]	TLR7/9	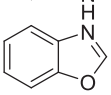
Chromene[p36]	TLR8/9	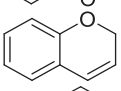
Dihydropyrrolo[2,3-d] pyrimidines[p37]	TLR9	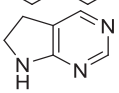
Furopyridines[p36]	TLR8	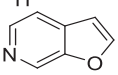
Imidazoles[p36]	TLR8	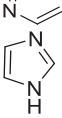
Imidazopyridine[p35]	TLR7/9	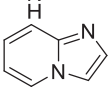
Imidazoquinoxalines[p35]	TLR7	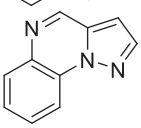
Imidazoquinolines[p30],[p31],[p32],[p38]	TLR7/8	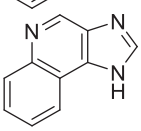
Imidazo-thienopyridines[p33]	TLR7	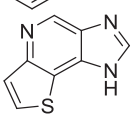
Indazoles[p35]	TLR7/8	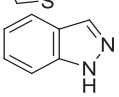
Indoles[p35]	TLR7/8	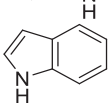
Isoxazole[p39]	TLR8	
Isoxazolopyrimidines[p40]	TLR7	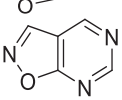
8-Oxoadenines[p41]	TLR7	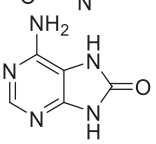
Pteridinones[p41]	TLR7	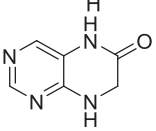

TABLE 1 (*CONTINUED*)

Scaffold class	Target	Structure
Purines[p35]	TLR7/9	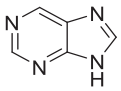
Pyrazolopyridines[p35]	TLR7/8	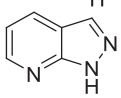
Pyrazolopyrimidines[p35]	TLR7/8	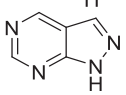
Pyridones[p35]	TLR7/8	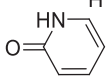
Pyridopyrimidines[p36]	TLR7/8	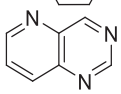
Pyrimidines[p42]	TLR8	
Pyrollopyridines[p43]	TLR7/9	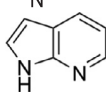
Pyrrolopyrimidine[p36]	TLR7	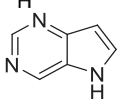
Triazoles[p36]	TLR8	
Quinazolines[p35]	TLR7/8/9	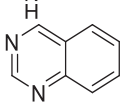
Quinolines[p35],[p44]	TLR7/8	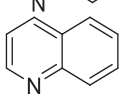

TLR7 stimulators (Table 1).[p40] Such novel agonists illustrate the ongoing innovation in TLR ligand design, with diverse scaffolds being explored to maximize efficacy and selectivity for therapeutic use (Table 1).[p35],[p36] The understanding of how agonists bind and dimerize TLRs has led to the design of more-effective analogs, and even antibody–drug conjugates carrying TLR7 agonist payloads for targeted immunotherapy. This emerging strategy involves localization of the 'danger signal' to tumors, and has been successfully applied, resulting in the discovery of novel TLR7/8 agonists.[p46],[p47],[p48] Moreover, recent progress in nanomedicine has facilitated targeted delivery of TLR agonists within the tumor microenvironment. Core-crosslinked diselenide nanoparticles can deliver TLR7/8 agonists in a radio-responsive manner, enhancing the efficacy of tumor radioimmunotherapy through spatiotemporal immune activation while limiting systemic inflammation.[p35] In another approach, polyphenylene sulfide (PPS)-based nanoparticles encapsulating TLR7/8 agonists induce selectively prolonged activation of DCs, thereby amplifying antigen presentation and promoting durable anticancer immunity in preclinical models. This underscores the therapeutic potential of engineering delivery systems to refine innate immune activation.[p49] Additionally, chemical modification of oligoribonucleotides at specific sugar positions enables the

TABLE 2

Selected TLR7/8/9-targeting compounds in clinical development Agonistic or antagonistic activity and the primary disease area under investigation of key clinical-stage TLR7, TLR8 and TLR9 modulators. Trial identifiers (e.g., NCT numbers) link to ongoing studies.

TLR7/8/9-targeting compounds in clinical development					
TLRs	**Agonists**	**Antagonists**	**Structure**	**Target disease or treatment**	**Clinical trial if available**
TLR7	CAN1012		/	Solid tumors	NCT05580991
	Imiquimod		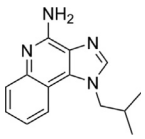	Human papillomavirus (HPV)-associated carcinoma	NCT06686043 NCT06252857
				Basal cell carcinoma	NCT05838599
				Mycosis fungoides	
TLR8	TQA3810		/	Chronic hepatitis B	NCT06566248
	Selgantolimod		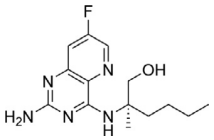	Chronic hepatitis B	NCT05551273
TLR7/8		M5049 (enpatoran)	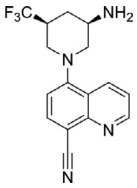	SLE	NCT05540327
				Idiopathic inflammatory myopathies (IIM)	NCT05650567
		BMS-986256 (afimetoran)	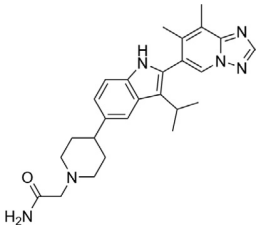	SLE	NCT04895696
		E6742	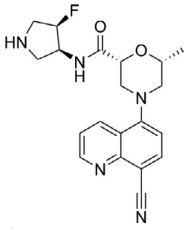	SLE	NCT05278663
	3M-052-AF		/	Vaccine adjuvant	NCT06613789
	EIK1001		/	Solid tumors	NCT06246110
				Advanced melanoma	NCT06697301
	STM-416p (resiquimod)		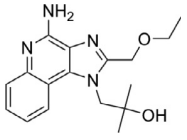	Prostatectomy	NCT06450106
TLR9	SD-101 (nelitolimod)		/	Hepatocellular carcinoma	NCT06710223
	IMO-2125 (tilsotolimod)		/	Malignant melanoma	NCT04126876

design of TLR7-selective ligands by preventing RNase-mediated cleavage that would otherwise generate TLR8-activating uridine monomers.[p50] An approach that also leverages the structural information of the TLR9 receptor for the development of TLR9 agonists consists in the design of DNA nanostructures, which are able to target the CpG motif binding site and the 5′-xCx DNA binding site.[p51]

Rational design of MydD88-dependent endosomal TLR antagonists for autoimmune disease

Significant advances have been made in small-molecule antagonists that inhibit MyD88-dependent endosomal TLRs. One strategy targets a hydrophobic pocket at the TLR dimer interface – a site that is accessible in the resting state and adjacent to the

agonist-binding cleft. For instance, the TLR8-selective antagonist CU-CPT8m was discovered to bind a hydrophobic pocket on the TLR8 dimer interface, locking the receptor in its preactivated state. Co-crystal structures showed CU-CPT8m occupies a cavity present only in the resting dimer, thereby preventing the conformational rearrangements needed for signaling.[p12] Similarly, a new class of isoxazole-based TLR8 antagonists was recently discovered (Table 1).[p39] *In silico* analysis revealed interactions of compound 10[[p39]] with the TLR8 dimer interface, stabilizing an inactive conformation and blocking receptor activation. The dual TLR7/8 antagonist E6742 binds non-covalently in a pocket at the interface of the TLR7 and TLR8 ectodomains, effectively 'freezing' the receptors in an inactive dimer orientation.[p52] E6742 potently suppresses TLR7/8-mediated cytokine release in human immune cells and markedly ameliorated lupus-like disease in mice, underscoring the therapeutic potential of interface-binding antagonists. Furthermore, a new imidazoloquinoline has been reported as a potent TLR7/8 antagonist, successfully reducing psoriasis-like skin inflammation in mice.[p38]

An alternative antagonist design is to modify known agonist scaffolds into competitive antagonists. Such findings outline the importance of TLR conformational dynamics, because an antagonist can bind without immediately altering the ectodomain arrangement, yet still shifts the equilibrium toward an inhibited state. Exploiting this, drug designers created numerous heterocyclic TLR7 antagonists (Table 1) that compete at the ligand-binding site but prevent the conformational changes needed for signaling.[p35] Another important aspect of the drug therapy is the lack or presence of a charge in the TLR modulators, which has effects on their unbinding and permeability. One emerging compound, D2469079A, exemplifies the importance of membrane permeability in TLR-targeted drug design, displaying selective TLR7/8 antagonism alongside strong brain penetration.[p53]

The antagonist landscape for TLR9 has also expanded, although direct structural evidence of small molecules binding TLR9 is still emerging. Antimalarials like chloroquine have long been known to suppress endosomal TLR activation, and structure–function studies indicate chloroquine selectively antagonizes TLR9 by physically blocking the TLR9–DNA interaction, potentially through intercalation or obscurity of the CpG DNA ligand.[p54] This inspired the synthesis of TLR9 antagonists like CPG-52364, a quinazoline, and related derivates, improving potency and selectivity over chloroquine.[p35] Further optimization led to dihydropyrrolo[2,3-d]pyrimidine compounds that are nanomolar TLR9 antagonists (Table 1).[p37] Recently, a new benzimidazole structure was filed for patent,[p55] and another potent and selective quinoline-based TLR9 antagonist was discovered through a constructed homology model.[p44] Notably, several antagonists targeting TLR9 (and dual targeting TLR7/9) do not measurably bind DNA, implying they probably engage the receptor directly.[p56] This suggests that, analogous to TLR7/8, small-molecule TLR9 antagonists can occupy the internal ligand-binding pocket or an allosteric site to prevent activation.

Advances in scaffold design have led to new dual TLR7/8 antagonists, such as a benzimidazole-aryl ether hybrid with improved selectivity and pharmacokinetics.[p36] Indole-based dual antagonists like BMS-986256 (afimetoran), which features an indole scaffold with multiple heterocyclic substituents to simultaneously block TLR7/8, was shown to reverse autoimmune pathology in lupus-prone mice by shutting down TLR7/8-driven inflammation and has entered clinical trial for lupus.[p35] Similarly, a 2-phenylindole-piperidine (Table 1) series yielded compound 7f, a potent TLR7/8 antagonist with favorable pharmacokinetics[[p57]]. A co-crystal structure of 7f bound to TLR8 confirmed it stabilizes an 'apo-like' inactive conformation, consistent with the mechanism of interface-binding antagonists, therefore showing efficacy in rodent models of psoriasis and lupus.[p58] A recent study reported the structure-based design of novel reversible covalent dual TLR2/9 antagonists derived from salicylaldehyde fragments. These compounds target conserved lysine residues within the TIR domain via imine-bond formation, representing a non-DNA-binding mechanism of inhibition.[p59] Novel small-molecule TLR7/9 inhibitors were recently developed and demonstrated *in vivo* efficacy in preclinical mouse models of psoriasis and lupus.[p43]

Endogenous regulation of TLR7/8 activation has gained attention as a mechanism to prevent autoimmunity. A recent study identified 2′-O-methyl-guanosine-containing 3-mer RNA fragments as natural TLR7/8 antagonists. These short, modified RNAs bind a distinct inhibitory site on the receptors and effectively block ligand-induced signaling without triggering cytokine release. Importantly, patient-derived mutations in TLR7 or TLR8 can disrupt this antagonistic mechanism, linking defective endogenous inhibition to hyperinflammatory and autoimmune phenotypes.[p60]

Lately, more-advanced clinical candidates have emerged, such as enpatoran (M5049), an oral dual TLR7/8 antagonist, which demonstrated significant efficacy in reducing cutaneous lupus erythematosus symptoms and IFN signatures in a Phase II trial, prompting further exploration in systemic autoimmune conditions (Table 2). By contrast, another selective TLR7/8 antagonist, MHV-370, was terminated in Phase II (NCT04988087) owing to administrative reasons rather than safety or efficacy concerns.

Overcoming translational barriers in TLR7/8/9 therapeutics

Despite substantial advancements in the structure-guided drug discovery and clinical development of MyD88-dependent endosomal TLRs modulators, several crucial challenges continue to impede therapeutic progress. Achieving high target specificity without triggering excessive systemic immune activation or suppression remains a significant obstacle, exacerbated by the structural similarities between agonists and antagonists. This similarity complicates rational drug design, necessitating highly detailed structural insights and meticulous chemical optimization.

A persistent hurdle is the absence of a functional murine model for TLR8, largely attributed to pronounced species-specific differences.[p1],[p3] Human TLR8 robustly responds to ssRNA and synthetic ligands, whereas mouse TLR8 is essentially inactive owing to structural divergence. This species-specific difference significantly complicates preclinical studies, often requiring alternative models to reliably predict human responses.

Clinically, TLR7/8/9 modulators frequently face challenges related to insufficient selectivity, unfavorable pharmacokinetics and pronounced immune-related toxicities, including cytokine release syndromes and systemic inflammation. This complexity is further heightened by the inherent context-dependence of TLR signaling, which varies substantially by cell type, anatomical site and disease stage, complicating clinical trial design and patient stratification. Consequently, a high attrition rate in clinical trials persists, despite initial encouraging preclinical results. For example, the broad-spectrum antagonist CPG-52364 demonstrated promising early-stage target engagement but was discontinued after a Phase I lupus trial.[p35] Similarly, TLR9 agonist IMO-2055 was halted owing to unacceptable adverse effects.[p24] Even innovative delivery systems, such as HER2-targeted TLR7 agonist conjugates, have encountered setbacks owing to dose-limiting toxicities including cytokine storms and neuroinflammation.[p61] Furthermore, structure-based drug discovery for TLR9 remains limited by the absence of resolved human receptor structures. Current efforts predominantly rely on homology modeling derived from available bovine, equine or primate receptor structures, which points to an urgent need for improved structural data to facilitate rational ligand design.

Concluding remarks and future perspectives

The therapeutic potential of endosomal TLR modulation remains significant, with potential applications in oncology, autoimmune diseases and infectious disease management. To achieve this potential, future research must present advancing delivery strategies such as antibody–drug conjugates and nanoparticle-based formulations, enhancing tissue-specific targeting and minimizing off-target effects. Combining TLR modulators with immune checkpoint inhibitors or traditional immunotherapies holds promise to amplify therapeutic efficacy further. Detailed mechanistic studies on endosomal trafficking, receptor regulation and context-specific signaling will be essential to inform rational therapeutic design and precise patient stratification. Notably, recent findings highlight that double knockout of TASL and TASL2 impairs antiviral immunity while offering protection from lupus-like disease in mouse models, underscoring their therapeutic relevance.[p20]

Furthermore, novel endogenous TLR ligands and their cellular regulators have been identified. For example, natural 2′-O-methylated RNA fragments act as TLR7/8 antagonists,[p60] whereas pseudouridine-modified RNA, widely used in mRNA therapeutics, avoids immune detection by TLR7/8,[p62] offering potential templates for next-generation drug design. Trafficking regulators such as UNC93B1, through its YxxΦ motif, and signaling adaptors like TASL and SLC15A4 have been proposed as new targets to modulate receptor localization and downstream signaling selectively.[p63],[p64]

Emerging insights into TLR8 biology suggest it plays a unique part in sensing endogenously derived ssRNA during tissue damage and viral infection. These studies point to cell-type-specific expression patterns and a potential role in chronic inflammation and autoimmunity, emphasizing the need for selective modulation strategies.[p65],[p66] Structural advancements have illuminated crucial insights into TLR7/8/9 pathways, particularly revealing novel allosteric and hydrophobic pockets at receptor dimer interfaces. Concurrently, significant progress in ligand optimization and delivery technologies is overcoming previous barriers: chemically optimized TLR7/8 antagonists are now entering advanced clinical trials with improved selectivity and safety profiles (Table 2), whereas engineered oligonucleotide agonists delivered via nanoparticles demonstrate enhanced local immune responses without systemic toxicity.[p49]

Clinically, biomarker-driven patient selection and targeted delivery systems are becoming integral to maximizing therapeutic outcomes. TLR agonists combined with checkpoint inhibitors have begun converting immunologically ‘cold’ tumors into ‘hot’ ones, showing objective responses even in PD-1-resistant cancers during early-phase trials.[p24] Similarly, TLR7/8/9 agonists continue to serve effectively as adjuvants in vaccines and antiviral strategies (Table 2).[p67] In the future, the precise and targeted application of TLR modulators will be essential. Armed with deeper mechanistic understanding, structural insights and clinical learnings, researchers are well-positioned to overcome existing hurdles and unlock the full therapeutic potential of TLR7/8/9-targeted therapies, significantly advancing their utility across oncology, autoimmune and infectious diseases.

Conflicts of interest

We have no conflicts of interest to disclose. All the authors comply with ethical policies regarding conflicts of interest, informed consent and the ethical treatment of humans and animals in research.

Declaration of generative AI and AI-assisted technologies in the writing process

During the preparation of this work, the authors used ChatGPT to correct or edit already written text. After using this tool, the authors reviewed and edited the content as needed and take full responsibility for the content of the published article.

Acknowledgments

We apologize to colleagues whose work could not be included due to space limits.

Author contributions

T.M. and **V.T.** contributed equally to this work. **T.M.**, **V.T.**, **G. Wobler** and **G. Weindl** conceived the topic, designed the main idea and wrote the manuscript. All authors have given approval to the final version of the manuscript.

Data availability

No data was used for the research described in the article.

References

1. Kawai T, Ikegawa M, Ori D, Akira S. Decoding Toll-like receptors: recent insights and perspectives in innate immunity. *Immunity*. 2024;57:649–673. https://doi.org/10.1016/j.immuni.2024.03.004.
2. Fitzgerald KA, Kagan JC. Toll-like receptors and the control of immunity. *Cell*. 2020;180:1044–1066. https://doi.org/10.1016/j.cell.2020.02.041.
3. Lind NA, Rael VE, Pestal K, Liu B, Barton GM. Regulation of the nucleic acid-sensing Toll-like receptors. *Nat Rev Immunol*. 2022;22:224–235. https://doi.org/10.1038/s41577-021-00577-0.
4. McWhirter SM, Jefferies CA. Nucleic acid sensors as therapeutic targets for human disease. *Immunity*. 2020;53:78–97. https://doi.org/10.1016/j.immuni.2020.04.004.
5. Hsieh ML, Nishizaki D, Adashek JJ, Kato S, Kurzrock R. Toll-like receptor 3: a double-edged sword. *Biomark Res*. 2025;13. https://doi.org/10.1186/s40364-025-00739-5.
6. Botos I, Segal DM, Davies DR. The structural biology of toll-like receptors. *Structure*. 2011;19:447–459. https://doi.org/10.1016/j.str.2011.02.004.
7. Latz E et al. Ligand-induced conformational changes allosterically activate Toll-like receptor 9. *Nat Immunol*. 2007;8:772–779. https://doi.org/10.1038/ni1479.
8. Tanji H, Ohto U, Shibata T, Miyake K, Shimizu T. Structural reorganization of the toll-like receptor 8 dimer induced by agonistic ligands. *Science*. 2013;339:1426–1429. https://doi.org/10.1126/science.1229159.
9. Ishida H et al. Cryo-EM structures of Toll-like receptors in complex with UNC93B1. *Nat Struct Mol Biol*. 2021;28:173–180. https://doi.org/10.1038/s41594-020-00542-w.
10. Zhang Z et al. Structural analysis reveals that toll-like receptor 7 is a dual receptor for guanosine and single-stranded RNA. *Immunity*. 2016;45:737–748. https://doi.org/10.1016/j.immuni.2016.09.011.
11. Tojo S et al. Structural analysis reveals TLR7 dynamics underlying antagonism. *Nat Commun*. 2020;11:5204. https://doi.org/10.1038/s41467-020-19025-z.
12. Zhang S et al. Small-molecule inhibition of TLR8 through stabilization of its resting state. *Nat Chem Biol*. 2018;14:58–64. https://doi.org/10.1038/nchembio.2518.
13. Talagayev V, Wolber G, Nunes-Alves A. Agonists and antagonists show different unbinding paths from the TLR8 receptor. *J Chem Inf Model*. 2025. https://doi.org/10.1021/acs.jcim.5c00496.
14. Tanji H et al. Toll-like receptor 8 senses degradation products of single-stranded RNA. *Nat Struct Mol Biol*. 2015;22:109–115. https://doi.org/10.1038/nsmb.2943.
15. Ohto U, Ishida H, Shibata T, Sato R, Miyake K, Shimizu T. Toll-like receptor 9 contains two DNA binding sites that function cooperatively to promote receptor dimerization and activation. *Immunity*. 2018;48:649–658.e4. https://doi.org/10.1016/j.immuni.2018.03.013.
16. Ohto U et al. Structural basis of CpG and inhibitory DNA recognition by Toll-like receptor 9. *Nature*. 2015;520:702–705. https://doi.org/10.1038/nature14138.
17. Fisch D et al. Molecular definition of the endogenous Toll-like receptor signalling pathways. *Nature*. 2024;631:635–644. https://doi.org/10.1038/s41586-024-07614-7.
18. Lau L et al. An essential role for TASL in mouse autoimmune pathogenesis and Toll-like receptor signaling. *Nat Commun*. 2025;16:968. https://doi.org/10.1038/s41467-024-55690-0.
19. Stocks CJ, Li X, Stow JL. New advances in innate immune endosomal trafficking. *Curr Opin Cell Biol*. 2024;89, 102395. https://doi.org/10.1016/j.ceb.2024.102395.
20. Drobek A et al. The TLR7/9 adaptors TASL and TASL2 mediate IRF5-dependent antiviral responses and autoimmunity in mouse. *Nat Commun*. 2025;16:967. https://doi.org/10.1038/s41467-024-55692-y.
21. Boeszoermenyi A et al. A conformation-locking inhibitor of SLC15A4 with TASL proteostatic anti-inflammatory activity. *Nat Commun*. 2023;14:6626. https://doi.org/10.1038/s41467-023-42070-3.
22. Chakraborty S et al. Application of toll-like receptors (TLRs) and their agonists in cancer vaccines and immunotherapy. *Front Immunol*. 2023;14, 1227833. https://doi.org/10.3389/fimmu.2023.1227833.
23. Scheiermann J, Klinman DM. Clinical evaluation of CpG oligonucleotides as adjuvants for vaccines targeting infectious diseases and cancer. *Vaccine*. 2014;32:6377–6389. https://doi.org/10.1016/j.vaccine.2014.06.065.
24. Rolfo C, Giovannetti E, Martinez P, McCue S, Naing A. Applications and clinical trial landscape using Toll-like receptor agonists to reduce the toll of cancer. *npj Precis Oncol*. 2023;7:26. https://doi.org/10.1038/s41698-023-00364-1.
25. Kayesh MEH, Kohara M, Tsukiyama-Kohara K. TLR agonists as vaccine adjuvants in the prevention of viral infections: an overview. *Front Microbiol*. 2023;14, 1249718. https://doi.org/10.3389/fmicb.2023.1249718.
26. Wen L et al. Toll-like receptors 7 and 9 regulate the proliferation and differentiation of B cells in systemic lupus erythematosus. *Front Immunol*. 2023;14, 1093208. https://doi.org/10.3389/fimmu.2023.1093208.
27. Hawtin S et al. Preclinical characterization of the Toll-like receptor 7/8 antagonist MHV370 for lupus therapy. *Cell Rep Med*. 2023;4, 101036. https://doi.org/10.1016/j.xcrm.2023.101036.
28. Klopp-Schulze L et al. Asia-inclusive global development of enpatoran: results of an ethno-bridging study, intrinsic/extrinsic factor assessments and disease trajectory modeling to inform design of a phase II multiregional clinical trial. *Clin Pharmacol Ther*. 2024;115:1346–1357. https://doi.org/10.1002/cpt.3216.
29. Fillatreau S, Manfroi B, Dörner T. Toll-like receptor signalling in B cells during systemic lupus erythematosus. *Nat Rev Rheumatol*. 2021;17:98–108. https://doi.org/10.1038/s41584-020-00544-4.
30. DeYoung EG et al. Synthesis and optimization of 1-substituted imidazo[4,5-*c*]quinoline TLR7 agonists. *ACS Med Chem Lett*. 2023;14:1358–1368. https://doi.org/10.1021/acsmedchemlett.3c00260.
31. Avoni A et al. Synthesis and immunopharmacological evaluation of novel TLR7 agonistic triazole tethered imidazoquinolines. *RSC Adv*. 2023;13:1066–1077. https://doi.org/10.1039/D2RA06395F.
32. Kaushik D et al. Structure–activity relationships toward the identification of a high-potency selective human toll-like receptor-7 agonist. *J Med Chem*. 2024;67:8346–8360. https://doi.org/10.1021/acs.jmedchem.4c00464.
33. Brant MG et al. Generation and structure-activity relationships of novel imidazo-thienopyridine based TLR7 agonists: application as payloads for immunostimulatory antibody drug-conjugates. *Bioorg Med Chem Lett*. 2023;91, 129348. https://doi.org/10.1016/j.bmcl.2023.129348.
34. Tsukidate T, Hespen CW, Hang HC. Small molecule modulators of immune pattern recognition receptors. *RSC Chem Biol*. 2023;4:1014–1036. https://doi.org/10.1039/D3CB00096F.
35. Zheng H, Wu P, Bonnet P-A. Recent advances on small-molecule antagonists targeting TLR7. *Molecules*. 2023;28:634. https://doi.org/10.3390/molecules28020634.
36. Talukdar A, Ganguly D, Roy S, Das N, Sarkar D. Structural evolution and translational potential for agonists and antagonists of endosomal toll-like receptors. *J Med Chem*. 2021;64:8010–8041. https://doi.org/10.1021/acs.jmedchem.1c00300.
37. Watanabe M et al. Dihydropyrrolo[2,3-*d*]pyrimidines: selective toll-like receptor 9 antagonists from scaffold morphing efforts. *ACS Med Chem Lett*. 2014;5:1235–1239. https://doi.org/10.1021/ml5003184.
38. Wu P, Fu Q, Zhou S, Huang L, Cheng K, Chen Z. Structure-based rational design of TLR7/8 antagonists through agonist scaffold reengineering for psoriasis therapy. *Eur J Med Chem*. 2025;299, 118063. https://doi.org/10.1016/j.ejmech.2025.118063.
39. Matziol T et al. Discovery of novel isoxazole-based small-molecule toll-like receptor 8 antagonists. *J Med Chem*. 2025;68:4888–4907. https://doi.org/10.1021/acs.jmedchem.4c03148.
40. Strašek Benedik N, Dolšak A, Švajger U, Sosič I, Gobec S, Sova M. Structural optimization and biological evaluation of isoxazolo[5,4-*d*]pyrimidines as selective toll-like receptor 7 agonists. *ACS Omega*. 2024;9:2362–2382. https://doi.org/10.1021/acsomega.3c06343.
41. Patinote C et al. Agonist and antagonist ligands of toll-like receptors 7 and 8: Ingenious tools for therapeutic purposes. *Eur J Med Chem*. 2020;193, 112238. https://doi.org/10.1016/j.ejmech.2020.112238.
42. Benedik NS et al. Optimization of 6-(trifluoromethyl)pyrimidine derivatives as TLR8 antagonists. *Acta Pharm*. 2025;75:159–183. https://doi.org/10.2478/acph-2025-0011.
43. Jeong U et al. Discovery of ETI41 and ETI60: novel selective endosomal Toll-like receptor inhibitors for the treatment of autoimmune diseases. *Exp Mol Med*. 2025. https://doi.org/10.1038/s12276-025-01526-w.
44. Song X, Feng C-G, Wang C, Cheng J, Lin G-Q. Discovery of potent and selective quinoline-based toll-like receptor 9 antagonists. *ACS Med Chem Lett*. 2025;16:1747–1755. https://doi.org/10.1021/acsmedchemlett.5c00248.
45. Zhang Z et al. Structural analyses of toll-like receptor 7 reveal detailed RNA sequence specificity and recognition mechanism of agonistic ligands. *Cell Rep*. 2018;25:3371–3381.e5. https://doi.org/10.1016/j.celrep.2018.11.081.
46. Patel AM et al. Design and optimization of selectivity-tunable toll-like receptor 7/8 agonists as novel antibody–drug conjugate payloads. *J Med Chem*. 2024;67:15756–15779. https://doi.org/10.1021/acs.jmedchem.4c01384.

47. Poudel YB et al. Structure-based design of novel TLR7/8 agonist payloads enabling an immunomodulatory conjugate approach. *ACS Med Chem Lett*. 2025;16:80–88. https://doi.org/10.1021/acsmedchemlett.4c00463.
48. Yamazoe S et al. Discovery and characterization of a first-in-class LIV1-TLR7/8 immunomodulatory conjugate with robust myeloid activation and antitumor activity. *J Med Chem*. 2025;68:11322–11339. https://doi.org/10.1021/acs.jmedchem.5c00264.
49. Zhang Y et al. PPS-TLR7/8 agonist nanoparticles equip robust anticancer immunity by selectively prolonged activation of dendritic cells. *Biomaterials*. 2025;316, 123032. https://doi.org/10.1016/j.biomaterials.2024.123032.
50. Tong A-J et al. Nucleotide modifications enable rational design of TLR7-selective ligands by blocking RNase cleavage. *J Exp Med*. 2024;221, e20230341. https://doi.org/10.1084/jem.20230341.
51. C. Chen, C. Tian, Z. Jin, Y. Wen, C.Z. Huang and H. Zuo, Rational Design of DNA nanostructures as TLR9 Agonists, Biomacromolecules, 2025, https://doi.org/10.1021/acs.biomac.5c00919.
52. Ishizaka ST et al. A novel Toll-like receptor 7/8–specific antagonist E6742 ameliorates clinically relevant disease parameters in murine models of lupus. *Eur J Pharmacol*. 2023;957, 175962. https://doi.org/10.1016/j.ejphar.2023.175962.
53. Deng X et al. Discovery of D2469079A, A novel selective toll-like receptor 7/8 antagonist with brain penetrance 2025.04.12.648517. *bioRxiv*. 2025. https://doi.org/10.1101/2025.04.12.648517.
54. Chandler L, Yusuf I, McClements M, Barnard A, MacLaren R, Xue K. Immunomodulatory effects of hydroxychloroquine and chloroquine in viral infections and their potential application in retinal gene therapy. *Int J Mol Sci*. 2020;21:4972. https://doi.org/10.3390/ijms21144972.
55. Sabnis RW. Novel substituted benzimidazole compounds as TLR9 inhibitors for treating fibrotic diseases, particularly idiopathic pulmonary fibrosis. *ACS Med Chem Lett*. 2024;15:1804–1805. https://doi.org/10.1021/acsmedchemlett.4c00473.
56. Haseeb M et al. Discovery of novel small molecule dual inhibitor targeting toll-like receptors 7 and 9. *J Chem Inf Model*. 2024;64:5090–5107. https://doi.org/10.1021/acs.jcim.4c00578.
57. Mussari CP et al. Discovery of Potent and Orally Bioavailable Small Molecule Antagonists of Toll-like Receptors 7/8/9 (TLR7/8/9). *ACS Med Chem Lett*. 2020;11. https://doi.org/10.1021/acsmedchemlett.0c00264.
58. Sreekantha RK et al. Identification of 2-pyridinylindole-based dual antagonists of toll-like receptors 7 and 8 (TLR7/8). *ACS Med Chem Lett*. 2022;13:812–818. https://doi.org/10.1021/acsmedchemlett.2c00049.
59. Natala SR et al. Structure based design, synthesis and identification of novel covalent reversible dual TLR2/TLR9 small molecule antagonists. *Bioorg Med Chem Lett*. 2025;124, 130259. https://doi.org/10.1016/j.bmcl.2025.130259.
60. Alharbi AS et al. 2′-O-Methyl-guanosine 3-base RNA fragments mediate essential natural TLR7/8 antagonism. *bioRxiv*. 2024. https://doi.org/10.1101/2024.07.25.605091.
61. Janku F et al. Preclinical characterization and phase I study of an anti–HER2-TLR7 immune-stimulator antibody conjugate in patients with HER2+ malignancies. *Cancer Immunol Res*. 2022;10:1441–1461. https://doi.org/10.1158/2326-6066.cir-21-0722.
62. Bérouti M et al. Pseudouridine RNA avoids immune detection through impaired endolysosomal processing and TLR engagement. *Cell*. 2025. https://doi.org/10.1016/j.cell.2025.05.032.
63. Zhang H et al. SLC15A4 controls endolysosomal TLR7–9 responses by recruiting the innate immune adaptor TASL. *Cell Rep*. 2023;42, 112916. https://doi.org/10.1016/j.celrep.2023.112916.
64. Rael VE et al. Large-scale mutational analysis identifies UNC93B1 variants that drive TLR-mediated autoimmunity in mice and humans. *J Exp Med*. 2024;221. https://doi.org/10.1084/jem.20232005.
65. Schmidt A et al. Toll-like receptor 8 activation induces a neutrophil inflammatory phenotype: therapeutic implications for the utility of toll-like receptor 8 inhibition. *J Leukoc Biol*. 2025;117, qiaf036. https://doi.org/10.1093/jleuko/qiaf036.
66. Maserumule C et al. Phagosomal RNA sensing through TLR8 controls susceptibility to tuberculosis, *Cell Rep*, 44, 2025, https://doi.org/10.1016/j.celrep.2025.115657.
67. Zhao T et al. Vaccine adjuvants: mechanisms and platforms. *Signal Transduct Target Ther*. 2023;8. https://doi.org/10.1038/s41392-023-01557-7.

Appendix II. Publication II: Optimization of 6-(trifluoromethyl)pyrimidine derivatives as TLR8 antagonists

The following pages include the article “Optimization of 6-(trifluoromethyl)pyrimidine derivatives as TLR8 antagonists” as it was published in Acta Pharmaceutica by De Gruyter.

Reprinted with permission from:

Nika Strašek Benedik, Valerij Talagayev, Troy Matziol, Ana Dolšak, Izidor Sosič, Günther Weindl, Gerhard Wolber, Matej Sova. Optimization of 6-(trifluoromethyl)pyrimidine derivatives as TLR8 antagonists. Acta Pharm. 2025;75(2):159–183.

Doi: 10.2478/acph-2025-0011

sciendo

HRVATSKO FARMACEUTSKO DRUŠTVO
CROATIAN PHARMACEUTICAL SOCIETY

Acta Pharm. **75** (2025) 159–183
https://doi.org/10.2478/acph-2025-0011

Original research paper

Optimization of 6-(trifluoromethyl)pyrimidine derivatives as TLR8 antagonists

NIKA STRAŠEK BENEDIK[1,a]
VALERIJ TALAGAYEV[2,a]
TROY MATZIOL[3]
ANA DOLŠAK[1]
IZIDOR SOSIČ[1]
GÜNTHER WEINDL[3,*]
GERHARD WOLBER[2,*]
MATEJ SOVA[1,*]

[1] *University of Ljubljana, Faculty of Pharmacy, Department of Pharmaceutical Chemistry, 1000 Ljubljana, Slovenia*

[2] *Freie Universität Berlin, Institute of Pharmacy, Pharmaceutical and Medicinal Chemistry, 14195 Berlin, Germany*

[3] *University of Bonn, Pharmaceutical Institute, Pharmacology and Toxicology Section, 53121 Bonn, Germany*

Accepted March 28, 2025
Published online March 28, 2025

ABSTRACT

Toll-like receptors (TLRs) are essential for the innate immune system as they recognize pathogen-associated molecular patterns and trigger immune responses. Overactivation of TLR8 by endogenous nucleic acids is associated with the development of autoimmune diseases and promotes inflammatory responses. This study presents the design, synthesis, and evaluation of a series of TLR8 antagonists based on the optimization of previously reported 6-(trifluoromethyl)pyrimidin-2-amines, with targeted modifications to further explore structure-activity relationships (SAR) and increase potency. A two-step synthesis involving nucleophilic aromatic substitution and Suzuki coupling was used to prepare two series of new compounds. The biological evaluation revealed that compounds **14** and **26** exhibited promising TLR8 antagonistic activity with IC_{50} values of 6.5 and 8.7 μmol L^{-1}, respectively. Compound **14** showed reduced cell viability at higher concentrations, while compound **26** showed no cytotoxic effects, making it a promising candidate for further investigation.

Keywords: Toll-like receptors, TLR8 antagonists, autoimmune disorders, immunomodulation, pyrimidines

INTRODUCTION

Toll-like receptors (TLRs) are an important component of the innate immune system, responsible for the recognition of pathogen-associated molecular patterns (PAMPs) derived from bacteria, viruses, fungi, and parasites (1). This recognition process is crucial for initiating the body's immune defense mechanisms against infections and contributes to the regulation of inflammatory responses. In humans, ten different TLRs (TLR1-TLR10) have been identified, which are either expressed on the cell surface, where they recognize microbial membrane components such as lipoproteins and lipopolysaccharides, or within intracellular endosomes, where they primarily recognize nucleic acids derived from viruses and other intracellular pathogens (1–3). Among these, TLR7 and TLR8 have received considerable attention due to their involvement in several disease pathologies (4–8). Overactivation of

* Correspondence; e-mail: matej.sova@ffa.uni-lj.si, gerhard.wolber@fu-berlin.de, guenther.weindl@uni-bonn.de
[a] These authors contributed equally.

these receptors by endogenous nucleic acids has been associated with autoimmune disorders such as systemic lupus erythematosus, psoriasis, and rheumatoid arthritis (5, 9, 11). In particular, activation of TLR8 has been associated with the promotion of pro-inflammatory responses that not only exacerbate autoimmune conditions but also facilitate the replication and persistence of viruses such as human immunodeficiency virus type 1 (HIV-1), making it an important target for therapeutic intervention (12, 13).

Given the significant role of TLR8 in both immune regulation and disease progression, the development of selective small-molecule inhibitors has become an area of growing interest. Over the past decade, we and others have reported several chemotypes of TLR8 antagonists, including 5-indazol-5-yl pyridines (14), 3-arylpyrazolopyrimidin-6-amines (15), 2-phenyl-indole-5-piperidines (16), and benzylbenzothiazoles (17). Despite these advancements, only a limited number of TLR8-selective small-molecule antagonists have been developed to date. Furthermore, achieving favorable pharmacokinetic properties and minimizing potential off-target effects are critical hurdles that need to be addressed in the design of next-generation TLR8 modulators.

In this study, we present the design, synthesis, and biological evaluation of a novel series of TLR8 antagonists that show low micromolar potency. Building on our previous research (18, 19), we investigated SAR of 6-(trifluoromethyl)pyrimidin-2-amine-based TLR8 antagonists by introducing modifications at two key positions of the core structure, which were selected from MD simulations.

EXPERIMENTAL

Chemistry

Reagents and solvents for the synthesis were purchased from commercial sources (BLD Pharmatech, Enamine, Apollo Scientific, TCI, Sigma-Aldrich, Merck) and used for the reactions without further purification. Compounds **1** and **6** were purchased from BLD Pharmatech and used without further purification. Reaction progress was monitored *via* thin-layer chromatography (TLC) using silica-gel plates (Merck DC Fertigplatten Kieselgel 60 GF254), visualized under UV light, or stained with appropriate reagents. Flash column chromatography was carried out on silica gel 60 (70–230 mesh, Merck). ^{1}H and ^{13}C{^{1}H} NMR spectra were recorded at 295 K in DMSO-d_6 using an Advance III NMR spectrometer (Bruker, USA) with a decoupling inverse ^{1}H probe (Broadband). The coupling constants (J) are given in Hz, with splitting patterns indicated as: s (singlet), d (doublet), dd (double doublet), t (triplet), and m (multiplet). LC-MS was performed on Agilent 1260 Infinity II (Agilent Technologies, USA), coupled with Advion Expression CMSL Mass Spectrometer (Advion Inc, USA). High-resolution mass measurements were performed on an Exactive Plus orbitrap mass spectrometer at the Faculty of Pharmacy, University of Ljubljana.

General procedures

General procedure I: Reduction. – The starting reagent (1 eq) was dissolved in anhydrous THF and cooled to 0 °C. $AlCl_3$ (3 eq) and $LiAlH_4$ (2.5–3.5 eq) were added portionwise. The reaction mixture was stirred overnight at room temperature. The next day, the reaction was

quenched by the addition of 10 % citric acid solution and extracted with EtOAc. NaOH (2 mol L^{-1}) was added to the water phase, and the product was extracted with CH_2Cl_2. The organic phase was dried over anhydrous Na_2SO_4, and concentrated under reduced pressure. The product obtained was used for the subsequent reactions without further purification.

General procedure II: Suzuki coupling. – A mixture of boronic acid (1 eq), 4-aryl-2-chloropyrimidine (1.15 eq), K_2CO_3 (2–3 eq), and the catalyst tetrakis(triphenylphosphine)palladium (0.05 eq) was dissolved in a solution of H_2O and dioxane. The reaction mixture was heated to reflux and stirred for 18 hours under an inert atmosphere. After completion of the reaction, the mixture was extracted from H_2O with ethyl acetate. The combined organic layers were washed with brine, dried over anhydrous Na_2SO_4, and concentrated under reduced pressure. The crude product was then purified by flash column chromatography.

General procedure III: Nucleophilic substitution A. – To a solution containing 2,4-dichloro-6-(trifluoromethyl)pyrimidine (**6**) or another suitably substituted 2-chloro-6-(trifluoromethyl) pyrimidine (1 eq) in MeCN, amine (1.5 eq) and K_2CO_3 (2–3 eq) were added. The reaction mixture was stirred for 18 hours at room temperature under an inert atmosphere. After completion of the reaction, the solvent was evaporated under reduced pressure. The product was purified by column chromatography.

General procedure IV: Nucleophilic substitution B. – Amine (2 eq) and 2,4-dichloro-6-(trifluoromethyl)pyrimidine (**6**) or another suitably substituted 2-chloro-6-(trifluoromethyl) pyrimidine (1 eq) were dissolved in MeCN (15 mL) and DMF (7 mL) and Et_3N (2 eq) was added. The reaction mixture was stirred overnight at 82 °C. The next day, EtOAc and H_2O were added, and the phases were separated. The organic phase was washed with brine and dried over Na_2SO_4. The product was purified by column chromatography.

General procedure V: Removal of the Boc protecting group. – A solution of the Boc-protected compound in CH_2Cl_2 (5 mL) was treated with HCl in dioxane (> 30 eq) and the mixture was stirred for 2 h at room temperature. After removal of the volatiles under reduced pressure, the product was extracted from an aqueous solution of $NaHCO_3$ with CH_2Cl_2, dried over anhydrous Na_2SO_4, and concentrated under reduced pressure.

General procedure VI: 2-step synthesis of the final compounds ***24***–***28***. – Amine (2 eq) and suitably substituted 2-chloro-6-(trifluoromethyl)pyrimidine (1 eq) were dissolved in MeCN (15 mL). K_2CO_3 (2 eq) was added and the reaction mixture was stirred overnight at 82 °C. The next day, EtOAc and H_2O were added, and the phases were separated. The organic phase was washed with brine and dried over Na_2SO_4. The crude product obtained was dissolved in 4 mol L^{-1} HCl in dioxane and the mixture was stirred for 2 h at room temperature. After removal of the volatiles under reduced pressure, the product was extracted from the aqueous solution of $NaHCO_3$ with CH_2Cl_2, dried over anhydrous Na_2SO_4, and concentrated under reduced pressure. The product was purified by column chromatography.

Synthetic procedures for the preparation of intermediates

*Synthesis of (4-(2-aminoethyl)phenyl)methanol (***2***).* – Synthesized according to general procedure I with the addition of $AlCl_3$ to the reaction mixture. Prepared from methyl 4-(cyanomethyl)benzoate (**1**) (0.900 g, 5.14 mmol), $AlCl_3$ (2.050 g, 15.4 mmol, 3 eq) and $LiAlH_4$ (0.580 g, 15.4 mmol). Colorless oil. Yield: 52 %.

*Synthesis of (4-(2-aminoethyl)-2-chlorophenyl)methanol (**3**).* – Synthesized according to general procedure I from methyl 2-chloro-4-cyanobenzoate (0.391 g, 2.0 mmol) and $LiAlH_4$ (0.243 g, 6.4 mmol). Orange oil. Yield: 64 %.

*Synthesis of (4-(2-aminoethyl)-2-bromophenyl)methanol (**4**).* – Synthesized according to general procedure I from methyl 2-bromo-4-cyanobenzoate (0.720 g, 3.0 mmol) and $LiAlH_4$ (0.365 g, 9.6 mmol). Yellow oil. Yield: 42 %.

*Synthesis of (4-(2-aminoethyl)-3-fluorophenyl)methanol (**5**).* – Synthesized according to general procedure I from methyl 4-cyano-3-fluorobenzoate (0.538 g, 3.0 mmol) and $LiAlH_4$ (0.365 g, 9.6 mmol). Yellow oil. Yield: 84 %.

*Synthesis of N-benzyl-2-chloro-6-(trifluoromethyl)pyrimidin-4-amine (**7**).* – Synthesized according to general procedure III from 2,4-dichloro-6-(trifluoromethyl)pyrimidine (**6**) (0.620 mL, 4.6 mmol), benzylamine (0.550 mL, 5.0 mmol, 1.1 eq) and K_2CO_3 (1.910 g, 13.8 mmol) at room temperature. The product was purified by column chromatography, using EtOAc/*n*-hexane = 1/4 as the mobile phase. Yellow oil. Yield: 60 %.

Synthesis of (4-(2-((2-chloro-6-(trifluoromethyl)pyrimidin-4-yl)amino)ethyl)phenyl)methanol (**8**). – Synthesized according to general procedure III from 2,4-dichloro-6-(trifluoromethyl) pyrimidine (**6**) (0.180 mL, 1.3 mmol), **2** (0.200 g, 1.3 mmol) and K_2CO_3 (0.448 g, 4.6 mmol) at room temperature. The product was purified by column chromatography, using EtOAc/ *n*-hexane = 1/3 as the mobile phase. Yellow oil. Yield: 22 %.

Synthesis of 4-(2-((2-chloro-6-(trifluoromethyl)pyrimidin-4-yl)amino)ethyl)phenol (**9**). – Synthesized according to general procedure III from 2,4-dichloro-6-(trifluoromethyl)pyrimidine (**6**) (1.050 mL, 7.2 mmol), 4-(2-aminoethyl)phenol (1.000 g, 1.3 mmol) and K_2CO_3 (3.020 g, 21.6 mmol) at room temperature. The product was purified by column chromatography using CH_2Cl_2/MeOH/AcOH = 20/1/0.1 as the mobile phase. Yellow oil. Yield: 47 %.

Synthesis of N-(2-([1,1'-biphenyl]-4-yl)ethyl)-2-chloro-6-(trifluoromethyl)pyrimidin-4-amine (**10**). – Synthesized according to general procedure IV from 2-([1,1'-biphenyl]-4-yl)ethan-1-amine (0.395 g, 2.0 mmol), 2,4-dichloro-6-(trifluoromethyl)pyrimidine (**6**) (0.273 mL, 2.0 mmol) and Et_3N (0.278 mL, 2.0 mmol). The product was purified by column chromatography using (EtOAc/*n*-hexane =1/4) as the mobile phase. White solid. Yield: 50 %.

Synthesis of tert-butyl 2-(4-((4-hydroxyphenethyl)amino)-6-(trifluoromethyl)pyrimidin-2-yl)-1H-pyrrole-1-carboxylate (**15**). – Synthesized according to general procedure II from **9** (0.150 g, 0.47 mmol, 1.1 eq), (1-(*tert*-butoxycarbonyl)-1*H*-pyrrol-3-yl)boronic acid (0.090 g, 0.42 mmol, K_2CO_3 (0.200 g, 1.26 mmol) and $Pd(PPh_3)_4$ (0.024 g, 0.021 mmol, 0.05 eq). The product was purified by column chromatography, using EtOAc/*n*-hexane = 1/2 as the mobile phase. Yellow oil. Yield: 40 %.

Synthesis of tert-butyl (4-((4-(benzylamino)-6-(trifluoromethyl)pyrimidin-2-yl)oxy)benzyl) carbamate (**17**). – Synthesized according to general procedure III from **7** (0.150 g, 0.52 mmol, 1 eq), *tert*-butyl (4-hydroxybenzyl)carbamate (0.200 g, 0.089 mmol, 1.7 eq), and K_2CO_3 (0.216 g, 1.56 mmol, 3 eq) in DMF. The product was purified by column chromatography, using EtOAc/*n*-hexane = 1/2 as the mobile phase. White solid. Yield: 24 %.

Synthesis of tert-butyl 2-(2-chloro-6-(trifluoromethyl)pyrimidin-4-yl)-1H-pyrrole-1-carboxylate (**23**). – Synthesized according to general procedure II from 2,4-dichloro-6-(trifluoromethyl)

pyrimidine (**6**) (0.068 mL, 0.5 mmol), (1-(*tert*-butoxycarbonyl)-1*H*-pyrrol-2-yl)boronic acid (0.106 g, 0.5 mmol), K_2CO_3 (0.207 g, 1.5 mmol) and $Pd(PPh_3)_4$ (0.003 mg, 0.005 mmol). The product was purified by column chromatography, using EtOAc/*n*-hexane = 1/2 as the mobile phase. Yellow oil. Yield: 40 %.

Analytical data of intermediates **2–5**, **7–10**, **15**, **17** and **23** are given in Tables I and II.

Synthetic procedures for preparation of the final compounds

Synthesis of 4-(((4-(benzylamino)-6-(trifluoromethyl)pyrimidin-2-yl)amino)methyl)phenol (**11**). – Synthesized according to general procedure III from **7** (0.250 g, 0.88 mmol), 4-(aminomethyl)phenol (0.110 g, 0.88 mmol) and K_2CO_3 (0.366 g, 2.64 mmol) at 80 °C. The product was purified by column chromatography, using EtOAc/*n*-hexane = 1/4 as the mobile phase. Yellow oil. Yield: 11 %. R_f (EtOAc/*n*-hexane = 1/4) = 0.40.

Synthesis of (4-(2-((4-(benzylamino)-6-(trifluoromethyl)pyrimidin-2-yl)amino)ethyl)phenyl) methanol (**12**). – Synthesized according to general procedure III from **7** (0.380 g, 1.32 mmol), **2** (0.200 g, 1.32 mmol), and K_2CO_3 (0.365 g, 2.64 mmol, 2 eq) at 80 °C. The product was purified by column chromatography, using EtOAc/*n*-hexane = 1/1 as the mobile phase. White solid. Yield: 20 %. R_f (EtOAc/*n*-hexane = 1/1) = 0.45.

Synthesis of (4-(2-((2-phenyl-6-(trifluoromethyl)pyrimidin-4-yl)amino)ethyl)phenyl)methanol (**13**). – Synthesized according to general procedure II from **8** (0.045 g, 0.13 mmol), phenylboronic acid (0.020 g, 0.12 mmol), K_2CO_3 (0.056 g, 0.26 mmol), and $Pd(PPh_3)_4$ (0.010 g, 0.006 mmol). The product was purified by column chromatography, using EtOAc/*n*-hexane = 1/1 as the mobile phase. White solid. Yield: 63 %. R_f (EtOAc/*n*-hexane = 1/1) = 0.30.

Synthesis of 4-(2-((2-phenyl-6-(trifluoromethyl)pyrimidin-4-yl)amino)ethyl)phenol (**14**). – Synthesized according to general procedure II from **9** (0.100 g, 0.31 mmol, 1.1 eq), phenylboronic acid (0.042 g, 0.28 mmol, 1 eq), K_2CO_3 (0.130 g, 0.56 mmol, 2 eq) and $Pd(PPh_3)_4$ (0.016 g, 0.014 mmol, 0.05 eq). The product was purified by column chromatography, using EtOAc/*n*-hexane = 1/2 as the mobile phase. White solid. Yield: 56 %. R_f (EtOAc/*n*-hexane = 1/1) = 0.65.

Synthesis of 4-(2-((2-(1H-pyrrol-2-yl)-6-(trifluoromethyl)pyrimidin-4-yl)amino)ethyl)phenol (**16**). – Synthesized according to general procedure V from **15** (0.090 g, 0.20 mmol, 1 eq) and 4 mol L^{-1} HCl in dioxane (5 mL). Yellow oil. Yield: 64 %. R_f (CH_2Cl_2/MeOH = 9/1) = 0.20.

Synthesis of 2-(4-(aminomethyl)phenoxy)-N-benzyl-6-(trifluoromethyl)pyrimidin-4-amine (**18**). – Synthesized according to general procedure V from **17** (0.050 g, 0.1 mmol, 1 eq) and 4 mol L^{-1} HCl in dioxane (5 mL). Yellow oil. Yield: 97 %. R_f (CH_2Cl_2/MeOH = 9/1) = 0.0.

Synthesis of 4-(2-((4-(benzylamino)-6-(trifluoromethyl)pyrimidin-2-yl)amino)ethyl)phenol (**19**). – Synthesized according to general procedure III from **7** (0.380 g, 1.32 mmol, 1 eq), 4-(2-aminoethyl)phenol (0.200 g, 1.32 mmol, 1 eq) and K_2CO_3 (0.365 g, 2.64 mmol, 2 eq) at 80 °C. The product was purified by column chromatography, using EtOAc/*n*-hexane = 1/1 as the mobile phase. Yellow oil. Yield: 20 %. R_f (EtOAc/*n*-hexane = 1/1) = 0.45.

Synthesis of (4-(2-((2-((4-(hydroxymethyl)benzyl)amino)-6-(trifluoromethyl)pyrimidin-4-yl) amino) ethyl)phenyl)methanol (**20**). – Synthesized according to general procedure IV from **8** (0.150 g, 0.45 mmol), (4-(aminomethyl)phenyl)methanol (0.060 g, 0.45 mmol) and Et_3N

Table I. Analytical data of intermediates ***2****–****5***

Compd.	Chemical name	Molecular formula	M_r	^{1}H NMR (400 MHz, $CDCl_3$): δ (ppm)	R_f value
2	(4-(2-aminoethyl) phenyl)methanol	$C_9H_{13}NO$	151.21	2.74 (t, J = 6.9 Hz, 2H), 2.94 (t, J = 6.9 Hz, 2H), 3.66–3.84 (m, 1H) 4.66 (s, 2H), 7.07–7.20 (m, 2H), 7.26–7.38 (m, 2H); 2H (NH_2) exchanged with H_2O ^{1}H NMR is in accordance with literature (20)	0.0 (EtOAc)
3	(4-(aminomethyl)-2-chlorophenyl) methanol	$C_8H_{10}ClNO$	171.62	3.86 (s, 2H), 4.77 (s, 2H), 7.23 (dd, J_1 = 1.6 Hz, J_2 = 7.7 Hz, 1H), 7.35 (d, J = 1.8 Hz, 1H), 7.44 (d, J = 7.8 Hz, 1H), 3H from OH and NH_2 are exchanged	0.28 (EtOAc/*n*-hexane = 1/1)
4	(4-(aminomethyl)-2-bromophenyl) methanol	$C_8H_{10}BrNO$	216.08	3.85 (s, 2H), 4.73 (s, 2H), 7.31–7.33 (m, 1H), 7.41–7.44 (m, 1H), 7.52–7.54 (m, 1H), 3H from NH_2 and OH are exchanged	0.27 (EtOAc/*n*-hexane = 1/1)
5	(4-(aminomethyl)-3-fluorophenyl) methanol	$C_8H_{10}FNO$	155.17	3.86 (s, 2H), 4.65 (s, 2H), 7.03–7.09 (m, 2H), 7.28–7.33 (m, 1H), 3H from NH_2 and OH are exchanged ^{1}H NMR is in accordance with literature (21)	0.27 (EtOAc/*n*-hexane = 1/1)

Table II. Analytical data of intermediates ***7****–****10****,* ***15****,* ***17*** *and* ***23***

Compd.	Chemical name	Molecular formula	M_r	^{1}H NMR	MS	R_f value
7	*N*-benzyl-2-chloro-6-(trifluoromethyl) pyrimidin-4-amine	$C_{12}H_9ClF_3N_3$	287.67	^{1}H NMR (400 MHz, DMSO-d_6): δ (ppm) 4.58 (d, J = 5.7 Hz, 2H), 6.94 (s, 1H), 7.23 – 7.44 (m, 5H), 8.98 (t, J = 5.8 Hz, 1H)	MS (ESI-): m/z calc. for $C_{12}H_8ClF_3N_3$ $[M\text{-}H]^-$ 286.0, found 285.8. MS (ESI+) m/z calc. for $C_{12}H_9ClF_3N_3$ $[M+H]^+$ 288.0, found 287.9	0.40 (EtOAc/*n*-hexane = 1/4)

Compd.	Chemical name	Molecular formula	M_r	^{1}H NMR	MS	R_f value
8	(4-(2-((2-chloro-6-(trifluoromethyl) pyrimidin-4-yl) amino)ethyl)phenyl) methanol	$C_{14}H_{13}ClF_3N_3O$	331.72	^{1}H NMR (400 MHz, $CDCl_3$): δ (ppm) 2.95 (t, J = 6.7 Hz, 2H), 3.56 (s, 1H), 3.73–3.89 (m, 1H), 4.69 (d, J = 5.8 Hz, 2H), 5.20 (bs, 1H), 5.66 (bs, 1H), 6.48 (s, 1H), 7.21 (d, J = 7.7 Hz, 2H), 7.35 (d, J = 7.9 Hz, 2H)	MS (ESI-): *m/z* calc. for $C_{14}H_{12}ClF_3N_3O$ $[M-H]^-$ 330.1, found 330.0; MS (ESI+) *m/z* calc. for $C_{14}H_{14}ClF_3N_3O$ $[M+H]^+$ 332.1, found 332.1	0.40 (EtOAc/ *n*-hexane = 1/3)
9	4-(2-((2-chloro-6-(trifluoromethyl) pyrimidin-4-yl) amino)ethyl)phenol	$C_{13}H_{11}ClF_3N_3O$	317.70	^{1}H NMR (400 MHz, $CDCl_3$): δ (ppp) 2.87 (t, J = 6.9 Hz, 2H), 3.50 (s, 1H), 3.76 (s, 1H), 5.24 (s, 1H), 6.30–6.54 (m, 1H), 6.80 (d, J = 7.8 Hz, 2H), 7.07 (d, J = 7.8 Hz, 2H), 7.26 (t, J = 1.2 Hz, 1H)	MS (ESI-): *m/z* calc. for $C_{13}H_{10}ClF_3N_3O$ $[M-H]^-$ 316.0, found 315.8; MS (ESI+) *m/z* calc. for $C_{13}H_{12}ClF_3N_3O$ $[M+H]^+$ 318.0, found 317.9	0.30 (CH_2Cl_2/ MeOH/AcOH = 20/1/0.1)
10	*N*-(2-([1,1'-biphenyl]-4-yl)ethyl)-2-chloro-6-(trifluoromethyl) pyrimidin-4-amine	$C_{19}H_{15}ClF_3N_3$	377.80	^{1}H NMR (400 MHz, $CDCl_3$): δ (ppm) 2.99 (t, J = 6.7 Hz, 2H), 3.55–3.90 (m, 2H), 5.17–5.75 (m, 1H), 6.51 (s, 1H), 7.27–7.30 (m, 2H), 7.33–7.38 (m, 1H), 7.42–7.47 (m, 2H), 7.54–7.60 (m, 4H)	MS (ESI-): *m/z* calc. for $C_{19}H_{14}ClF_3N_3$ $[M-H]^-$ 376.1, found 376.2; MS (ESI+) *m/z* calc. for $C_{19}H_{16}ClF_3N_3$ $[M+H]^+$ 378.1, found 378.3	0.18 (EtOAc/*n* -hexane = 1/4)
15	*tert*-butyl 2-(4-((4-hydroxyphenethyl) amino)-6-(trifluoromethyl) pyrimidin-2-yl)-1*H*-pyrrole-1-carboxylate	$C_{22}H_{23}F_3N_4O_3$	448.45	^{1}H NMR (400 MHz, $CDCl_3$): δ (ppm) 1.42 (s, 9H), 2.86 (t, J = 6.8 Hz, 2H), 3.76 – 3.45 (m, 2H), 5.01 (s, 1H), 6.22 (t, J = 3.3 Hz, 1H), 6.45 (s, 1H), 6.71 (s, 1H), 6.76–6.82 (m, 2H), 6.98–7.12 (m, 2H), 7.31 (dd, J = 3.1, 1.7 Hz, 1H); 1H exchanged with H_2O	MS (ESI-): *m/z* calc. for $C_{22}H_{22}F_3N_4O_3$ $[M-H]^-$ 447.2, found 447.1; MS (ESI+) *m/z* calc. for $C_{22}H_{24}F_3N_4O_3$ $[M+H]^+$ 449.2, found 449.1	0.50 (EtOAc/ *n*-hexane = 1/1)
17	*tert*-butyl (4-((4-(benzylamino)-6-(trifluoromethyl) pyrimidin-2-yl)oxy) benzyl)carbamate	$C_{24}H_{25}F_3N_4O_3$	474.48	^{1}H NMR (400 MHz, $CDCl_3$): δ (ppm) 1.45 (s, 9H), 4.32 (bs, 2H), 4.47 (d, J = 5.5 Hz, 2H), 4.97 (bs, 1H), 5.47 (bs, 1H), 6.43 (s, 1H), 7.04–7.20 (m, 4H), 7.24–7.49 (m, 5H)	MS (ESI-): *m/z* calc. for $C_{24}H_{24}F_3N_4O_3$ $[M-H]^-$ 473.2, found 472.9; MS (ESI+) *m/z* calc. for $C_{24}H_{26}F_3N_4O_3$ $[M+H]^+$ 475.2, found 474.9	0.20 (EtOAc/ *n*-hexane = 1/2)
23	*tert*-butyl 2-(2-chloro-6-(trifluoromethyl) pyrimidin-4-yl)-1*H*-pyrrole-1-carboxylate	$C_{14}H_{13}ClF_3N_3O_2$	347.72	^{1}H NMR (400 MHz, $CDCl_3$): δ (ppm) 1.51 (s, 9H), 6.34 (t, J = 3.4 Hz, 1H), 6.90 (dd, J_1 = 1.7 Hz, J_2 = 3.6 Hz, 1H), 7.50 (dd, J_1 = 1.7 Hz, J_2 = 3.2 Hz, 1H), 7.63 (s, 1H)	MS (ESI-): *m/z* calc. for $C_{19}H_{14}ClF_3N_3$ $[M-H]^-$ 346.1, found 346.2; MS (ESI+): *m/z* calc. for $C_{19}H_{16}ClF_3N_3$ $[M+H]^+$ 348.1, found 348.3	0.67 (EtOAc/ *n*-hexane = 1/1)

(0.063 mL, 0.45 mmol). The product was purified by column chromatography, using EtOAc/*n*-hexane = 1/1 as the mobile phase. White solid. Yield: 21 %. R_f = 0.14 (EtOAc/*n*-hexane = 1/1).

Synthesis of (4-(((4-((2-([1,1'-biphenyl]-4-yl)ethyl)amino)-6-(trifluoromethyl)pyrimidin-2-yl) amino)methyl)phenyl)methanol (**21**). – Synthesized according to general procedure IV from **10** (0.289 g, 0.5 mmol), (4-(aminomethyl)phenyl)methanol (0.137 g, 1.0 mmol) and Et_3N (0.140 mL, 0.45 mmol). The product was purified by column chromatography, using EtOAc/*n*-hexane = 1/2 as the mobile phase. Colorless oil. Yield: 46 %.

Synthesis of (4-(2-((2-(furan-2-yl)-6-(trifluoromethyl)pyrimidin-4-yl)amino)ethyl)phenyl) methanol (**22**). – Synthesized according to general procedure II from **8** (0.080 g, 0.24 mmol), 2-furanylboronic acid (0.027 g, 0.24 mmol), K_2CO_3 (0.100 g, 0.72 mmol) and $Pd(PPh_3)_4$ (0.008 g, 0.007 mmol). The product was purified by column chromatography, using EtOAc/*n*-hexane = 1/2 as the mobile phase. Orange oil. Yield: 46 %. R_f = 0.22 (EtOAc/*n*-hexane = 1/2, *V/V).*

Synthesis of (4-(((4-(1H-pyrrol-2-yl)-6-(trifluoromethyl)pyrimidin-2-yl)amino)methyl)-2-chlorophenyl)methanol (**24**). – Synthesized according to general procedure VI from **23** (0.150 g, 0.4 mmol), **3** (0.172 g, 1.00 mmol) and K_2CO_3 (0.165 g, 1.2 mmol). The product was purified by column chromatography, using MTBE/PE= 1/2 as the mobile phase. Pale yellow oil. Yield: 7 %. R_f = 0.20 (MTBE/petroleum ether = 2/1, *V/V*).

Synthesis of (4-(((4-(1H-pyrrol-2-yl)-6-(trifluoromethyl)pyrimidin-2-yl)amino)methyl)-2-bromophenyl)methanol (**25**). – Synthesized according to general procedure VI from **23** (0.174 g, 0.5 mmol), **4** (0.216 g, 1.00 mmol) and K_2CO_3 (0.207 g, 1.5 mmol). The product was purified by column chromatography, using Et_2O as the mobile phase. Yellow solid. Yield: 5 %. R_f = 0.55 (Et_2O).

Synthesis of (4-(((4-(1H-pyrrol-2-yl)-6-(trifluoromethyl)pyrimidin-2-yl)amino)methyl)-3-fluorophenyl)methanol (**26**). – Synthesized according to general procedure VI from **23** (0.174 g, 0.5 mmol), **5** (0.156 g, 1.00 mmol) and K_2CO_3 (0. 207 g, 1.5 mmol). The product was purified by column chromatography, using EtOAc/*n*-hexane = 1/1 as the mobile phase. Orange solid. Yield: 45 %. R_f = 0.31 (EtOAc/*n*-hexane = 1/1).

Synthesis of N-((1H-pyrazol-5-yl)methyl)-4-(1H-pyrrol-2-yl)-6-(trifluoromethyl)pyrimidin-2-amine (**27**). – Synthesized according to general procedure VI from **23** (0.174 g, 0.5 mmol), (1*H*-pyrazol-5-yl)methanamine (0.097 g, 1.00 mmol) and K_2CO_3 (0.207 g, 1.5 mmol). The product was purified by column chromatography, using EtOAc/*n*-hexane = 1/1 as the mobile phase. Pale yellow solid. Yield: 30 %. R_f = 0.16 (DCM/*i*-PrOH=15/1).

Synthesis of (4-(2-((4-(1H-pyrrol-2-yl)-6-(trifluoromethyl)pyrimidin-2-yl)amino)ethyl)phenyl) methanol (**28**). – Synthesized according to general procedure VI from **23** (0.140 g, 0.4 mmol), **2** (0.121 g, 0.8 mmol) and K_2CO_3 (0.165 g, 1.2 mmol). The product was purified by column chromatography, using EtOAc/*n*-hexane = 1/1 as the mobile phase. Yellow oil. Yield: 12 %.

Spectral data of the final compounds are given in Table III.

Table III. Spectral data of final compounds

Compd.	Chemical name	^{1}H NMR	^{13}C{^{1}H} NMR	HRMS
11	4-(((4-(benzylamino)-6-(trifluoromethyl) pyrimidin-2-yl)amino) methyl)phenol	^{1}H NMR (400 MHz, $CDCl_3$): δ (ppm) 4.48 (d, J = 5.8 Hz, 2H), 5.05–5.40 (m, 2H), 5.30 (bs, 1H), 5.70 (s, 1H), 6.05 (s, 1H), 6.73 (d, J = 8.4 Hz, 2H), 7.13 (d, J = 7.8 Hz, 2H), 7.29–7.39 (m, 5H); 1H exchanged with H_2O	^{13}C NMR (101 MHz, DMSO-d_6): δ (ppm) 21.14, 43.29, 114.13, 126.71, 127.85, 128.08, 128.51, 128.62, 129.40, 134.33, 136.35, 136.55, 142.28, 153.02, 164.46	HRMS (ESI): m/z calc. for $C_{19}H_{18}N_4OF_3$ $[M+H]^+$ 375.14272; found 375.14167
12	(4-(2-((4-(benzylamino)-6-(trifluoromethyl) pyrimidin-2-yl)amino) ethyl)phenyl)methanol	^{1}H NMR (400 MHz, $CDCl_3$): δ (ppm) 2.91 (t, J = 7.4 Hz, 2H), 3.62–3.94 (m, 2H), 4.37–4.59 (m, 1H), 4.59–4.85 (m, 3H), 6.12 (s, 1H), 6.91–7.10 (m, 1H), 7.13–7.26 (m, 2H), 7.25–7.46 (m, 7H). 1H exchanged with H_2O	^{13}C NMR (101 MHz, DMSO-d_6): δ (ppm) 34.81, 40.66, 42.51, 62.73, 126.50, 126.83, 127.28, 128.08, 128.23, 128.32, 132.41, 138.04, 140.14, 145.44, 158.34, 162.60, 163.25	HRMS (ESI): m/z calc. for $C_{21}H_{22}N_4OF_3$ $[M+H]^+$ 403.17402; found 403.17295
13	(4-(2-((2-phenyl-6-(trifluoromethyl) pyrimidin-4-yl)amino) ethyl)phenyl)methanol	^{1}H NMR (400 MHz, $CDCl_3$): δ (ppm) 2.97 (t, J = 6.9 Hz, 2H), 3.49–3.94 (m, 2H), 4.50–4.78 (m, 2H), 4.97–5.42 (m, 1H), 6.45 (s, 1H), 7.23 (t, J = 8.2 Hz, 2H), 7.29–7.35 (m, 2H), 7.46 (dt, J = 5.7, 2.9 Hz, 3H), 8.42 (bs, 2H). 1H exchanged with H_2O	^{13}C NMR (101 MHz, DMSO-d_6): δ (ppm) 34.67, 42.41, 63.19, 101.09, 121.64 (q, J = 274.0 Hz), 123.01, 127.10, 128.27, 128.89, 128.99, 131.48, 137.40, 138.06, 140.92, 163.27, 164.42	HRMS (ESI): m/z calc. for $C_{20}H_{19}N_3OF_3$ $[M+H]^+$ 374.14747; found 374.14651
14	4-(2-((2-phenyl-6-(trifluoromethyl) pyrimidin-4-yl)amino) ethyl)phenol	^{1}H NMR (400 MHz, DMSO-d_6): δ (ppm) 2.81 (t, J = 7.3 Hz, 2H), 3.67 (q, J = 6.7 Hz, 2H), 6.69–6.71 (m, 2H), 6.80 (s, 1H), 7.07–7.09 (m, 2H), 7.49–7.53 (m, 3H), 8.11 (t, J = 5.4 Hz, 1H), 8.32–8.34 (m, 2H), 9.19 (s, 1H)	^{13}C NMR (101 MHz, DMSO-d_6): δ (ppm) 33.62, 42.07, 100.46, 115.08, 121.08 (q, J = 274.4 Hz), 127.69, 128.40, 129.19, 129.50, 130.89, 136.85, 155.65, 162.68, 163.83	HRMS (ESI): m/z calc. for $C_{19}H_{17}N_3OF_3$ $[M+H]^+$ 360.13182; found 360.13070
16	4-(2-((2-(1*H*-pyrrol-2-yl)-6-(trifluoromethyl) pyrimidin-4-yl)amino) ethyl)phenol	^{1}H NMR (400 MHz, DMSO-d_6): δ (ppm) 2.76 (t, J = 7.3 Hz, 2H), 3.67 (q, J = 6.6 Hz, 1H), 6.16 (dd, J = 5.6, 2.4 Hz, 1H), 6.57 (s, 1H), 6.69 (d, J = 8.3 Hz, 2H), 6.85–6.87 (m, 1H), 6.92–6.94 (m, 1H), 7.08 (d, J = 8.3 Hz, 2H), 7.85 (t, J = 5.1 Hz, 2H), 9.17 (s, 1H), 11.35 (bs, 1H)	^{13}C NMR (101 MHz, DMSO-d_6): δ (ppm) 33.34, 41.17, 97.82, 108.91, 111.11, 114.50, 120.44 (q, J = 274.2), 121.64, 128.75, 128.95, 129.03, 129.45, 155.10, 158.68, 161.75	HRMS (ESI): m/z calc. for $C_{17}H_{16}N_4OF_3$ $[M+H]^+$ 349.12707; found 349.126143
18	2-(4-(aminomethyl) phenoxy)-*N*-benzyl-6-(trifluoromethyl) pyrimidin-4-amine	^{1}H NMR (400 MHz, DMSO-d_6): δ (ppm) 4.05 (q, J = 5.8 Hz, 2H), 4.43 (d, J = 5.8 Hz, 2H), 6.72 (s, 1H), 7.11–7.40 (m, 7H), 7.45–7.68 (m, 2H), 8.26 (s, 2H), 8.80 (t, J = 5.9 Hz, 1H)	^{13}C NMR (101 MHz, DMSO-d_6): δ (ppm) 41.14, 43.07, 120.94, 121.12, 126.44, 126.54, 127.10, 127.83, 129.49, 130.01, 137.57, 151.99, 158.59, 163.80	HRMS (ESI): m/z calc. for $C_{19}H_{18}N_4OF_3$ $[M+H]^+$ 375.14272; found 375.14172

Compd.	Chemical name	^{1}H NMR	^{13}C{^{1}H} NMR	HRMS
19	4-(2-((4-(benzylamino)-6-(trifluoromethyl) pyrimidin-2-yl)amino) ethyl)phenol	^{1}H NMR (400 MHz, $CDCl_3$): δ (ppm) 2.81 (t, J = 7.2 Hz, 2H), 3.63 (s, 2H), 4.36–4.95 (m, 3H), 6.09 (bs, 1H), 6.56–6.83 (m, 2H), 7.04 (bs, 3H), 7.27–7.54 (m, 5H)	^{13}C NMR (101 MHz, DMSO-d_6): δ (ppm) 34.35, 42.79, 43.36, 115.06, 121.18 (q, J = 276.0 Hz), 126.86, 127.34, 128.34, 129.42, 129.73, 139.38, 155.53, 158.30 (q, J = 32.0 Hz), 161.93, 163.05	HRMS (ESI): m/z calc. for $C_{20}H_{20}N_4OF_3$ $[M+H]^+$ 389.15837; found 389.15728
20	(4-(2-((2-((4-(hydroxy-methyl)benzyl) amino)-6-(trifluoromethyl) pyrimidin-4-yl)amino) ethyl)phenyl)methanol	^{1}H NMR (400 MHz, $CDCl_3$): δ (ppm) 1.63–1.73 (m, 2H), 2.85 (t, J = 6.9 Hz, 2H), 3.54–3.66 (m, 2H), 4.61 (d, J = 6.0 Hz, 2H), 4.67 (s, 4H), 4.84 (bs, 1H), 5.38 (bs, 1H), 5.96 (s, 1H), 7.10–7.18 (m, 2H), 7.28–7.37 (m, 6H)	^{13}C NMR (100 MHz, $CDCl_3$): δ (ppm) 31.09, 35.26, 45.32, 65.22, 65.27, 100.13, 121.12 (q, $J_{C\text{-}F}$ = 274.6 Hz), 127.36, 127.60, 127.86, 129.09, 138.94, 139.39, 139.43, 139.93, 156.13 (q, $J_{C\text{-}F}$ = 35.8 Hz), 161.36, 162.57	HRMS (ESI+): m/z calc. for $C_{22}H_{24}O_2N_4F_3$ $[M+H]^+$ 433.1846, found 433.1830
21	(4-(((4-((2-([1,1'-biphenyl]-4-yl)ethyl)amino)-6-(trifluoromethyl) pyrimidin-2-yl)amino) methyl)phenyl)methanol	^{1}H NMR (400 MHz, $CDCl_3$): δ (ppm) 1.72 (bs, 1H), 2.90 (t, J = 6.8 Hz, 2H), 3.57–3.72 (m, 2H), 4.61 (d, J = 4.9 Hz, 2H), 4.67 (s, 2H), 4.90 (bs, 1H), 5.40 (bs, 1H), 6.00 (s, 1H), 7.18–7.25 (m, 2H), 7.30–7.37 (m, 5H), 7.41–7.46 (m, 2H), 7.51–7.60 (m, 4H)	^{13}C NMR (100 MHz, $CDCl_3$): δ (ppm) 35.19, 42.40, 45.33, 65.26, 94.87, 121.13 (q, $J_{C\text{-}F}$ = 274.9 Hz), 127.11, 127.15, 127.38, 127.42, 127.59, 127.89, 128.94, 129.32, 130.18, 138.93, 139.82, 139.96, 140.89, 154.69 (q, $J_{C\text{-}F}$ = 32.6 Hz), 162.57	HRMS (ESI+): m/z calc. for $C_{27}H_{26}ON_4F_3$ $[M+H]^+$ 479.2053, found 479.2048
22	(4-(2-((2-(furan-2-yl)-6-(trifluoromethyl) pyrimidin-4-yl)amino) ethyl)phenyl) methanol	^{1}H NMR (400 MHz, $CDCl_3$): δ (ppm) 2.97 (t, J = 6.9 Hz, 2H), 3.55–3.90 (m, 3H), 4.69 (s, 2H), 5.56 (bs, 1H), 6.41 (s, 1H), 6.54 (dd, J_1 = 1.8 Hz, J_2 = 3.4 Hz, 1H), 7.21–7.25 (m, 2H), 7.30–7.36 (m, 3H), 7.59–7.62 (m, 1H)	^{13}C NMR (100 MHz, $CDCl_3$): δ (ppm) 29.84, 35.15, 65.16, 99.08, 112.21, 114.40, 120.92 (q, $J_{C\text{-}F}$ = 274.9 Hz), 127.71, 129.12, 139.70, 145.30, 151.77, 155.25, 158.09, 162.98	HRMS (ESI+): m/z calc. for $C_{18}H_{17}O_2N_3F_3$ $[M+H]^+$ 364.1267, found 364.1260
24	(4-(((4-(1*H*-pyrrol-2-yl)-6-(trifluoromethyl) pyrimidin-2-yl)amino) methyl)-2-chlorophenyl) methanol	^{1}H NMR (400 MHz, $CDCl_3$): δ (ppm) 2.97 (t, J = 6.9 Hz, 2H), 3.55–3.90 (m, 3H), 4.69 (s, 2H), 5.56 (bs, 1H), 6.41 (s, 1H), 6.54 (dd, J_1 = 1.8 Hz, J_2 = 3.4 Hz, 1H), 7.21–7.25 (m, 2H), 7.30–7.36 (m, 3H), 7.59–7.62 (m, 1H)	^{13}C NMR (100 MHz, $CDCl_3$): δ (ppm) 45.99, 62.76, 100.66, 111.54, 112.38, 120.89 (q, $J_{C\text{-}F}$ = 275.1 Hz), 122.61, 126.18, 128.46, 129.15, 129.21, 133.07, 137.34, 140.30, 156.35 (q, $J_{C\text{-}F}$ = 36.2 Hz), 159.32, 162.13	HRMS (ESI+): m/z calc. for $C_{17}H_{15}ON_4ClF_3$ $[M+H]^+$ 383.0881, found 383.0873

Compd.	Chemical name	^{1}H NMR	^{13}C{^{1}H} NMR	HRMS
25	(4-(((4-(1*H*-pyrrol-2-yl)-6-(trifluoromethyl) pyrimidin-2-yl)amino) methyl)-2-bromophenyl) methanol	^{1}H NMR (400 MHz, $CDCl_3$): δ (ppm) 1.98 (t, J = 6.3 Hz, 1H), 4.67 (d, J = 6.0 Hz, 2H), 4.74 (d, J = 5.7 Hz, 2H), 5.62 (bs, 1H), 6.32–6.35 (m, 1H), 6.89–6.91 (m, 1H), 6.98–6.99 (m, 1H), 7.05 (s, 1H), 7.34 (dd, J_1 = 1.7 Hz, J_2 = 7.8 Hz, 1H), 7.45 (d, J = 7.8 Hz, 1H), 7.59 (d, J = 1.7 Hz, 1H), 9.41 (bs, 1H)	^{13}C NMR (100 MHz, $CDCl_3$): δ (ppm) 44.93, 64.98, 100.71, 111.55, 112.35, 119.54, 120.30 (q, $J_{C\text{-}F}$ = 274.0 Hz), 122.59, 122.87, 129.24, 129.29, 131.72, 138.95, 140.55, 156.26, 159.32, 162.13	HRMS (ESI+): m/z calc. for $C_{17}H_{15}ON_4BrF_3$ $[M+H]^+$ 427.0376, found 427.0370
26	(4-(((4-(1*H*-pyrrol-2-yl)-6-(trifluoromethyl) pyrimidin-2-yl)amino) methyl)-3-fluorophenyl) methanol	^{1}H NMR (400 MHz, $CDCl_3$): δ (ppm) 1.73 (t, J = 5.9 Hz, 1H), 4.68 (d, J = 5.4 Hz, 2H), 4.71 (d, J = 6.2 Hz, 2H), 5.68 (bs, 1H), 6.32–6.34 (m, 1H), 6.88–6.90 (m, 1H), 6.98–7.01 (m, 1H), 7.02 (s, 1H), 7.07–7.13 (m, 2H), 7.36–7.42 (m, 1H), 9.54 (bs, 1H)	^{13}C NMR (100 MHz, $CDCl_3$): δ (ppm) 39.14, 64.37, 100.43, 111.45, 112.33, 113.79 (d, $J_{C\text{-}F}$ = 22.2 Hz), 120.92 (q, $J_{C\text{-}F}$ = 275.0 Hz), 122.54, 122.65, 125.03 (d, $J_{C\text{-}F}$ = 14.9 Hz), 129.25, 130.04, 142.80 (d, $J_{C\text{-}F}$ = 7.2 Hz), 156.30 (q, $J_{C\text{-}F}$ = 35.0 Hz), 159.31, 161.17 (d, $J_{C\text{-}F}$ = 247.4 Hz), 162.05	HRMS (ESI+): m/z calc. for $C_{17}H_{15}ON_4F_4$ $[M+H]^+$ 367.1177, found 367.1173
27	*N*-((1*H*-pyrazol-5-yl) methyl)-4-(1*H*-pyrrol-2-yl)-6-(trifluoromethyl) pyrimidin-2-amine	^{1}H NMR (400 MHz, $CDCl_3$): δ (ppm) 4.72 (d, J = 5.7 Hz, 2H), 5.93 (bs, 1H), 6.30 (bs, 1H), 6.33 (dt, J_1 = 2.6 Hz, J_2 = 3.8 Hz, 1H), 6.90–6.92 (m, 1H), 6.98–7.01 (m, 1H), 7.05 (s, 1H), 7.53 (bs, 1H), 9.60 (s, 1H), 1H from NH is exchanged with H_2O	^{13}C NMR (100 MHz, $CDCl_3$): δ (ppm) 38.92, 100.37, 104.19, 111.50, 112.41, 121.00 (q, $J_{C\text{-}F}$ = 274.9 Hz), 122.69, 129.30, 132.19, 148.02, 156.11 (q, $J_{C\text{-}F}$ = 33.6 Hz), 159.40, 162.09	HRMS (ESI+): m/z calc. for $C_{13}H_{12}N_6F_3$ $[M+H]^+$ 309.1070, found 309.1063;
28	(4-(2-((4-(1*H*-pyrrol-2-yl)-6-(trifluoromethyl) pyrimidin-2-yl)amino) ethyl)phenyl) methanol	^{1}H NMR (400 MHz, $CDCl_3$): δ (ppm) 2.94 (t, J = 7.0 Hz, 2H), 3.73–3.78 (m, 2H), 4.67 (s, 2H), 5.29 (bs, 1H), 6.33–6.35 (m, 1H), 6.88–6.90 (m, 1H), 6.97–6.99 (m, 1H), 6.99 (s, 1H), 7.22–7.26 (m, 2H), 7.30–7.36 (m, 2H), 9.47 (bs, 1H); 1H is exchanged with H_2O	^{13}C NMR (100 MHz, $CDCl_3$): δ (ppm) 35.62, 42.91, 65.29, 100.08, 111.45, 112.04, 118.23 (q, $J_{C\text{-}F}$ = 274.0 Hz), 122.26, 127.58, 129.18, 129.36, 138.74, 139.28, 156.35 (q, $J_{C\text{-}F}$ = 36.0 Hz),159.16, 162.29	HRMS (ESI+): m/z calc. for $C_{18}H_{18}N_4F_3O$ $[M+H]^+$ 363.14272, found 363.14215

Biological assays

TLR8 antagonist activity evaluation. – Human embryonic kidney (HEK)-Blue cells stably transfected with hTLR8 and an NF-κB SEAP reporter (#hkb-htlr8, InvivoGen, France) were used to assess the potency of the compounds, as described previously (18, 19, 22, 23). The cell line (passage 5–12) was cultured in Dulbecco's modified Eagle's medium (PAN-Biotech, Germany) containing 10 % (*V*/*V*) heat-inactivated fetal bovine serum (FBS; S0615, Sigma-Aldrich, Germany), 100 U mL^{-1} penicillin, 100 mg mL^{-1} streptomycin (P4333, Sigma-Aldrich), 2 mmol L^{-1} L-glutamine (G7513, Sigma-Aldrich), 100 μg mL^{-1} normocin (#ant-nr-05, InvivoGen) and the selective antibiotics 100 μg mL^{-1} zeocin (#ant-zn-05, InvivoGen) and 30 μg mL^{-1} blasticidin (#ant-bl-05, InvivoGen). The cell line was maintained at 37 °C in a humidified atmosphere of 5 % CO_2 and 95 % air and was regularly tested negative for mycoplasma contamination (#11-1025, Venor GeM Classic Mycoplasma PCR detection kit, Minerva Biolabs, Germany).

Cells were seeded in 96-well plates at a density of 4×10^4 cells per well. After 24 h, the cells were preincubated with the test compounds for 1 h. Afterwards, cells were stimulated with the TLR8 agonist TL8-506 (#tlrl-tl8506, InvivoGen). After 24 h, SEAP activity in the cell supernatants was measured using the Quanti-Blue reagent (#rep-qbs, InvivoGen) according to the manufacturer's instructions. The optical density was measured using a Mithras LB 940 reader (Berthold Technologies, Germany). All test compounds were dissolved in DMSO (A994.1, Carl Roth, Germany) at a concentration of 50 mol mL^{-1} to prepare stock solutions.

Cytotoxicity assessment. – The MTT (3-(4,5-dimethylthiazol-2-yl)-2,5-diphenyltetrazolium bromide) assay was used to determine the effects of the compounds on cell viability. HEK-Blue hTLR8 cells were seeded in 96-well plates at a density of 4×10^4 cells per well. After 24 h, the test compounds were added to the cells for 20 h. Afterwards, the MTT reagent (5 mg mL^{-1}, M5655, Sigma Aldrich) was then added to the cells and incubated for 4 h at 37 °C. After removing supernatants, DMSO (4720.1, Carl Roth) was added and absorption at 540 nm was measured on a Mithras LB 940 reader (Berthold Technologies). The viability of the non-stimulated cells was defined as 100 %. DMSO (10 % *V*/*V*; A994.1, Carl Roth) served as a positive (cytotoxic) control.

Statistical analysis

Data are presented as means or means + SEM. For studies assessing relative TLR8 inhibitory effects, TL8-506-induced NF-κB activity was set to 100 %, with all other values calculated accordingly. Curve fitting was performed using four-parameter nonlinear regression. Data visualization was done using GraphPad Prism (version 8.0, GraphPad Software Inc., USA).

Computational studies

Protein structure preparation. – The protein structure for in silico modeling was selected according to the best resolution of 2.30 A (PDB ID: 5WYZ (39)). Structure preparation was performed with MOE 20222.02 (Chemical Computing Group, Canada). Co-crystallized oligosaccharides and water were removed. Modeling of the missing side chain and

capping were performed using the Structure Preparation utility. The protein-ligand complex was protonated at the temperature of 300 K and pH of 7.4 using the protonate 3D function (24).

Molecular docking studies. – Molecular docking was performed with GOLD (25). Compounds were docked using 50 genetic algorithm runs with the ChemPLP (26) scoring function. The binding pocket for the docking experiment was defined as a sphere with a radius of 10 Å around the co-crystallized ligand. The obtained binding modes were minimized with the MMFF94 force field (27) implemented in Ligandscout 4.4.3 (28). The binding poses were selected by filtering according to their interactions, with the binding pose required to have a hydrogen bond acceptor between the pyrimidine and the backbone of Gly351 in addition to undergoing a visual inspection with a focus on the conformational plausibility, interaction geometry, and shape complementarity of the binding modes.

Molecular dynamics simulations. – The protein-ligand complexes were prepared for molecular dynamics (MD) simulations by using Maestro 11.7 (Schrödinger, LLC, USA). The hydrogen bond network in the systems was optimized at a pH of 7.0. The protein was placed in a cubic box keeping the edges at a 10 Å distance to the protein surface. The box was filled with the TIP3P water model (29), sodium, and chloride ions to neutralize the system and obtain isotonic conditions (0.15 mol L^{-1} NaCl). The system was parameterized using the OPLS 2005 force field (30) and relaxed using the default Desmond protocol. MD simulations were carried out with a constant number of particles, pressure, and temperature (NPT ensemble). The Nose-Hoover thermostat (31, 32) was used to keep a constant keeping with a constant temperature of 298 K. The constant pressure of 1.01325 was preserved using the Martyna-Tobias-Klein method (33). The MD simulations were carried out with Desmond in version 2022-1 on RTX 2080Ti and RTX 3090 graphics processing units (NVIDIA Corporation, USA). The MD simulations for the protein-ligand complexes were performed in 5 replicates, 50 ns each, generating 1000 frames per replica and were post-processed in VMD (34) through alignment and concatenation. The trajectories of the protein-ligand complex simulations were analyzed using Dynophores (35–37) implemented in Ligandscout 4.4.3 (28) to obtain the protein-ligand interaction frequencies.

RESULTS AND DISCUSSION

In our previous study (18), we discovered pyrimidine-based TLR8 modulators that targeted the TLR8 uridine binding site (Fig. 1a) (38). The most promising compound with furan at position 4 and (4-(aminomethyl)phenyl)methanol at position 2 (Fig. 1b) showed an IC_{50} value in the low micromolar range (IC_{50} = 6.2 μmol L^{-1}) (18). The idea behind the new series of compounds was to further explore the SAR by introducing different aromatic rings and amines at both positions, R^1 and R^2 (Fig. 1b, Fig. 2).

The rationale for targeting R^1 and R^2 was based on the potential for additional interactions, considering the steric size of the moieties and their impact on protein binding. The R^1 modifications aimed to (*i*) explore the effect of linker length, (*ii*) assess the role of hydrogen bonding in R^1, and (*iii*) evaluate the impact of halogen substitution on the phenyl ring. For R^2, initial modifications focused on extending the moiety to further sterically probe the binding site in the first series. Additionally, hydroxyl groups were incorporated to inves-

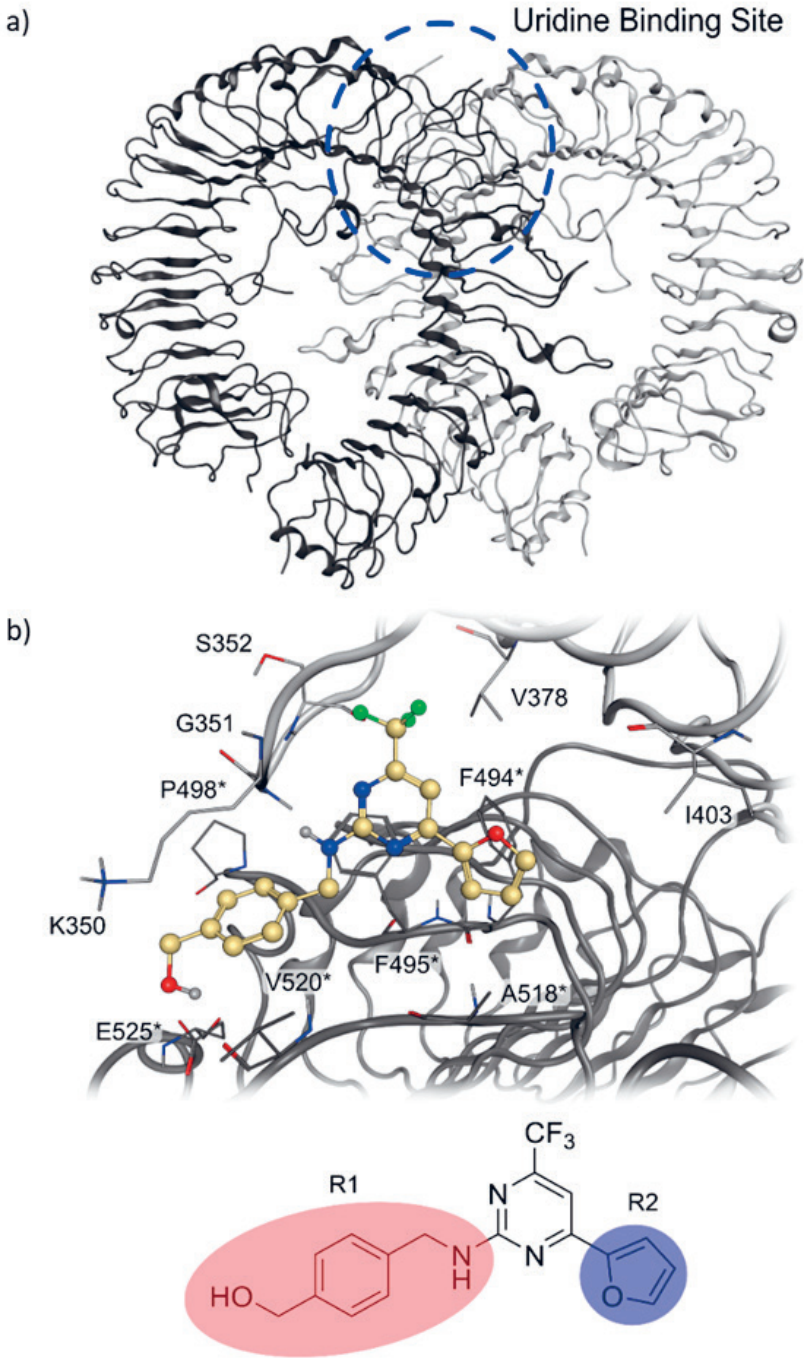

Fig. 1. a) Protein structure of the inactive state of TLR8 with the uridine binding site (circled) (38) (PDB ID: 5WYZ) (39); b) Predicted binding pose of the most promising compound from the previous series with the substituents R^1 and R^2, which were used for SAR. Color code: light and dark grey ribbons and atoms: TLR8 protein structure.

tigate their potential for hydrogen bonding with the protein. In the second series, modifications primarily involved replacing the furan with a pyrrole ring to establish an additional hydrogen bond.

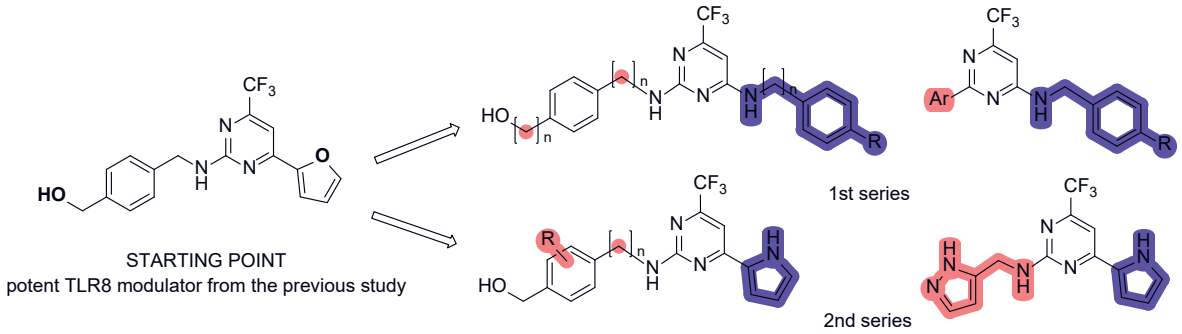

Fig. 2. General structures of two novel series of TLR8 antagonists obtained from structural modifications on the most potent TLR8 modulator from the previous study (18); R is halogen, Ar is aryl (benzene, pyrrole or furan).

Synthesis

The starting amines (**2–5**) were synthesized *via* the reduction of methyl 4-(cyanomethyl)benzoate (**1**) and three different methyl 4-cyanobenzoates using $LiAlH_4$ (Scheme 1A). Subsequently, a two-step synthetic procedure was used to prepare a series of pyrimi-

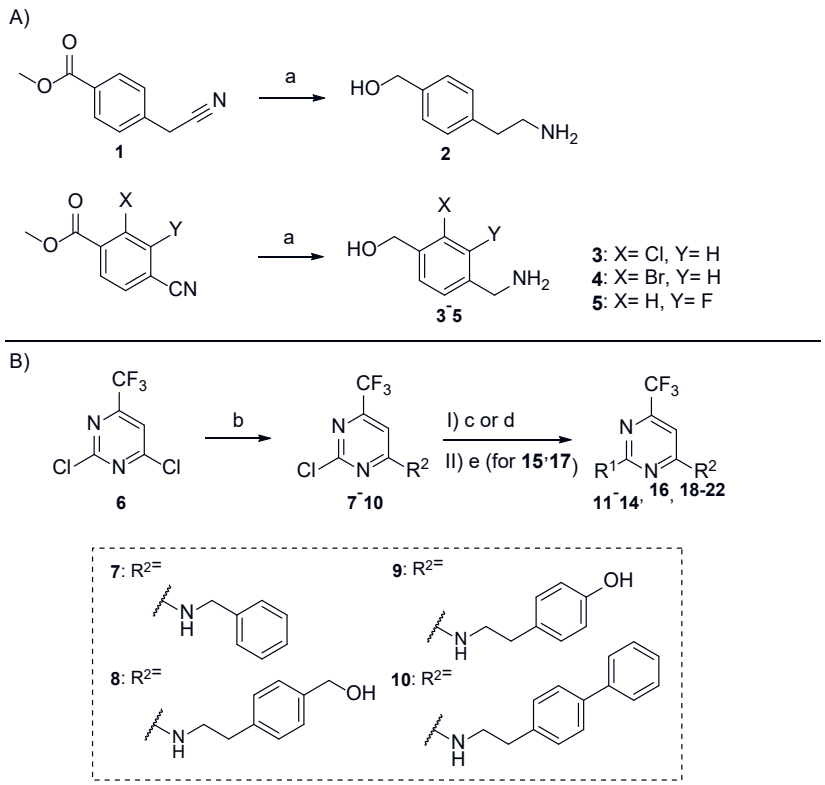

Scheme 1. A) Reagents and conditions: Preparation of starting compounds **2–5**. Reagents and conditions: a) $AlCl_3$, $LiAlH_4$, THF, 0 °C to rt, 18 h; B) Synthetic route for preparation of compounds **11–22**. Reagents and conditions: b) amine **2–5**, K_2CO_3, MeCN, rt, 18 h; c) appropriate amine, K_2CO_3, MeCN, 85 °C, 18 h; d) $Pd(PPh_3)_4$, appropriate boronic acid K_2CO_3, dioxane, H_2O, MW, 20 min; e) 4 mol L^{-1} HCl in dioxane – for the synthesis of compounds **16** and **18** (from **15** and **17**, respectively).

dine-based compounds (Scheme 1B, Table IV). In the first step, various amines were introduced at position 4 of 2,4-dichloro-6-(trifluoromethyl)pyrimidine (**6**) by nucleophilic aromatic substitution to give compounds **7–10**. Compounds **11–12**, **17,** and **19–21** were prepared by another nucleophilic aromatic substitution between the obtained 4-aryl-2--chloropyrimidines and suitable amines or *tert*-butyl (4-hydroxybenzyl)carbamate. Compounds **13–15** and **22** were synthesized by Suzuki coupling between the obtained 4-aryl-2-chloropyrimidines and selected boronic acids. The final compounds **16** and **18** were obtained after the removal of a Boc protecting group in **15** and **17**.

*Table IV. Structures of final compounds **11–14**, **16**, **18–22** from the first series*

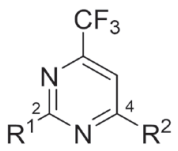

Compd.	R^1	R^2
11	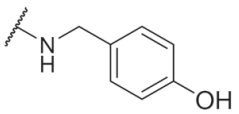	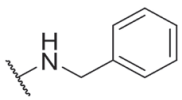
12	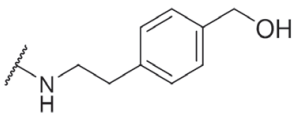	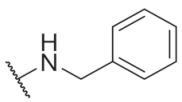
13	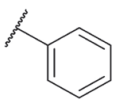	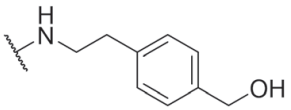
14	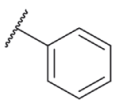	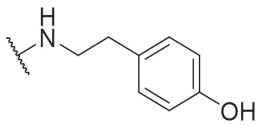
16	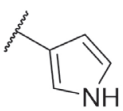	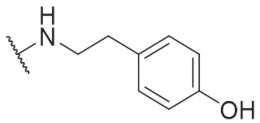
18	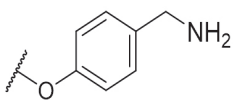	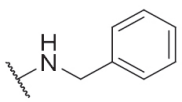
19	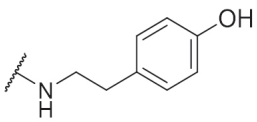	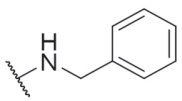

20	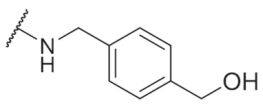	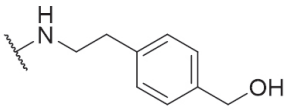
21	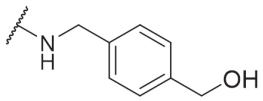	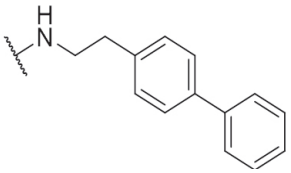
22	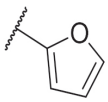	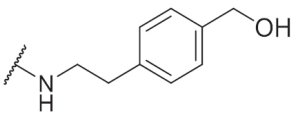

In the second series of compounds, a pyrrole ring was introduced at position 4, along with various aromatic substituents at position 2. The intermediate 2-chloro-4-(1*H*-pyrrole--5-yl)-6-(trifluoromethyl)pyrimidine (**23**) was synthesized by Suzuki coupling of the (1-(*tert*-butoxycarbonyl)-1*H*-pyrrol-2-yl)boronic acid and 2,4-dichloro-6-(trifluoromethyl) pyrimidine (**6**). The final compounds (**24**–**28**) were prepared by nucleophilic aromatic substitution, followed by acidic deprotection of the Boc group (Scheme 2).

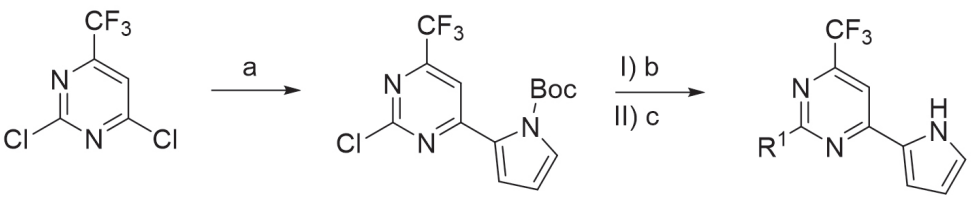

6 **23** **24-28**

Scheme 2. Synthetic route for preparation of compounds **24**–**28** from second series. Reagents and conditions: a) $Pd(PPh_3)_4$, boronic acid, K_2CO_3, dioxane, H_2O, MW, 100 °C, 20 min; b) appropriate amine, K_2CO_3, MeCN, 82 °C, 18 h; c) 4 M HCl in dioxane.

Biological evaluation

The synthesized compounds were biologically evaluated and tested in hTLR8-HEK293 reporter cells. hTLR8-HEK293 reporter cells are HEK293 cells, that express the human TLR8 gene and an inducible SEAP (secreted embryonic alkaline phosphatase) reporter gene and are used to monitor the activation of human TLR8. None of the compounds showed agonistic effects at 10 and 25 μmol L^{-1} (Fig. S1). The compounds from the first series showed slightly weaker antagonistic activity compared to the previously reported antagonists (18). Compounds **14** and **19** showed promising antagonistic activity on TLR8, with IC_{50} values of 6.5 and 15.5 μmol L^{-1} (Table VI, Fig. 3b), respectively. Both compounds contain a 4-(2-aminoethyl)phenol substituent, compound **14** at position 4 and compound **19** at

*Table V. Structures of final compounds **24**–**28** from the second series*

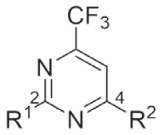

Compd.	R^1	R^2
24	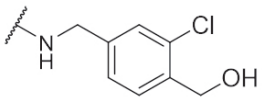	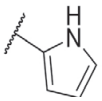
25	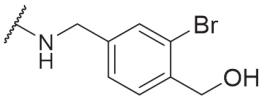	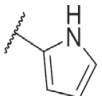
26	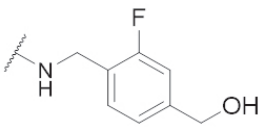	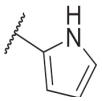
27	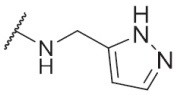	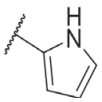
28	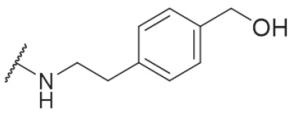	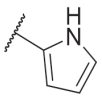

position 2, suggesting that a 4-hydroxyphenyl ring at a distance of two carbon atoms appears to be essential for binding. Compounds **11**, **20**, and **21** with a shorter linker showed lower affinity, whereas compounds **12**, **13**, and **20** with benzyl alcohol lost their antagonistic effect

Table VI. Potencies for inhibition of NF-κB activity in hTLR8-HEK293 reporter cells. IC_{50} values were calculated from concentration-response curves

Compd.	IC_{50} (μmol L^{-1}) hTLR8-HEK293
14	6.5
19	15.5
25	12.0
26	8.7
28	16.0

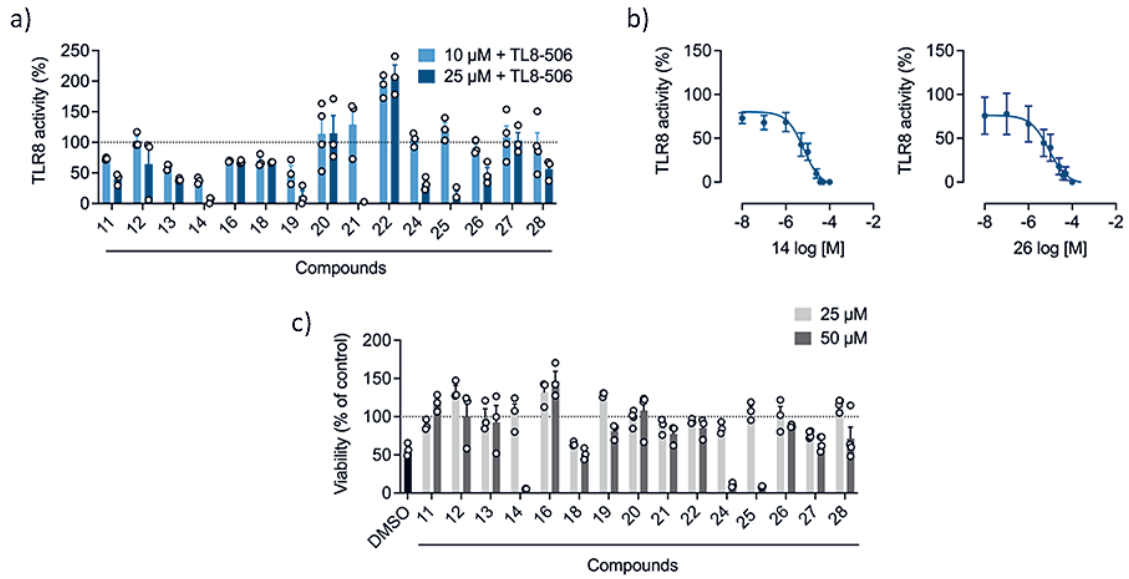

Fig. 3. a) Inhibition of TL8-506-stimulated NF-κB activity in hTLR8-HEK293 reporter cells. HEK-Blue hTLR8 cells were preincubated with the compounds (10 or 25 μmol L^{-1}) for 1 h, and then stimulated with the TLR8 agonist TL8-506 (0.6 μmol L^{-1}) for 24 h. Supernatants were analyzed for TLR8-mediated NF-κB activation by SEAP reporter assay using QuantiBlue (OD_{620}). Data are normalized to TL8--506-stimulated cells. Mean + SEM (n = 3–4); b) Inhibition of TL8-506-stimulated NF-κB activity in hTLR8-HEK293 reporter cells. HEK-Blue hTLR8 cells were preincubated with increasing concentrations of the compound **14** or **26** for 1 h and then stimulated with TL8-506 (0.6 μmol L^{-1}) for 24 h. Supernatants were analyzed for TLR8-mediated NF-κB activation by SEAP reporter assay using QuantiBlue (OD_{620}). Data are normalized to TL8-506-stimulated cells. For the calculation of the concentration-response curves nonlinear regression with variable slope (four parameters) was used. Mean ± SEM (n = 3). The IC_{50} values are shown as means in Table VI; c) Cell viability for the tested compounds. HEK-Blue hTLR8 cells were incubated with the compounds (25, 50 μmol L^{-1}) for 24 h. Cell viability was analyzed using the MTT assay, and normalized to non-stimulated cells (vehicle control). DMSO (10 %, *V*/*V*) was used as the cytotoxic control. Mean ± SEM (n = 3).

completely. We also tried replacing the phenyl ring at position 2 with furan (compound **22**), but this also resulted in a loss of activity. Replacing the hydroxyl group with a free amino group (compound **18**) at position 2 or introducing a larger biphenyl substituent at position 4 (compound **21**) also did not lead to an improvement in potency.

The effect of the synthesized compounds on the viability of hTLR8-HEK293 reporter cells was evaluated to exclude possible false-positive results due to cytotoxicity (Fig. 3c). Compound **14** reduced cell viability at 50 μmol L^{-1} but had no effect at 25 μmol L^{-1}, indicating that its IC_{50} value of 6.5 μmol L^{-1} was not related to cytotoxicity. Compound **19** showed no reduction in cell viability at any of the concentrations tested.

In the second series, we introduced a pyrrole ring at position 4 and introduced various aromatic substituents at position 2. Compounds **25**, **26**, and **28** showed IC_{50} values between 8 and 16 μmol L^{-1}, and no cytotoxic effects except compound **25** at 50 μmol L^{-1}. Among them, compound **26**, which contains a (4-(aminomethyl)-3-fluorophenyl)methanol at position 2, demonstrated the most potent TLR8 antagonistic activity with an IC_{50} value of 8.7 μmol L^{-1}, outperforming the analog with bromine (compound **25**).

The main difference between the first and second series is the substitution at position 4 on the main pyrimidine scaffold. The first series is substituted with various benzyl or phenethylamines, whereas the second series has a pyrrole ring at position 4, which is most likely important for the inhibition of TL8-506-stimulated, TLR8-dependent NF-κB activity. In addition, the most potent compounds of the first series have a 4-hydroxyphenethylamine substituent (compounds **14** and **19**), while the most potent compounds from the second series are substituted with a (4-(aminomethyl)phenyl)methanol derivative that has an additional halogen atom on a benzene ring (compounds **24**–**26**), or with (4-(2-aminoethyl)phenyl)methanol (compound **28**), which has a linker that is one carbon atom longer compared to the starting compound from Fig. 2. The activity in the second series is lost when a pyrazole ring is introduced at position 2 (compound **27**). According to the biological results obtained from both series, the future optimization strategy for the second series could be the substitution of pyrrole (R^2) and/or the introduction of substituted 4-hydroxyphenethylamine (R^1), preferably with halogen atoms. As far as cytotoxicity is concerned, the bromo and chloro derivatives from the second series (compounds **24** and **25**) are cytotoxic at 50 μmol L^{-1} so substitution with fluorine (as in compound **26**) should be made. The compounds from the first series are less cytotoxic with the exception of compound **14**, which has a phenyl ring at position 2.

Computational evaluation

In silico studies were performed to determine the binding modes of **14** and **26** within the uridine binding site of TLR8 (Fig. 4) (38). Their binding modes both show a hydrogen bond between the pyrimidine of **14** and **26** acting as the hydrogen bond acceptor and the backbone amide of G351 backbone amide acting as a hydrogen bond donor. The trifluoromethyl groups of **14** and **26** show hydrophobic interactions with Y348, V378, and F495*. The phenyl ring at position 2 of **14** displays additional hydrophobic interactions with F261, K350, and V520*, while the phenyl ring at position 4 displays hydrophobic interactions with Y567* and F405, and the hydroxyl group acts as a hydrogen bond donor with the oxygen backbone atom of I403. The amine of **14** forms a hydrogen bond with the backbone oxygen atom of A518*. The binding mode of **26** shows that the pyrrole forms a hydrogen bond with the backbone oxygen atom of F494*, while simultaneously showing a hydrophobic interaction with F405, A518*, and Y567*. The phenyl ring of **26** shows a hydrophobic interaction with K350, while the *ortho*-fluoro substituent shows a hydrophobic interaction with P498*. The hydroxyl group acts as a hydrogen donor with the side chain of E525* and as a hydrogen bond acceptor with the side chain of T524*, while the amine forms a hydrogen bond with the backbone of Q519* (Fig. 4a,b).

Molecular dynamics simulations were performed to analyze the frequency of interactions of compounds **14** and **26** with the protein using our recently developed method Dynophores (35–37). The analysis shows that the hydrogen acceptor between the pyrimidine of **14** and **26** and the backbone amine of G351 is present during 69.5 % of the simulation for **14** and 91.4 % for compound **26**. The trifluoromethyl maintains hydrophobic interactions throughout the whole simulation in both **14** and **26** and acts as a hydrogen bond acceptor for 56.7 % of the simulation time in **14** and 49.8 % of the simulation time in **26**. The phenyl rings of **14** both show hydrophobic interactions with the phenyl ring at position 2 showing hydrophobic interactions during 72.9 % of the simulation time. In contrast, the phenyl ring at position 4 shows hydrophobic interactions throughout the entire duration

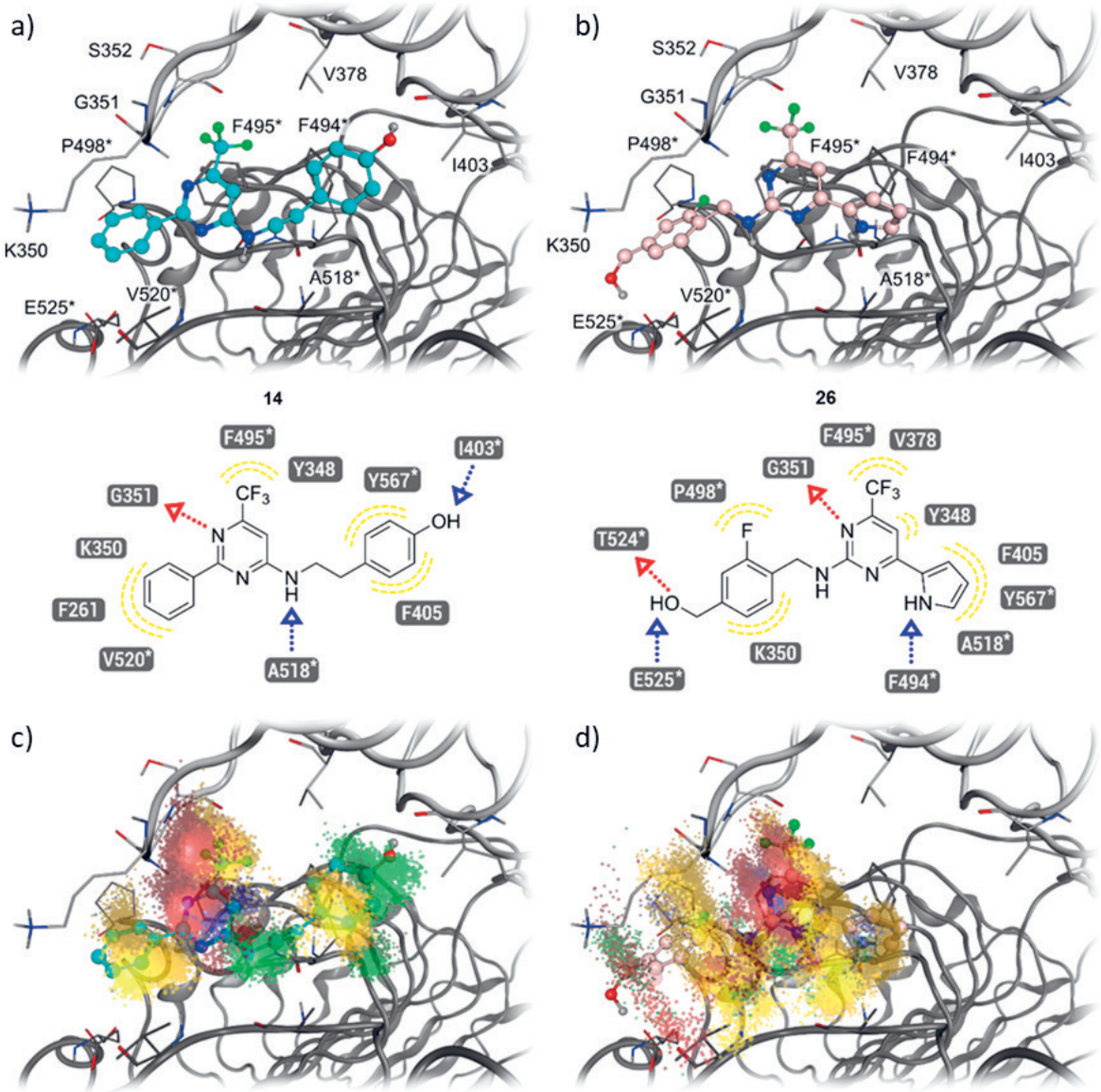

Fig. 4. a) 3D and 2D representation of the predicted binding mode of compound **14**; b) 3D and 2D representation of the predicted binding mode of compound **26**; c) representation of protein-ligand interaction frequencies of **14** through Dynophore clouds; d) Representation of protein-ligand interaction frequencies of **26** through Dynophore clouds. Color code: light and dark grey ribbons and atoms: TLR8. yellow clouds: hydrophobic interactions, blue clouds: aromatic interactions, red clouds: hydrogen bond acceptors, green clouds: hydrogen bond donors.

of the simulation. The hydroxyl group of **14** acts as both a hydrogen bond donor for 79.9 % of the simulation time and as a hydrogen bond acceptor for 6.9 % of the simulation time. The amine at position 4 maintains a hydrogen bond with the backbone of A518* during 36.9 % of the simulation time. The pyrimidine ring of **14** shows πinteractions in 16.5 % of the simulation time, while the pyrimidine ring of **26** maintains πinteractions in 21.0 % of the simulation time. The pyrrole at position 4 shows hydrophobic interactions throughout the whole simulation and maintains hydrogen bond interactions during 12.8 % of the

simulation time. The amine at position 2 of **26** acts as a hydrogen bond donor in 21.1 % of the simulation time, while the hydroxyl group acts as a hydrogen bond acceptor during 13.5 % of the simulation time. The fluorine shows hydrophobic interactions in 82.3 % of the simulation time and maintains a hydrogen bond in 16.4 % of the simulation time. The phenyl ring at position 2 of **26** shows hydrophobic interactions in 41.4 % of the simulation time (Fig. 4c,d, Table S1 and S2).

CONCLUSIONS

In this study, we successfully designed, synthesized, and evaluated a novel series of TLR8 antagonists, building on previous research to increase the potency of this class of antagonists. Compounds **14** and **26** demonstrated the most promising activity, with IC_{50} values of 6.5 and 8.7 μmol L^{-1}, respectively. While compound **14** reduced cell viability at higher concentrations, compound **26** showed no effect on cell viability, highlighting its potential for further development as a TLR8 antagonist. Even though these compounds are less potent compared to some previously reported TRL8 antagonists, *e.g.* isoxazole derivatives (40), 5-indazol-5-yl pyridines (14), or the quinoline derivative CU-CPT9a (41), which show the IC_{50} values in the nanomolar or picomolar range, there is still room for further optimization of our compounds to improve the potency. One possibility is to explore the substitutions at position 6 by replacing the trifluoromethyl group with different amines or aromatic rings to gain additional interactions with amino acid residues in the active site. Similarly, the substitutions on the pyrrole ring at position 2 of the main scaffold could also improve the potency. To avoid potential cytotoxicity, substitution with benzene, chlorine, and bromine should not be used. This study was based on the previously reported TLR8 modulator (18), which showed selective activity towards TLR7, so our compounds most likely retain this selectivity. To confirm this, future experiments could also include the determination of selectivity against TLR7 and also other TLRs. Nonetheless, the results of this study provide valuable insights into the SAR of TLR8 antagonists and form the basis for future therapeutic applications targeting TLR8-mediated diseases.

Supplementary information includes biological data, computational data, and NMR spectra of the active final compounds. Supplementary material is available upon request.

Acknowledgements and funding. – This work was funded by the Slovenian Research and Innovation Agency (research core funding No. P1-0208, grant to M.S. J1-4417, bilateral project grant BI-DE/23-24-011, and a grant to N.S.B.).

Conflict of interest. – The authors declare no competing financial interest in connection with this manuscript.

Authors contributions. – Conceptualization, N.S.B. and M.S.; synthesis, A.D. and N.S.B.; biological experiments, T.M. and G. Weindl; computational studies, V.T. and G. Wolber; writing, original draft preparation, N.S.B, I.S., and M.S.; writing, review and editing, N.S.B, V.T, T.M., G. Weindl, G. Wolber and M.S.; supervision, I.S., G. Weindl, G. Wolber and M.S. All authors have read and agreed to the published version of the manuscript.

REFERENCES

1. K. A. Fitzgerald and J. C. Kagan, Toll-like receptors and the control of immunity, *Cell* **180**(6) (2020) 1044–1066; https://doi.org/10.1016/j.cell.2020.02.041
2. C. A. Janeway and R. Medzhitov, Innate immune recognition, *Annu. Rev. Immunol.* **20** (2002) 197–216; https://doi.org/10.1146/annurev.immunol.20.083001.084359
3. R. Medzhitov, Toll-like receptors and innate immunity, *Nat. Rev. Immunol.* **1** (2001) 135–145; https://doi.org/10.1038/35100529
4. T. Kawai and S. Akira, Toll-like receptors and their crosstalk with other innate receptors in infection and immunity, *Immunity* **34**(5) (2011) 637–650; https://doi.org/10.1016/j.immuni.2011.05.006
5. F. J. Barrat and R. L. Coffman, Development of TLR inhibitors for the treatment of autoimmune diseases, *Immunol. Rev.* **223**(1) (2008) 271–283; https://doi.org/10.1111/j.1600-065X.2008.00630.x
6. I. Martínez-Espinoza and A. Guerrero-Plata, The relevance of TLR8 in viral infections, *Pathogens* **11**(2) (2022) Article ID 134; https://doi.org/10.3390/pathogens11020134
7. M. J. Braunstein, J. Kucharczyk and S. Adams, Targeting Toll-like receptors for cancer therapy, *Targ. Oncol.* **13** (2018) 583–598; https://doi.org/10.1007/s11523-018-0589-7
8. J. A. Hamerman and G. M. Barton, The path ahead for understanding Toll-like receptor-driven systemic autoimmunity, *Curr. Opin. Immunol.* **91** (2024) Article ID 102482; https://doi.org/10.1016/j.coi.2024.102482
9. J.-Q. Chen, P. Szodoray and M. Zeher, Toll-like receptor pathways in autoimmune diseases, *Clinic Rev. Allerg. Immunol.* **50** (2016) 1–17; https://doi.org/10.1007/s12016-015-8473-z
10. C.-Y. Lai, Y.-W. Su, K.-I. Lin, L.-C. Hsu and T.-H. Chuang, Natural modulators of endosomal Toll-like receptor-mediated psoriatic skin inflammation, *J. Immunol. Res.* **2017** (2017) Article ID 7807313 (15 pages); https://doi.org/10.1155/2017/7807313
11. T. Celhar and A.-M. Fairhurst, Toll-like receptors in systemic lupus erythematosus: Potential for personalized treatment, *Front. Pharmacol.* **5** (2014) Article ID 265 (8 pages); https://doi.org/10.3389/fphar.2014.00265
12. D. -Y. Oh, S. Taube, O. Hamouda, C. Kücherer, G. Poggensee, H. Jessen, J. K. Eckert, K. Neumann, A. Storek, M. Pouliot, P. Borgeat, N. Oh, E. Schreier, A. Pruss, K. Hattermann and R. R. Schumann, A functional Toll-like receptor 8 variant is associated with HIV disease restriction, *J. Infecty. Dis.* **198**(5) (2008) 701–709; https://doi.org/10.1086/590431
13. H. Z. Meås, M. Haug, M. S. Beckwith, C. Louet, L. Ryan, Z. Hu, J. Landskron, S. A. Nordbø, K. Taskén, H. Yin, J. K. Damås and T. H. Flo, Sensing of HIV-1 by TLR8 activates human T cells and reverses latency, *Nat. Commun.* **11** (2020) Article ID 147 (16 pages); https://doi.org/10.1038/s41467-019-13837-4
14. T. Knoepfel, P. Nimsgern, S. Jacquier, M. Bourrel, E. Vangrevelinghe, R. Glatthar, D. Behnke, P. B. Alper, P.-Y. Michellys, J. Deane, T. Junt, G. Zipfel, S. Limonta, S. Hawtin, C. Andre, T. Boulay, P. Loetscher, M. Faller, J. Blank, R. Feifel and C. Betschart, Target-based identification and optimization of 5-indazol-5-yl pyridones as Toll-like receptor 7 and 8 antagonists using a biochemical TLR8 antagonist competition assay, *J. Med. Chem.* **63**(15) (2020) 8276–8295; https://doi.org/10.1021/acs.jmedchem.0c00130
15. P. B. Alper, J. Deane, C. Betschart, D. Buffet, G. Collignon Zipfel, P. Gordon, J. Hampton, S. Hawtin, M. Ibanez, T. Jiang, T. Junt, T. Knoepfel, B. Liu, J. Maginnis, U. McKeever, P.-Y. Michellys, D. Mutnick, B. Nayak, S. Niwa, W. Richmond and X. Zhu, Discovery of potent, orally bioavailable in vivo efficacious antagonists of the TLR7/8 pathway, *Bioorg. Med. Chem. Lett.* **30**(17) (2020) Article ID 127366; https://doi.org/10.1016/j.bmcl.2020.127366
16. C. P. Mussari, D. S. Dodd, R. K. Sreekantha, L. Pasunoori, H. Wan, S. L. Posy, D. Critton, S. Ruepp, M. Subramanian, A. Watson, P. Davies, G. L. Schieven, L. M. Salter-Cid, R. Srivastava, D. M.

Tagore, S. Dudhgaonkar, M. A. Poss, P. H. Carter and A. J. Dickman, Discovery of potent and orally bioavailable small molecule antagonists of Toll-like receptors 7/8/9 (TLR7/8/9), *ACS Med. Chem. Lett.* **11**(9) (2020) 1751–1758; https://doi.org/10.1021/acsmedchemlett.0c00264

17. M. Grabowski, M. Bermudez, T. Rudolf, D. Šribar, P. Varga, M. S. Murgueitio, G. Wolber, J. Rademann and G. Weindl, Identification and validation of a novel dual small-molecule TLR2/8 antagonist, *Biochem. Pharmacol.* **177** (2020) Article ID 113957; https://doi.org/10.1016/j.bcp.2020.113957
18. A. Dolšak, D. Šribar, A. Scheffler, M. Grabowski, U. Švajger, S. Gobec, J. Holze, G. Weindl, G. Wolber and M. Sova, Further hit optimization of 6-(trifluoromethyl)pyrimidin-2-amine based TLR8 modulators: Synthesis, biological evaluation and structure–activity relationships, *Eur. J. Med. Chem.* **225** (2021) Article ID 113809; https://doi.org/10.1016/j.ejmech.2021.113809
19. D. Šribar, M. Grabowski, M. S. Murgueitio, M. Bermudez, G. Weindl and G. Wolber, Identification and characterization of a novel chemotype for human TLR8 inhibitors, *Eur. J. Med. Chem.* **179** (2019) 744–752; https://doi.org/10.1016/j.ejmech.2019.06.084
20. J. J. Naleway, Y. Jiang and R. Link-Cole, Reagents and methods for direct labeling of nucleotides; Retrieved from https://patents.google.com/patent/US20130150254A1/en?oq=US20130150254
21. N. Varga, I. Sutkeviciute, C. Guzzi, J. McGeagh, I. Petit-Haertlein, S. Gugliotta, J. Weiser, J. Angulo, F. Fieschi and A. Bernardi, Selective targeting of dendritic cell-specific intercellular adhesion molecule-3-grabbing nonintegrin (DC-SIGN) with mannose-based glycomimetics: Synthesis and interaction studies of bis(benzylamide) derivatives of a pseudomannobioside, *Chem. Eur. J.* **19**(15) (2013) 4786–4797; https://doi.org/10.1002/chem.201202764
22. M. Grabowski, M. S. Murgueitio, M. Bermudez, J. Rademann, G. Wolber and G. Weindl, Identification of a pyrogallol derivative as a potent and selective human TLR2 antagonist by structure-based virtual screening, *Biochem. Pharmacol.* **154** (2018) 148–160; https://doi.org/10.1016/j.bcp.2018.04.018
23. J. Holze, F. Lauber, S. Soler, E. Kostenis and G. Weindl, Label-free biosensor assay decodes the dynamics of Toll-like receptor signaling, *Nat. Commun.* **15** (2024) Article ID 9554 (18 pages); https://doi.org/10.1038/s41467-024-53770-9
24. P. Labute, Protonate3D: Assignment of ionization states and hydrogen coordinates to macromolecular structures, *Proteins* **75**(1) (2009) 187–205; https://doi.org/10.1002/prot.22234
25. G. Jones, P. Willett, R. C. Glen, A. R. Leach and R. Taylor, Development and validation of a genetic algorithm for flexible docking, *J. Mol. Biol.* **267**(3) (1997) 727–748; https://doi.org/10.1006/jmbi.1996.0897
26. O. Korb, T. Stützle and T. E. Exner, Empirical scoring functions for advanced protein-ligand docking with PLANTS, *J. Chem. Inf. Model.* **49**(1) (2009) 84–96; https://doi.org/10.1021/ci800298z
27. T. A. Halgren, Merck molecular force field. I. Basis, form, scope, parameterization, and performance of MMFF94, *J. Comput. Chem.* **17**(5–6) (1996) 490–519; https://doi.org/10.1002/(SICI)1096-987X(199604)17:5/6<490::AID-JCC1>3.0.CO;2-P
28. G. Wolber and T. Langer, LigandScout: 3-D pharmacophores derived from protein-bound ligands and their use as virtual screening filters, *J. Chem. Inf. Model.* **45**(1) (2005) 160–169; https://doi.org/10.1021/ci049885e
29. P. Mark and L. Nilsson, Structure and dynamics of the TIP3P, SPC, and SPC/E water models at 298 K, *J. Phys. Chem. A* **105**(43) (2001) 9954–9960; https://doi.org/10.1021/jp003020w
30. E. Harder, W. Damm, J. Maple, C. Wu, M. Reboul, J. Y. Xiang, L. Wang, D. Lupyan, M. K. Dahlgren, J. L. Knight, J. W. Kaus, D. S. Cerutti, G. Krilov, W. L. Jorgensen, R. Abel and R. A. Friesner, OPLS3: A force field providing broad coverage of drug-like small molecules and proteins, *J. Chem. Theory Comput.* **12**(1) (2016) 281–296; https://doi.org/10.1021/acs.jctc.5b00864
31. S. Nosé, A molecular dynamics method for simulations in the canonical ensemble, *Mol. Phys.* **52**(2) (1984) 255–268; https://doi.org/10.1080/00268978400101201

32. W. G. Hoover, Canonical dynamics: Equilibrium phase-space distributions, *Phys. Rev. A Gen. Phys.* **31** (1985) 1695–1697; https://doi.org/10.1103/physreva.31.1695
33. G. J. Martyna, M. E. Tuckerman, D. J. Tobias and M. L. Klein, Explicit reversible integrators for extended systems dynamics, *Mol. Phys.* **87**(5) (1996) 1117–1157; https://doi.org/10.1080/00268979600100761
34. W. Humphrey, A. Dalke and K. Schulten, VMD: Visual molecular dynamics, *J. Mol. Graph.* **14**(1) (1996) 33–38; https://doi.org/10.1016/0263-7855(96)00018-5
35. A. Bock, M. Bermudez, F. Krebs, C. Matera, B. Chirinda, D. Sydow, C. Dallanoce, U. Holzgrabe, M. De Amici, M. J. Lohse, G. Wolber and K. Mohr, Ligand binding ensembles determine graded agonist efficacies at a G protein-coupled receptor, *J. Biol. Chem.* **291**(31) (2016) 16375–16389; https://doi.org/10.1074/jbc.M116.735431
36. M. Janežič, K. Valjavec, K. B. Loboda, B. Herlah, I. Ogris, M. Kozorog, M. Podobnik, S. G. Grdadolnik, G. Wolber and A. Perdih, Dynophore-based approach in virtual screening: A case of human DNA topoisomerase IIα, *Int. J. Mol. Sci.* **22**(24) (2021) Article ID 13474; https://doi.org/10.3390/ijms222413474
37. N. Fuchs, L. Calvo-Barreiro, V. Talagayev, S. Pach, G. Wolber and M. T. Gabr, From virtual screens to cellular target engagement: New small molecule ligands for the immune checkpoint LAG-3, *ACS Med. Chem. Lett.* **15**(11) (2024) 1884–1890; https://doi.org/10.1021/acsmedchemlett.4c00350
38. H. Tanji, U. Ohto, T. Shibata, K. Miyake and T. Shimizu, Structural reorganization of the Toll-like receptor 8 dimer induced by agonistic ligands, *Science* **339**(6126) (2013) 1426–1429; https://doi.org/10.1126/science.1229159
39. S. Zhang, Z. Hu, H. Tanji, S. Jiang, N. Das, J. Li, K. Sakaniwa, J. Jin, Y. Bian, U. Ohto, T. Shimizu and H. Yin, Small-molecule inhibition of TLR8 through stabilization of its resting state, *Nat. Chem. Biol.* **14** (2018) 58–64; https://doi.org/10.1038/nchembio.2518
40. T. Matziol, V. Talagayev, T. Slokan, N. Strašek Benedik, J. Holze, M. Sova, G. Wolber and G. Weindl, Discovery of novel isoxazole-based small-molecule Toll-like receptor 8 antagonists, *J. Med. Chem.* **68**(4) (2025) 4888–4907; https://doi.org/10.1021/acs.jmedchem.4c03148
41. Z. Hu, H. Tanji, S. Jiang, S. Zhang, K. Koo, J. Chan, K. Sakaniwa, U. Ohto, A. Candia, T. Shimizu and H. Yin, Small-molecule TLR8 antagonists via structure-based rational design, *Cell. Chem. Biol.* **25**(10) (2018) 1286–1291; https://doi.org/10.1016/j.chembiol.2018.07.004

Supplementary information

Optimization of 6-(trifluoromethyl)pyrimidine derivatives as TLR8 antagonists

Nika Strašek Benedik[#1], Valerij Talagayev[#2], Troy Matziol[3], Ana Dolšak[1], Izidor Sosič[1], Günther Weindl[3*], Gerhard Wolber[2*], Matej Sova[1*]

[1]*University of Ljubljana, Faculty of Pharmacy, The Department of Pharmaceutical Chemistry, Aškerčeva 7, SI-1000 Ljubljana, Slovenia*

[2]*Freie Universität Berlin, Institute of Pharmacy, Pharmaceutical and Medicinal Chemistry, Königin-Luise-Str. 2+4, 14195 Berlin, Germany*

[3]*University of Bonn, Pharmaceutical Institute, Pharmacology and Toxicology Section, Gerhard-Domagk-Str. 3, 53121 Bonn, Germany*

[*]*Corresponding authors. e-mail: matej.sova@ffa.uni-lj.si, guenther.weindl@uni-bonn.de or gerhard.wolber@fu-berlin.de*

[#]*Authors contributed equally*

Table of contents

1. Biological data

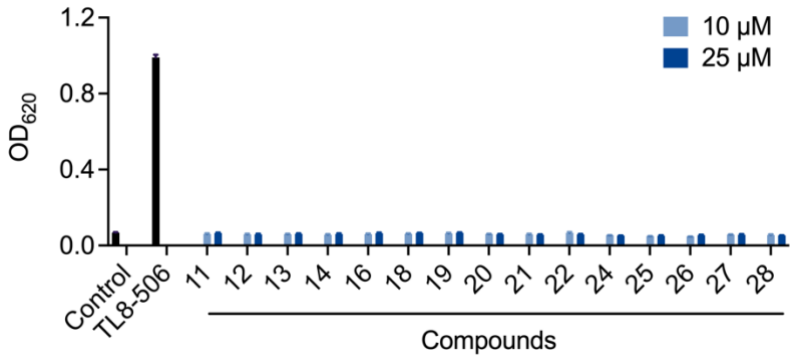

Fig. S1. Activation of NF-κB activity in hTLR8-HEK293 cells.
HEK-Blue hTLR8 cells were stimulated with TL8-506 (0.6 µM) or the test compounds (10 µM, 25 µM) for 24 h. Supernatants were analyzed for TLR8-mediated NF-κB activation by SEAP reporter assay using QuantiBlue (OD_{620}). Mean + SEM (n=4).

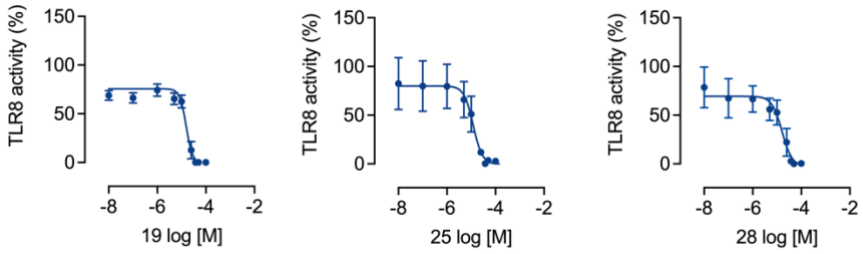

Fig. S2. Concentration-response curves in hTLR8-HEK293 cells for **19**, **25**, and **28**.
HEK-Blue hTLR8 cells were preincubated with increasing concentrations of the test compounds for 1 h, and then stimulated with TL8-506 (0.6 µM) for 24 h. Supernatants were analyzed for TLR8-mediated NF-κB activation by SEAP reporter assay using QuantiBlue (OD_{620}). For the calculation of the concentration-response curves nonlinear regression with variable slope (four parameters) was used. IC_{50} values are shown in Table 3. Mean ± SEM (n=3-4).

2. Computational data

Table S1. Interaction frequencies of **14** with TLR8 homodimer during MD simulation.

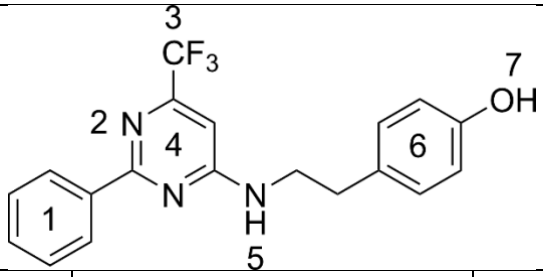

Ligand Moiety	Interaction Type	Interaction Frequency (%)
Phenyl ring 1	Hydrophobic	72.9
Pyrimidine nitrogen 2	Hydrogen bond acceptor	91.4
Trifluoromethyl 3	Hydrophobic	100.0
Trifluoromethyl 3	Hydrogen bond acceptor	56.7
Pyrimidine 4	Aromatic	16.5
Amine 5	Hydrogen bond donor	36.9
Phenyl ring 6	Hydrophobic	100.0
Hydroxyl group 7	Hydrogen bond acceptor	6.9
Hydroxyl group 7	Hydrogen bond donor	79.9

Table S2. Interaction frequencies of **26** with TLR8 homodimer during MD simulation.

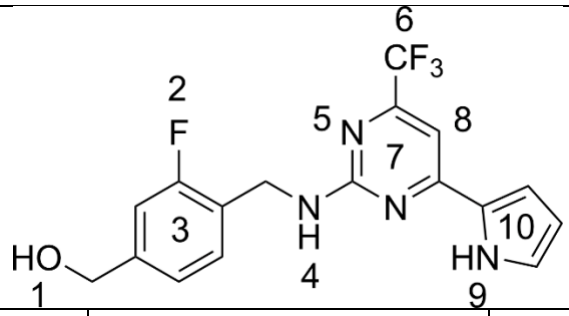

Ligand Moiety	Interaction Type	Interaction Frequency (%)
Hydroxyl group 1	Hydrogen bond acceptor	13.5
Fluorine 2	Hydrophobic	82.3
Fluorine 2	Hydrogen bond acceptor	16.4
Phenyl ring 3	Hydrophobic	41.4
Amine 4	Hydrogen bond donor	21.1
Pyrimidine nitrogen 5	Hydrogen bond acceptor	69.5
Trifluoromethyl 6	Hydrogen bond acceptor	49.8
Trifluoromethyl 6	Hydrophobic	100.0
Pyrimidine 7	Aromatic	21.0
Pyrimidine carbon 8	Hydrophobic	98.5
Pyrrole nitrogen 9	Hydrogen bond donor	12.8
Pyrrole 10	Hydrophobic	100.0

3. NMR spectra of active final compounds (compounds with IC_{50} values - 14, 19, 25, 26, 28)

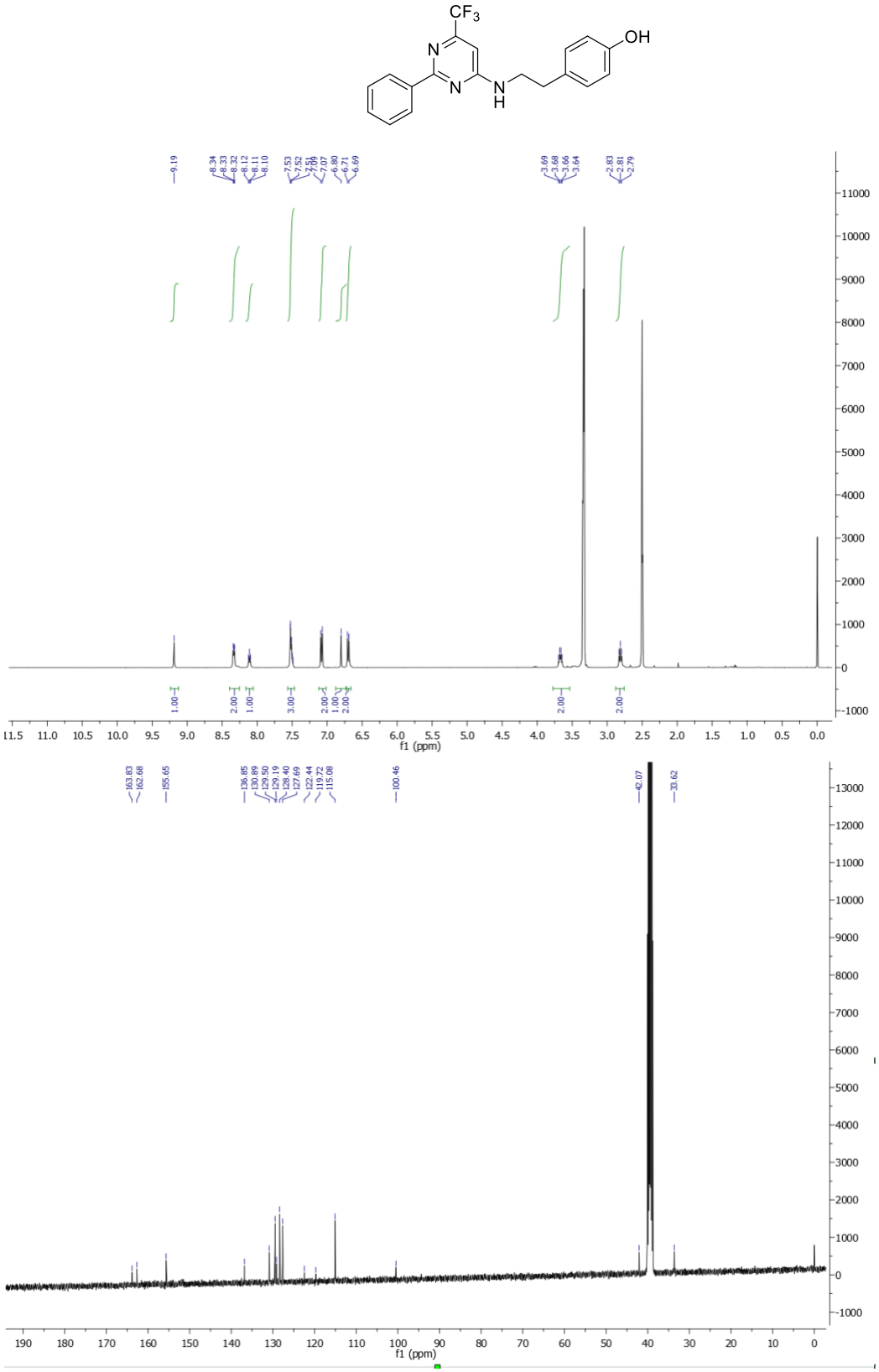

^{1}H and $^{13}C\{^{1}H\}$ NMR spectrum of compound **14**.

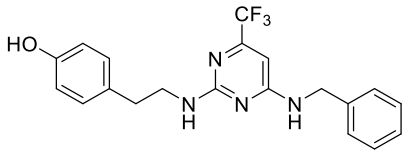

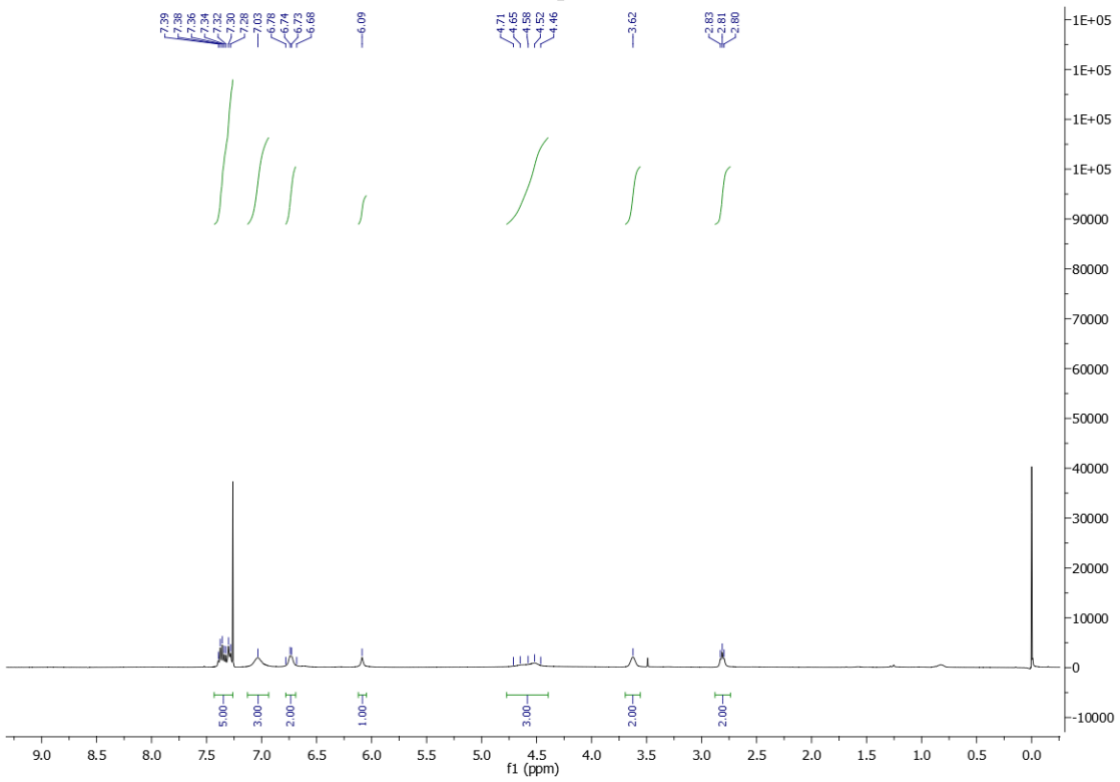

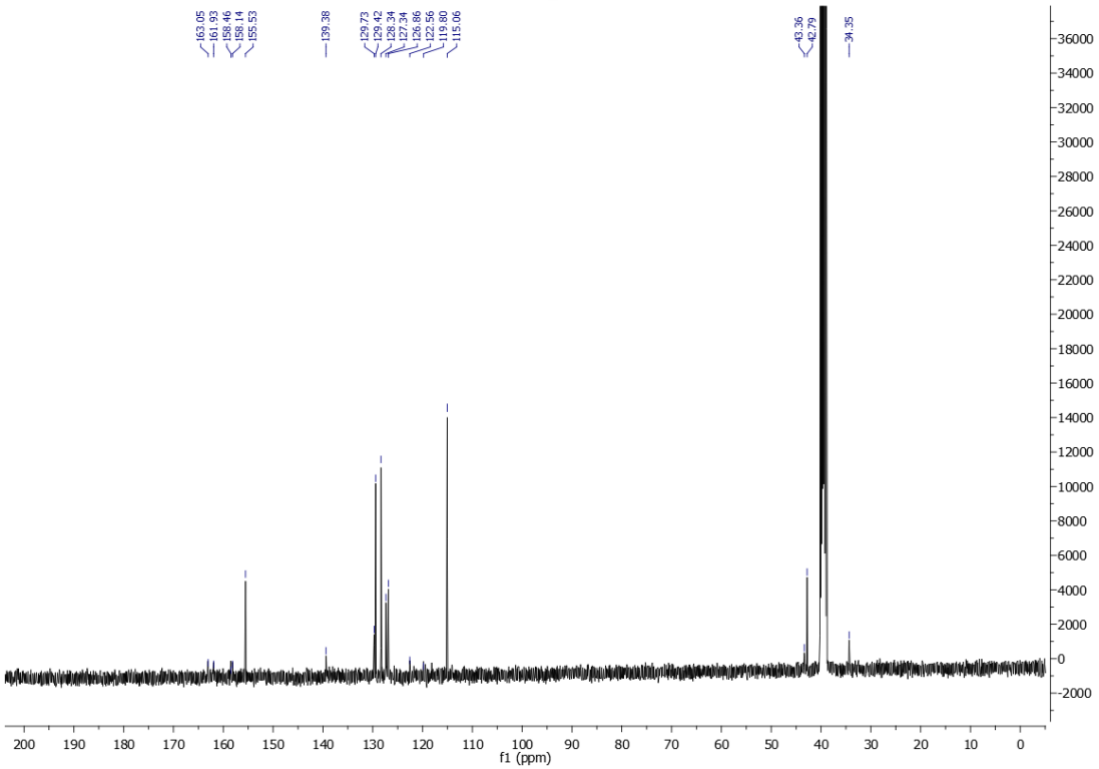

^{1}H and ^{13}C{^{1}H} NMR spectrum of compound **19**.

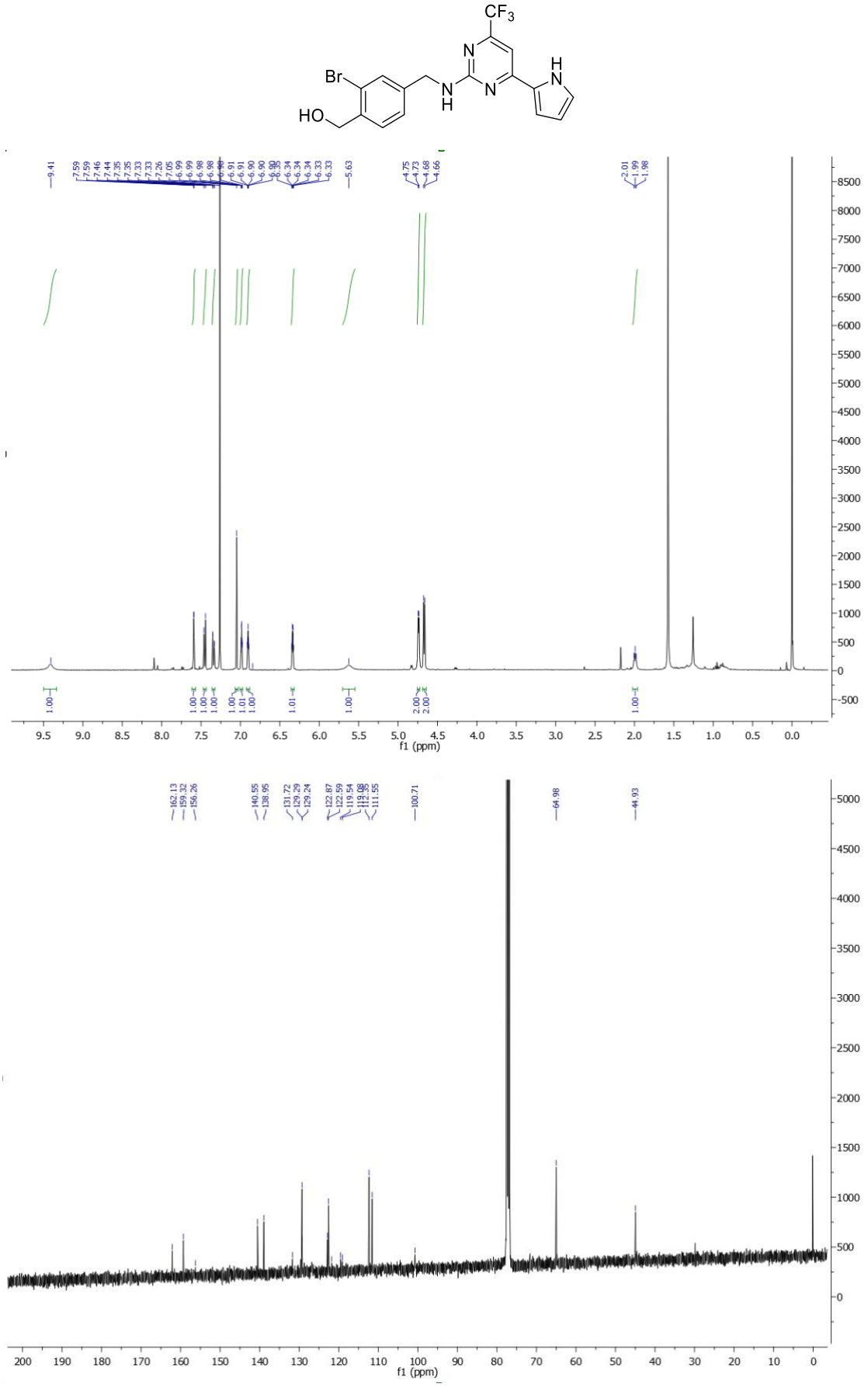

^{1}H and $^{13}C\{^{1}H\}$ NMR spectrum of compound **25**.

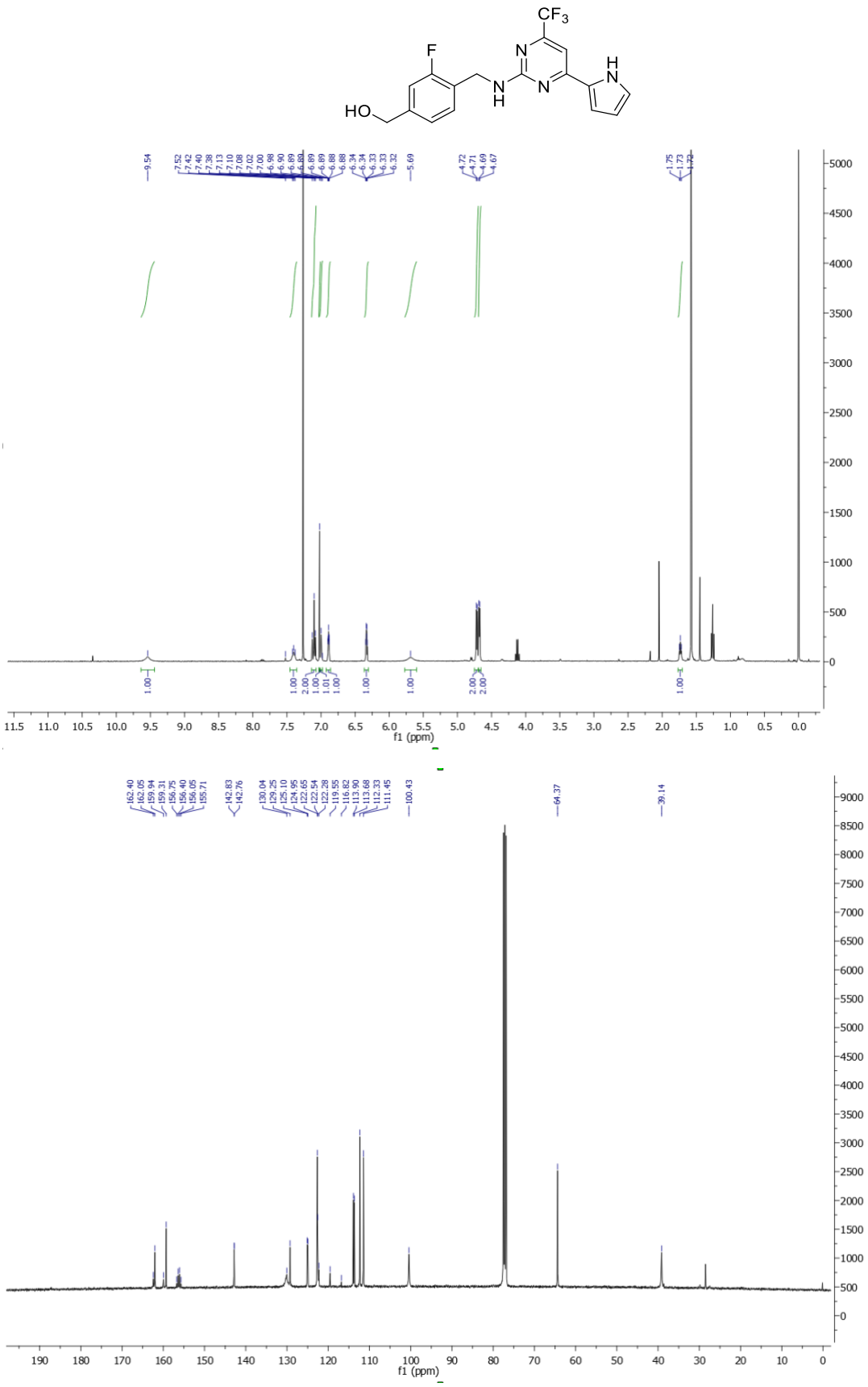

^{1}H and $^{13}C\{^{1}H\}$ NMR spectrum of compound **26.**

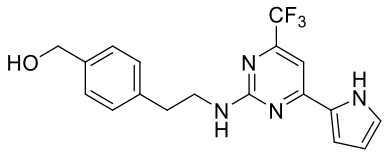

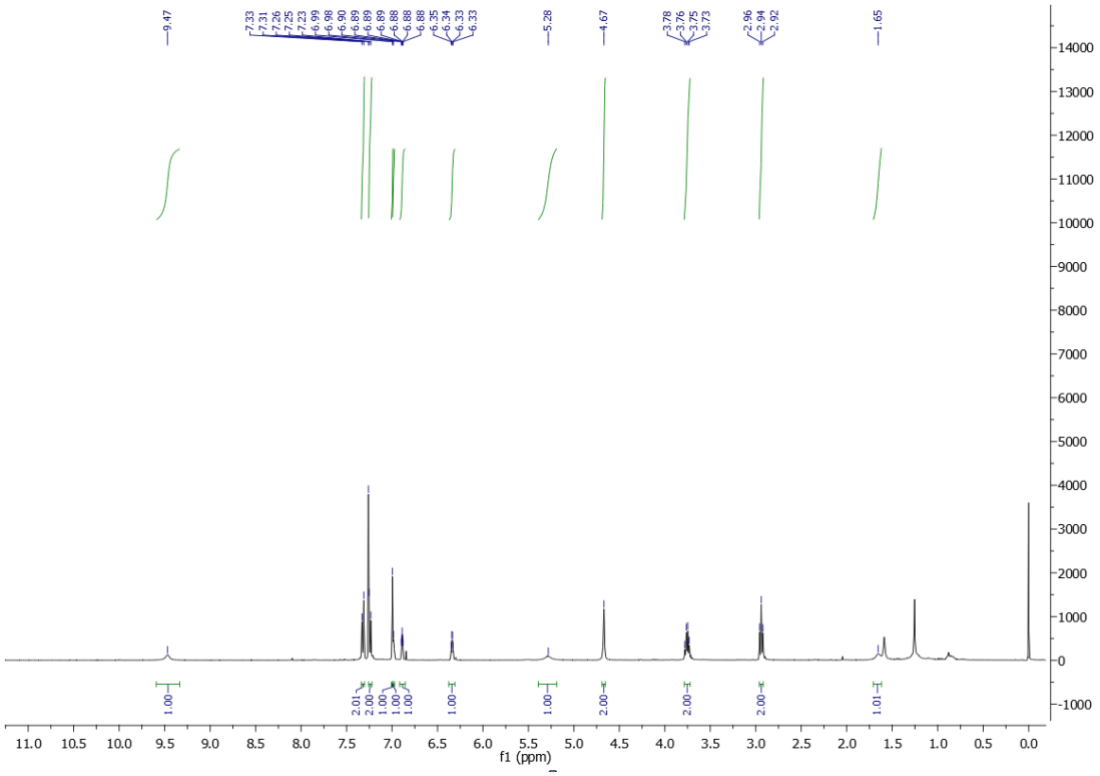

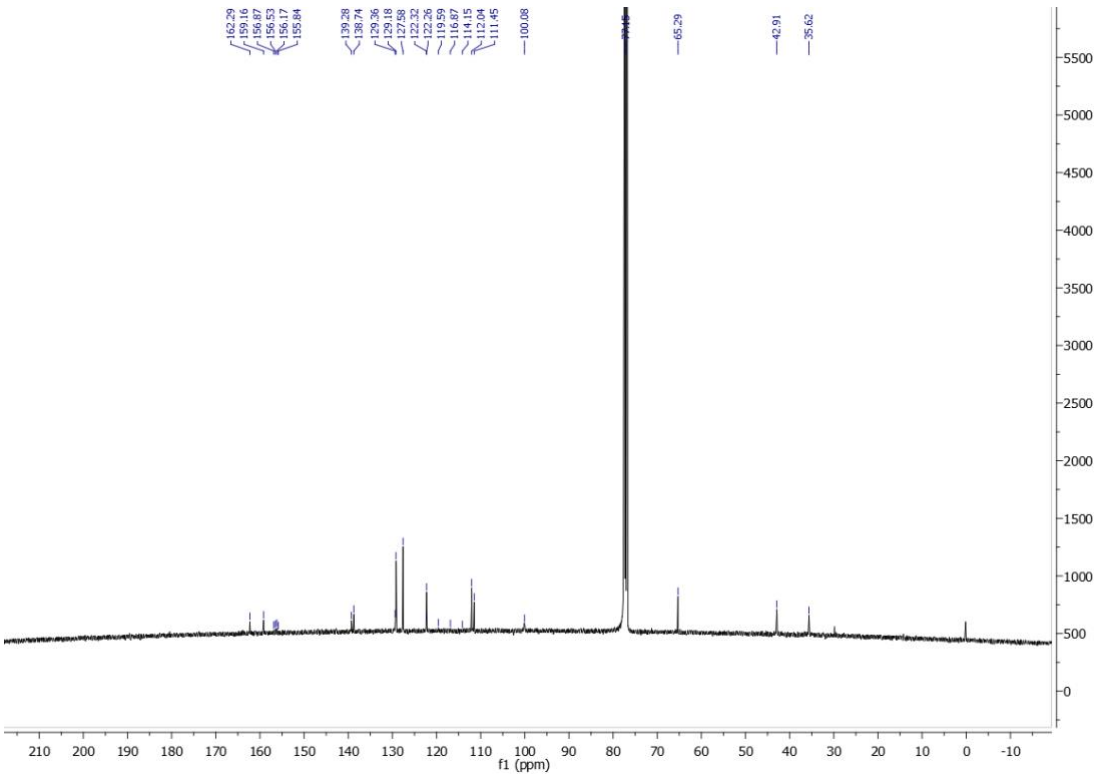

^{1}H and $^{13}C\{^{1}H\}$ spectrum of compound **28.**

Appendix III. Publication III: Discovery of Novel Isoxazole-Based Small-Molecule Toll-Like Receptor 8 Antagonists

The following pages include the article “Discovery of Novel Isoxazole-Based Small-Molecule Toll-Like Receptor 8 Antagonists” as it was published in Journal of Medicinal Chemistry by the American Chemical Society.

Reprinted with permission from:

Troy Matziol, Valerij Talagayev, Tjaša Slokan, Nika Strašek Benedik, Janine Holze, Matej Sova, Gerhard Wolber, Günther Weindl. Discovery of Novel Isoxazole-Based Small-Molecule Toll-Like Receptor 8 Antagonists. J Med Chem. 2025;68(4):4888–4907.

Doi: 10.1021/acs.jmedchem.4c03148

Journal of Medicinal Chemistry

pubs.acs.org/jmc

Article

Discovery of Novel Isoxazole-Based Small-Molecule Toll-Like Receptor 8 Antagonists

Troy Matziol,[‖] Valerij Talagayev,[‖] Tjaša Slokan, Nika Strašek Benedik, Janine Holze, Matej Sova,* Gerhard Wolber,* and Günther Weindl*

Cite This: *J. Med. Chem.* 2025, 68, 4888−4907

Read Online

ACCESS | Metrics & More | Article Recommendations | Supporting Information

ABSTRACT: Toll-like receptor 8 (TLR8) recognizes viral and bacterial RNA, initiating inflammatory responses that are crucial for innate immunity. Dysregulated TLR8 signaling contributes to autoimmune diseases, including systemic lupus erythematosus and rheumatoid arthritis, driving chronic inflammation and tissue damage. Therefore, targeting TLR8 has gained attention as a promising therapeutic strategy. We report a novel selective TLR8 antagonist scaffold identified through computational modeling and simulation. In silico-guided rational drug design and synthesis led to potent isoxazole-based compounds that were characterized by structure−activity relationships. The most active compounds inhibited TLR8-mediated signaling in cell lines and primary cells, reduced MyD88 recruitment, suppressed NF-κB- and IRF-dependent signaling, and decreased inflammatory responses. In silico and pharmacological analyses demonstrated competitive binding to the pocket of chemical ligands within the TLR8 dimerization interface. These highly selective and potent TLR8 antagonists possess favorable physicochemical properties, representing potential clinical candidates for TLR8-targeted therapy.

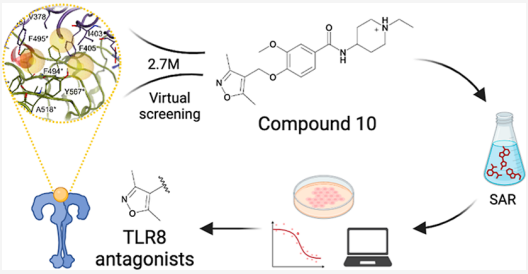

INTRODUCTION

Toll-like receptors (TLRs) are germline-encoded pattern recognition receptors (PRRs) that initiate immune responses by recognizing pathogen-associated molecular patterns (PAMPs) and damage-associated molecular patterns (DAMPs) derived from pathogens or damaged cells. As critical components of the innate immune system, TLRs play a key role in immune defense.[1,2] The human TLR family consists of TLR1-10, with TLR3/7/8/9 localized on endosomal membranes.[3] Among the endosomal TLRs, TLR8 has emerged as a pivotal regulator in various immune-mediated disorders due to its distinct signaling pathways and biological functions.[4,5] Primarily expressed in innate immune cells, such as monocytes, macrophages, and dendritic cells, TLR8 recognizes single-stranded RNA molecules from pathogens or damaged host cells.[6−8] This recognition leads to the recruitment of adaptor protein MyD88 and the activation of downstream signaling pathways involving nuclear factor-κB (NF-κB) and interferon regulatory factors (IRFs). Dysregulated TLR8 signaling has been implicated in the pathogenesis of autoimmune diseases, including systemic lupus erythematosus (SLE) and rheumatoid arthritis (RA), where persistent TLR8 activation contributes to chronic inflammation and tissue damage.[9−11] TLR8 has also been recognized to play a significant role in the regulation of viral infections.[12,13]

The therapeutic potential of targeting TLR8 has recently generated significant interest, particularly in the development of TLR8 antagonists.[6,14−17] Selective TLR8 antagonists are designed to modulate aberrant TLR8 signaling and restore immune homeostasis in diseases characterized by TLR8 hyperactivity. For example, small-molecule TLR8 antagonists have demonstrated potential for modulating cytokine levels in autoimmune diseases such as SLE and RA.[14,18] Several TLR7/8 ligands, including small molecules and antibodies, have been identified and are currently in preclinical and clinical trials.[19,20] Enpatoran (M5049), a synthetic small-molecule TLR7/8 antagonist, is currently being investigated as a potential treatment for SLE.[21] However, selective TLR8 antagonists have yet to be fully explored in clinical studies.

No naturally occurring antagonists of TLR8 have been identified to date. A recent preprint suggests that endogenous 2′-*O*-methyl guanosine RNA fragments might act as antagonists of TLR7/8.[22] Unlike agonists, which benefit from a synergistic effect that enhances the affinity of uridine, a common RNA-building block found in animals and viruses, similar synergistic mechanisms for antagonist recognition have yet to be identified. Nonetheless, advances in understanding TLR8 pharmacology have significantly facilitated the development of TLR8 antagonists. Structural studies of the inactivated

Received: December 20, 2024
Revised: February 3, 2025
Accepted: February 7, 2025
Published: February 14, 2025

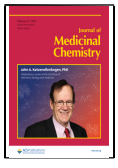

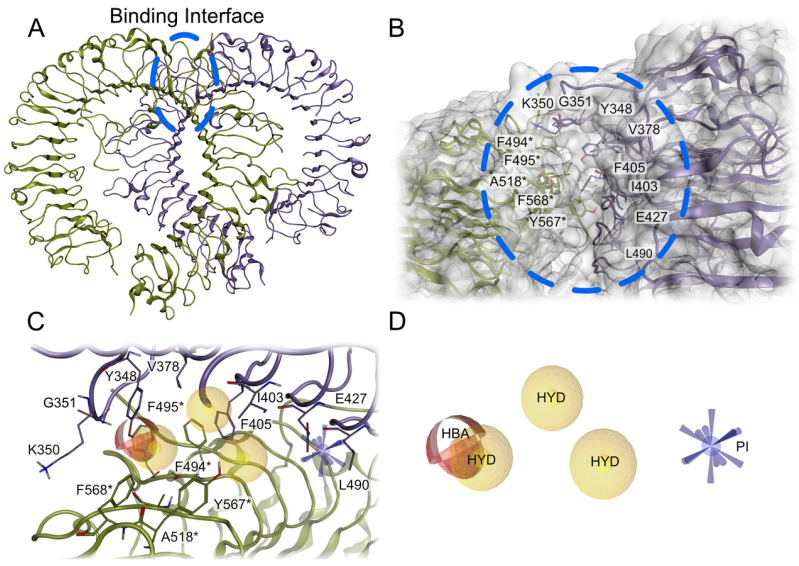

Figure 1. Structure of TLR8 binding interface with virtual screening 3D pharmacophore. (A) Structure of TLR8 with the binding interface of the homodimers. (B) Zoom view of the TLR8 antagonist binding site. (C) Binding site of TLR8 antagonists with the generated 3D pharmacophore. (D) 3D pharmacophore,[31−33] which was used for virtual screening. The asterisk denotes the chain B. Color code: yellow spheres, hydrophobic contacts (HYD); red spheres, hydrogen bond acceptor (HBA); blue sphere with cones, positive ionizable (PI); purple and green ribbons and atoms, TLR8 homodimers; gray surface, TLR8 protein surface.

TLR8 dimer bound to antagonists have offered valuable insights into how TLR8 activity can be regulated. Despite this progress, research into the inhibitory mechanisms of TLR8 remain in its early stages.[14,18] By targeting specific regions within the TLR8 receptor, novel antagonists can block ligand recognition and disrupt downstream signaling events.[23] Previously, we have identified selective TLR8 antagonists through structure-based virtual screening approaches, which inhibited TLR8-mediated responses in the low μM range,[16,17] and potent TLR8 antagonists have been described as tool compounds in the literature.[14,15]

In this study, we identified novel, highly potent small-molecule TLR8 antagonists through a structure−activity relationship (SAR)-based approach. Extensive biological characterization of the active virtual hits revealed compound **10** as a potential clinical candidate. Compound **10** demonstrated high selectivity, potency, and bioavailability as a competitive antagonist of TLR8 with no observed cytotoxic effects.

RESULTS

Virtual Screening Identifies Novel Isoxazole Scaffold. To investigate the interactions between known TLR8 antagonists and the receptor, we analyzed all recently published crystal structures containing cocrystallized TLR8 (RCSB PDB: 6KYA, 6TY5, 6V9U, 6ZJZ, 7R52, 7R53, 7R54, 7RC9)[21,24−27] (Figure S1). These structures consistently revealed that the antagonists bind at the uridine-binding site,[15,28,29] located at the interface of the TLR8 homodimer (Figure 1A). Within this binding site, all cocrystallized antagonists establish a key hydrogen bond acceptor interaction with the backbone amide of G351, a central feature of their binding mode.[18,21,24−27] Surrounding G351, residues such as F494, F495, Y348*, and V378* (where asterisks denote chain B residues) contribute additional hydrophobic contacts through their lipophilic side chains. Ionic interactions between E427 and the aliphatic amine groups of several antagonists (as observed in 6TY5, 6 V9U, 6ZJZ, 7R53, 7R54, and 7RC9)[21,24−27] further stabilize binding (Figure 1B). Using LigandScout,[30] we developed a 3D pharmacophore[31−33] to represent the common binding features of these antagonists, using the coordinate frame of PDB entry 7RC9[30] as a reference. The pharmacophore highlights essential interactions within the binding pocket including a hydrogen bond acceptor near G351, a positively ionizable feature adjacent to E427, and three hydrophobic features. These hydrophobic features align with key residues: the first near Y348, K350, and F494*; the second near V378 and F405; and the third close to I403, F494*, and A518* (Figure 1C,D). Together, these features encapsulate the shared interaction profile of TLR8 antagonists, providing a basis for a 3D pharmacophore virtual screening campaign.

To understand how the 3D pharmacophore would perform in discriminating between active and inactive compounds, we statistically validated the 3D pharmacophore using two sets of compounds: the first, Set A, consisted of 158 known active molecules retrieved from ChEMBL[34−36] (IC_{50} < 1000 nM), in addition to 231 known inactive compounds from ChEMBL (labeled as inactive or IC_{50} > 1000 nM), as well as 8406 decoys with physicochemical properties similar to the active molecules. The validation with both active and inactive compounds yielded only true positives, showing that all the active compounds were correctly recognized as active, while the validation of active molecules with diverse molecules with physicochemical properties similar to those of the active compounds yielded 58 false positives, showing that the pharmacophore recognizes diverse molecules with similar physicochemical properties as active molecules. To test the ability of the 3D pharmacophore to identify compounds that have low IC_{50} values, a second validation of Set B was performed using compounds with IC_{50} values below 50 nM. Thus, 47 compounds with IC_{50} values below 50 nM were labeled as actives and were validated with the previously mentioned 231 inactive compounds and 2538 molecules with

https://doi.org/10.1021/acs.jmedchem.4c03148
J. Med. Chem. 2025, 68, 4888−4907

physicochemical properties similar to the active compounds from Set B, generated from the active compounds of set B. This validation showed that against the inactive compounds, 19 out of 47 true positive compounds of the set B were retrieved with no false positive virtual screening hits, while the validation with the molecules with physicochemical properties similar to the active compounds from set B resulted in 29 false positive hits (Figure S2A−D), showing overall good performance in retrospective model validation.

Following the retrospective validation of the 3D pharmacophore model, we performed a prospective virtual screening using a commercial library of 2.7 million compounds to obtain potentially potent compounds, yielding 18310 virtual hits. These were then subjected to a two-step consensus molecular docking protocol using the crystal structure with the highest resolution (PDB entry 7RC9)[30] (see Experimental Section: Molecular Docking). This molecular docking protocol resulted in 42 compounds with 5 compounds containing an already known dimethoxyphenyl scaffold,[37] 22 compounds containing an already known pyridine scaffold,[37] and 12 compounds containing a novel isoxazole scaffold. We selected the isoxazole scaffold compounds for further experimental testing due to their novelty (Table S1).

Biological Characterization of Hit Compounds. To experimentally confirm our in silico predictions, the 12 hit compounds were tested for their activity and cell viability in hTLR8-HEK293 reporter cells. None of the compounds showed agonistic effects (Figure S3A). Four of the 12 compounds, representing a hit rate of 33%, showed no cytotoxic effects (Figure S3B) and over 75% inhibition of NF-κB at 10 μM (Figure S3C and Table S2) when stimulated with the TLR8 agonist TL8-506, and therefore were selected for IC_{50} testing (Figure S4). Compounds **10** and **12** demonstrated IC_{50} values below 0.5 μM (Table 1) and were comparable to Enpatoran, a TLR7/8 dual antagonist currently under clinical investigation for SLE and cutaneous lupus erythematosus (CLE).[38]

Given the strong homology between TLR7 and TLR8 and their many common ligands,[28] achieving high selectivity for TLR8 is challenging. To verify the selectivity, we tested compounds **10**, **11**, and **12** for IC_{50} in hTLR7-HEK293 reporter cells. Compounds **10** and **12** demonstrated >100-fold selectivity, indicating a strong preference for TLR8 over TLR7 (Table 1 and Figure S5). TLR8 preference was confirmed for compound **11**, a close analogue of compound **10** but with lower potency at TLR8. In contrast, Enpatoran preferentially inhibited TLR7-mediated responses with a TLR7/TLR8 selectivity factor below 0.05.

Structure−Activity Relationship of Isoxazole-Based TLR8 Antagonists. The promising inhibitory effects of compounds with an isoxazole scaffold prompted us to explore the chemical space by in silico-guided chemical synthesis to decipher the binding mode and structural basis of TLR8 inhibition. An in silico SAR evaluation was performed to analyze the binding modes of the derivatives and identify the differences in the interactions of those with the protein. For this, we performed molecular docking studies. The main differences in the derivatives consisted of the presence or absence of a methoxy group on the phenyl ring in addition to the difference of the substituent in the para position of the phenyl ring. The length of the substituent played an important role in the SAR as shown by compounds **34** and **35**. These compounds mainly differ in the substituent on the piperidine ring, with compound **34** having a methyl group, while **35** contains an isopropyl moiety (Figure 2A). The length of the isopropyl moiety allows **35** to form an additional hydrophobic interaction with Leu490, facilitated by the closer proximity of the isopropyl group compared to the shorter methyl group of **38**. Thus, the main difference in these compounds is the hydrophobic interaction with Leu490, which affects the activity of the compound. Another important aspect of the SAR analysis was the presence or absence of the methoxy group. Examples of this analysis are compounds **31** and **38**. Compound **31**, which contains the methoxy group, loses the hydrophobic contact with Ala518* that is present in compound **38**; thus, the absence of the methoxy group increases the potency of **31** (Figure 2B). These results highlight the importance of the substituent length and the methoxy group on the potency of the compounds.

Table 1. Potencies for Inhibition of NF-κB Activity in hTLR8- and hTLR7-HEK293 Reporter Cells[a]

Compound	Structure	IC_{50} [μM] (95% CI)		Selectivity factor
		hTLR8-HEK293	hTLR7-HEK293	IC_{50} (TLR7)/ IC_{50} (TLR8)
1	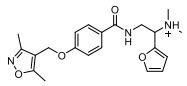	3.57 (1.99-5.66)	n.d.	n.d.
10	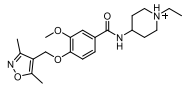	0.402 (0.254-0.613)	>50	>138
11	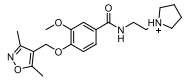	6.62 (4.23-9.81)	>50	>10
12	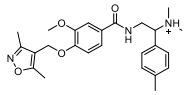	0.500 (0.236-0.957)	>50	>102
Enpatoran	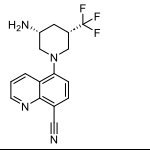	0.285 (0.232-0.347)	≤ 0.05	< 0.18

[a]IC_{50} values were calculated from concentration−response curves (Figures S4 and S5). n.d. = not determined.

The synthesis began with methyl 4-hydroxybenzoate or methyl 4-hydroxy-3-methoxybenzoate, which was alkylated with 4-(chloromethyl)-3,5-dimethylisoxazole (Scheme 1). In the second step, the esters **13** and **14** were hydrolyzed with 1 M NaOH and the obtained carboxylic acids **15** and **16** were coupled with the appropriate amine using HATU as a coupling reagent to give amides **17**-**39**. 4-((3,5-Dimethylisoxazol-4-yl)methoxy)benzoic acid was also coupled with *tert*-butyl 4-aminopiperidine-1-carboxylate to give the amide **42**, and in the next step, the Boc protecting group was removed with trifluoroacetic acid. The obtained 4-((3,5-dimethylisoxazol-4-yl)methoxy)-*N*-(piperidin-4-yl)benzamide (**43**) was then alkylated with butyl or allyl bromide to give amides **40** and **41**, respectively.

To optimize and evaluate the scaffold and in silico predictions, these synthesized compounds were screened as described above (Figure S6). Thirteen of 26 compounds showed over 80% inhibition at 10 μM (Table S3), and 12 were selected for IC_{50} testing (Figure S7). However, none of the compounds demonstrated IC_{50} values lower than those of

https://doi.org/10.1021/acs.jmedchem.4c03148
J. Med. Chem. 2025, 68, 4888−4907

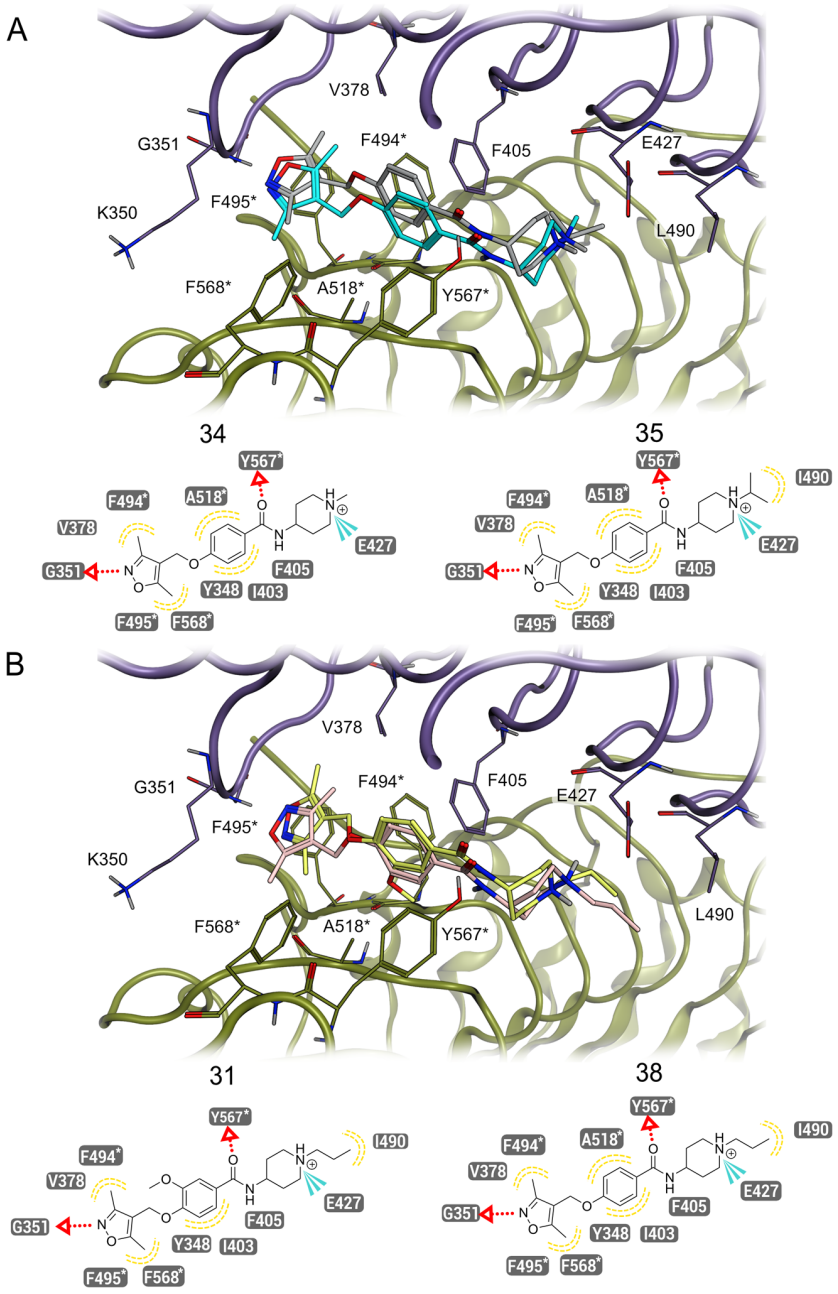

Figure 2. In silico SAR study of compounds **34**, **35**, **31**, and **38**. (A) Compound **34** has a methyl group at the piperidine ring and thus is not able to perform a hydrophobic interaction with Leu40, while compound **35** has an isopropyl group at the piperidine, which leads to an additional hydrophobic interaction with L490. (B) Compound **31** has a methoxy group at the phenyl ring, which leads to the loss of the hydrophobic interaction with Ala518*. Compound **38**, which lacks the methoxy group at the phenyl ring, shows a hydrophobic interaction with Ala518*. The asterisk denotes the chain B. Color code: purple and green ribbons atoms, TLR8 homodimers; turquoise atoms, compound **34**; gray atoms, compound **35**; yellow atoms, compound **31**; pink atoms, compound **38**.

compounds **10** and **12** from the initial screening (Table 2). Therefore, we proceeded with further biological characterization of these compounds. Nevertheless, we have obtained relevant information about the SAR. Among the synthesized compounds, the tertiary amines with piperidine ring (e.g., **26**, **31**, **34**, **35**, **38**−**41**; Tables S3 and S4) are the most potent TLR8 antagonists with IC_{50} values around 1 μM. As already mentioned above, the nature of the substituent on the piperidine ring is important since the compounds with a longer (e.g., **31**, **38**−**41**) or branched (e.g., **28** and **35**) substituent on the piperidine ring exhibited higher potency compared to the methyl-substituted or unsubstituted piperidine derivatives (e.g., **33**, **34**, **43**). The piperidine ring has to be alkylated since compound **43** with unsubstituted piperidine showed only 32% inhibition of NF-κB at 10 μM. The most optimal substituent on the piperidine ring is ethyl, which is present in compound **10** or allyl in the case of compounds without a methoxy group. In compounds **24** and **26**, the piperidine ring is inverted and bonded directly to the carbonyl group, resulting in the distance that is one atom shorter. The bound pyrrolidine and piperidine in the para position of the piperidine enable the activity of these compounds. In this case,

https://doi.org/10.1021/acs.jmedchem.4c03148
J. Med. Chem. 2025, 68, 4888−4907

Scheme 1. Synthesis of Isoxazole-Based Compounds.[a]

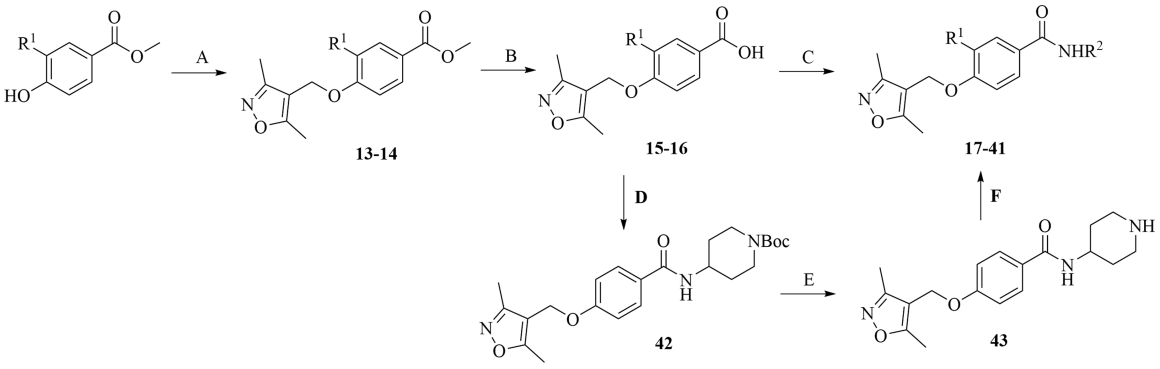

[a]Reagents and conditions:(A) K_2CO_3, 4-(chloromethyl)-3,5-dimethylisoxazole, KI, acetone, 50 °C, 24 h; (B) 1 M NaOH, 1,4-dioxane, rt, 24h.(C) HATU, amine (R^2NH_2), DIPEA, THF, rt, 24h;(D) HATU, tert-butyl 4-aminopiperidine-1-carboxylate, DIPEA, THF, rt, 24 h; (E) TFA, DCM, rt, 24 h; (F) alkyl bromide, K_2CO_3, KI, acetonitrile, reflux, 2 h

the methoxy group on the phenyl ring is beneficial since derivative without the methoxy group (e.g., **21**) is less potent. Likewise, the methoxy derivative **10** is more potent than compound **39**, which does not possess a methoxy group. Furthermore, replacing the piperidine with pyrrolidine results in the less potent isoxazole derivatives **19**, **27**, and **29**. Piperazine derivatives showed only moderate (compounds **17**, **22**, and **23**) or low inhibition (compounds **30** and **36**) of NF-κB at 10 μM.

Compounds 10 and 12 Selectively Inhibit TLR8-Mediated Inflammation and Signaling. Next, we examined the inhibitory effects of the two lead compounds across various assays, cell lines, and primary cells. Activation or inhibition of TLR8 modulates downstream signaling pathways, significantly influencing cytokine production.[39] In THP-1 macrophages, compounds **10** and **12** demonstrated potent TLR8-mediated TNF inhibition with IC_{50} values of 0.037 and 0.12 μM, respectively (Figure 3A and Table 3). Cell viability remained unaffected up to 100 μM (Figure S8A). TNF production was selectively inhibited at 10 μM in response to the TLR8 agonists TL8-506 or CL075, without influencing responses to TLR2 or TLR4 agonists (Figure 3B). To reflect more physiologically relevant conditions, we tested peripheral mononuclear blood cells (PBMCs), which express various TLRs. Both compounds **10** (IC_{50} = 1.02 μM) and **12** (IC_{50} = 1.15 μM) showed lower potency than Enpatoran (IC_{50} = 0.074 μM) (Figure 3C and Table 3) without affecting cell viability up to 100 μM (Figure S8B).

Since compound **10** showed improved potency over compound **12** in all pharmacological parameters, we decided to further characterize this compound. To evaluate TLR specificity, compound **10** was tested against ligands for TLR2/1, TLR2/6, TLR3, TLR4, TLR5, TLR7, TLR8, and TLR9 using HEK293 reporter cells. The results demonstrated selective inhibition of TLR8, with no significant activity against other TLRs, confirming its high selectivity (Figure 4A). To confirm cytokine inhibition at the gene level, we analyzed mRNA expression levels of *TNF* and *IL1B* in TL8-506-stimulated THP-1 macrophages, which were significantly inhibited in the presence of compound **10** (Figure 4B). In general, IL-1β is released after priming and activation of macrophages.[40] TLR8 priming and subsequent NLRP3 activation by nigericin or ATP triggered IL-1β release, which was blocked by compound **10** (Figure 4C). Cell death was induced by the inflammasome activators in both primed and unprimed cells to the same extent and not reduced by the TLR8 antagonist (Figure 4D). Further investigation of upstream proteins involved in the NF-κB pathway demonstrated that compound **10** reduced p-NF-κB p65 and increased IκBα levels following TLR8 activation with TL8-506 (Figure 4E). When stimulated, respectively, with TLR8 and TLR4 agonists in THP1-Dual TLR4/MD-2/CD14 cells (hereafter referred to as THP-1 Dual cells), compound **10** showed selective and potent inhibition of TLR8-but not TLR4-mediated activation of the NF-κB and interferon regulatory factor (IRF) pathways (Figure 4F). Given that NF-κB and IRF activation in TLR8 occurs through the MyD88 pathway, we sought to determine whether compound **10** reduces the level of recruitment of MyD88 to the TLR8 receptor. While it is increasingly clear that TLR-induced myddosomes are long-lived and highly dynamic,[41] coimmunoprecipitation analysis in THP-1 macrophages demonstrated reduced MyD88 recruitment to TLR8 in the presence of compound **10** (Figure 4G). To complement the traditional single-end point assays, we used optical biosensor technology to measure whole TLR-mediated cell responses in a label-free environment.[42] In THP-1 Dual cells, no DMR signal was detected in the presence of compound **10** alone (Figure S9A), whereas TL8-506 and LPS induced a robust DMR signal during the recording period (Figure S9B,C). DMR signals were fully inhibited by high concentrations of compound **10** in TL8-506-stimulated cells (Figure S9B), while no inhibition was observed in the presence of LPS (Figure S9C). The concentration−effect curve for DMR signals at 250 min (Figure 4H) showed an IC_{50} of 0.855 μM (95% CI: 0.459−1.59 μM) for compound **10** in TLR8-activated cells.

Binding Mode Characterization of Compound 10. We performed in silico analysis of the binding mode of compound **10** to gain insight into the interactions between **10** and TLR8. We found that compound **10** shows a hydrogen bond interaction of the isoxazole with the backbone amide of G351 and a charge interaction of the protonated amine with the side chain of E427. The methyl groups of **10** form hydrophobic contacts with the side chains of Y348, K350, V378, F494*, F495*, and F568*. The phenyl ring forms hydrophobic contacts with the side chains of I403, F405, A518*, and Y567*, while the ethyl moiety establishes a hydrophobic contact with L490 (Figure 5A).

https://doi.org/10.1021/acs.jmedchem.4c03148
J. Med. Chem. 2025, 68, 4888−4907

Table 2. Potencies for Inhibition of NF-κB Activity in hTLR8-HEK293 Reporter Cells[a]

Compound	Structure	IC_{50} [μM] (95% CI) hTLR8-HEK293
19	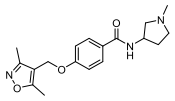	3.06 (1.34-4.79)
24	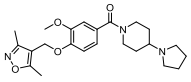	3.46 (2.53-4.73)
26	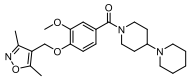	18.3 (13.0-25.8)
27	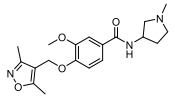	8.15 (6.04-11.2)
28	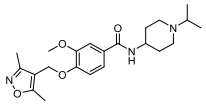	1.73 (1.41-2.13)
31	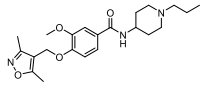	1.66 (1.40-1.97)
34	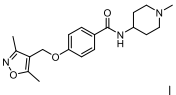	1.68 (1.39-2.06)
35	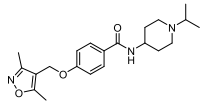	0.99 (0.87-1.13)
38	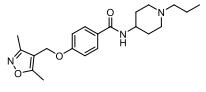	0.78 (0.69-0.89)
39	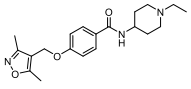	1.10 (0.97-1.25)
40	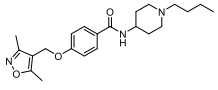	0.73 (0.45-1.21)
41	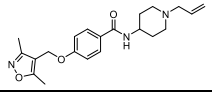	0.50 (0.32-0.79)

[a]IC_{50} values were calculated from concentration−response curves (Figure S7).

To further characterize these interactions, we performed molecular dynamics (MD) simulations and analyzed the frequency of the interactions using our recently developed method Dynophores.[43−47] This analysis method allowed us to evaluate the stability of the interactions throughout the simulation. The Dynophore analysis revealed that the isoxazole nitrogen maintains a hydrogen bond with the backbone amide of G351 for 80% of the simulation time. The methyl groups of the isoxazole show hydrophobic contacts with residues F261, Y348, V378, I403, F494*, F495*, A518*, and V520* during 100% of the simulation. The isoxazole ring shows π-interactions with Y348 and F495* during 44% of the simulation time. The phenyl ring shows hydrophobic contacts throughout the entire simulation duration with residues F261, I403, F405, F494*, A518*, and Y567*, while the charge interaction between the amine of **10** and E427 is formed during 92% of the simulation length (Figure 5B and Table S5).

To further evaluate the MD simulation results and to explore the binding cavity of TLR8, we conducted mutation studies. The starting point was an in silico inspection of the binding site of the cocrystallized ligand of PDB ID: 5WYZ.[48] This structure was selected because of the size of the ligand and its suitability in the binding site. Additionally, it was a crystal structure that was not used in generating the 3D pharmacophore for the virtual screening campaign. We analyzed the binding site to identify potential residues that could be modified to affect the activity of compound **10**. The residues G351, V378, F495, and A518 were selected for in silico mutation studies based on their interactions with **10**. Among those residues, G351 is notable for forming a hydrogen bond acceptor interaction with compound **10**. Introducing a G351P mutation would disrupt the hydrogen bond interaction with **10** and allow us to evaluate the importance of this hydrogen bond interaction for TLR8 inhibition. V378 and A518 have hydrophobic contacts with the methyl groups and the phenyl ring, respectively; therefore, their modification to amino acids with longer chains, such as methionine and leucine, would sterically affect the binding site and the binding mode of compound **10**. F495 is a residue that has hydrophobic contacts as well as aromatic interactions with **10**, so changing it to valine or leucine would prevent aromatic interactions and induce steric changes in the binding site.

To verify the in silico studies, plasmids with mutations in glycine (G351P), valine (V378M), and phenylalanine (F495L) were transfected into HEK293 cells. TLR8-mediated activity was observed only in the F495L mutation, while other mutations, as well as dual or triple combinations, showed no activity when stimulated with the agonist TL8-506 (Figure 6A). This indicates that G351 and V378 are critical amino acids for TLR8 ligand binding. Next, we focused on the F495L mutation to determine whether compound **10** could fit into the TLR8 binding cavity. TLR8 activation, triggered by the well-characterized agonists CL075 and TL8-506, was reduced by compound **10** and Enpatoran (Figure 6B). Both agonists are known to bind to TLR8 receptor binding site, as demonstrated by crystal structures.[49] Since Enpatoran is also characterized by a crystal structure,[21] this suggests that compound **10** binds to the same pocket in TLR8 as the two agonists and Enpatoran. This, together with our predicted modeling studies, indicates that TL8-506 and compound **10** compete for binding to the same receptor binding site. To further determine the binding mode, Schild analysis of both compounds in hTLR8-HEK293 reporter cells was performed. Compound **10** was able to shift the concentration−response curve parallel to the right (Figure 6C). The corresponding Schild plot was linear (Figure 6D). This is supported by significantly higher EC_{50} values and unchanged E_{max} values of TL8-506 in the presence of compound **10** (Table S6), indicating competitive antagonism.

Additional in silico studies were performed with compound **10** to explain the change of activity with the mutated HEK293 cells. The three main residues G351, V378, and F495* were separately mutated, and molecular docking studies were performed (Figure 7A). The G351P affects the backbone of residue 351. This leads to P351 not being able to establish a hydrogen bond with compound **10**. Consequently, we hypothesized that compound **10** would show no activity against the G351P mutant (Figure 7B,C). The V378 M

https://doi.org/10.1021/acs.jmedchem.4c03148
J. Med. Chem. 2025, 68, 4888−4907

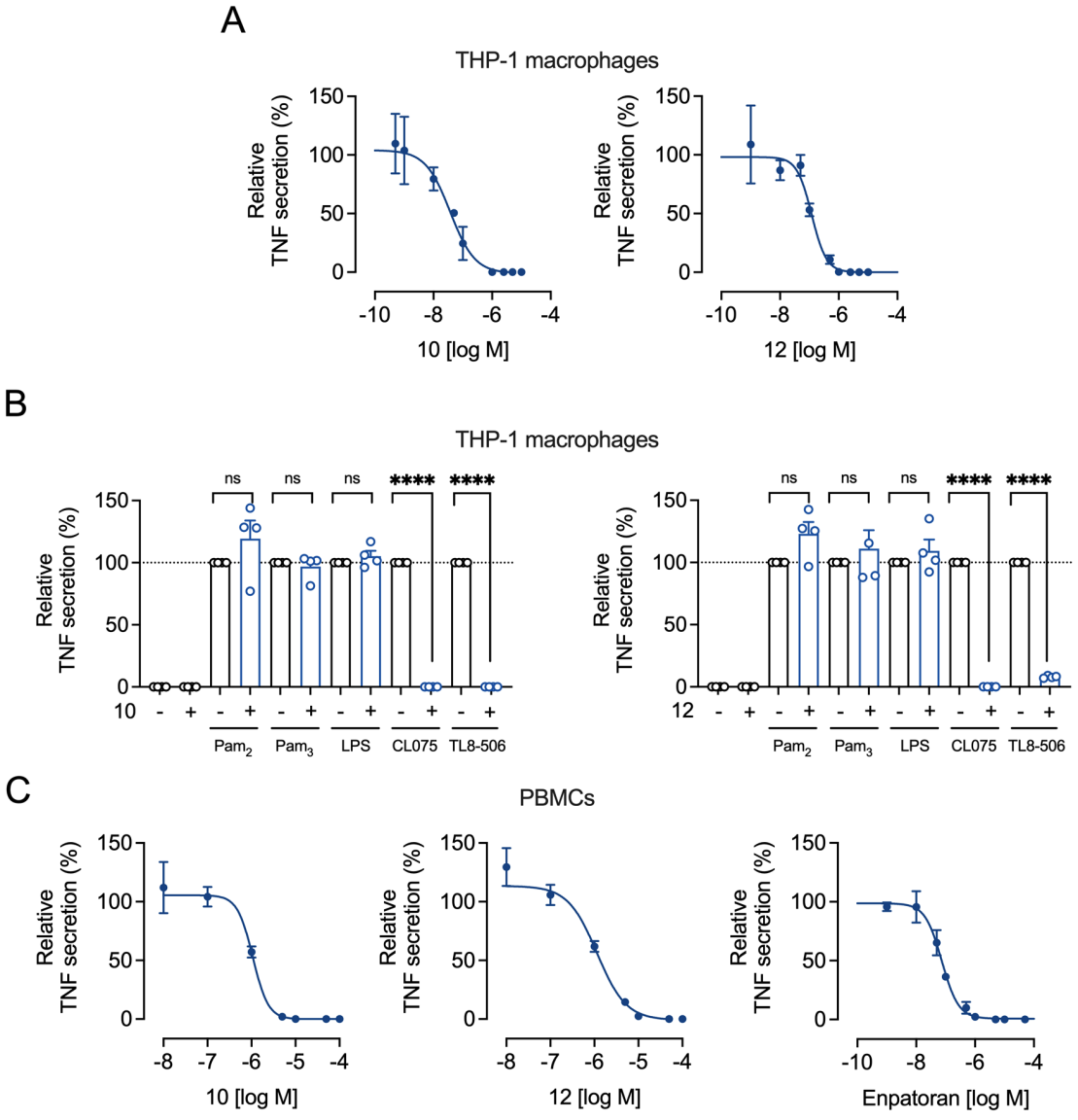

Figure 3. Potency and selectivity of compounds **10** and **12** in THP-1 macrophages and PBMCs. (A) THP-1 macrophages or (C) PBMCs were preincubated with increasing concentrations of the test compounds for 1 h and then stimulated with TL8-506 (0.6 μM) for 4 h. TNF release in the cell culture supernatants was determined by ELISA. For the calculation of concentration−response curves, nonlinear regression with variable slope (four parameters) was used. IC_{50} values are shown in Table 3. Mean ± SEM (n = 3). (B) THP-1 macrophages were preincubated with 10 μM of compound **10** or **12** for 1 h and then stimulated with TLR ligands Pam_3CSK_4 (100 ng/mL), Pam_2CSK_4 (10 ng/mL), LPS (10 ng/mL), CL075 (4 μM), and TL8-506 (3 μM) for 24 h. TNF release in the cell culture supernatants was determined by ELISA. Mean + SEM (n = 4). One-sample t-test, ns ≥0.05, *$P \leq 0.05$, **$P \leq 0.01$ ***$P \leq 0.001$, ****$P \leq 0.0001$.

Table 3. Potencies for Inhibition of TL8-506-Stimulated TNF Release in THP-1 Macrophages and PBMCs[a]

compound	IC_{50} [μM] (95% CI)	
	THP-1 macrophages	PBMCs
10	0.037 (0.020−0.066)	1.07 (0.76−1.53)
12	0.120 (0.090−0.172)	1.15 (0.71−1.76)
Enpatoran	n.d.	0.074 (0.058−0.096)

[a]IC_{50} values were calculated from concentration−response curves (Figure 3A, C). n.d. = not determined.

mutation increases the size of the side chain of residue 378, potentially obstructing compound **10** from assessing the TLR8 binding site. Thus, we hypothesized that compound **10** would be inactive in the presence of this mutation (Figure 7D,E). Conversely, the mutation F495L decreases the size of residue 495, similarly sterically affecting the TLR8 binding site as observed with the V378 M mutation. However, the mutation to the residue L495* does not hinder compound **10** from binding in the molecular docking experiment, allowing for a binding pose of compound **10** to be identified with the F495L mutation (Figure 7F,G).

The docking pose of compound **10** with TLR8 mutation F495L shows a hydrogen bond interaction with G351 in addition to an ionic interaction with E427. The hydrophobic interactions are identical to the interactions present in the wild-type TLR8 with the methyl groups displaying hydrophobic interactions with Y348, K350, V378, F494*, L495*, and F568*. The phenyl ring shows hydrophobic contacts with the side chains of I403, F405, A518*, and Y567*. The change

https://doi.org/10.1021/acs.jmedchem.4c03148
J. Med. Chem. 2025, 68, 4888−4907

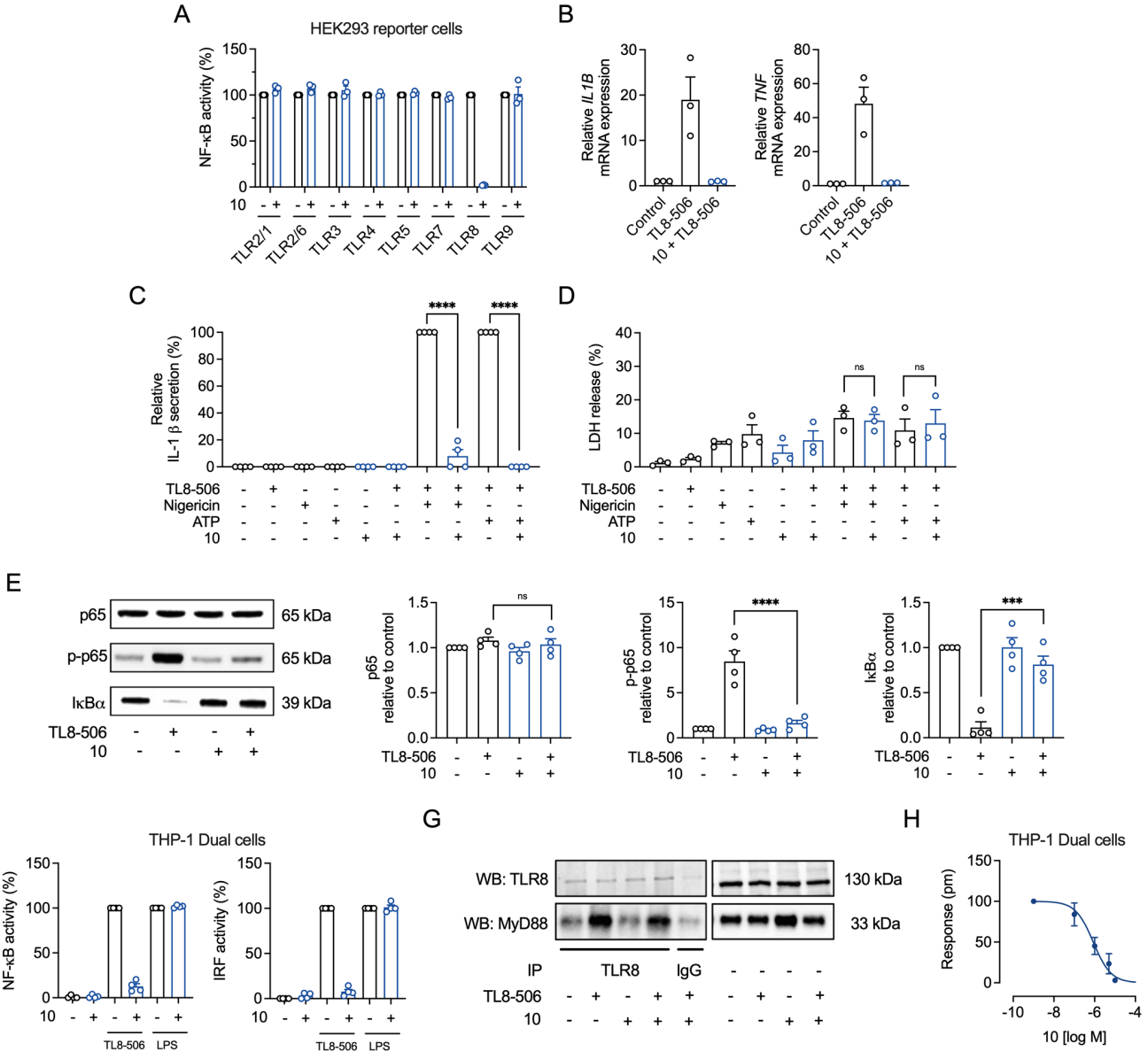

Figure 4. Compound **10** inhibits TLR8-mediated inflammation and signaling. (A) hTLR-HEK293 reporter cells were preincubated with or without compound **10** (10 μM) for 1 h and then stimulated with ligands for TLR2/1 (Pam_3CSK_4, 10 ng/mL), TLR2/6 (Pam_2CSK_4, 1 ng/mL), TLR3 (poly(I:C) HMW, 10 μg/mL), TLR4 (LPS *E. coli*, 10 ng/mL), TLR5 (flagellin *B. subtilits*, 100 ng/mL), TLR7 (CL307, 0.8 μM), TLR8 (TL8-506, 1.5 μM), or TLR9 (ODN2006, 5 μM). Supernatants were analyzed for TLR-mediated NF-κB activation by the SEAP reporter assay using QuantiBlue (OD_{620}) and normalized to the respective TLR agonist alone. Mean + SEM (n = 3). (B) THP-1 macrophages were preincubated with 10 μM of compound **10** for 1 h and then stimulated with TL8-506 (6 μM) for 1 h. *IL1B* and *TNF* gene expression was normalized to the housekeeping gene *GAPDH*, and values were compared to control (designated with a value of 1). Bar graphs show mean + SEM (n = 3). (C,D) THP-1 macrophages were primed with TL8-506 (0.6 μM) for 3 h and then stimulated for 3 h with ATP (5 mM). Compound **10** (10 μM) was added after priming for 1 h before stimulation. (C) IL-1β release in the cell culture supernatants was determined by ELISA. (D) LDH release was determined in cell culture supernatants. Results are shown as percentage of the maximum LDH release. Mean + SEM (n = 4). (E) THP-1 macrophages were incubated with compound **10** (10 μM) for 1 h and stimulated with TL8-506 (0.6 μM) for 15 min. Whole-cell lysates were used for WB. Bar graphs were obtained by densitometric analysis of Western blot data. Uncropped Western blots are shown in Figure S10A. Mean + SEM (n = 4). One-way ANOVA followed by Tukey's post-test, ns $\geq$0.05, *$P \leq 0.05$, **$P \leq 0.01$ ***$P \leq 0.001$, ****$P \leq 0.0001$. (F) THP1-Dual TLR4/MD-2/CD14 cells (THP-1 Dual cells) were preincubated with 10 μM of compound **10** for 1 h and then stimulated with TL8-506 (6 μM) or LPS from *E. coli* (10 ng/mL) for 24 h. Supernatants were analyzed for NF-κB activation by the SEAP reporter assay using QuantiBlue (OD_{620}) or for IRF activation by lucia luciferase using QuantiLuc. (G) THP-1 macrophages were incubated with compound **10** (10 μM) for 1 h, followed by TL8-506 (0.6 μM) stimulation for 30 min. Co-IP was performed using anti-hTLR8 antibodies and is depicted as Western blots (WB) for hTLR8 and MyD88. Uncropped Western blots are shown in Figure S10B. Mean + SEM (n = 4). (H) Inhibitory concentration−response curves resulting from DMR traces. THP1-Dual TLR4/MD-2/CD14 cells (THP-1 Dual cells) were preincubated with increasing concentration of compound **10** and afterward stimulated with 6 μM TL8-506. The concentration−response curve was derived from DMR signals recorded at 250 min shown in Figure S9B. Mean ± SEM (n = 3).

https://doi.org/10.1021/acs.jmedchem.4c03148
J. Med. Chem. 2025, 68, 4888−4907

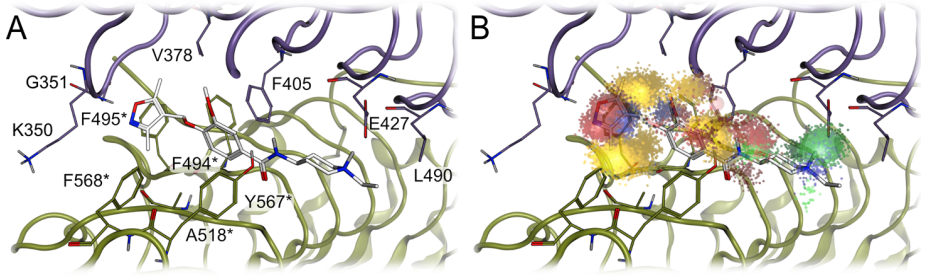

Figure 5. Toll-like receptor 8 binding interface with proposed binding mode of compound **10**. (A) TLR8 binding site interface with the hypothetical binding pose of **10**. (B) TLR8 binding site interface with the surmised binding pose of **10** and the Dynophore clouds representing the interactions between **10** and the TLR8 homodimer. The asterisk denotes the chain B. Color code: yellow clouds, hydrophobic contact; red clouds, hydrogen bond acceptor; green clouds, hydrogen bond donor; dark blue clouds, aromatic interaction; light blue cloud, ionic interaction; white atoms, compound **10**; purple and dark green ribbons and atoms, TLR8 homodimers.

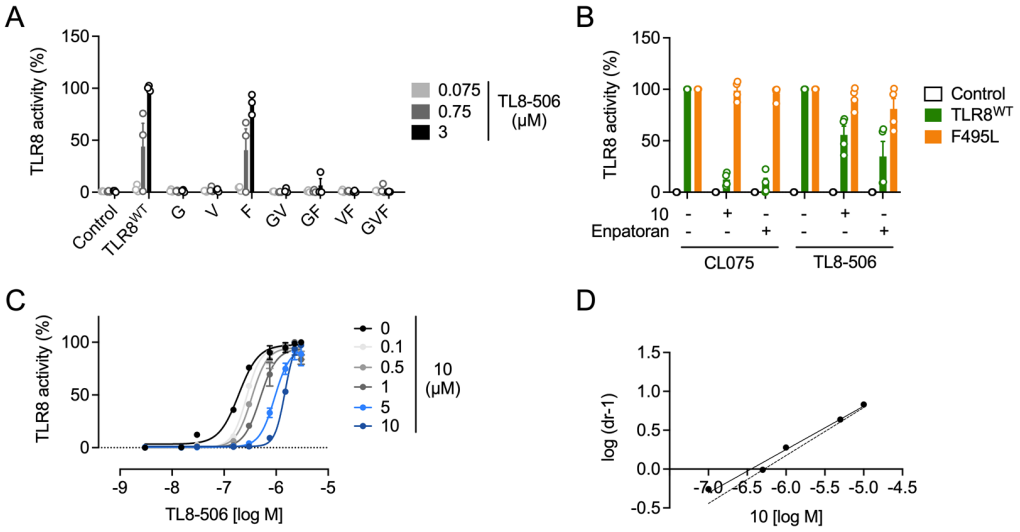

Figure 6. Compound **10** is a competitive antagonist of TL8-506. (A) HEK293 reporter control cells were transfected with mutant (G = Glycin351, V = Valin378, F = Phenylalanine495; GV, GF, VF, and GVF = dual or triple mutations of amino acids) or wildtype TLR8 plasmid ($TLR8^{WT}$). Cells were stimulated with indicated concentrations of TL8-506 for 24 h. Supernatants were analyzed for TLR8-mediated NF-κB activation by SEAP reporter assay using QuantiBlue (OD_{620}) and normalized to TL8-506. Mean + SEM (n = 3). (B) HEK293 reporter control cells were transfected with mutant or wildtype TLR8 plasmid. Cells were preincubated with either compound **10** (2 μM) or Enpatoran (1 μM) for 1 h and then stimulated with TL8-506 (3 μM) or CL075 (4 μM) for 24 h. Supernatants were analyzed for TLR8-mediated NF-κB activation by the SEAP reporter assay using QuantiBlue (OD_{620}) and normalized to TL8-506 or CL075, respectively. Mean + SEM (n = 4). (C) hTLR8-HEK293 reporter cells were preincubated with indicated concentrations of compound **10** for 1 h and stimulated with increasing concentrations of TL8-506 for 24 h. Supernatants were analyzed for TLR8-mediated NF-κB activation by the SEAP reporter assay using QuantiBlue (OD_{620}). Calculated pharmacological parameters of the concentration−effect curves are depicted in Table S6. (D) Schild plot of (C). The lines show linear regression, with Schild slopes unconstrained (solid) or constrained to unity (dashed) (n = 3).

of F495* to leucine disrupts an aromatic interaction between compound **10** and residue 495* (Figure 7H).

DISCUSSION AND CONCLUSIONS

Since the identification of the first small-molecule TLR8 antagonist,[15] little progress has been made for the exploration of selective antagonists. Given the crucial role of TLR8 in inflammatory and autoimmune diseases, the development of selective and bioavailable antagonists holds significant therapeutic potential. However, this poses a challenge, as there is currently no model to adequately address TLR8 signaling in mice, where the receptor appears to be nonfunctional.[50]

In this study, we aimed to discover and characterize novel, potent, and selective TLR8 antagonists, with solubility and bioactivity profiles that have not been previously documented.

We performed a virtual screening campaign that involved generating a 3D pharmacophore based on available crystal structures. This pharmacophore was then used for a primary virtual screening, followed by molecular docking, which led to the identification of novel compounds. These compounds contain an isoxazole scaffold that forms hydrogen bonds with the backbone of Gly351, ultimately inhibiting TLR8. The compounds also contain an aliphatic amine, which is responsible for a key ionic interaction with the Glu427 residue. The SAR studies revealed that the length of the substitute at the para position of the phenyl ring influences the activity of the compounds, which is mainly due to the hydrophobic interaction with the Leu490 residue, which is shown to be present in the docking poses of compounds that display higher activity. The most optimal substituent is *N*-ethylpiperidine, attached to the phenyl ring via an amide group. It was also observed that the presence of a methoxy

https://doi.org/10.1021/acs.jmedchem.4c03148
J. Med. Chem. 2025, 68, 4888−4907

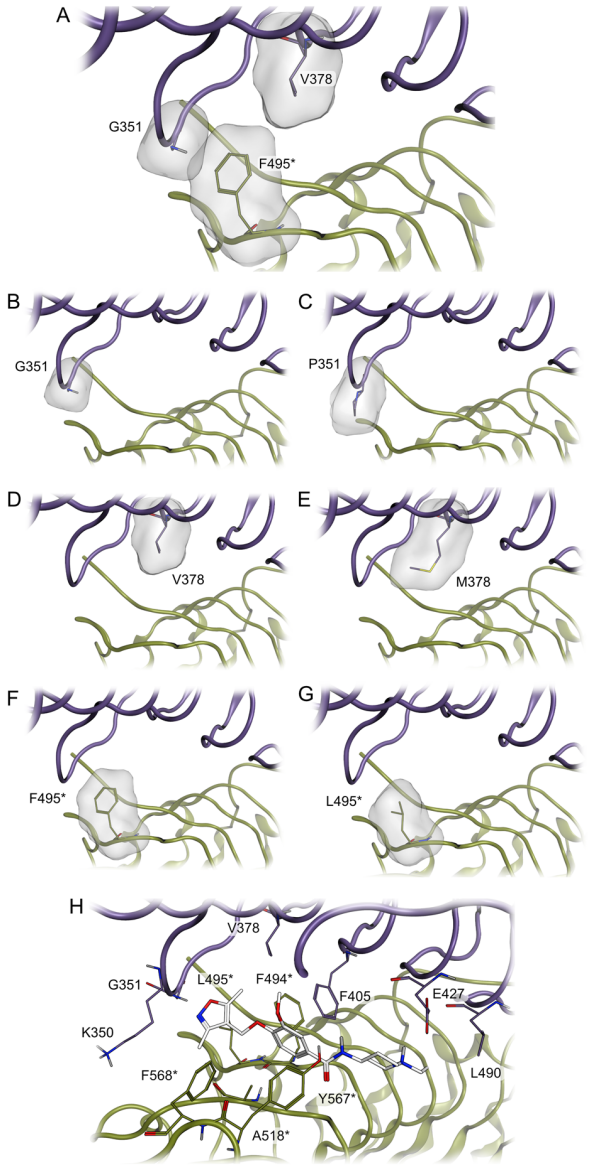

Figure 7. Illustration of the mutation studies of TLR8 and compound **10** binding mode with F495L mutation. TLR8 binding site interface with the highlighted surface shape of (A) residues G351, V378, and F495*; (B) residue G351 and (C) mutated residue P351; (D) residue V378 and (E) mutated residue M378; (F) residue F495* and (G) mutated residue L495*. (H) TLR8 binding site interface with the hypothetical binding pose of compound **10** with the F495L mutation. The asterisk denotes the chain B. Color code: white atoms, compound **10**; purple and dark green ribbons, TLR8 homodimers; gray surface, TLR8 protein surface.

group at the phenyl ring reduces the activity of some compounds. This reduction was attributed to the methoxy group pushing the phenyl ring further from the Ala518 residue, thereby losing the hydrophobic interaction between the phenyl ring and Ala518, which in turn affects the activity of the compounds. Consequently, removing the methoxy group is preferred for higher potency in *N*-alkylated piperidines. Additionally, the size of the ring is important, with piperidine being favored over pyrrolidine.

Among 12 isoxazole analogues selected based on SAR studies and biologically screened, along with an additional 26 analogues synthesized to explore the chemical space within the TLR8 binding cavity, two compounds showed significant, concentration-dependent, and highly selective inhibition of TLR8-mediated signaling in HEK293 reporter cells overexpressing TLR8, with IC_{50} values in the nanomolar range. Compound **10** and **12** showed significant reduction of cytokines in various cell lines and human primary cells without affecting responses of other TLRs, particularly TLR7.

To demonstrate that compound **10** effectively inhibits TLR8-mediated pathways in the innate immune system, we evaluated its effect on TLR8 signaling and key signaling proteins using a panel of end point assays and real-time analysis with label-free optical biosensor technology. Co-immunoprecipitation confirmed that compound **10** inhibited TLR8 activation by reducing MyD88 recruitment and inhibited the activation of NF-κB and IRF pathways. Furthermore, our findings suggest that TL8-506 as TLR8 activator can be used for priming in the activation of the inflammasome pathway. We demonstrate that compound **10** reduces IL-1β secretion when incubated together with a TLR8 agonist and either nigericin or ATP. This finding highlights the possibility in treating autoimmune diseases such as RA,[51] which warrants further investigation.

Since the exploration of TLR8, the existence of at least two highly conserved binding sites for this receptor has been reported, one for ssRNA and small chemical ligands like TL8-506 or CL075, while the second site binds preferably to dinucleotide UG.[6,49] An additional binding site has been proposed, which is only formed during the resting state of TLR8 homodimer.[15] We hypothesized that our antagonist binds to this specific binding pocket. A SAR-based binding approach, combined with mutations in the TLR8 binding cavity, confirmed the ligand−receptor interaction within this pocket. We further addressed the mechanism of antagonism of compound **10**. CuCPT9a, highly potent TLR8 antagonist, has been reported to bind to the TLR8 ectodomain, as demonstrated by crystal structure analysis and ITC; however, the type of antagonism has not been experimentally confirmed.[15] In the Schild analysis, a parallel shift for compound **10** was observed, indicating that the analyzed parameters are most consistent with competitive antagonism. Although our study did not employ a direct binding assay, a potential limitation, our comprehensive methodological approach, combining pharmacological and in silico binding exploration, suggests that compound **10** binds within the TLR8 binding cavity.

Our findings provide strong evidence that compound **10** is a potent and highly bioavailable antagonist for TLR8. Overall, our study significantly advances our understanding of the mechanisms involved in designing and evolving new TLR8 antagonists that can regulate cytokine secretion and serve as therapeutic candidates for clinical applications.

EXPERIMENTAL SECTION

Pharmacophore Generation. The crystal structures of known TLR8 antagonists[18,21,24−27] were each separately loaded into LigandScout 4.4.[30] A structure-based 3D pharmacophore[31−33] for one of each cocrystallized ligand was generated. The 3D pharmacophores were overlapped with the reference pharmacophore of PDB ID: 7RC9[52] and the features, which were present in more than four of the overlapped 3D pharmacophores, were retained.

Pharmacophore Validation. TLR8 antagonists were retrieved from ChEMBL[34−36] and categorized into actives consisting of compounds with IC_{50} values below 1 μM and inactives for

https://doi.org/10.1021/acs.jmedchem.4c03148
J. Med. Chem. 2025, 68, 4888−4907

pharmacophore validation in addition to a set of decoys based upon actives generated in the DUD-E Decoys webpage.[52] The second validation set contained compounds with an IC_{50} value below 50 nM as actives with the previously used set of inactives. DUD-E Decoys were generated for the compounds with an IC_{50} value below 50 nM. The validation of the pharmacophore model and ROC (receiver operating characteristic) curves generation was performed in Ligandscout 4.4.[30]

Pharmacophore Virtual Screening. The 3D pharmacophore was used for a virtual screening campaign of the Enamine Screening collection database (version 2022, retrieved from enamine.com) consisting of 2.7 million compounds. The compounds protonation states were directly taken over from the Enamine screening collection and the salt remover module from RDKit[53] was applied to the compounds. The library was prepared using idbgen implemented in Ligandscout 4.4[30] with the settings generating 25 conformations for each ligand with a minimal surface accessibility threshold for a hydrophobicity score of 0.25. The virtual screening was performed using iScreen of LigandScout 4.4 with the default settings that consist of a minimum number of required features of 3 with 0 allowed features to omit. The scoring function used in iScreen was the absolute scoring function.

Protein Structure Preparation. The protein structure of the human TLR8 with a cocrystallized ligand fulfilling the 3D pharmacophore used for virtual screening with the highest resolution of 2.76 Å (PDB ID: 7RC9)[27] was prepared using MOE 2022 (Chemical Computing Group, Montreal, Canada). The crystallographic waters and buffer additives were removed, while the ligand was retained. The missing side chain modeling and capping was performed using the Structure Preparation utility. The protein was protonated using the Protonate 3D function[54] at pH 7 and temperature 300 K.

Molecular Docking. The obtained hits were docked into the prepared crystal structure of 7RC9[27] using GOLD 5.8.2[48] with the binding site being defined with the radius of 6 Å around the cocrystallized ligand. For the two-step consensus molecular docking protocol, 25 genetic algorithm runs per molecule were conducted using the ChemPLP scoring function.[55] The docking poses were selected by fulfillment of the interaction points in the respective 3D pharmacophore, consisting of a hydrogen bond acceptor, three hydrophobic features, and a positive ionizable. The selected docking poses were minimized with the Merck molecular force field 94 (MMFF94).[56] Compounds were selected from the minimized docking poses by visual inspection according to the fulfillment of the interaction points in the respective 3D pharmacophores in addition to conformational and structural sanity, resulting in 92 selected compounds. Subsequently, the selected compounds underwent a consecutive docking with GoldScore scoring function[37] and ChemScore scoring function.[48] Finally, all docking poses underwent the docking pose selection, docking pose minimization, and visual inspection with the selection criteria described above.

For the SAR in silico studies, the 25 genetic algorithm runs per molecule were conducted using the ChemPLP scoring function.[55] All docking poses underwent the docking pose selection, docking pose minimization, and visual inspection with the selection criteria described above.

Mutation Studies. For the mutation studies the crystal structure PDB ID: 5WYZ[48] was used. Point mutations G351P, V378L, F495V, and A518L were generated with Protein builder tool in MOE 2022 (Chemical Computing Group, Montreal, Canada) with the selection of the mutation residue followed by a side chain minimization with backbone tethering with the cocrystallized ligand being inactive, thus not affecting the mutation. The cocrystallized ligand was redocked into the crystal structure with the mutations with GOLD 5.8.2.[48] The binding site was defined with the radius of 6 Å around the cocrystallized ligand in the crystal structure with the mutation. For the molecular docking, 15 genetic algorithm runs per molecule were conducted using the GoldScore scoring function.[37] The docking poses were minimized with the Merck molecular force field 94 (MMFF94).[56] The final docking pose was selected by visual inspection according to fulfillment of conformational sanity.

The crystal structure PDB ID: 7RC9[30] was used for the molecular docking studies with compound **10**. The mutations G351P, V378L, and F495L were generated with Protein builder tool in MOE 2022 (Chemical Computing Group, Montreal, Canada) with the selection of the mutation residue followed by a side chain minimization with backbone tethering with the cocrystallized ligand being inactive, thus not affecting the mutation. Compound **10** was docked into the crystal structure with the mutations with GOLD 5.8.2.[48] The binding site was defined with the radius of 10 Å around the cocrystallized ligand in the crystal structure with the mutation. For the molecular docking, 25 genetic algorithm runs per molecule were conducted using the ChemPLP scoring function.[55] The docking poses were minimized with the Merck molecular force field 94 (MMFF94).[56] The final docking pose was selected by visual inspection according to the fulfillment of conformational sanity.

Molecular Dynamics Simulations. The molecular dynamics (MD) simulations were performed on RTX4090 and RTX3090 graphics processing units (NVIDIA Corporation, Santa Clara). The simulations for the TLR8 complex with **10** were prepared for molecular dynamics (MD) simulations using Maestro 11.7 (Schrödinger, LLC, New York, USA). The hydrogen bond network in both systems was optimized at pH 7.0 and temperature 300 K. The complex was placed in a TIP3P[57] water box with a 10 Å padding distance to the protein surface. The system was isotonized with 0.15 M NaCl. The system was parametrized using the OPLS 2005 force field[58] and relaxed using the default Desmond protocol. MD simulations were carried out with a constant number of particles, pressure, and temperature (*NPT* ensemble). During the main MD simulation, the constant temperature of 300 K was held using the Nose−Hoover thermostat.[59,60] The constant pressure of 1.01325 bar was preserved using the Martyna-Tobias-Klein method.[61] Three replicas with a duration of 50 ns each were simulated, each generating 1000 frames. The replicas were concatenated using VMD[62] and the combined trajectory of the protein and ligand was analyzed using the DynophoreApp in LigandScout 4.4.[30]

Virtual Screening Compound Purity Testing. The purification of virtual screening compounds **1**-**12** with HPLC was performed using an Agilent 1290 Infinity system with a binary pump, autosampler, column compartment, and Agilent 1260 DAD VL + detector. Mass spectrometric detection was performed using an Agilent 6130B Single Quadrupole MS. Compound purification was achieved with an Agilent Poroshell C18 column (100 × 2.1 mm, 2.7 μm particle size) at 30 °C with a flow rate of 0.400 mL/min. The mobile phase consisted of solvent A (water with 0.1% formic acid) and solvent B (acetonitrile with 0.1% formic acid). The gradient for the purification started with 5% solvent B, held for 1 min, and followed by a linear increase to 95% solvent B over 8 min. The gradient was maintained at 95% solvent B for 2 min before returning to 5% solvent B in 0.5 min. The total runtime was 11 min. The injection volume was 0.5 μL. The DAD signals were monitored at 254, 210, and 220 nm, with a scan rate of 40 Hz. MS detection was performed in both positive and negative ion modes, scanning a mass range of m/z 50−700. All compounds were >95% pure by HPLC analysis (Figure S12). ^{1}H NMR spectra for purchased active compounds **1** and **10**-**12** are provided in Figure S13.

General Methods and Analytical Data for Synthesized Compounds. Reagents and solvents were purchased from commercial sources (e.g., BLDpharm, Sigma-Aldrich, Acros Organics, Apollo Scientific, Fluorochem, Enamine, and TCI). Reactions were monitored by thin-layer chromatography on silica gel plates (Merck DC Fertigplatten Kieselgel 60 GF254) and visualized under UV light or stained with the appropriate staining reagents. Flash column chromatography was performed on silica gel 60 (mesh size 70−230; Merck) using the indicated solvents. Yields are for the purified products and were not optimized. 1H and 13C NMR spectra were recorded at 295 K in $CDCl_3$, DMSO-d_6 or acetone-d_6 (Avance III NMR spectrometer; Bruker, MA, USA) using a decoupling inverse 1H probe (Broadband). The coupling constants (J) are given in Hz,

https://doi.org/10.1021/acs.jmedchem.4c03148
J. Med. Chem. 2025, 68, 4888−4907

and the splitting patterns are designated as follows: s, singlet; bs, broad singlet; d, doublet; t, triplet; q, quartet; dd, doublet of doublets; dt, doublet of triplets; m, multiplet. Mass spectra (Expression CMS mass spectrometer; Advion, NY, USA) and high-resolution mass measurements (Exactive Plus Orbitrap mass spectrometer; Thermo Fischer Scientific, MA, USA) were performed at the Faculty of Pharmacy, University of Ljubljana, Slovenia. HPLC analyses were performed on the Thermo Scientific UltiMate 3000 modular system (Thermo Fisher Scientific Inc.) equipped with a quaternary pump and a multiple wavelength detector. An ACQUITY UPLC HSS C18 column (2.1 × 50 mm; 1.8 μm), thermostated at 40 °C, was used with a flow rate of 0.4 mL/min; detection at 254 nm; and an eluent system of: A, 0.1% aqueous trifluoroacetic acid; B, acetonitrile. The following gradient was applied: 0−7 min, 5−95% B; 7−8 min, 95% B. All compounds were >95% pure by HPLC analysis. ^{1}H NMR, ^{13}C NMR, and HPLC traces for the synthesized active compounds are provided in Figure S14.

General Procedure A. Methyl 4-hydroxy-3-methoxybenzoate or methyl 4-hydroxybenzoate (1 equiv) was dissolved in acetone, and then K_2CO_3 (1.1 equiv), 4-(chloromethyl)-3,5-dimethylisoxazole (1 equiv), and KI (cat.) were added. The reaction mixture was stirred overnight at 50 °C. The solvent was evaporated and EtOAc was added to the residue. The organic phase was washed with water (2×) and brine, dried over anhydrous Na_2SO_4, filtered, and evaporated under reduced pressure. The product was used in the next step without further purification.

*Methyl 4-((3,5-Dimethylisoxazol-4-yl)methoxy)benzoate (**13**).* The compound was synthesized from methyl 4-hydroxybenzoate (32.86 mmol, 5.00 g), K_2CO_3 (36.15 mmol, 5.00 g), 4-(chloromethyl)-3,5-dimethylisoxazole (32.86 mmol, 4.78 g), and KI (cat.) according to general procedure A. Yield 53%; yellow solid; R_f = 0.43 (EtOAc/*n*-Hex, 2:1, v/v); ^{1}H NMR (400 MHz, DMSO-d_6): δ (ppm) = 2.22 (s, 3H), 2.42 (s, 3H), 3.82 (s, 3H), 5.02 (s, 2H), 6.99−7.23 (m, 2H), 7.75−8.12 (m, 2H).

*Methyl 4-((3,5-Dimethylisoxazol-4-yl)methoxy)-3-methoxybenzoate (**14**).* The compound was synthesized from methyl 4-hydroxy-3-methoxybenzoate (36.00 mmol, 6.56 g), K_2CO_3 (40 mmol, 5.53 g), 4-(chloromethyl)-3,5-dimethylisoxazole (36.00 mmol, 5.24 g) and KI (cat.) according to general procedure A. Yield 95%; white solid; R_f = 0.60 (EtOAc/*n*-Hex, 1:1, v/v); ^{1}H NMR (400 MHz, DMSO-d_6): δ (ppm) 2.22 (s, 3H), 2.41 (s, 3H), 3.81 (s, 3H), 3.83 (s, 3H), 5.00 (s, 2H), 7.21 (d, J = 8.5 Hz, 1H), 7.47 (d, J = 2.0 Hz, 1H), 7.61 (dd, J = 8.4, 2.0 Hz, 1H).

General Procedure B. An appropriate benzoate (1 equiv) was dissolved in 1 M NaOH and 1,4-dioxane and stirred overnight at room temperature. Diethyl ether was added to the reaction mixture, and phases were separated. One M HCl was added to the water phase, and the product precipitated.

*4-((3,5-Dimethylisoxazol-4-yl)methoxy)benzoic Acid (**15**).* The compound was synthesized from methyl 4-((3,5-dimethylisoxazol-4-yl)methoxy)benzoate (17.54 mmol, 4.58 g) and 1 M NaOH according to general procedure B. Yield 90%; white solid; R_f = 0.19 (EtOAc/*n*-Hex, 2:1, v/v); ^{1}H NMR (400 MHz, DMSO-d_6): δ (ppm) = 2.21 (s, 3H), 2.42 (s, 3H), 5.00 (s, 2H), 6.96−7.23 (m, 2H), 7.71−8.03 (m, 2H), 12.67 (br s, 1H).

*4-((3,5-Dimethylisoxazol-4-yl)methoxy)-3-methoxybenzoic Acid (**16**).* The compound was synthesized from methyl 4-((3,5-dimethylisoxazol-4-yl)methoxy)-3-methoxybenzoate (36.00 mmol, 10.50 g) and 1 M NaOH according to general procedure B. Yield 78%; white solid; R_f = 0.21 (EtOAc/*n*-Hex, 1:1, v/v); ^{1}H NMR (400 MHz, DMSO-d_6): δ (ppm) = 2.22 (s, 3H), 2.40 (s, 3H), 3.80 (s, 3H), 4.99 (s, 2H), 7.18 (d, J = 8.5 Hz, 1H), 7.47 (d, J = 1.9 Hz, 1H), 7.58 (dd, J = 8.4, 1.9 Hz, 1H), 12.75 (br s, 1H).

General Procedure C. An appropriate acid (1 equiv) was dissolved in anhydrous THF under an argon atmosphere, and then HATU (1.5 equiv) was added. An appropriate amine (1 equiv) and DIPEA (4 equiv) were then added to the stirred solution. The reaction mixture was stirred overnight at room temperature. EtOAc was then added and the obtained solution was washed with saturated $NaHCO_3$ solution. The organic phase was dried over anhydrous Na_2SO_4 and filtered, and the solvent was removed under reduced pressure. The residue was purified by flash column chromatography.

*4-Benzylpiperazin-1-yl(4-((3,5-Dimethylisoxazol-4-yl)methoxy)-phenyl)methanone (**17**).* The compound was synthesized from 4-((3,5-dimethylisoxazol-4-yl)methoxy)benzoic acid (0.22 mmol, 0.054 g), HATU (0.33 mmol, 0.126 g), 1-benzylpiperazine (0.22 mmol, 0.039 mL), and DIPEA (0.88 mmol, 0.153 mL) according to general procedure C. The compound was purified by flash column chromatography with EtOAc/*n*-Hex = 4/1 (v/v) as eluent. Yield 34%; white solid; R_f = 0.51 (EtOAc/*n*-Hex, 4:1, v/v); ^{1}H NMR (400 MHz, $CDCl_3$): δ (ppm) = 2.29 (s, 3H), 2.41 (s, 3H), 2.46 (br s, 4H), 3.51 (br s, 2H), 3.54 (s, 2H), 3.70 (br s, 2H), 4.80 (s, 2H), 6.92−6.96 (m, 2H), 7.27−7.35 (m, 5H), 7.37−7.41 (m, 2H); ^{13}C NMR (100 MHz, $CDCl_3$): δ (ppm) = 10.16, 11.19, 53.06, 59.57, 62.94, 77.22, 109.96, 114.47, 127.31, 128.35, 128.78, 129.14, 129.22, 137.57, 159.42, 159.69, 167.59, 169.99; HRMS (ESI$^+$) m/z calcd for $C_{24}H_{28}N_3O_3$ $[M + H]^+$ 406.21252; found, 406.21149; HPLC purity 100% at 254 nm (t_R = 3.373 min).

*4-((3,5-Dimethylisoxazol-4-yl)methoxy)-N-(2-(pyrrolidin-1-yl)-ethyl)benzamide (**18**).* The compound was synthesized from 4-((3,5-dimethylisoxazol-4-yl)methoxy)benzoic acid (0.61 mmol, 0.150 g), HATU (0.92 mmol, 0.348 g), 2-(pyrrolidine-1-yl)ethan-1-amine (0.61 mmol, 0.077 mL), and DIPEA (2.44 mmol, 0.425 mL) according to general procedure C. The compound was purified by flash column chromatography with DCM/MeOH = 9/1 (v/v) as eluent. Yield 14%; yellow oil; R_f = 0.20 (DCM/MeOH, 9:1, v/v); ^{1}H NMR (400 MHz, acetone-d_6): δ (ppm) = 2.07−2.13 (m, 4H), 2.24 (s, 3H), 2.43 (s, 3H), 3.45−3.47 (m, 6H), 3.77−3.81 (m, 2H), 5.04 (s, 2H), 7.08−7.12 (m, 2H), 7.89−7.93 (m, 2H), 8.15 (br s, 1H); ^{13}C NMR (100 MHz, acetone-d_6): δ (ppm) = 10.06, 10.94, 23.85, 38.01, 55.55, 57.45, 60.38, 111.04, 115.45, 127.19, 130.11, 160.30, 162.33, 168.35, 169.01; HRMS (ESI$^+$) m/z calcd for $C_{19}H_{26}N_3O_3$ $[M + H]^+$ 344.19687; found, 344.19599; HPLC purity 100.00% at 254 nm (t_R = 3.030 min).

*4-((3,5-Dimethylisoxazol-4-yl)methoxy)-N-(1-methylpyrrolidin-3-yl)benzamide (**19**).* The compound was synthesized from 4-((3,5-dimethylisoxazol-4-yl)methoxy)benzoic acid (0.61 mmol, 0.150 g), HATU (0.92 mmol, 0.348 g), 1-methylpyrrolidin-3-amine (0.61 mmol, 0.061 g), and DIPEA (2.44 mmol, 0.425 mL) according to general procedure C. The compound was purified by flash column chromatography with DCM/MeOH = 9/1 (v/v) as eluent. Yield 11%; white solid; R_f = 0.36 (DCM/MeOH, 9:1, v/v); ^{1}H NMR (400 MHz, acetone-d_6): δ (ppm) = 1.73−1.82 (m, 1H), 2.24 (s, 3H), 2.26−2.30 (m, 1H), 2.32 (s, 3H), 2.35−2.41 (m, 1H), 2.43 (s, 3H), 2.57 (dd, J = 9.6, 4.1 Hz, 1H), 2.67−2.77 (m, 2H), 4.45−4.64 (m, 1H), 5.00 (s, 2H), 7.02−7.06 (m, 2H), 7.69 (d, J = 6.2 Hz, 1H), 7.89−7.93 (m, 2H); ^{13}C NMR (100 MHz, acetone-d_6): δ (ppm) = 10.06, 10.94, 33.11, 42.01, 50.26, 55.70, 60.27, 63.34, 111.14, 115.13, 128.60, 128.62, 129.90, 160.32, 161.75, 166.24, 166.30, 168.30; HRMS (ESI$^+$) m/z calcd for $C_{18}H_{24}N_3O_3$ $[M + H]^+$ 330.18122; found, 330.18044; HPLC purity 99.38% at 254 nm (t_R = 2.873 min).

*4-((3,5-Dimethylisoxazol-4-yl)methoxy)-N-(4-methylpiperazin-1-yl)benzamide (**20**).* The compound was synthesized from 4-((3,5-dimethylisoxazol-4-yl)methoxy)benzoic acid (0.61 mmol, 0.150 g), HATU (0.92 mmol, 0.348 g), 4-methylpiperazin-1-amine (0.61 mmol, 0.073 mL), and DIPEA (2.44 mmol, 0.425 mL) according to general procedure C. The compound was purified by flash column chromatography with DCM/MeOH = 9/1 (v/v) as eluent. Yield 20%; white solid; R_f = 0.27 (DCM/MeOH, 9:1, v/v); ^{1}H NMR (400 MHz, acetone-d_6): δ (ppm) = 2.22 (s, 3H), 2.24 (s, 3H), 2.43 (s, 3H), 2.46 (s, 4H), 2.98 (s, 4H), 5.01 (s, 2H), 7.04 (d, J = 8.8 Hz, 2H), 7.82 (d, J = 8.5 Hz, 2H), 8.45 (s, 1H); ^{13}C NMR (100 MHz, acetone-d_6): δ (ppm) = 10.15, 11.19, 45.70, 54.31, 55.62, 59.60, 109.84, 114.52, 126.64, 129.03, 159.65, 160.97, 164.89, 167.65; HRMS (ESI$^+$) m/z calcd for $C_{18}H_{25}N_4O_3$ $[M + H]^+$ 345.19212; found, 345.19122; HPLC purity 99.67% at 254 nm (t_R = 2.760 min).

*(4-((3,5-Dimethylisoxazol-4-yl)methoxy)phenyl)(4-(pyrrolidin-1-yl)piperidin-1-yl)methanone (**21**).* The compound was synthesized from 4-((3,5-dimethylisoxazol-4-yl)methoxy)benzoic acid (0.61 mmol, 0.150 g), HATU (0.92 mmol, 0.348 g), 4-(pyrrolidin-1-

https://doi.org/10.1021/acs.jmedchem.4c03148
J. Med. Chem. 2025, 68, 4888−4907

yl)piperidine (0.61 mmol, 0.094 g), and DIPEA (2.44 mmol, 0.425 mL) according to general procedure C. The compound was purified by flash column chromatography with DCM/MeOH = 9/1 (v/v) as eluent. Yield 26%; yellow oil; R_f = 0.31 (DCM/MeOH, 9:1, v/v); ^{1}H NMR (400 MHz, $CDCl_3$): δ (ppm) = 1.50−1.62 (m, 2H), 1.80−1.85 (m, 4H), 2.05 (br s, 4H), 2.28 (s, 3H), 2.34−2.40 (m, 1H), 2.41 (s, 3H), 2.60−2.70 (m, 4H), 2.97 (br s, 2H), 4.81 (s, 2H), 6.93−6.95 (m, 2H), 7.36−7.38 (m, 2H); ^{13}C NMR (100 MHz, $CDCl_3$): δ (ppm) = 10.28, 11.30, 23.33, 31.41, 51.64, 59.71, 61.82, 110.12, 114.68, 129.05, 129.11, 159.54, 159.83, 167.72, 170.21; HRMS (ESI$^+$) m/z calcd for $C_{22}H_{30}N_3O_3$ $[M + H]^+$ 384.22817; found, 384.22718; HPLC purity 100.00% at 254 nm (t_R = 3.047 min).

*(4-Benzylpiperazin-1-yl)(4-((3,5-dimethylisoxazol-4-yl)methoxy)-3-methoxyphenyl)methanone (**22**).* The compound was synthesized from 4-((3,5-dimethylisoxazol-4-yl)methoxy)-3-methoxybenzoic acid (0.54 mmol, 0.150 g), HATU (0.81 mmol, 0.308 g), 1-benzylpiperazine (0.54 mmol, 0.094 mL), and DIPEA (2.16 mmol, 0.376 mL) according to general procedure C. The compound was purified by flash column chromatography with EtOAc/*n*-Hex = 4/1 (v/v) as eluent. Yield 14%; white solid; R_f = 0.25 (EtOAc/*n*-Hex, 4:1, v/v); ^{1}H NMR (400 MHz, $CDCl_3$): δ (ppm) = 2.30 (s, 3H), 2.38 (s, 3H), 2.46 (br s, 4H), 3.52 (br s, 2H), 3.54 (s, 2H), 3.74 (br s, 2H), 3.86 (s, 3H), 4.85 (s, 2H), 6.89 (d, J = 8.2 Hz, 1H), 6.94 (dd, J = 8.1, 1.8 Hz, 1H), 7.00 (d, J = 1.8 Hz, 1H), 7.28−7.35 (m, 5H); ^{13}C NMR (100 MHz, $CDCl_3$): δ (ppm) = 10.14, 11.16, 53.14, 55.95, 61.05, 62.93, 110.13, 111.52, 114.35, 119.81, 127.32, 128.35, 129.13, 129.73, 137.55, 148.71, 150.20, 159.81, 167.68, 169.92; HRMS (ESI$^+$) m/z calcd for $C_{25}H_{30}N_3O_4$ $[M + H]^+$ 436.22308; found, 436.22217; HPLC purity 98.60% at 254 nm (t_R = 3.333 min).

*4-((3,5-Dimethylisoxazol-4-yl)methoxy)-3-methoxy-N-(4-methylpiperazin-1-yl)benzamide (**23**).* The compound was synthesized from 4-((3,5-dimethylisoxazol-4-yl)methoxy)-3-methoxybenzoic acid (1.44 mmol, 0.400 g), HATU (2.16 mmol, 0.821 g), 4-methylpiperazin-1-amine (1.44 mmol, 0.121 mL), and DIPEA (5.76 mmol, 1.00 mL) according to general procedure C. The compound was purified by flash column chromatography with DCM/MeOH = 9/1 (v/v) as eluent. Yield 30%; white solid; R_f = 0.34 (DCM/MeOH, 9:1, v/v); ^{1}H NMR (400 MHz, $CDCl_3$): δ (ppm) = 2.30 (s, 3H), 2.34 (s, 3H), 2.39 (s, 3H), 2.65 (br s, 4H), 2.97 (br s, 4H), 3.90 (s, 3H), 4.88 (s, 2H), 6.70 (br s, 1H), 6.90 (d, J = 8.3 Hz, 1H), 7.19−7.24 (m, 1H), 7.39 (br s, 1H); ^{13}C NMR (100 MHz, $CDCl_3$): δ (ppm) = 10.15, 11.18, 45.75, 54.33, 55.69, 56.07, 60.99, 109.98, 111.52, 114.00, 119.09, 127.79, 150.37, 159.77, 165.04, 167.73; HRMS (ESI$^+$) m/z calcd for $C_{19}H_{27}N_4O_4$ $[M + H]^+$ 375.20268; found, 375.20167; HPLC purity 100.00% at 254 nm (t_R = 2.727 min).

*(4-((3,5-Dimethylisoxazol-4-yl)methoxy)-3-methoxyphenyl)(4-(pyrrolidin-1-yl)piperidin-1-yl)methanone (**24**).* The compound was synthesized from 4-((3,5-dimethylisoxazol-4-yl)methoxy)-3-methoxybenzoic acid (1.00 mmol, 0.277 g), HATU (1.50 mmol, 0.570 g), 4-(pyrrolidin-1-yl)piperidine (1.00 mmol, 0.154 g), and DIPEA (4.00 mmol, 0.697 mL) according to general procedure C. The compound was purified by flash column chromatography with DCM/MeOH = 9/1 (v/v) as eluent. Yield 56%; white solid; R_f = 0.33 (DCM/MeOH, 9:1, v/v); ^{1}H NMR (400 MHz, $CDCl_3$): δ (ppm) = 1.51−1.62 (m, 2H), 1.83−1.87 (m, 4H), 1.97 (br s, 4H), 2.30 (s, 3H), 2.39 (s, 3H), 2.40−2.48 (m, 1H), 2.63−2.75 (m, 4H), 2.98 (br s, 2H), 3.85 (s, 3H), 4.86 (s, 2H), 6.91 (d, J = 8.2 Hz, 1H), 6.94 (dd, J = 8.1, 1.7 Hz, 1H), 6.98 (d, J = 1.7 Hz, 1H); ^{13}C NMR (100 MHz, acetone-d_6): δ (ppm) = 10.04, 10.89, 23.96, 31.79, 51.94, 56.23, 61.38, 62.20, 111.40, 112.29, 115.52, 120.58, 131.25, 149.70, 151.00, 160.46, 168.32, 169.95; HRMS (ESI$^+$) m/z calcd for $C_{23}H_{32}N_3O_4$ $[M + H]^+$ 414.23873; found, 414.23751; HPLC purity 100.00% at 254 nm (t_R = 2.993 min).

*(4-((3,5-Dimethylisoxazol-4-yl)methoxy)-3-methoxyphenyl)(5-methylhexahydropyrrolo[3,4-c]pyrrol-2(1H)-yl)methanone (**25**).* The compound was synthesized from 4-((3,5-dimethylisoxazol-4-yl)methoxy)-3-methoxybenzoic acid (0.500 mmol, 0.139 g), HATU (0.75 mmol, 0.285 g), 2-methyloctahydropyrrolo[3,4-*c*]pyrrole (0.500 mmol, 0.063 g), and DIPEA (2.00 mmol, 0.348 mL) according to general procedure C. The compound was purified by flash column chromatography with DCM/MeOH = 9/1 (v/v) as eluent. Yield 49%; yellow oil; R_f = 0.22 (DCM/MeOH, 9:1, v/v); ^{1}H NMR (400 MHz, acetone-d_6): δ (ppm) = 2.26 (s, 3H), 2.37 (s, 3H), 2.39 (s, 3H), 2.52−2.69 (m, 4H), 2.85−2.93 (m, 2H), 3.45−3.54 (m, 2H), 3.74−3.82 (m, 2H), 3.83 (s, 3H), 4.97 (s, 2H), 7.08 (d, J = 1.1 Hz, 2H), 7.10−7.14 (m, 1H); ^{13}C NMR (100 MHz, acetone-d_6): δ (ppm) = 10.04, 10.89, 40.16, 41.74, 49.70, 56.21, 61.34, 62.85, 111.39, 112.64, 115.20, 121.13, 131.94, 149.92, 150.77, 160.46, 168.32, 168.76; HRMS (ESI$^+$) m/z calcd for $C_{21}H_{28}N_3O_4$ $[M + H]^+$ 386.20743; found, 386.20639; HPLC purity 100.00% at 254 nm (t_R = 2.740 min).

*[1,4′-Bipiperidin]-1′-yl(4-((3,5-dimethylisoxazol-4-yl)methoxy)-3-methoxyphenyl)methanone (**26**).* The compound was synthesized from 4-((3,5-dimethylisoxazol-4-yl)methoxy)-3-methoxybenzoic acid (1.44 mmol, 0.400 g), HATU (2.16 mmol, 0.821 g), 1,4′-bipiperidine (1.44 mmol, 0.243 g), and DIPEA (5.76 mmol, 1.00 mL) according to general procedure C. The compound was purified by flash column chromatography with DCM/MeOH = 9/1 (v/v) as eluent. Yield 27%; white solid; R_f = 0.25 (DCM/MeOH, 9:1, v/v); ^{1}H NMR (400 MHz, acetone-d_6): δ (ppm) = 1.59−1.64 (m, 2H), 1.71−1.86 (m, 6H), 2.12 (bd, J = 12.2 Hz, 2H), 2.26 (s, 3H), 2.39 (s, 3H), 3.13−3.25 (m, 5H), 3.33−3.39 (m, 4H), 3.83 (s, 3H), 4.97 (s, 2H), 6.99 (dd, J = 8.1, 1.9 Hz, 1H), 7.03 (d, J = 1.9 Hz, 1H), 7.09 (d, J = 8.2 Hz, 1H); ^{13}C NMR (100 MHz, acetone-d_6): δ (ppm) = 10.02, 10.87, 23.37, 25.08, 27.75, 46.40, 51.04, 56.25, 61.24, 64.29, 111.29, 112.05, 115.38, 120.60, 130.36, 149.86, 150.92, 160.44, 168.31, 170.27; HRMS (ESI$^+$) m/z calcd for $C_{24}H_{34}N_3O_4$ $[M + H]^+$ 428.25438; found, 428.25360; HPLC purity 100.00% at 254 nm (t_R = 3.127 min).

*4-((3,5-Dimethylisoxazol-4-yl)methoxy)-3-methoxy-N-(1-methylpyrrolidin-3-yl)benzamide (**27**).* The compound was synthesized from 4-((3,5-dimethylisoxazol-4-yl)methoxy)-3-methoxybenzoic acid (1.08 mmol, 0.300 g), HATU (1.62 mmol, 0.616 g), 1-methylpyrrolidin-3-amine (1.08 mmol, 0.112 mL), and DIPEA (4.32 mmol, 0.753 mL) according to general procedure C. The compound was purified by flash column chromatography with DCM/MeOH = 9/1 (v/v) as eluent. Yield 39%; white solid; R_f = 0.33 (DCM/MeOH, 9:1, v/v); ^{1}H NMR (400 MHz, methanol-d_4): δ (ppm) = 1.87−1.95 (m, 1H), 2.28 (s, 3H), 2.35−2.44 (m, 1H), 2.39 (s, 3H), 2.48 (s, 3H), 2.62−2.68 (m, 1H), 2.74 (dd, J = 10.4, 4.7 Hz, 1H), 2.91−2.98 (m, 2H), 3.88 (s, 3H), 4.53−4.59 (m, 1H), 4.97 (s, 2H), 7.09−7.11 (m, 1H), 7.45−7.48 (m, 2H), 1H from NH is exchanged; ^{13}C NMR (100 MHz, methanol-d_4): δ (ppm) = 9.94, 10.80, 32.55, 42.09, 50.97, 56.05, 56.44, 61.67, 62.82, 111.80, 112.28, 115.57, 121.72, 129.08, 151.32, 151.96, 161.45, 169.41, 169.56; HRMS (ESI$^+$) m/z calcd for $C_{19}H_{26}N_3O_4$ $[M + H]^+$ 360.19178; found, 360.19084; HPLC purity 97.63% at 254 nm (t_R = 2.850 min).

*4-((3,5-Dimethylisoxazol-4-yl)methoxy)-N-(1-isopropylpiperidin-4-yl)-3-methoxybenzamide (**28**).* The compound was synthesized from 4-((3,5-dimethylisoxazol-4-yl)methoxy)-3-methoxybenzoic acid (0.54 mmol, 0.150 g), HATU (0.81 mmol, 0.308 g), 1-isopropylpiperidin-4-amine (0.54 mmol, 0.077 g), and DIPEA (2.16 mmol, 0.376 mL) according to general procedure C. The compound was purified by flash column chromatography with DCM/MeOH = 9/1 (v/v) as eluent. Yield 33%; white solid; R_f = 0.20 (DCM/MeOH, 9:1, v/v); ^{1}H NMR (400 MHz, $CDCl_3$): δ (ppm) = 1.06 (d, J = 6.6 Hz, 6H), 1.49−1.56 (m, 2H), 2.01−2.15 (m, 2H), 2.30 (s, 3H), 2.34 (dd, J = 11.5, 2.2 Hz, 2H), 2.38 (s, 3H), 2.71−2.81 (m, 1H), 2.83−2.93 (m, 2H), 3.91 (s, 3H), 3.92−4.04 (m, 1H), 4.88 (s, 2H), 5.87 (d, J = 8.3 Hz, 1H), 6.90 (d, J = 8.3 Hz, 1H), 7.19 (dd, J = 8.3, 2.0 Hz, 1H), 7.43 (d, J = 2.0 Hz, 1H); ^{13}C NMR (100 MHz, $CDCl_3$): δ (ppm) = 10.15, 11.17, 18.42, 32.69, 47.39, 47.57, 54.58, 56.04, 61.03, 110.02, 111.39, 114.08, 118.76, 128.97, 150.15, 150.25, 159.78, 166.23, 167.73; HRMS (ESI$^+$) m/z calcd for $C_{22}H_{32}N_3O_4$ $[M + H]^+$ 402.23873; found, 402.23742; HPLC purity 98.91% at 254 nm (t_R = 2.803 min).

*4-((3,5-Dimethylisoxazol-4-yl)methoxy)-N-(1-ethylpyrrolidin-3-yl)-3-methoxybenzamide (**29**).* The compound was synthesized from 4-((3,5-dimethylisoxazol-4-yl)methoxy)-3-methoxybenzoic acid (0.54 mmol, 0.150 g), HATU (0.81 mmol, 0.308 g), 1-ethylpyrrolidin-3-amine dihydrochloride (0.54 mmol, 0.101 g), and DIPEA (2.16

https://doi.org/10.1021/acs.jmedchem.4c03148
J. Med. Chem. 2025, 68, 4888−4907

mmol, 0.376 mL) according to general procedure C. The compound was purified by flash column chromatography with DCM/MeOH = 9/1 (v/v) as eluent. Yield 10%; colorless oil; R_f = 0.22 (DCM/MeOH, 9:1, v/v); ^{1}H NMR (400 MHz, $CDCl_3$): δ (ppm) = 1.32 (t, J = 7.3 Hz, 3H), 1.97−2.11 (m, 1H), 2.30 (s, 3H), 2.38 (s, 3H), 2.55−2.65 (m, 1H), 2.75−2.82 (m, 1H), 2.78 (q, J = 7.3 Hz, 2H), 3.03−3.11 (m, 1H), 3.28−3.34 (m, 1H), 3.46−3.54 (m, 1H), 3.90 (s, 3H), 4.63−4.72 (m, 1H), 4.88 (s, 2H), 6.93 (d, J = 8.4 Hz, 1H), 7.18−7.26 (m, 1H), 7.24 (br s, 3H), 7.37 (dd, J = 8.3, 2.1 Hz, 1H), 7.41 (d, J = 2.0 Hz, 1H); ^{13}C NMR (100 MHz, $CDCl_3$): δ (ppm) = 10.15, 11.17, 12.60, 31.30, 49.10, 49.51, 53.47, 56.03, 59.96, 60.89, 109.95, 110.86, 113.88, 119.93, 127.13, 150.07, 150.71, 159.81, 167.68, 167.80; HRMS (ESI$^+$) m/z calcd for $C_{20}H_{28}N_3O_4$ $[M + H]^+$ 374.20743; found, 374.20677; HPLC purity 98.44% at 254 nm (t_R = 2.733 min).

*(4-((3,5-Dimethylisoxazol-4-yl)methoxy)-3-methoxyphenyl)(4-(2-hydroxyethyl)piperazin-1-yl)methanone (**30**).* The compound was synthesized from 4-((3,5-dimethylisoxazol-4-yl)methoxy)-3-methoxybenzoic acid (1.08 mmol, 0.300 g), HATU (1.62 mmol, 0.616 g), 2-(piperazin-1-yl)ethan-1-ol (1.08 mmol, 0.133 mL), and DIPEA (4.32 mmol, 0.753 mL) according to general procedure C. The compound was purified by flash column chromatography with DCM/MeOH = 20/1 (v/v) as eluent. Yield 24%; orange oil; R_f = 0.14 (DCM/MeOH, 20:1, v/v); ^{1}H NMR (400 MHz, $CDCl_3$): δ (ppm) = 2.31 (s, 3H), 2.39 (s, 3H), 2.55 (br s, 4H), 2.59−2.63 (m, 2H), 3.58−3.74 (m, 6H), 3.87 (s, 3H), 4.86 (s, 2H), 6.91 (d, J = 8.2 Hz, 1H), 6.95 (dd, J = 8.2, 1.8 Hz, 1H), 7.01 (d, J = 1.7 Hz, 1H), 1H from OH is exchanged; ^{13}C NMR (100 MHz, $CDCl_3$): δ (ppm) = 10.15, 11.17, 50.82, 53.02, 55.97, 57.79, 59.35, 61.00, 110.11, 111.47, 114.26, 119.83, 129.39, 148.84, 150.21, 159.83, 167.72, 170.03; HRMS (ESI$^+$) m/z calcd for $C_{20}H_{28}N_3O_5$ $[M + H]^+$ 390.20235; found, 390.20140; HPLC purity 100.00% at 254 nm (t_R = 2.427 min).

*4-((3,5-Dimethylisoxazol-4-yl)methoxy)-3-methoxy-N-(1-propylpiperidin-4-yl)benzamide (**31**).* The compound was synthesized from 4-((3,5-dimethylisoxazol-4-yl)methoxy)-3-methoxybenzoic acid (0.54 mmol, 0.150 g), HATU (0.81 mmol, 0.308 g), 1-propylpiperidin-4-amine (0.54 mmol, 0.086 mL), and DIPEA (2.16 mmol, 0.376 mL) according to general procedure C. The compound was purified by flash column chromatography with DCM/MeOH = 9/1 (v/v) as eluent. Yield 49%; white solid; R_f = 0.19 (DCM/MeOH, 9:1, v/v); ^{1}H NMR (400 MHz, $CDCl_3$): δ (ppm) = 0.94 (t, J = 7.4 Hz, 3H), 1.57−1.69 (m, 4H), 2.07−2.14 (m, 2H), 2.30 (s, 3H), 2.31−2.39 (m, 2H), 2.39 (s, 3H), 2.44−2.53 (m, 2H), 3.08 (bd, J = 12.0 Hz, 2H), 3.91 (s, 3H), 4.00−4.10 (m, 1H), 4.88 (s, 2H), 5.99 (d, J = 8.0 Hz, 1H), 6.91 (d, J = 8.3 Hz, 1H), 7.22 (dd, J = 8.3, 2.0 Hz, 1H), 7.41 (d, J = 2.0 Hz, 1H); ^{13}C NMR (100 MHz, $CDCl_3$): δ (ppm) = 10.15, 11.18, 11.76, 19.74, 31.60, 46.59, 52.59, 56.05, 60.51, 60.98, 110.00, 111.27, 113.98, 118.99, 128.56, 150.20, 150.28, 159.80, 166.40, 167.76; HRMS (ESI$^+$) m/z calcd for $C_{22}H_{32}N_3O_4$ $[M + H]^+$ 402.23873; found, 402.23753; HPLC purity 100.00% at 254 nm (t_R = 2.857 min).

*4-((3,5-Dimethylisoxazol-4-yl)methoxy)-3-methoxy-N-((1-methylpyrrolidin-3-yl)methyl)benzamide (**32**).* The compound was synthesized from 4-((3,5-dimethylisoxazol-4-yl)methoxy)-3-methoxybenzoic acid (0.54 mmol, 0.150 g), HATU (0.81 mmol, 0.308 g), (1-methylpyrrolidin-3-yl)methanamine (0.54 mmol, 0.062 g), and DIPEA (2.16 mmol, 0.376 mL) according to general procedure C. The compound was purified by flash column chromatography with DCM/MeOH = 9/1 (v/v) as eluent. Yield 15%; white solid; R_f = 0.04 (DCM/MeOH, 9:1, v/v); ^{1}H NMR (400 MHz, $CDCl_3$): δ (ppm) = 1.61−1.69 (m, 1H), 2.06−2.17 (m, 1H), 2.30 (s, 3H), 2.38 (s, 3H), 2.39 (s, 3H), 2.45−2.52 (m, 1H), 2.53−2.59 (m, 1H), 2.70 (dd, J = 9.2, 2.4 Hz, 1H), 2.90 (td, J = 8.8, 3.7 Hz, 1H), 3.38−3.44 (m, 1H), 3.37−3.51 (m, 2H), 3.90 (s, 3H), 4.88 (s, 2H), 6.92 (d, J = 8.3 Hz, 1H), 7.29 (dd, J = 8.3, 2.0 Hz, 1H), 7.46 (d, J = 1.9 Hz, 1H), 7.61 (br s, 1H); ^{13}C NMR (100 MHz, $CDCl_3$): δ (ppm) = 10.24, 11.26, 28.84, 36.38, 42.05, 45.75, 56.04, 56.31, 61.03, 61.12, 110.20, 111.24, 114.36, 119.29, 128.99, 150.13, 150.21, 159.91, 167.25, 167.86; HRMS (ESI$^+$) m/z calcd for $C_{20}H_{28}N_3O_4$ $[M + H]^+$ 374.20743; found, 374.20630; HPLC purity 100.00% at 254 nm (t_R = 2.657 min).

*4-((3,5-Dimethylisoxazol-4-yl)methoxy)-3-methoxy-N-(1-methylpiperidin-4-yl)benzamide (**33**).* The compound was synthesized from 4-((3,5-dimethylisoxazol-4-yl)methoxy)-3-methoxybenzoic acid (0.54 mmol, 0.150 g), HATU (0.81 mmol, 0.308 g), 1-methylpiperridin-4-amine (0.54 mmol, 0.068 mL), and DIPEA (2.16 mmol, 0.376 mL) according to general procedure C. The compound was purified by flash column chromatography with DCM/MeOH = 9/1 (v/v) as eluent. Yield 48%; white solid; R_f = 0.09 (DCM/MeOH, 9:1, v/v); ^{1}H NMR (400 MHz, $CDCl_3$): δ (ppm) = 1.54−1.65 (m, 2H), 2.01−2.09 (m, 2H), 2.14−2.23 (m, 2H), 2.30 (s, 3H), 2.32 (s, 3H), 2.38 (s, 3H), 2.85 (bd, J = 11.6 Hz, 2H), 3.91 (s, 3H), 3.94−4.04 (m, 1H), 4.88 (s, 2H), 5.92 (d, J = 7.8 Hz, 1H), 6.90 (d, J = 8.3 Hz, 1H), 7.21 (dd, J = 8.3, 2.1 Hz, 1H), 7.43 (d, J = 2.0 Hz, 1H); ^{13}C NMR (100 MHz, $CDCl_3$): δ (ppm) = 10.28, 11.30, 32.48, 46.32, 46.76, 54.69, 56.18, 61.16, 110.15, 111.50, 114.21, 118.97, 129.00, 150.32, 150.38, 159.91, 166.45, 167.87; HRMS (ESI$^+$) m/z calcd for $C_{20}H_{28}N_3O_4$ $[M + H]^+$ 374.20743; found, 374.20634; HPLC purity 100.00% at 254 nm (t_R = 2.643 min).

*4-((3,5-Dimethylisoxazol-4-yl)methoxy)-N-(1-methylpiperidin-4-yl)benzamide (**34**).* The compound was synthesized from 4-((3,5-dimethylisoxazol-4-yl)methoxy)benzoic acid (0.61 mmol, 0.150 g), HATU (0.92 mmol, 0.348 g), 1-methylpiperidin-4-amine (0.61 mmol, 0.077 mL), and DIPEA (2.44 mmol, 0.425 mL) according to general procedure C. The compound was purified by flash column chromatography with DCM/MeOH = 9/1 (v/v) as eluent. Yield 13%; white solid; R_f = 0.10 (DCM/MeOH, 9:1, v/v); ^{1}H NMR (400 MHz, $CDCl_3$): δ (ppm) = 1.51−1.61 (m, 2H), 2.00−2.07 (m, 2H), 2.12−2.18 (m, 2H), 2.28 (s, 3H), 2.29 (s, 3H), 2.41 (s, 3H), 2.79−2.84 (m, 2H), 3.93−4.02 (m, 1H), 4.82 (s, 2H), 5.90 (d, J = 7.7 Hz, 1H), 6.94−6.97 (m, 2H), 7.72−7.76 (m, 2H); ^{13}C NMR (100 MHz, $CDCl_3$): δ (ppm) = 10.27, 11.31, 32.57, 46.35, 46.71, 54.68, 59.77, 110.00, 114.63, 127.92, 128.89, 159.77, 160.96, 166.32, 167.75; HRMS (ESI$^+$) m/z calcd for $C_{19}H_{26}N_3O_3$ $[M + H]^+$ 344.19687; found,344.19585; HPLC purity 100.00% at 254 nm (t_R = 2.680 min).

*4-((3,5-Dimethylisoxazol-4-yl)methoxy)-N-(1-isopropylpiperidin-4-yl)benzamide (**35**).* The compound was synthesized from 4-((3,5-dimethylisoxazol-4-yl)methoxy)benzoic acid (0.61 mmol, 0.150 g), HATU (0.92 mmol, 0.348 g), 1-isopropylpiperidin-4-amine (0.61 mmol, 0.086 g), and DIPEA (2.44 mmol, 0.425 mL) according to general procedure C. The compound was purified by flash column chromatography with DCM/MeOH = 9/1 (v/v) as eluent. Yield 39%; white solid; R_f = 0.11 (DCM/MeOH, 9:1, v/v); ^{1}H NMR (400 MHz, $CDCl_3$): δ (ppm) = 1.06 (d, J = 6.6 Hz, 6H), 1.52−1.62 (m, 2H), 2.02−2.08 (m, 2H), 2.27 (s, 3H), 2.31−2.37 (m, 2H), 2.40 (s, 3H), 2.73−2.83 (m, 1H), 2.86−2.92 (m, 2H), 3.92−4.02 (m, 1H), 4.81 (s, 2H), 5.90 (d, J = 8.0 Hz, 1H), 6.93−6.96 (m, 2H), 7.71−7.74 (m, 2H); ^{13}C NMR (100 MHz, $CDCl_3$): δ (ppm) = 10.25, 11.29, 18.45, 32.61, 47.31, 47.73, 54.85, 59.74, 109.99, 114.60, 127.90, 128.89, 159.75, 160.92, 166.28, 167.73; HRMS (ESI$^+$) m/z calcd for $C_{21}H_{30}N_3O_3$ $[M + H]^+$ 372.22817; found,372.22702; HPLC purity 99.67% at 254 nm (t_R = 2.843 min).

*(4-((3,5-Dimethylisoxazol-4-yl)methoxy)phenyl)(4-(2-hydroxyethyl)piperazin-1-yl)methanone (**36**).* The compound was synthesized from 4-((3,5-dimethylisoxazol-4-yl)methoxy)benzoic acid (0.61 mmol, 0.150 g), HATU (0.92 mmol, 0.348 g), 2-(piperazin-1-yl)ethan-1-ol (0.61 mmol, 0.075 mL), and DIPEA (2.44 mmol, 0.425 mL) according to general procedure C. The compound was purified by flash column chromatography with DCM/MeOH = 20/1 (v/v) as eluent. Yield 22%; yellow solid; R_f = 0.08 (DCM/MeOH, 20:1, v/v); ^{1}H NMR (400 MHz, $CDCl_3$): δ (ppm) = 2.29 (s, 3H), 2.42 (s, 3H), 2.55 (br s, 4H), 2.59−2.62 (m, 2H), 3.49−3.83 (m, 6H), 4.82 (s, 2H), 6.94−6.97 (m, 2H), 7.39−7.43 (m, 2H); ^{13}C NMR (100 MHz, $CDCl_3$): δ (ppm) = 10.31, 11.43, 53.09, 56.00, 57.89, 59.46, 59.72, 110.08, 114.67, 128.67, 129.40, 159.67, 159.83, 167.74, 170.19; HRMS (ESI$^+$) m/z calcd for $C_{19}H_{26}N_3O_4$ $[M + H]^+$ 360.19178; found,360.19092; HPLC purity 97.84% at 254 nm (t_R = 2.453 min).

*4-((3,5-Dimethylisoxazol-4-yl)methoxy)-N-((1-methylpyrrolidin-3-yl)methyl)benzamide (**37**).* The compound was synthesized from 4-((3,5-dimethylisoxazol-4-yl)methoxy)benzoic acid (0.61 mmol, 0.150 g), HATU (0.92 mmol, 0.348 g), (1-methylpyrrolidin-3-yl)methanamine (0.61 mmol, 0.075 mL), and DIPEA (2.44 mmol, 0.425 mL) according to general procedure C. The compound was

https://doi.org/10.1021/acs.jmedchem.4c03148
J. Med. Chem. 2025, 68, 4888−4907

purified by flash column chromatography with DCM/MeOH = 9/1 (v/v) as eluent. Yield 22%; yellow solid; R_f = 0.02 (DCM/MeOH, 9:1, v/v); ^{1}H NMR (400 MHz, $CDCl_3$): δ (ppm) = 1.55−1.64 (m, 1H), 2.00−2.09 (m, 1H), 2.25 (s, 3H), 2.27−2.32 (m, 1H), 2.35 (s, 3H), 2.38 (s, 3H), 2.44−2.48 (m, 1H), 2.50−2.54 (m, 1H), 2.59 (dd, J = 8.8, 2.7 Hz, 1H), 2.82 (td, J = 8.7, 3.9 Hz, 1H), 3.33−3.46 (m, 2H), 4.80 (s, 2H), 6.91−6.95 (m, 2H), 7.58 (t, J = 4.8 Hz, 1H), 7.73−7.77 (m, 2H); ^{13}C NMR (100 MHz, $CDCl_3$): δ (ppm) = 10.14, 11.17, 28.66, 36.57, 41.85, 45.07, 50.49, 56.01, 59.56, 60.54, 109.94, 114.42, 127.67, 128.85, 159.70, 160.71, 167.21, 167.64; HRMS (ESI$^+$) m/z calcd for $C_{19}H_{26}N_3O_3$ $[M + H]^+$ 344.19687; found,344.19525; HPLC purity 99.02% at 254 nm (t_R = 2.683 min).

*4-((3,5-Dimethylisoxazol-4-yl)methoxy)-N-(1-propylpiperidin-4-yl)benzamide (**38**).* The compound was synthesized from 4-((3,5-dimethylisoxazol-4-yl)methoxy)benzoic acid (0.61 mmol, 0.150 g), HATU (0.92 mmol, 0.348 g), 1-propylpiperidin-4-amine (0.61 mmol, 0.096 mL), and DIPEA (2.44 mmol, 0.425 mL) according to general procedure C. The compound was purified by flash column chromatography with DCM/MeOH = 9/1 (v/v) as eluent. Yield 40%; white solid; R_f = 0.23 (DCM/MeOH, 9:1, v/v); ^{1}H NMR (400 MHz, $CDCl_3$): δ (ppm) = 0.93 (t, J = 7.4 Hz, 3H), 1.54−1.72 (m, 4H), 2.08−2.13 (m, 2H), 2.27−2.33 (m, 2H), 2.29 (s, 3H), 2.42 (s, 3H), 2.44−2.47 (m, 2H), 3.01−3.08 (m, 2H), 4.01−4.09 (m, 1H), 4.83 (s, 2H), 5.98 (d, J = 7.9 Hz, 1H), 6.95−6.98 (m, 2H), 7.73−7.76 (m, 2H); ^{13}C NMR (100 MHz, $CDCl_3$): δ (ppm) = 10.17, 11.20, 11.81, 19.86, 31.80, 46.63, 52.53, 59.63, 60.54, 109.85, 114.51, 127.56, 128.80, 159.67, 160.89, 166.27, 167.66; HRMS (ESI$^+$) m/z calcd for $C_{21}H_{30}N_3O_3$ $[M + H]^+$ 372.22817; found,372.22724; HPLC purity 97.87% at 254 nm (t_R = 2.900 min).

*4-((3,5-Dimethylisoxazol-4-yl)methoxy)-N-(1-ethylpiperidin-4-yl)benzamide (**39**).* The compound was synthesized from 4-((3,5-dimethylisoxazol-4-yl)methoxy)benzoic acid (0.81 mmol, 0.200 g), HATU (1.22 mmol, 0.462 g), 1-ethylpiperidin-4-amine (0.81 mmol, 0.104 g), and DIPEA (3.24 mmol, 0.564 mL) according to general procedure D. The compound was purified by flash column chromatography using DCM/MeOH = 9/1 (v/v) as eluent. Yield 31%; white solid; R_f = 0.18 (DCM/MeOH, 9:1, v/v); ^{1}H NMR (400 MHz, $CDCl_3$): δ (ppm) = 1.10 (t, J = 7.2 Hz, 3H), 1.51−1.61 (m, 2H), 2.05−2.17 (m, 4H), 2.29 (s, 3H), 2.42 (s, 3H), 2.43 (q, J = 7.2 Hz, 2H), 2.92 (bd, J = 11.4 Hz, 2H), 3.92−4.08 (m, 1H), 4.83 (s, 2H), 5.86 (d, J = 7.6 Hz, 1H), 6.95−6.98 (m, 2H), 7.72−7.76 (m, 2H); ^{13}C NMR (100 MHz, $CDCl_3$): δ (ppm) = 10.17, 11.21, 12.27, 32.44, 47.12, 52.06, 52.35, 59.62, 109.85, 114.48, 127.79, 128.75, 159.67, 160.81, 166.15, 167.64; HRMS (ESI$^+$) m/z calcd for $C_{20}H_{28}N_3O_3$ $[M + H]^+$ 358.21252; found,358.21224; HPLC purity 100.00% at 254 nm (t_R = 2.737 min).

*tert-Butyl 4-(4-((3,5-dimethylisoxazol-4-yl)methoxy)-benzamido)piperidine-1-carboxylate (**42**).* The compound was synthesized from 4-((3,5-dimethylisoxazol-4-yl)methoxy)benzoic acid (1.21 mmol, 0.300 g), HATU (1.82 mmol, 0.690 g), *tert*-butyl 4-aminopiperidine-1-carboxylate (1.21 mmol, 0.243 g), and DIPEA (4.84 mmol, 0.843 mL) via general procedure D. The compound was purified by flash column chromatography using EtOAc/*n*-Hex = 2/1 (v/v) as eluent. Yield 72%; colorless oil; R_f = 0.23 (EtOAc/*n*-hex, 2:1, v/v); ^{1}H NMR (400 MHz, $CDCl_3$): δ (ppm) = 1.22−1.42 (m, 2H), 1.47 (s, 9H), 1.98−2.07 (m, 2H), 2.29 (s, 3H), 2.42 (s, 3H), 2.92 (s, 2H), 4.00−4.24 (m, 3H), 4.83 (s, 2H), 5.87 (d, J = 7.9 Hz, 1H), 6.94−6.97 (m, 2H), 7.72−7.76 (m, 2H).

*4-((3,5-Dimethylisoxazol-4-yl)methoxy)-N-(piperidin-4-yl)-benzamide (**43**).* *tert*-Butyl 4-(4-((3,5-dimethylisoxazol-4-yl)-methoxy)benzamido)piperidine-1-carboxylate (**42**) (0.39 mmol, 0.168 g) was dissolved in DCM (10 mL) and trifluoroacetic acid (3.90 mmol, 0.300 mL) and stirred at room temperature for 24 h. Solvents were evaporated, and the compound was purified by flash column chromatography using DCM/isopropanol = 7/3 (v/v)+ 1% NH_3 as an eluent. Yield 21%; colorless oil; R_f = 0.24 ((DCM/isopropanol, 7:3, v/v) + 1% NH_3); ^{1}H NMR (400 MHz, acetone-d_6): δ (ppm) = 1.92−2.02 (m, 2H), 2.14−2.18 (m, 2H), 2.24 (s, 3H), 2.42 (s, 3H), 3.20 (td, J = 12.7, 3.0 Hz, 2H), 3.55 (dt, J = 12.8, 3.3 Hz, 2H), 4.18−4.28 (m, 1H), 5.00 (s, 2H), 5.23 (br s, 1H), 7.02−7.06 (m, 2H), 7.90−7.95 (m, 3H); ^{13}C NMR (100 MHz, acetone-d_6): δ (ppm) = 10.05, 10.93, 29.33, 43.73, 45.74, 60.28, 111.09, 115.16, 128.05, 130.16, 160.32, 161.97, 166.66, 168.31; HRMS (ESI$^+$) m/z calcd for $C_{18}H_{24}N_3O_3$ $[M + H]^+$ 330.18122; found,330.18053; HPLC purity 100.00% at 254 nm (t_R = 2.643 min).

General Procedure D: Alkylation of Amine. 4-((3,5-Dimethylisoxazol-4-yl)methoxy)-*N*-(piperidin-4-yl)benzamide (**43**) (1 equiv) was dissolved in anhydrous acetonitrile, and an appropriate alkyl bromide (2 equiv), K_2CO_3 (1.5 equiv), and KI (catalytic amount) were added. The reaction mixture was stirred at reflux for 2 h. The solvent was removed under reduced pressure, and the residue was dissolved in DCM and extracted with water. The organic phase was dried over anhydrous Na_2SO_4, filtered, and evaporated under reduced pressure. The residue was purified by flash column chromatography.

*N-(1-Butylpiperidin-4-yl)-4-((3,5-dimethylisoxazol-4-yl)-methoxy)benzamide (**40**).* The compound was synthesized from 4-((3,5-dimethylisoxazol-4-yl)methoxy)-*N*-(piperidin-4-yl)benzamide (**43**) (0.46 mmol, 0.150 g), K_2CO_3 (0.68 mmol, 0.094 g), 1-chlorobutane (0.91 mmol, 0.096 mL), and KI (cat.) according to general procedure D. The compound was purified by flash column chromatography using DCM/MeOH = 9/1 (v/v) as eluent. Yield 8%; white solid; R_f = 0.37 (DCM/MeOH, 9:1, v/v); ^{1}H NMR (400 MHz, $CDCl_3$): δ (ppm) = 0.94 (t, J = 7.3 Hz, 3H), 1.30−1.39 (m, 2H), 1.75 (br s, 4H), 2.05−2.12 (m, 2H), 2.28 (br s, 2H), 2.29 (s, 3H), 2.42 (s, 3H), 2.48 (s, 2H), 3.05 (br s, 2H), 4.02−4.10 (m, 1H), 4.83 (s, 2H), 5.95 (d, J = 7.6 Hz, 1H), 6.95−6.99 (m, 2H), 7.72−7.76 (m, 2H); ^{13}C NMR (100 MHz, $CDCl_3$): δ (ppm) = 10.16, 11.20, 13.94, 20.69, 28.51, 31.59, 46.54, 52.41, 58.25, 59.63, 109.86, 114.49, 127.56, 128.83, 159.66, 160.88, 166.21, 167.64; HRMS (ESI$^+$) m/z calcd for $C_{22}H_{32}N_3O_3$ $[M + H]^+$ 386.24382; found,386.24272; HPLC purity 100.00% at 254 nm (t_R = 3.110 min).

*N-(1-Allylpiperidin-4-yl)-4-((3,5-dimethylisoxazol-4-yl)methoxy)-benzamide (**41**).* The compound was synthesized from 4-((3,5-dimethylisoxazol-4-yl)methoxy)-*N*-(piperidin-4-yl)benzamide (**43**) (0.91 mmol, 0.300 g), K_2CO_3 (1.37 mmol, 0.189 g), 3-bromoprop-1-ene (1.82 mmol, 0.158 mL), and KI (cat.) according to general procedure D. The compound was purified by flash column chromatography using DCM/MeOH = 9/1 (v/v) as eluent. Yield 26%; white solid; R_f = 0.34 (DCM/MeOH, 9:1, v/v); ^{1}H NMR (400 MHz, $CDCl_3$): δ (ppm) = 1.60−1.70 (m, 2H), 2.03−2.11 (m, 2H), 2.17−2.26 (m, 2H), 2.29 (s, 3H), 2.42 (s, 3H), 2.96−2.99 (m, 2H), 3.06−3.09 (m, 2H), 3.98−4.08 (m, 1H), 4.83 (s, 2H), 5.19−5.25 (m, 2H), 0.86−5.96 (m, 2H), 6.95−6.98 (m, 2H), 7.72−7.76 (m, 2H); ^{13}C NMR (100 MHz, $CDCl_3$): δ (ppm) = 10.17, 11.20, 31.78, 46.62, 52.18, 59.61, 61.44, 109.86, 114.47, 119.43, 127.55, 128.84, 133.59, 159.66, 160.85, 166.24, 167.64; HRMS (ESI$^+$) m/z calcd for $C_{21}H_{28}N_3O_3$$[M + H]^+$ 370.21252; found,370.21145. HPLC purity, 98.08% at 254 nm (t_R = 2.867 min).

Cell Culture. Human embryonic Kidney (HEK)-Blue Null1, HEK-Blue hTLR2-TLR1, HEK-Blue hTLR2-TLR6, HEK-Blue hTLR4, HEK-Blue hTLR5, HEK-Blue hTLR7, HEK-Blue hTLR8, and HEK-Blue hTLR9 (InvivoGen, Toulouse, France) were cultured in Dulbecco's modified Eagle's medium (PAN-Biotech, Aidenbach, Germany) containing 10% (v/v) heat inactivated fetal bovine serum (FBS; S0615), 100 U/mL penicillin, 100 mg/mL streptomycin (P4333), 2 mM 1-glutamine (G7513) (all from Sigma-Aldrich, Taufkirchen, Germany), 100 μg/mL Normocin and selective antibiotics HEK-Blue Selection (hTLR2-TLR1, hTLR2-TLR6, hTLR4), 100 μg/mL zeocin (Null1), 100 μg/mL zeocin with 10 μg/mL (hTLR7, hTLR9), and 30 μg/mL (hTLR5, hTLR8) blasticidin (all from InvivoGen, Toulouse, France). THP1-Dual TLR4/MD-2/CD14 cells (InvivoGen, Toulouse, France) were cultured in RPMI-1640 medium supplemented with 10% fetal bovine serum (FBS), penicillin (100U/mL), streptomycin (100 μg/mL), L-glutamine (2 mM), HEPES (25 mM), Normocin (100 μg/mL), and selective antibiotics (blasticidin: 10 μg/mL, zeocin: 100 μg/mL) following the manufacturer's instructions.

THP-1 cells (ACC 16, DSMZ-German Collection of Microorganisms and Cell Cultures GmbH, Braunschweig, Germany) were

https://doi.org/10.1021/acs.jmedchem.4c03148
J. Med. Chem. 2025, 68, 4888−4907

cultured in RPMI 1640 (11530586, Fisher scientific, Schwerte, Germany) containing 100 U/mL penicillin, 100 μg/mL streptomycin (P4333), 2 mM L-glutamine (G7513, both from Sigma-Aldrich, Taufkirchen, Germany), and 10% heat-inactivated fetal bovine serum (FBS; S0615, Sigma- Aldrich, Taufkirchen, Germany) at a density of 4 × 10^5 cells/mL to 2 × 10^6 cells/mL. For generating THP-1-derived macrophages, THP-1 monocytes were seeded into 24-well plates at a density of 4 × 10^5 cells/mL in growth medium including 25 ng/mL PMA (phorbol 12-myristate 13-acetate; tlrl-pma, Invivogen, Toulouse, France). After 48 h, adherent cells were carefully washed with PBS (phosphate buffered saline; P04-53500, Pan Biotechne, Aidenbach, Germany) and rested in PMA-free medium for 24 h. All cell lines were maintained at 37 °C in a humidified atmosphere of 5% CO2 and 95% air and were regularly tested negative for mycoplasma contamination (VenorGeM Classic Mycoplasma PCR detection kit, Minerva Biolabs, Berlin, Germany).

PBMCs (peripheral blood mononuclear cells) were obtained from buffy-coat donations (Institute of Experimental Haematology and Transfusion Medicine, University Clinic Bonn) and isolated by density gradient centrifugation using Biocoll separation media (Bio&Sell, Nuremberg, Germany). PMBCs were washed three times with PBS containing ETDA and afterward seeded in 24-well plates (5 × 10^6 cells/well). The studies with human blood were approved by the ethics committee of the University Clinic Bonn (315/22) and written informed consent was obtained from all healthy donors.

Plasmids. Human embryonic Kidney (HEK)-Blue Null1 Cells (InvivoGen, Toulouse, France) were seeded into 6-well plates at a density of 1 × 10^6 cells/mL. After 24 h, adherent cells were washed with PBS and afterward transfected with plasmids using PEI Max. After another 24 h, cells were detached with TrypLE Express (Thermo Fisher Scientific, Darmstadt, Germany), seeded into 96-well plates at a density of 4 × 10^4 cells/mL, and rested for 24 h in medium containing selective antibiotics for hTLR8 cells (as described above). Plasmids encoding mutant TLR8 ($TLR8^{F513L}$) were prepared from the $TLR8^{WT}$ construct (pUNO1-hTLR08a, NM_016610.4, InvivoGen, Toulouse, France) by site-directed mutagenesis (Q5 Site-Directed Mutagenesis Kit, NEB, Frankfurt am Main, Germany) using the primer pairs 5′-AAGAGGTTATATGTTCCAGGAAC-3′ and 5′-AAATGCAATGCCCGTAGAG-3′ (synthesized by Thermo Fisher Scientific, Darmstadt, Germany). Successful mutagenesis was confirmed by Sanger sequencing. TLR8 transfection and overexpression was confirmed using Western Blot (Figure S11).

Cell Stimulation. HEK-Blue cells (4 × 10^4 cells/well) and THP-1 macrophages (4 × 10^4 cells/well, 4 × 10^5 cells/well and 8 × 10^5 cells/well) were seeded in 96-well plates, 24-well plates, or 6-well plates (PS, Sarsted, Germany), respectively. For stimulation experiments, cells were washed with phosphate-buffered saline (PBS, Sigma-Aldrich) and media was replaced with OptiMEM (Thermo Fisher Scientific, Darmstadt, Germany). For inhibition studies, the cells were preincubated with TLR8 antagonists for 1 h and afterward stimulated with TLR agonists for 24 h. The following TLR ligands were used: Pam_2CSK_4, Pam_3CSK_4, poly(I:C) (HMW), LPS from *Escherichia coli* O111:B4 (LPS-EB Ultrapure), flagellin from *Bacillus subtilis* (flagellin-BS Ultrapure), CL307, CL075, R848, TL8-506, ODN2006 (all from InvivoGen, Toulouse, France), and Enpatoran (BIOZOL Diagnostika, Germany). After 24 h, NF-κB activity was measured using QuantiBlue solution (InvivoGen, Toulouse, France) following the manufacturer's instructions.

THP1-Dual TLR4/MD-2/CD14 cells (InvivoGen, Toulouse, France) were seeded in 96-well plates at a density of 1 × 10^5 cells per well and were immediately preincubated with designated antagonists for 1 h and afterward stimulated with TLR agonists. After 24 h, NF-κB activity was measured via the SEAP reporter assay using QuantiBlue solution (InvivoGen, Toulouse, France) and ISRE activity was measured via lucia luciferase using QuantiLuc solution (InvivoGen, Toulouse, France), both following the manufacturer's instructions.

The TLR8 antagonists synthesized and commercially purchased were dissolved in DMSO as a 50 mM stock solution. Final DMSO concentrations in the cell culture were below 0.2% (v/v). The cells were first incubated with the antagonists for 1 h and afterward stimulated with the respective TLR agonist.

Cell Viability. Effects on cell viability were assessed by the MTT assay. HEK-Blue hTLR7, HEK-Blue hTLR8 cells, or differentiated THP-1 macrophages (40,000 cells/well, 96 well plate) were preincubated with TLR8 antagonists for 1 h and afterward stimulated for 20 h with TLR7 or TLR8 agonists. Subsequently, 25 μL of MTT (3-(4,5-dimethylthiazol-2-yl)-2,5-diphenyltetrazolium bromide, 5 mg/mL) was added and incubated for 4 h at 37 °C. After the supernatants were removed, DMSO (4720.1, Carl Roth, Karlsruhe, Germany) was added and absorption at 540 nm was measured. Viability of the untreated cells was defined as 100%. DMSO (10% (v/v); A994.1, Carl Roth, Karlsruhe, Germany) served as a positive control.

In selected experiments, LDH assay was performed according to the manufacturer's instructions (Thermo fisher Scientific, Darmstadt, Germany). The percentage of LDH release was calculated compared to the 100% cell lysis control.

Enzyme-Linked Immunosorbent Assay. After 4 h of stimulation of THP-1 macrophages or PBMCs with the respective TLR agonists, cell culture supernatants were collected and analyzed using commercially available human TNF or IL-1β secretion ELISA kits (88-7346-88, 88-7261-88; Thermo Fisher Scientific, Darmstadt, Germany).

Dynamic Mass Redistribution (DMR) Label-Free Assay. DMR assays were conducted using the EPIC system (Corning) in accordance with established protocols.[42,63,64] On the day of the assay, THP-1 Dual TLR4-MD2-CD14 cells were seeded as suspension cells at a density of 40,000 cells per well in assay buffer (Hank's Balanced Salt Solution (HBSS) with 20 mM HEPES, pH 7.0) into an Epic 384-well uncoated glass microplate (Corning, New York, NY, USA). Cells were briefly centrifuged for 10 s to ensure proper contact with the bottom biosensor and prevent drops from adhering to the sides of the wells. Each well had a final volume of 30 μL. After cell seeding, the Epic microplates were incubated in the EPIC instrument at 37 °C for 1.5 h. Serial dilutions of compounds were prepared in the same assay buffer. DMR measurements were performed using the Epic biosensor, and following baseline readings, 10 μL of compounds were added to each well (40 μL total volume) using a semiautomated liquid handler, Selma (Analytik Jena AG, Jena, Germany). The antagonist was preincubated for 1.5 h before the addition of the agonist. DMR signals were recorded for 15,000 s, and the data were analyzed and exported using the Epic Analyzer Software (Corning, New York, NY, USA). All signals were baseline-corrected, and compound responses were represented as picometer (picosecond) shifts over time (minutes) following baseline normalization. Experiments were performed at 37 °C in triplicate or quadruplicate.

Western Blotting. The protein amount was quantified by a bicinchoninic acid assay (Pierce BCA Protein Assay Kit; 23227, Thermo Fisher Scientific, Darmstadt, Germany). Twenty-five μg protein per lane was separated on a 10% TGX Stain-Free FastCast acrylamide gel (1610183, Bio-Rad, Feldkirchen, Germany) containing TEMED (2367, Carl Roth, Karlsruhe, Germany) and ammonium persulfate (A3678, Sigma-Aldrich, Taufkirchen, Germany) using MiniPROTEAN electrophoresis system (Bio-Rad). Gels were blotted on low fluorescence polyvinylidene difluoride membranes (Immobilon-FL PVDF low fluorescence; 05317, Merck, Darmstadt, Germany) using the Trans-Blot Turbo System (Bio-Rad, Feldkirchen, Germany). Membranes were blocked using 5% milk (T145.2, Carl Roth, Karlsruhe, Germany) in TBS-T buffer consisting of TRIS HCl (T3253, Sigma-Aldrich, Taufkirchen, Germany), NaCl (27810.295, VWR, Darmstadt, Germany), and Tween 20 (9127.1, Carl Roth, Karlsruhe, Germany). Membranes were incubated overnight at 4 °C with either mouse anti-TLR8 mAb (sc-373760, SCBT), rabbit anti-MyD88 mAb (4283, CST), rabbit anti-Phospho-NF-κB p65 (Ser536) (no. 93H1), rabbit anti-NF-κB p65 (D14E12) XP (no. 8242), or rabbit anti-IκBα antibody (no. 9242) in 5% BSA. Afterward, they were washed three times with TBS-T and incubated with either rabbit anti-IgG HRP conjugated antibody (no. 7074) or mouse anti-IgG HRP conjugated antibody (no. 7076), all from Cell Signaling Technology (CST, Leiden, The Netherlands), for one h at RT. Blots were

https://doi.org/10.1021/acs.jmedchem.4c03148
J. Med. Chem. 2025, 68, 4888−4907

developed with ECL reagent (Clarity Western ECL Substrate; 1705060, Bio-Rad, Feldkirchen, Germany) and imaged using ChemiDoc imaging system (Bio-Rad, Feldkirchen, Germany). Values of protein expression were analyzed by densitometry and normalized to total protein levels using Image lab 6.1 Bio-Rad, Feldkirchen, Germany. Uncropped Western blots are provided in Figure S10A.

Co-Immunoprecipitation. THP-1 macrophages were lysed in cell lysis buffer (RIPA) with a protease/phosphatase inhibitor cocktail (NEB, Frankfurt am Main, Germany). The total amount of protein was quantified by using bicinchoninic acid assay (Pierce BCA Protein Assay Kit; 23227, Thermo Fisher Scientific, Darmstadt, Germany) and equivalent amounts of each sample were used for coimmunoprecipitation. Lysates were incubated with mouse anti-TLR8 mAb (sc-373760, SCBT, Heidelberg, Germany) for 2 h at 4 °C. Mouse anti-IgG2b mAb (no. 53484, CST, Leiden, The Netherlands) served as the isotype control. Next, protein A/G PLUS agarose beads (sc-2003, SCBT, Heidelberg, Germany) were added for overnight incubation at 4 °C followed by washing with RIPA buffer 4 times. The immunoprecipitated proteins were removed from the beads with standard SDS-PAGE sample buffer in the presence of DTT by boiling for 5 min at 95 °C. Afterward, the samples were analyzed by Western blot. The nonimmunoprecipitated cell lysate was used as loading control. Uncropped Western blots are provided in Figure S10B.

RNA Isolation, cDNA Synthesis, and qRT-PCR. Total RNA isolation was performed using innuPREP RNA mini kit 2.0 (845-KS-2040050, AnalytikJena, Jena, Germany) according to the manufacturer's protocol. Synthesis of cDNA was carried out using an iScript cDNA synthesis kit (1708891, Bio-Rad, Feldkirchen, Germany). Quantitative real-time RT-PCR (qRT-PCR) was performed as described before.[65] Primers (synthesized by TIB Molbiol, Berlin, Germany or Eurofins Genomics, Ebersberg, Germany) with the following sequences were used: *GAPDH*, 5′-CTCTCTGCTCCTCCTGTTCGAC-3′ and 5′- TGAGC-GATGTGGCTCGGCT-3′; *TNF*, 5′-CCCAGGGACCTCTC-TAATC-3′ and 5′-GCTACAGGCTTGTCACTCGG-3′, *IL1B*, 5′-TGGAGCAACAAGTGGTGT-3′ and 5′-TTGGGATCTA-CACTCTCCAGC-3′. Fold difference in gene expression was normalized to the housekeeping gene *GAPDH* showing the most constant expression levels. The reaction mix containing cDNA template, primers, and SYBR green (iTaq Universal SYBR Green Supermix; 172−5125, Bio-Rad, Feldkirchen, Germany) was run under the conditions as described.

Statistical Analysis. Data are expressed as mean ± SEM. For multiple comparisons, statistically significant differences were determined by one-way ANOVA followed by a Dunnett's or Tukey's post-test and considered significant at $*P \leq 0.05$, $**P \leq 0.01$, $***P \leq 0.001$, $****P \leq 0.0001$. All other values were calculated accordingly. Statistical differences were assessed by a one-sample *t*-test against 100%. Statistical analysis was performed using GraphPad Prism (version 8.0, GraphPad software, San Diego, USA).

■ ASSOCIATED CONTENT

Data Availability Statement

All data generated or analyzed during this study are included in the article and its Supporting Information.

Supporting Information

The Supporting Information is available free of charge at https://pubs.acs.org/doi/10.1021/acs.jmedchem.4c03148.

Chemical structures of known cocrystallized TLR8 antagonists; validation of the virtual screening 3D pharmacophore; NF-κB activity and cell viability in hTLR8-HEK293 cells for compounds **1-12**; concentration−response curves in hTLR8-HEK293 cells for compounds **1**, **10−12**; concentration−response curves in hTLR7-HEK293 cells for compounds **10−12**; NF-κB activity and cell viability in hTLR8-HEK293 cells for compounds **17−41**, **43**; concentration−response curves in hTLR8-HEK293 cells for synthesized compounds; cell viability of compounds **10** and **12** in THP-1 macrophages and PMBCs; inhibition of TLR8-dependent activity in THP-1 Dual cells; whole uncropped images of the original Western blots; transfection of mutant and wildtype TLR8 plasmids into HEK293 cells; HPLC traces for compounds **1−12**; ^{1}H NMR spectra for purchased active compounds **1**, **10−12**; ^{1}H NMR, ^{13}C NMR, and HPLC traces for synthesized active compounds; chemical structures of compounds **1−12** containing the isoxazole scaffold; inhibition of NF-κB activity in hTLR8-HEK293 cells by compounds **1−12**; inhibition of NF-κB activity in hTLR8-HEK293 cells by compounds **17−41**, **43**; chemical structures of synthesized compounds **17−41**, **43**; interaction frequencies of **10** with TLR8 homodimer during MD simulation; pharmacological parameters (EC_{50}, E_{max}) of compound **10**, and references (PDF)

Docking model (7rc9_1_12) (PDB)

Docking model (7rc9_17_42) (PDB)

Molecular formula strings (CSV)

■ AUTHOR INFORMATION

Corresponding Authors

Matej Sova − *Faculty of Pharmacy, the Department of Pharmaceutical Chemistry, University of Ljubljana, SI-1000 Ljubljana, Slovenia;* orcid.org/0000-0002-8977-3450; Email: matej.sova@ffa.uni-lj.si

Gerhard Wolber − *Institute of Pharmacy, Pharmaceutical and Medicinal ChemistryFreie, Universität Berlin, 14195 Berlin, Germany;* orcid.org/0000-0002-5344-0048; Email: gerhard.wolber@fu-berlin.de

Günther Weindl − *Pharmaceutical Institute, Pharmacology and Toxicology Section, University of Bonn, 53121 Bonn, Germany;* orcid.org/0000-0002-4493-7597; Email: guenther.weindl@uni-bonn.de

Authors

Troy Matziol − *Pharmaceutical Institute, Pharmacology and Toxicology Section, University of Bonn, 53121 Bonn, Germany*

Valerij Talagayev − *Institute of Pharmacy, Pharmaceutical and Medicinal ChemistryFreie, Universität Berlin, 14195 Berlin, Germany*

Tjaša Slokan − *Faculty of Pharmacy, the Department of Pharmaceutical Chemistry, University of Ljubljana, SI-1000 Ljubljana, Slovenia*

Nika Strašek Benedik − *Faculty of Pharmacy, the Department of Pharmaceutical Chemistry, University of Ljubljana, SI-1000 Ljubljana, Slovenia*

Janine Holze − *Pharmaceutical Institute, Pharmacology and Toxicology Section, University of Bonn, 53121 Bonn, Germany*

Complete contact information is available at: https://pubs.acs.org/10.1021/acs.jmedchem.4c03148

Author Contributions

[‖]T.M. and V.T.contributed equally to this work. T.M, V.T., T.S., N.S.B., and J.H. performed experiments; T.M., V.T., T.S., N.S.B., J.H., and G. Weindl analyzed the data; M.S., G. Wolber, and G. Weindl directed the study; T.M., V.T., M.S., G. Wolber, and G. Weindl wrote the manuscript. All authors have given

https://doi.org/10.1021/acs.jmedchem.4c03148
J. Med. Chem. 2025, 68, 4888−4907

approval to the final version of the manuscript. M.S., G. Wolber, and G. Weindl contributed equally and share the senior and corresponding authorship.

Notes

The authors declare no competing financial interest.

■ ACKNOWLEDGMENTS

We thank Eicke Latz (Deutsches Rheuma Forschungszentrum Berlin) for kindly providing reagents. This work was funded by the Slovenian Research and Innovation Agency (research core funding no. P1-0208, grant to M.S. J1-4417, bilateral project grant BI-DE/23-24-011, and a grant to N.S.B.) and supported by the German Research Foundation to G.W. and G.W. (grant RA 895/16-1). The Table of Contents Graphic was created in BioRender. Weindl, G. (2025) https://BioRender.com/d11h423.

■ ABBREVIATIONS

CD14, cluster of differentiation 14; CLE, cutaneous lupus erythematosus; DAMP, damage-associated molecular pattern; ELISA, enzyme-linked immunosorbent assay; HBA, hydrogen bond acceptor; HEK, human embryonic kidney; HYD, hydrophobic contacts; IC50, half-maximal inhibitory concentration; IFN, interferon; IL, interleukin; IRF, Interferon regulatory factor; LDH, lactate dehydrogenase; MD, molecular dynamics; NF-κB, nuclear factor κB; PAMP, pathogen-associated molecular pattern; PBMC, peripheral blood mononuclear cell; PDB, protein data bank; PI, positive ionizable; PRR, pattern recognition receptor; RA, rheumatoid arthritis; SAR, structure−activity relationship; SEAP, secreted alkaline phosphatase; SLE, systemic lupus erythematosus; TLR, Toll-like receptor; TNF, tumor necrosis factor

■ REFERENCES

(1) Fitzgerald, K. A.; Kagan, J. C. Toll-like Receptors and the Control of Immunity. *Cell* **2020**, *180* (6), 1044−1066.
(2) Kawai, T.; Ikegawa, M.; Ori, D.; Akira, S. Decoding Toll-like Receptors: Recent Insights and Perspectives in Innate Immunity. *Immunity* **2024**, *57* (4), 649−673.
(3) Lind, N. A.; Rael, V. E.; Pestal, K.; Liu, B.; Barton, G. M. Regulation of the Nucleic Acid-Sensing Toll-like Receptors. *Nat. Rev. Immunol.* **2022**, *22* (4), 224−235.
(4) Hamerman, J. A.; Barton, G. M. The Path Ahead for Understanding Toll-like Receptor-Driven Systemic Autoimmunity. *Curr. Opin. Immunol.* **2024**, *91*, 102482.
(5) Liang, J.; Wan, Y.; Gao, J.; Zheng, L.; Wang, J.; Wu, P.; Li, Y.; Wang, B.; Wang, D.; Ma, Y.; Shen, B.; Lv, X.; Wang, D.; An, N.; Ma, X.; Geng, G.; Tong, J.; Liu, J.; Chen, G.; Gao, M.; Kurita, R.; Nakamura, Y.; Zhu, P.; Yin, H.; Zhu, X.; Shi, L. Erythroid-Intrinsic Activation of TLR8 Impairs Erythropoiesis in Inherited Anemia. *Nat. Commun.* **2024**, *15* (1), 5678.
(6) Tanji, H.; Ohto, U.; Shibata, T.; Taoka, M.; Yamauchi, Y.; Isobe, T.; Miyake, K.; Shimizu, T. Toll-like Receptor 8 Senses Degradation Products of Single-Stranded RNA. *Nat. Struct. Mol. Biol.* **2015**, *22* (2), 109−115.
(7) Greulich, W.; Wagner, M.; Gaidt, M. M.; Stafford, C.; Cheng, Y.; Linder, A.; Carell, T.; Hornung, V. TLR8 Is a Sensor of RNase T2 Degradation Products. *Cell* **2019**, *179* (6), 1264−1275.
(8) Krüger, A.; Oldenburg, M.; Chebrolu, C.; Beisser, D.; Kolter, J.; Sigmund, A. M.; Steinmann, J.; Schäfer, S.; Hochrein, H.; Rahmann, S.; Wagner, H.; Henneke, P.; Hornung, V.; Buer, J.; Kirschning, C. J. Human TLR 8 Senses UR/URR Motifs in Bacterial and Mitochondrial RNA. *EMBO Rep.* **2015**, *16* (12), 1656−1663.
(9) Vollmer, J.; Tluk, S.; Schmitz, C.; Hamm, S.; Jurk, M.; Forsbach, A.; Akira, S.; Kelly, K. M.; Reeves, W. H.; Bauer, S.; Krieg, A. M. Immune Stimulation Mediated by Autoantigen Binding Sites within Small Nuclear RNAs Involves Toll-like Receptors 7 and 8. *J. Exp. Med.* **2005**, *202* (11), 1575−1585.
(10) Junt, T.; Barchet, W. Translating Nucleic Acid-Sensing Pathways into Therapies. *Nat. Rev. Immunol.* **2015**, *15* (9), 529−544.
(11) Ehlers, C.; Thiele, T.; Biermann, H.; Traidl, S.; Bruns, L.; Ziegler, A.; Schefzyk, M.; Bartsch, L. M.; Kalinke, U.; Witte, T.; Graalmann, T. Toll-Like Receptor 8 Is Expressed in Monocytes in Contrast to Plasmacytoid Dendritic Cells and Mediates Aberrant Interleukin-10 Responses in Patients With Systemic Sclerosis. *Arthritis Rheumatol.* **2024**, *77*, 59−66.
(12) De Marcken, M.; Dhaliwal, K.; Danielsen, A. C.; Gautron, A. S.; Dominguez-Villar, M. TLR7 and TLR8 Activate Distinct Pathways in Monocytes during RNA Virus Infection. *Sci. Signaling* **2019**, *12* (605), No. eaaw1347.
(13) Garcia, G.; Irudayam, J. I.; Jeyachandran, A. V.; Dubey, S.; Chang, C.; Castillo Cario, S.; Price, N.; Arumugam, S.; Marquez, A. L.; Shah, A.; Fanaei, A.; Chakravarty, N.; Joshi, S.; Sinha, S.; French, S. W.; Parcells, M. S.; Ramaiah, A.; Arumugaswami, V. Innate Immune Pathway Modulator Screen Identifies STING Pathway Activation as a Strategy to Inhibit Multiple Families of Arbo and Respiratory Viruses. *Cell Rep. Med.* **2023**, *4* (5), 101024.
(14) Hu, Z.; Tanji, H.; Jiang, S.; Zhang, S.; Koo, K.; Chan, J.; Sakaniwa, K.; Ohto, U.; Candia, A.; Shimizu, T.; Yin, H. Small-Molecule TLR8 Antagonists via Structure-Based Rational Design. *Cell Chem. Biol.* **2018**, *25* (10), 1286−1291.
(15) Zhang, S.; Hu, Z.; Tanji, H.; Jiang, S.; Das, N.; Li, J.; Sakaniwa, K.; Jin, J.; Bian, Y.; Ohto, U.; Shimizu, T.; Yin, H. Small-Molecule Inhibition of TLR8 through Stabilization of Its Resting State. *Nat. Chem. Biol.* **2018**, *14* (1), 58−64.
(16) Šribar, D.; Grabowski, M.; Murgueitio, M. S.; Bermudez, M.; Weindl, G.; Wolber, G. Identification and Characterization of a Novel Chemotype for Human TLR8 Inhibitors. *Eur. J. Med. Chem.* **2019**, *179*, 744−752.
(17) Dolšak, A.; Šribar, D.; Scheffler, A.; Grabowski, M.; Švajger, U.; Gobec, S.; Holze, J.; Weindl, G.; Wolber, G.; Sova, M. Further Hit Optimization of 6-(Trifluoromethyl)Pyrimidin-2-Amine Based TLR8Modulators: Synthesis, Biological Evaluation and Structure−Activity Relationships. *Eur. J. Med. Chem.* **2021**, *225*, 113809.
(18) Jiang, S.; Tanji, H.; Yin, K.; Zhang, S.; Sakaniwa, K.; Huang, J.; Yang, Y.; Li, J.; Ohto, U.; Shimizu, T.; Yin, H. Rationally Designed Small-Molecule Inhibitors Targeting an Unconventional Pocket on the TLR8 Protein−Protein Interface. *J. Med. Chem.* **2020**, *63* (8), 4117−4132.
(19) Sun, H.; Li, Y.; Zhang, P.; Xing, H.; Zhao, S.; Song, Y.; Wan, D.; Yu, J. Targeting Toll-like Receptor 7/8 for Immunotherapy: Recent Advances and Prospectives. *Biomark. Res.* **2022**, *10* (1), 89.
(20) Hawtin, S.; André, C.; Collignon-Zipfel, G.; Appenzeller, S.; Bannert, B.; Baumgartner, L.; Beck, D.; Betschart, C.; Boulay, T.; Brunner, H. I.; Ceci, M.; Deane, J.; Feifel, R.; Ferrero, E.; Kyburz, D.; Lafossas, F.; Loetscher, P.; Merz-Stoeckle, C.; Michellys, P.; Nuesslein-Hildesheim, B.; Raulf, F.; Rush, J. S.; Ruzzante, G.; Stein, T.; Zaharevitz, S.; Wieczorek, G.; Siegel, R.; Gergely, P.; Shisha, T.; Junt, T. Preclinical Characterization of the Toll-like Receptor 7/8 Antagonist MHV370 for Lupus Therapy. *Cell Rep. Med.* **2023**, *4* (5), 101036.
(21) Vlach, J.; Bender, A. T.; Przetak, M.; Pereira, A.; Deshpande, A.; Johnson, T. L.; Reissig, S.; Tzvetkov, E.; Musil, D.; Morse, N. T.; Haselmayer, P.; Zimmerli, S. C.; Okitsu, S. L.; Walsky, R. L.; Sherer, B. Discovery of M5049: A Novel Selective Toll-Like Receptor 7/8 Inhibitor for Treatment of Autoimmunity. *J. Pharmacol. Exp. Ther.* **2021**, *376* (3), 397−409.
(22) Alharbi, A. S.; Sapkota, S.; Zhang, Z.; Jin, R.; Jayasekara, W. S. N.; Rupasinghe, E.; Speir, M.; Wilkinson-White, L.; Gamsjaeger, R.; Cubeddu, L.; Ellyard, J. I.; Wenholz, D. S.; McAllan, A. L.; Rezwan, R.; Ying, L.; Far, H. H.; Bones, J.; He, S.; Yu, D.; Lennox, K. A.; Hertzog, P. J.; Vinuesa, C. G.; Behlke, M. A.; Ohto, U.; Laczka, O. F.; Corry, B.; Shimizu, T.; Gantier, M. P. 2'-O-Methyl-Guanosine 3-Base

https://doi.org/10.1021/acs.jmedchem.4c03148
J. Med. Chem. 2025, 68, 4888−4907

RNA Fragments Mediate Essential Natural TLR7/8 Antagonism. *bioRxiv* **2024**, bioRxiv:605091.
(23) Sakaniwa, K.; Shimizu, T. Targeting the Innate Immune Receptor TLR8 Using Small-Molecule Agents. *Acta Crystallogr., Sect. D:Struct. Biol.* **2020**, *76* (7), 621−629.
(24) Knoepfel, T.; Nimsgern, P.; Jacquier, S.; Bourrel, M.; Vangrevelinghe, E.; Glatthar, R.; Behnke, D.; Alper, P. B.; Michellys, P.-Y.; Deane, J.; Junt, T.; Zipfel, G.; Limonta, S.; Hawtin, S.; Andre, C.; Boulay, T.; Loetscher, P.; Faller, M.; Blank, J.; Feifel, R.; Betschart, C. Target-Based Identification and Optimization of 5-Indazol-5-Yl Pyridones as Toll-like Receptor 7 and 8 Antagonists Using a Biochemical TLR8 Antagonist Competition Assay. *J. Med. Chem.* **2020**, *63* (15), 8276−8295.
(25) Mussari, C. P.; Dodd, D. S.; Sreekantha, R. K.; Pasunoori, L.; Wan, H.; Posy, S. L.; Critton, D.; Ruepp, S.; Subramanian, M.; Watson, A.; Davies, P.; Schieven, G. L.; Salter-Cid, L. M.; Srivastava, R.; Tagore, D. M.; Dudhgaonkar, S.; Poss, M. A.; Carter, P. H.; Dyckman, A. J. Discovery of Potent and Orally Bioavailable Small Molecule Antagonists of Toll-like Receptors 7/8/9 (TLR7/8/9). *ACS Med. Chem. Lett.* **2020**, *11* (9), 1751−1758.
(26) Betschart, C.; Faller, M.; Zink, F.; Hemmig, R.; Blank, J.; Vangrevelinghe, E.; Bourrel, M.; Glatthar, R.; Behnke, D.; Barker, K.; Heizmann, A.; Angst, D.; Nimsgern, P.; Jacquier, S.; Junt, T.; Zipfel, G.; Ruzzante, G.; Loetscher, P.; Limonta, S.; Hawtin, S.; Andre, C. B.; Boulay, T.; Feifel, R.; Knoepfel, T. Structure-Based Optimization of a Fragment-like TLR8 Binding Screening Hit to an *In Vivo* Efficacious TLR7/8 Antagonist. *ACS Med. Chem. Lett.* **2022**, *13* (4), 658−664.
(27) Sreekantha, R. K.; Mussari, C. P.; Dodd, D. S.; Pasunoori, L.; Hegde, S.; Posy, S. L.; Critton, D.; Ruepp, S.; Subramanian, M.; Salter-Cid, L. M.; Tagore, D. M.; Sarodaya, S.; Dudhgaonkar, S.; Poss, M. A.; Schieven, G. L.; Carter, P. H.; Macor, J. E.; Dyckman, A. J. Identification of 2-Pyridinylindole-Based Dual Antagonists of Toll-like Receptors 7 and 8 (TLR7/8). *ACS Med. Chem. Lett.* **2022**, *13* (5), 812−818.
(28) Zhang, Z.; Ohto, U.; Taoka, M.; Yamauchi, Y.; Sato, R.; Shukla, N. M.; David, S. A.; Isobe, T.; Miyake, K.; Shimizu, T. Structural Analyses of Toll-like Receptor 7 Reveal Detailed RNA Sequence Specificity and Recognition Mechanism of Agonistic Ligands. *Cell Rep.* **2018**, *25* (12), 3371−3381.
(29) Zhang, Z.; Ohto, U.; Shibata, T.; Krayukhina, E.; Taoka, M.; Yamauchi, Y.; Tanji, H.; Isobe, T.; Uchiyama, S.; Miyake, K.; Shimizu, T. Structural Analysis Reveals That Toll-like Receptor 7 Is a Dual Receptor for Guanosine and Single-Stranded RNA. *Immunity* **2016**, *45* (4), 737−748.
(30) Wolber, G.; Langer, T. LigandScout: 3-D Pharmacophores Derived from Protein-Bound Ligands and Their Use as Virtual Screening Filters. *J. Chem. Inf. Model.* **2005**, *45* (1), 160−169.
(31) Schaller, D.; Šribar, D.; Noonan, T.; Deng, L.; Nguyen, T. N.; Pach, S.; Machalz, D.; Bermudez, M.; Wolber, G. Next Generation 3D Pharmacophore Modeling. *Wiley Interdiscip. Rev.: Comput. Mol. Sci.* **2020**, *10* (4), No. e1468.
(32) Kutlushina, A.; Khakimova, A.; Madzhidov, T.; Polishchuk, P. Ligand-Based Pharmacophore Modeling Using Novel 3D Pharmacophore Signatures. *Molecules* **2018**, *23* (12), 3094.
(33) Noonan, T.; Denzinger, K.; Talagayev, V.; Chen, Y.; Puls, K.; Wolf, C. A.; Liu, S.; Nguyen, T. N.; Wolber, G. Mind the Gap—Deciphering GPCR Pharmacology Using 3D Pharmacophores and Artificial Intelligence. *Pharmaceuticals* **2022**, *15* (11), 1304.
(34) Mendez, D.; Gaulton, A.; Bento, A. P.; Chambers, J.; De Veij, M.; Félix, E.; Magariños, M. P.; Mosquera, J. F.; Mutowo, P.; Nowotka, M.; Gordillo-Marañón, M.; Hunter, F.; Junco, L.; Mugumbate, G.; Rodriguez-Lopez, M.; Atkinson, F.; Bosc, N.; Radoux, C. J.; Segura-Cabrera, A.; Hersey, A.; Leach, A. R. ChEMBL: Towards Direct Deposition of Bioassay Data. *Nucleic Acids Res.* **2019**, *47* (D1), D930−D940.
(35) Gaulton, A.; Hersey, A.; Nowotka, M.; Bento, A. P.; Chambers, J.; Mendez, D.; Mutowo, P.; Atkinson, F.; Bellis, L. J.; Cibrián-Uhalte, E.; Davies, M.; Dedman, N.; Karlsson, A.; Magariños, M. P.; Overington, J. P.; Papadatos, G.; Smit, I.; Leach, A. R. The ChEMBL Database in 2017. *Nucleic Acids Res.* **2017**, *45* (D1), D945−D954.
(36) Gaulton, A.; Bellis, L. J.; Bento, A. P.; Chambers, J.; Davies, M.; Hersey, A.; Light, Y.; McGlinchey, S.; Michalovich, D.; Al-Lazikani, B.; Overington, J. P. ChEMBL: A Large-Scale Bioactivity Database for Drug Discovery. *Nucleic Acids Res.* **2012**, *40* (D1), D1100−D1107.
(37) Verdonk, M. L.; Cole, J. C.; Hartshorn, M. J.; Murray, C. W.; Taylor, R. D. Improved Protein−Ligand Docking Using GOLD. *Proteins:Struct., Funct., Bioinf.* **2003**, *52* (4), 609−623.
(38) Port, A.; Shaw, J. V.; Klopp-Schulze, L.; Bytyqi, A.; Vetter, C.; Hussey, E.; Mammasse, N.; Ona, V.; Bachmann, A.; Strugala, D.; Reh, C.; Goteti, K. Phase 1 Study in Healthy Participants of the Safety, Pharmacokinetics, and Pharmacodynamics of Enpatoran (M5049), a Dual Antagonist of Toll-like Receptors 7 and 8. *Pharmacol. Res. Perspect.* **2021**, *9* (5), No. e00842.
(39) Cervantes, J. L.; Weinerman, B.; Basole, C.; Salazar, J. C. TLR8: The Forgotten Relative Revindicated. *Cell. Mol. Immunol.* **2012**, *9* (6), 434−438.
(40) He, Y.; Hara, H.; Núñez, G. Mechanism and Regulation of NLRP3 Inflammasome Activation. *Trends Biochem. Sci.* **2016**, *41* (12), 1012−1021.
(41) Fisch, D.; Zhang, T.; Sun, H.; Ma, W.; Tan, Y.; Gygi, S. P.; Higgins, D. E.; Kagan, J. C. Molecular Definition of the Endogenous Toll-like Receptor Signalling Pathways. *Nature* **2024**, *631* (8021), 635−644.
(42) Holze, J.; Lauber, F.; Soler, S.; Kostenis, E.; Weindl, G. Label-Free Biosensor Assay Decodes the Dynamics of Toll-like Receptor Signaling. *Nat. Commun.* **2024**, *15* (1), 9554.
(43) Bock, A.; Bermudez, M.; Krebs, F.; Matera, C.; Chirinda, B.; Sydow, D.; Dallanoce, C.; Holzgrabe, U.; De Amici, M.; Lohse, M. J.; Wolber, G.; Mohr, K. Ligand Binding Ensembles Determine Graded Agonist Efficacies at a G Protein-Coupled Receptor. *J. Biol. Chem.* **2016**, *291* (31), 16375−16389.
(44) Janežič, M.; Valjavec, K.; Loboda, K. B.; Herlah, B.; Ogris, I.; Kozorog, M.; Podobnik, M.; Grdadolnik, S. G.; Wolber, G.; Perdih, A. Dynophore-Based Approach in Virtual Screening: A Case of Human DNA Topoisomerase IIα. *Int. J. Mol. Sci.* **2021**, *22* (24), 13474.
(45) Puls, K.; Olivé-Marti, A.-L.; Pach, S.; Pinter, B.; Erli, F.; Wolber, G.; Spetea, M. In Vitro, In Vivo and In Silico Characterization of a Novel Kappa-Opioid Receptor Antagonist. *Pharmaceuticals* **2022**, *15* (6), 680.
(46) Koçak Aslan, E.; Lam, K.; Dengiz, C.; Denzinger, K.; Dicle Erdamar, I. Y.; Huang, S.; Zamponi, G. W.; Wolber, G.; Gündüz, M. G. Synthesis, Molecular Modeling, DFT Studies, and EPR Analysis of 1,4-Dihydropyridines as Potential Calcium Channel Blockers. *J. Mol. Struct.* **2024**, *1307*, 137983.
(47) Machalz, D.; Li, H.; Du, W.; Sharma, S.; Liu, S.; Bureik, M.; Wolber, G. Discovery of a Novel Potent Cytochrome P450 CYP4Z1 Inhibitor. *Eur. J. Med. Chem.* **2021**, *215*, 113255.
(48) Jones, G.; Willett, P.; Glen, R. C.; Leach, S.; Liu, A. R. Development and Validation of a Genetic Algorithm for Flexible Docking. *J. Mol. Biol.* **1997**, *267*, 727.
(49) Tanji, H.; Ohto, U.; Shibata, T.; Miyake, K.; Shimizu, T. Structural Reorganization of the Toll-Like Receptor 8 Dimer Induced by Agonistic Ligands. *Science* **2013**, *339* (6126), 1426−1429.
(50) Forsbach, A.; Nemorin, J.-G.; Montino, C.; Müller, C.; Samulowitz, U.; Vicari, A. P.; Jurk, M.; Mutwiri, G. K.; Krieg, A. M.; Lipford, G. B.; Vollmer, J. Identification of RNA Sequence Motifs Stimulating Sequence-Specific TLR8-Dependent Immune Responses. *J. Immunol.* **2008**, *180* (6), 3729−3738.
(51) Kay, J. The Role of Interleukin-1 in the Pathogenesis of Rheumatoid Arthritis. *Rheumatology* **2004**, *43* (suppl_3), iii2−iii9.
(52) Mysinger, M. M.; Carchia, M.; Irwin, J. J.; Shoichet, B. K. Directory of Useful Decoys, Enhanced (DUD-E): Better Ligands and Decoys for Better Benchmarking. *J. Med. Chem.* **2012**, *55* (14), 6582−6594.
(53) *RDKit: Open-Source Cheminformatics*. https://www.rdkit.org.

https://doi.org/10.1021/acs.jmedchem.4c03148
J. Med. Chem. 2025, 68, 4888−4907

(54) Labute, P. Protonate3D: Assignment of Ionization States and Hydrogen Coordinates to Macromolecular Structures. *Proteins:Struct., Funct., Bioinf.* **2009**, *75* (1), 187−205.
(55) Korb, O.; Stützle, T.; Exner, T. E. Empirical Scoring Functions for Advanced Protein−Ligand Docking with PLANTS. *J. Chem. Inf. Model.* **2009**, *49* (1), 84−96.
(56) Halgren, T. A. Merck Molecular Force Field. I. Basis, Form, Scope, Parameterization, and Performance of MMFF94. *J. Comput. Chem.* **1996**, *17* (5−6), 490−519.
(57) Mark, P.; Nilsson, L. Structure and Dynamics of the TIP3P, SPC, and SPC/E Water Models at 298 K. *J. Phys. Chem. A* **2001**, *105* (43), 9954−9960.
(58) Harder, E.; Damm, W.; Maple, J.; Wu, C.; Reboul, M.; Xiang, J. Y.; Wang, L.; Lupyan, D.; Dahlgren, M. K.; Knight, J. L.; Kaus, J. W.; Cerutti, D. S.; Krilov, G.; Jorgensen, W. L.; Abel, R.; Friesner, R. A. OPLS3: A Force Field Providing Broad Coverage of Drug-like Small Molecules and Proteins. *J. Chem. Theory Comput.* **2016**, *12* (1), 281−296.
(59) Nosé, S. A Molecular Dynamics Method for Simulations in the Canonical Ensemble. *Mol. Phys.* **1984**, *52* (2), 255−268.
(60) Hoover, W. G. Canonical Dynamics: Equilibrium Phase-Space Distributions. *Phys. Rev. A* **1985**, *31* (3), 1695−1697.
(61) Martyna, G. J.; Tuckerman, M. E.; Tobias, D. J.; Klein, M. L. Explicit Reversible Integrators for Extended Systems Dynamics. *Mol. Phys.* **1996**, *87* (5), 1117−1157.
(62) Humphrey, W.; Dalke, A.; Schulten, K. VMD: Visual Molecular Dynamics. *J. Mol. Graphics* **1996**, *14* (1), 33−38.
(63) Schröder, R.; Schmidt, J.; Blättermann, S.; Peters, L.; Janssen, N.; Grundmann, M.; Seemann, W.; Kaufel, D.; Merten, N.; Drewke, C.; Gomeza, J.; Milligan, G.; Mohr, K.; Kostenis, E. Applying Label-Free Dynamic Mass Redistribution Technology to Frame Signaling of G Protein−Coupled Receptors Noninvasively in Living Cells. *Nat. Protoc.* **2011**, *6* (11), 1748−1760.
(64) Huber, W.; Carey, V. J.; Gentleman, R.; Anders, S.; Carlson, M.; Carvalho, B. S.; Bravo, H. C.; Davis, S.; Gatto, L.; Girke, T.; Gottardo, R.; Hahne, F.; Hansen, K. D.; Irizarry, R. A.; Lawrence, M.; Love, M. I.; MacDonald, J.; Obenchain, V.; Oleś, A. K.; Pagès, H.; Reyes, A.; Shannon, P.; Smyth, G. K.; Tenenbaum, D.; Waldron, L.; Morgan, M. Orchestrating High-Throughput Genomic Analysis with Bioconductor. *Nat. Methods* **2015**, *12* (2), 115−121.
(65) Müller, G.; Lübow, C.; Weindl, G. Lysosomotropic Beta Blockers Induce Oxidative Stress and IL23A Production in Langerhans Cells. *Autophagy* **2020**, *16* (8), 1380−1395.

https://doi.org/10.1021/acs.jmedchem.4c03148
J. Med. Chem. 2025, 68, 4888−4907

Supporting Information

Discovery of novel isoxazole-based small-molecule Toll-like receptor 8 antagonists

Troy Matziol[1#], Valerij Talagayev[2#], Tjaša Slokan[3], Nika Strašek Benedik[3], Janine Holze[1], Matej Sova[3*], Gerhard Wolber[2*], Günther Weindl[1*]

[1] University of Bonn, Pharmaceutical Institute, Pharmacology and Toxicology Section, Gerhard-Domagk-Str. 3, 53121 Bonn, Germany
[2] Freie Universität Berlin, Institute of Pharmacy, Pharmaceutical and Medicinal Chemistry, Königin-Luise-Str. 2+4, 14195 Berlin, Germany
[3] University of Ljubljana, Faculty of Pharmacy, The Department of Pharmaceutical Chemistry, Aškerčeva 7, 1000 Ljubljana, Slovenia

[#]These authors contributed equally to this work

[*]Corresponding authors. e-mail: matej.sova@ffa.uni-lj.si, gerhard.wolber@fu-berlin.de, guenther.weindl@uni-bonn.de

Table of contents

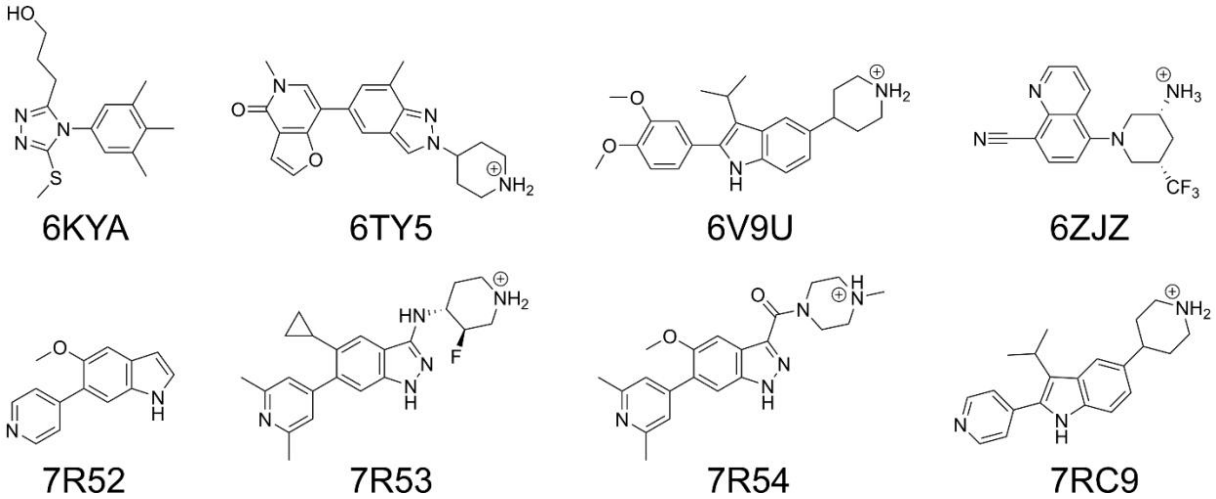

Figure S1. Chemical structures of known co-crystalized TLR8 antagonists.

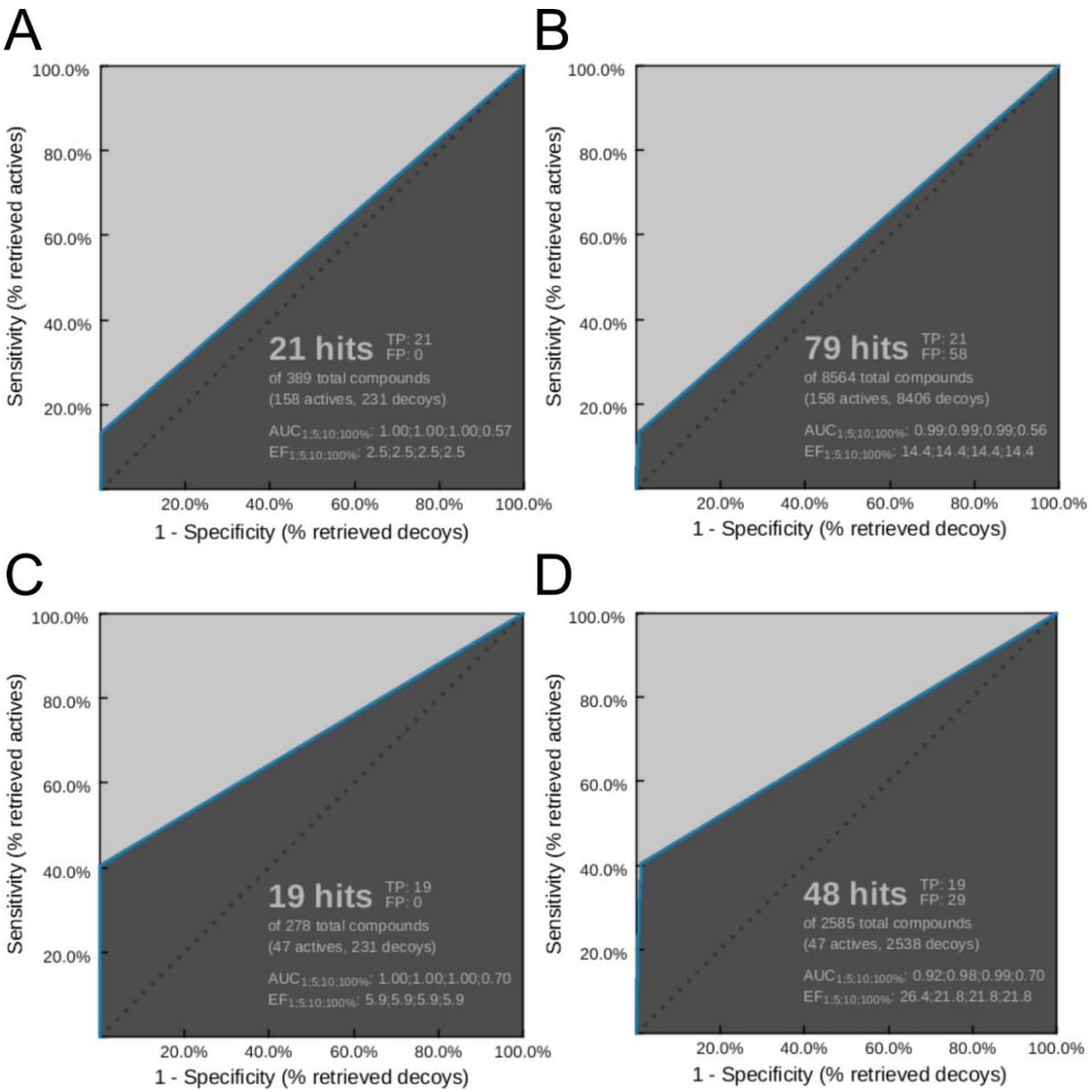

Figure S2. Validation of the virtual screening 3D pharmacophore.

(A) Validation of the 3D pharmacophore[1–3] with set A actives with an IC_{50} below 1000 nM and inactives obtained from ChEMBL.[4–6] (B) Validation of the 3D pharmacophore with set A actives and decoys obtained from DUD-E.[7] (C) Validation of the 3D pharmacophore with set B actives with an IC_{50} below 50 nM and inactives obtained from ChEMBL. (D) Validation of the 3D pharmacophore with set B actives with an IC_{50} below 50 nM and decoys obtained from DUD-E.

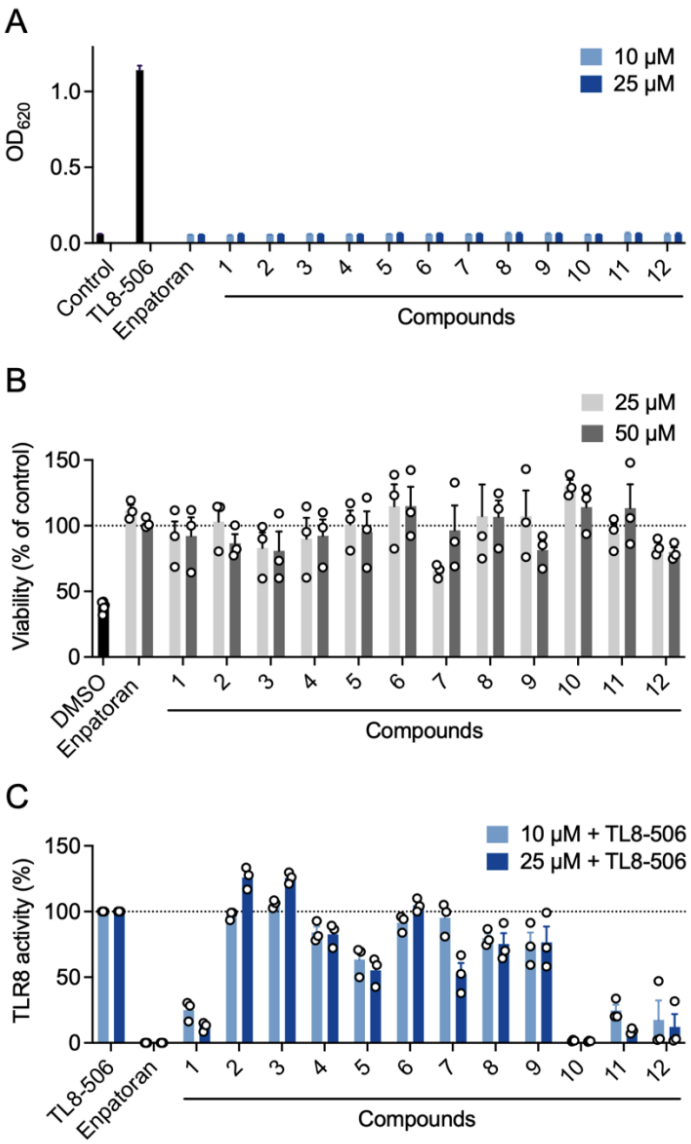

Figure S3. NF-κB activity and cell viability in hTLR8-HEK293 cells for compounds **1-12**.

(A) Activation of TLR8-dependent NF-κB activity in cells. HEK-Blue hTLR8 cells were stimulated with TL8-506 (0.6 µM) or the compounds (10 µM, 25 µM) for 24 h. Supernatants were analyzed for TLR8-mediated NF-κB activation by SEAP reporter assay using QuantiBlue (OD_{620}). Mean + SEM (n=3). (B) HEK-Blue hTLR8 cells were incubated with the compounds (25, 50 µM) for 24 h. Cell viability was analyzed using the MTT assay, and normalized to non-stimulated cells (vehicle control). DMSO (10%, v/v) was used as the cytotoxic control. Mean + SEM (n=3). (C) HEK-Blue hTLR8 cells were preincubated with the compounds (10 µM, 25 µM) for 1 h, and then stimulated with TL8-506 (0.6 µM) for 24 h. Supernatants were analyzed for TLR8-mediated NF-κB activation by SEAP reporter assay using QuantiBlue (OD_{620}), and normalized to TL8-506 alone. Mean + SEM (n=3).

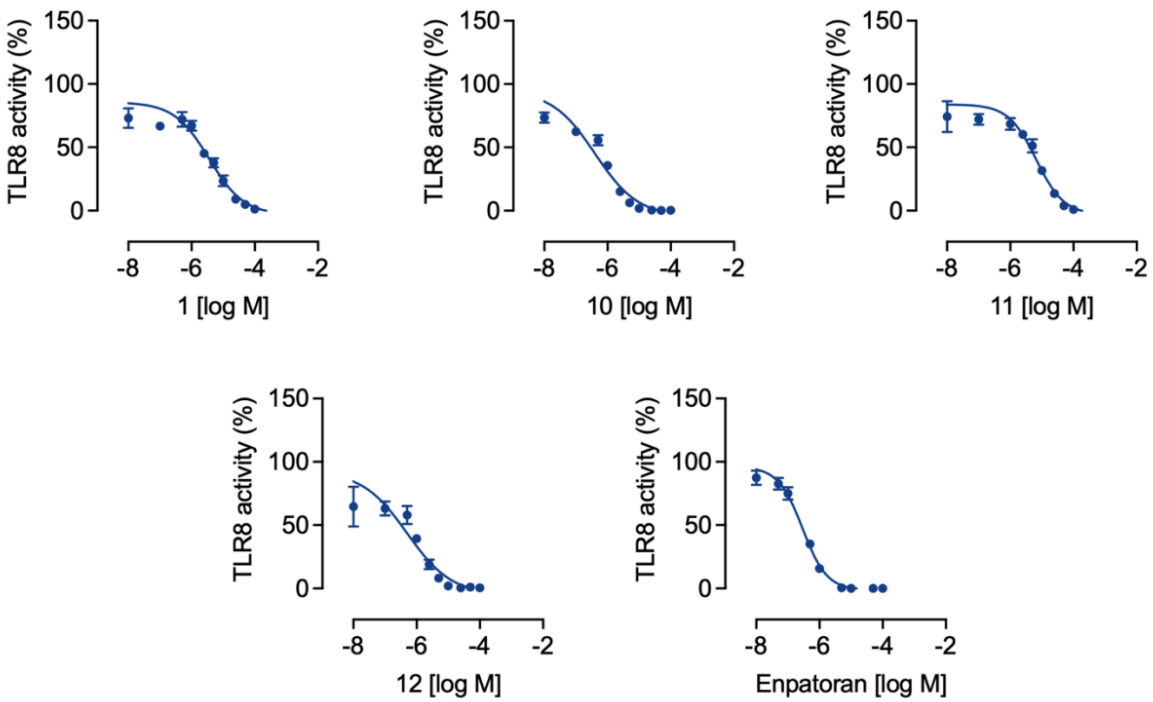

Figure S4. Concentration-response curves in hTLR8-HEK293 cells for compounds **1**, **10**-**12**.

HEK-Blue hTLR8 cells were preincubated with increasing concentrations of the compounds for 1 h, and then stimulated with TL8-506 (0.6 μM) for 24 h. Supernatants were analyzed for TLR8-mediated NF-κB activation by SEAP reporter assay using QuantiBlue (OD_{620}). For the calculation of the concentration-response curve nonlinear regression with variable slope (four parameters) was used. IC_{50} values are shown in Table 1. Mean ± SEM (n=3-4).

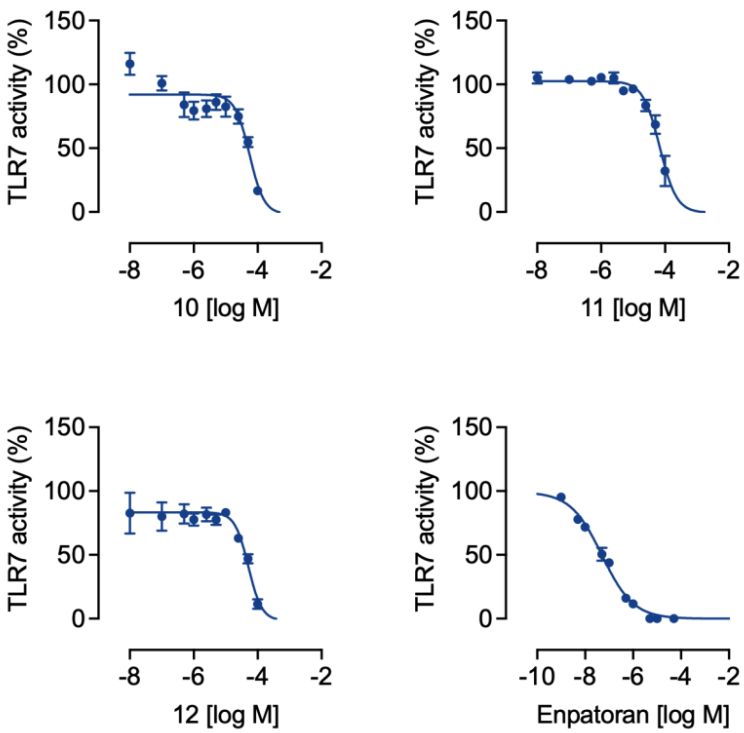

Figure S5. Concentration-response curves in hTLR7-HEK293 cells for compounds **10**-**12**.

HEK-Blue hTLR7 cells were preincubated with increasing concentrations of the compounds for 1 h, and then stimulated with CL307 (1.7 µM) for 24 h. Supernatants were analyzed for TLR7-mediated NF-κB activation by SEAP reporter assay using QuantiBlue (OD_{620}). For the calculation of the concentration-response curve nonlinear regression with variable slope (four parameters) was used. IC_{50} values are shown in Table 1. Mean ± SEM (n=4).

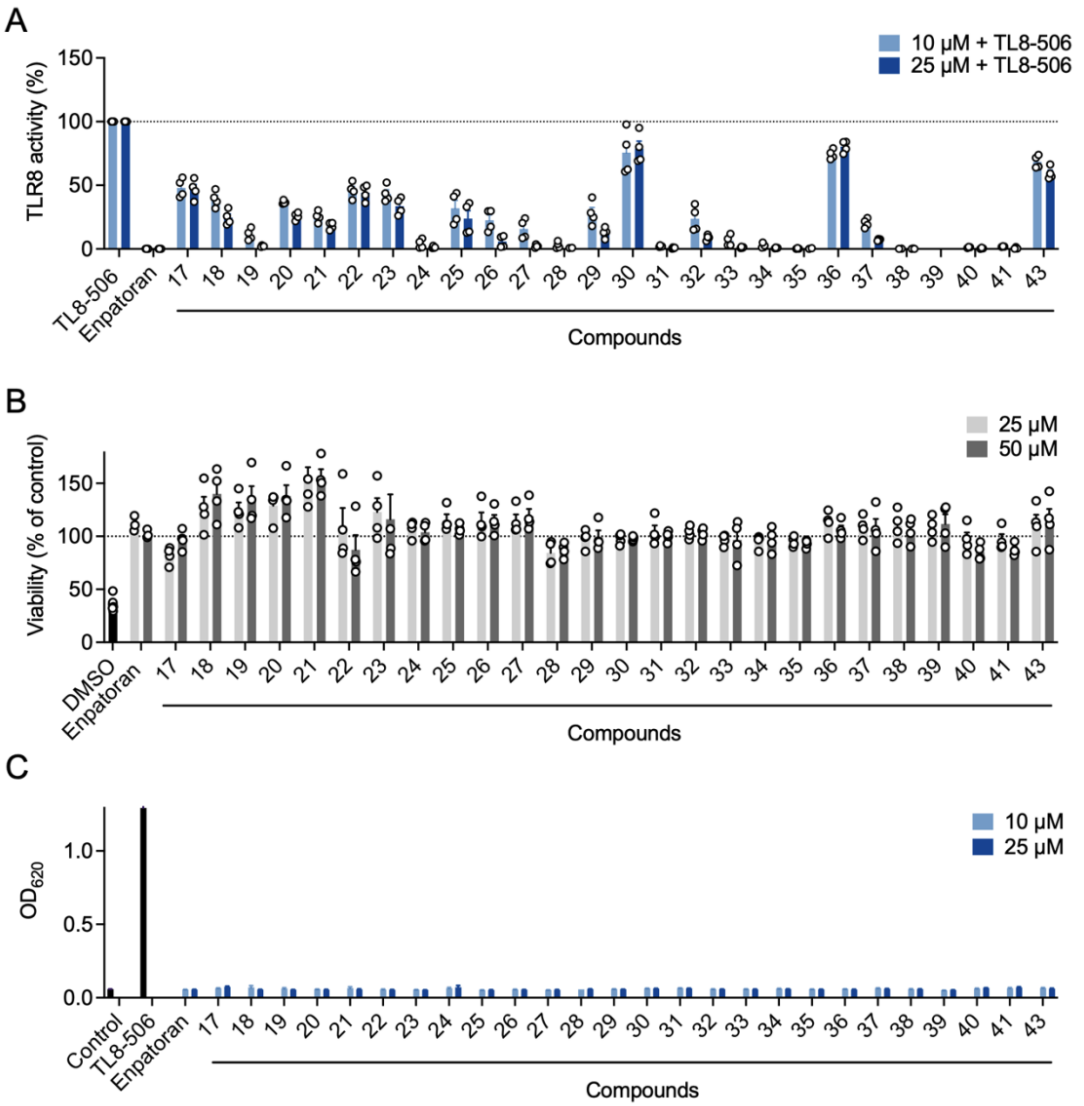

Figure S6. NF-κB activity and cell viability in hTLR8-HEK293 cells for compounds **17-41, 43**. (A) HEK-Blue hTLR8 cells were preincubated with the compounds (10 µM, 25 µM) for 1 h, and then stimulated with TL8-506 (0.6 µM) for 24 h. Supernatants were analyzed for TLR8-mediated NF-κB activation by SEAP reporter assay using QuantiBlue (OD_{620}), and normalized to TL8-506 alone. Mean + SEM (n=4). (B) HEK-Blue hTLR8 cells were incubated with the compounds (25, 50 µM) for 24 h. Cell viability was analyzed using the MTT assay, and normalized to non-stimulated cells (vehicle control). DMSO (10%, v/v) was used as the cytotoxic control. Mean + SEM (n=4). (C) Activation of TLR8-dependent NF-κB activity in cells. HEK-Blue hTLR8 cells were stimulated with TL8-506 (0.6 µM) or the compounds (10 µM, 25 µM) for 24 h. Supernatants were analyzed for TLR8-mediated NF-κB activation by SEAP reporter assay using QuantiBlue (OD_{620}). Mean + SEM (n=4).

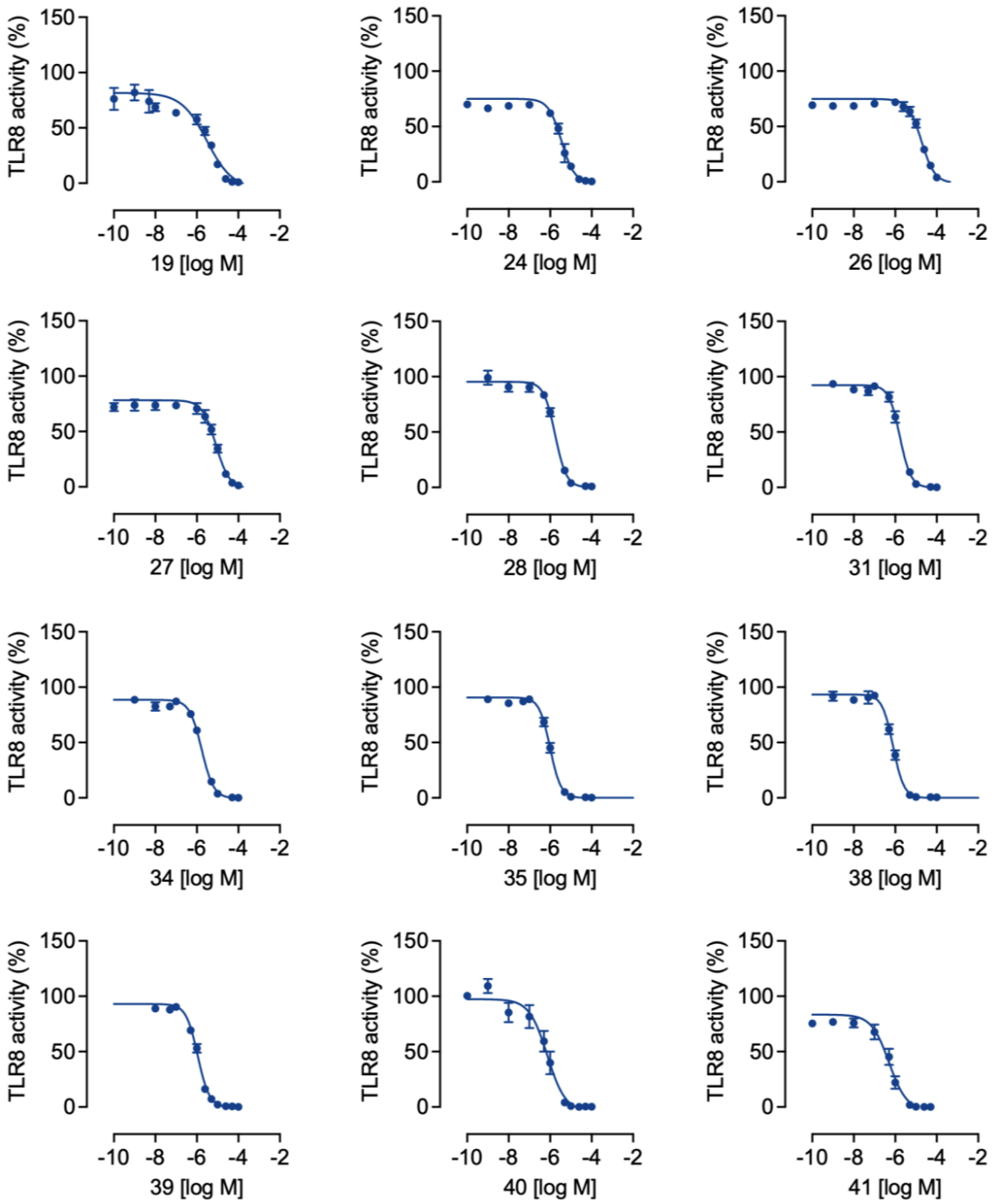

Figure S7. Concentration-response curves in hTLR8-HEK293 cells for synthesized compounds. HEK-Blue hTLR8 cells were preincubated with increasing concentrations of the compounds **19**, **24**, **26-28**, **31**, **34**, **35**, **38-41** for 1 h, and then stimulated with TL8-506 (0.6 μM) for 24 h. Supernatants were analyzed for TLR8-mediated NF-κB activation by SEAP reporter assay using QuantiBlue (OD_{620}). For the calculation of the concentration-response curves nonlinear regression with variable slope (four parameters) was used. IC_{50} values are shown in Table 2. Mean ± SEM (n=3-4).

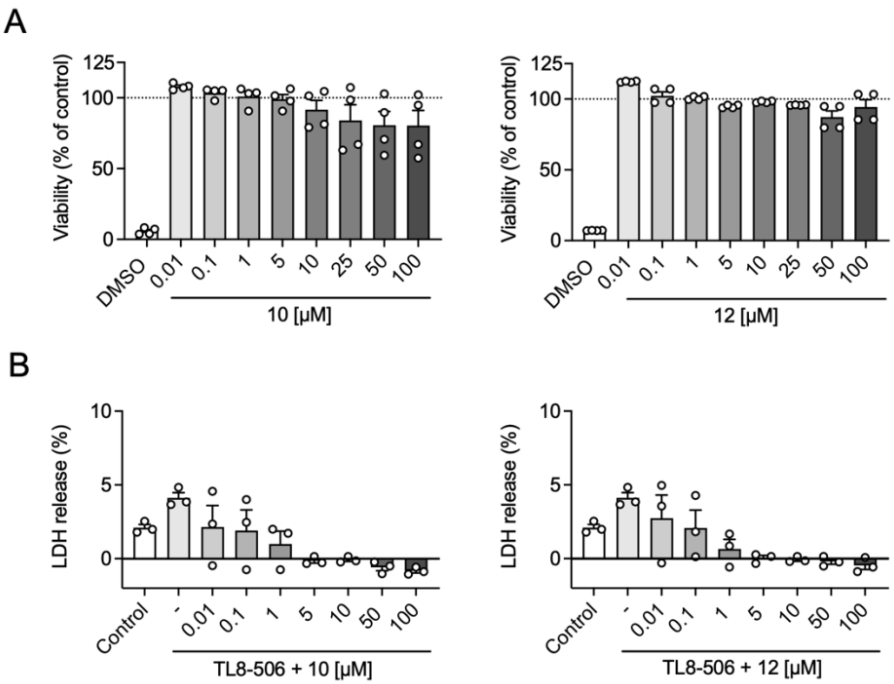

Figure S8. Cell viability of compounds **10** and **12** in THP-1 macrophages and PMBCs.

(A) THP-1 Macrophages were incubated with increasing concentrations of **10** and **12** for 24 h. Cell viability was analyzed using the MTT assay, and normalized to non-stimulated cells (vehicle control). DMSO (10%, v/v) was used as the cytotoxic control. Mean + SEM (n=3). (B) PBMCs were incubated with 0.6 µM TL8-506 or increasing concentrations of **10** and **12** for 24 h. LDH release was determined in cell culture supernatants. Results are shown as percentage of the maximum LDH release. Mean + SEM (n=3-4).

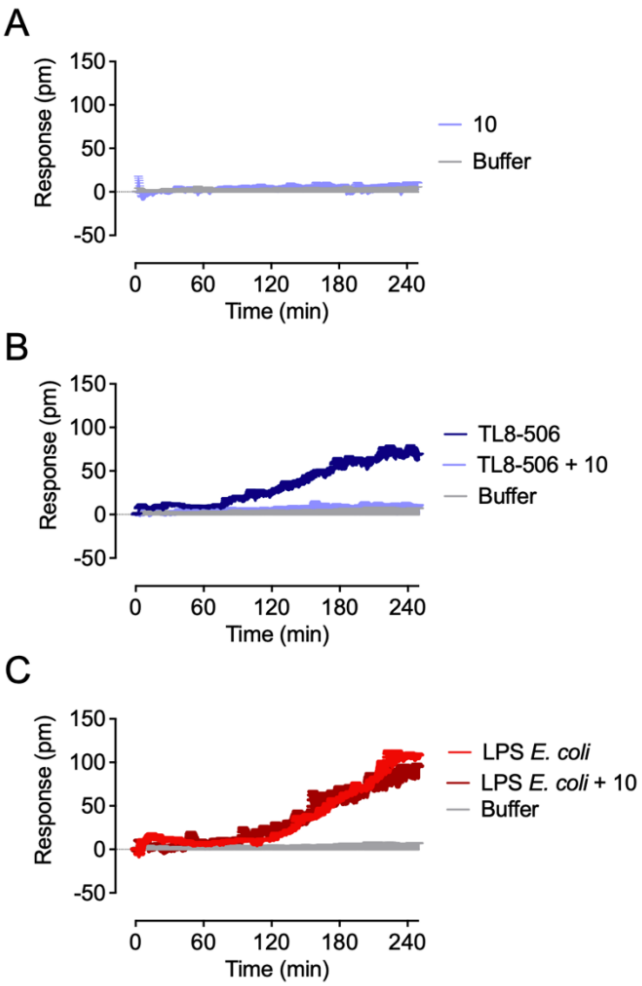

Figure S9. Inhibition of TLR8-dependent activity in THP-1 Dual cells.

Baseline corrected DMR representative recordings of THP-1 Dual MD2-CD14-TLR4 cells stimulated with (A) compound **10** (10 µM) or after 1.5 h preincubation with compound **10** (10 µM) with either (B) TL8-506 (6 µM) or (C) LPS from *E. coli* (1 µg/ml). Calculated pharmacological parameters of the concentration-response curves are depicted in Table S6. Data are mean ± SEM of four independent experiments.

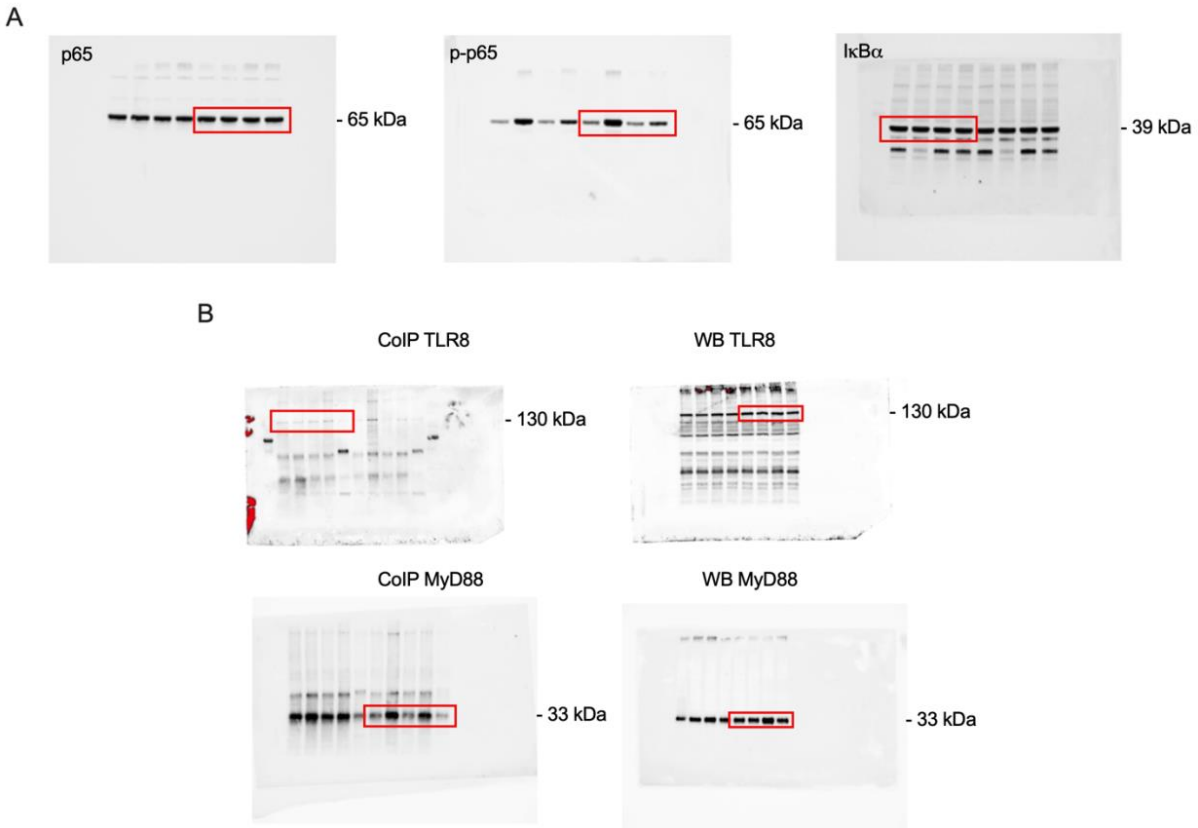

Figure S10. Whole uncropped images of the original western blots.

(A) Complete western blots of NF-κB p65, NF-κB phospho-p65, and IκBα shown in Figure 4E.
(B) Complete western blots of TLR8 and MyD88 after immunoprecipitation shown in Figure 4G.

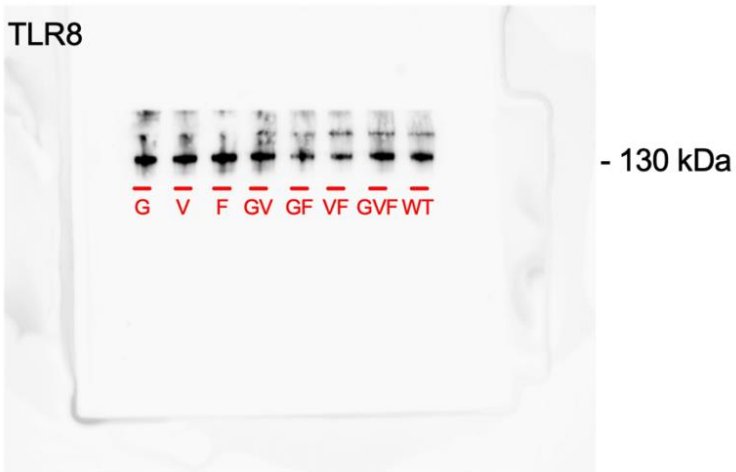

Figure S11. Transfection of mutant and wildtype TLR8 plasmids into HEK293 cells.

HEK293 reporter control cells (Null1) were transfected with mutant (G=Glycin351Prolin, V=Valin378Methionine, F=Phenylalanine495Leucin; GV, GF, VF and GVF=dual- or triple-mutated combinations) or wildtype TLR8 plasmid (WT).

Figure S12. HPLC traces for purchased compounds **1-12**.

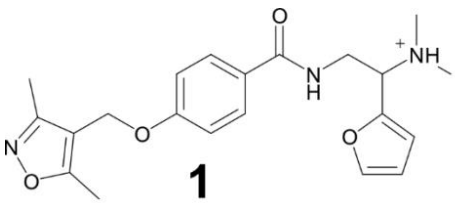

1

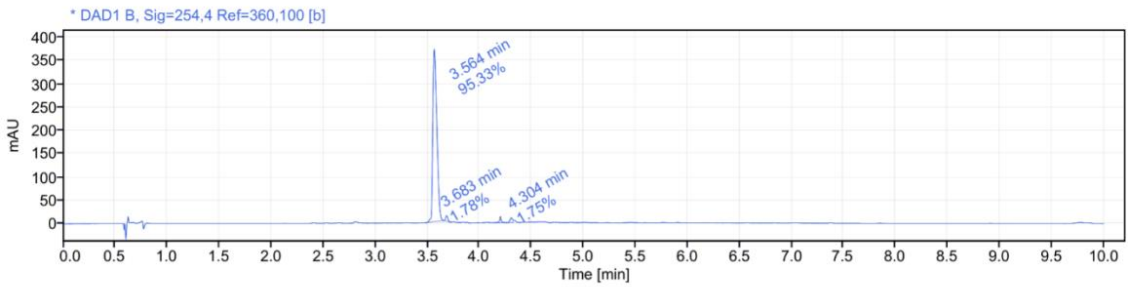

Signal: *DAD1 B, Sig=254,4 Ref= 360,100 [b]

RT	Peak area	Area %
3.564	998.726	95.33
3.683	18.692	1.78
4.156	11.921	1.14
4.304	18.311	1.75
Sum	1047.65	

HPLC trace for compound **1**.

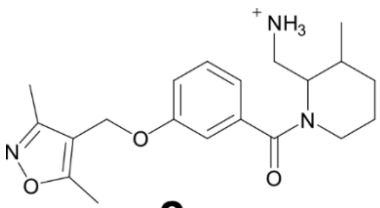

2

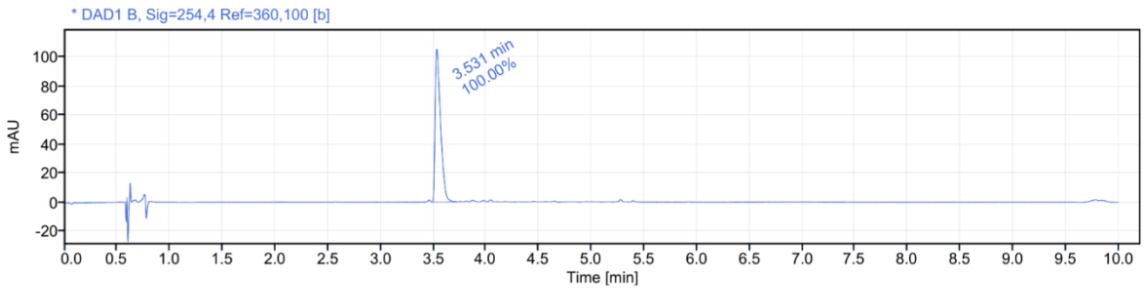

Signal: *DAD1 B, Sig=254,4 Ref= 360,100 [b]

RT	Peak area	Area %
3.531	379.3	100.00
Sum	379.3	

HPLC trace for compound **2**.

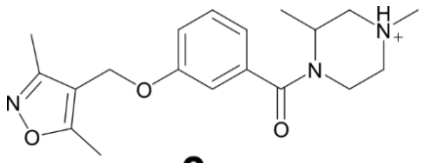

3

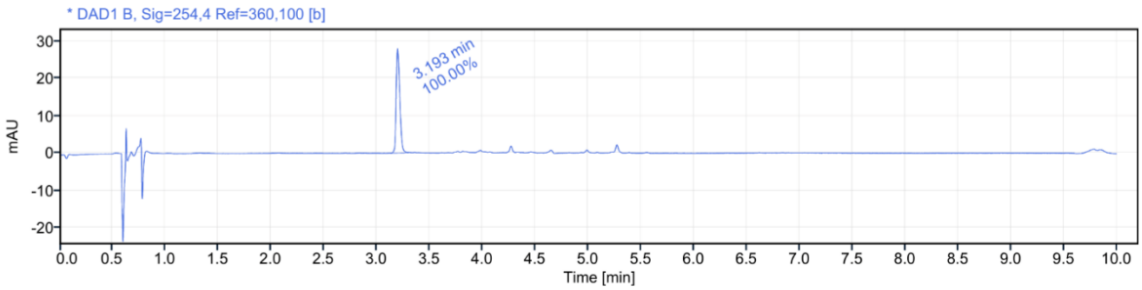

Signal: *DAD1 B, Sig=254,4 Ref= 360,100 [b]

RT	Peak area	Area %
3.193	67.29	100.00
Sum	67.29	

HPLC trace for compound **3**.

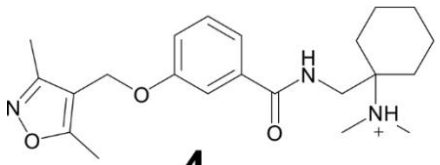

4

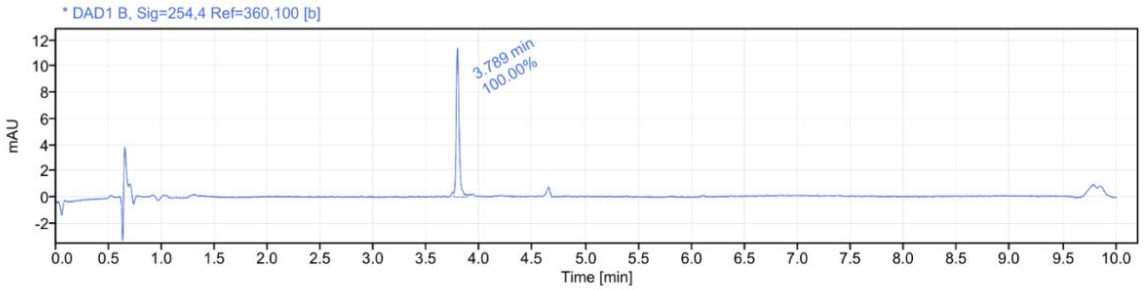

Signal: *DAD1 B, Sig=254,4 Ref= 360,100 [b]

RT	Peak area	Area %
3.789	21.72	100.00
Sum	21.72	

HPLC trace for compound **4**.

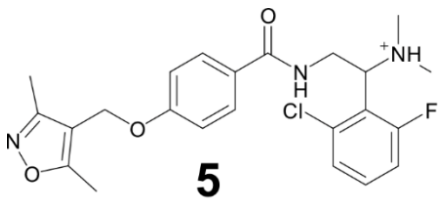

5

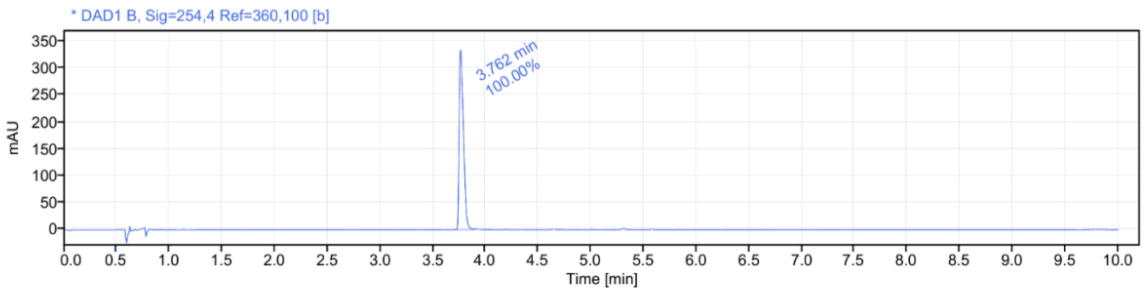

Signal: *DAD1 B, Sig=254,4 Ref= 360,100 [b]

RT	**Peak area**	**Area %**
3.762	954.9	100.00
Sum	954.9	

HPLC trace for compound **5**.

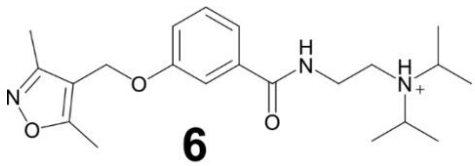

6

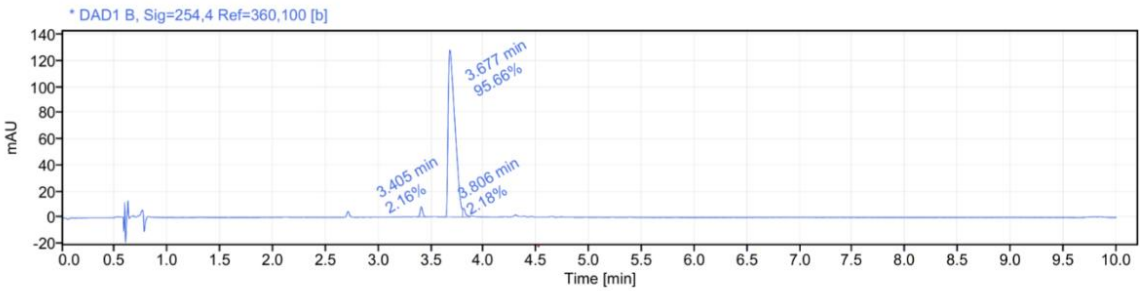

Signal: *DAD1 B, Sig=254,4 Ref= 360,100 [b]

RT	Peak area	Area %
3.405	12.97	2.16
3.677	574.1	95.66
3.806	13.05	2.18
Sum	600.12	

HPLC trace for compound **6**.

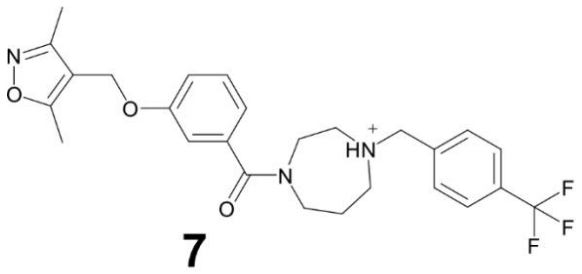

7

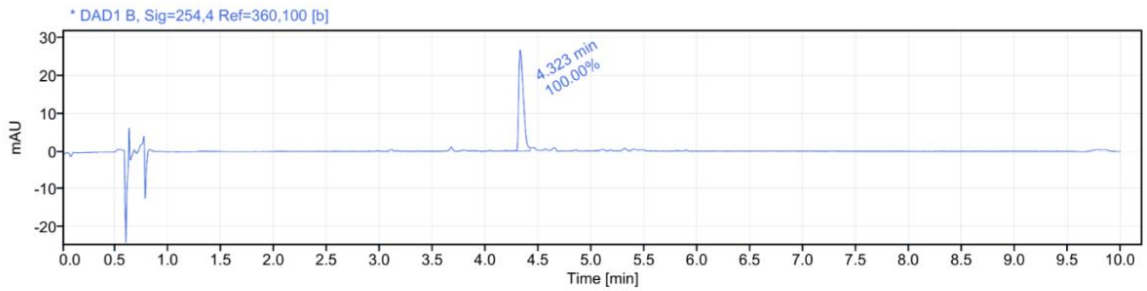

Signal: *DAD1 B, Sig=254,4 Ref= 360,100 [b]

RT	**Peak area**	**Area %**
4.323	81.04	100.00
Sum	81.04	

HPLC trace for compound **7**.

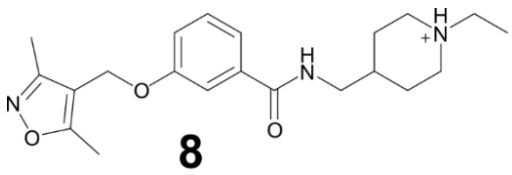

8

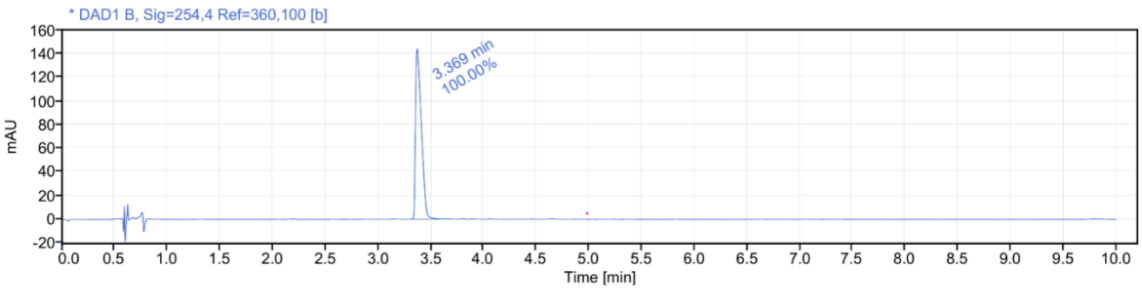

Signal: *DAD1 B, Sig=254,4 Ref= 360,100 [b]

RT	Peak area	Area %
3.369	554.1	100.00
Sum	554.1	

HPLC trace for compound **8**.

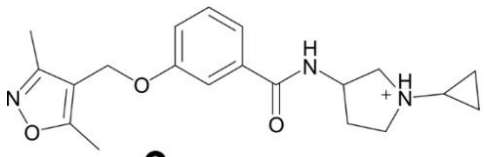

9

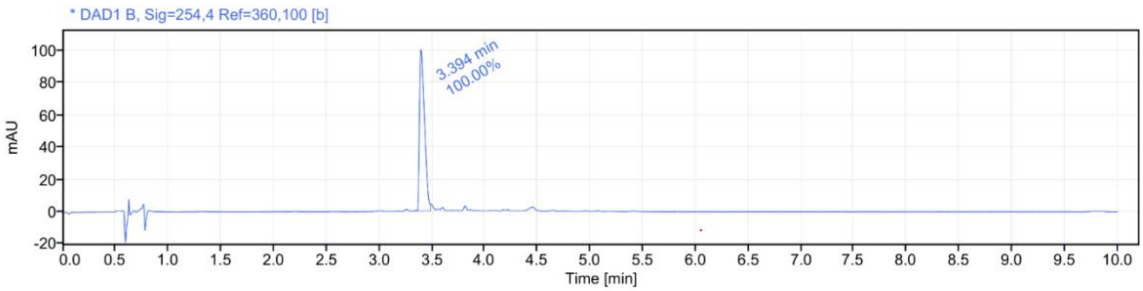

Signal: *DAD1 B, Sig=254,4 Ref= 360,100 [b]

RT	Peak area	Area %
3.394	337.2	100.00
Sum	337.2	

HPLC trace for compound **9**.

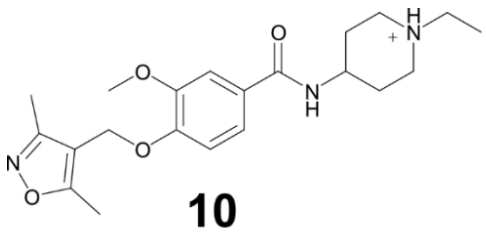

10

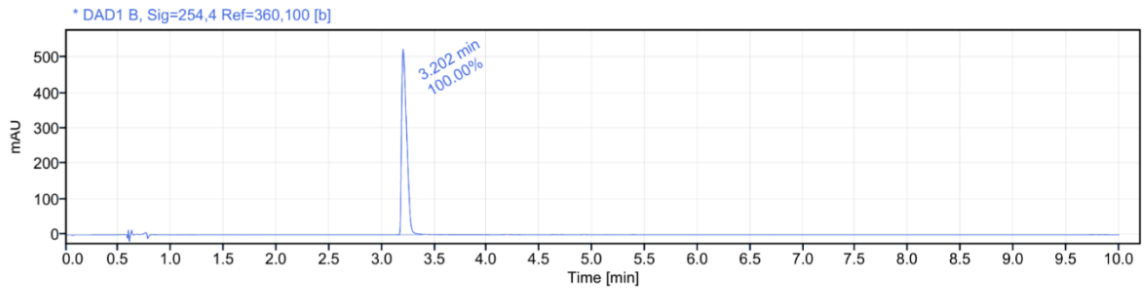

Signal: *DAD1 B, Sig=254,4 Ref= 360,100 [b]

RT	Peak area	Area %
3.202	1768	100.00
Sum	1768	

HPLC trace for lead compound **10**.

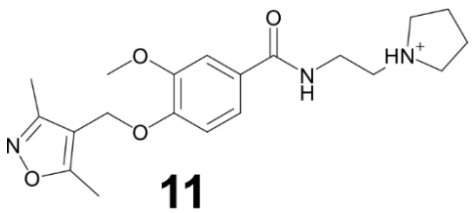

11

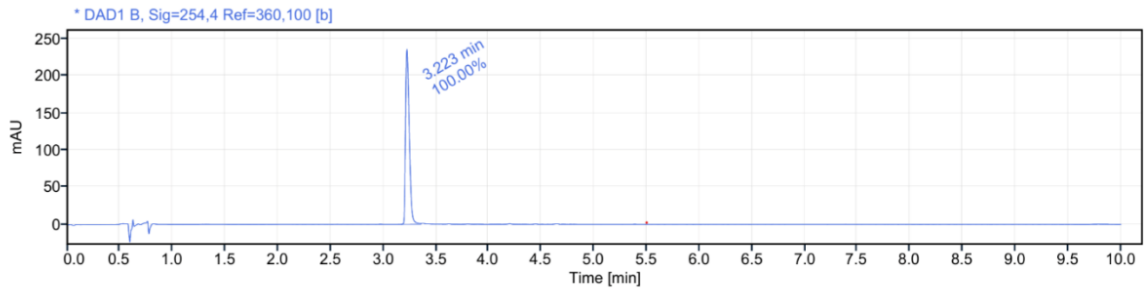

Signal: *DAD1 B, Sig=254,4 Ref= 360,100 [b]

RT	Peak area	Area %
3.223	584.0	100.00
Sum	584.0	

HPLC trace for compound **11**.

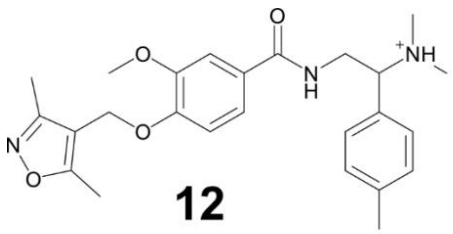

12

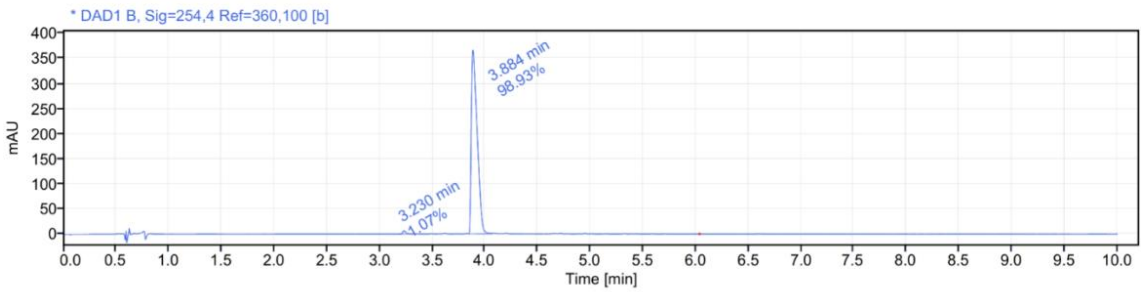

Signal: *DAD1 B, Sig=254,4 Ref= 360,100 [b]

RT	**Peak area**	**Area %**
3.230	15.48	1.07
3.884	1429	98.93
Sum	1444.48	

HPLC trace for compound **12**.

Figure S13. ^{1}H NMR spectra for purchased active compounds **1**, **10**-**12**.

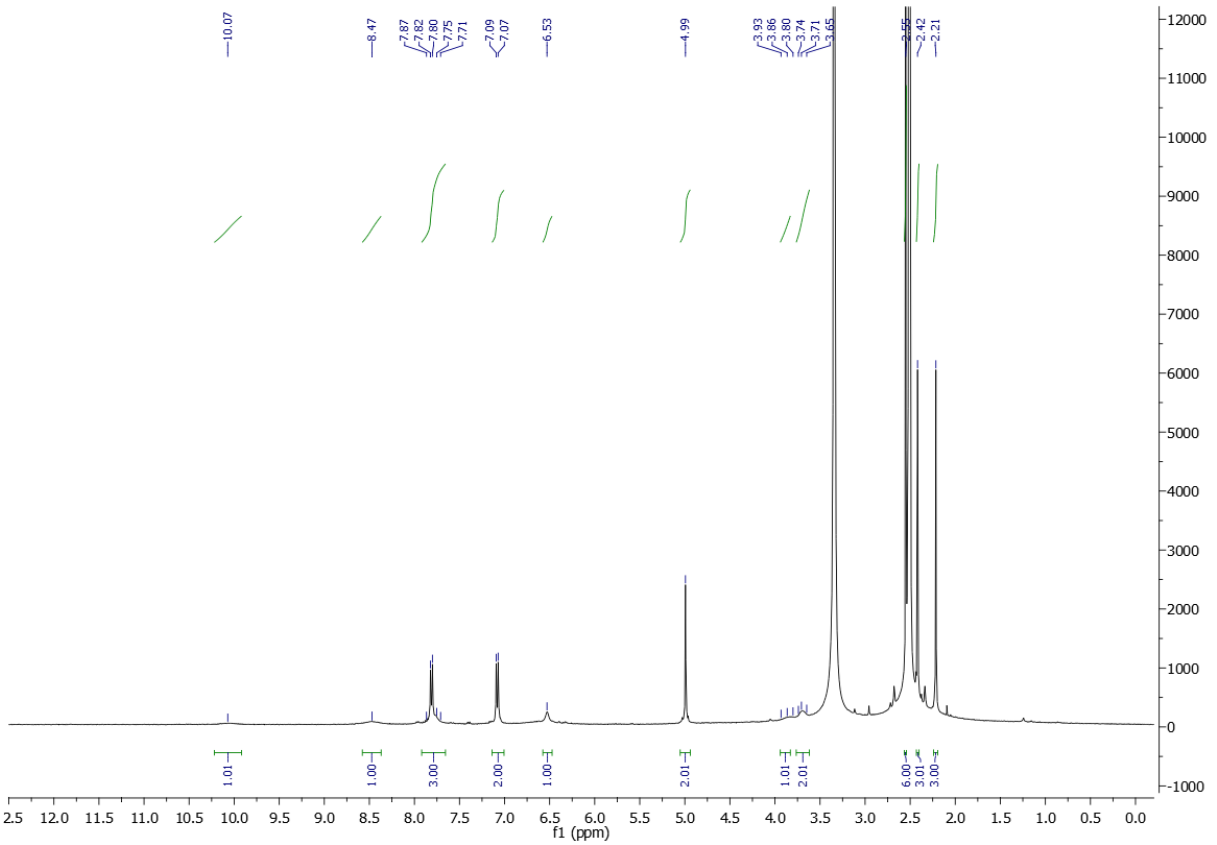

^{1}H NMR for compound **1**.

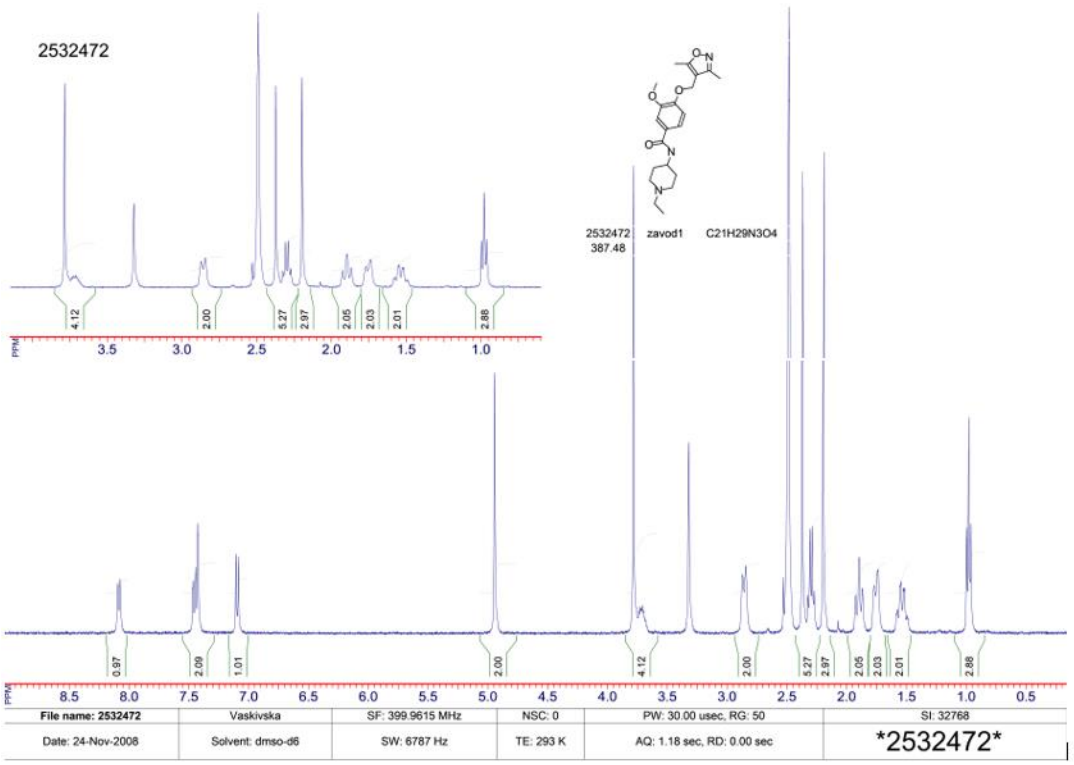

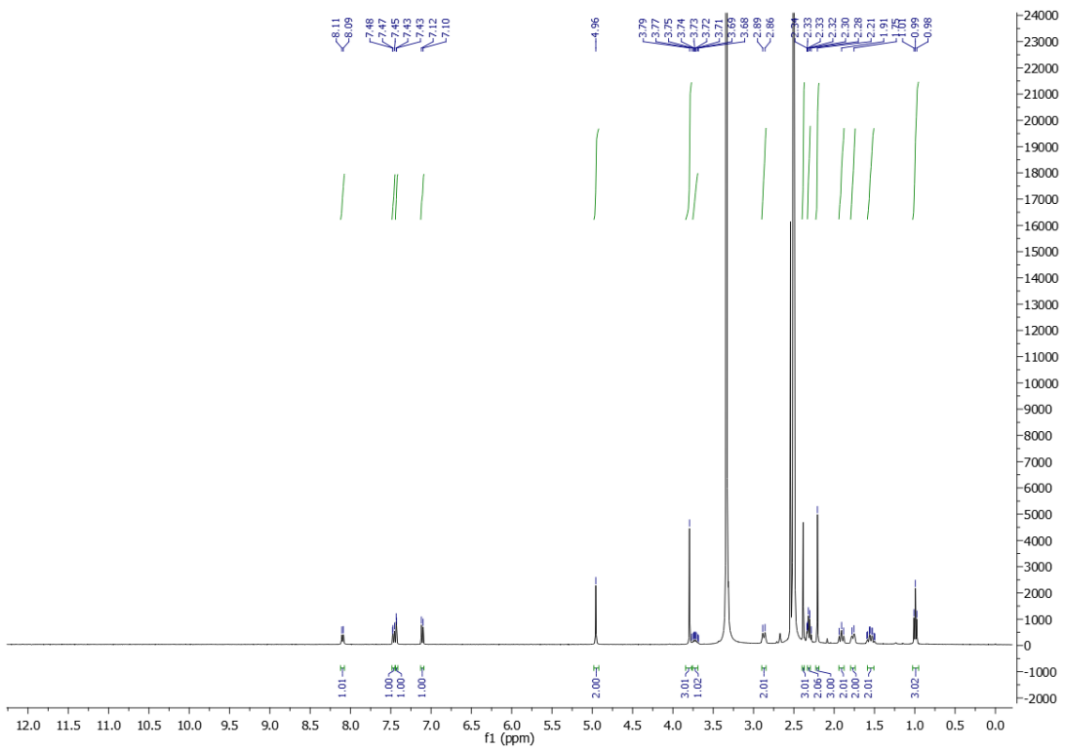

^{1}H NMR for lead compound **10** (top: provided by vendor, bottom: in-house analysis).

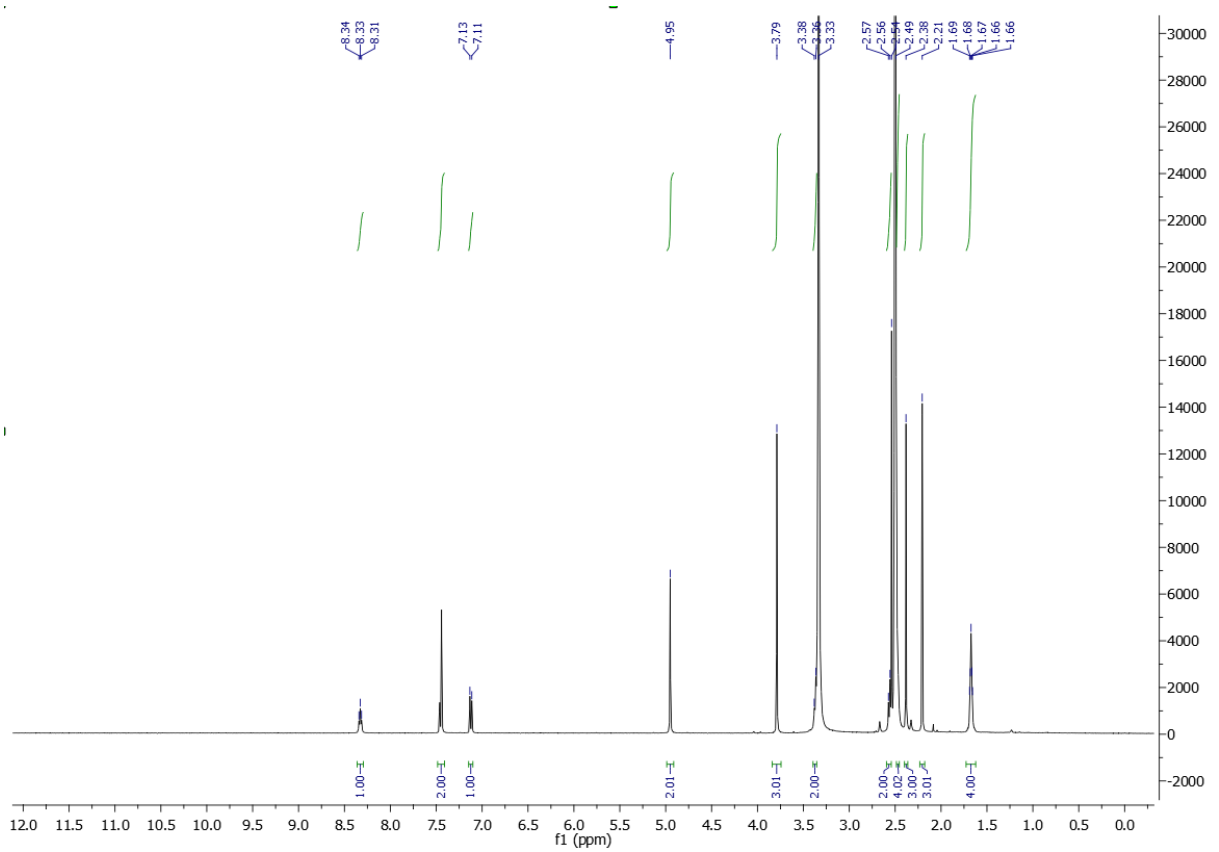

^{1}H NMR for compound **11**.

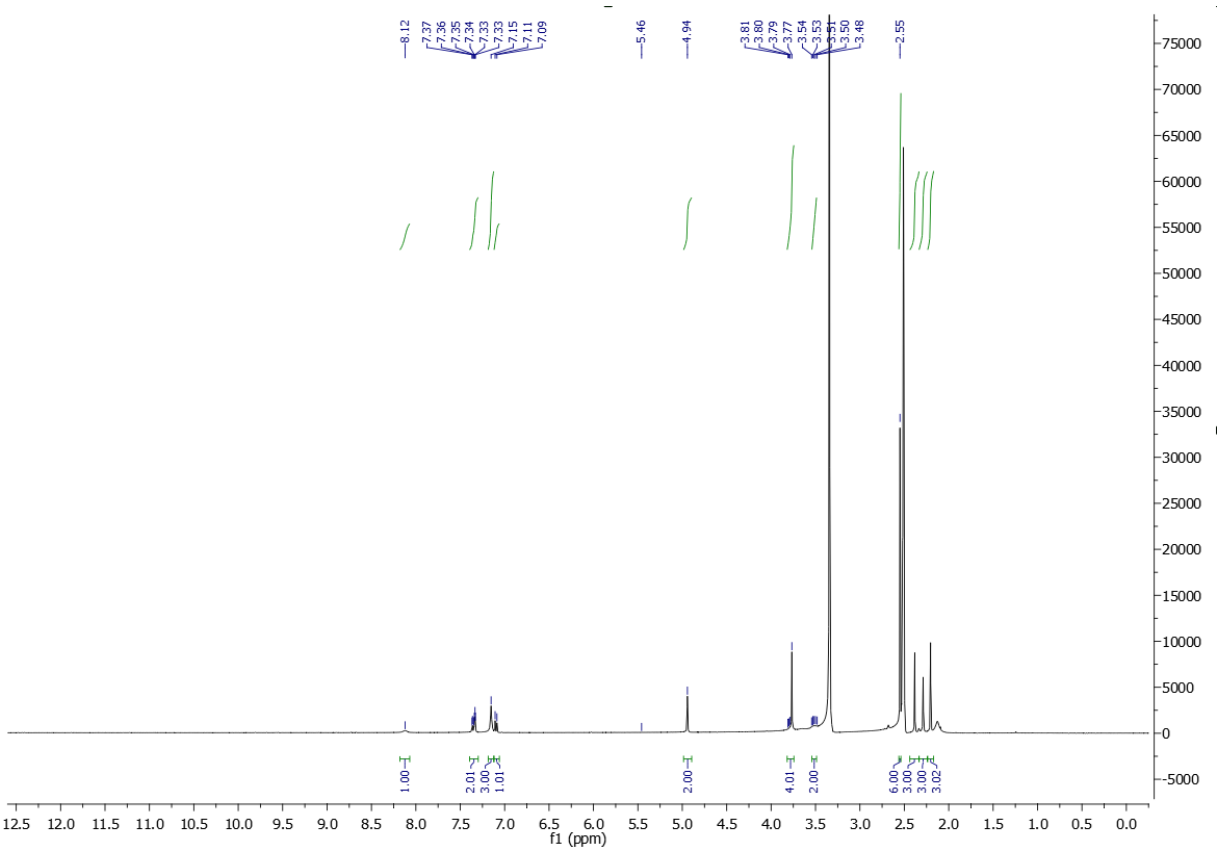

^{1}H NMR for compound **12**.

Figure S14. ^{1}H NMR, ^{13}C NMR and HPLC traces for synthesized active compounds.

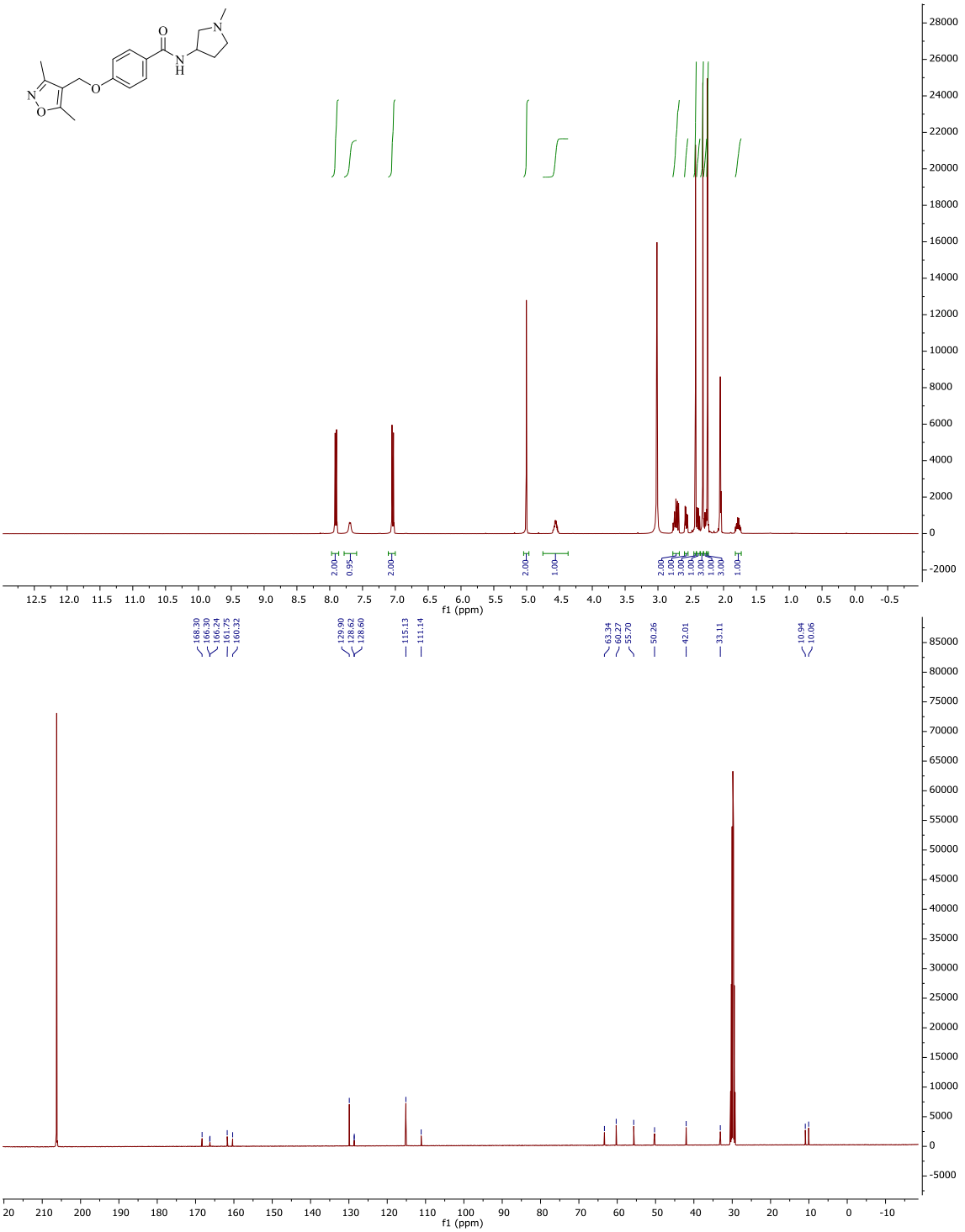

^{1}H and ^{13}C NMR for compound **19**.

Chromatogram

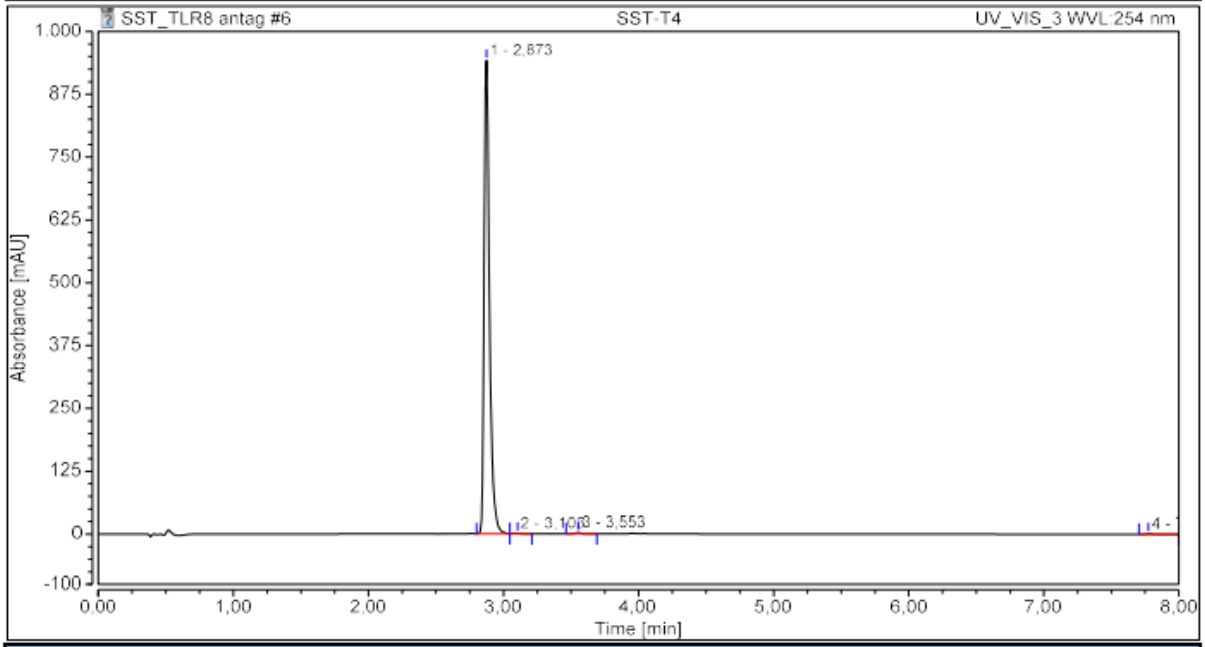

Integration Results

No.	Peak Name	Retention Time min	Area mAU*min	Height mAU	Relative Area %	Relative Height %	Amount n.a.
1		2,873	43,304	942,087	99,38	99,48	n.a.
2		3,103	0,079	1,027	0,18	0,11	n.a.
3		3,553	0,124	2,671	0,28	0,28	n.a.
4		7,773	0,066	1,258	0,15	0,13	n.a.
Total:			**43,573**	**947,042**	**100,00**	**100,00**	

HPLC trace for compound **19**.

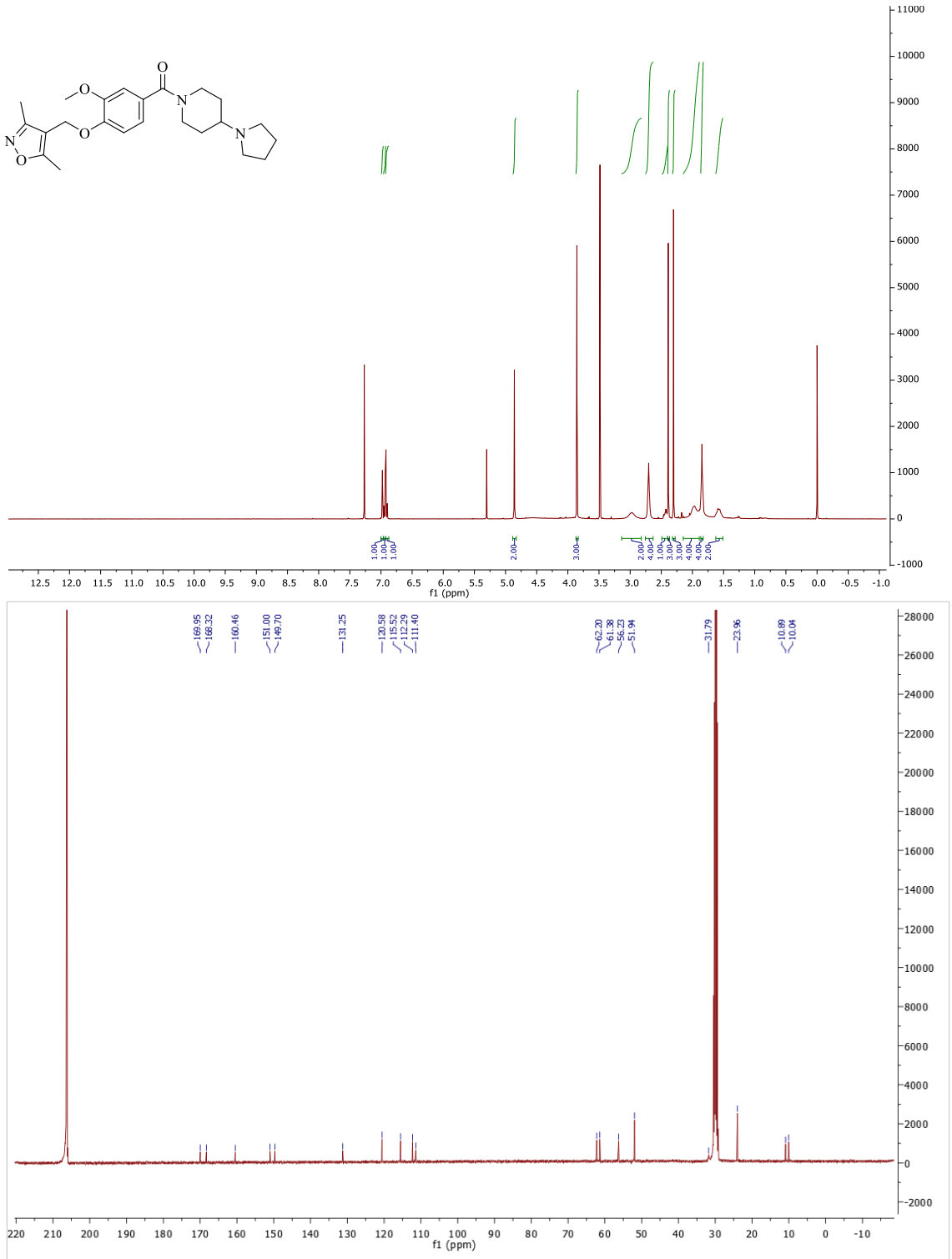

^{1}H and ^{13}C NMR for compound **24**.

Chromatogram

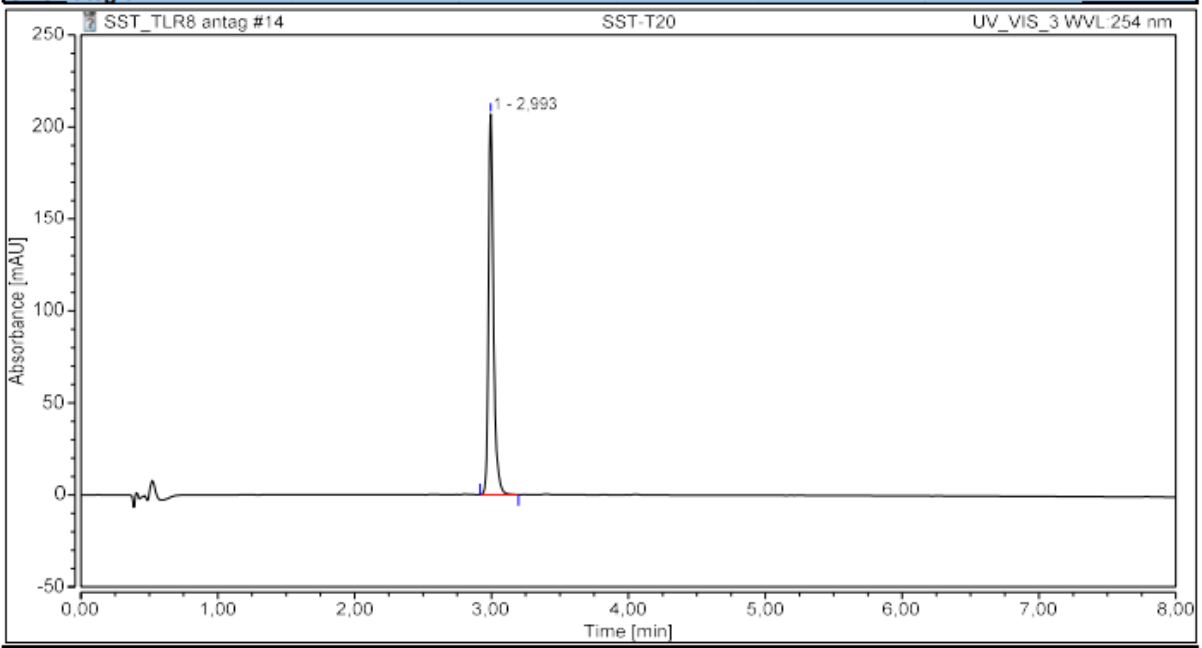

Integration Results

No.	Peak Name	Retention Time min	Area mAU*min	Height mAU	Relative Area %	Relative Height %	Amount n.a.
1		2,993	8,708	206,790	100,00	100,00	n.a.
Total:			**8,708**	**206,790**	**100,00**	**100,00**	

HPLC trace for compound **24**.

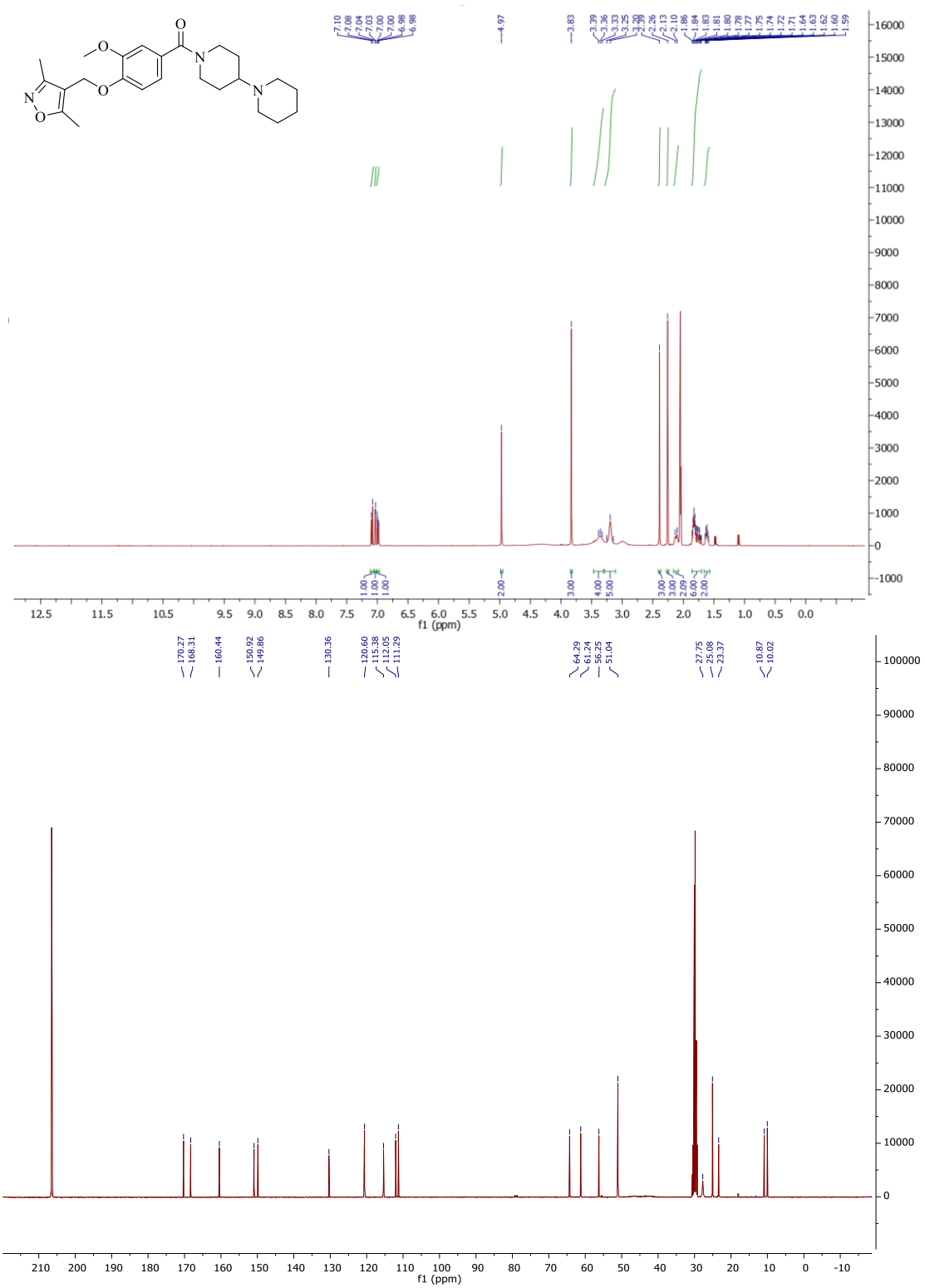

^{1}H and ^{13}C NMR for compound **26**.

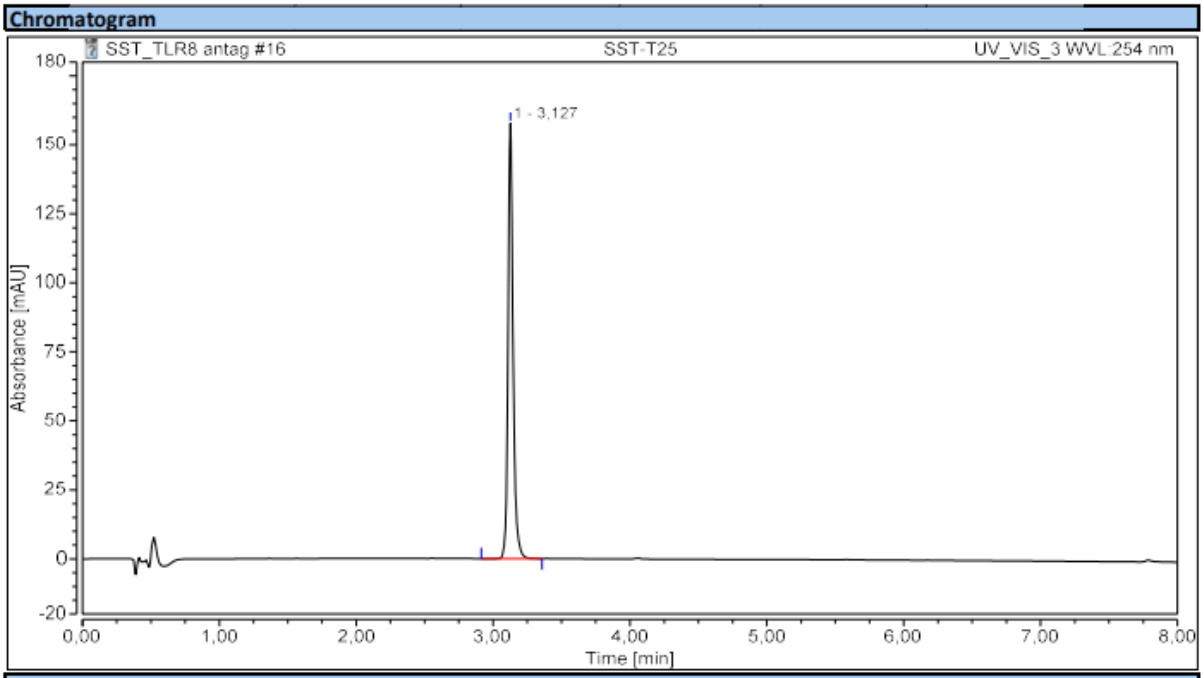

Integration Results

No.	Peak Name	Retention Time min	Area mAU*min	Height mAU	Relative Area %	Relative Height %	Amount n.a.
1		3,127	6,716	157,672	100,00	100,00	n.a.
Total:			**6,716**	**157,672**	**100,00**	**100,00**	

HPLC trace for compound **26**.

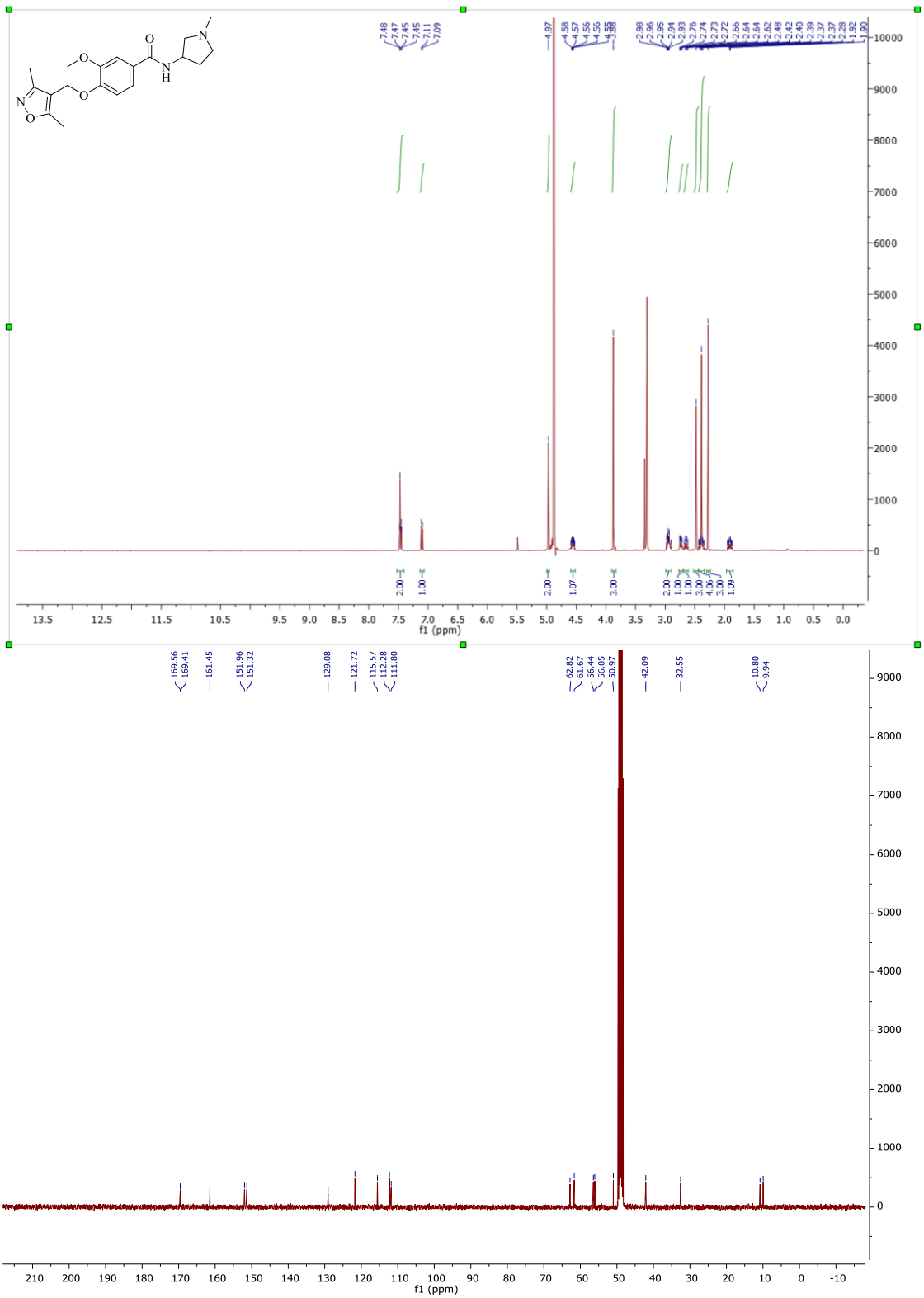

^{1}H and ^{13}C NMR for compound **27**.

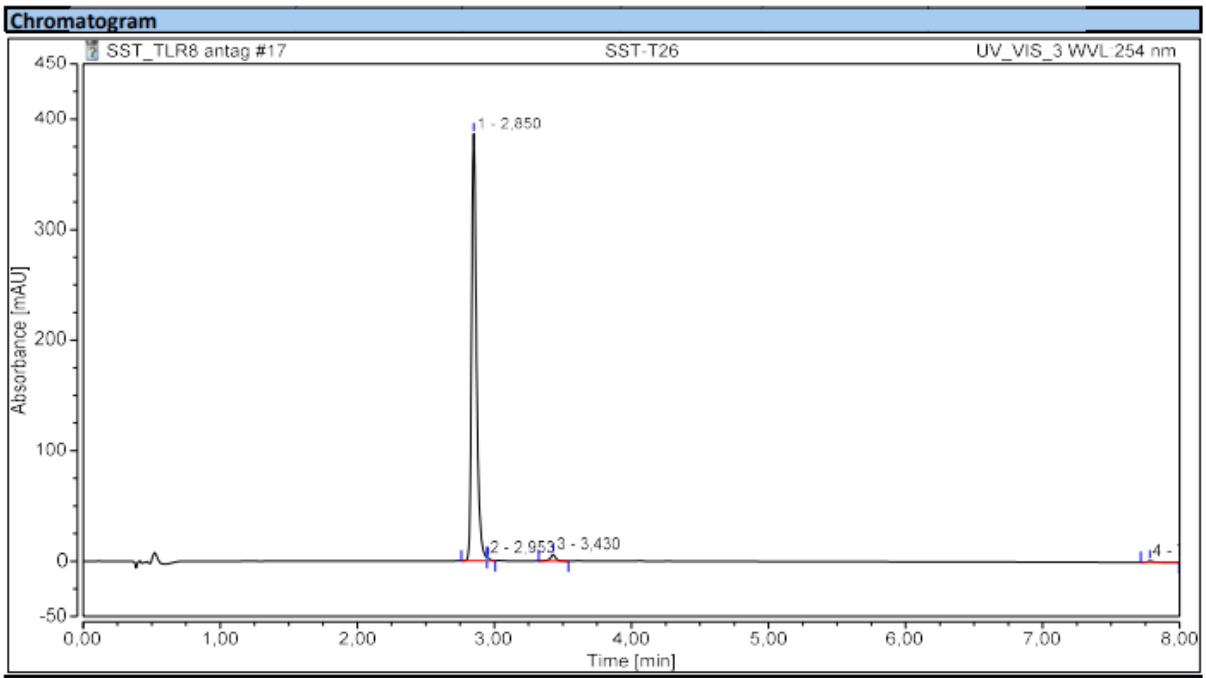

Integration Results

No.	Peak Name	Retention Time min	Area mAU*min	Height mAU	Relative Area %	Relative Height %	Amount n.a.
1		2,850	15,950	386,276	97,63	97,55	n.a.
2		2,953	0,056	2,426	0,35	0,61	n.a.
3		3,430	0,266	6,085	1,63	1,54	n.a.
4		7,783	0,065	1,181	0,40	0,30	n.a.
Total:			**16,338**	**395,968**	**100,00**	**100,00**	

HPLC trace for compound **27**.

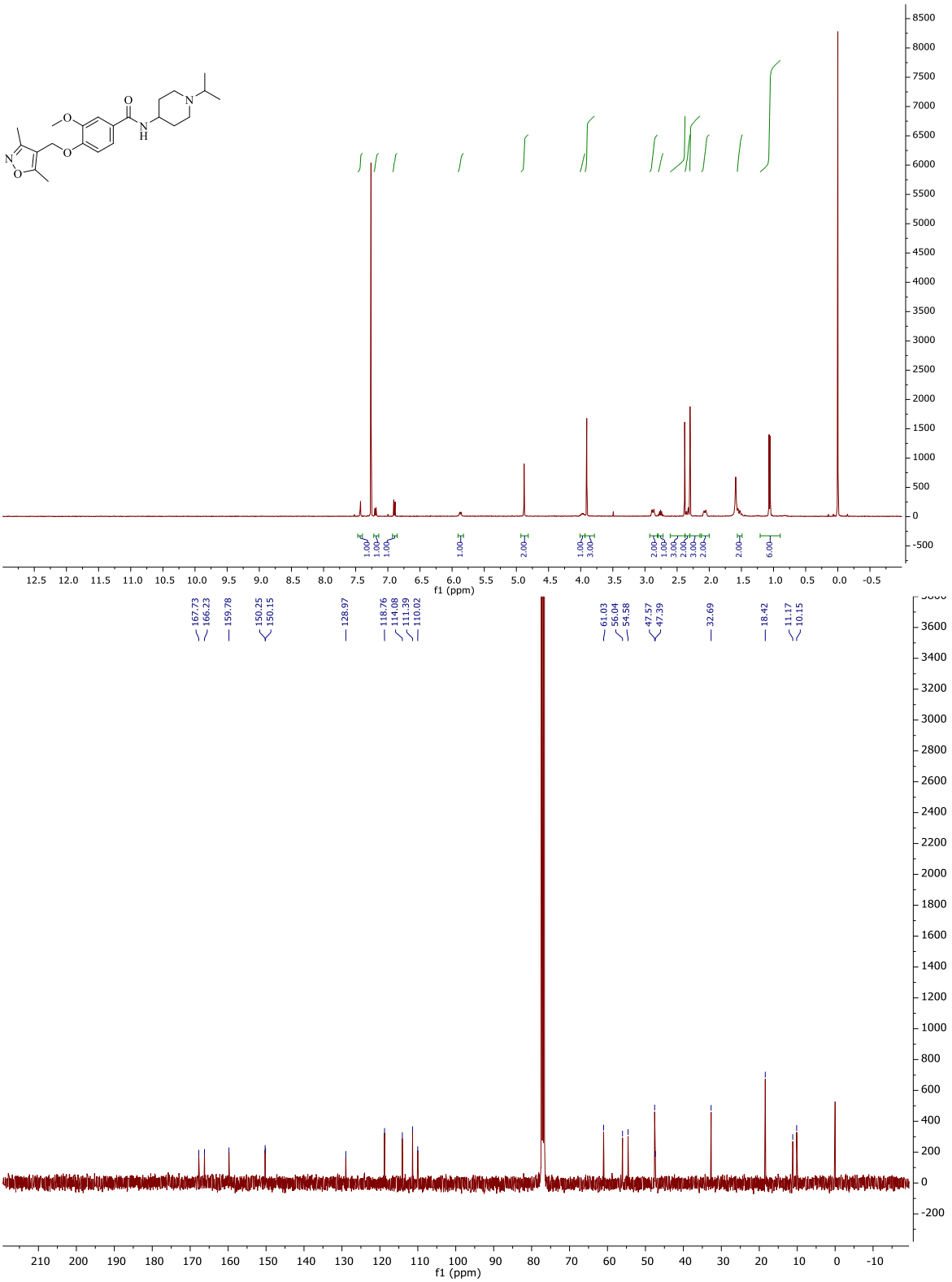

^{1}H and ^{13}C NMR for compound **28**.

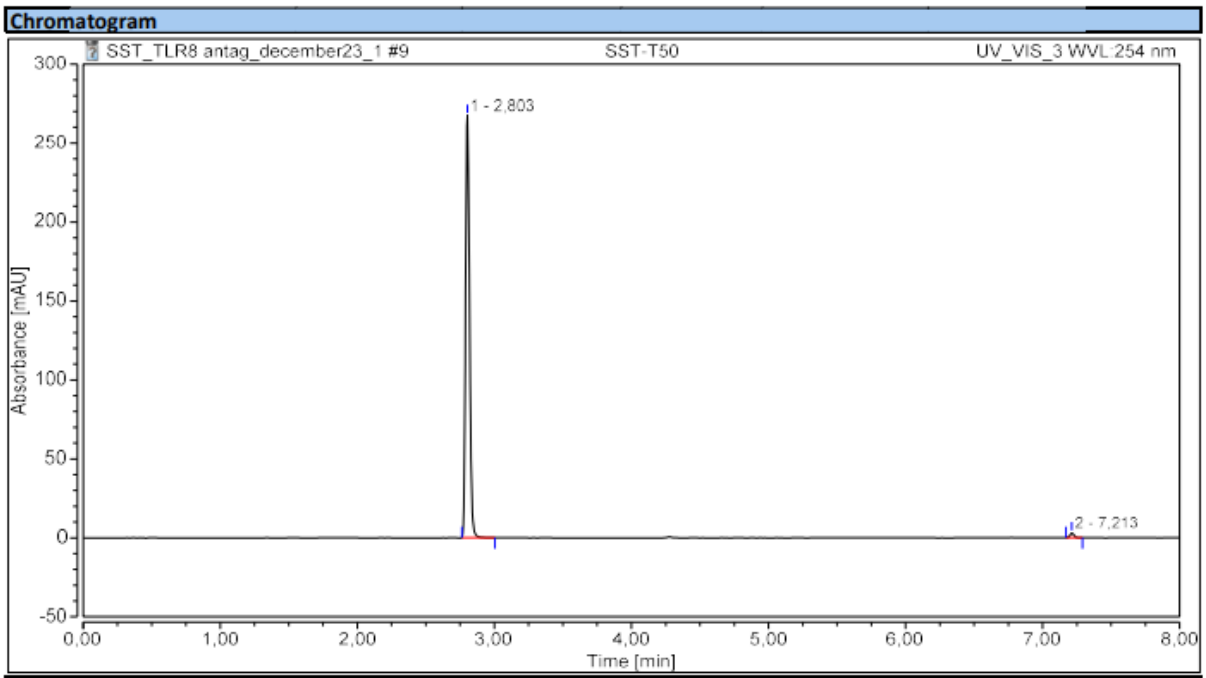

Integration Results

No.	Peak Name	Retention Time min	Area mAU*min	Height mAU	Relative Area %	Relative Height %	Amount n.a.
1		2,803	8,987	267,233	98,91	98,88	n.a.
2		7,213	0,099	3,030	1,09	1,12	n.a.
Total:			**9,086**	**270,263**	**100,00**	**100,00**	

HPLC trace for compound **28**.

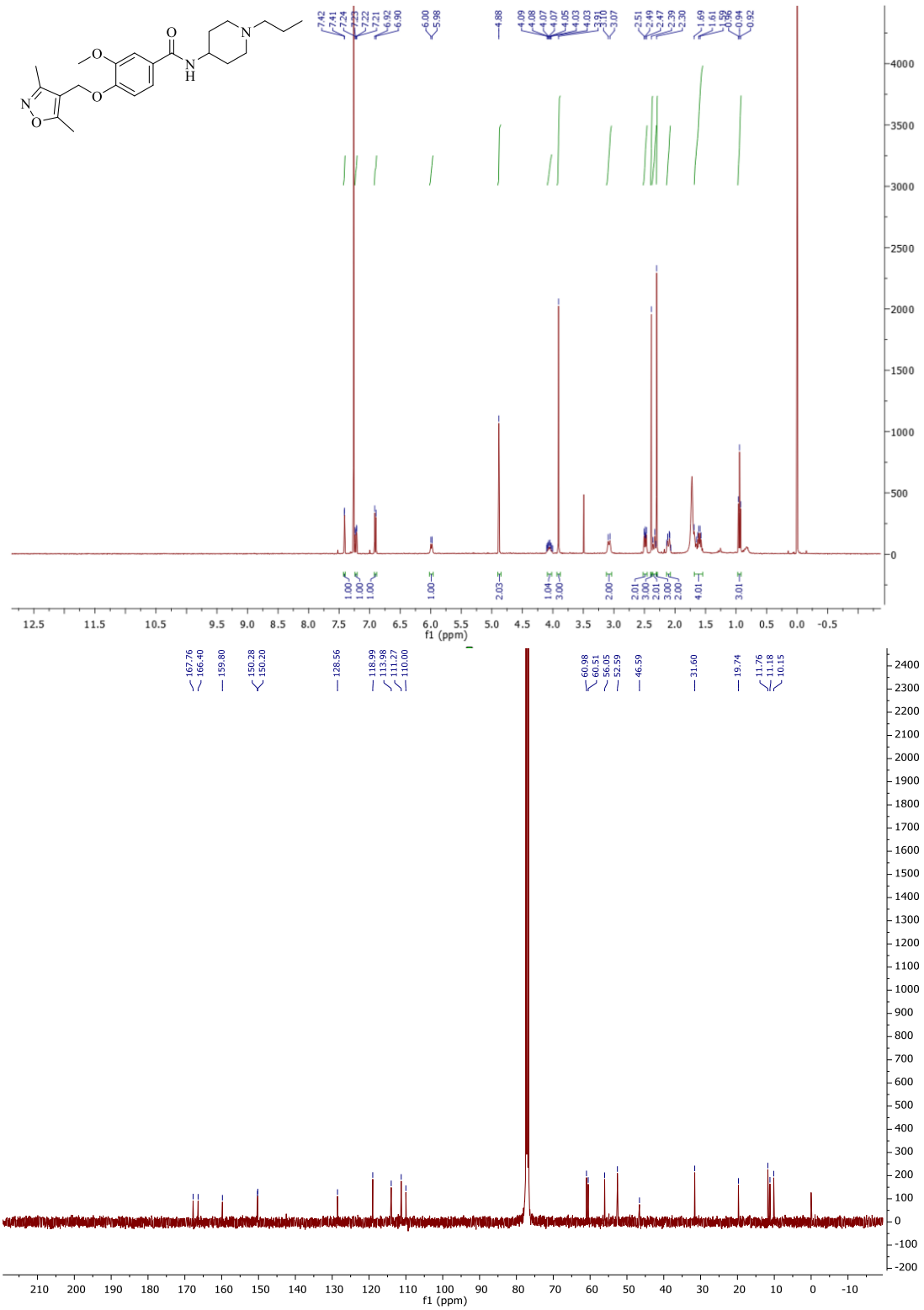

^{1}H and ^{13}C NMR for compound **31**.

Chromatogram

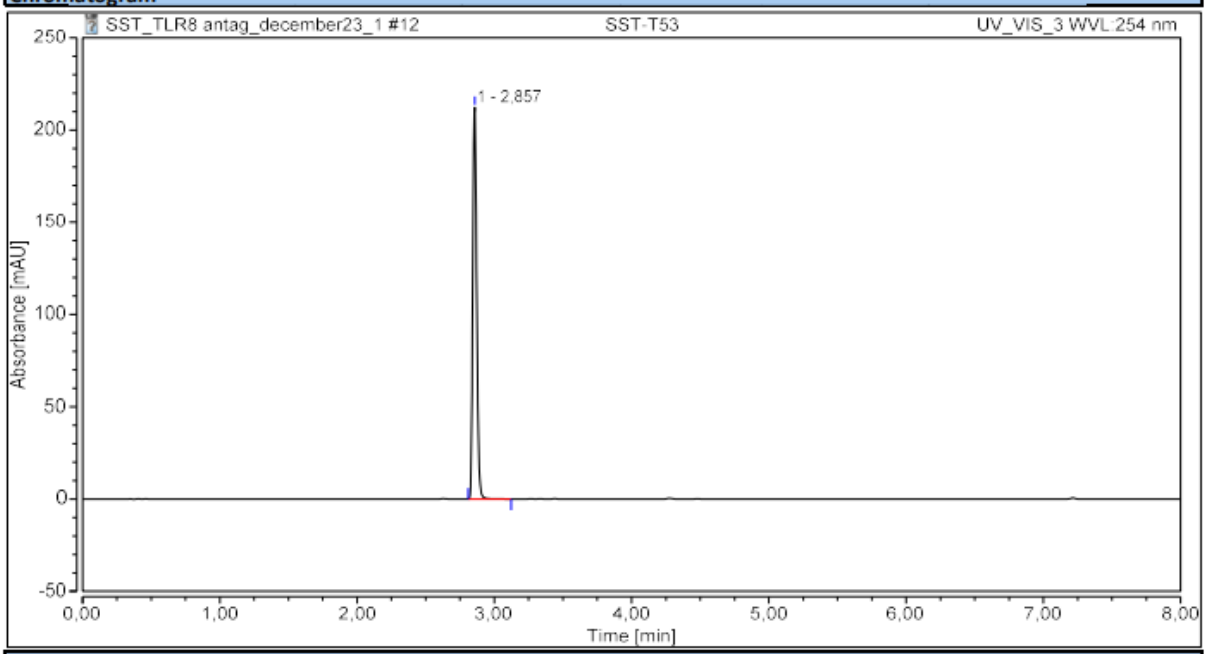

Integration Results

No.	Peak Name	Retention Time min	Area mAU*min	Height mAU	Relative Area %	Relative Height %	Amount n.a.
1		2,857	7,069	212,251	100,00	100,00	n.a.
Total:			**7,069**	**212,251**	**100,00**	**100,00**	

HPLC trace for compound **31**.

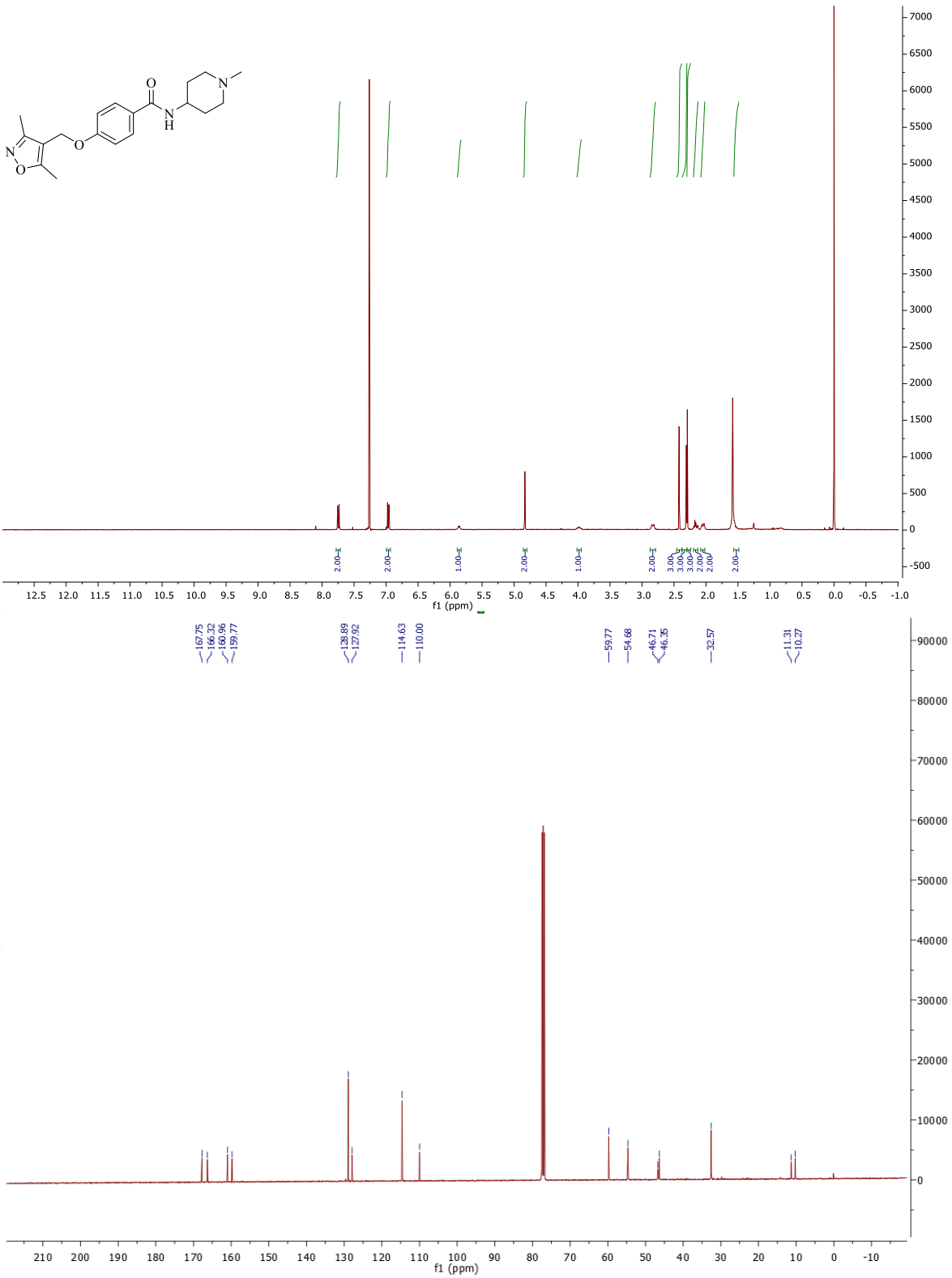

^{1}H and ^{13}C NMR for compound **34**.

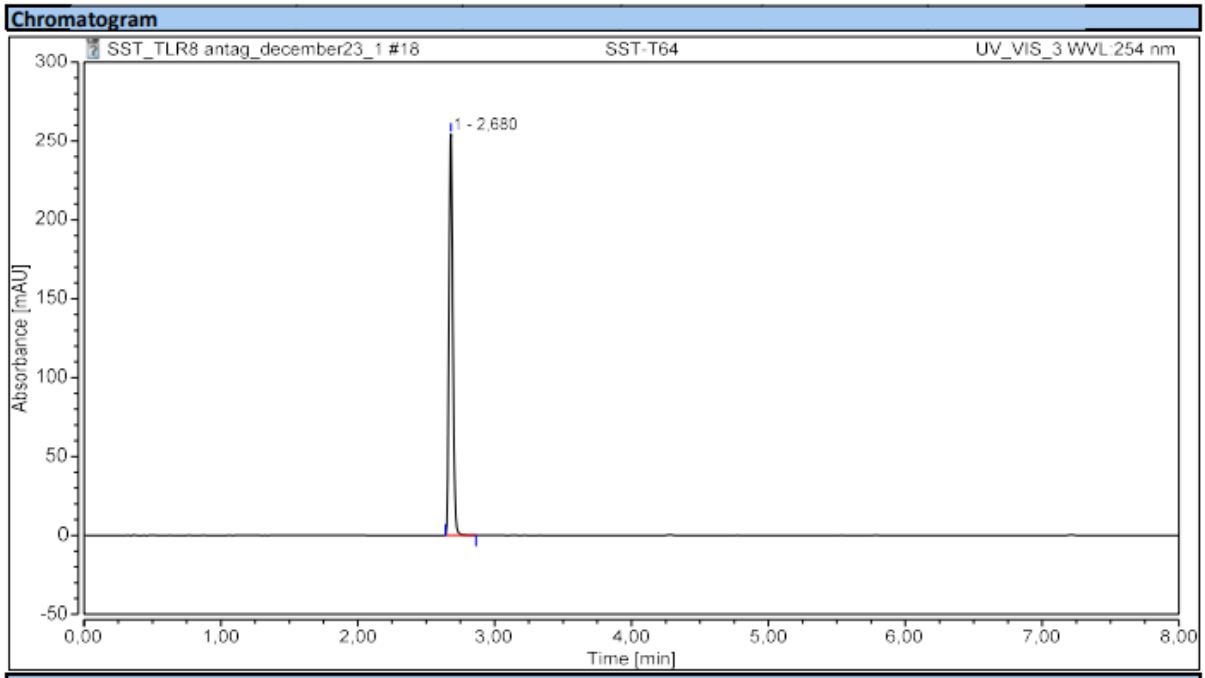

Integration Results

No.	Peak Name	Retention Time min	Area mAU*min	Height mAU	Relative Area %	Relative Height %	Amount n.a.
1		2,680	8,217	254,166	100,00	100,00	n.a.
Total:			**8,217**	**254,166**	**100,00**	**100,00**	

HPLC trace for compound **34**.

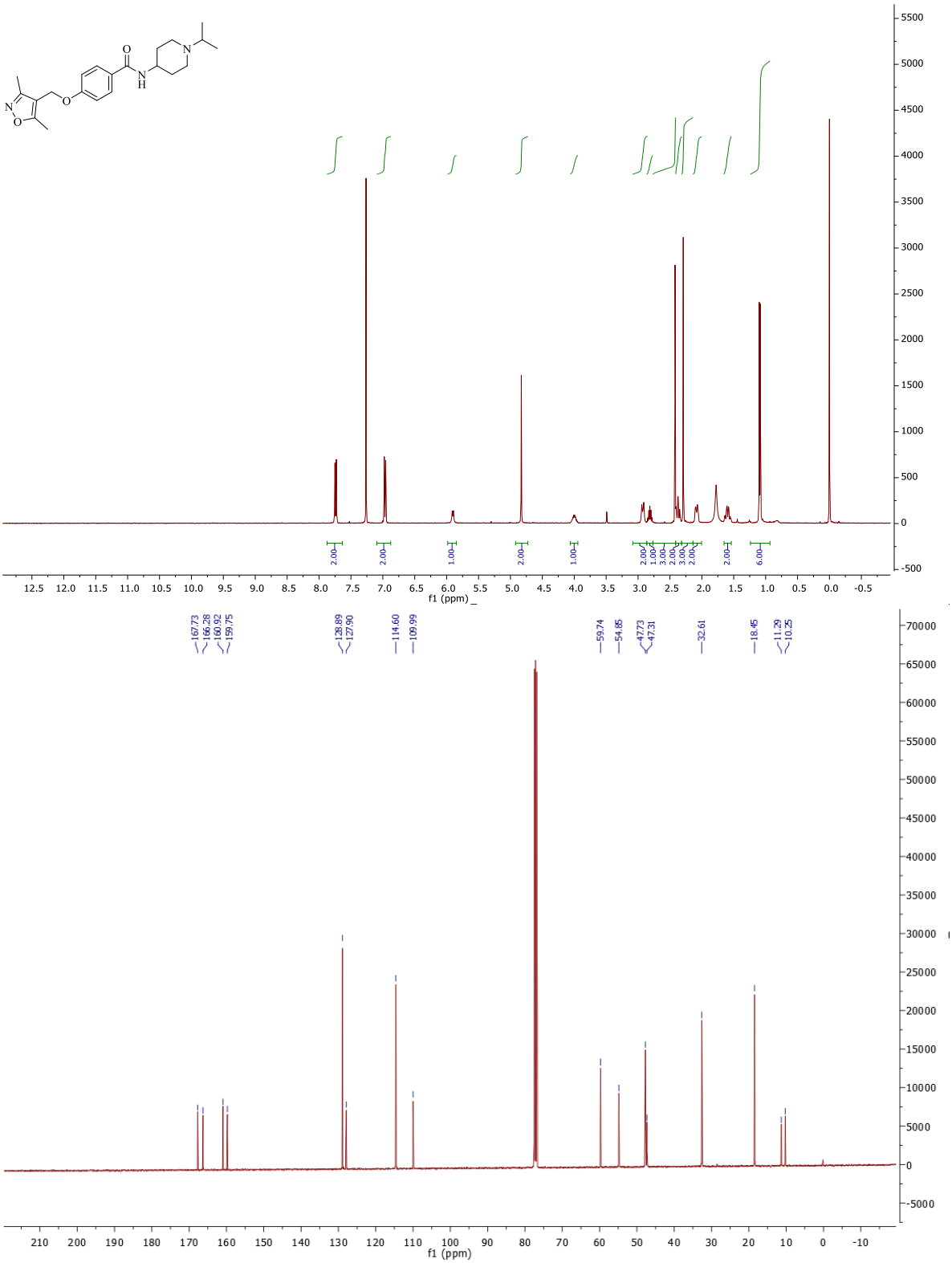

^{1}H and ^{13}C NMR for compound **35**.

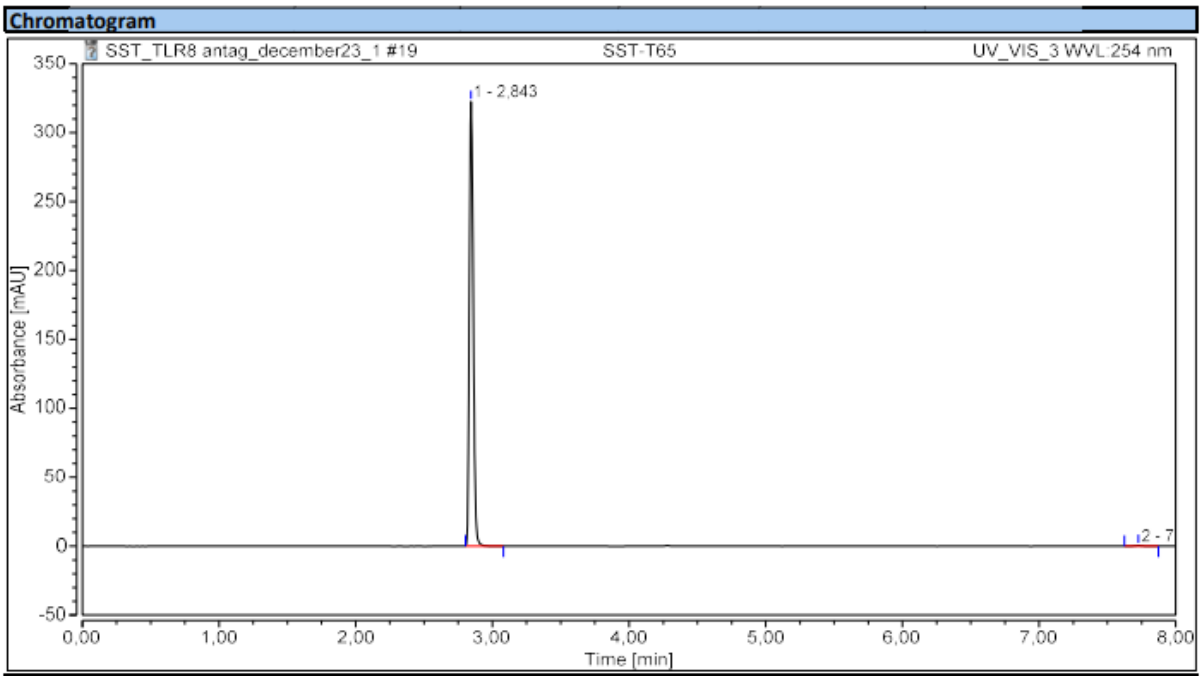

Integration Results

No.	Peak Name	Retention Time min	Area mAU*min	Height mAU	Relative Area %	Relative Height %	Amount n.a.
1		2,843	10,785	322,530	99,67	99,87	n.a.
2		7,727	0,035	0,415	0,33	0,13	n.a.
Total:			**10,821**	**322,945**	**100,00**	**100,00**	

HPLC trace for compound **35**.

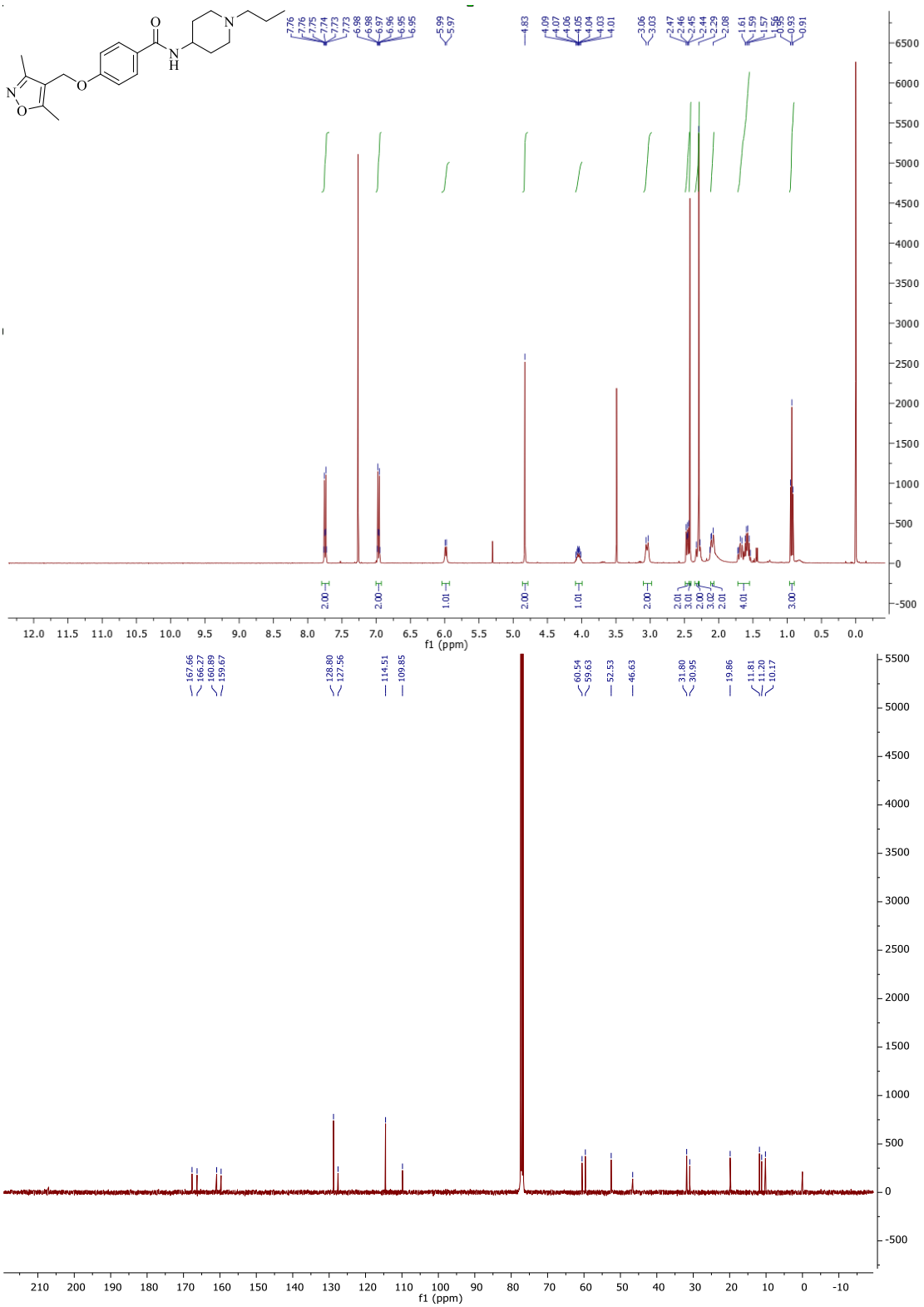

^{1}H and ^{13}C NMR for compound **38**.

Chromatogram

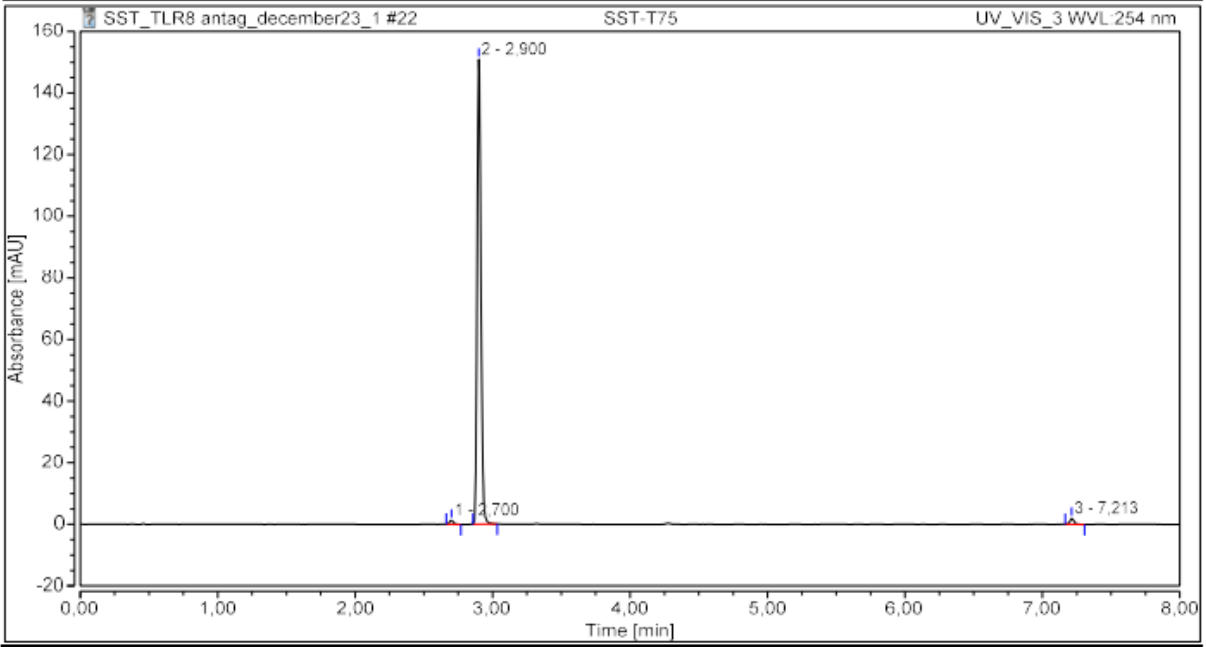

Integration Results

No.	Peak Name	Retention Time min	Area mAU*min	Height mAU	Relative Area %	Relative Height %	Amount n.a.
1		2,700	0,042	1,335	0,84	0,87	n.a.
2		2,900	4,870	150,941	97,87	97,87	n.a.
3		7,213	0,064	1,954	1,29	1,27	n.a.
Total:			**4,976**	**154,230**	**100,00**	**100,00**	

HPLC trace for compound **38**.

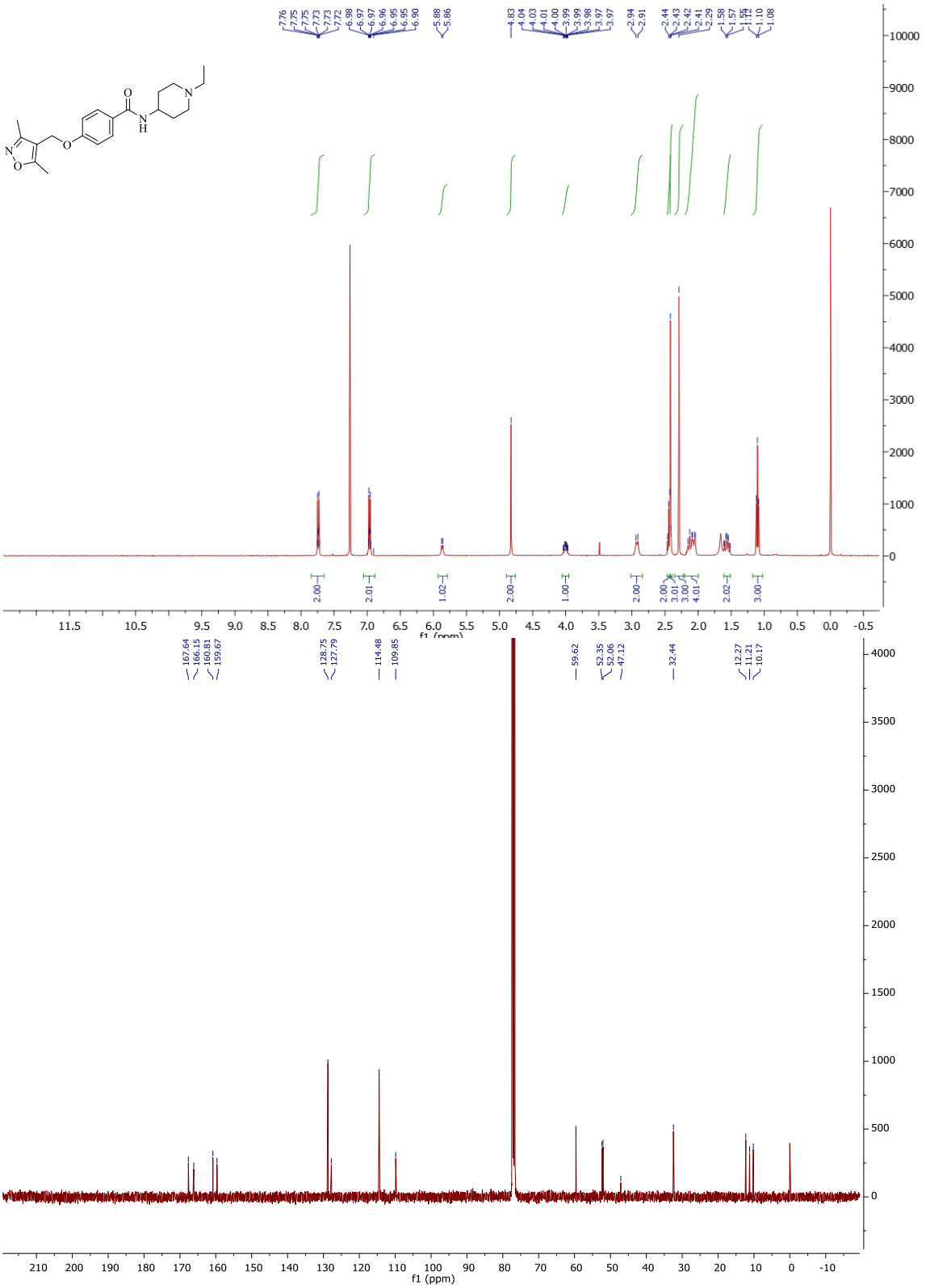

^{1}H and ^{13}C NMR for compound **39**.

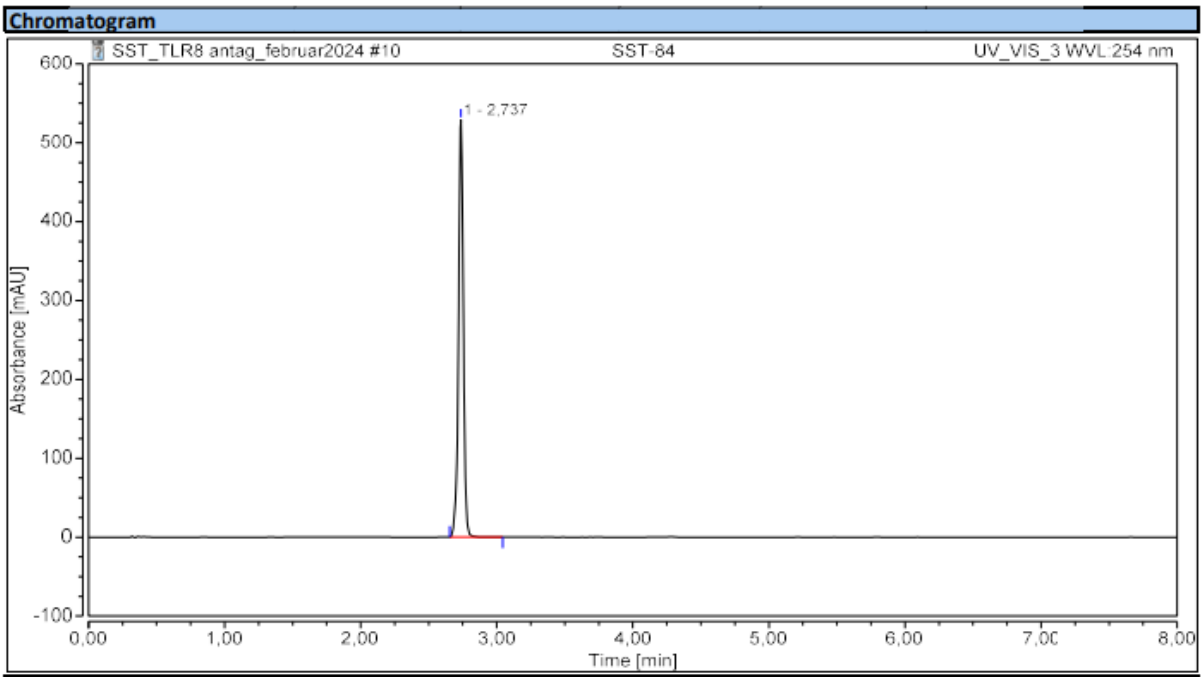

Integration Results

No.	Peak Name	Retention Time min	Area mAU*min	Height mAU	Relative Area %	Relative Height %	Amount n.a.
1		2,737	22,045	528,905	100,00	100,00	n.a.
Total:			**22,045**	**528,905**	**100,00**	**100,00**	

HPLC trace for compound **39**.

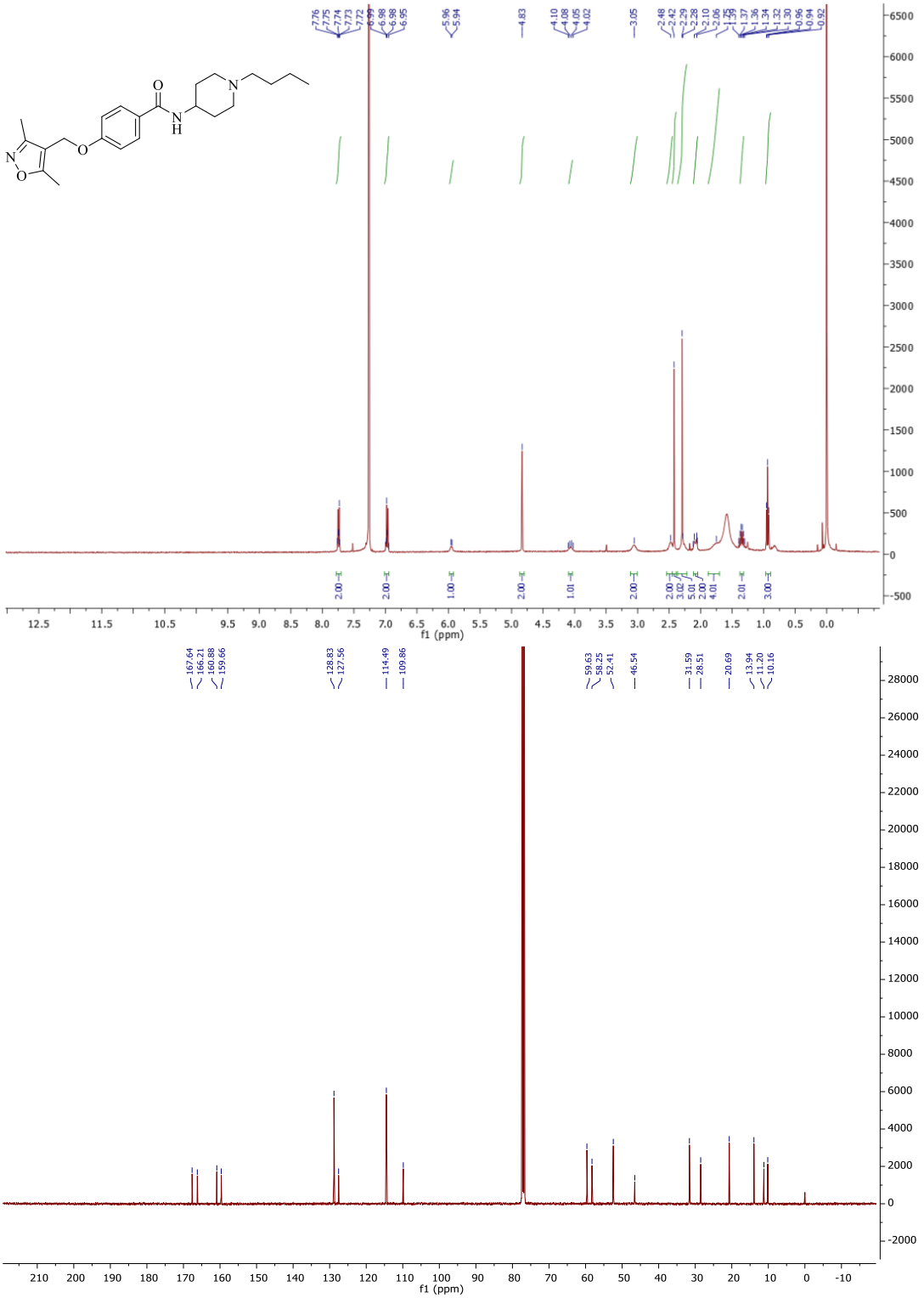

^{1}H and ^{13}C NMR for compound **40**.

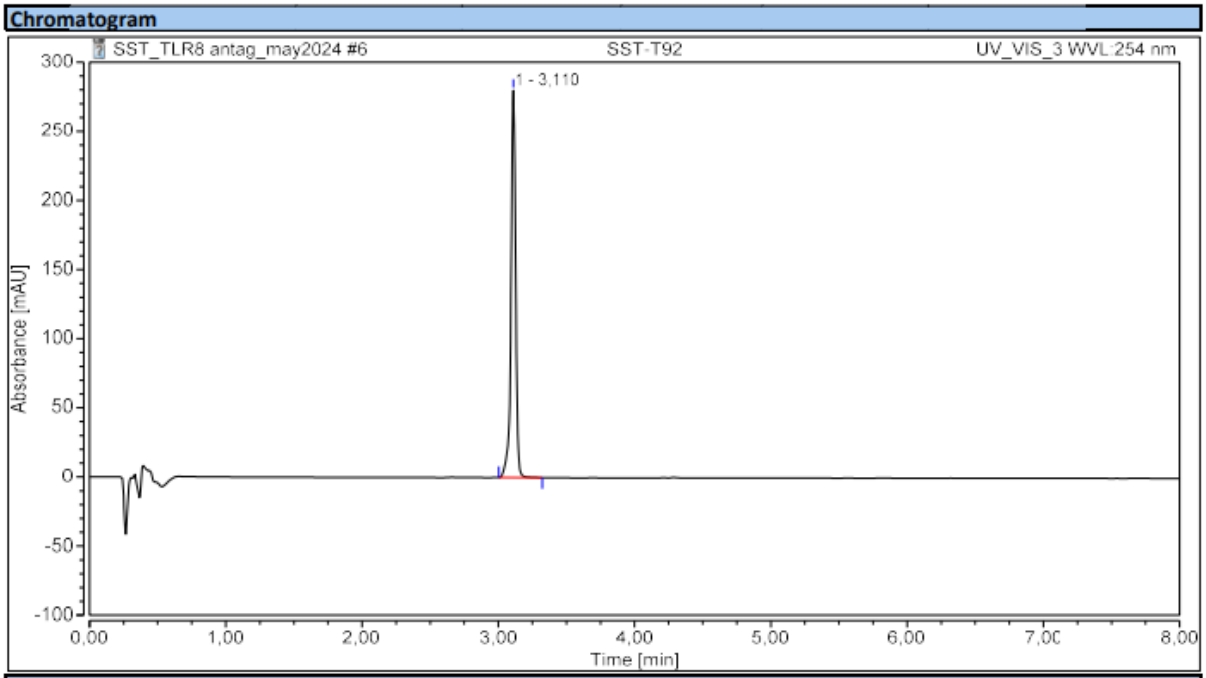

Integration Results

No.	Peak Name	Retention Time min	Area mAU*min	Height mAU	Relative Area %	Relative Height %	Amount n.a.
1		3,110	11,035	280,051	100,00	100,00	n.a.
Total:			**11,035**	**280,051**	**100,00**	**100,00**	

HPLC trace for compound **40**.

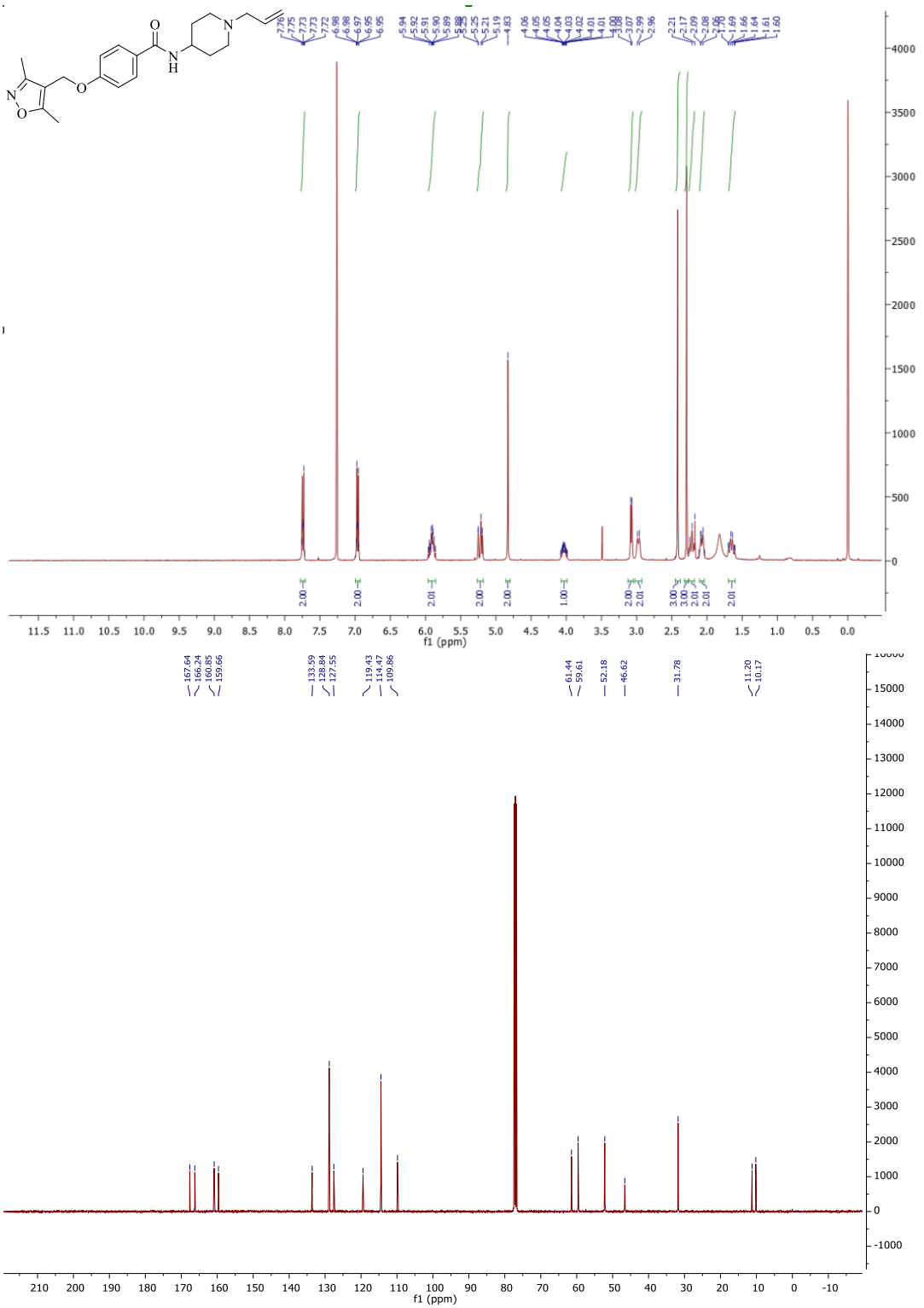

^{1}H and ^{13}C NMR for compound **41**.

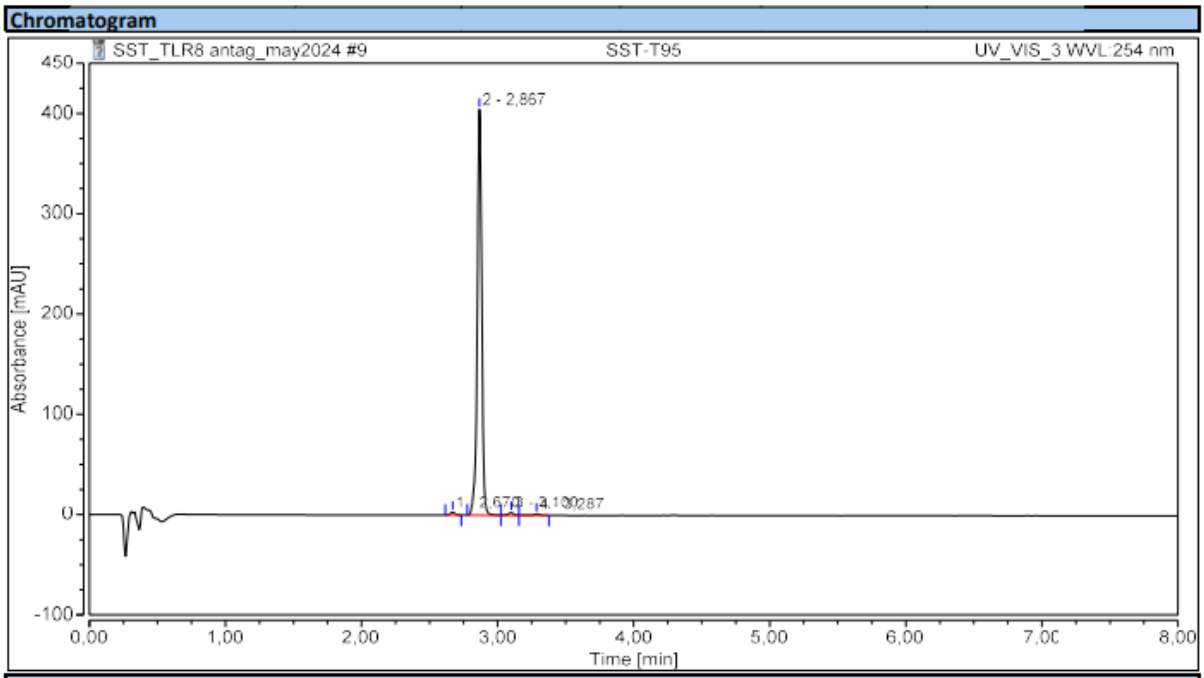

Integration Results

No.	Peak Name	Retention Time min	Area mAU*min	Height mAU	Relative Area %	Relative Height %	Amount n.a.
1		2,670	0,102	2,796	0,65	0,68	n.a.
2		2,867	15,440	404,575	98,08	98,31	n.a.
3		3,100	0,117	2,623	0,74	0,64	n.a.
4		3,287	0,083	1,529	0,53	0,37	n.a.
Total:			**15,742**	**411,523**	**100,00**	**100,00**	

HPLC trace for compound **41**.

Table S1. Chemical structures of compounds **1-12** containing the isoxazole scaffold.

Compound	Chemical Structure
1	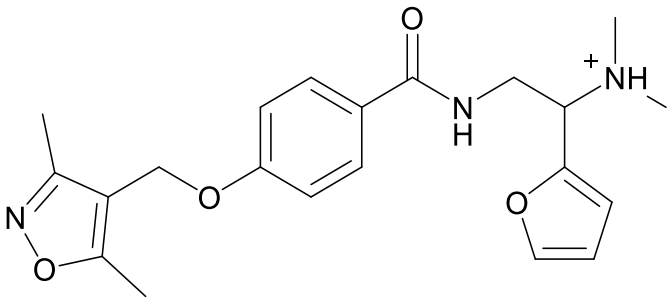
2	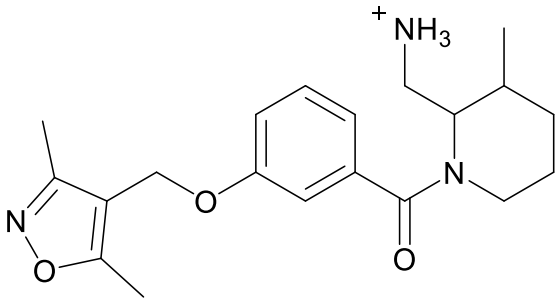
3	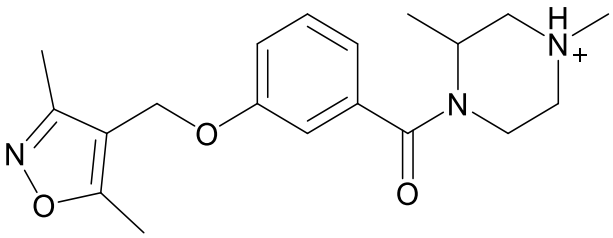
4	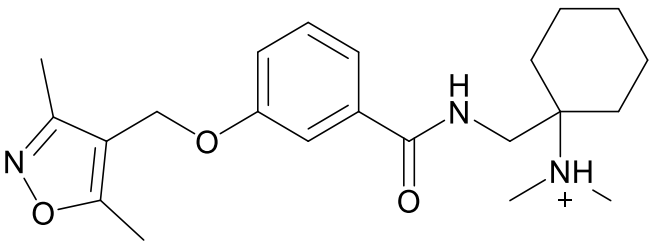

5	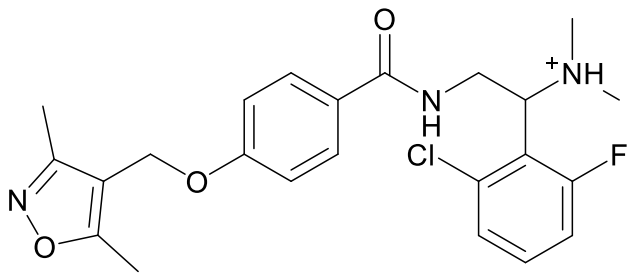
6	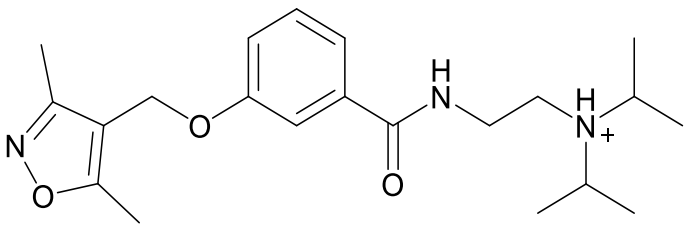
7	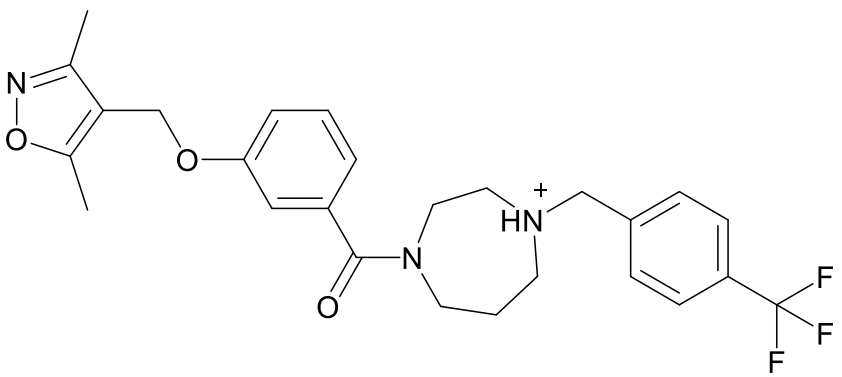
8	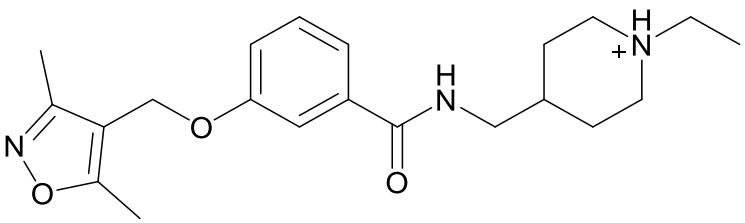
9	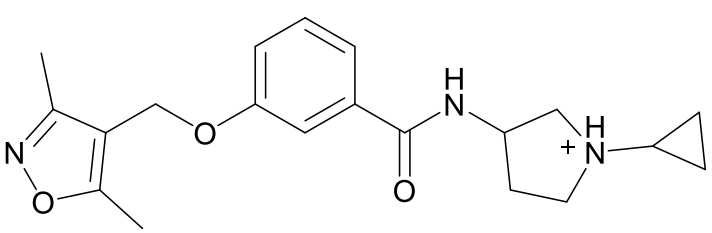

10	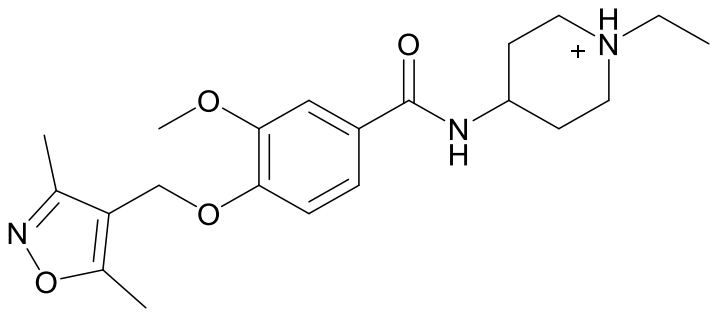
11	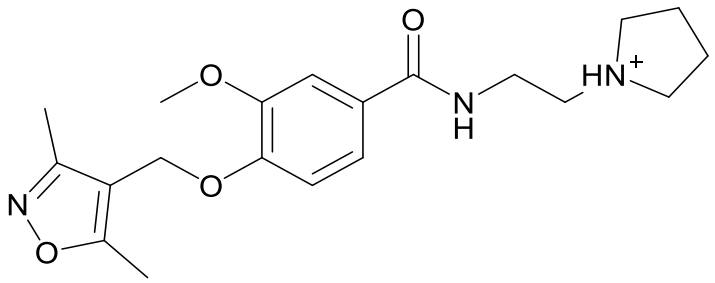
12	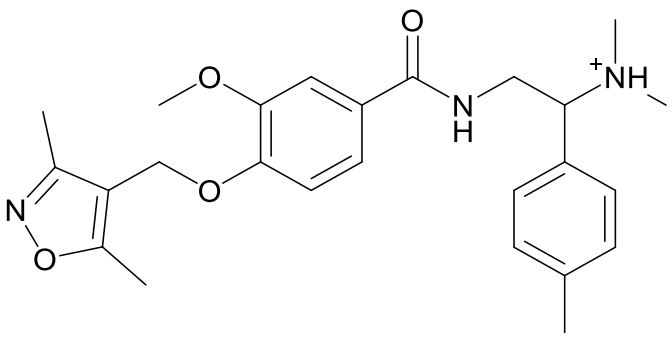

Table S2. Inhibition of NF-κB activity in hTLR8-HEK293 cells by compounds **1-12**.

Data are mean ± SEM of three independent experiments (Figure S3). One-sample *t*-test against 100% NF-κB activity. *P ≤ 0.05, ***P ≤ 0.001, ****P ≤ 0.0001.

Compound	**% inhibition at 10 µM ± SEM**
1	75 ± 4**
2	3 ± 2
3	-6 ± 2
4	16 ± 4
5	37 ± 7*
6	9 ± 4
7	5 ± 7
8	20 ± 4*
9	25 ± 9
10	98 ± 0.3****
11	75 ± 5**
12	83 ± 15*
Enpatoran	100 ± 0

Table S3. Inhibition of NF-κB activity in hTLR8-HEK293 cells by compounds **17-41**, **43**.

Data are mean ± SEM of three to four independent experiments (Figure S6). One-sample *t*-test against 100% NF-κB activity. *P ≤ 0.05, **P ≤ 0.01 ***P ≤ 0.001, ****P ≤ 0.0001.

Compound	**% inhibition at 10 μM ± SEM**
17	52 ± 4***
18	61 ± 3***
19	89 ± 2****
20	63 ± 0.7****
21	75 ± 2****
22	54 ± 3****
23	57 ± 3***
24	96 ± 2**
25	68 ± 6****
26	77 ± 4**
27	84 ± 4***
28	97 ± 1****
29	72 ± 5***
30	24 ± 9
31	98 ± 0.3****
32	77 ± 5***
33	94 ± 2 ****
34	97 ± 0.9****
35	99 ± 0.2****
36	26 ± 2***
37	80 ± 2****
38	100 ± 0.1****
39	100 ± 0.2****
40	99 ± 0.4****
41	99 ± 0.7****
43	32 ± 2**
Enpatoran	100 ± 0****

Table S4. Chemical structures of synthesized compounds **17**-**41**, **43**.

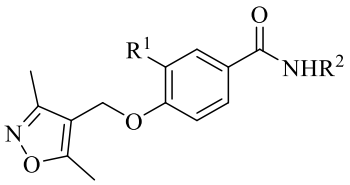

Compound	R^1	Amine (R_2NH_2)
17	H	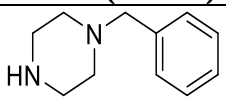
18	H	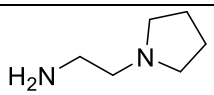
19	H	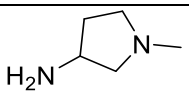
20	H	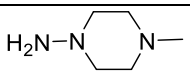
21	H	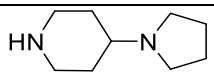
22	OMe	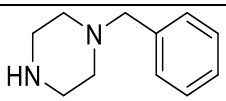
23	OMe	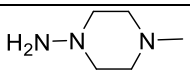
24	OMe	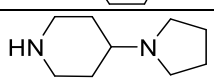
25	OMe	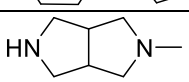
26	OMe	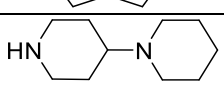
27	OMe	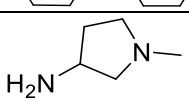
28	OMe	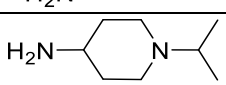
29	OMe	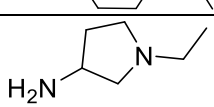
30	OMe	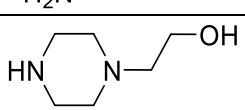
31	OMe	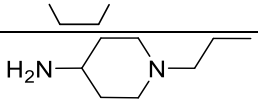
32	OMe	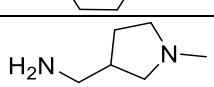

33	OMe	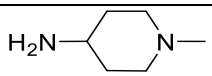
34	H	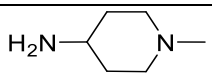
35	H	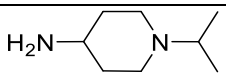
36	H	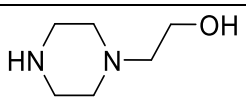
37	H	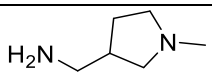
38	H	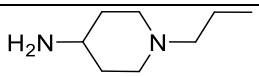
39	H	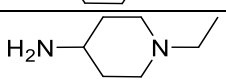
40	H	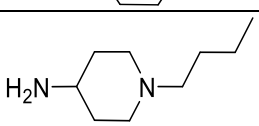
41	H	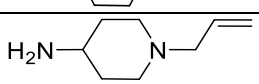
43	H	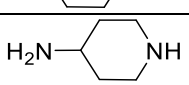

Table S5. Interaction frequencies of **10** with TLR8 homodimer during MD simulation.

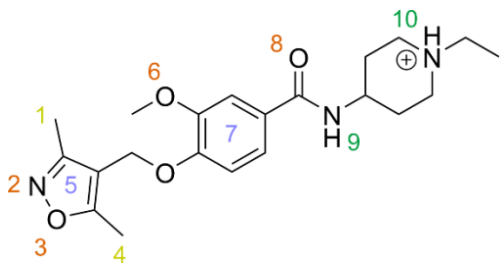

Ligand Moiety	**Interaction type**	**Frequency**
Methyl 1	Hydrophobic	100.0%
Isoxazole nitrogen 2	Hydrogen bond acceptor	60.1%
Isoxazole oxygen 3	Hydrogen bond acceptor	80.2%
Methyl 4	Hydrophobic	100.0%
Isoxazole 5	Aromatic	43.5%
Methoxy 6	Hydrogen bond acceptor	7.3%
Phenyl 7	Hydrophobic	100.0%
Carbamide oxygen 8	Hydrogen bond acceptor	20.5%
Carbamide amide 9	Hydrogen bond donor	8.3%
Amine 10	Hydrogen bond donor	84.4%
Amine 10	Positive ionizable	91.6%

Table S6. Pharmacological parameters (EC_{50}, E_{max}) of compound **10.**
Values were calculated from curves shown in Figure 6C.

	EC_{50} [µM] (95% CI)	**EC_{max} [%] (95% CI)**
TL8-506	0.19 (0.16-0.22)	97.6 (92.9-104.7)
+ **10** (0.1 µM)	0.27 (0.24-030)	95.42 (91.6-99.8)
+ **10** (0.5 µM)	0.33 (0.29-0.39)	94.8 (89.9-100.4)
+ **10** (1 µM)	0.49 (0.40-0.60)	93.9 (86.9-102.1)
+ **10** (5 µM)	0.93 (0.79-1.16)	94.26 (84.5-111.8)
+ **10** (10 µM)	1.45 (1.39-1.58)	103.7 (95.5-114.2)

References

(1) Schaller, D.; Šribar, D.; Noonan, T.; Deng, L.; Nguyen, T. N.; Pach, S.; Machalz, D.; Bermudez, M.; Wolber, G. Next Generation 3D Pharmacophore Modeling. *WIREs Comput Mol Sci* **2020**, *10* (4), e1468. https://doi.org/10.1002/wcms.1468.

(2) Kutlushina, A.; Khakimova, A.; Madzhidov, T.; Polishchuk, P. Ligand-Based Pharmacophore Modeling Using Novel 3D Pharmacophore Signatures. *Molecules* **2018**, *23* (12), 3094. https://doi.org/10.3390/molecules23123094.

(3) Noonan, T.; Denzinger, K.; Talagayev, V.; Chen, Y.; Puls, K.; Wolf, C. A.; Liu, S.; Nguyen, T. N.; Wolber, G. Mind the Gap—Deciphering GPCR Pharmacology Using 3D Pharmacophores and Artificial Intelligence. *Pharmaceuticals* **2022**, *15* (11), 1304. https://doi.org/10.3390/ph15111304.

(4) Mendez, D.; Gaulton, A.; Bento, A. P.; Chambers, J.; De Veij, M.; Félix, E.; Magariños, M. P.; Mosquera, J. F.; Mutowo, P.; Nowotka, M.; Gordillo-Marañón, M.; Hunter, F.; Junco, L.; Mugumbate, G.; Rodriguez-Lopez, M.; Atkinson, F.; Bosc, N.; Radoux, C. J.; Segura-Cabrera, A.; Hersey, A.; Leach, A. R. ChEMBL: Towards Direct Deposition of Bioassay Data. *Nucleic Acids Research* **2019**, *47* (D1), D930–D940. https://doi.org/10.1093/nar/gky1075.

(5) Gaulton, A.; Hersey, A.; Nowotka, M.; Bento, A. P.; Chambers, J.; Mendez, D.; Mutowo, P.; Atkinson, F.; Bellis, L. J.; Cibrián-Uhalte, E.; Davies, M.; Dedman, N.; Karlsson, A.; Magariños, M. P.; Overington, J. P.; Papadatos, G.; Smit, I.; Leach, A. R. The ChEMBL Database in 2017. *Nucleic Acids Res* **2017**, *45* (D1), D945–D954. https://doi.org/10.1093/nar/gkw1074.

(6) Gaulton, A.; Bellis, L. J.; Bento, A. P.; Chambers, J.; Davies, M.; Hersey, A.; Light, Y.; McGlinchey, S.; Michalovich, D.; Al-Lazikani, B.; Overington, J. P. ChEMBL: A Large-Scale Bioactivity Database for Drug Discovery. *Nucleic Acids Research* **2012**, *40* (D1), D1100–D1107. https://doi.org/10.1093/nar/gkr777.

(7) Mysinger, M. M.; Carchia, M.; Irwin, John. J.; Shoichet, B. K. Directory of Useful Decoys, Enhanced (DUD-E): Better Ligands and Decoys for Better Benchmarking. *J. Med. Chem.* **2012**, *55* (14), 6582–6594. https://doi.org/10.1021/jm300687e.

Appendix IV. Supporting information of chapter 5: Design, synthesis and biological evaluation of novel pyrimidine and quinazoline-based small-molecule Toll-like receptor 8 antagonists

Troy Matziol[1#], Valerij Talagayev[2#], Nika Strašek Benedik[3], Paula von Kempis[1], Tjaša Slokan[3], Janine Holze[1], Günther Weindl[1], Gerhard Wolber[2], Matej Sova[3]

[#]Troy Matziol and Valerij Talagayev contributed equally to this work.

[1] University of Bonn, Pharmaceutical Institute, Pharmacology and Toxicology Section, Gerhard-Domagk-Str. 3, 53121 Bonn, Germany

[2] Freie Universität Berlin, Institute of Pharmacy, Pharmaceutical and Medicinal Chemistry, Königin-Luise-Str. 2+4, 14195 Berlin, Germany

[3] University of Ljubljana, Faculty of Pharmacy, The Department of Pharmaceutical Chemistry, Aškerčeva 7, SI-1000 Ljubljana, Slovenia

Reprinted with permission from:

Troy Matziol, Valerij Talagayev, Nika Strašek Benedik, Paula von Kempis, Tjaša Slokan, Janine Holze, Günther Weindl, Gerhard Wolber and Matej Sova.

Supporting Information

Design, Synthesis and biological evaluation of novel pyrimidine and quinazoline-based small-molecule Toll-like receptor 8 antagonists

Troy Matziol[1#], Valerij Talagayev[2#], Nika Strašek Benedik[3], Paula von Kempis[1], Tjaša Slokan[3], Janine Holze[1], Günther Weindl[1*], Gerhard Wolber[2*], Matej Sova[3*]

[1] University of Bonn, Pharmaceutical Institute, Pharmacology and Toxicology Section, Gerhard-Domagk-Str. 3, 53121 Bonn, Germany

[2] Freie Universität Berlin, Institute of Pharmacy, Pharmaceutical and Medicinal Chemistry, Königin-Luise-Str. 2+4, 14195 Berlin, Germany

[3] University of Ljubljana, Faculty of Pharmacy, The Department of Pharmaceutical Chemistry, Aškerčeva 7, SI-1000 Ljubljana, Slovenia

[#]These authors contributed equally to this work

[*]Corresponding authors. e-mail: guenther.weindl@uni-bonn.de, gerhard.wolber@fu-berlin.de, matej.sova@ffa.uni-lj.si

Table of contents

1. ^{1}H NMR, ^{13}C NMR spectra and HPLC traces for compounds 9–17, 20–23, 30–32, 35, 38.

^{1}H NMR (400 MHz, $CDCl_3$)

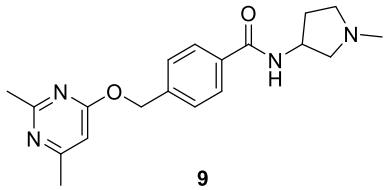

9

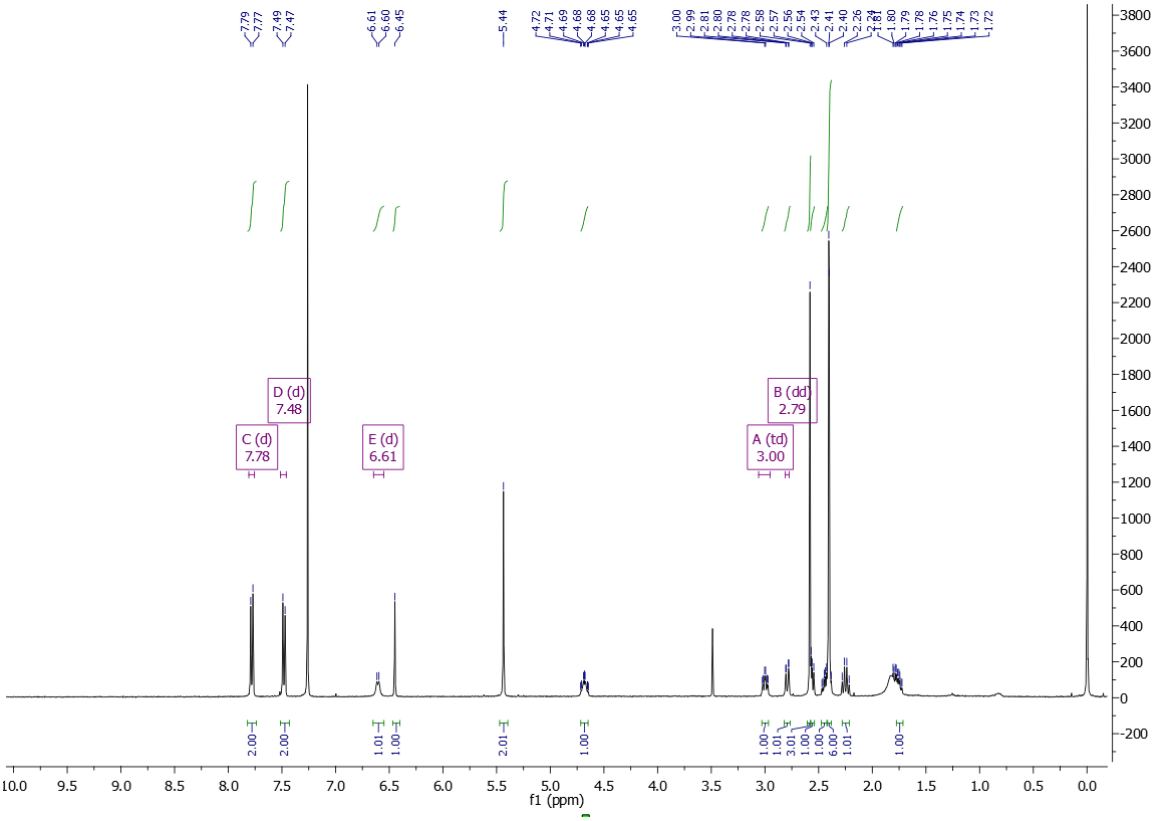

^{13}C NMR (400 MHz, $CDCl_3$)

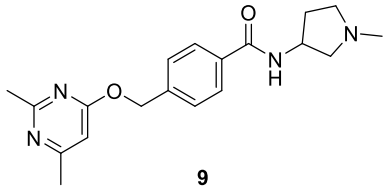

9

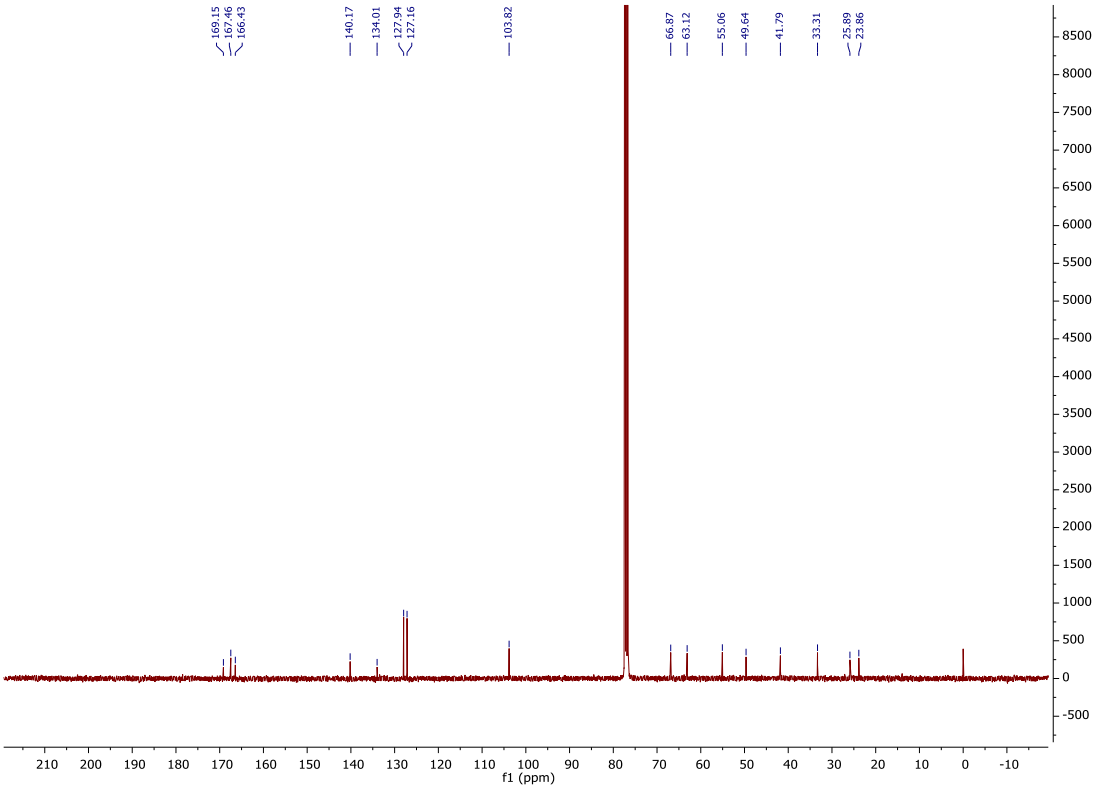

HPLC trace for **9**

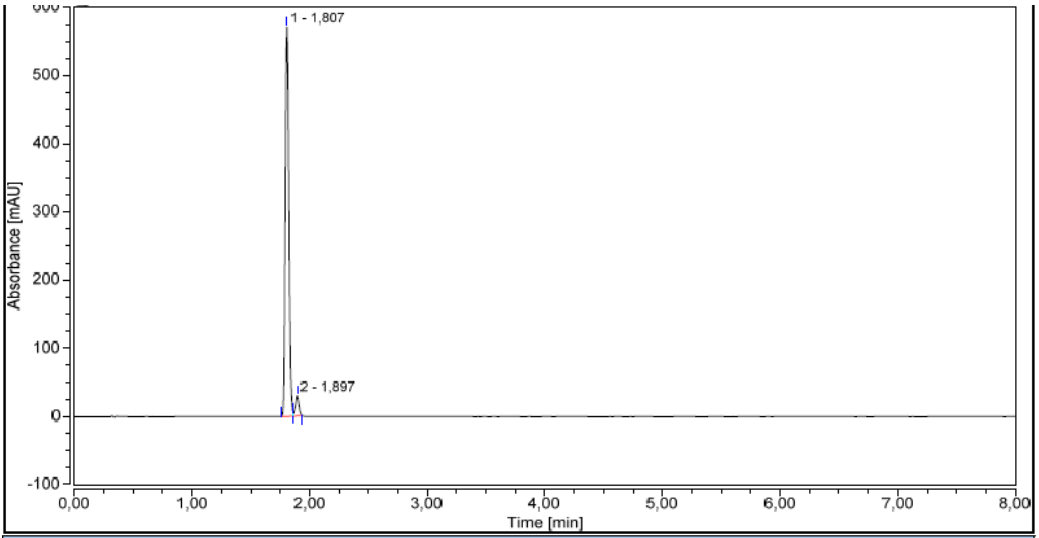

Integration Results							
No.	Peak Name	Retention Time min	Area mAU*min	Height mAU	Relative Area %	Relative Height %	Amount n.a.
1		1,807	19,903	570,433	95,30	95,12	n.a.
2		1,897	0,982	29,290	4,70	4,88	n.a.
Total:			**20,885**	**599,723**	**100,00**	**100,00**	

^{1}H NMR (400 MHz, $CDCl_3$)

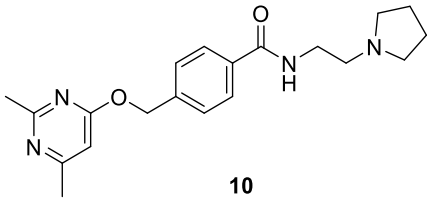

10

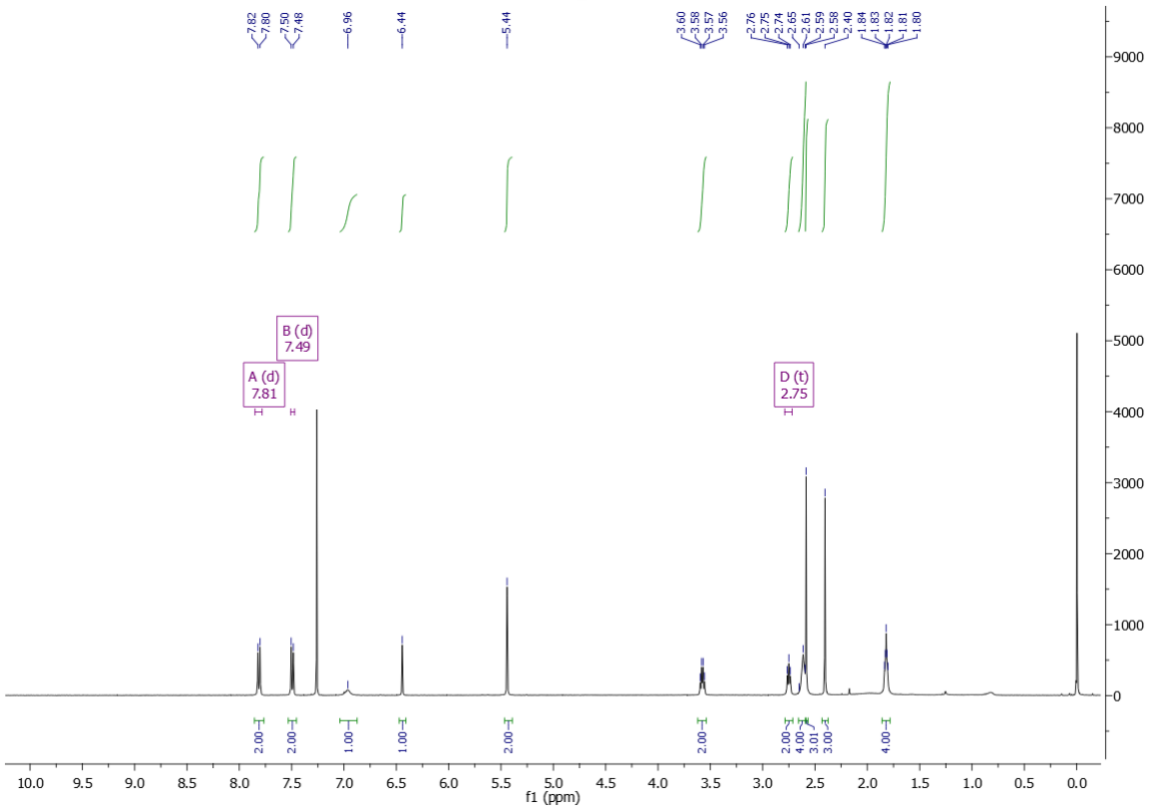

^{13}C NMR (400 MHz, $CDCl_3$)

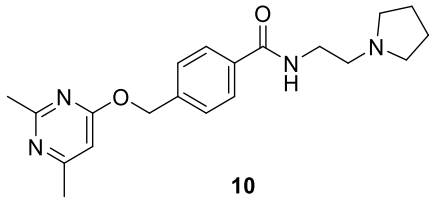

10

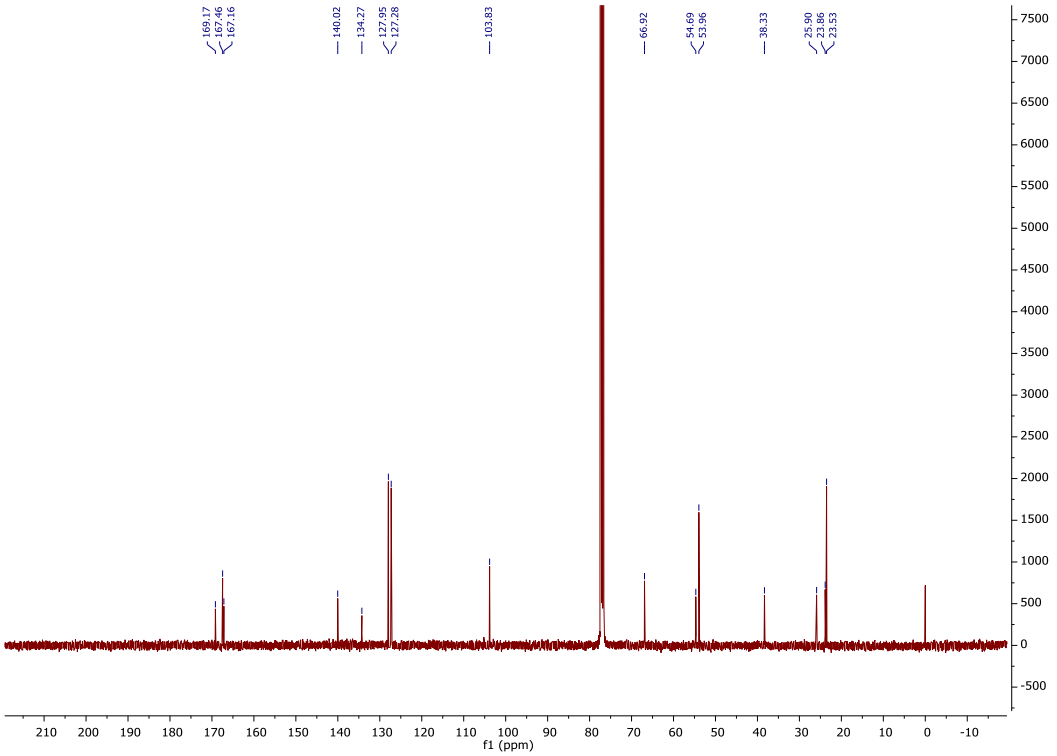

HPLC trace for **10**

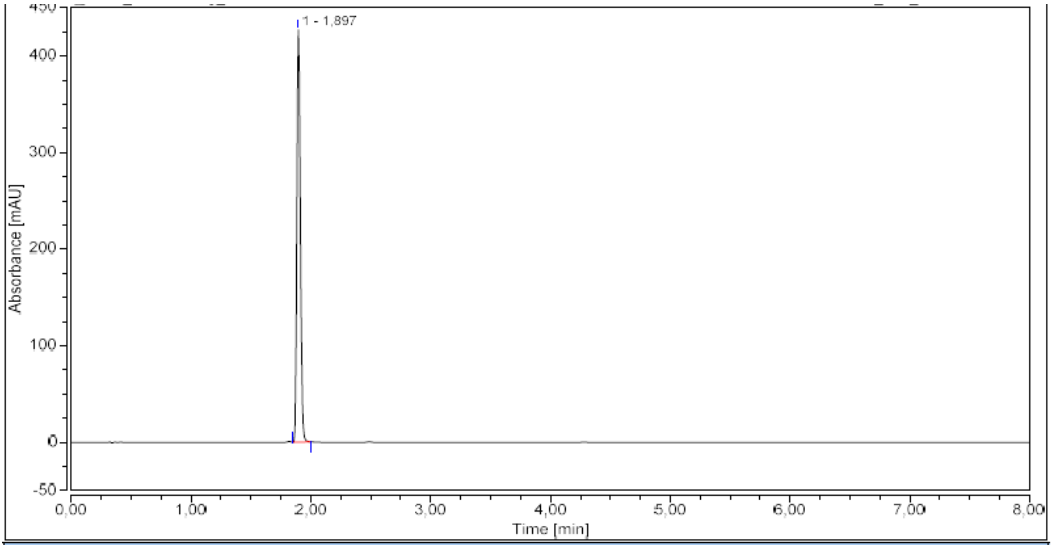

Integration Results

No.	Peak Name	Retention Time min	Area mAU*min	Height mAU	Relative Area %	Relative Height %	Amount n.a.
1		1,897	14,700	426,828	100,00	100,00	n.a.
Total:			**14,700**	**426,828**	**100,00**	**100,00**	

^{1}H NMR (400 MHz, $(CD_3)_2CO$)

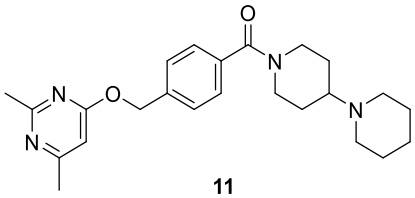

11

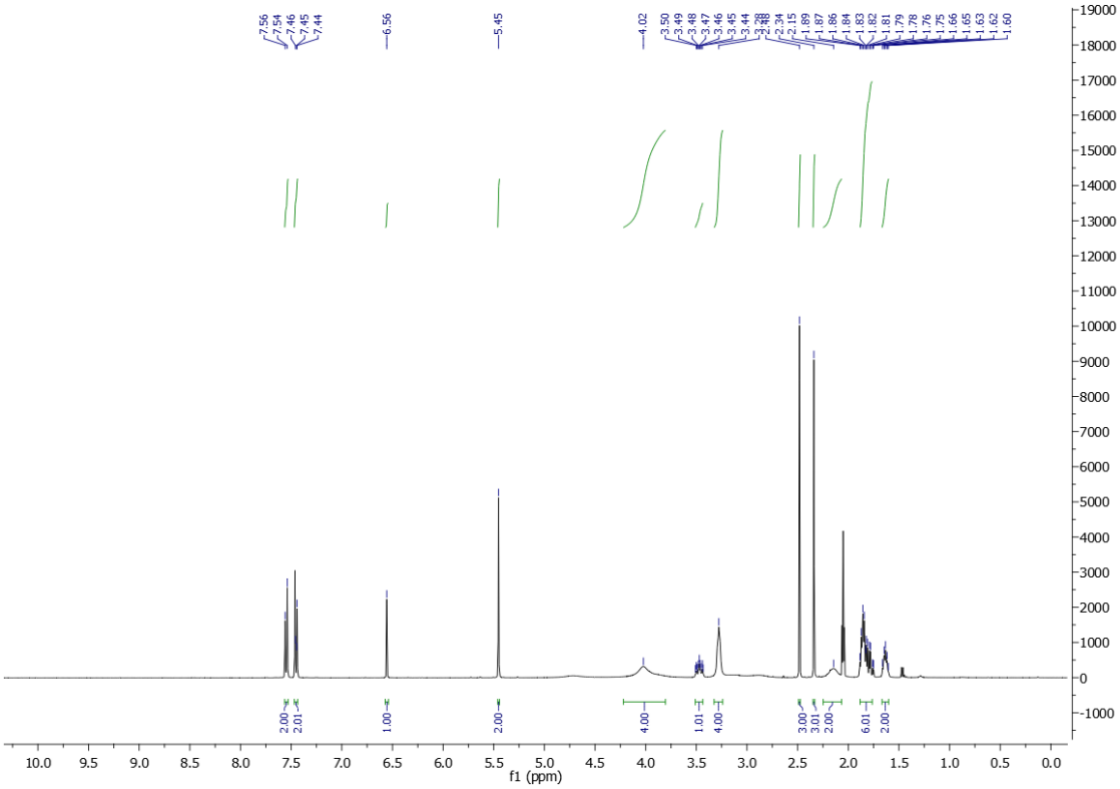

^{13}C NMR (100 MHz, $(CD_3)_2CO$)

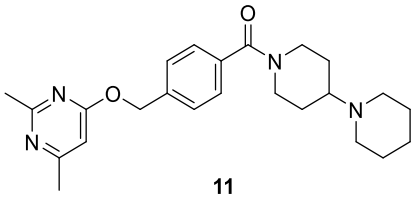

11

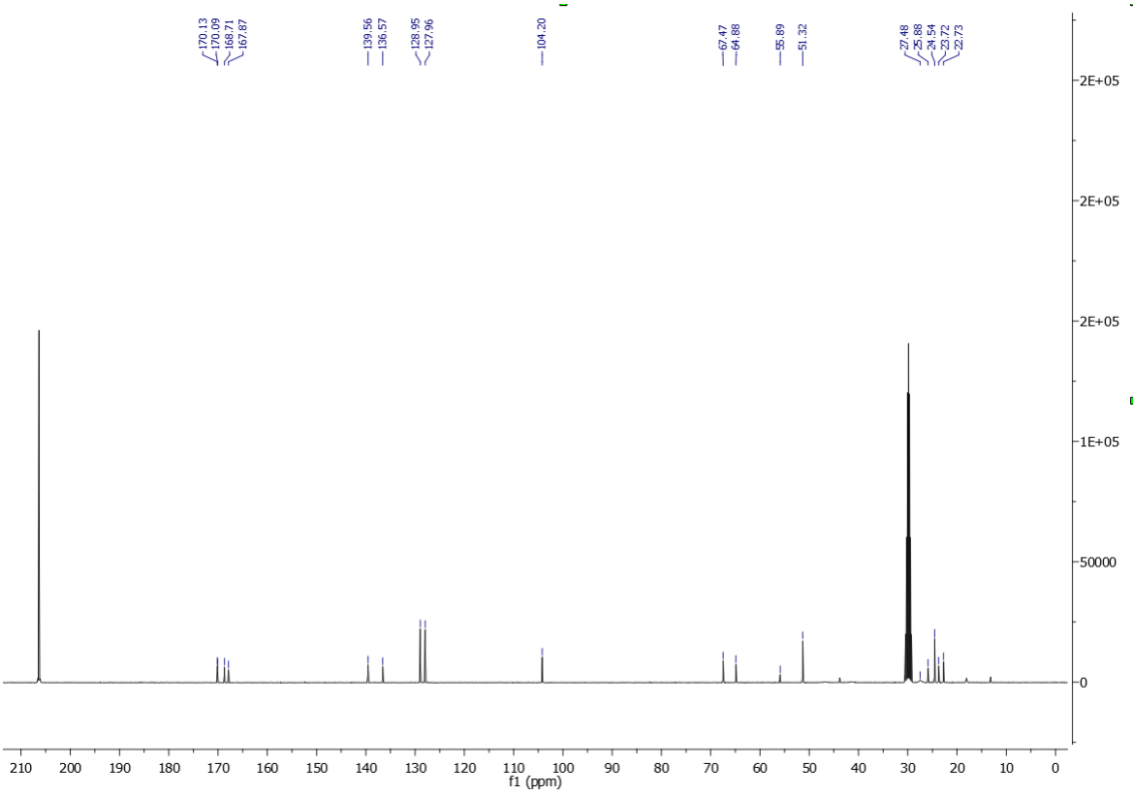

HPLC trace for **11**

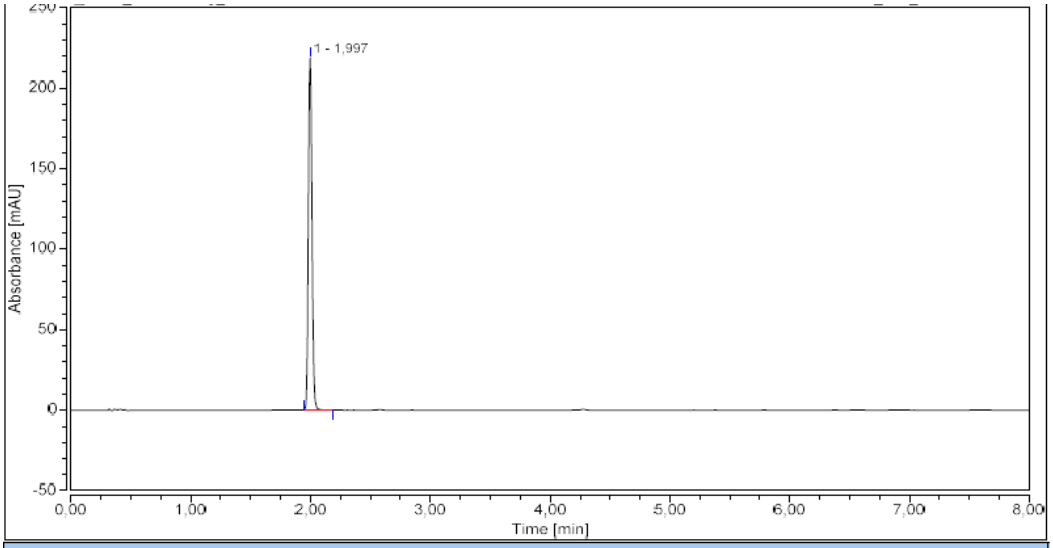

Integration Results

No.	Peak Name	Retention Time min	Area mAU*min	Height mAU	Relative Area %	Relative Height %	Amount n.a.
1		1,997	7,586	218,783	100,00	100,00	n.a.
Total:			**7,586**	**218,783**	**100,00**	**100,00**	

^{1}H NMR (400 MHz, $(CD_3)_2CO$)

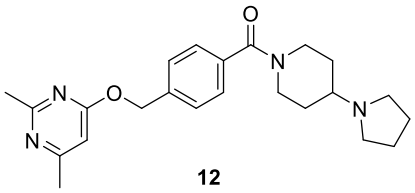

12

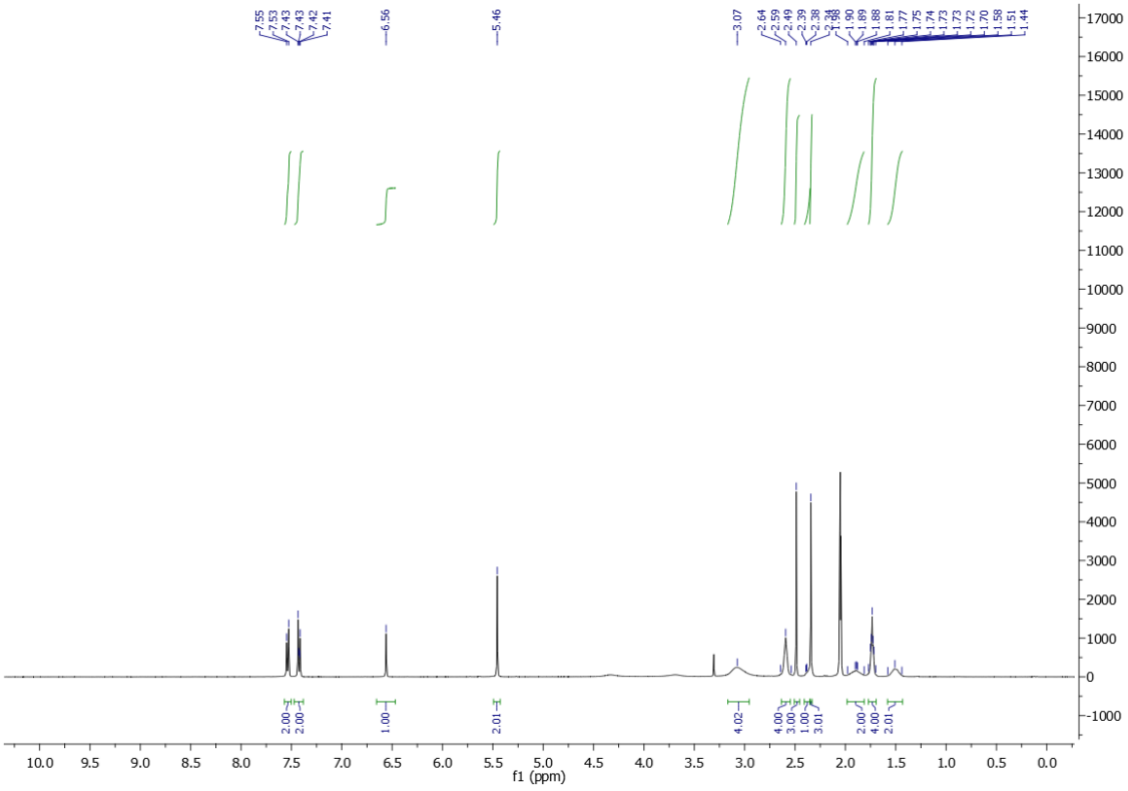

^{13}C NMR (100 MHz, $(CD_3)_2CO$)

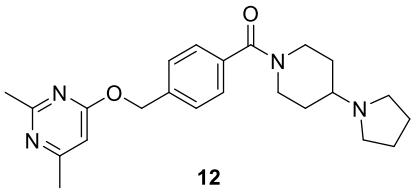

12

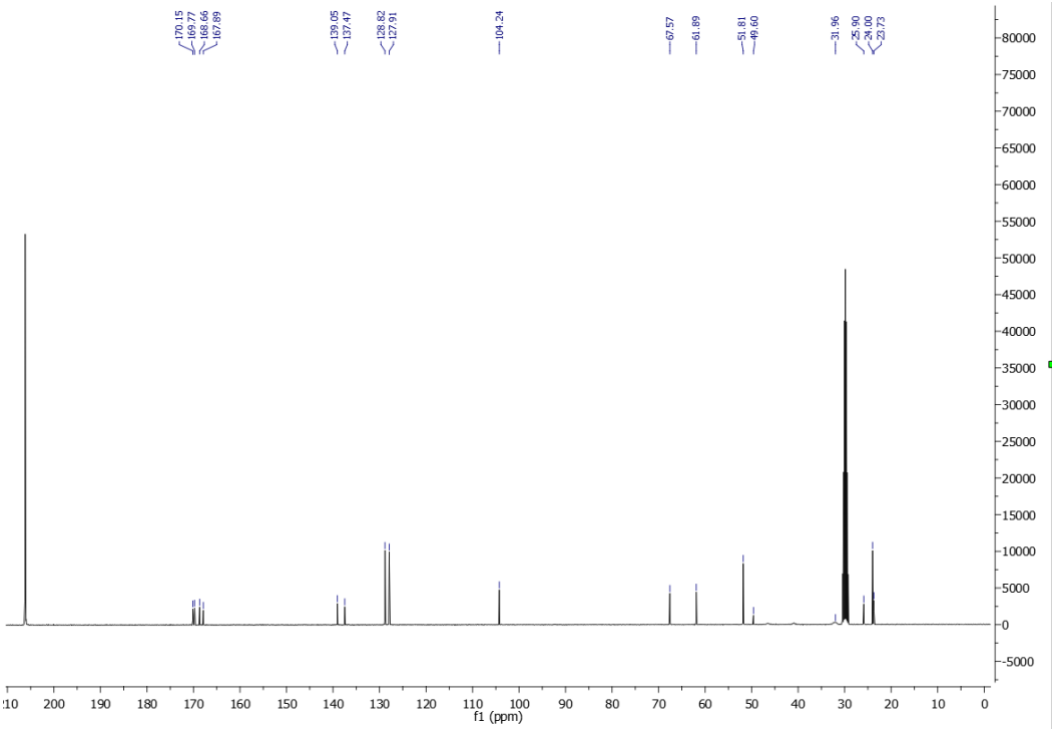

HPLC trace for **12**

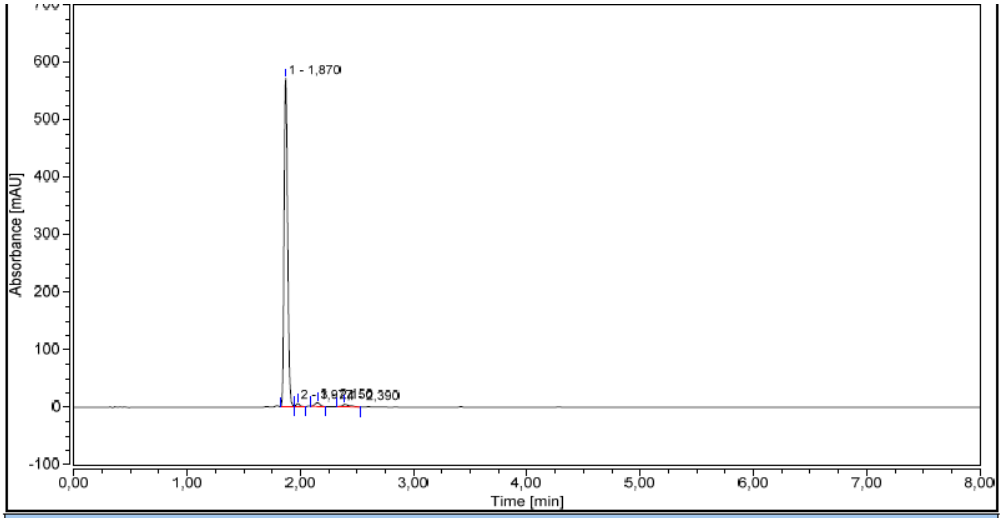

Integration Results

No.	Peak Name	Retention Time min	Area mAU*min	Height mAU	Relative Area %	Relative Height %	Amount n.a.
1		1,870	20,477	571,369	95,96	97,07	n.a.
2		1,977	0,214	5,810	1,00	0,99	n.a.
3		2,150	0,341	6,760	1,60	1,15	n.a.
4		2,390	0,308	4,688	1,44	0,80	n.a.
Total:			**21,340**	**588,627**	**100,00**	**100,00**	

^{1}H NMR (400 MHz, $CDCl_3$)

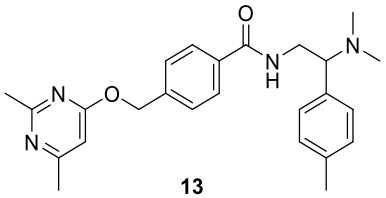

13

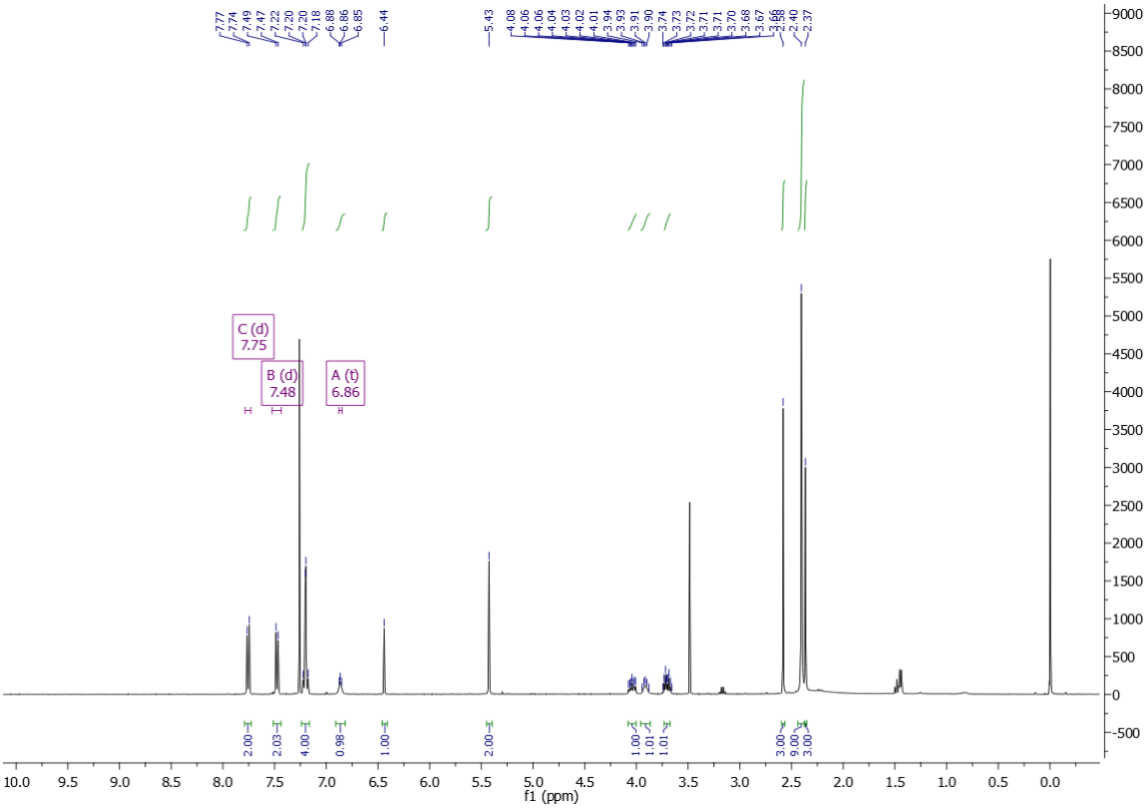

^{13}C NMR (400 MHz, $CDCl_3$)

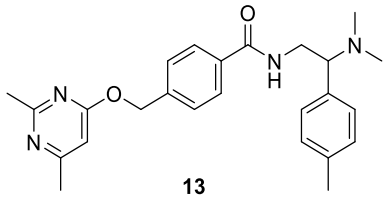

13

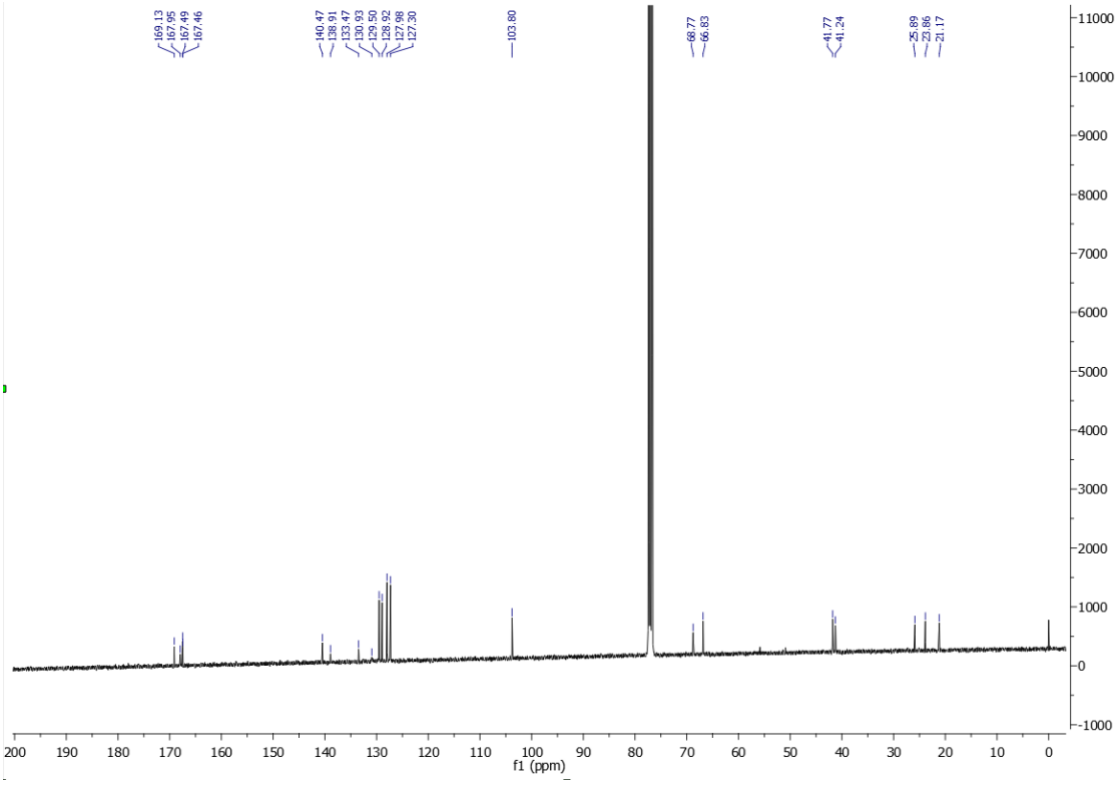

HPLC trace for **13**

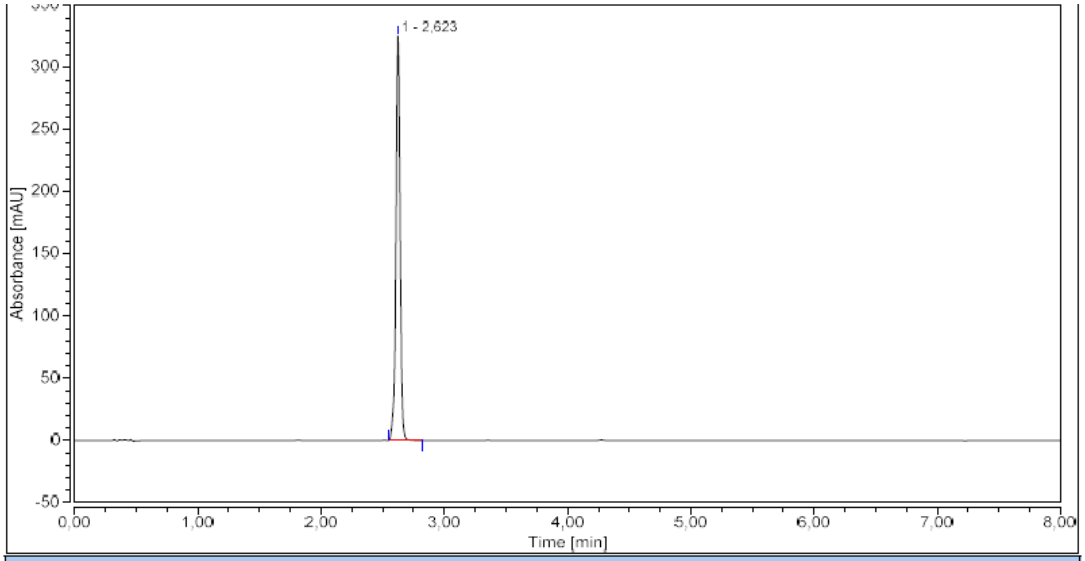

Integration Results

No.	Peak Name	Retention Time min	Area mAU*min	Height mAU	Relative Area %	Relative Height %	Amount n.a.
1		2,623	12,776	325,504	100,00	100,00	n.a.
Total:			**12,776**	**325,504**	**100,00**	**100,00**	

^{1}H NMR (400 MHz, $CDCl_3$)

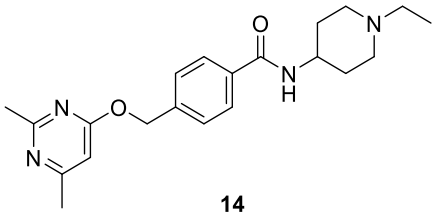

14

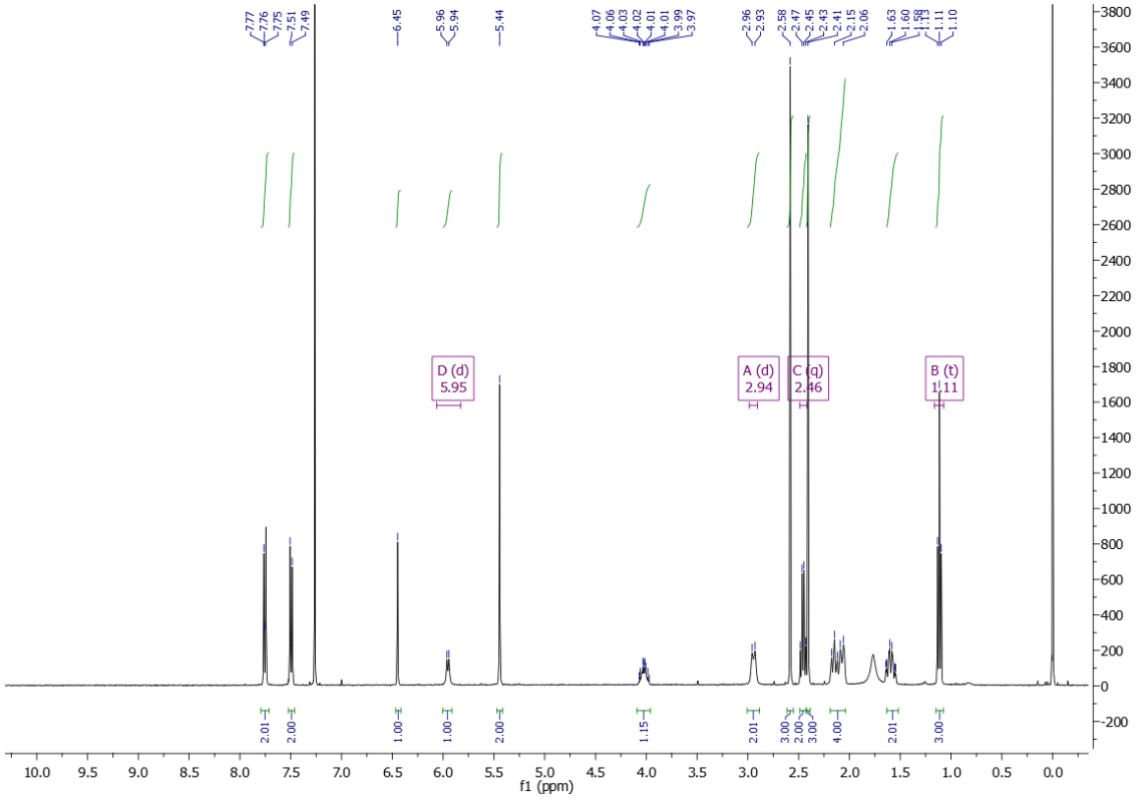

^{13}C NMR (100 MHz, $CDCl_3$)

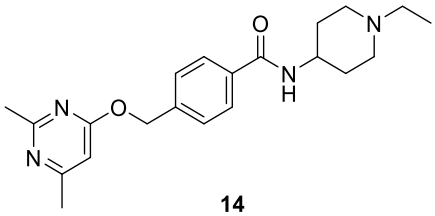

14

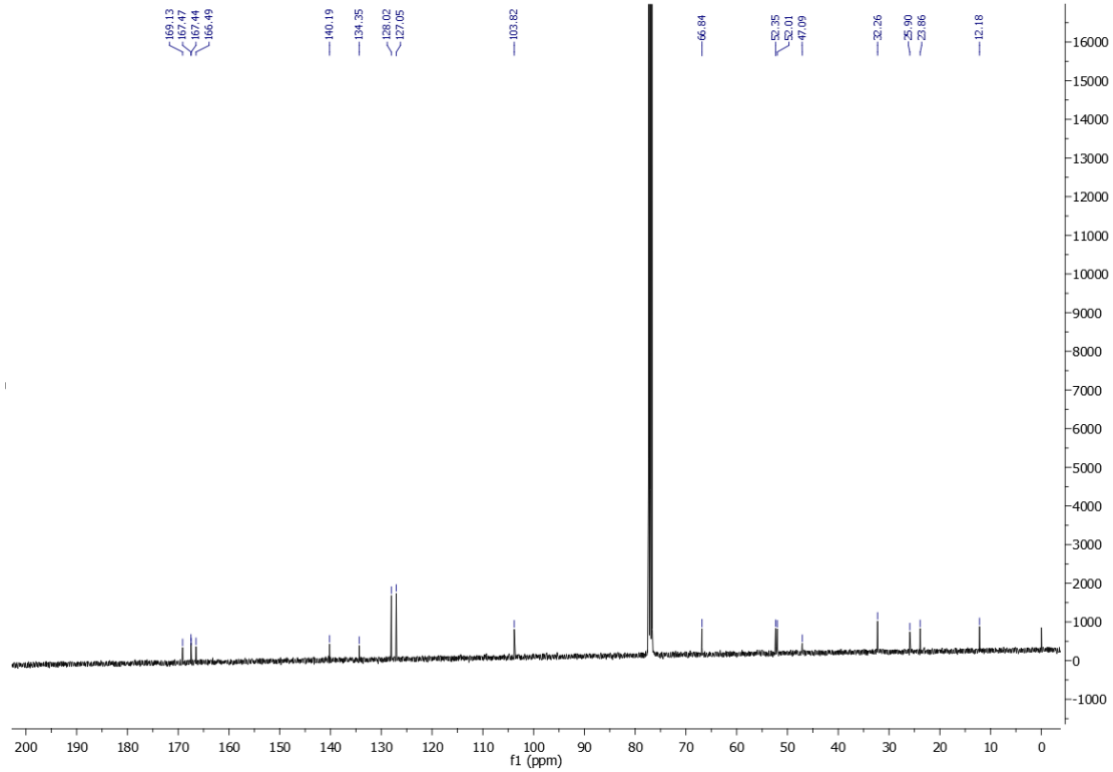

HPLC trace for **14**

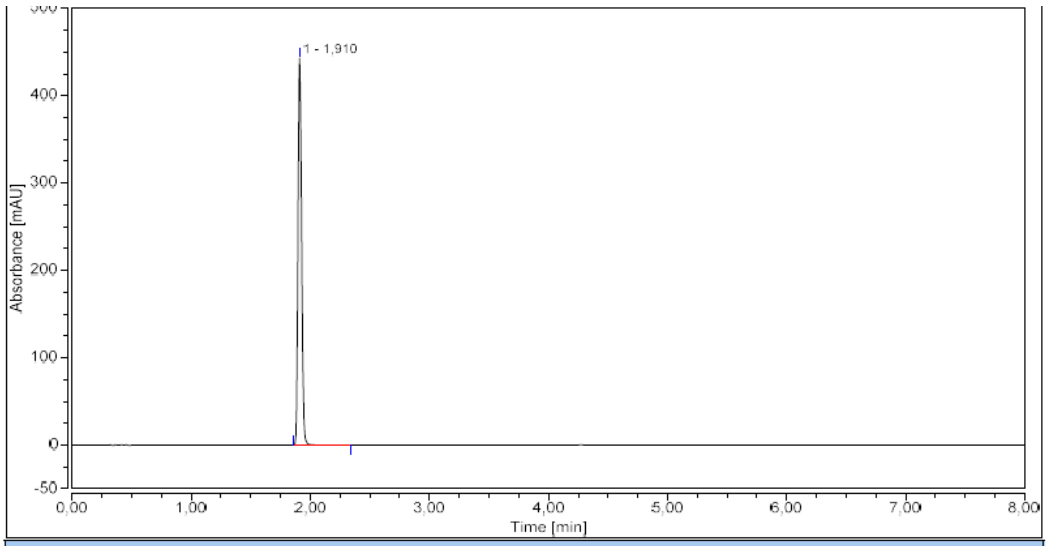

Integration Results							
No.	Peak Name	Retention Time min	Area mAU*min	Height mAU	Relative Area %	Relative Height %	Amount n.a.
1		1,910	15,558	442,788	100,00	100,00	n.a.
Total:			**15,558**	**442,788**	**100,00**	**100,00**	

^{1}H NMR (400 MHz, $CDCl_3$)

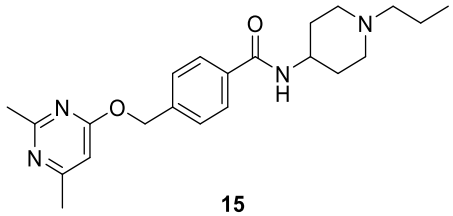

15

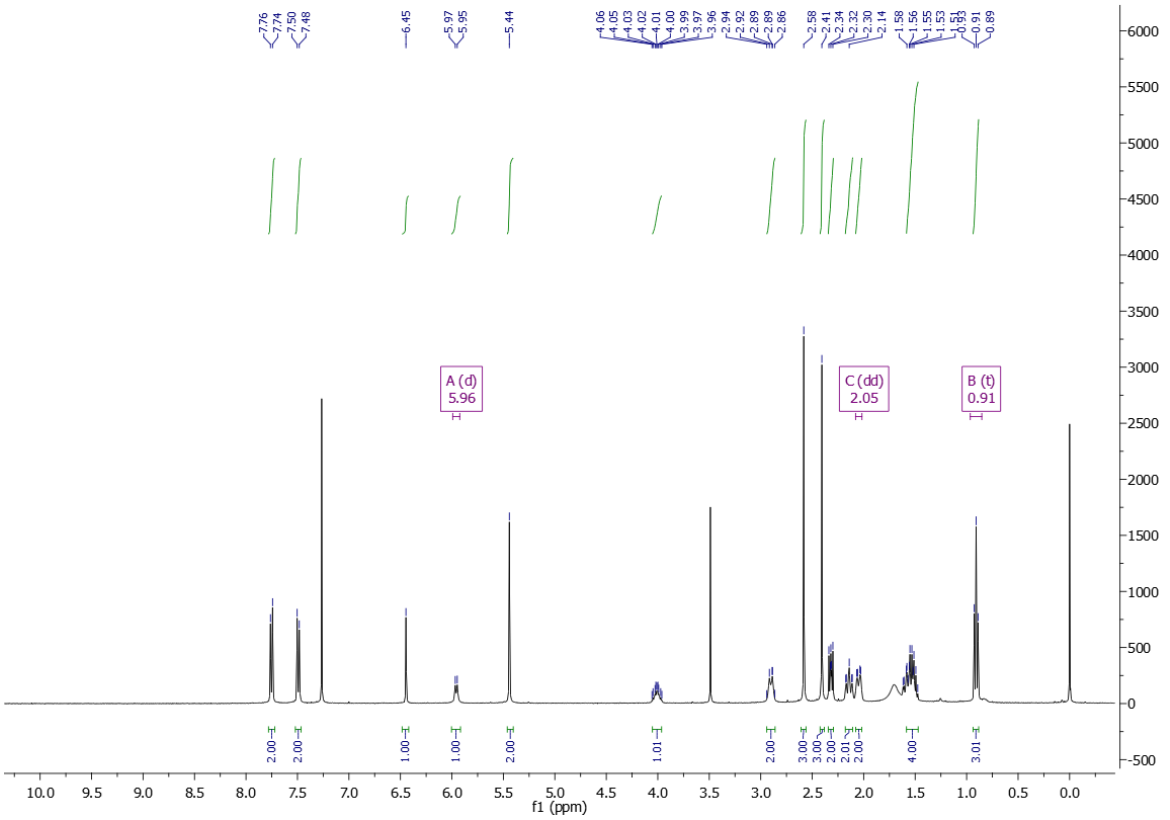

^{13}C NMR (100 MHz, $CDCl_3$)

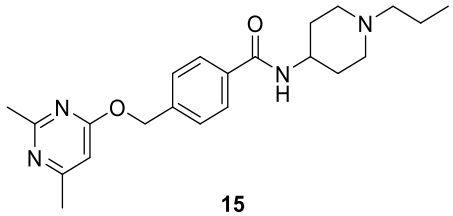

15

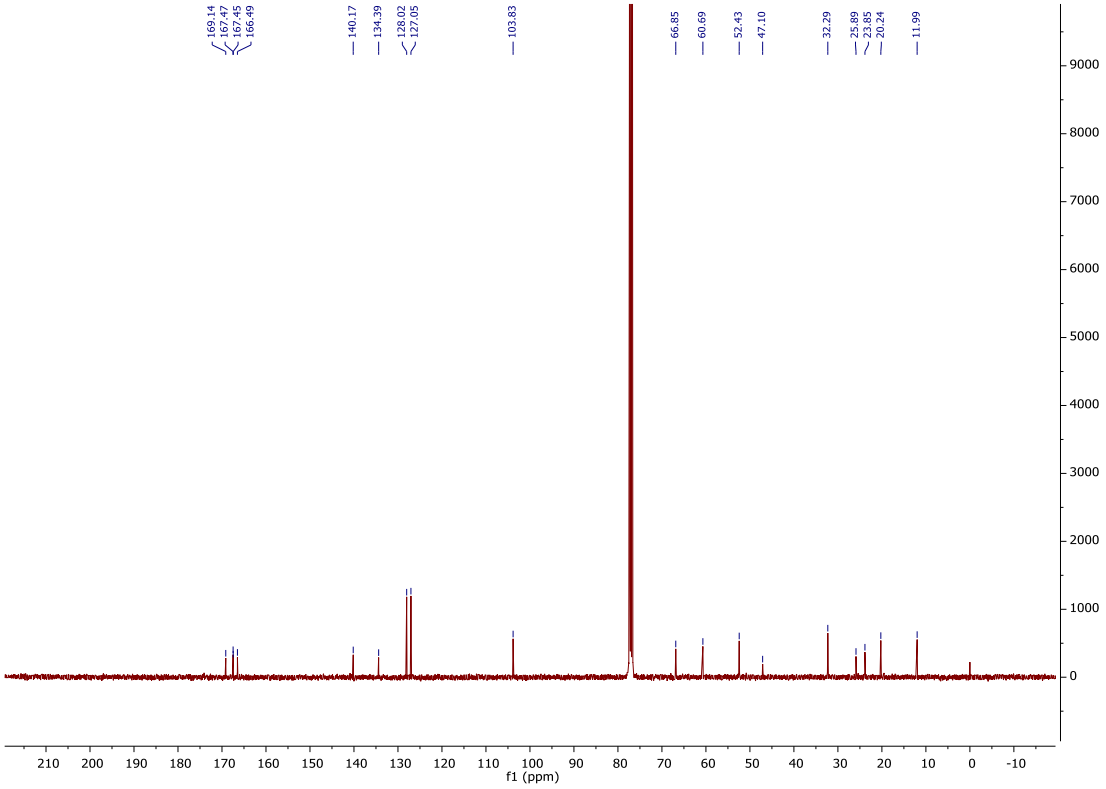

HPLC trace for **15**

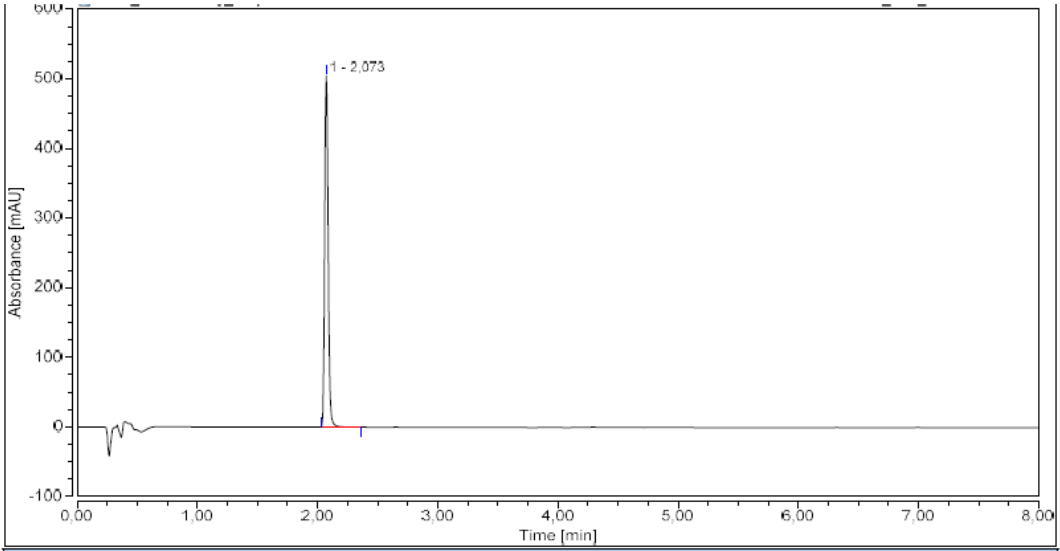

Integration Results

No.	Peak Name	Retention Time min	Area mAU*min	Height mAU	Relative Area %	Relative Height %	Amount n.a.
1		2,073	17,139	504,472	100,00	100,00	n.a.
Total:			**17,139**	**504,472**	**100,00**	**100,00**	

^{1}H NMR (400 MHz, $CDCl_3$)

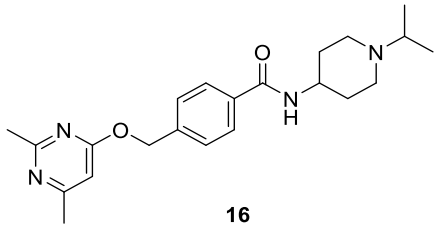

16

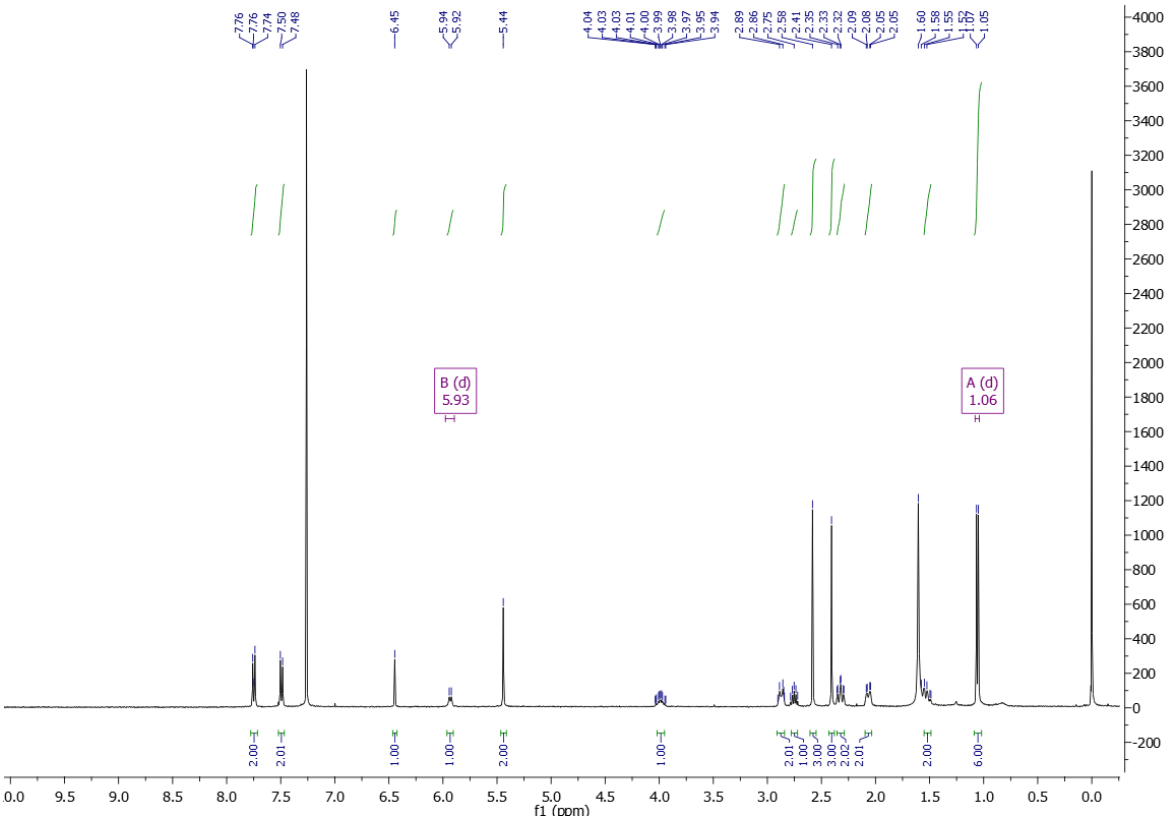

^{13}C NMR (100 MHz, $CDCl_3$)

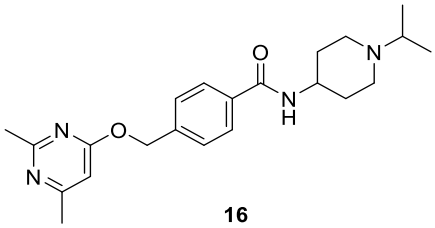

16

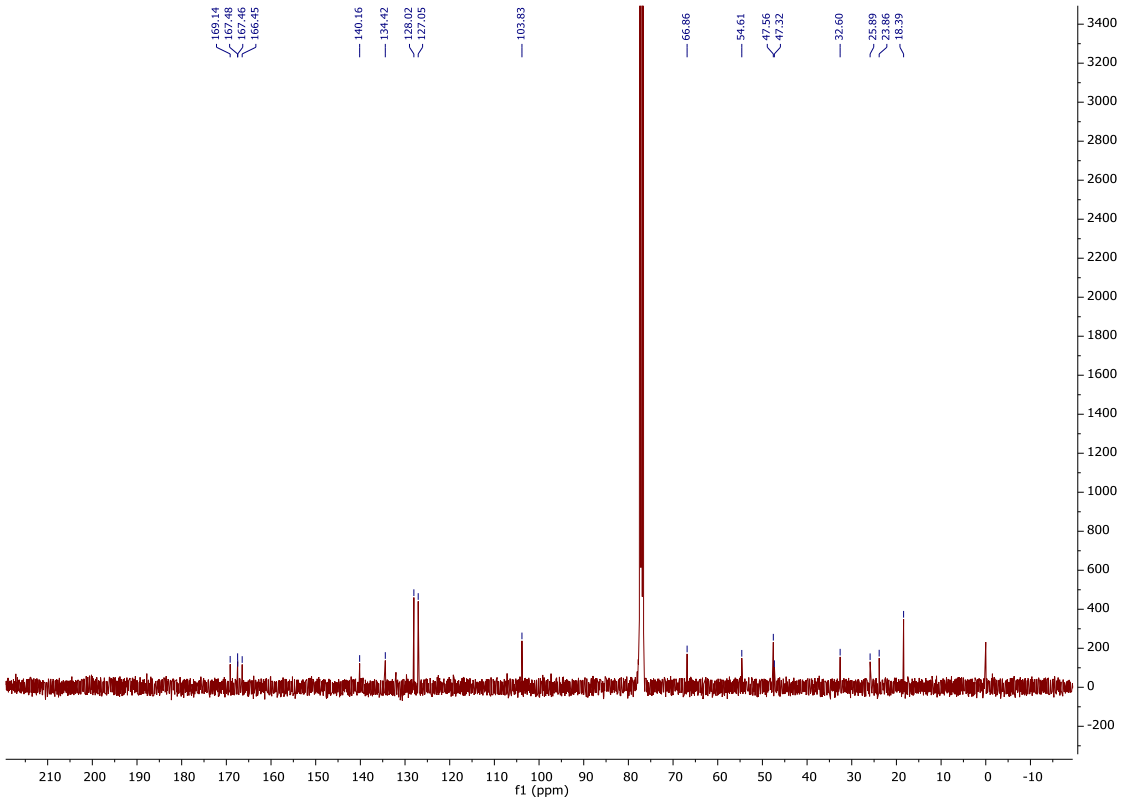

HPLC trace for **16**

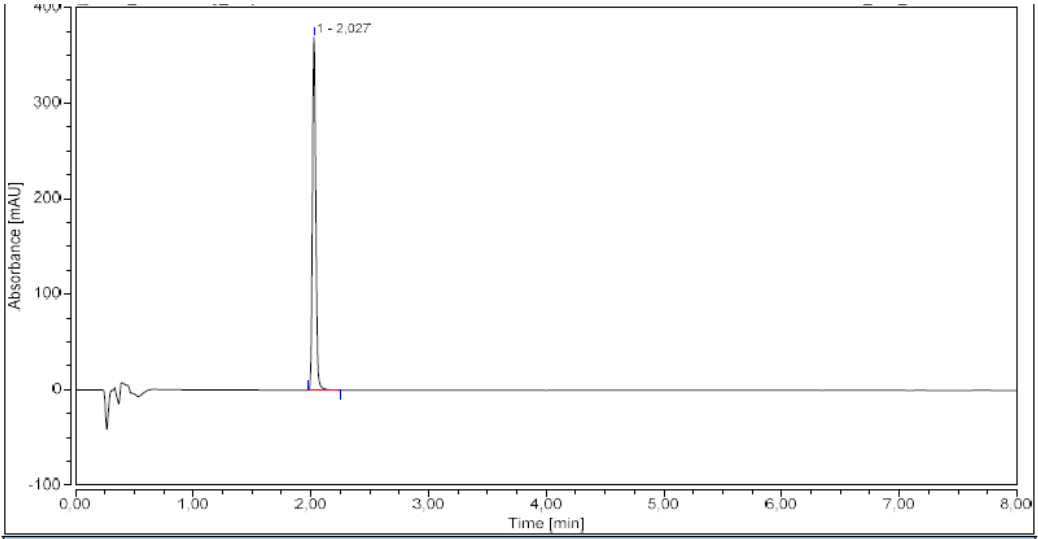

Integration Results

No.	Peak Name	Retention Time min	Area mAU*min	Height mAU	Relative Area %	Relative Height %	Amount n.a.
1		2,027	12,232	369,104	100,00	100,00	n.a.
Total:			**12,232**	**369,104**	**100,00**	**100,00**	

^{1}H NMR (400 MHz, $CDCl_3$)

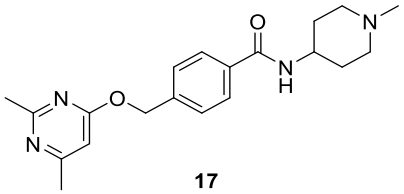

17

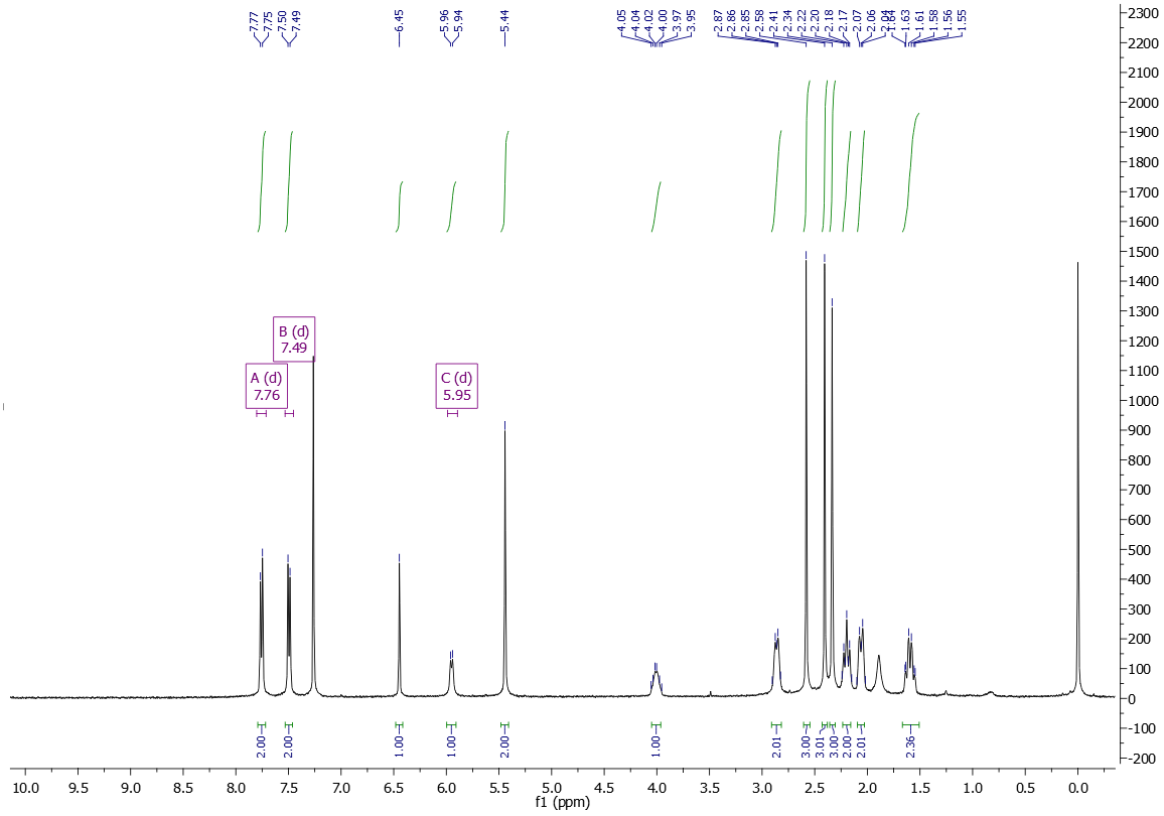

^{13}C NMR (100 MHz, $CDCl_3$)

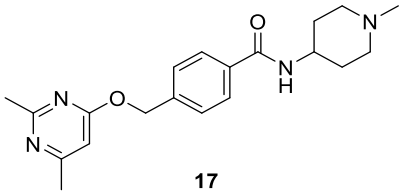

17

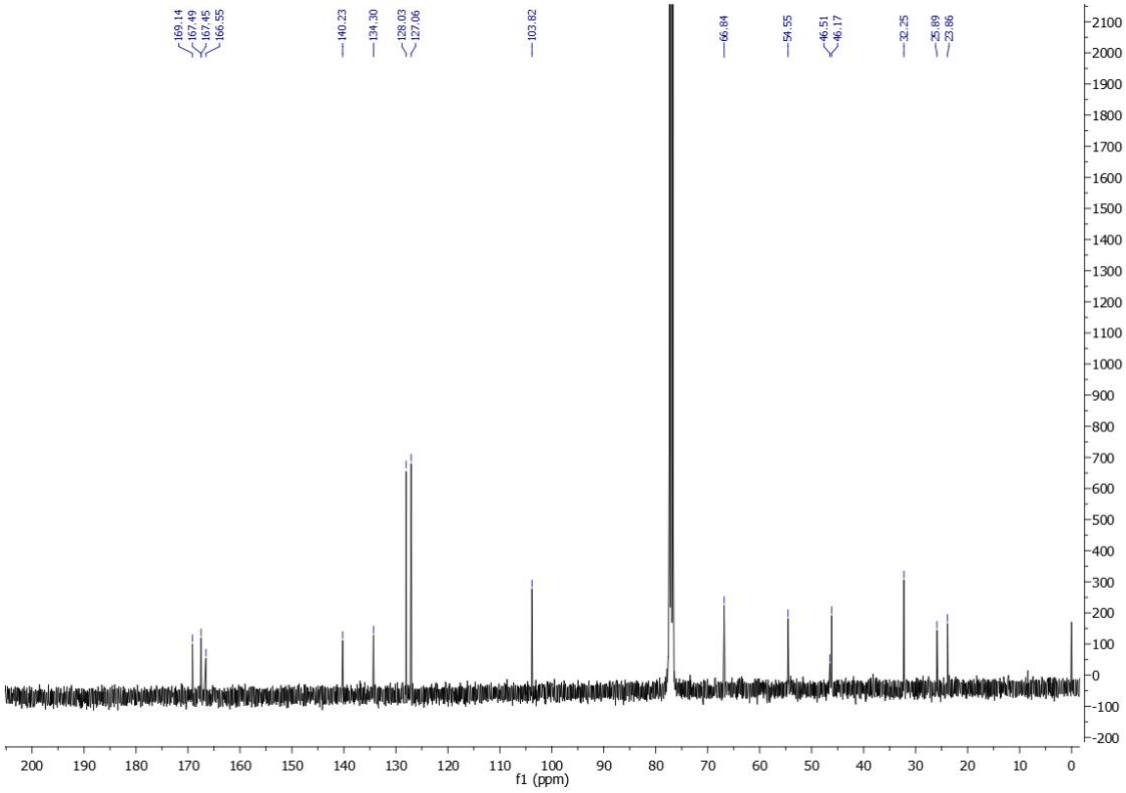

HPLC trace for **17**

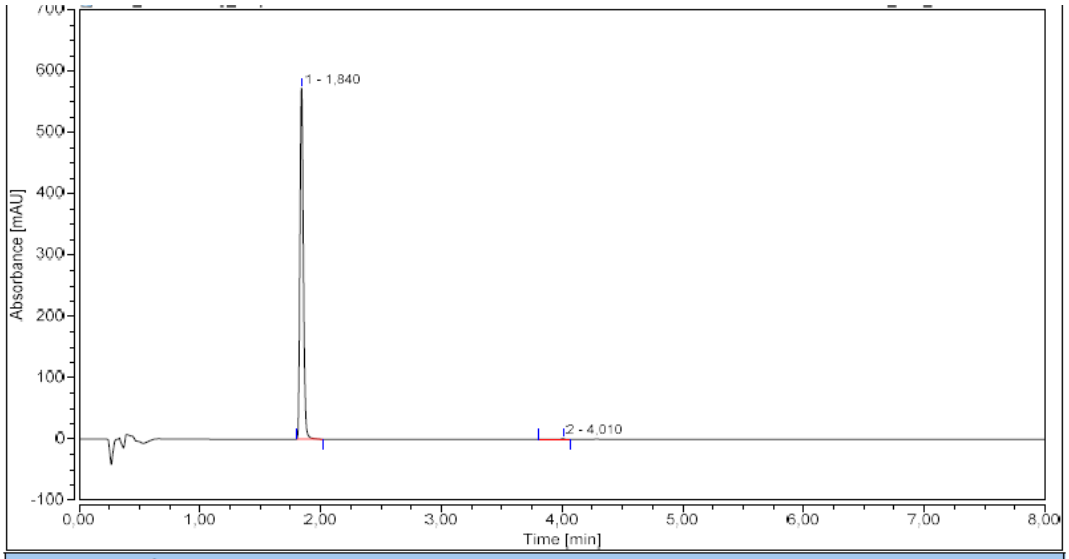

Integration Results

No.	Peak Name	Retention Time min	Area mAU*min	Height mAU	Relative Area %	Relative Height %	Amount n.a.
1		1,840	18,964	572,265	99,68	99,76	n.a.
2		4,010	0,060	1,389	0,32	0,24	n.a.
Total:			**19,024**	**573,653**	**100,00**	**100,00**	

^{1}H NMR (400 MHz, $CDCl_3$)

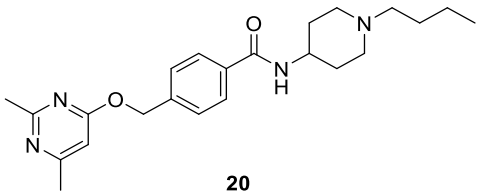

20

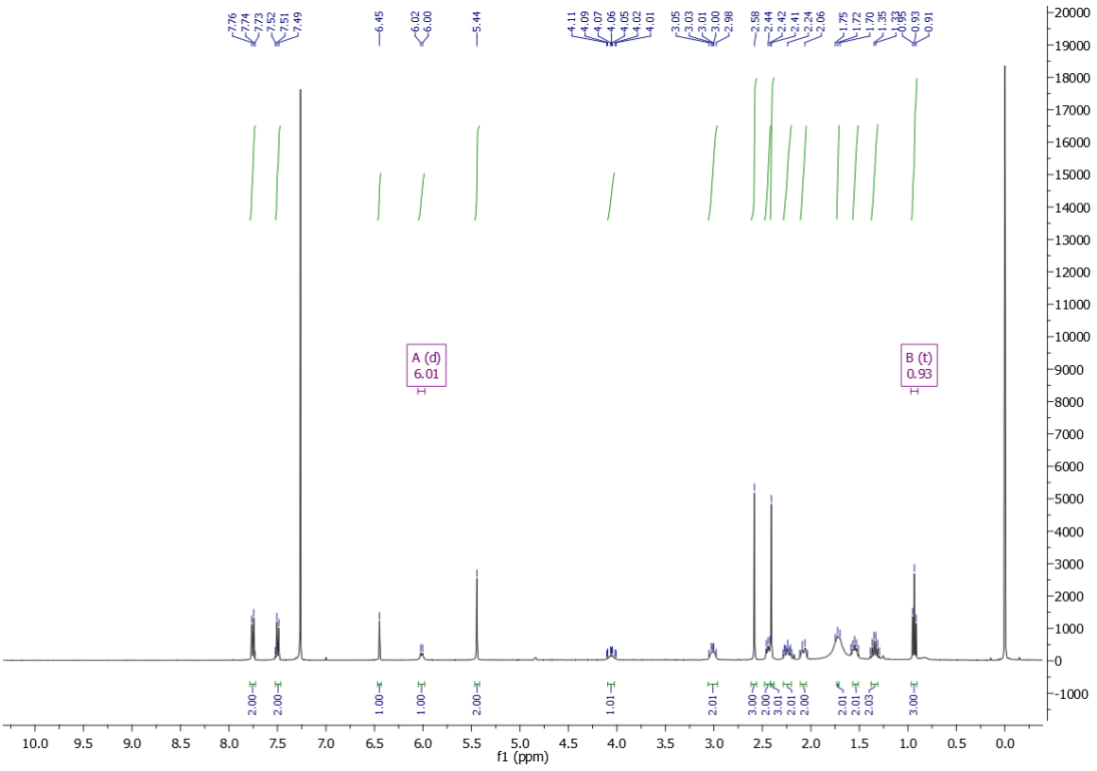

^{13}C NMR (100 MHz, $CDCl_3$)

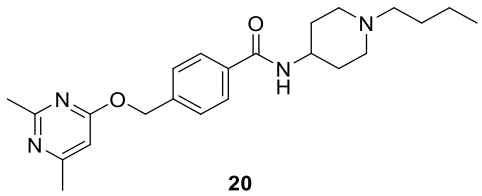

20

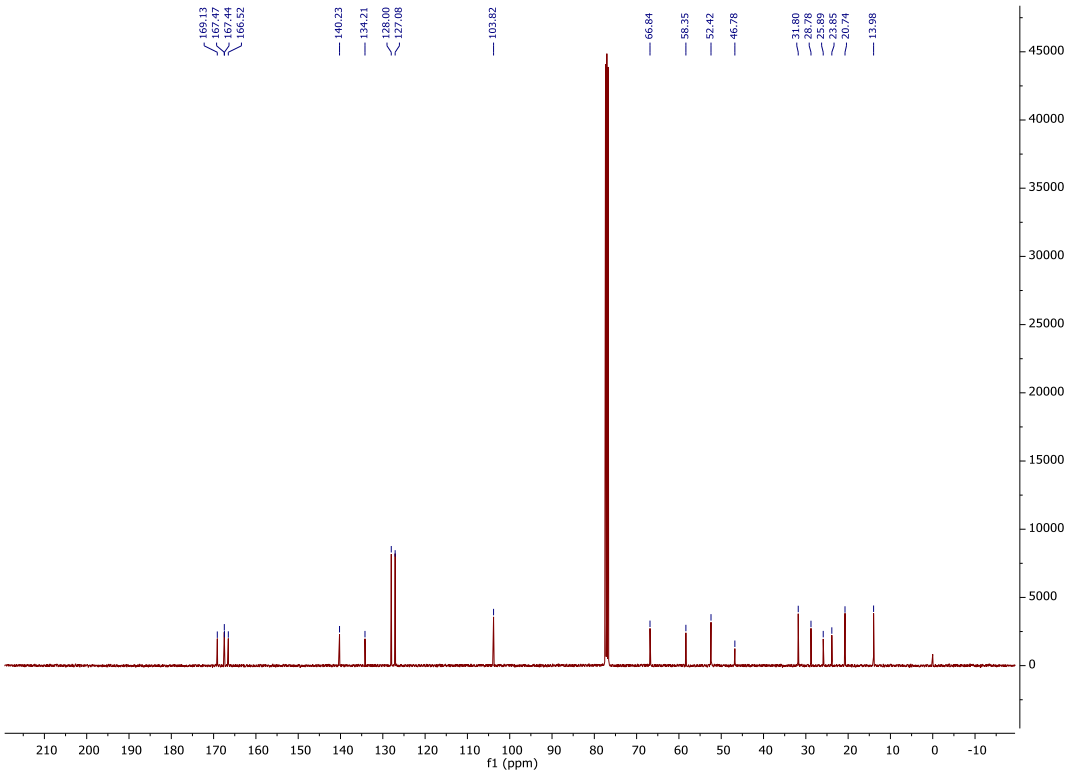

HPLC trace for **20**

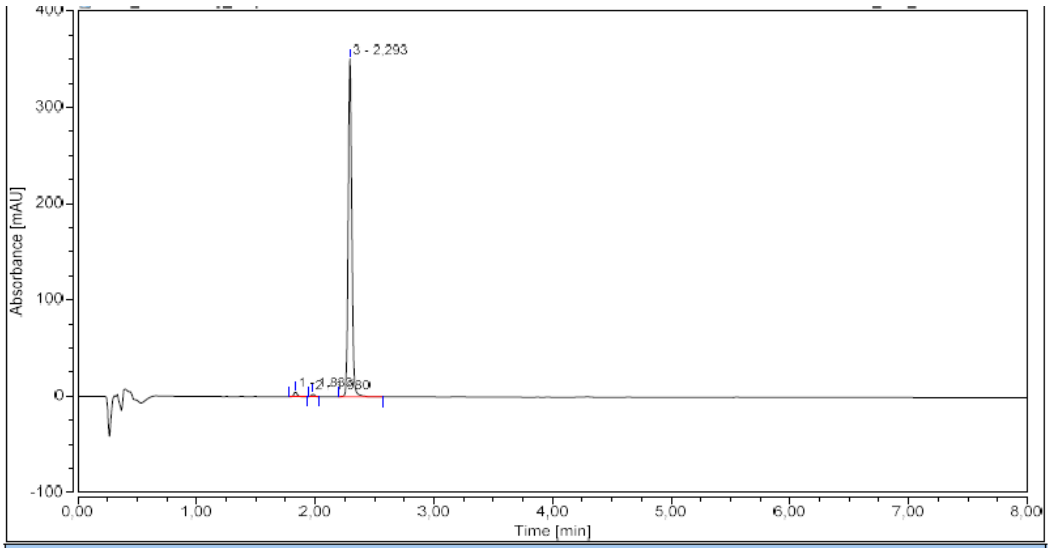

Integration Results							
No.	Peak Name	Retention Time min	Area mAU*min	Height mAU	Relative Area %	Relative Height %	Amount n.a.
1		1,833	0,157	4,906	1,25	1,37	n.a.
2		1,980	0,078	2,554	0,62	0,71	n.a.
3		2,293	12,308	350,679	98,13	97,92	n.a.
Total:			**12,543**	**358,139**	**100,00**	**100,00**	

^{1}H NMR (400 MHz, $CDCl_3$)

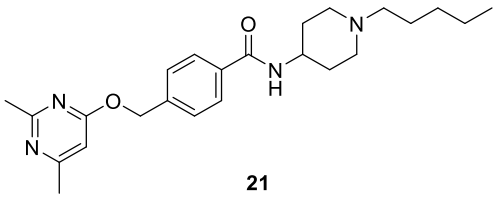

21

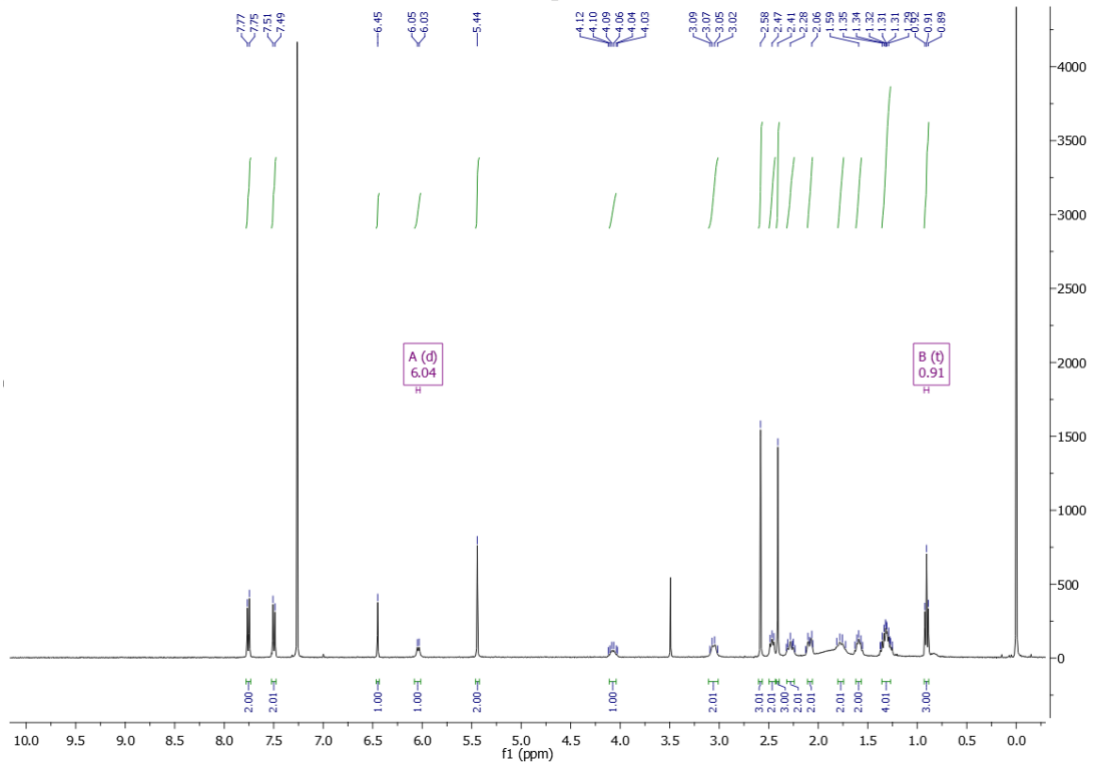

^{13}C NMR (100 MHz, $CDCl_3$)

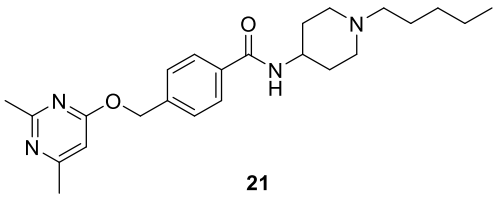

21

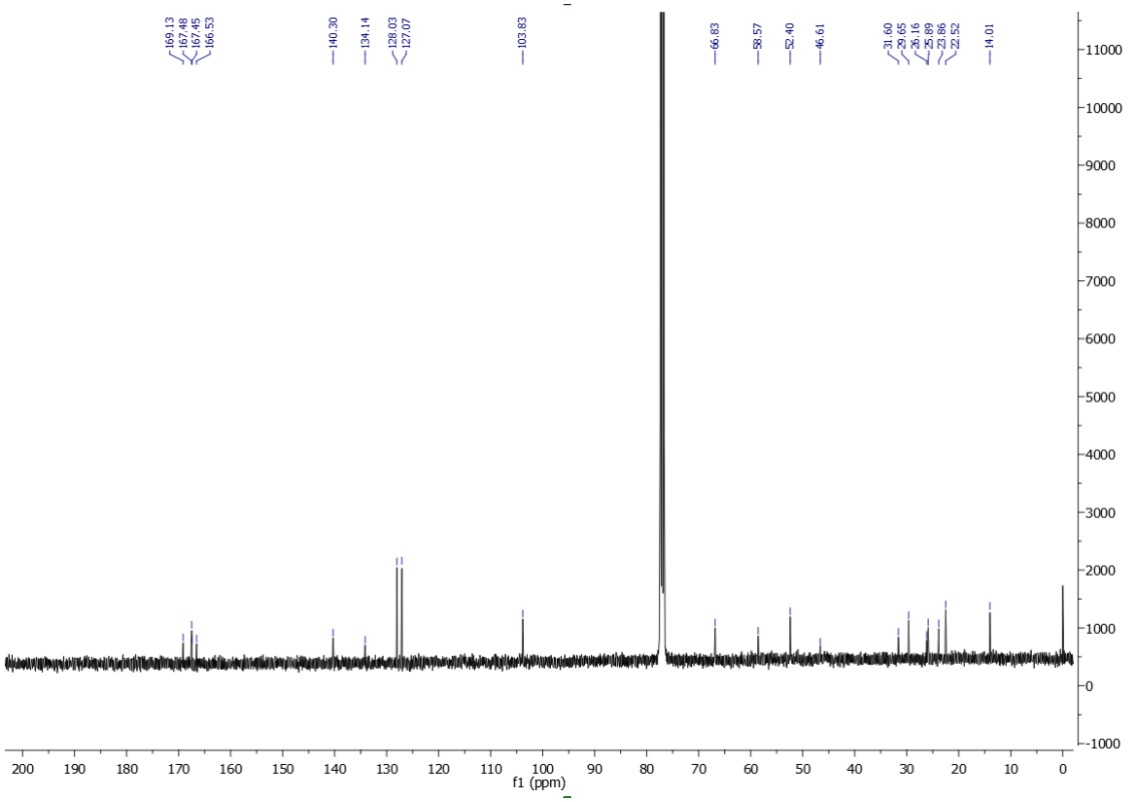

HPLC trace for **21**

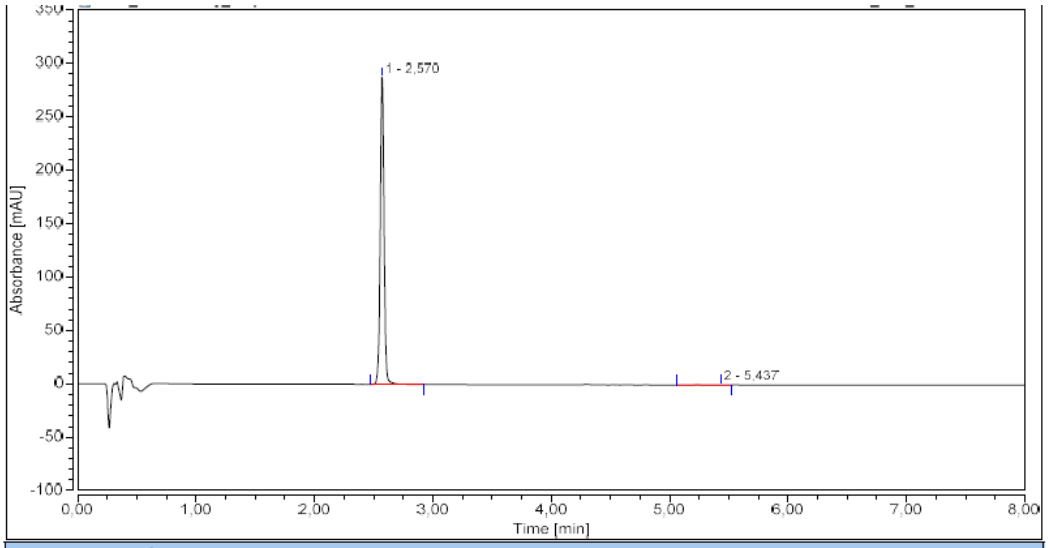

Integration Results

No.	Peak Name	Retention Time min	Area mAU*min	Height mAU	Relative Area %	Relative Height %	Amount n.a.
1		2,570	10,635	287,720	99,48	99,93	n.a.
2		5,437	0,056	0,196	0,52	0,07	n.a.
Total:			**10,691**	**287,916**	**100,00**	**100,00**	

^{1}H NMR (400 MHz, $CDCl_3$)

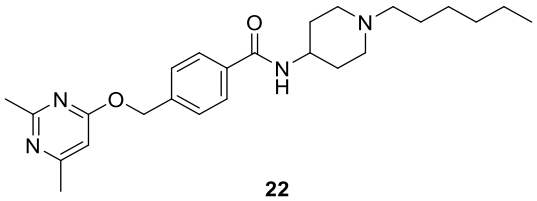

22

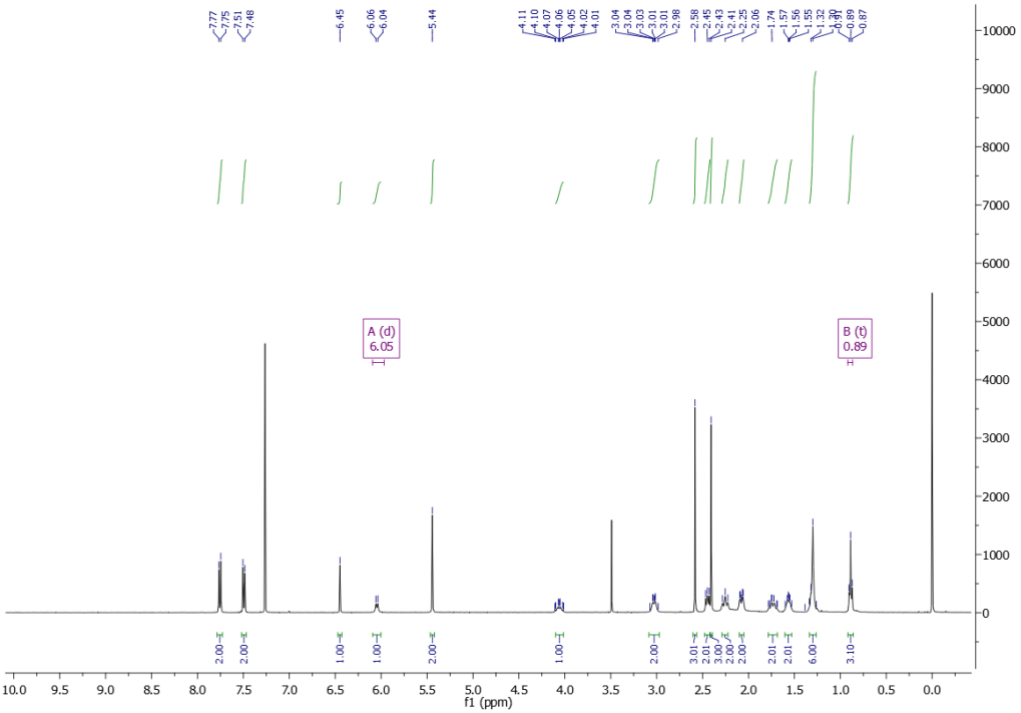

^{13}C NMR (100 MHz, $CDCl_3$)

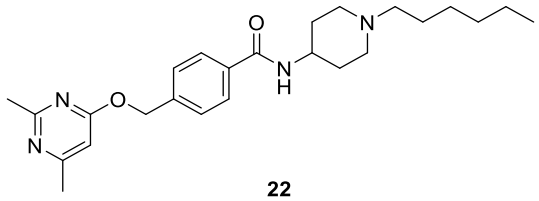

22

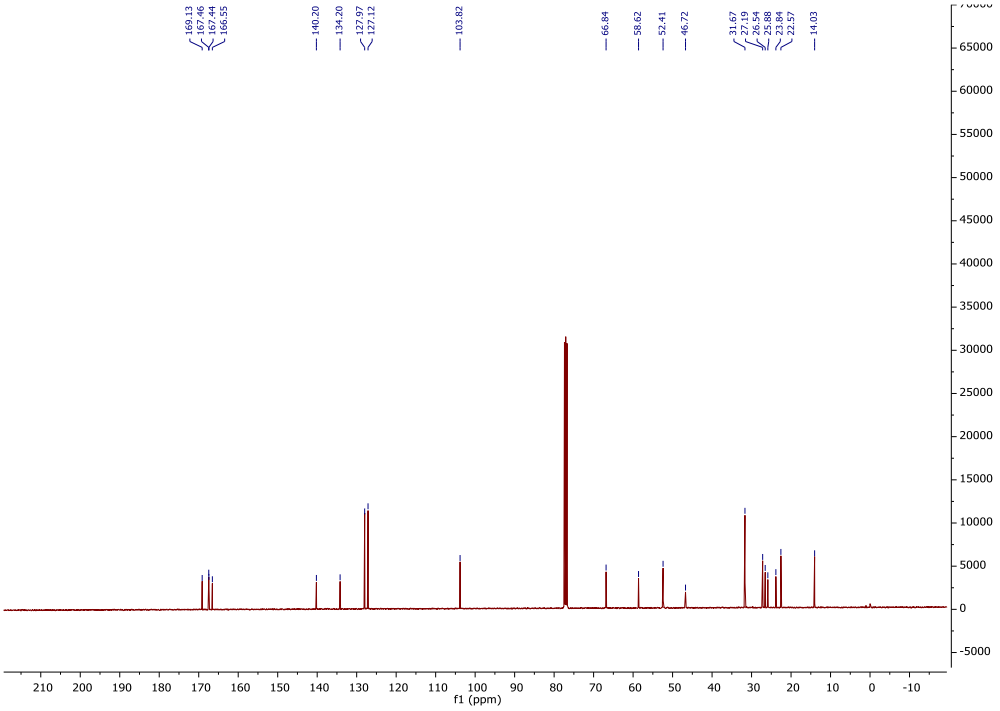

HPLC trace for **22**

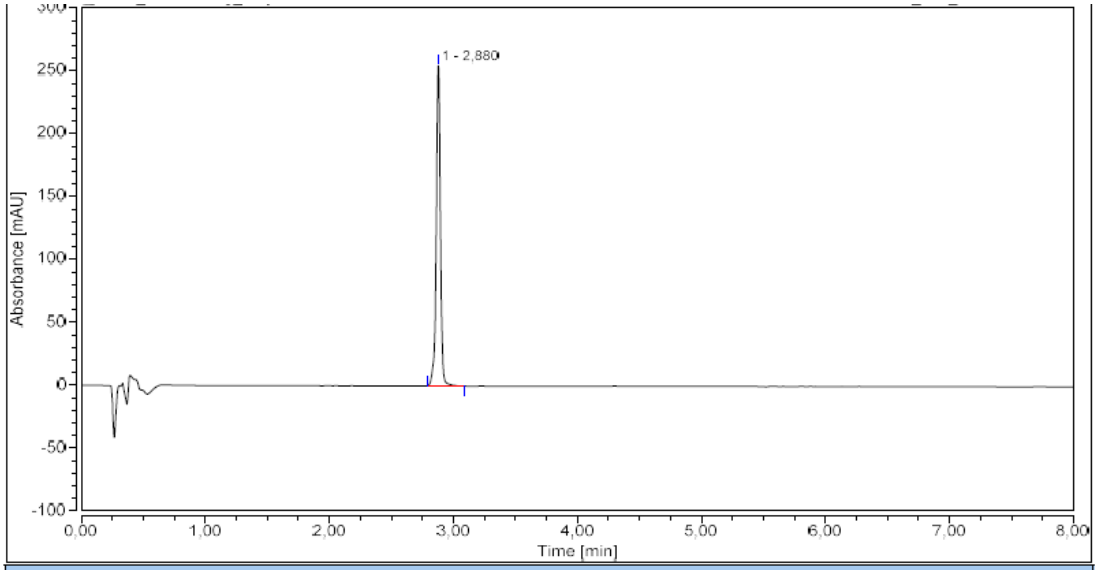

Integration Results

No.	Peak Name	Retention Time min	Area mAU*min	Height mAU	Relative Area %	Relative Height %	Amount n.a.
1		2,880	9,992	254,559	100,00	100,00	n.a.
Total:			**9,992**	**254,559**	**100,00**	**100,00**	

^{1}H NMR (400 MHz, $CDCl_3$)

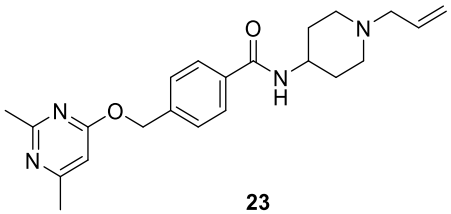

23

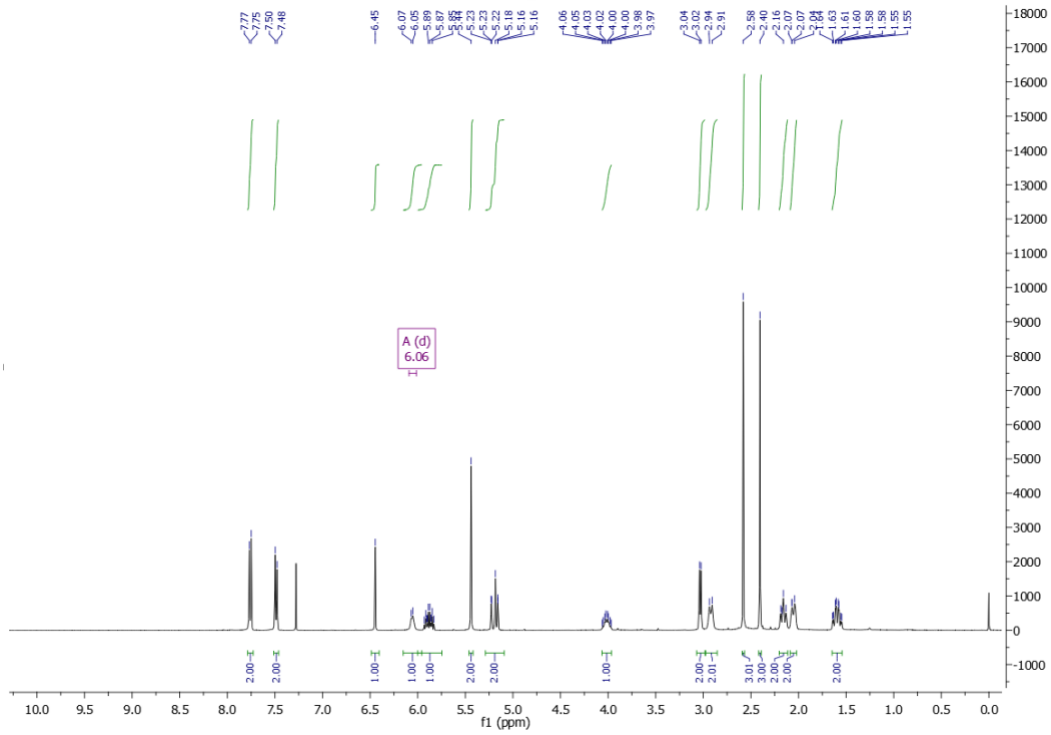

^{13}C NMR (100 MHz, $CDCl_3$)

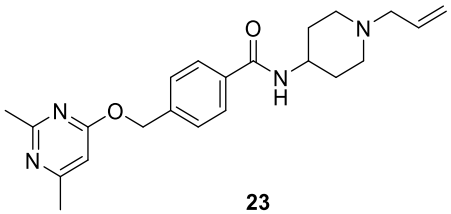

23

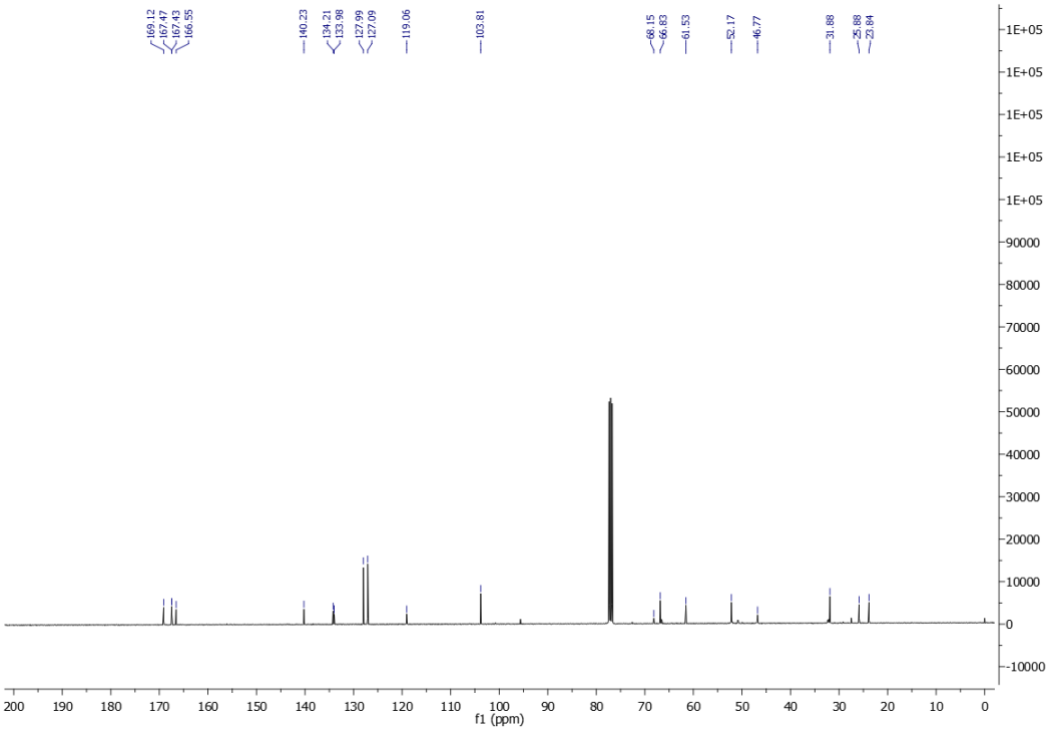

HPLC trace for **23**

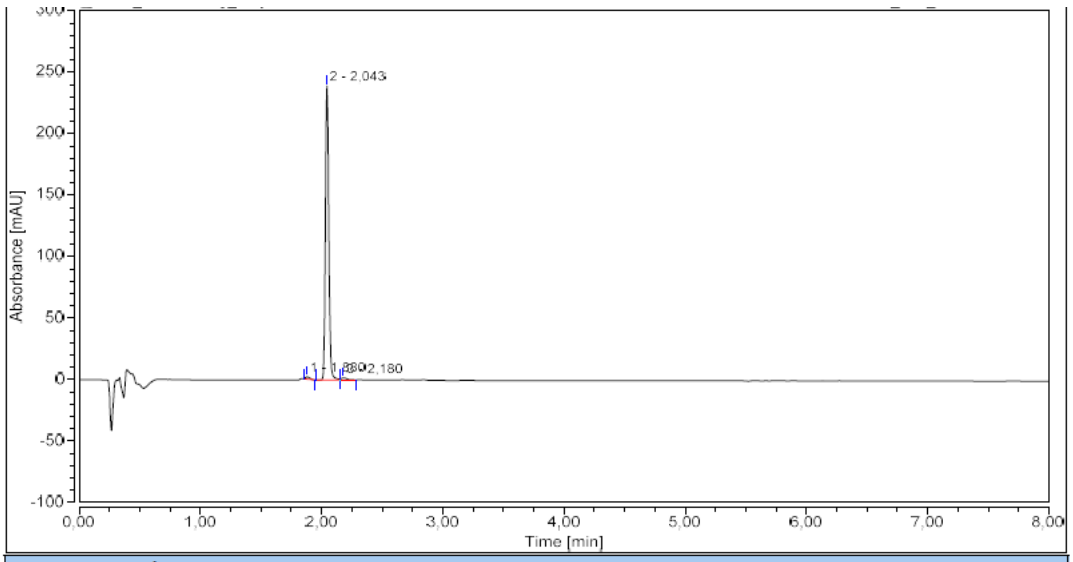

Integration Results

No.	Peak Name	Retention Time min	Area mAU*min	Height mAU	Relative Area %	Relative Height %	Amount n.a.
1		1,880	0,082	2,010	1,04	0,83	n.a.
2		2,043	7,711	239,123	97,78	98,44	n.a.
3		2,180	0,092	1,773	1,17	0,73	n.a.
Total:			**7,886**	**242,906**	**100,00**	**100,00**	

^{1}H NMR (400 MHz, $CDCl_3$)

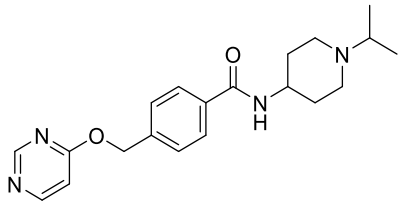

30

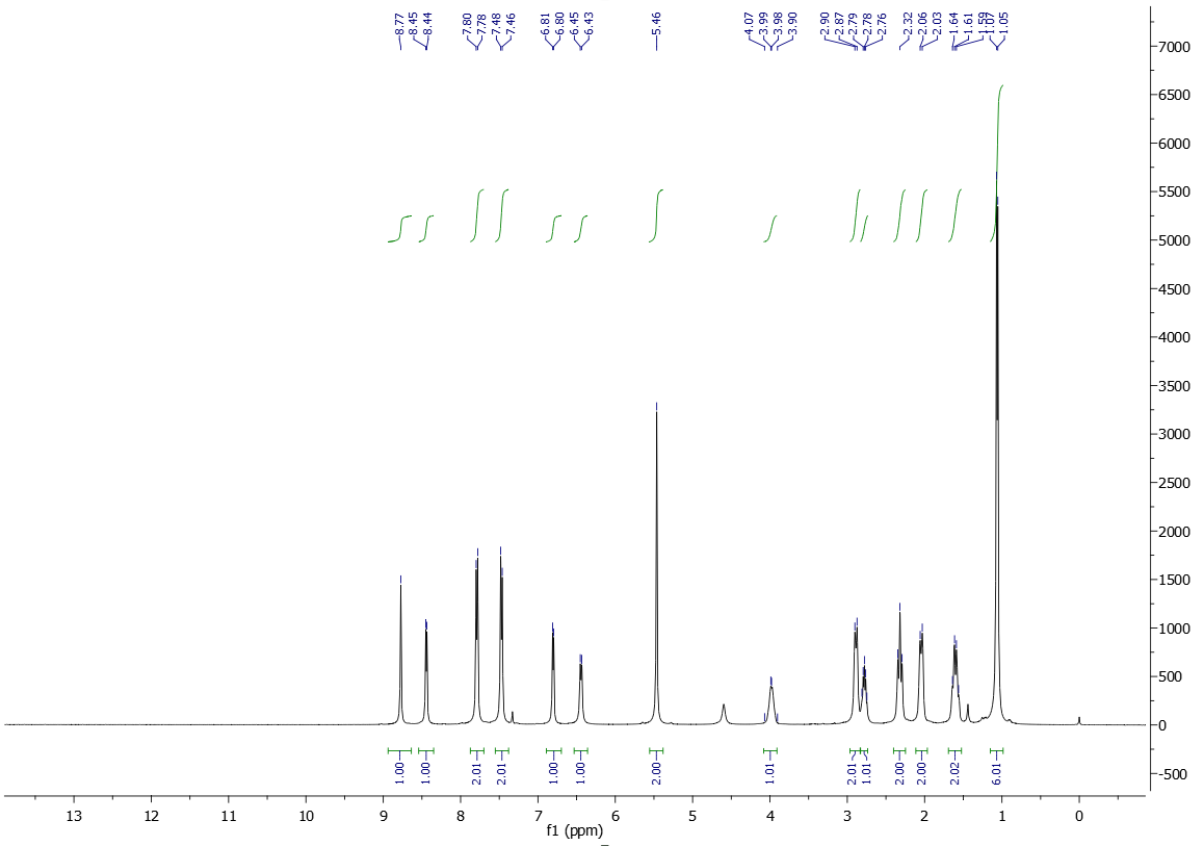

^{13}C NMR (100 MHz, $CDCl_3$)

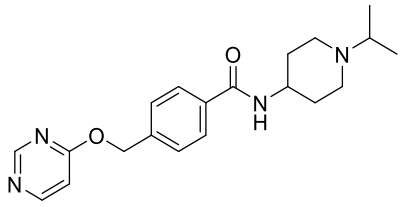

30

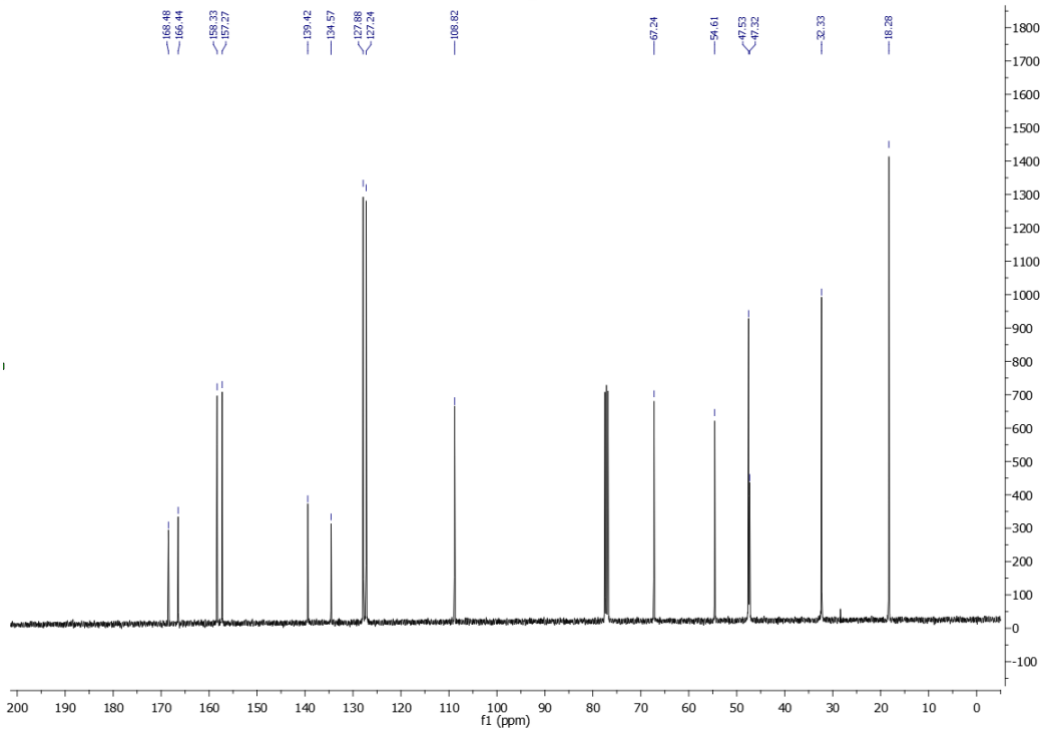

HPLC trace for **30**

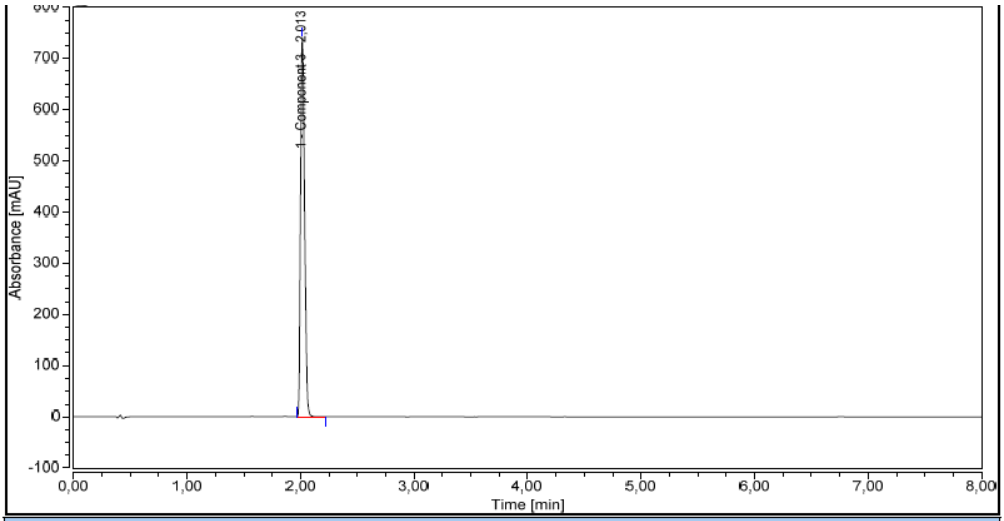

Integration Results							
No.	Peak Name	Retention Time min	Area mAU*min	Height mAU	Relative Area %	Relative Height %	Amount
n.a.	Component 1	n.a.	n.a.	n.a.	n.a.	n.a.	n.a.
n.a.	Component 2	n.a.	n.a.	n.a.	n.a.	n.a.	n.a.
1	Component 3	2,013	30,706	741,154	100,00	100,00	n.a.
n.a.	Component 4	n.a.	n.a.	n.a.	n.a.	n.a.	n.a.
Total:			**30,706**	**741,154**	**100,00**	**100,00**	

^{1}H NMR (400 MHz, $CDCl_3$)

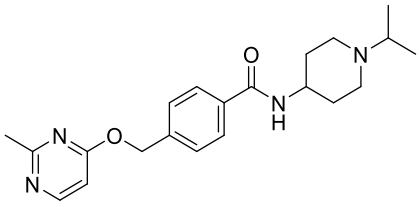

31

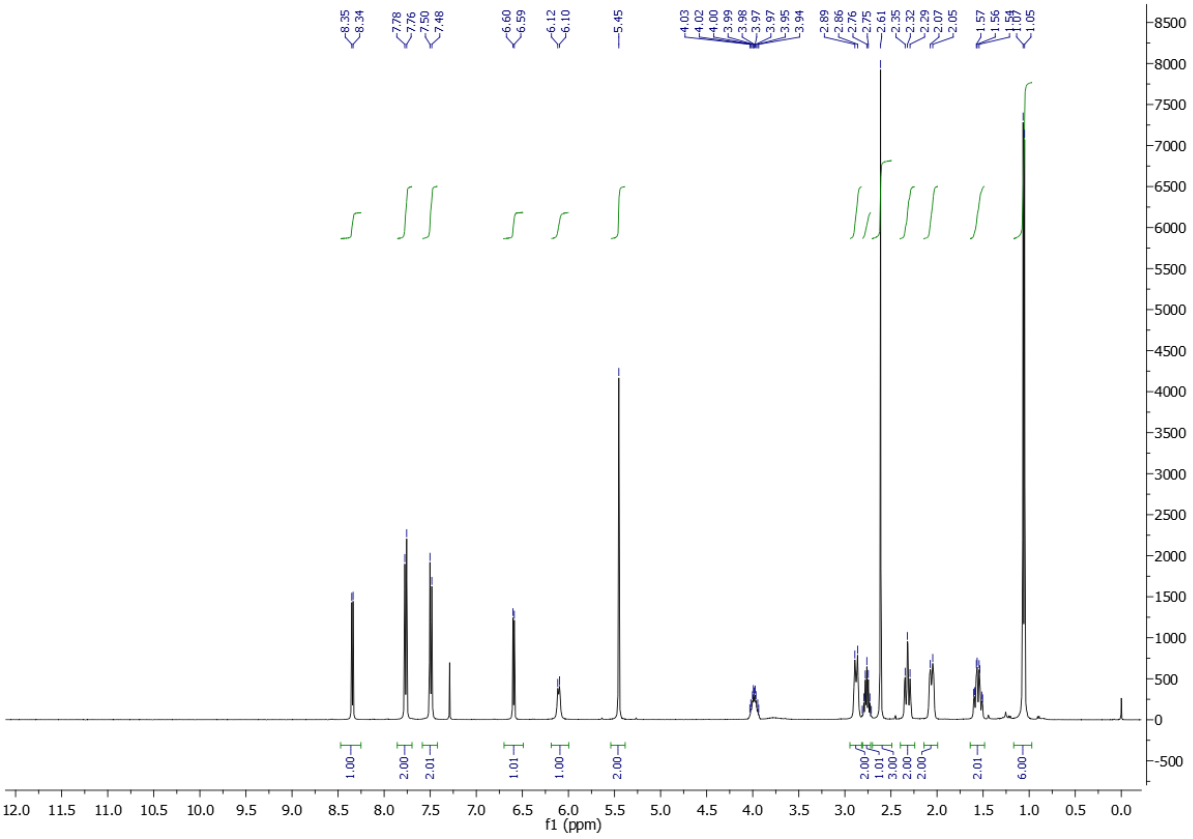

^{13}C NMR (100 MHz, $CDCl_3$)

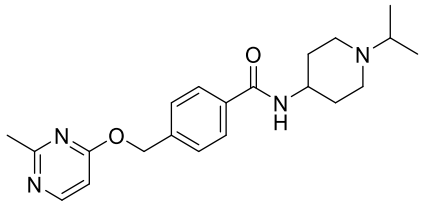

31

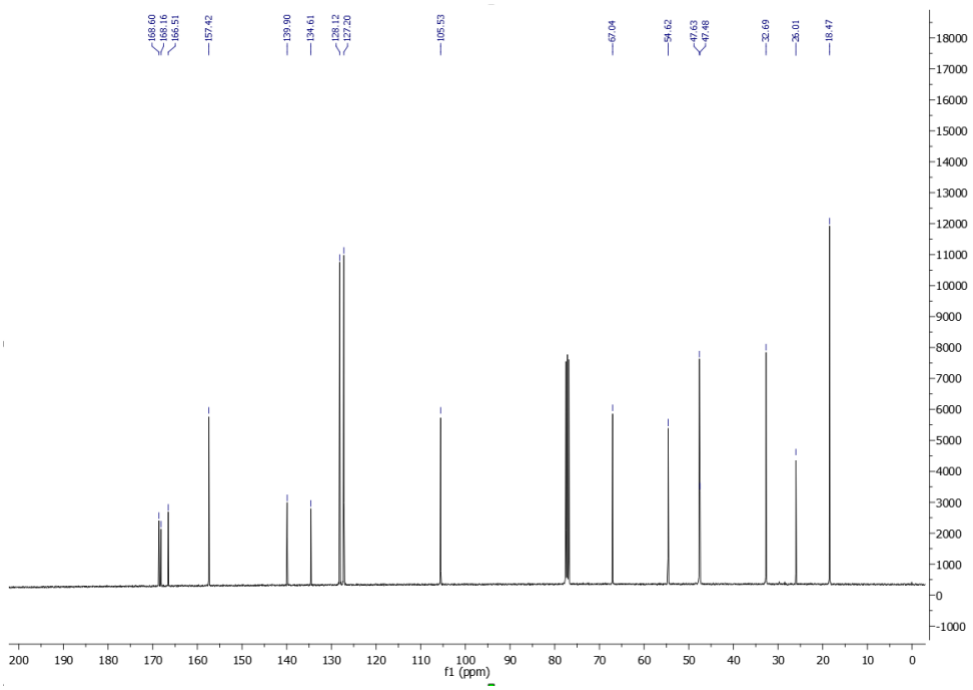

HPLC trace for **31**

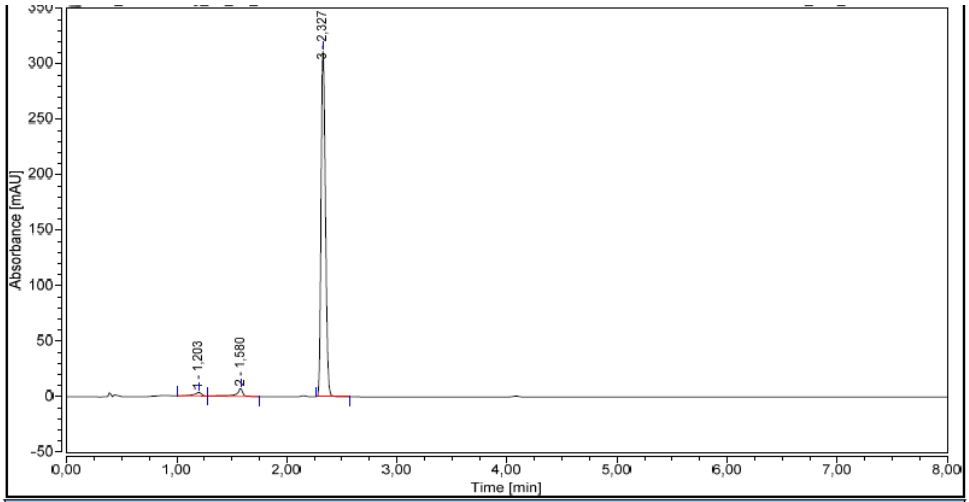

Integration Results

No.	Peak Name	Retention Time min	Area mAU*min	Height mAU	Relative Area %	Relative Height %	Amount
1		1,203	0,259	3,302	1,72	1,03	n.a.
2		1,580	0,493	7,295	3,28	2,26	n.a.
n.a.	Component 1	n.a.	n.a.	n.a.	n.a.	n.a.	n.a.
n.a.	Component 2	n.a.	n.a.	n.a.	n.a.	n.a.	n.a.
n.a.	Component 3	n.a.	n.a.	n.a.	n.a.	n.a.	n.a.
3		2,327	14,264	311,476	95,00	96,71	n.a.
n.a.	Component 4	n.a.	n.a.	n.a.	n.a.	n.a.	n.a.
Total:			**15,016**	**322,073**	**100,00**	**100,00**	

^{1}H NMR (400 MHz, $CDCl_3$)

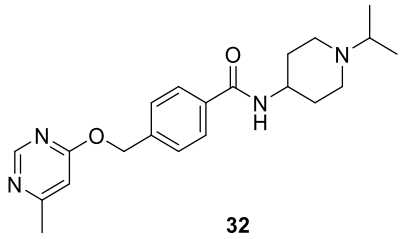

32

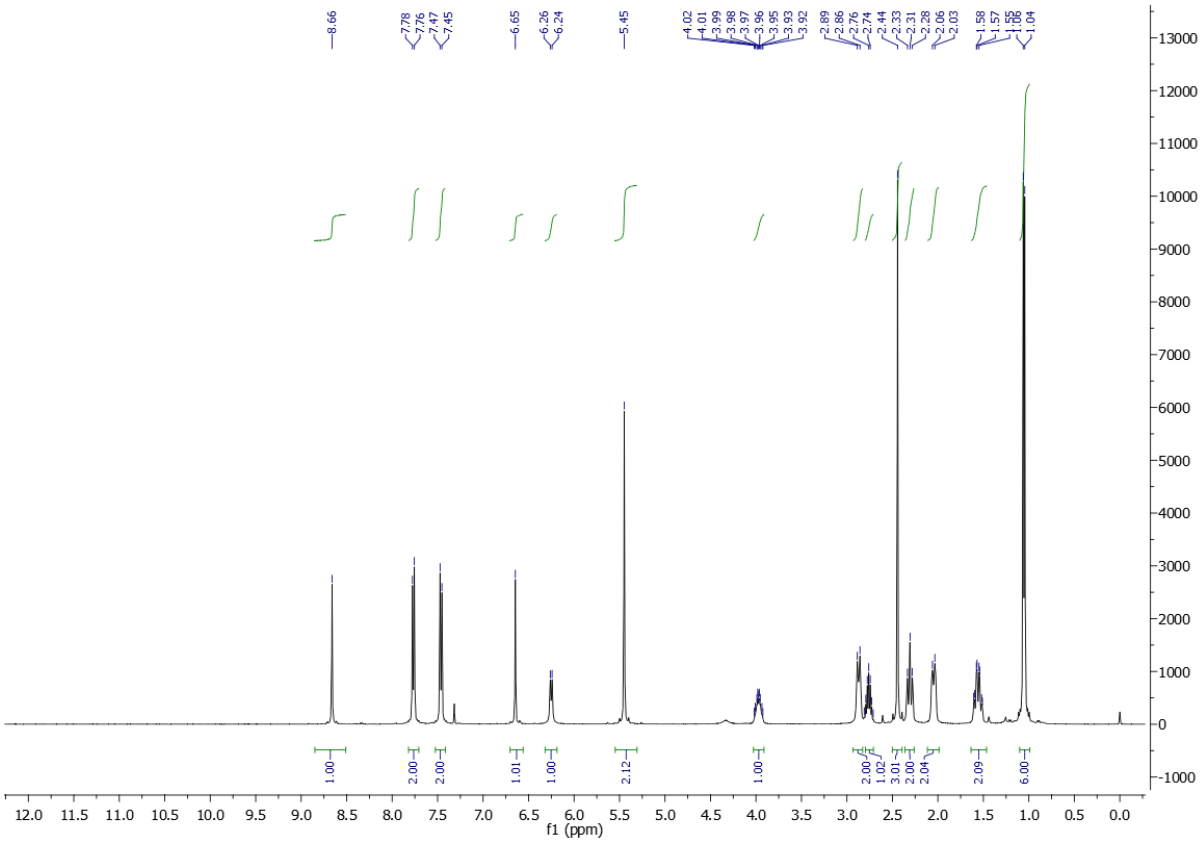

^{13}C NMR (100 MHz, $CDCl_3$)

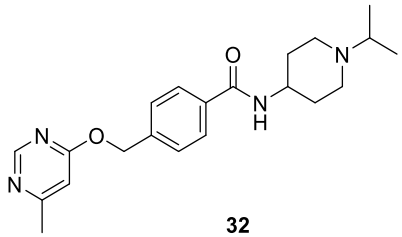

32

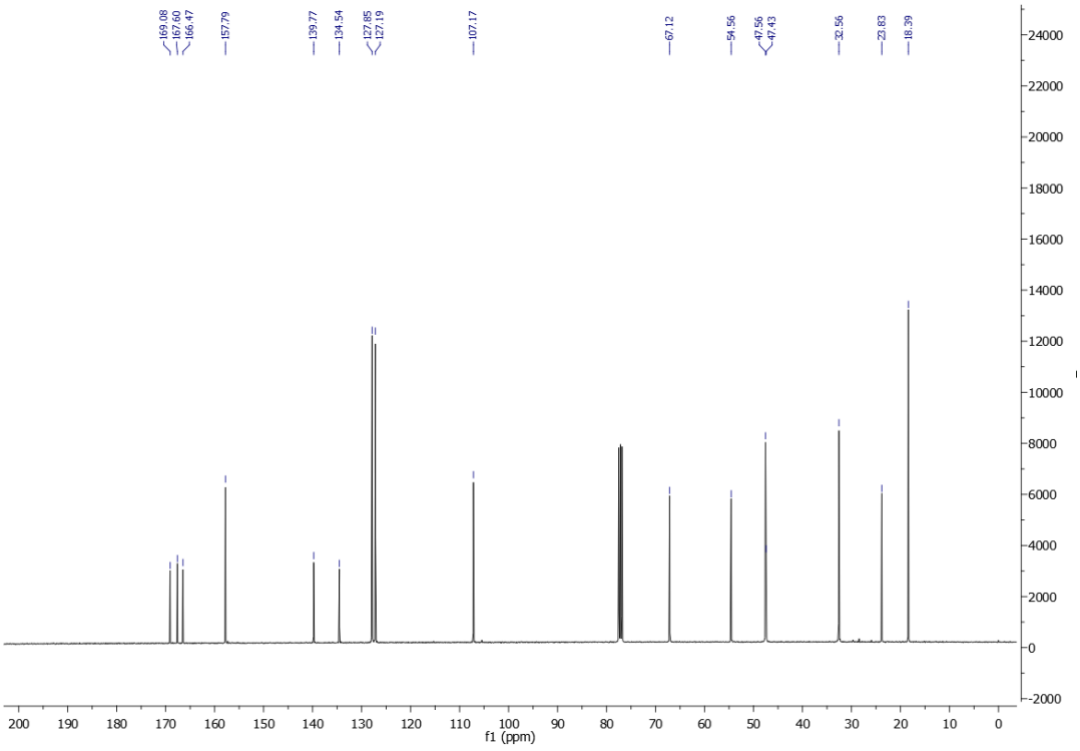

HPLC trace for **32**

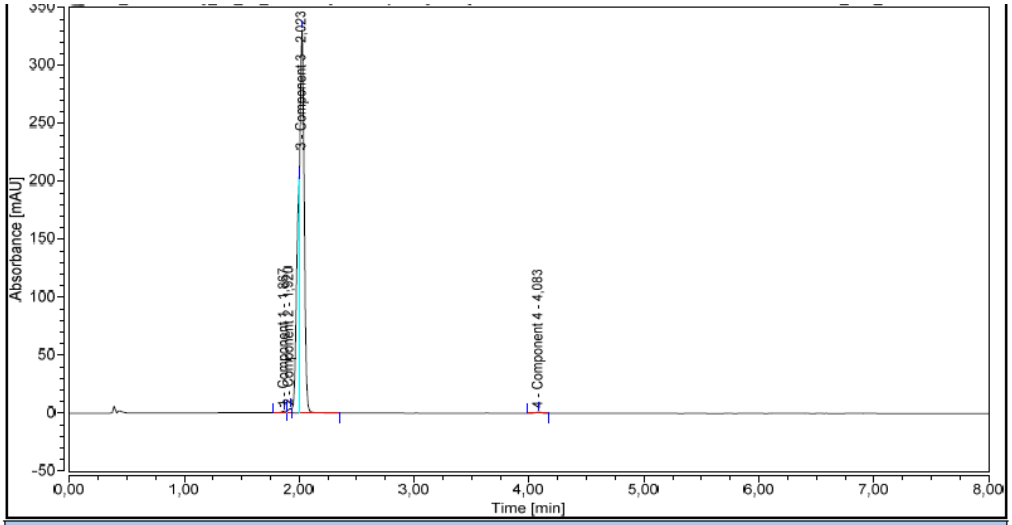

Integration Results

No.	Peak Name	Retention Time min	Area mAU*min	Height mAU	Relative Area %	Relative Height %	Amount
1	Component 1	1,867	0,079	1,521	0,55	0,45	n.a.
2	Component 2	1,920	0,127	3,613	0,89	1,07	n.a.
3	Component 3	2,023	14,060	330,213	98,18	98,16	n.a.
4	Component 4	4,083	0,055	1,042	0,39	0,31	n.a.
Total:			**14,322**	**336,389**	**100,00**	**100,00**	

^{1}H NMR (400 MHz, $CDCl_3$)

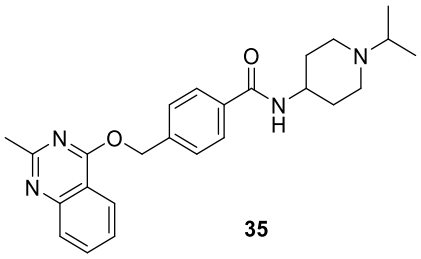

35

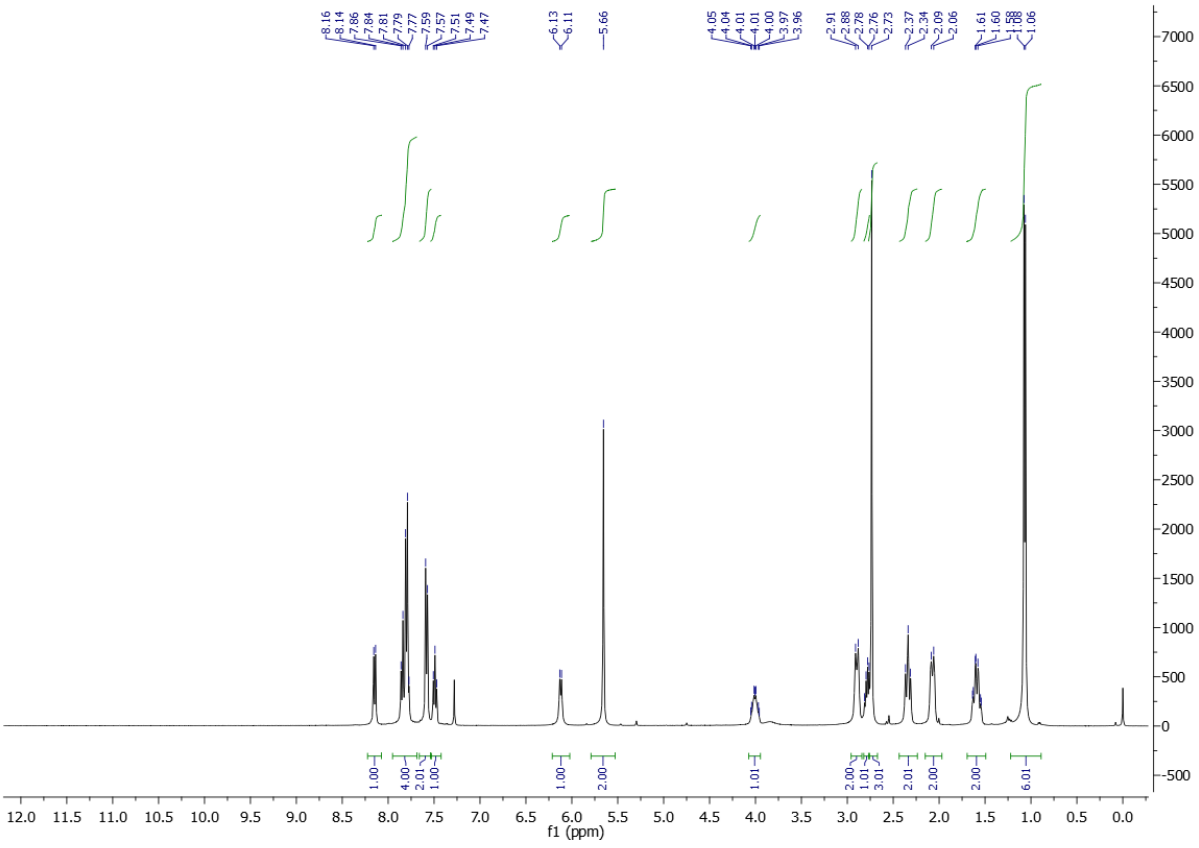

^{13}C NMR (100 MHz, $CDCl_3$)

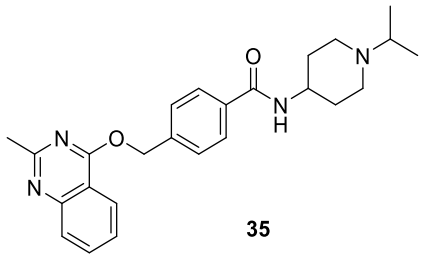

35

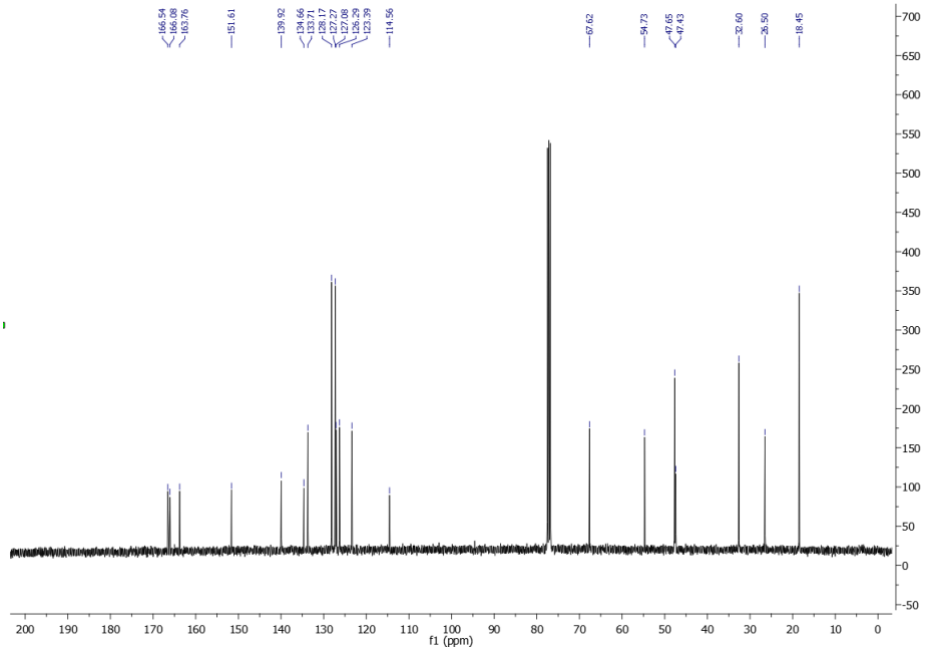

HPLC trace for 35

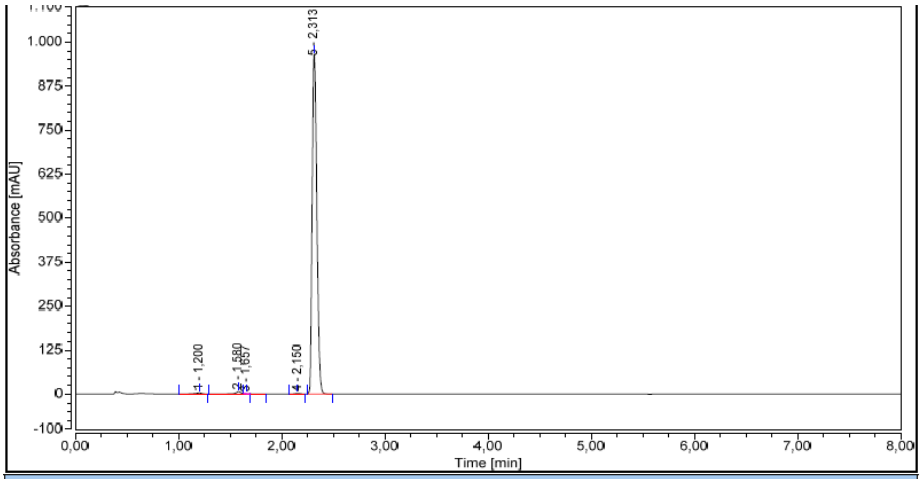

Integration Results

No.	Peak Name	Retention Time min	Area mAU*min	Height mAU	Relative Area %	Relative Height %	Amount
1		1,200	0,244	3,228	0,47	0,33	n.a.
2		1,580	0,545	7,498	1,06	0,77	n.a.
3		1,657	0,003	0,102	0,01	0,01	n.a.
n.a.	Component 1	n.a.	n.a.	n.a.	n.a.	n.a.	n.a.
n.a.	Component 2	n.a.	n.a.	n.a.	n.a.	n.a.	n.a.
n.a.	Component 3	n.a.	n.a.	n.a.	n.a.	n.a.	n.a.
4		2,150	0,115	2,190	0,22	0,22	n.a.
5		2,313	50,734	965,776	98,24	98,67	n.a.
n.a.	Component 4	n.a.	n.a.	n.a.	n.a.	n.a.	n.a.
Total:			**51,641**	**978,795**	**100,00**	**100,00**	

^{1}H NMR (400 MHz, $CDCl_3$)

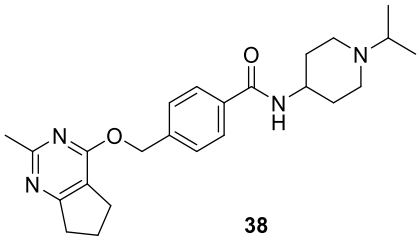

38

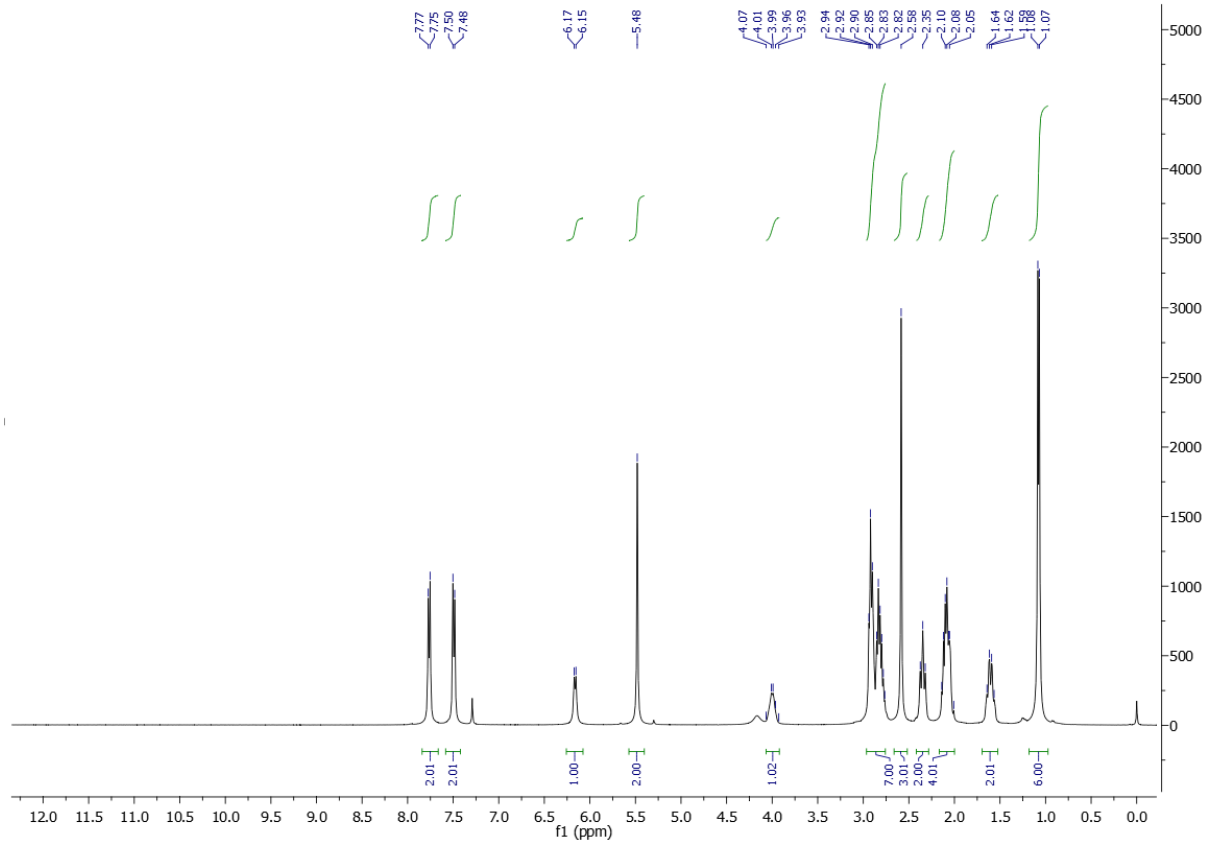

^{13}C NMR (100 MHz, $CDCl_3$)

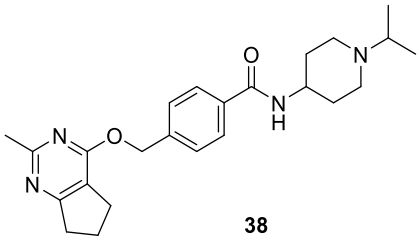

38

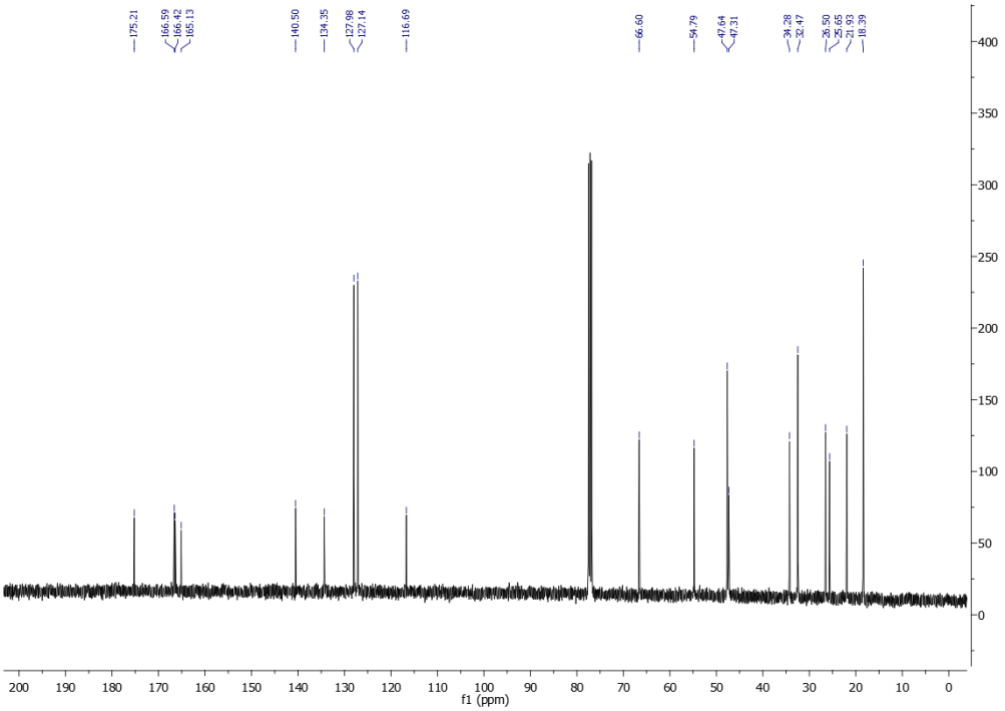

HPLC trace for **38**

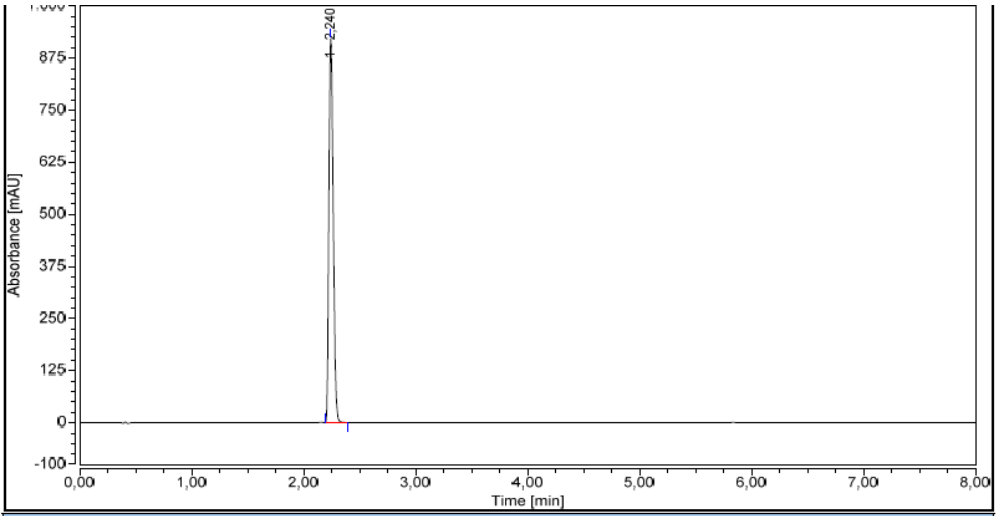

Integration Results							
No.	Peak Name	Retention Time min	Area mAU*min	Height mAU	Relative Area %	Relative Height %	Amount
n.a.	Component 1	n.a.	n.a.	n.a.	n.a.	n.a.	n.a.
n.a.	Component 2	n.a.	n.a.	n.a.	n.a.	n.a.	n.a.
n.a.	Component 3	n.a.	n.a.	n.a.	n.a.	n.a.	n.a.
1		2,240	41,448	920,579	100,00	100,00	n.a.
n.a.	Component 4	n.a.	n.a.	n.a.	n.a.	n.a.	n.a.
Total:			**41,448**	**920,579**	**100,00**	**100,00**	

2. Supplementary Figures

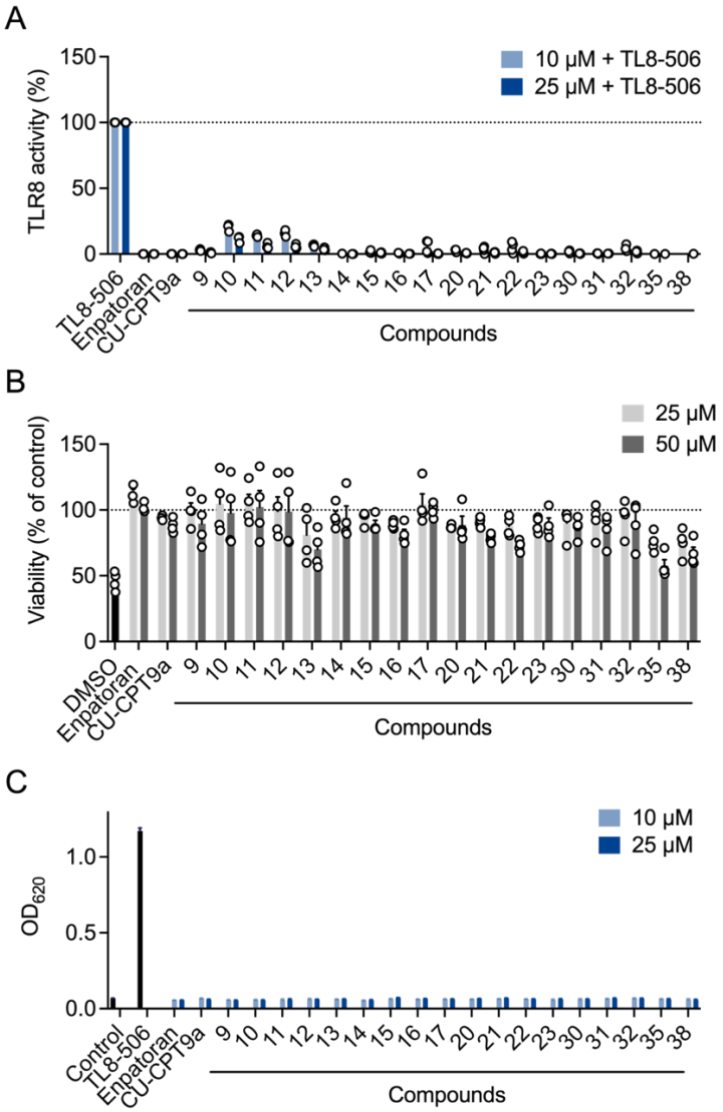

Figure S1. NF-κB activity and cell viability in hTLR8-HEK293 cells for **9**–**17**, **20–23**, **30**–**32**, **35**, **38**.
(A) HEK-Blue hTLR8 cells were preincubated with the compounds (10 µM, 25 µM) for 1 h and then stimulated with TL8-506 (0.6 µM) for 24 h. Supernatants were analyzed for TLR8-mediated NF-κB activation by SEAP reporter assay using QuantiBlue (OD_{620}) and normalized to TL8-506 alone. (B) HEK-Blue hTLR8 cells were incubated with the compounds (25, 50 µM) for 24 h. Cell viability was analyzed using the MTT assay and normalized to non-stimulated cells (vehicle control). DMSO (10 %, v/v) was used as the cytotoxic control. Mean + SEM (n=4). (C) Activation of TLR8-dependent NF-κB activity in cells. HEK-Blue hTLR8 cells were stimulated with TL8-506 (0.6 µM) or the compounds (10 µM, 25 µM) for 24 h. Supernatants were analyzed for TLR8-mediated NF-κB activation by SEAP reporter assay using QuantiBlue (OD_{620}). The TLR7/8 antagonist enpatoran and TLR8 antagonist CU-CPT9a served as control. Mean + SEM (n=3–4).

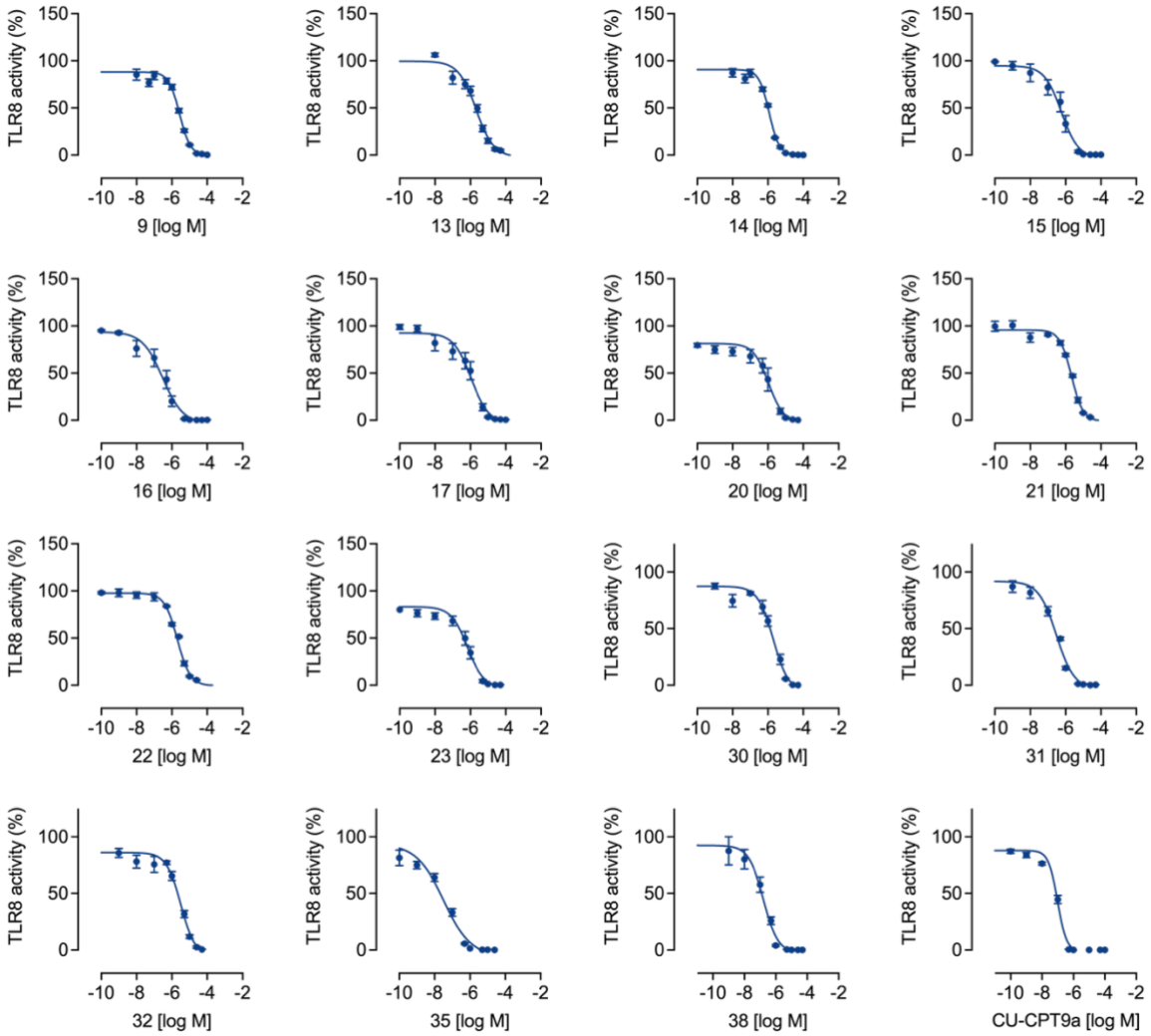

Figure S2. Concentration-response curves in hTLR8-HEK293 cells for **9**, **13**–**17**, **20**–**23**, **30**–**32**, **35**, **38** and **CuCPT9a**.
HEK-Blue hTLR8 cells were preincubated with increasing concentrations of the compounds **9**, **13**–**17**, **20**–**23**, **30**–**32**, **35**, **38** and **CuCPT9a** for 1 h, and then stimulated with TL8-506 (0.6 μM) for 24 h. Supernatants were analyzed for TLR8-mediated NF-κB activation by SEAP reporter assay using QuantiBlue (OD_{620}). For the calculation of the concentration-response curve nonlinear regression with variable slope (four parameters) was used. Mean ± SEM (n=3–4).

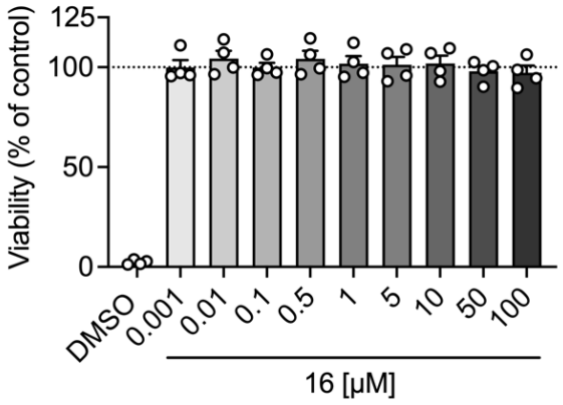

Figure S3. Cell viability of **16** in hTLR8-HEK293 cells.
HEK Blue hTLR8 cells were incubated for 24 h with increasing concentrations of **16**. Viability was analyzed using the MTT assay and normalized to non-stimulated cells (vehicle control, dashed line). DMSO (10% v/v) was used as the cytotoxic control. Mean + SEM (n=4).

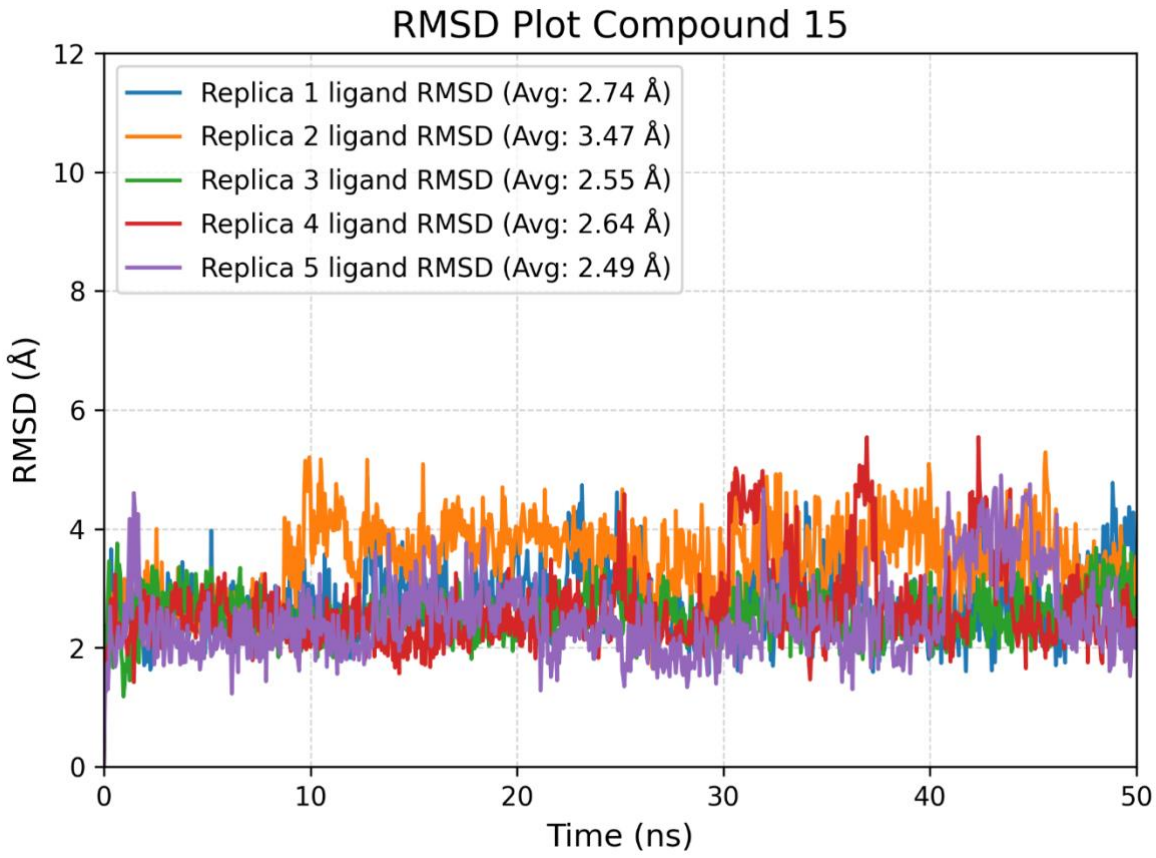

Figure S4. RMSD plot of **15** in TLR8 binding interface.
Compound **15** showed an average root mean square deviation (RMSD) of 2.78 Å during the simulation, indicating a stable binding mode of **15** in the binding pocket of the TLR8 homodimer.

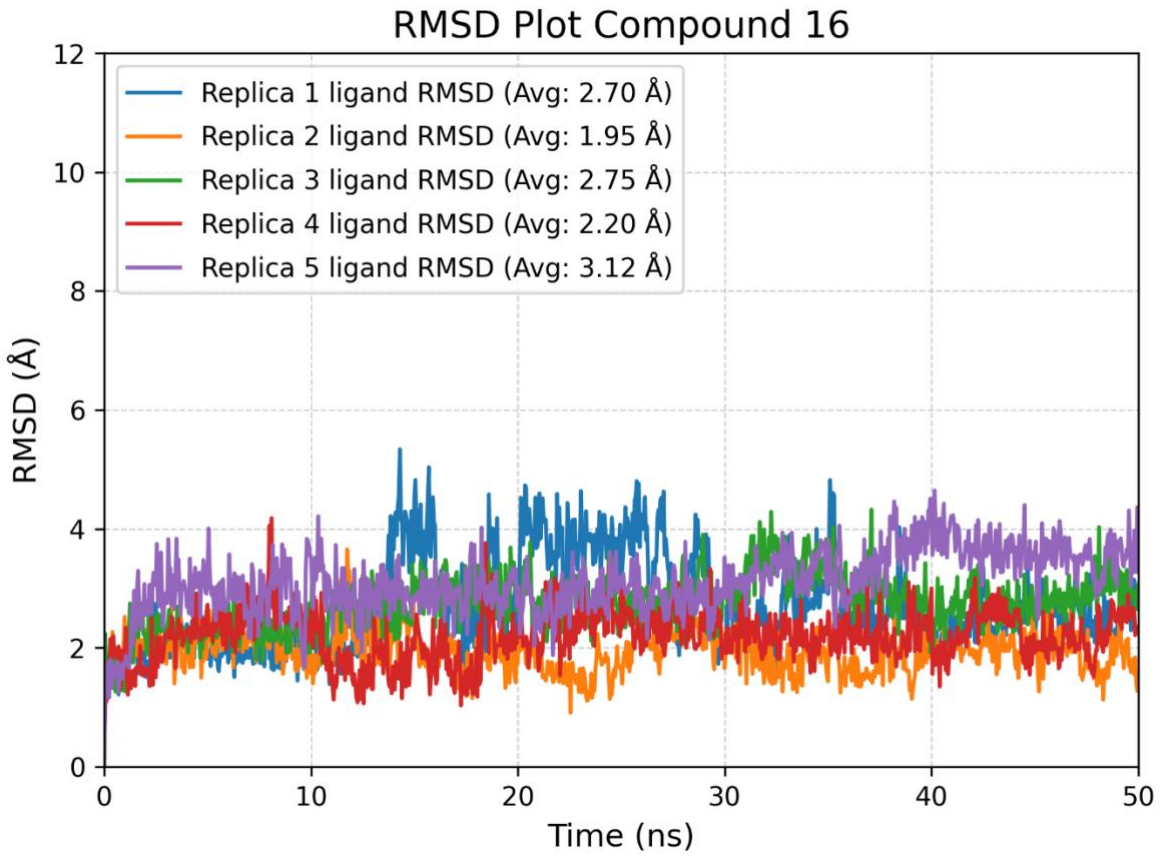

Figure S5. RMSD plot of **16** in TLR8 binding interface.
Compound **16** showed an average root mean square deviation (RMSD) of 2.54 Å during the simulation, indicating a stable binding mode of **16** in the binding pocket of the TLR8 homodimer.

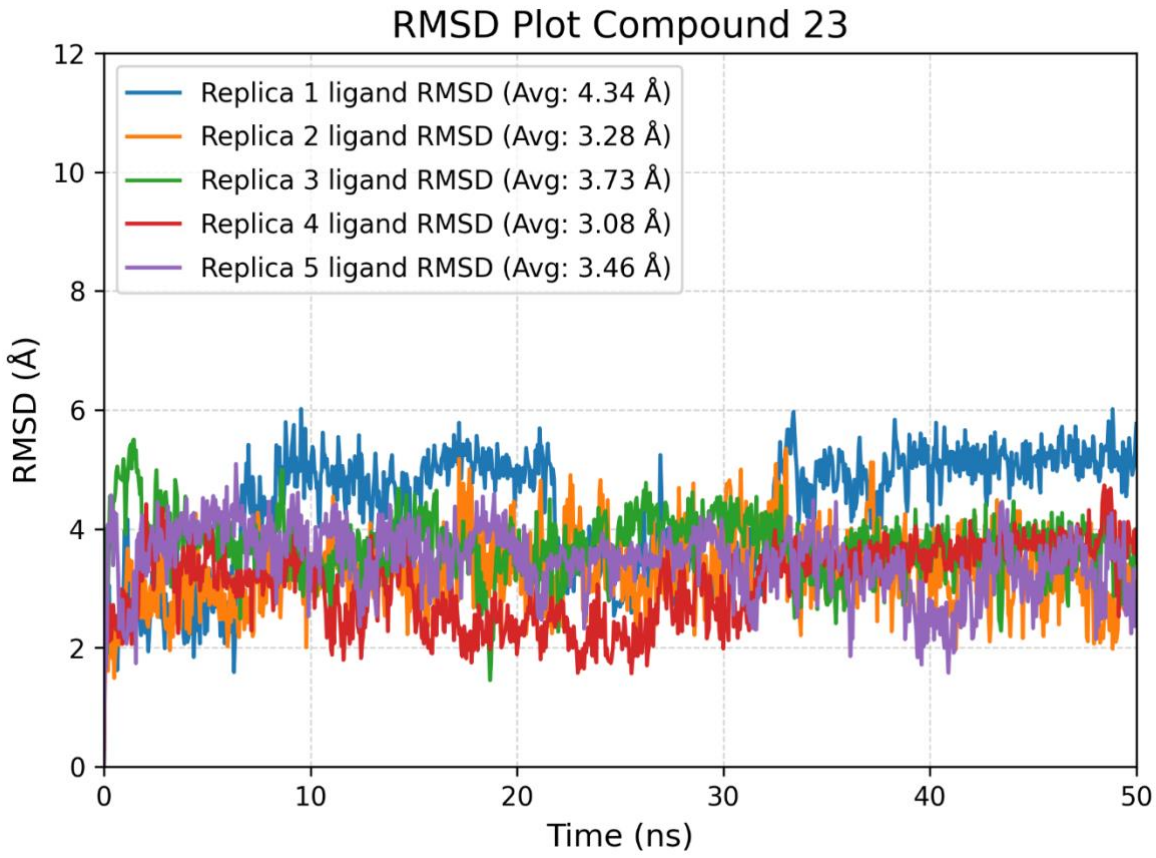

Figure S6. RMSD plot of **23** in TLR8 binding interface.
Compound **23** showed an average root mean square deviation (RMSD) of 3.58 Å during the simulation, indicating a stable binding mode of **23** in the binding pocket of the TLR8 homodimer.

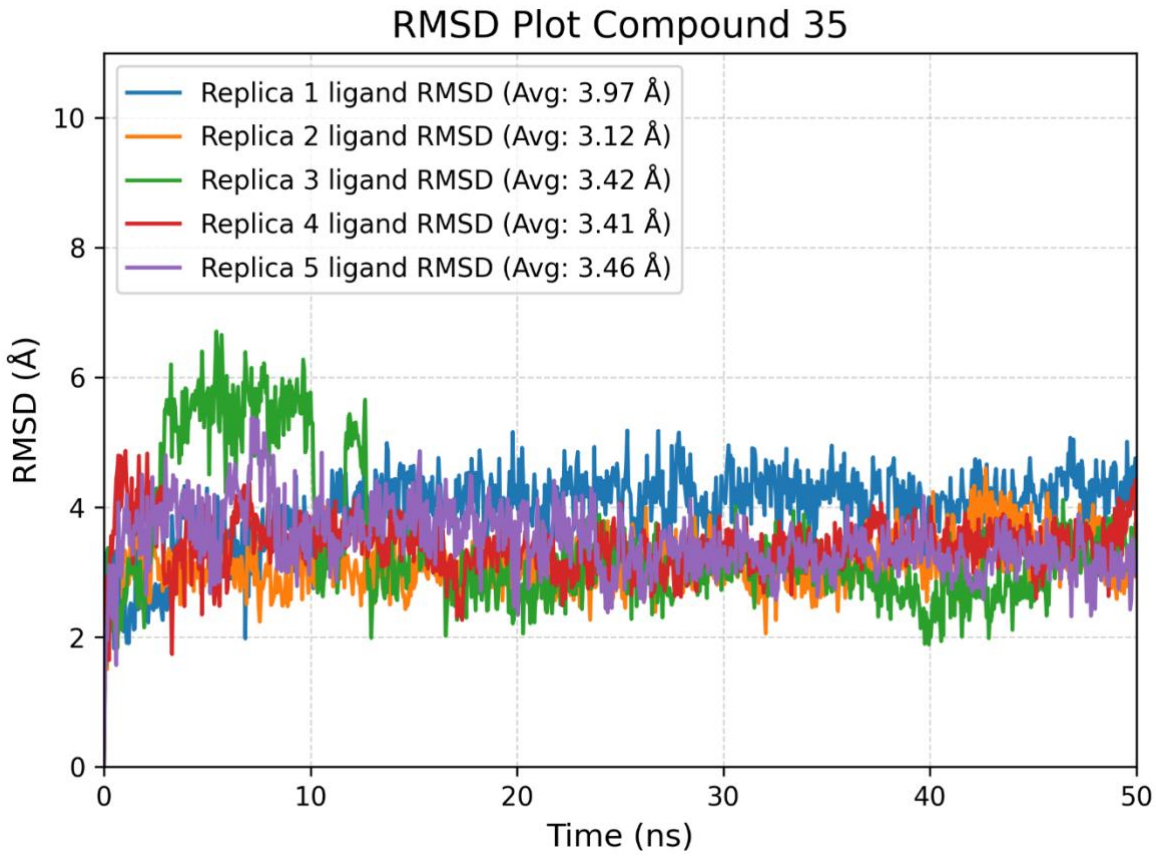

Figure S7. RMSD plot of **35** in TLR8 binding interface.
Compound **35** showed an average root mean square deviation (RMSD) of 3.48 Å during the simulation, indicating a stable binding mode of **35** in the binding pocket of the TLR8 homodimer.

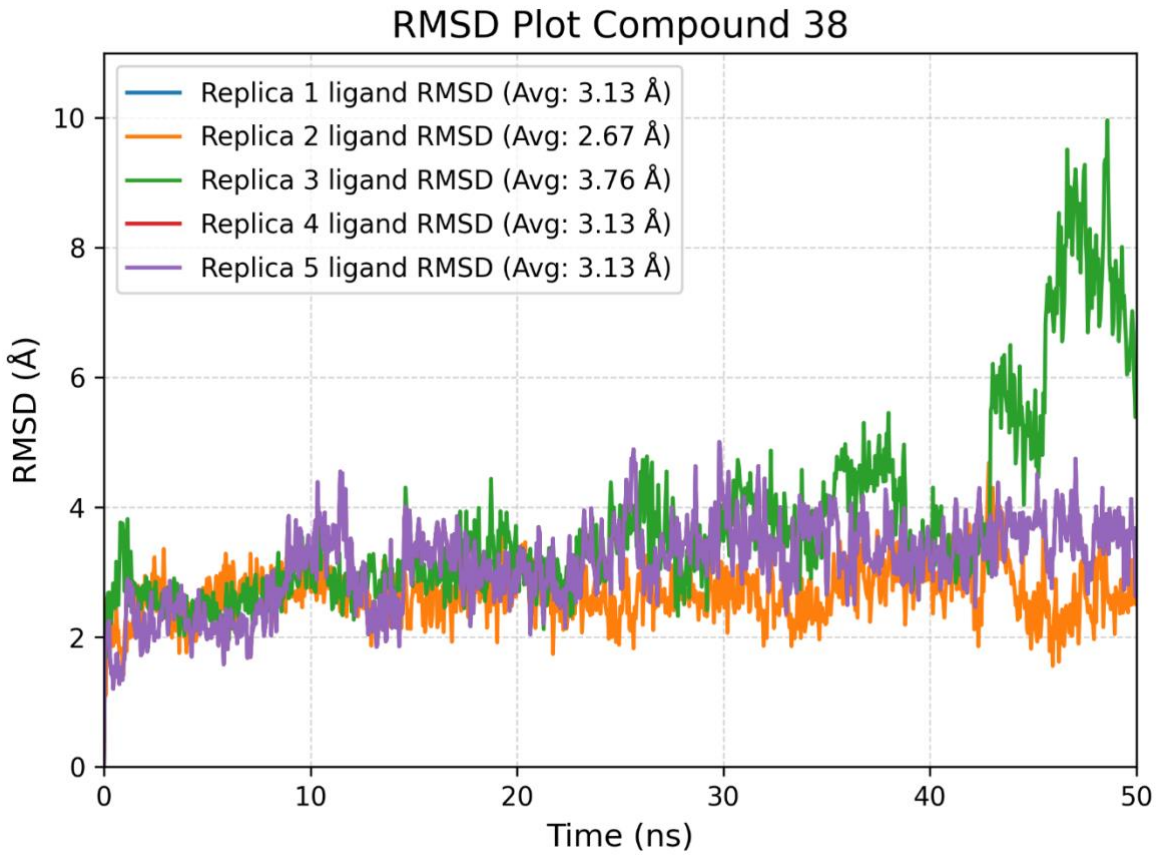

Figure S8. RMSD plot of **38** in TLR8 binding interface.
Compound **38** showed an average root mean square deviation (RMSD) of 3.16 Å during the simulation, indicating a stable binding mode of **38** in the binding pocket of the TLR8 homodimer. During the simulation of Replica 3 an increase in the RMSD can be noticed, with the average RMSD of replica 3 consisting of 3.76 Å. This increase is related to the movement of the piperazine rest of **38** to maintain the positive ionizable interaction.

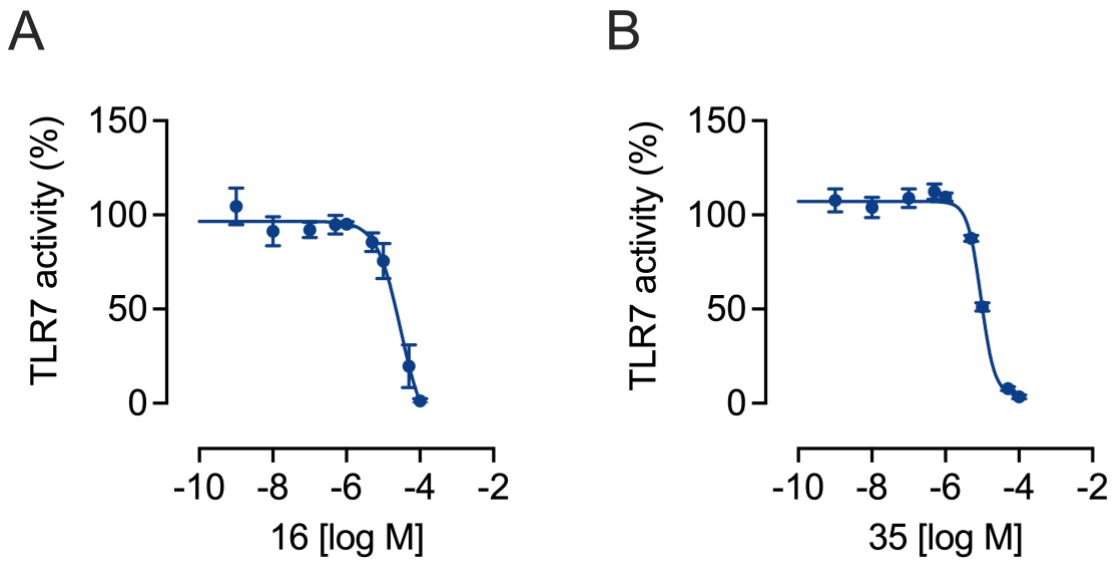

Figure S9. Concentration-response curve in hTLR7-HEK293 cells for **16** and **35**.
HEK-Blue hTLR7 cells were preincubated with increasing concentrations of compound **16** (A) or **35** (B) for 1 h and then stimulated with CL307 (1.7 μM) for 24 h. Supernatants were analyzed for TLR7-mediated NF-κB activation by SEAP reporter assay using QuantiBlue (OD_{620}). For the calculation of the concentration-response curve nonlinear regression with variable slope (four parameters) was used. Mean ± SEM (n=4).

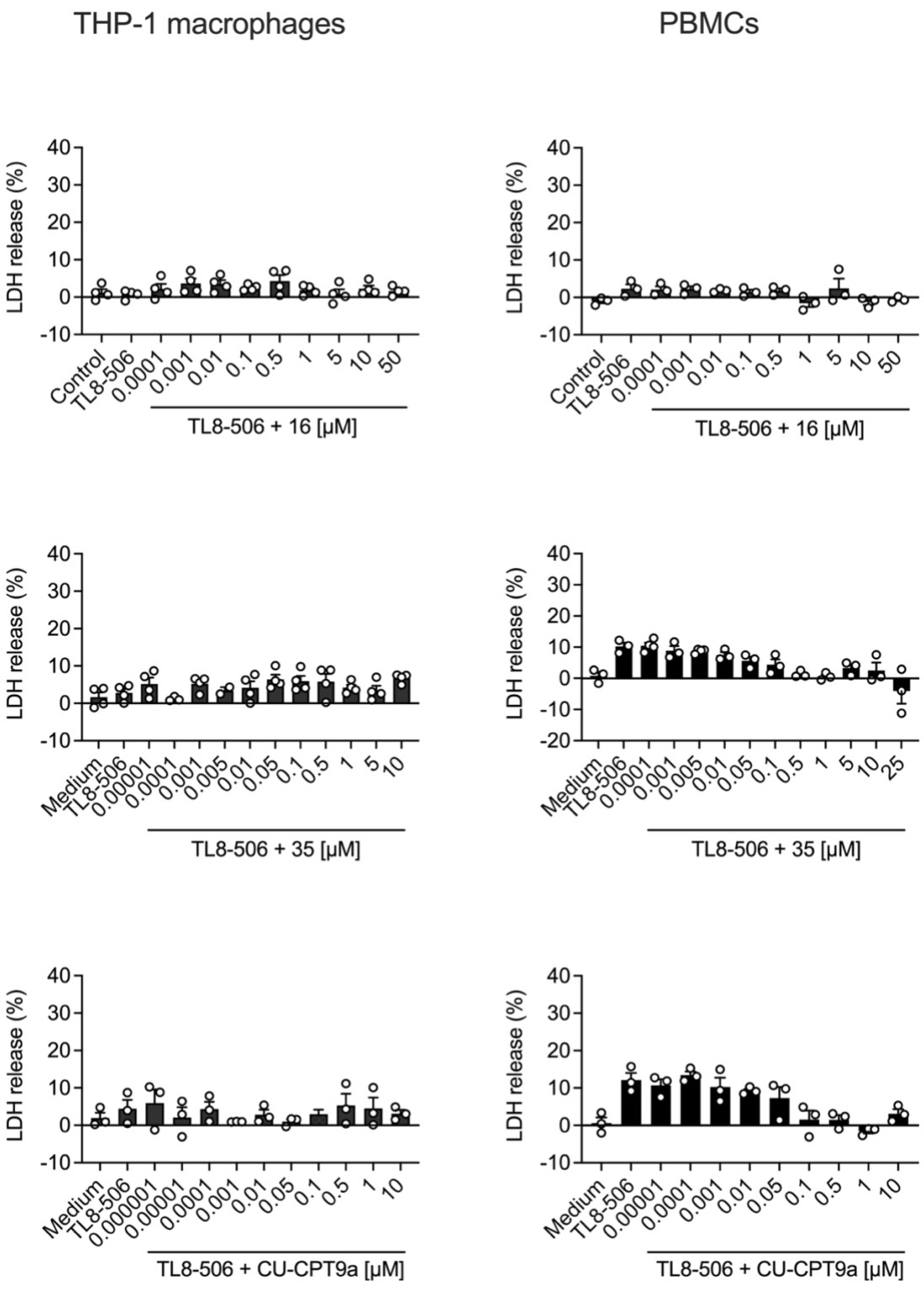

Figure S10. Cell viability of **16**, **35** and **CU-CPT9a** in PBMCs and THP-1 macrophages. THP-1 macrophages or PBMCs were incubated with 0.6 µM TL8-506 or increasing concentrations of compound **16**, **35** and **CU-CPT9a** for 4 h. LDH release was determined in cell culture supernatants. Results are shown as percentage of the maximum LDH release. Mean + SEM (n=3–4).

3. Supplementary Tables

Table S1. Molecular docking scores of compounds **9–17** and **20–23**.

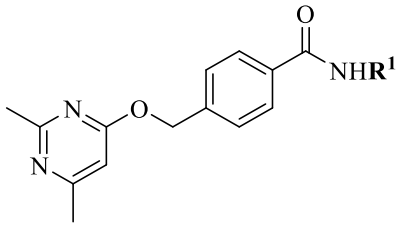

Compound	Amine (R^1NH_2)	ChemPLP Fitness Score
9	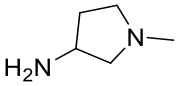	74.32
10	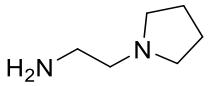	75.58
11	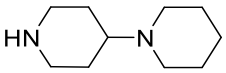	74.68
12	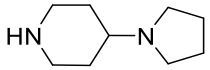	74.45
13	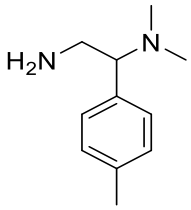	86.06
14	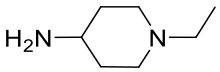	76.26
15	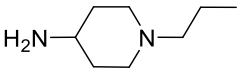	75.62
16	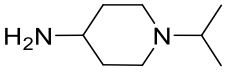	73.42
17	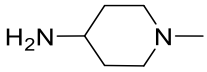	75.94
20	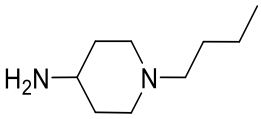	70.65
21	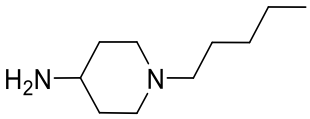	76.17
22	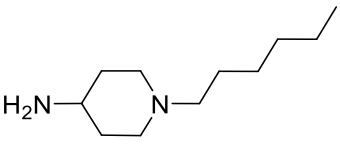	79.56
23	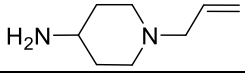	80.00

Table S2. Interaction frequencies of **15** with TLR8 homodimer during MD simulation.

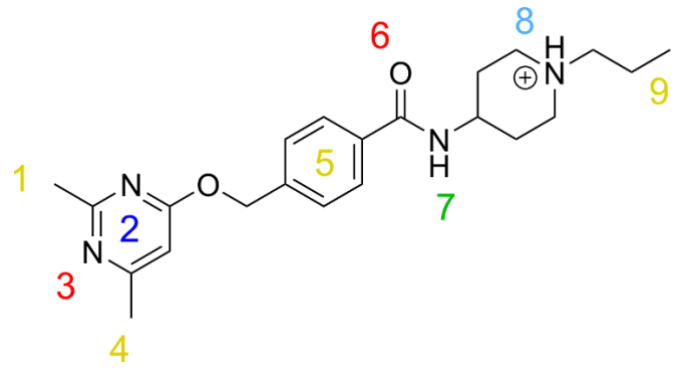

Ligand Moiety	**Interaction type**	**Frequency**
Methyl 1	Hydrophobic	93.8%
Pyrimidine 2	Hydrophobic	39.7%
Pyrimidine 2	Aromatic	5.9%
Pyrimidine nitrogen 3	Hydrogen bond acceptor	99.0%
Methyl 4	Hydrophobic	73.0%
Phenyl 5	Hydrophobic	96.8%
Carbamide oxygen 6	Hydrogen bond acceptor	22.8%
Carbamide amide 7	Hydrogen bond donor	3.1%
Amine 8	Positive ionizable	97.9%
Propyl 9	Hydrophobic	46.0%

Table S3. Interaction frequencies of **16** with TLR8 homodimer during MD simulation.

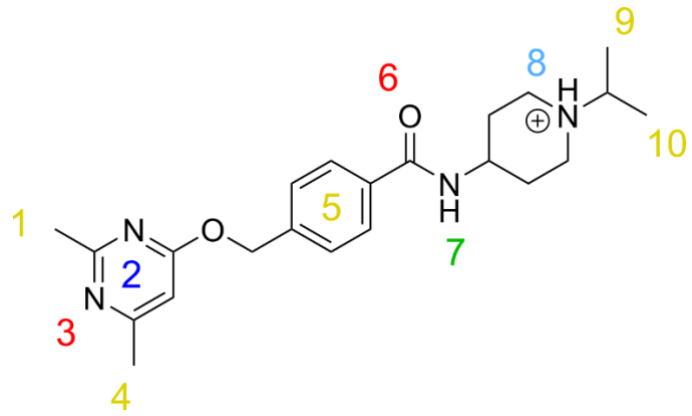

Ligand Moiety	**Interaction type**	**Frequency**
Methyl 1	Hydrophobic	91.8%
Pyrimidine 2	Hydrophobic	43.9%
Pyrimidine 2	Aromatic	3.3%
Pyrimidine nitrogen 3	Hydrogen bond acceptor	98.9%
Methyl 4	Hydrophobic	74.4%
Phenyl 5	Hydrophobic	97.8%
Carbamide oxygen 6	Hydrogen bond acceptor	29.6%
Carbamide amide 7	Hydrogen bond donor	8.6%
Amine 8	Positive ionizable	88.8%
Methyl 9	Hydrophobic	34.8%
Methyl 10	Hydrophobic	23.1%

Table S4. Interaction frequencies of **23** with TLR8 homodimer during MD simulation.

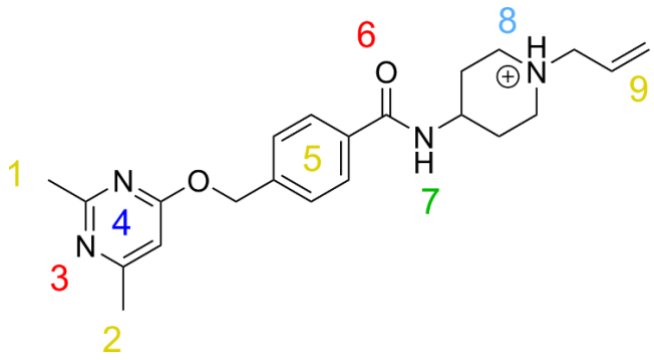

Ligand Moiety	**Interaction type**	**Frequency**
Methyl 1	Hydrophobic	93.3%
Pyrimidine 2	Hydrophobic	32.9%
Pyrimidine 2	Aromatic	2.8%
Pyrimidine nitrogen 3	Hydrogen bond acceptor	98.4%
Methyl 4	Hydrophobic	76.0%
Phenyl 5	Hydrophobic	98.3%
Carbamide oxygen 6	Hydrogen bond acceptor	28.1 %
Carbamide amide 7	Hydrogen bond donor	3.7%
Amine 8	Positive ionizable	10.7%
Ethyl 9	Hydrophobic	38.3%

Table S5. Interaction frequencies of **35** with TLR8 homodimer during MD simulation.

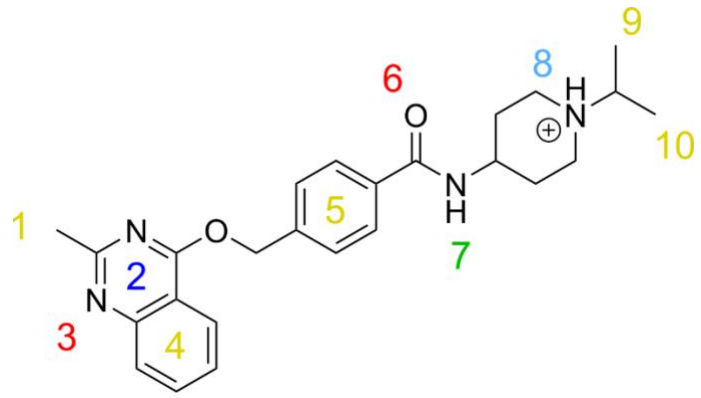

Ligand Moiety	**Interaction type**	**Frequency**
Methyl 1	Hydrophobic	95.7%
Pyrimidine 2	Hydrophobic	52.4%
Pyrimidine 2	Aromatic	65.9%
Pyrimidine nitrogen 3	Hydrogen bond acceptor	94.7%
Phenyl 4	Hydrophobic	98.1%
Phenyl 5	Hydrophobic	97.6%
Carbamide oxygen 6	Hydrogen bond acceptor	16.0%
Carbamide amide 7	Hydrogen bond donor	0.3%
Amine 8	Positive ionizable	91.6%
Methyl 9	Hydrophobic	14.1%
Methyl 10	Hydrophobic	27.5%

Table S6. Interaction frequencies of **38** with TLR8 homodimer during MD simulation.

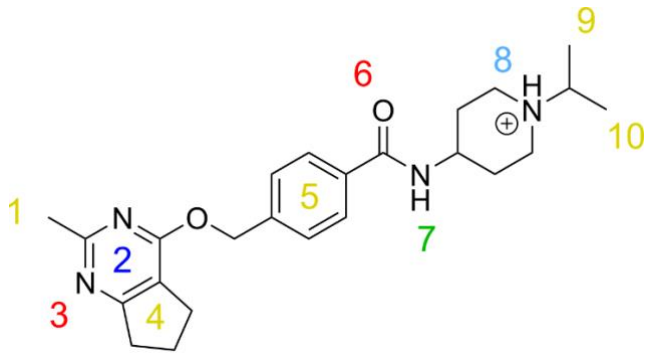

Ligand Moiety	**Interaction type**	**Frequency**
Methyl 1	Hydrophobic	93.7%
Pyrimidine 2	Hydrophobic	55.5%
Pyrimidine 2	Aromatic	34.9%
Pyrimidine nitrogen 3	Hydrogen bond acceptor	94.8%
Cyclopentan 4	Hydrophobic	92.9%
Phenyl 5	Hydrophobic	97.6%
Carbamide oxygen 6	Hydrogen bond acceptor	20.4%
Carbamide amide 7	Hydrogen bond donor	0.9%
Amine 8	Positive ionizable	91.0%
Methyl 9	Hydrophobic	16.3%
Methyl 10	Hydrophobic	23.3%

Danksagung

Die vorliegende Arbeit wäre ohne die Unterstützung zahlreicher Menschen nicht möglich gewesen. Ihnen allen möchte ich an dieser Stelle meinen aufrichtigen Dank aussprechen.

Mein besonderer Dank gilt zuallererst Prof. Dr. Günther Weindl für seine außergewöhnliche Betreuung während der gesamten Promotionsphase. Deine ständige Verfügbarkeit, fachliche Expertise und motivierenden Gespräche haben dazu beigetragen, dass diese Arbeit trotz aller Herausforderungen erfolgreich abgeschlossen werden konnte. Dein mir entgegengebrachtes Vertrauen hat nicht nur die Qualität dieser Dissertation gestärkt, sondern auch meine persönliche Entwicklung als Wissenschaftler nachhaltig geprägt.

Herrn Prof. Dr. Gerhard Wolber danke ich herzlich für die enge Zusammenarbeit an den zentralen Publikationen dieser Arbeit sowie für die Übernahme der Zweitkorrektur. Seine Erfahrung und seine inspirierende Art in unseren gemeinsamen Projekten haben die wissenschaftliche Aussagekraft der Untersuchungen entscheidend vorangebracht und wertvolle neue Perspektiven eröffnet.

Der Prüfungskommission gilt mein aufrichtiger Dank für die kritische Begutachtung dieser Arbeit. Ein herzlicher Gruß gilt dabei Herrn Prof. Dr. Bartholomaeus, dessen exzellente Lehre ich bereits während meines Biologiestudiums kennenlernen durfte. Dass Sie trotz Ihres wohlverdienten Ruhestands an meiner Disputation teilgenommen haben, bedeutet mir viel.

Ein besonderer Dank gilt Valerij Talagayev, auf den ich mich im Zuge unserer gemeinsamen Projekte jederzeit blind verlassen konnte. Deine beeindruckende Arbeitsweise und respektvolle Art haben die Kooperation zu einem Vergnügen gemacht und unsere gemeinsamen Erfolge erst ermöglicht.

Jonas Engelhardt und Judith Bockstiegel danke ich herzlich für ihre hervorragende Unterstützung in meiner Anfangszeit. Ihr umfassendes Wissen, ihre praktischen Tipps und euer moralischer Beistand haben mir diese Zeit erheblich erleichtert. Mit dir, Jonas, ist gleichzeitig eine tiefe Freundschaft entstanden. Als Patenonkel deines Sohnes Leo verbindet uns nun etwas, das weit über die Wissenschaft und Promotionszeit hinaus Bestand hat.

Weiterhin hervorheben möchte ich Felicitas Lauber, deren außergewöhnliches Organisationstalent unsere großartigen Arbeitsgruppenausflüge und insbesondere die unvergessliche Karnevalsfeier 2025 erst möglich gemacht hat. Solche Momente haben den Arbeitsalltag bereichert und für den nötigen Ausgleich gesorgt.

Allen Bürokolleginnen und -kollegen danke ich für ihre ständige Unterstützung, ihren Rat und ihre tatkräftige Hilfe in allen Phasen, besonders in den stressigen Momenten. Das herzliche, humorvolle Miteinander und die gegenseitige Hilfsbereitschaft in diesem besonderen Arbeitskreis haben die tägliche Arbeit enorm bereichert.

Mein tiefster Dank gilt schließlich meiner Familie und meinen Freunden für ihre unerschütterliche Geduld, emotionale Stütze und den unermüdlichen Zuspruch. Ihr habt mir in schwierigen Momenten den Rücken gestärkt und immer an mich geglaubt. Mit eurer Liebe, eurem Verständnis und eurer Ermutigung habe ich das Ziel nie aus den Augen verloren und so war dieser Weg nicht nur machbar, sondern hat mir auch Freude bereitet.